CALIX[4]PYRROLE CAVITANDS FOR SUPRAMOLECULAR SENSING AND CATALYSIS

Andrés Felipe Sierra Ramos

UNIVERSITAT ROVIRA i VIRGILI

Calix[4]pyrrole cavitands for supramolecular sensing and catalysis

Andrés Felipe Sierra Ramos

DOCTORAL THESIS
2022

UNIVERSITAT ROVIRA I VIRGILI
CALIX[4]PYRROLE CAVITANDS FOR SUPRAMOLECULAR SENSING AND CATALYSIS
Andrés Felipe Sierra Ramos

UNIVERSITAT ROVIRA I VIRGILI
CALIX[4]PYRROLE CAVITANDS FOR SUPRAMOLECULAR SENSING AND CATALYSIS
Andrés Felipe Sierra Ramos

DOCTORAL THESIS

Andrés Felipe Sierra Ramos

CALIX[4]PYRROLE CAVITANDS FOR SUPRAMOLECULAR SENSING AND CATALYSIS

Supervised by Prof. Pablo Ballester Balaguer

UNIVERSITAT
ROVIRA i VIRGILI

Tarragona

2022

UNIVERSITAT ROVIRA I VIRGILI
CALIX[4]PYRROLE CAVITANDS FOR SUPRAMOLECULAR SENSING AND CATALYSIS
Andrés Felipe Sierra Ramos

ICIQ
Institut Català d'Investigació Química

Av. Països Catalans, 16
43007 Tarragona, Spain
Tel. (+34) 977 920 200
email: iciq@iciq.es

UNIVERSITAT ROVIRA i VIRGILI
Dept. de Química Analítica i Química Orgànica

Carrer de Marcel·lí Domingo, 1
43007 Tarragona, Spain
Tel. (+34) 977 55 97 69
email: sdn4@urv.cat

I STATE that the present study, entitled "Calix[4]pyrrole cavitands for supramolecular sensing and catalysis", presented by Andrés Felipe Sierra Ramos for the award of the degree of Doctor, has been carried out under my supervision at the Institute of Chemical Research of Catalonia (ICIQ).

Tarragona, January 2022

Doctoral Thesis Supervisor

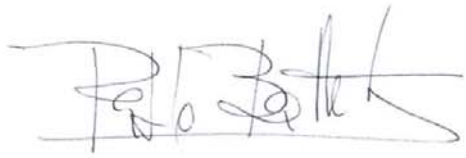

Prof. Pablo Ballester Balaguer

UNIVERSITAT ROVIRA I VIRGILI
CALIX[4]PYRROLE CAVITANDS FOR SUPRAMOLECULAR SENSING AND CATALYSIS
Andrés Felipe Sierra Ramos

Acknowledgements

Los resultados presentados en esta tesis son la consecuencia de las contribuciones realizadas por un gran número de personas. Por esta razón, quiero dedicar estas líneas a todos aquellos que gracias a dichas contribuciones han hecho posible la culminación de esta maravillosa etapa.

Agradezco en primer lugar al profesor **Pau Ballester** por haberme dado la oportunidad de trabajar en su grupo de investigación. Profe Pau, muchas gracias por todas tus enseñanzas académicas y personales. Tu enorme conocimiento e inigualable dedicación y compromiso serán siempre una referencia a seguir. Gracias también por tu paciencia y por estar siempre disponible para atendernos sin importar que tan ocupado o cansado estés.

Quiero realizar un reconocimiento muy especial a **Gemma Aragay**. Gemma, gracias por toda tu ayuda, particularmente por las correcciones de los reportes, introducciones, cálculos, ajustes de titulaciones, capítulos de tesis y demás. Quisiera ser al menos la mitad de productivo que tú.

Me gustaría también agradecer a todos los miembros del PB4 por los momentos compartidos dentro y fuera del laboratorio. **Ricardo Molina**, **Dragoş Dăbuleanu**, **Andrea Rivoli**, **Chiara Mirabella**, **Pedro Ferreira**, **Lluis Martínez**, **Guillem Peñuelas**, **Giulia Moncelsi**, **Yifan Li**, **Qingqing Sun, Hayley Kay Frost**, **Sven van Vliet**, **Anna Brzechwa**, **Alicia Geburzi** y **Luis Escobar**. A todos ustedes, gracias por tanto y perdón por tan poco.

Extiendo mis agradecimientos a **Beatriz Martin**, por todo su apoyo y amabilidad para ayudarnos con todo tipo de documentación.

I would like also thanks to professors **Uwe Pischel**, **Pascal Blondeau** and **Enrico Dalcanale** for the productive collaborations.

Mis más sinceros agradecimientos al Institutut Català d´Investigació Química (**ICIQ**) y a todo su personal. Especialmente quiero agradecer a las unidades de apoyo. **Gabriel Gonzales**, **Israel Macho** y **Kerman Gómez** por todo su soporte en la medición y análisis de experimentos RMN. **Simona Curreli**, **María José Hueso**, **Meritxell Diaz** y **Marta Serrano** por el análisis y separación de muestras por HPLC y la capacitación recibida en el equipo de GC-FID. **Noemi Cabello** por los resultados de masas exactas de nuestros compuestos. **Eduardo Escudero**, **Jordi Benet** y **Marta**

Martinez por los análisis y consejos recibidos en la difracción de rayos-x de nuestros receptores y complejos supramoleculares.

Gracias a todo el personal de logística y limpieza quienes cumplen una labor determinante para el correcto funcionamiento del instituto. Muchas gracias a **Xavi Asensio** por su increíble amabilidad y disponibilidad al momento de recibirnos para la reparación del material de vidrio.

Finalmente, quiero agradecer a las personas externas al instituto que han sido también parte esencial de este proyecto. A mi familia por ser el motor de mi vida, especialmente a mi madre **Rosa Ramos**, a quien le debo todo y le profeso el más puro e infinito amor. A **Emilio**, **JuanDi** y **AnaLu**, mis hermosos sobrinos quienes llenan de alegría mis días. A mis hermanos **Rafa** e **Ivonne** por tanto amor y apoyo incondicional. A mis amigos **Jorge**, **Camila**, **Raiana**, **Santi**, **Richard**, **Sandrita**, **Aleix**, **Karen**, **Reyda** y **Ralu** por los planes y viajes compartidos. A **Jimmy** y **Sarita** por hacer del apartamento y de Tarragona un lugar aún más agradable. A todos mis amigos en Colombia, particularmente a **Luisa María**, **Francis**, **Tatiana**, **Heider** y **Manuel Gonzalo**, con quienes conservo intacta la amistad a pesar de la distancia.

A mi familia,

UNIVERSITAT ROVIRA I VIRGILI
CALIX[4]PYRROLE CAVITANDS FOR SUPRAMOLECULAR SENSING AND CATALYSIS
Andrés Felipe Sierra Ramos

Table of Contents

Chapter 1

Introduction

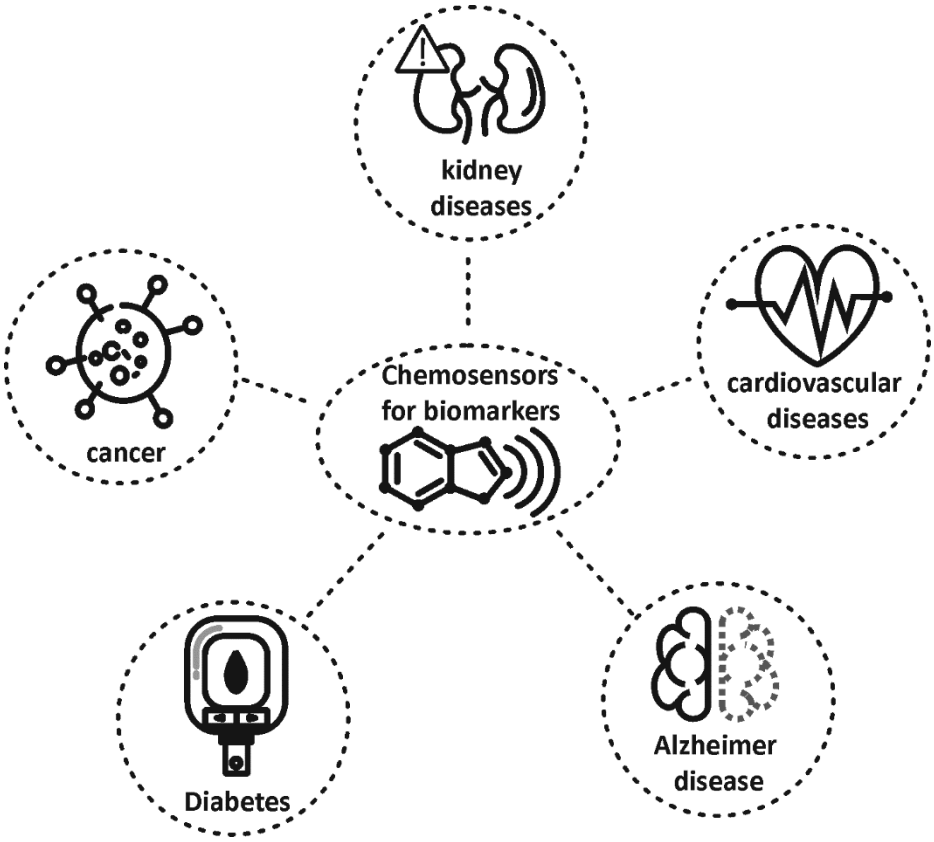

UNIVERSITAT ROVIRA I VIRGILI
CALIX[4]PYRROLE CAVITANDS FOR SUPRAMOLECULAR SENSING AND CATALYSIS
Andrés Felipe Sierra Ramos

1.1. Calix[4]pyrrole scaffolds

Calix[4]pyrroles (C4Ps) are synthetic tetrapyrrolic macrocyclic structures connected by sp^3 carbon atoms (*meso* carbons).[1] These compounds are conformationally flexible and non-planar. The origin of C4Ps dates back to 1886 when Baeyer reported the HCl catalyzed cyclo-condensation reaction of pyrrole and acetone (OMC4P, *Figure 1.1*).[2] The presence of two meso-substituents (alkyl or aryl) confers these compounds with stability to further oxidation yielding the well-known porphyrin scaffolds.

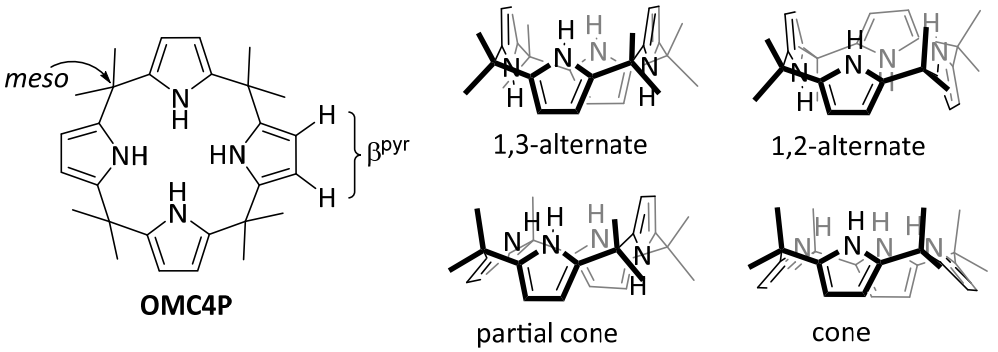

Figure 1.1 Line-drawing structures of meso-octamethylcalix[4]pyrrole (OMC4P) and its four different conformers.

More than a century later of Baeyer´s work, Sessler et al. described for the first time the use of C4Ps in the field of supramolecular chemistry as effective receptors for anions.[3] In fact, the name of "calixpyrrole" was coined by Sessler and co-workers due to the analogy existing between the conformations displayed by these compounds and those of the calix[4]arene counterparts.[4]

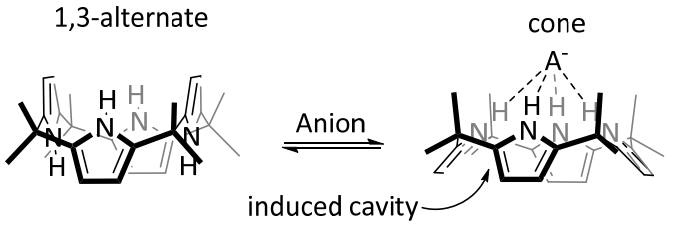

Figure 1.2 Line-drawing structures of free (1,3-alternate conformer) and bound (cone conformer) OMC4 in the equilibrium producing an anionic complex. The structures of the receptor highlight the conformational change experienced by the C4P core upon anion binding.

C4Ps are conformationally flexible and can exist in four conformations (cone, partial cone, and 1,3- or 1,2-alternate *Figure 1.1*). X-ray diffraction studies and quantum chemical calculations, demonstrated that the 1,3-alternate conformation is energetically favorable both in the solid state and in non-polar aprotic solvents.[1,5] However, the complexation of an anion to the C4P core induces a change in the macrocycle's conformation from 1,3-alternate to the cone. The bound anion establishes four convergent hydrogen bonding interactions with the pyrrole NHs stabilizing the cone. The formed 1:1 anionic complex displays an electron rich and shallow aromatic cavity defined by the pyrrole rings of the C4P (*Figure 1.2*), that is opposed to the bound anion. This cavity is suitable for the inclusion of electropositive species.[6,7]

The binding properties of the C4Ps towards anions,[8,9,10] as well as neutral[11,12] substrates have been extensively explored. In most cases, hydrogen bonding interactions between the pyrrole NHs of the receptor and an electron rich atom of the substrates are present in the formed complexes. In recent years, C4P scaffolds were used as components of molecular cages,[13,14,15,16] containers,[16,17] switches,[18,19] carriers,[20,21,22] potentiometric[23,24] and optical[25,26,27] sensors, as well as supramolecular catalysts[28,29]. Among these applications, we draw our attention to the use of C4P scaffolds in the development of optical molecular sensors. The main reason being that a wide range of chromophoric and fluorophoric units can be incorporated to the C4P receptor scaffolds by means of simple synthetic transformations. In this chapter, we will review recent literature for relevant examples of the detection of molecular biomarkers using optical sensors operating through Indicator Displacement Assays (IDAs).

1.2. Sensing approaches: Supramolecular fluorescent sensors and Indicator Displacement Assays (IDAs).

In general terms, a "sensor" is a device able to detect events or changes (inputs or stimulus) from its environment and translate them to a resulting impulse (output). In the macromolecular world, we are surrounded by plenty of them, in our homes, offices, cars, etc. We can find sensors in our daily life performing simple tasks. For example, turning on the lights, detecting smoke or fire, adjusting the room temperature, detecting our presence, making our coffee and many others. Sensors can also be useful to control patient´s health status, in particular, body temperature, pulse rate, respiration rate and blood pressure are the most common vital signs monitored by using medical sensors.

In the molecular world, we can similarly find molecular sensors, also called chemical sensors or chemosensors. A chemical sensor, defined by the International Union of Pure and Applied Chemistry (IUPAC), "is a device that transforms chemical information, ranging from the concentration of a specific sample component to total composition analysis, into an analytically useful signal". The chemical information may come from a chemical reaction of the analyte or from a physical property of the system investigated.[30]

Design of a chemosensor consist of four main components as shown; a **chemical receptor** able to selectively recognize the substrate (analyte of interest), a **signaling unit** which transduces the binding event into a measurable physical or chemical change, a **spacer** connecting the receptor unit with the signaling unit, and finally a **method** of measuring the change and converting it into useful information. The selection of the receptor component is a pivotal step in developing an effective chemosensor. Receptors with high sensitivity and selectivity towards a specific substrate are desirable. In addition, a transduction mechanism exclusively activated by the molecular recognition event is mandatory.[31]

Semiochemistry refers to the area of supramolecular chemistry concerning with the development of signaling and sensing using molecules and devices. The term derives from "semiotics", which is the study of signs and symbols, their use and interpretation. The natural world makes use of molecular recognition events for the signaling and sensing of a wide variety of compounds. For example, by establishing a supramolecular complex between a chemical messenger molecule i.e. a hormone or pheromone and a protein-based receptor.[32]

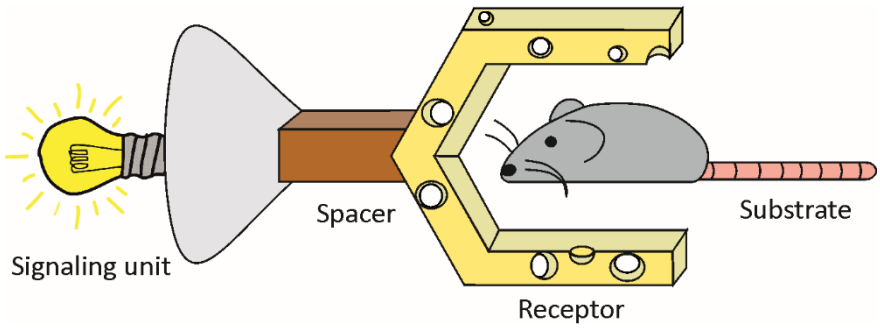

Figure 1.3 Cartoon representation of a chemical sensor. Adapted from ref. 32

The basic units of a molecular sensor are showed in *Figure 1.3*. During the sensing event, a molecular recognition process between the substrate (guest or analyte) and

the receptor is stablished. This process occurs *via* the establishment of intermolecular forces. The recognition process has to be energetically more favorable for the target molecule than for other potential guests (interferents). The selectivity of the binding event includes size, shape and functional complementarity between the host and the guest. However, the existence of the binding event is not always enough to modify the properties of the complex with respect to those of the free sensor. The receptor unit and the signaling unit must experience some sort of communication. In short, when the receptor binds the substrate the event has to be transduced to the properties of the signaling unit.[32] According to the changes experienced by the signaling unit, molecular sensors can be classified as: 1) optical (change in the absorbance, reflectance, fluorescence) or 2) electrochemical (changes in electrical potentials, current).

The combination of a binding site with a fluorophore, as signaling unit, and the existence of a mechanism communicating both components produces a "supramolecular fluorescent sensor".[33] The development of a supramolecular fluorescent sensor involves the understanding of the communication mechanism. The modulation of the optical response can occur by means of one or more mechanisms. These include photoinduced electron transfer (PET),[34] fluorescence resonance energy transfer (FRET),[35] energy transfer (ET),[36] and aggregation-enhanced emission (AEE)[37] among others.[33]

In the present thesis, we will use the term "binding-based sensing (BBS)" suggested by Chang et al. to refer to the sensing methodology involving the covalent attachment of the binding-site with the signaling unit.[38]

Many examples of binding-based fluorescent sensors can be found in the literature.[39,40,41,42] However, the adequate functionalization of synthetic receptors with fluorophores, as signaling units, still represents a synthetic challenge. Moreover, in some of the synthesized constructs the binging event produces minimal changes in the optical properties of the signaling unit.[43] An elegant strategy to overcome this limitation relies on the use of Indicator Displacement Assays (IDAs) The components of an IDA are illustrated in *Figure 1.4*.

The methodology of the IDAs, involves an indicator (guest with optical properties) that is reversibly bound to the receptor (receptor-indicator complex). In the presence of the target (analyte), the indicator is displaced from the binding site of the host and released to the bulk solution. The change in the optical properties of

the bound and free indicator (e.g. quenching of the fluorescence upon binding) is used for the signaling (detection and quantification) of the target molecule in solution.

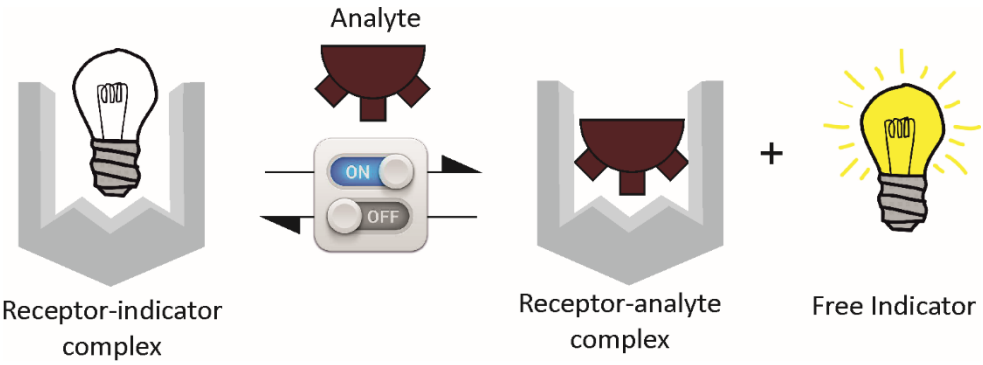

Figure 1.4 Cartoon representation of "turn-on" Indicator Displacement Assay (IDA) as an alternative approach to BBS for molecular sensing.

Therefore, the use of IDAs does not demand the covalent connection between the receptor and signaling units. This connection is replaced by the selection of a suitable indicator able to reversibly bind the receptor (e.g. H-bonding, π-π stacking, hydrophobic interaction) or forming dynamically covalent bonds[44]. In 2011 Nau, Pischel and Dsouza, [45] published an interesting review describing a series of fluorescent dyes and various water-soluble receptors, as well as, their multiple combinations for the development of IDAs.

One of the first indicator displacement assays was introduced by Inouye et al. for the fluorescence sensing (PET mechanism) of acetylcholine in protic media (*Figure 1.5a*). The emission of a pyrene-modified *N*-alkylpyridinium cation (**a**)[46] is quenched upon complex formation with the tetra-anionic calix[4]resorcinarene (**1**)[47]. The addition of acetylcholine, causes the displacement of the indicator and the competitive formation of a complex with the target analyte. The displacement process induces the recovery of the indicator emission ("turn on" sensing).[48] The group of Anslyn popularized this sensing methodology and coined the term "indicator displacement assay". For example, they used IDAs for fluorescent sensing of citrate. The used ensemble was based on 5-carboxyfluorescein (**b**, a fluorescent probe) and the tri-guanidinium receptor (**2**) (*Figure 1.5b*).[49]

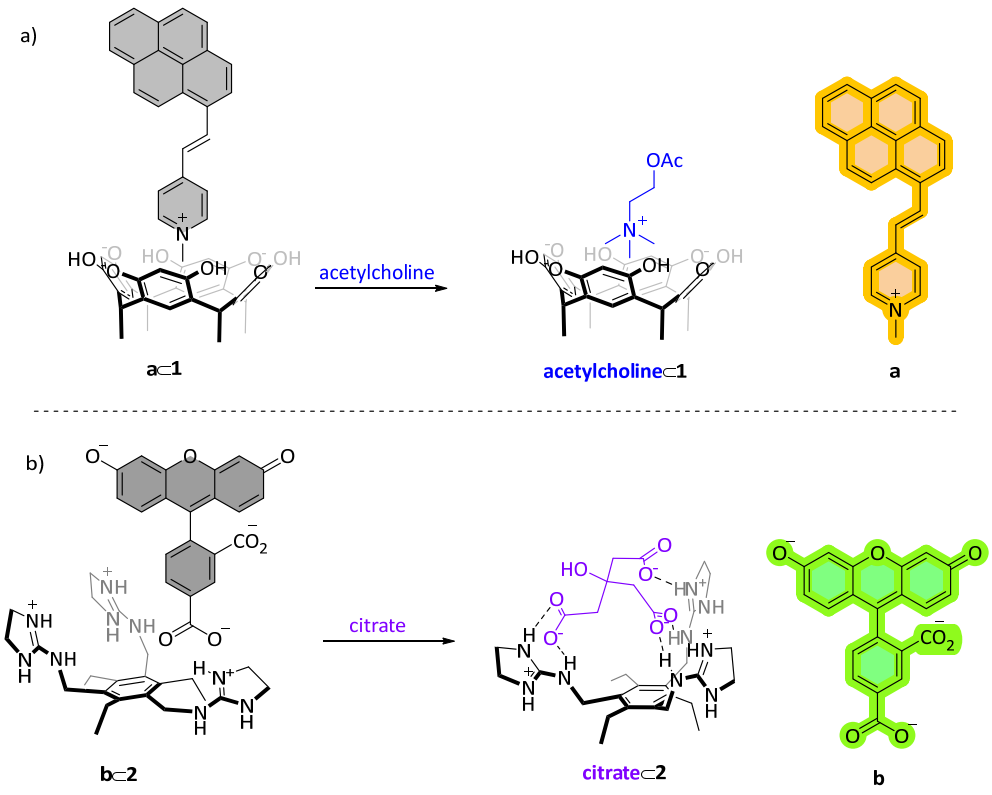

Figure 1.5 Line-drawing structures of the compounds used in the pioneering studies of supramolecular fluorescent sensors based on indicator displacement assays. a) IDA reported by Inouye et al for acetylcholine sensing using receptor **1** and pyrene derivative **a**. b) Citrate sensor developed by Anslyn et al. using 5-carboxyfluorescein **b** as a fluorescent probe and the guanidinium receptor **2**.

1.3. IDAs for Optical Supramolecular Sensing of Biomarkers.

Numerous IDAs have been reported for the sensing of biologically relevant molecules. Some of these compounds are biomarkers, that is they are measurable indicators of health status. Sensing of biomarkers for disease diagnosis requires simple, accurate, and reliable analytical techniques. In this section, we will review recent and relevant studies using IDA-based sensors of biomarkers for early disease detection.

We selected biomarkers involved in the early detection and monitoring of diseases causing high levels of deaths worldwide. In this regard, we relied on the most recent report published by the World Health Organization (WHO).[50] The reported estimates reveal mortality trends over the last 2 decades (2000-2019) caused by diseases. The

top 10 leading causes of death are depicted in *Figure 1.6*a. They accounted for the 55% of the deaths registered worldwide (55.4 million).

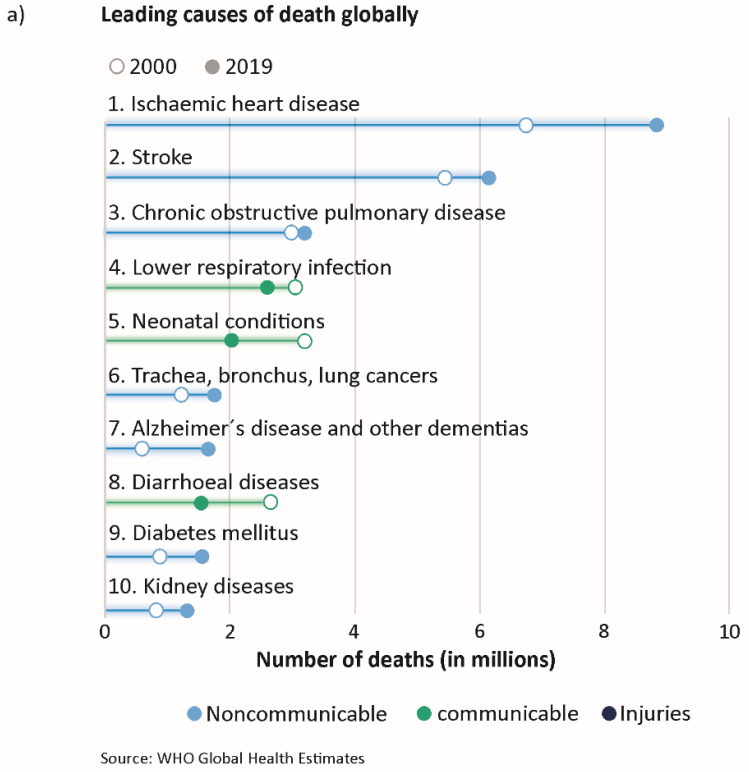

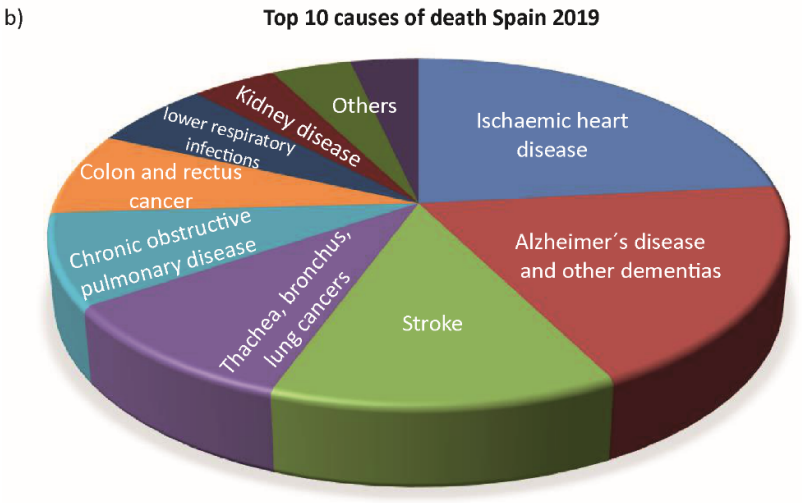

Figure 1.6 Top 10 causes of death a) worldwide and b) Spain in 2019. Source: WHO Global Health.

Being pre-pandemic data, these estimates do not include an assessment of the direct or indirect effect caused by COVID-19 on mortality rate. However, there is evidence that people living with pre-existing health conditions like heart disease,[51] diabetes[52] and respiratory conditions[53] are at higher risk of complications and death due to COVID-19. To the best of our knowledge, no IDA-based molecular sensor has been developed so far for detection or/and monitoring of COVID-19.

IDAs for the sensing of biomarkers of secondary diseases like HIV/AIDS,[54,55] bone diseases,[56] or endocrine diseases[57] fall out of the scope of this review.

Diseases like ischaemic heart disease (IHD), Alzheimer, diabetes and kidney disease, have shown a significant increase over a period of almost two decades (from 2000 to 2019). Conversely, neonatal conditions and diarrheal diseases have displayed a considerable decrease in the same period of time.

In the particular case of Spain (*Figure 1.6*b), it is worthy to note that Alzheimer and other dementias conditions are ranked as the second leading cause of death. Kidney diseases climbed two positions compared to worldwide statistics (ranking 8th, compared to the 10th place in global statistics).

Therefore, the development of effective and simple methodologies for the detection of biomarkers would facilitate early diagnosis of diseases and improve its therapeutic treatments (i.e. theranostics). In this vein, supramolecular chemists have taken a leading position in the development of IDA sensing approaches for a wide range of biomarkers.

1.3.1 Sensing of biomarkers related to kidney diseases.

In almost 20 years, kidney diseases rose from the 13th to the 10th world´s leading cause of death. Mortality increased from 813,000 in 2000 to 1.3 million in 2019.[50]

- *Citrate*

One of the most common biomarkers associated with kidney malfunction is citrate.[58,59] Citrate is an intermediate conjugate metabolite in the Krebs cycle (citric acid cycle, CAC). CAC plays an important role in the cell in relation to the generation and harvesting of chemical energy and in the provision of different biomolecules (e.g. amino acids, NADH).[60] Low levels of citrate in urine have been related with nephrolithiasis and nephrocalcinosis.[61] Citrate has also been considered a good biomarker for the early stage detection of prostate cancer[62] and bone diseases.[63]

Inspired by the work of Anslyn et al. described in the previous section, in 2006, Schwegmann et al., reported a "naked eye" IDA for the detection of citrate. They used 5-carboxyfluorescein **b** as indicator and receptor **3**, a cationic variation of the Anslyn´s pinwheel receptor **2**. Schwegmann´s team replaced the tri-guanidinium moiety of the Anslyn´s original design (Figure 1.5) by acyl guanidinio-carbonyl pyrroles (receptor **3** in *Figure 1.7*). The three binding sites of receptor **3** are rigid and planar, reducing conformational changes and increasing pre-organization for the ditopic interaction with the also planar carboxylate groups. As a result of this elegant modification, the authors reached an increase of two orders of magnitude for citrate binding in pure water with **3** compared to receptor **2**.[64]

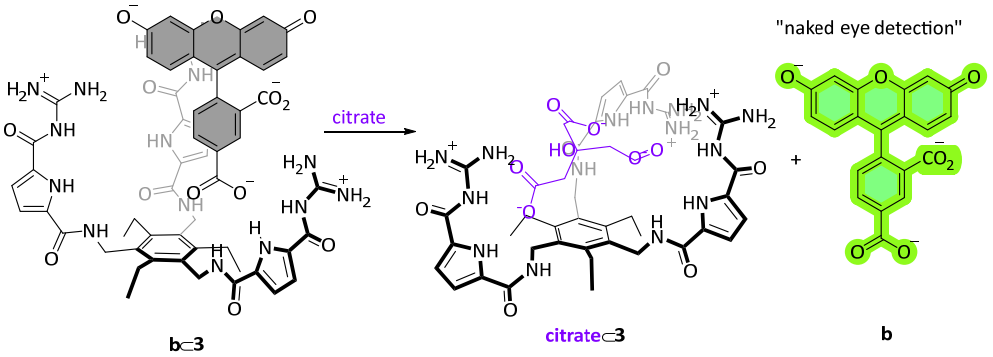

Figure 1.7 Line-drawing structures of the tripodal cationic receptor **3,** bearing guanidinocarbonyl pyrrole binding sites, and 5-carboxyfluorescein **b** as indicator engages in an IDA for citrate detection.

On a different note, in 2015, the Yang´s group reported the use of the di-nuclear zinc receptor (**4**) in an IDA assay for citrate. The receptor is based on a 9,10-distyrylanthracene (DSA) spacer equipped with two zinc(II)-dipicolylamine (DPA) arms (*Figure 1.8*).[65] The florescent receptor **4** displays an emission band with a maximum centered at 550 nm. The fluorescence of **4** is quenched upon binding to phenol red (**c**), most likely, due to Energy Transfer (ET) owing to the good overlap between the emission of **4** and the absorption of the anionic form of **c**. Addition of citrate induces the competitive displacement of the indicator **c** from the receptor's binding site. The competitive binding resulted in a significant recovery of the fluorescence. A linear response in the range of 0-10 µM of citrate was observed, allowing not only its detection but also its quantification. The developed IDA featured a limit of detection (LOD) as low as 0.1 µM.

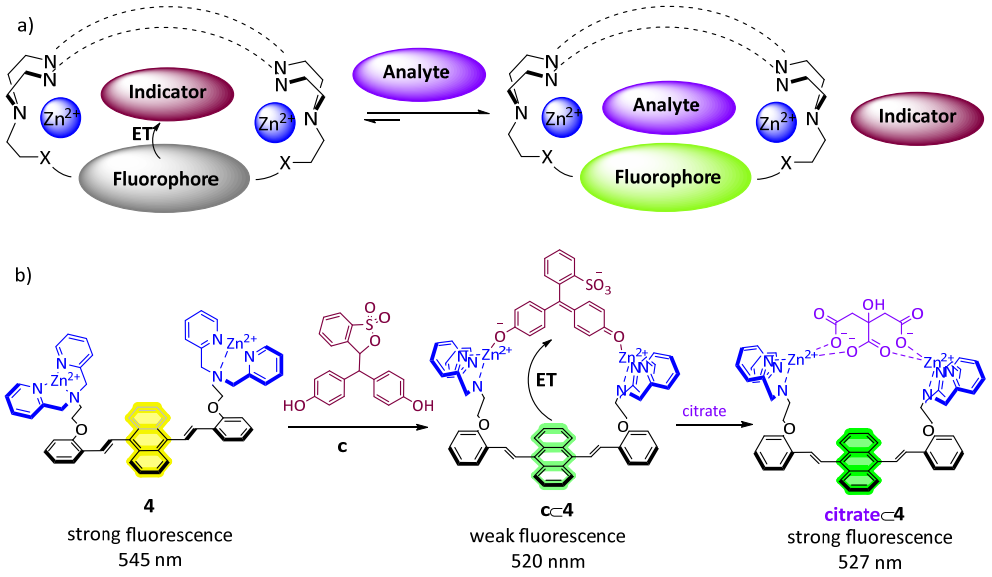

Figure 1.8 a) Schematic IDA approach and b) line-drawing structures of the dinuclear zinc complex **4** and phenol red **c** used in the IDA-based sensor for citrate detection. Adapted from reference 65

The emission changes observed upon addition of succinate and glutarate (dicarboxylates that are related to the tricarboxylate citrate structure) to the **c⊂4** ensemble were not noticeable. These results demonstrated the large selectivity of the ensemble for citrate over the two dicarboxylate analogues. Remarkably, the presence of the pyrophosphate (PPi) anion also provoked the recovery of the emission of **4** starting from the **c⊂4** ensemble. However, the authors did not find the existence of a linear relationship between the fluorescence's intensity and the PPi concentration. The titration experiments of the **c⊂4** ensemble with PPi showed that the maximum of the recovered emission band was different from that obtained using citrate suggesting the potential use of the IDA for the differentiation of the two anions. Finally, the authors highlighted the importance of the different location of the zinc(II)-dipicolylamine (DPA) substituents in the 9,10-distyrylanthracene (DSA) spacer for the binding and sensing of anions. In brief, when the zinc(II)-dipicolylamine (DPA) substituent of the DSA spacer are placed in the *para*-positions instead of the *ortho*-counterparts, as in **4**, the resulting chemosensor ensemble displayed a minor recovery of its emission and a non-linear fluorescence response upon incremental addition of citrate.

- *Oxalate*

Another important biomarker for the diagnosis of kidney disease is oxalate ($C_2O_4^{2-}$),[66] a dicarboxylate produced as by-product by the metabolism of glyoxalate and ascorbate. Urinary oxalate comes mainly from the diet and the endogenous synthesis. Vitamin C may increase the urinary oxalate total concentration by increasing its production by the body.[67] High levels of oxalate in urine or blood cause several disorders including kidney stones and renal failure.[68] The most common compound found in kidney stones is calcium oxalate (CaC_2O_4).[69] There is evidence supporting that beer consumption reduce risk by 40% of developing kidney stones.[70,71]

In 2012, Hu and Feng reported IDAs enabling the effective fluorescent sensing of oxalate in water.[72] The addition of 1 equiv. of the di-nuclear copper (II) complex of cyclophane **5**, **[Cu₂●5]²⁺**, to a water solution (10 mM HEPES buffer, pH = 7.0) of the fluorescent indicators **d** (Fluorescein) and **e** (Eosin Y) induced the complete quenching of their emissions. The subsequent addition of oxalate to the ensembles prepared by mixing equimolar amounts of the receptor and the indicator induced the recovery of the indicator's, **d** and **e**, emissions. (*Figure 1.9*). These results were indicative of the successful competitive binding of the oxalate and the displacement of the indicators from the complexes with **[Cu₂●5]²⁺**. Using Job's plots, the complexes of the indicators, **d** and **e**, with the di-nuclear cyclophane **[Cu₂●5]²⁺,** as well as that of the oxalate were assigned 1:1 binding stoichiometries**.**

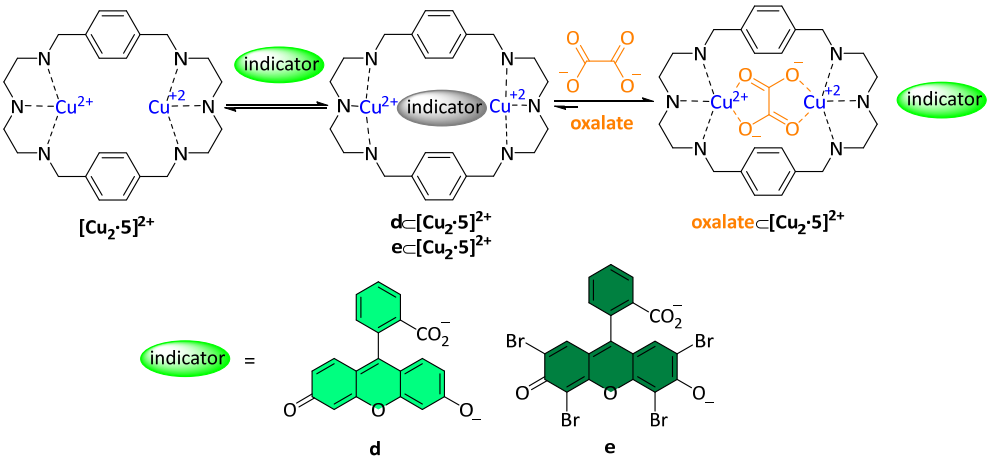

Figure 1.9 Line-drawing structures of di-nuclear cyclophane complex **[Cu₂●5]²⁺** fluorescent indicators **d** and **e**, and the complexes involved in the oxalate sensing. Adapted from reference 72.

The IDAs assays involving Eosin Y, **e**, showed a superior selectivity for the sensing of oxalate in water at neutral pH. Even in the presence of large excess of other anions including structurally similar dicarboxylates such as malonate, the Eosin ensemble selectively recognized and sensed oxalate. The analysis of the displacement data using a competitive binding model assigned a binding affinity larger than 10^7 M^{-1} to the complex formed by the di-nuclear receptor **[Cu₂●5]²⁺** and oxalate. According to the authors, the magnitude of the determined binding constant represented the largest value ever reported for an oxalate chemosensor complex under the operational conditions. More precisely, the reported value for the chemosensor complex **oxalate⊂[Cu₂●5]²⁺** exceeded in more than two orders of magnitude previous values reported for a related oxalate chemosensor complexes.[73] Similar magnitudes for the apparent 1:1 binding constants of oxalate complexes were recently disclosed using poly-amine bicyclic receptors bearing an anthracene strap (azacryptands).[74] The designed receptors featured an ellipsoidal cavity that can accommodate one oxalate dianion. However, acidic media (pH = 3.6) was necessary to reach such high binding constants with azacryptands. The secondary amine groups of the receptor must be protonated in order to establish multiple coulombic interactions with the bound oxalate. The azacryptand receptor bearing an anthracene spacer in its scaffold constitutes a fluorescent chemosensor for the direct binding sensing of oxalate.

In a more recent study, Tavallali and coworkers reported the development of a simple and selective colorimetric chemosensor for oxalate both in solution and in the solid state. The authors used the Cu(II) complex of Reactive Blue 4, **f**, as the chemosensing ensemble, **f●Cu²⁺**, for the selective recognition of oxalate over other competitive analytes.[75]

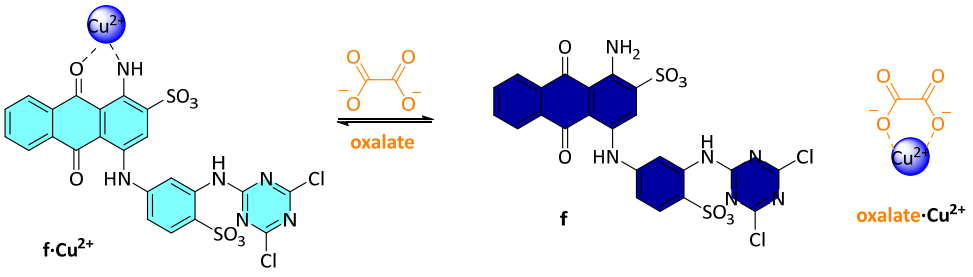

Figure 1.10 Line-drawing structures of the compounds involved in the metal-based IDA for the colorimetric oxalate detection reported by Tavallali et al.

The coordination complex **f●Cu^{2+}** exhibited a sky-blue color in water buffered solution (pH = 7.0). Its UV/vis spectrum showed a broad absorption band with a maximum at 619 nm. The calculated binding constant for **f●Cu^{2+}** complex was (4.46 ± 0.12) × 10^5 M^{-1}. The gradual addition of oxalate to the ensemble obtained with equimolar concentrations of [**f**]=[**Cu^{2+}**]= 50 μM produced a blue shift of the maximum of the initial absorption band (607 nm, Δλ = - 12 nm). As a result, the solution turned dark blue, which corresponds to the inherent color of free **f**. The competitive chelation of the **Cu^{2+}** cation by the oxalate dianion resulted in the formation of the **oxalate●Cu^{2+}** complex (K_a = (2.3 ± 0.1) × 10^7 M^{-1}) and the release of the indicator **f** to the bulk solution (*Figure 1.10*). The absorbance band increased linearly with the oxalate concentration from 1.76 to 49.9 μM. The LOD was calculated to be 0.62 μM. The developed IDA was successfully applied for oxalate determination in different real samples in solution (aqueous medium) and the solid-state (paper-based-experiments).

- *Creatinine*

Creatinine (**Cr**) is a byproduct of creatine, which helps muscles obtaining energy. Creatinine is toxic for the cells and it must be transported by the bloodstream and eliminated through renal filtration.[25] In consequence, the determination of creatinine concentration in body fluids (urine, plasma) is useful for the diagnosis and monitoring of kidney performance.

In 2020, we reported two different IDAs for the recognition of **Cr** and its lipophilic version hexylcreatinine (**HexCr**) in organic media. The developed IDAs share in common the use of a mono-phosphonate calix[4]pyrrole cavitand as the receptor unit..[26]

In the development of the first IDA, we relied on the well-known optical properties of the dansyl fluorophore. We covalently attached a dansyl unit to a mono-phosphonate calix[4]pyrrole cavitand via a sulfonamide bond obtaining the fluorescent receptor **6**. It is worth mentioning that the direct sensing of creatinine using receptor **6** produces negligible changes in its emission and absorption spectra.

However, the addition of incremental amounts of the pyridyl-*N*-oxide DABCYL derivative (**BHQ**) to a μM dichloromethane solution of **6** produced the quenching of its emission. Phosphonate calix[4]pyrrole cavitands are excellent receptors for pyridine-*N*-oxide derivatives producing inclusion complexes with 1:1 stoichiometry, which are highly stable thermodynamically (K_a > 10^6 M^{-1}). In turn, DABCYL

derivatives are known black-hole quenchers (**BHQ**). Thus, the formation of the **BHQ⊂6** complex deactivated the dansyl fluorescence, most likely, by Förster resonance energy transfer (FRET) (Figure 1.11, panel c).

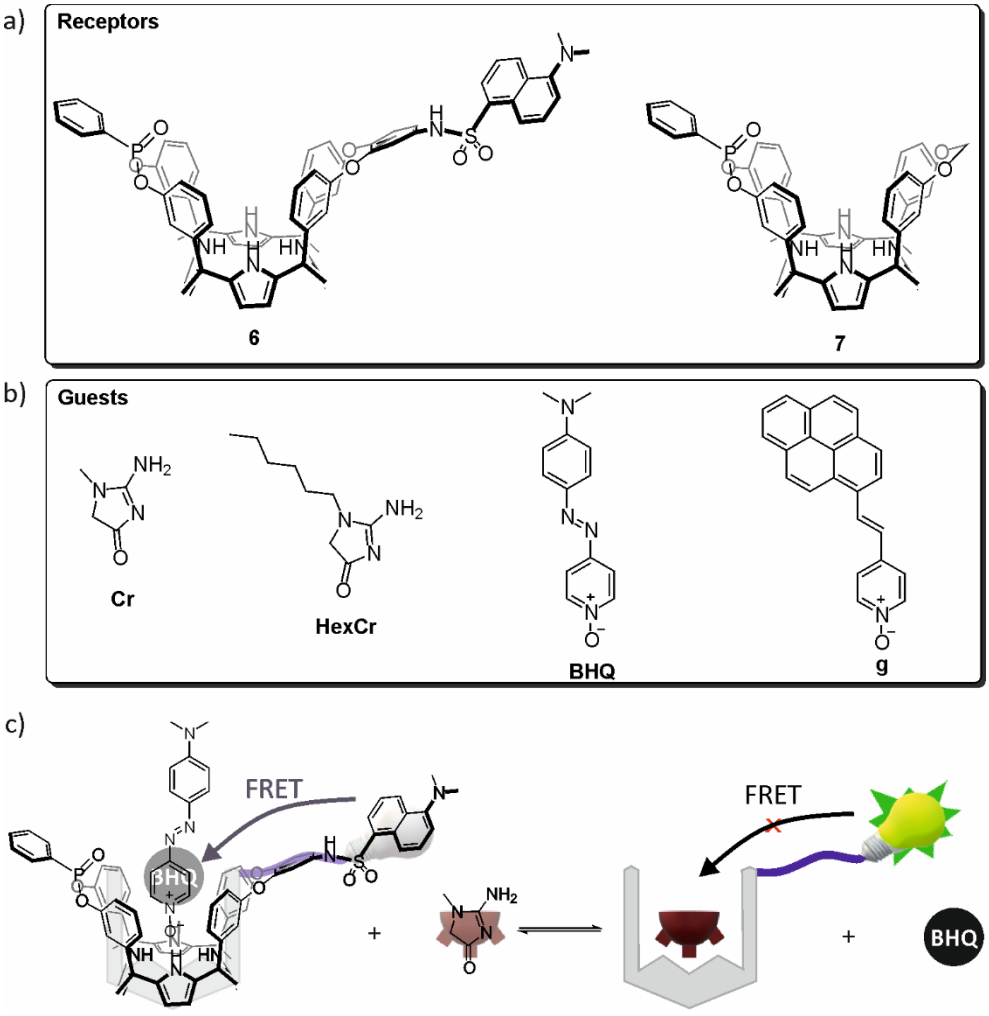

Figure 1.11 Line-drawing structures of a) phosphonate calix[4]pyrrole cavitands **6** and **7** b) creatinine(**Cr**), hexyl creatinine (**HexCr**), black-hole quencher (**BHQ**) and pyrene derivative **g.**, c) schematic representation of the FRET-based IDA developed for the sensing of creatinine in organic media.

A solution of the **BHQ⊂6** ensemble produced in an equimolar mixture of the components at 1 µM concentration was titrated with **HexCr**. The addition of the **HexCr** induced a "turn on" effect of the emission of the dansyl unit. This effect originated form the displacement of "quencher" **BHQ** from the ensemble and its

concomitant replacement by one molecule of **HexCr** producing the **HexCr⊂6** complex (*Figure 1.11*, panel c). Notably, the included **HexCr** does not produce any significant quenching effect on the dansyl fluorophore of the receptor. Thus, the observed fluorescence enhancement (4-fold, in the presence of 70 equiv of **HexCr**) corresponds to the undisturbed emission of the dansyl group. Similar results were obtained using **Cr** as competitive guest of the IDA. The binding of **HexCr**, **Cr** and the *N*-oxide DABCYL derivative with the fluorescent receptor **6** was also probed using ^{1}H and ^{31}P NMR spectroscopy titrations. The structures of the complexes formed in solution were characterized using 2D spectroscopy experiments (COSY, ROESY). We also used ITC experiment to assess accurate binding constant values of the formed 1:1 complexes. Notably, the binding constant values derived from the ITC experiments were in good agreement with those determined by fitting the direct fluorescent titration data to suitable binding models. In the particular case of the complexes **HexCr⊂6** and **Cr⊂6**, the data of the IDA experiments were fitted to a competitive binding model. Remarkably, the developed IDA displayed a LOD as low as 110 nM, which is in line with the concentrations of creatine found in the urine of healthy, as well as sick patients.

For the development of the second IDA we selected calix[4]pyrrole cavitand **7**, which is a non-fluorescent version of **6**. In this case, we designed the fluorescent indicator **g** suitable to integrate receptor **7** in a fluorescent "turn-on" IDA. Compound **g** contains a pyridyl-*N*-oxide covalently connected to a pyrene unit by an ethynyl spacer. The UV/vis titration of **g** with incremental amounts of **7** revealed a moderate decrease in the intensity of the absorption bands of the pyrene derivative and the existence of a quasi-isosbestic at 350 nm. We also monitored the interaction of **g** with **7** using emission spectroscopy (λ_{exc} = 350 nm). We observed a significant quenching of the dye (80% in the presence of 2.5 equiv. of **7**) and a reduced blue-shift of its emission band. Most likely, the intramolecular charge transfer state (ICT) of the excited dye is perturbed by complexation with receptor **7**. Dye **g** is bound to receptor **7** by inclusion of the pyridine-*N*-oxide residue. The mathematical analysis of the titration data assigned a binding constant value for the **g⊂7** complex larger than 10^{7} M^{-1}. This value was confirmed by ITC experiments. The sensing ensemble **g⊂7** (equimolar amount of each component at 1μM concentration) was tested in competitive IDAs with **HexCr** and **Cr**. The incremental addition of **HexCr** restored the fluorescence of the dye (2.5-fold enhancement with 50 equiv. **HexCr** and 1.8-fold enhancement with 50 equiv. of **Cr**). The analyses of the fluorescence data obtained in the IDAs using a competitive binding model provided the stability constants of the

complexes **HexCr⊂7** and **Cr⊂7** as 4.3×10^5 M^{-1} and 3.0×10^5 M^{-1}, respectively. In both cases. the complex formation was driven by the establishment of CH-π and hydrogen bonding interactions between the creatinine derivatives and the core of the polar aromatic cavity of the cavitand receptor **7**. The inwardly directed P=O group of receptors **6** and **7**, provided an extra hydrogen bonding interaction with the primary amino groups of the creatine derivatives**.**

1.3.2 Sensing of cancer related biomarkers.

According to the 2019 WHO statistics on main global causes of death, which is showed in *Figure 1.6*, trachea, bronchus and lung cancers are placed in the 6th place. Cancer is a disease older than even humanity itself. Scientists have documented how dinosaurs also suffered from cancer.[76] The first registered case of human cancer is found on an Ancient Egyptian papyrus written in 1500-1600 BC.[77] Early detection of any type of cancer offer the opportunity to increase effectivity of treatment and a curative intent.[78]

- *Pyrophosphate (**PPi**).*

Pyrophosphate (**PPi**), also known as diphosphate, is considered a potential biomarker for cancer diagnosis. **PPi** is a phosphorous oxyanion that contains two phosphorous atoms in a P-O-P linkage. It is the simplest of the polyphosphates and it is formed during the ATP hydrolysis into AMP to produce energy within living cells. **PPi** stands out among other biomarkers for the accuracy of cancer screening using body fluids. For example, in 2015 Miyamoto and co-workers described that the determination of levels of plasma pyrophosphate displayed 77.9% of accuracy in the detection of adenocarcinoma lung cancer using a single metabolite.[79]

Abnormal levels of pyrophosphate in body fluids have been also related with bone diseases,[80] and kidney malfunctions.[81]

In consequence, there has been a growing interest in the development of pyrophosphate chemosensors. Recently, Anbu et al[82] review the literature for reports dealing with colorimetric and fluorescent chemosensors for **PPi**. The covered period of time spans from 2010 to the end of 2019. In more recent years, zinc-terpyridine based chemosensors were successfully employed for the detection of **PPi** in aqueous media.[83,84] In this section we focus on examples of IDAs developed for the selective sensing of **PPi**. The selected examples involve the use of both metal-free and metal-based receptors.

a. IDA for **PPi** sensing based on a metal-free receptor.

In 2012, Ghosh and co-workers, reported the pyridinium-based fluorescent receptor **8** and a sensor bead **9**, based on the former, which allowed the naked eye detection of hydrogen pyrophosphate (**HPPi**). The authors used fluorescein, **d**, as indicator in IDAs experiments involving **8** and **9**(*Figure 1.12*). [85]

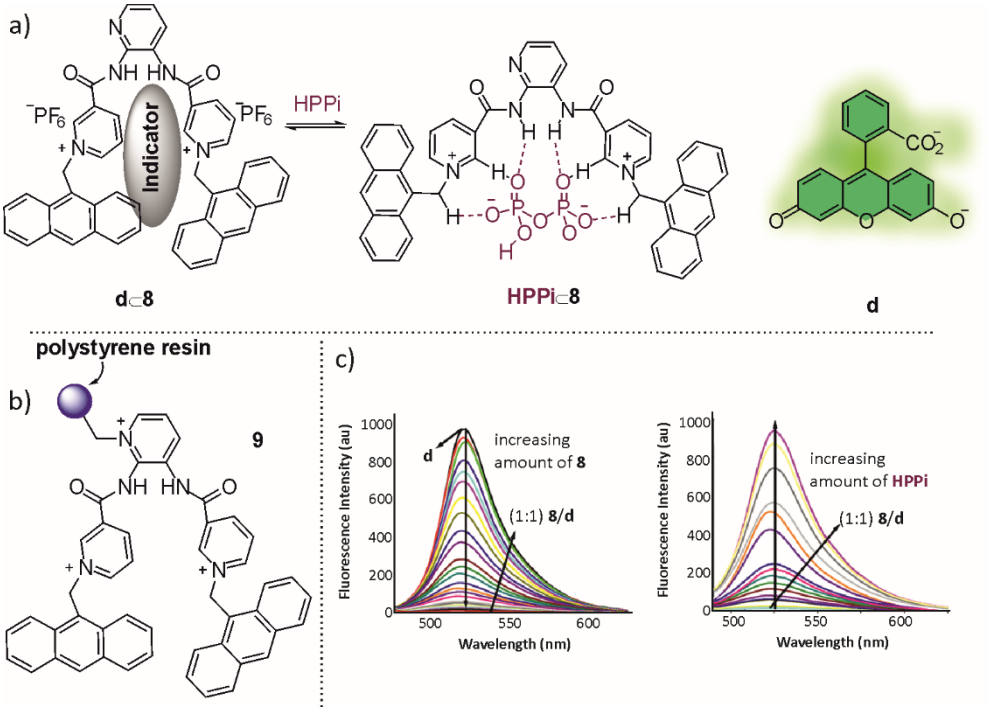

Figure 1.12 a) IDA equilibrium: line-drawing structures of the complex of hydrogen pyrophosphate (**HPPi**) with receptor **8**, as well as fluorescein **d**. The complex of fluorescein with the receptor is schematically shown. b) Schematic representation of the sensor bead **9**, c) (left panel) quenching experienced by the emission of indicator **d** upon incremental addition of receptor **8**; (right panel) recovery of the emission upon addition of **HPPi** as competitive guest. Experiments were performed in a CH_3CN/H_2O solution mixture (4/1 v/v 10 mM Tris HCl). The ensemble for the IDA was formed at equimolar concentrations of its components of 8.5×10^{-5} M.

The binding of fluorescein, **d**, into the cleft of **8** provoked the quenching of the emission of the dye. The incremental addition of **HPPi** to the ensemble, **d⊂8**, produced with equimolar concentrations of its components (8.5×10^{-5} M) in a CH_3CN/H_2O (4/1 v/v, 10 mM Tris HCl) solvents mixture, caused the gradual recovery of the emission of the dye. This observation indicated the competitive binding of the **HPPi** anion to the receptor and the release of the bound fluorescein **d** to the bulk solution. (Figure 1.12c). Using separate florescence titrations, the authors

determined that the binding constants of the **d⊂8** and **HPPi⊂8** complexes were of the same order of magnitude (~ 5.0×10^5 M^{-1} and 1.0×10^5 M^{-1}). This makes the **d⊂8** ensemble ideal for the naked-eye sensing of **HPPi**. Other phosphate analogues such us ATP, ADP or AMP did not restore the emission of the dye. The authors derived the molecular structure of the **HPPi⊂8** complex depicted in Figure 1.12a from the chemical shift values of its protons observed in ^{1}H the NMR spectrum and the results of DFT calculations. We consider that the putative structure of the complex would be better reflected by transferring the proton of the pyrophosphate to the *N*-atom of the pyridyl-bis-amide. This will also explain the recovery of the fluoresce for bound **8** to **HPPi** owing to the inhibition of the PET quenching. For practical purposes, Ghosh´s team developed the sensor bead **9**, as a solid support version of receptor **8**, by immobilizing a chloro-benzyl derivative on a Merrefield's resin. In this case, the IDA technique involved the treatment of a solution of fluorescein, 2.3 mL [**d**]= 8.0×10^{-5} M in CH_3CN/H_2O (4/1 v/v, 10 mM Tris HCl), with 5 mg of beads **9**. After 30 min, the absorption band of **d** reduced its intensity and the solution became colorless. The addition of the TBA salt of **HPPi** to the above heterogeneous mixture, induced the release of absorbed **d**, through competitive binding with the hydrogen pyrophosphate, and the consequent regeneration of the color of the solution. The sensor beads **9** were also used for **HPPi** sensing in a highly complex biological matrix such as blood serum. Using florescence microscopy, it was possible to observe the release of the green fluorescein dye from the outer surface of the beads. The control of the medium pH (neutral) resulted a key factor in accelerating the release of dye.

b. Metallopeptide-based **PPi** receptor.

Over the years, Joliffe and co-workers have exploited the use of peptide-based receptors containing bis[Zn(II)dipicolylamine] (Bis[Zn(II)DPA]) units owing to their selectivity in the binding of phosphate anions in aqueous solution. The studied receptors featured linear[86,87] and cyclic[88] peptide backbones. Their phosphate-binding properties were investigated under physiological conditions using IDAs involving pyrocatechol violet (PV) as colorimetric indicator.

Moving further in the **PPi** naked-eye detection, in 2017, Long and co-workers reported the use of a peptide synthesis resin as solid-support of the bis[Zn(II)DPA] peptide receptor **10**. This solid platform was used in heterogeneous IDAs also mediated by the pyrocatechol violet (**h**) as indicator (*Figure 1.13*a). [89]

The complexation of the indicator and its subsequent displacement by **PPi** was followed by clear color changes of the resin beads functionalized with the bis[Zn(II)DPA] peptide receptor **10**. The beads displayed blue color upon formation of **h●10** complexes at pH 7.4. The beads turned yellow when the indicator **h** was displaced from the solid-supported receptor **10** through competitive binding with **PPi** (*Figure 1.13*b). Noteworthily, color changes were not observed when solutions of analogous phosphonate anions, such as ATP, ADP or citrate were passed through loaded beads in a Pasteur pipette packed with glass fiber. These results evidenced the good selectivity of the functionalized beads for the naked-eye detection of **PPi**. Moreover, the obtained results are in line with those previously reported by Joliffe et al using analogous bis[Zn(II)DPA] peptide receptors in solution. [87] In short, an appropriate distance between the two Zn(II)DPA units is responsible for the good selectivity displayed by the bis-[Zn(II)DPA] peptides receptors in the binding of **PPi**.

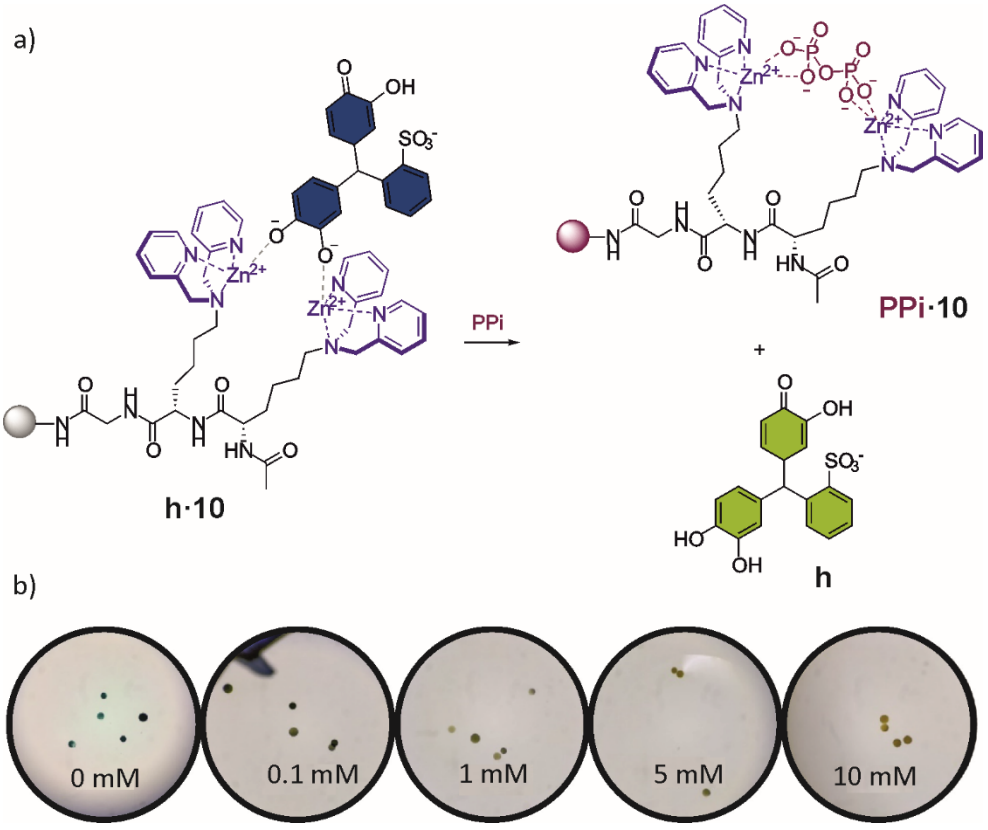

Figure 1.13 a) Line-drawing structures of the **h●10** and **PPi●10** complexes involved in the florescence IDA, b) dissection microscopy images (4 x magnifications) of the colorimetric threshold test for **PPi** detection at pH 7.4; the **PPi** concentration is shown in the images visualizing several resin beads.

Long and co-workers also prepared a resin functionalized with an acetamide group, which cannot bind Zn(II) nor the indicator **h**. Control experiments with the acetamide resin under the complexation conditions applied to the peptide functionalized beads did not produce a persistence color change.

In order to assess the LOD of the peptide functionalized beads, Long and co-workers developed a threshold test. 5-10 beads were treated with 50 µL of water solutions having different concentration of sodium **PPi** in 10 mM Tris buffer. The change of the color of the beads was monitored with a standard optical microscope or a smartphone equipped with a macro lens. On addition of concentrations above 1mM, a clear change in the color of the beads was observed. The threshold of the peptide functionalized beads in detecting **PPi** in artificial plasma and urine was also investigated. After 1 h of incubation time, the heterogenous IDA was able to detect **PPi** at 5 mM concentration in artificial plasma and at 2 mM concentration in real urine.

- *Glutathione*

Glutathione (**GSH**) is a thiolated tripeptide and the most abundant antioxidant molecule in living organisms. **GSH** plays an important role in multiple biological functions, such as in the cellular protection from damage by free radicals, peroxides and toxins.[90] In tumor cells prior to treatment, the **GSH** levels are often high. There is a strong correlation between elevated levels of intracellular glutathione/sustained glutathione-mediated redox activity and the resistance to pro-oxidant anticancer therapy.[91]

Carbon dots (**CD**) have been successfully employed for bioimaging of cancer cells[92] and recently emerged as promising nanomaterials for cancer therapy.[93] Anionic carbon dots (ACD) are interesting nanomaterials owing to their physicochemical properties and intrinsic fluorescence character. In 2016, Das and co-workers developed a “turn on” fluorescence IDA based on gold nanoparticles (**GNP**) protected with ACD, ACD-GNP.[94] The molecular recognition process involved in this example is limited to the interaction of the Au atoms at the surface of the GNP with the thiol group of the **GSH**. Nevertheless, we considered the example to be highly relevant due to the importance of **GSH** as cancer biomarker. Moreover, the use of nano-hybrid material instead of molecular compounds in the development of the IDA, the selectivity displayed by the ACD-GNP ensemble and its application in the selective labelling of cancer cells adds relevance to the study.

The ACD were synthesized using a reported protocol.[95](reference?) The ACD protected Gold nanoparticle (ACD-GNP) were synthesized following the conventional $NaBH_4$ reduction protocol of $HAuCl_4$ (1:2 ratio) using an aqueous solution of ACD at a concentration of 200 µg mL^{-1}. Lower concentrations of ACD produced dispersions most likely due to an insufficient amount of the capping agent.

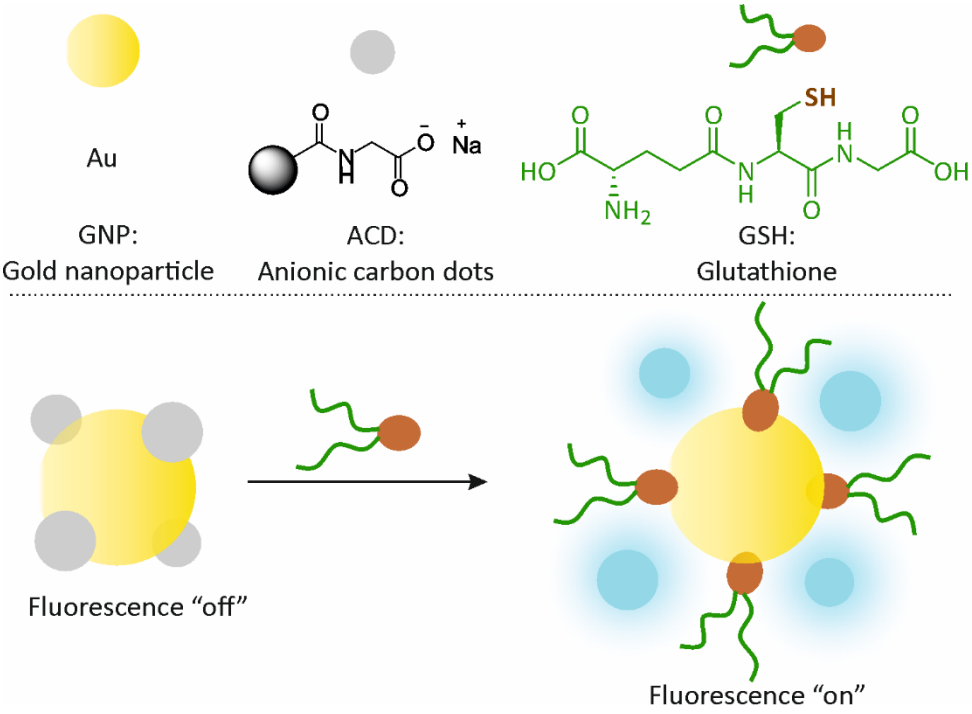

Figure 1.14 Schematic fluorescent IDA using **GNP** capped with **ACD** for selective detection of **GSH**. Adapted from reference 94.

The nano-hybrid ensemble used for the IDA had a final concentration of GNP (25µM) and ACD at 10 µg mL^{-1}, after optimal dilution of the standard solution used for its preparation. The florescence of the ACD-GNP nanoparticles is quenched compared to that of an ACD solution at 10 µg mL^{-1}. GNP are kwon fluorescence quenchers.[96] Firstly, the authors investigated the florescence response of the diluted solution of ACD-GNP nano-hybrids against a fixed concentration of 50 µM of **GSH** with time. They observed that the emission of the ACD at 420 nm increased with time and did not change any further after 5 min. For this reason, the **GSH** detection experiments involved a 10 min incubation time. Next, the fluoresce response of the optimized ACD-GNP ensemble was studied varying the concentration of **GSH** . The gradual increase of the concentration of **GSH** (0 - 50 µM) provoked an increase in the

fluorescence of the **ACD** at 420 nm. After the addition of 50 µM of **GSH**, almost 75 % fluorescence intensity was restored. This fluorescence enhancement was attributed to the competitive displacement of the fluorescent **ACD** nanomaterial indicator from the surface of the **GNP** by **GSH** molecules (*Figure 1.14*). The multidentate binding of **GSH** enables a stronger binding to the GNP surface. The detection limit of the methodology was determined to be as low as 6 nM in **GSH**. The replacement of the **GNP** capping agent (ACD for GSH) did not have an effect on its shape and size.

Other competitive biothiols like cysteine (Cys), homocysteine (Hcys) or gluthathione oxidized (GSSG) did not produced any observable fluorescence changes of the ACD-GNP nano-hybrid sensor when tested under similar experimental conditions. It is worthy to mention here that previous results revealed that Cys and Hcys have a higher capacity to induce aggregation of **GNP** than **GSH**.[97] Probably, the difference in steric hindrance and coordination capability of **GSH** is responsible of the observed selectivity with the **ACD-GNP** sensor ensemble. The competitive biotiols and a series of tested amino acids did not induce noticeable changes of **ACD-GNP** ensemble even at concentrations at high as 200 µM. Similar results were obtained when some biologically relevant molecules such us ascorbic acid, vitamin-E, DTT, BSA protein, glucose and ions such as Na^+, K^+, and S^{2-} were tested. Remarkably, the developed nano-hybrid sensor **ACD-GNP** ensemble was also used for the selective imaging of cancer cells over noncancerous counterparts. This result demonstrated its potential applications in biosensing and cancer diagnosis.

- *Carbonic anhydrase inhibitors*

Carbonic anhydrases (**CAs**) are widespread Zn^{2+} metalloenzymes in higher vertebrates including humans. **CAs** are involved in the catalytic hydration of carbon dioxide to carbonic acid, and numerous studies have demonstrated the important role of **CAs** in different tissues and physiological processes (respiration, digestion, production of body fluids etc.). Abnormal levels and/or activities of **CAs** are associated with cancer progression and response to therapy.[98] Koutnic et al. reported a fluorescent IDA to evaluate the efficacy of potential carbonic anhydrase II inhibitors.[99] This supramolecular chemistry approach bridges the gap between the inexpensive but simplified docking experiments and the accurate but complex catalytic activity studies.

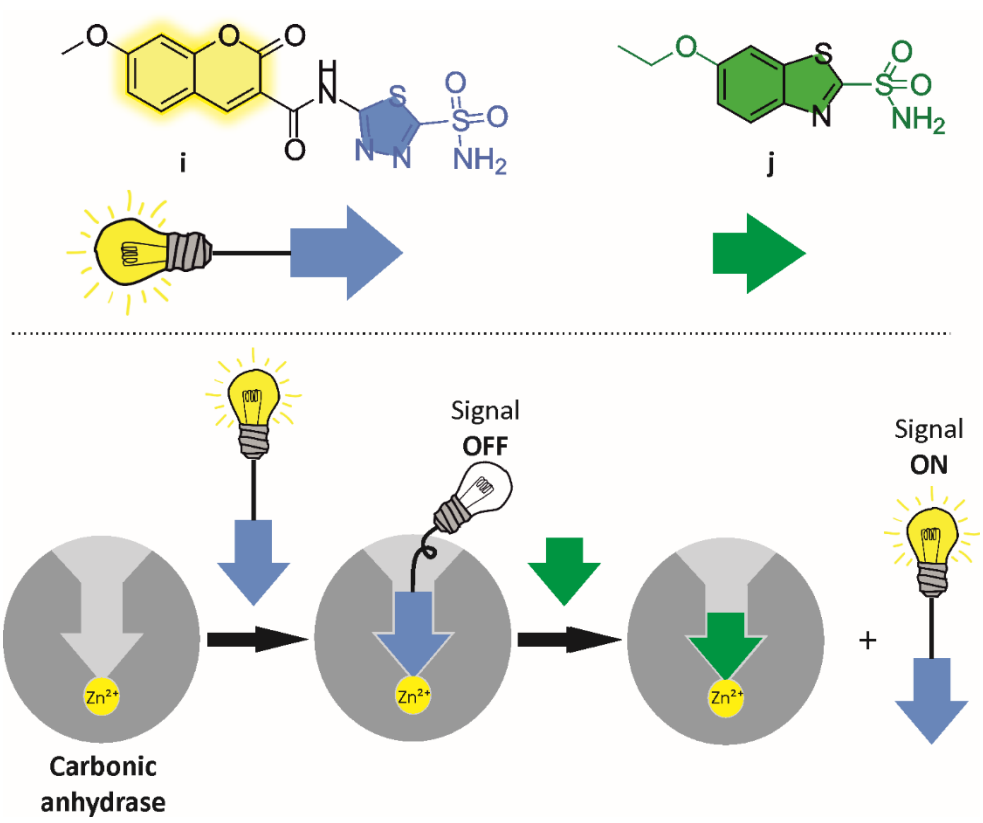

Figure 1.15 Schematic representation of a fluorescent IDA for the evaluation of the efficacy of organic compounds as inhibitors of carbonic anhydrase. Adapted from reference 99.

The designed indicators exploited the affinity of sulfonamide residues for the Zn^{2+} metal center in the catalytic site of **CA**. All of them included a 1,3,4-thiadiazol-5-yl-2-sulfonamide moiety, which was covalently attached to three fluorophores: 7-methoxycumrain, (dimethylamino)naphthalene and pyrene, either directly or through a six- or nine-atom linker. This provided a total of five fluorescent indicators (represented by the blue arrow with the light bulb in *Figure 1.15*). On the other hand, a library of fifteen non-fluorescent sulfonamide **CAs** inhibitors were selected (represented by the green arrow in *Figure 1.15*) to set-up binding competitive assays with the above-mentioned indicators. The structures of the inhibitors allowed the evaluation of steric and electronic effects on the competitive binding experiments. *Figure 1.15* depicts the structure of the fluorescent indicator **i** showing 90% quenching ([**i**]= 500 nM) upon incremental addition of bovine carbonic anhydrase isozyme II ([bCA II] = 0-1520 ng/mL) in aqueous HEPES solution (50 mM and pH 7.2) and the largest affinity constant (5.8×10^8 M^{-1}). The florescence of the indicator

displayed a negligible response when the experiment was repeated using human serum albumin (hSA). This result supported that the response of the fluorescence indicator was specifically related to the CA. We also depict in *Figure 1.15* the structure of the inhibitor **j** featuring the largest binding affinity calculated for the interaction with bCA II (2.4 x 10^{10} M^{-1}) using competitive binding experiment. The large changes in fluorescence between free and bound indicators were exploited to set-up IDAs. The recovery of the indicator's fluorescence was observed upon the addition of CAs inhibitor. The florescence data of the IDA experiments were used to calculated the binding affinities of the inhibitors to the CAs. The comparison between the results obtained from the IDAs and those deriving from ligand docking calculations, revealed that the displacement assay allows a better distinction between inhibitors having similar binding affinities. Moreover, the authors implement the IDAs of three indicators into a florescence microarray demonstrating its utility for the high-throughput screening of CAs inhibitors. The linear discriminant analysis (LDA) revealed an excellent capability of the indicators. The indicator array recognized the 14 used inhibitors and sorted them, in a 3D response space defined by the first canonical factors of the LDA, in three subgroups according to their structural features.

- *Sialic acid*

Due to the lack of suitable biomarkers for early detection, epithelial ovarian cancer is usually diagnosed at an advanced stage becoming a lethal disease. Recently, sialic acid (**SA**) has drawn the attention of doctors to be used as a blood biomarker for this type of cancer. **SA** plays an important role in biological processes including carcinogenesis. Consequently, there is a correlation between increased sialylation and ovarian cancer stages.[100] High **SA** levels can be observed even before the appearance of clinical symptoms.[101]

In this vein, the Yan´s group reported an IDA for ultrasensitive (ppb level) fluorescent detection of **SA** taking place inside a dye-functionalized covalent organic framework COF (**d⊂TpPa**).[102] The 2 D COF host **TpPa** is a weak luminescent material which is synthesized by the Schiff base reaction of 1,3,5-triformylphloroglucinol (Tp) with *p*-phenylenendiamine (Pa) in 1:1 mesitylene/dioxane.[103]

The reversible and expected enol-form of the Schiff bases underwent an irreversible proton tautomerism forming exclusively the keto-enamine form (see the "zoom-in" of the COF structure in Figure 1.16). The molecular material is resisting towards acid

and water owing to the absence of imine bonds. The hybrid material **d⊂TpPa** is obtained by soaking the 2D COF, **TpPa**, in an ethanol solution of [**d**]= 0.002 M for 9 days. The observation of a bathochromic shift (Δλ = 15 nm) for the main peak of the **d** dye after being absorbed into the **TpPa** material, potentially indicates the existence of π-π interaction between planar **TpPa** and the aromatic rings of the dye molecules explaining the high affinity of the composite.(*Figure 1.16*). The **d⊂TpPa** hybrid material was used to prepare a hydrogel composite material **11**, which is also composed by sodium alginate and Cr^{3+} metal ions. The Cr^{3+} metal plays a double role as cross-linking agent of the hydrogel **11** and quencher of the emission of the absorbed **d** dye. Other metal cations used in the hydrogel formation cannot completely quench the fluorescence (λ_{exc}= 437) of the absorbed **d** dye having an emission maximum at 514 nm.

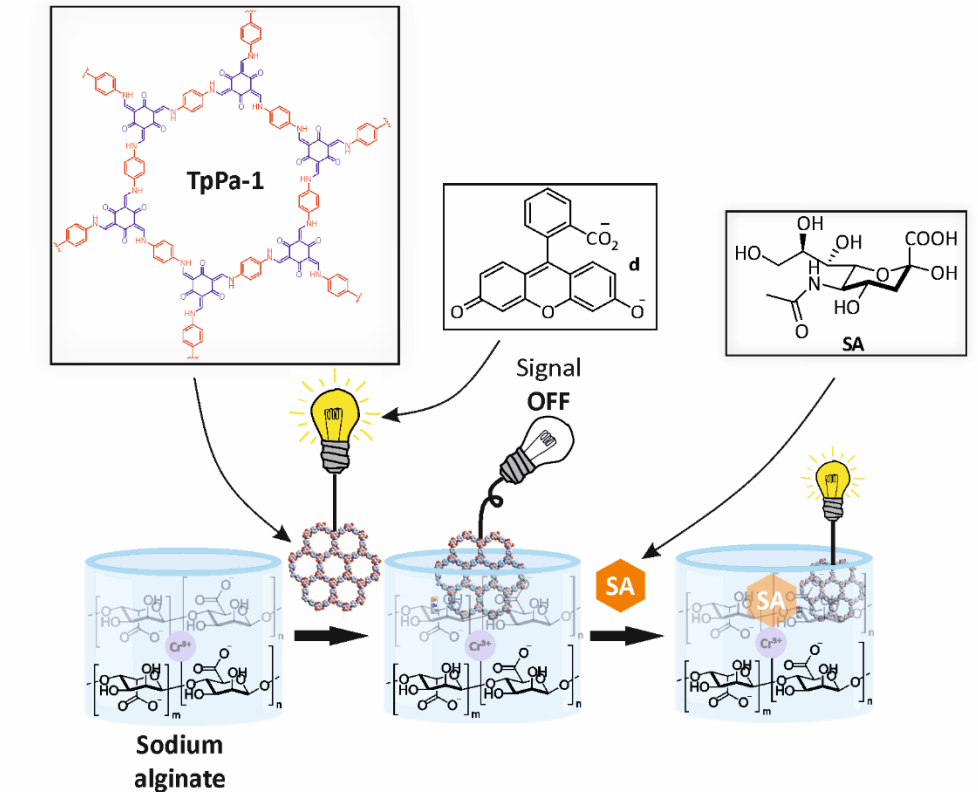

Figure 1.16 Schematic fluorescent IDA for selective detection of sialic acid (**SA**) an ovarian cancer biomarker. Adapted from reference 102.

An aqueous sample containing the composite hydrogel **11** was exposed to **SA** at a concentration of 10^{-2} M. A 19-fold enhancement of the fluorescence was observed.

The observed emission peak coincided with that of **d⊂TpPa.** This result indicated that when the **SA** was combined with the hydrogel the quenching of the fluorescence of the dye is modified. The authors suggested that a complexation of the mono-anionic **SA** with the Cr^{3+} cations of the hydrogel takes places. This process seems to weaken the interactions between the hybrid nanosensor **d⊂TpPa** and the Cr^{3+} cations producing a partial regeneration of the its fluorescence (19-fold).

Based on the affinity and selectivity obtained in aqueous media, the authors also evaluated the IDA with solutions of **SA** in the presence and absence of different interfering serum components and serum itself. Concentration-response experiment allowed the determination of a LOD as low as 8.71 nM for the hydrogel nanosensor composite **11**. The developed IDA also showed good stability with time and at different pHs.

- *Lysophosphatidic acid*

Lysophosphatidic acid (**LPA**) is a lipid mediator that functions as mitogen and motility factor for many cell types. This multifunctional lipid is well-known for its ability to stimulate proliferation, migration and survival of different types of cells, both normal and malignant. [104] Abnormal levels of **LPA** are directly related with breast,[105] ovarian,[106] and prostate cancer.[107]

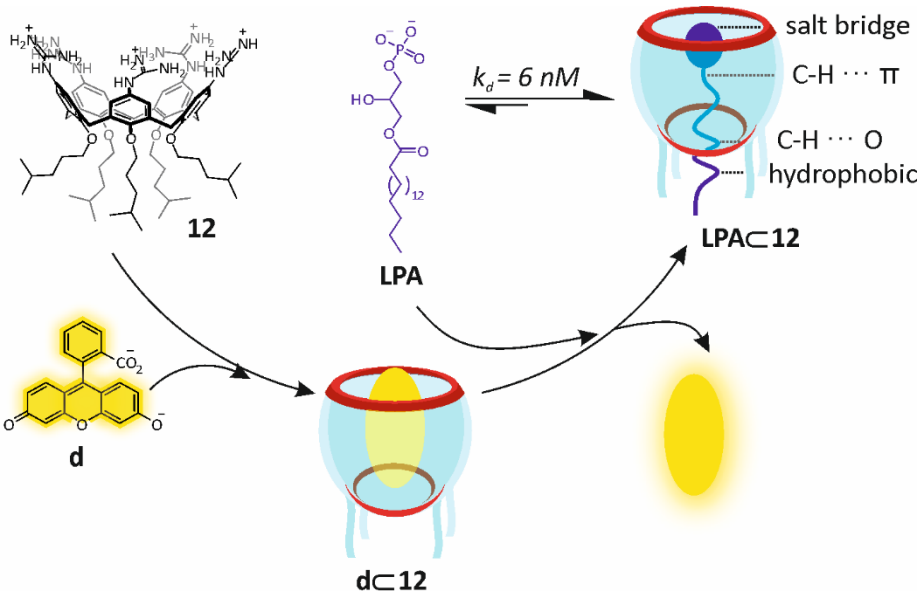

Figure 1.17 Schematic representation of the fluorescent IDA for the selective detection of lysophosphatidic acid (**LPA**). Adapted from reference 108.

The group of Guo designed and synthesized the water-soluble guanidinium-modified calix[5]arene (**12**) for the selective recognition of **LPA**. [108] The authors described that the critical aggregation concentrations (CAC) of both, host and guest, are low (< 0.4 mM). Thus, the measurement of the stability of the supramolecular complex **LPA⊂12** demanded the use of concentrations well below their CACs in order to avoid complications with the aggregation processes. The implementation of an IDA seemed to be a sensible alternative to ^{1}H NMR titrations. IDA experiments can be performed at low μM concentrations assuming that the biding constants of the complexes involved in the competitive binding assay are appropriate (~ 1/ μM). Moreover, the establishment of a fluorescent IDA would allow the fluorescent detection of **LPA**.

The structural features of receptor **12** fit well with the two potential binding sites in **LPA**: one phosphonate head and one long-chain fatty acid tail that can thread through the calix[5]arene lower-rim. Several intermolecular interactions are expected to be responsible for a strong binding of receptor **12** with **LPA**: charge-charge, charge-assisted hydrogen bonds (salt bridge), CH-π, CH-O, and hydrophobic interactions. (*Figure 1.17*).

The selected dye to be part of the IDA was fluorescein **d**. Fluorescein **d** formed a 1.1 complex with **12**, **d⊂12**, displaying a high stability constant ($5.0 \pm 1.0 \times 10^6$ M^{-1}), which is required for fluorescent IDA. In addition, the formation of **d⊂12** complex resulted in the complete quenching of the fluorescence of **d**. The displacement of **d** from the calix[5]arene cavity by **LPA** ([**d**]= 0.5 μM; [**12**]= 0.4 μM) took place efficiently and led to the formation of the competitive **LPA⊂12** complex, for which a binding constant value of $1.6 \pm 0.1 \times 10^8$ M^{-1} was determined. In aqueous media (pH =7.4), the displacement of fluorescein **d** from the cavity of the receptor **12** provoked a fluorescence “turn-on” sensing of **LPA**.

Moreover, binding studies and dynamic light scattering (DLS) measurements with two control hosts (guanidinium-calix[4]arene **13** and guanidinium-calix[5]arene-O-methylated **14**), confirmed that the cavity size and the conformational rigidity provided by the lower rim alkyl chains of receptor **12** played crucial roles in obtaining nanomolar binding of **LPA**. Notably, the developed sensor presented a LOD as low as 5.6 nM, which compared to other reported fluorescent probes, it represents the lowest LOD value in **LPA** detection. This result also indicated the high sensitivity of the **d⊂12** ensemble.

The study of the fluorescence changes of the **d⊂12** ensemble caused by other biologically important species found in serum (interferences) revealed that ATP produced an even more pronounced "turn-on" response that **LPA**. The ATP interference was solved by using "array sensing" *a.k.a.* differential sensing, which relies on the composite response of the analyte to an array of receptors/ensembles instead of a single one. As shown above (CA inhibitors section), IDAs are highly compatible with setting-up a differential sensing methodology. In the case at hand, the array of IDAs included the guanidinium-calix[4]arene **13** and the Al(III) phthalocyanine chloride tetrasulfonic acid (AlPcS4) as indicator dye. The AlPcS4 is strongly bound by the guanidinium calix receptors **12** and **13** with concomitant fluorescence quenching. Therefore, the reported pairs used in the "array sensing" to differentiate **LPA** to other species in plasma included: **d⊂12,** AlPcS4⊂**12** and AlPcS4⊂**13**. The score plot resulting from executing a principal component analysis *a.k.a.* linear discriminating analysis (LDA) of the sensing array showed that **LPA** was distinguished form other ATP and other plasma coexisting species. The rationale behind the differentiation is that **LPA** can only form a thermodynamically highly stable threading complex with receptor **12** and not with **13**. The ratio of the fluorescence responses (I_{LPA}/I_{ATP}) for receptor **12** is significantly larger than for **13**. To validate the application of the "array sensing" in real samples, the authors attempted the sensing of **LPA** in mouse serum containing different amounts of the analyte. Despite the existence of numerous interferences in the serum, the increase in the fluorescence of the reporter pair AlPcS4⊂**12** showed a liner relationship with the concentration of **LPA**. The authors calculated a LOD of 1.7 μM, which is well below the **LPA** concentration in serum of patients with ovarian and other gynecologic cancers. Inspired by these results, the authors used the reporter pair AlPcS4⊂**12** in the screening of cancerous and non-cancerous blood samples of mice. Consistently, the blood sample of cancerous mice provided a greater fluorescence response. The obtained results demonstrate the potential of the developed IDA in facilitating the diagnosis of ovarian cancer.

- *Glycolipids.*

Glycolipids (GLs) are lipids with a covalently attached carbohydrate. Elevated levels of glycolipids have been found on the cell surface of different types of cancer cells[109] such us gastric[110] and pancreatic[111] cancer. GLs are also important in infection, inflammation and cancer progression.[112]

Boronic acids (**BA**) were successfully employed as excellent receptors for the recognition of *cis*- 1,2 and 1,3-diols through the formation of dynamically covalent cyclic esters. Thus, they are also key components in the construction of chemosensors for monosaccharide detection. The Glass´s group exploited the use of **BA** in the detection of glycolipids using multicomponent IDAs (*Figure 1.18*).[113] The molecular components of the developed IDAs involve a cucurbit[8]uril (**CB**), a lipophilic boronic acid derivate (**BA**), as the selective carbohydrate receptor, and an electron-rich fluorescent indicator dye (**k**).

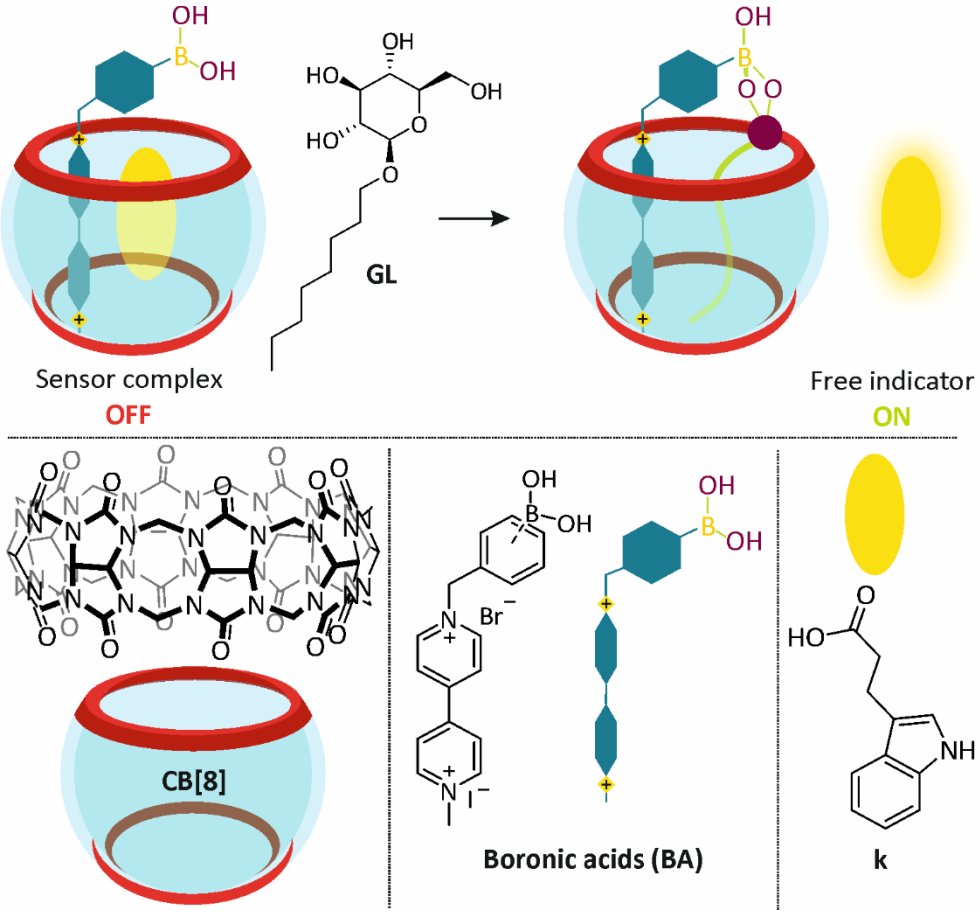

Figure 1.18 Multicomponent IDA sensor including a cucurbituril (**CB**), a boronic acid (**BA**) receptor and a fluorescent dye (**k**) for selective glycolipid detection.

In particular, the boronic acid derivative used as carbohydrate receptor contains a bis-pyridinium unit. On the one hand, the boronic acid is expected to form a cyclic boronic ester with the carbohydrate head-group of the lipid. On the other hand, the

bis-pyridinium cations are known to form 1:1 and 2:1 thermodynamically highly stable complexes with **CB** receptors that are soluble in water. Moreover, the interaction of the **CB[8]** with one bis-pyridinium "functionalizes" the receptor's cavity, making it suitable for the inclusion of complementary electron-rich substrates. It is known that pyridinium ions are good quenchers of electron-rich florescent dyes, providing a potential fluorescence "turn on" on complex dissociation. After screening several boronic acid receptors, the *para*-disubstituted phenyl boronic bis-pyridinum derivative **BA** was found to be optimal for complex solubility and 1:1 binding stoichiometry. Next, the 1:1 complex **BA⊂CB[8]** was tested for the formation of ternary complexes with electron-rich indicators. 3-indolepropionic acid (**k**) was selected as indicator because it made a water soluble ternary complex, **BA●k⊂CB[8]**, with a suitable binding constant for the inclusion of the dye (7×10^3 M^{-1}) and allowing its implementation in IDAsfor GLs. The formation of the ternary complex **BA●k⊂CB[8]** was fully characterized using ^{1}H NMR titrations. Its structure in the solid-state, as a boronate ester with citric acid of the buffer, was revealed by X-ray crystallography. The boronic acid receptor binds **CB[8]** with the boronic acid group outside the aromatic cavity. The indicator dye **k** binds inside the cavity together with the bis-pyridinium quenching residue of the included receptor. Next, the binding properties of the **BA⊂CB[8]** complex were investigated using fluorescence experiments. The titration of the selected fluorescent indicator, 3-indolepoprionic acid (25μM), with **BA⊂CB[8]** (0-350 μM) showed a 93% quenching of the fluorescence of the dye. When the ensemble **BA●k⊂CB[8]**, formed from an equimolar concentration of its components (2.5 mM), was titrated with increasing amounts of the octyl β-glucopyranoside (0-35 mM, **GL**) a threefold increase in fluorescence was observed. The fit of the florescence data to a competitive binding model returned a binding constant value of 1300 M^{-1} for the inclusion of the GL. The addition of other analytes such as glucose, methyl β-glucoside, pentanoic and hexanoic acid produced negligible changes in the fluorescence of the three-componentensemble. Glucose may bind to the boronic acid of the receptor but it does not displace the indicator. The carboxylic acids likely do not bind at all because the lack the glycoside group. In conclusion, the multicomponent sensor seems to be selective for glycolipids. Unfortunately, larger glycolipids caused precipitation and natural counterparts could not be tested.

1.3.3 Sensing of biomarkers related to cardiovascular diseases.

Cardiovascular diseases (CVD) are the leading cause of death worldwide in both developed and emerging countries (*Figure 1.6*). According to the 2019 WHO statistics, ischaemic heart disease (IHD) is the number-one killer in the world. It is responsible for 16% of the world's total deaths. This disease also presented the highest increase in deaths since 2000, going from more than 2 million to almost 9 million in 2019.[50]

- *Cysteine*

Cysteine (**Cys**) and homocysteine (**Hcys**), both sulfur-containing amino acids (AA) are produced from methionine, another sulfur-containing AA. Low levels of **Cys** and elevated levels of **Hcys** (i.e., hyperhomocysteinemia) have been associated with several CVD diseases like ischaemic stroke, neurological disorders, diabetes, lung and colorectal cancer, renal dysfunction and vitiligo.[114]

In a recent study, Ostrakhovitch and Tabibzadeh established that a concentration of **Hcys** of 10 µM or higher is considered a risk factor in the development of CVD and IHD.[115] More precisely, a 5 µM concentration of **Hcys** in plasma increases the relative risk of coronary heart disease by 1.6-1.8 times.[114,116]

Khajehsharifi and Sheini reported a metal-based IDA for the sensing and quantification of **Cys** using the zinc (II) complex of indicator **I** (Zincon, Figure 1.19a).[117] Complex **I●Zn^{2+}** produces a blue colored solution with a large absorption band centered at 617 nm. The binding constant for the complexation of **Zn^{2+}** to **I** was determined using absorption spectroscopy titrations in borate buffer (pH =9.0). The authors reported a value of 1.01×10^7 M^{-1} However, because the titration was performed at 50 µM concentration of **I** and the saturation of the absorbance changes was reached with 1 equiv. of Zn^{2+}, the reported value cannot be considered to be accurate. The detection of **Cys** involved the preparation of the **I●Zn^{2+}** ensemble using 0.1 mM Zincon and 0.05 mM Zn^{2+} concentrations in borate buffer. The resulting solution was titrated with incremental amount of **Cys** (0 - 0.15 mM or 0 – 3 equiv with respect to Zn^{2+}). The addition of **Cys** provoked the diminution of the absorbance of the band at 617 nm and the increase of the intensity of a broad band with maximum at 484 nm. Notably, isosbestic points were not observed during the displacement experiment. The color of the solution changed from blue to orange. These results supported the decoordination of the Zn^{2+} cation from Zincon due to a competitive binding with **Cys**. The authors assigned a 2:1 stoichiometry to the newly

formed complex with **Cys** based on a Job plot analysis. They also assigned a binding constant of 4.1×10^{11} to the complex without specifying units, we assume that they are M^{-2}. They compared the magnitude of the stability constant of the 1:1 complex, **I●Zn^{2+},** with that of **Cys$_2$●Zn^{2+}** counterpart. We consider that this comparison is not correct owing to the different units of the two constants. A fair comparison will involve the square root of the stability constant of **Zn^{2+}●Cys$_2$** with that of **Zn^{2+}●I**. Nevertheless, as stated before for the value of *K*(**I●Zn^{2+}**) that of *K*(**Cys$_2$●Zn^{2+}**) should also be considered as an estimate because the saturation of the complex was achieved in the presence of 2 equiv. of **Cys**. In any case, the formation of the competitive **Cys$_2$●Zn^{2+}** complex is very efficient, which indicates a high thermodynamic stability. Moreover, the kinetics of its formation are also fast because the florescence changes stabilizes after 2 min. The competitive binding was also substantiated using ^{1}H NMR spectroscopy.

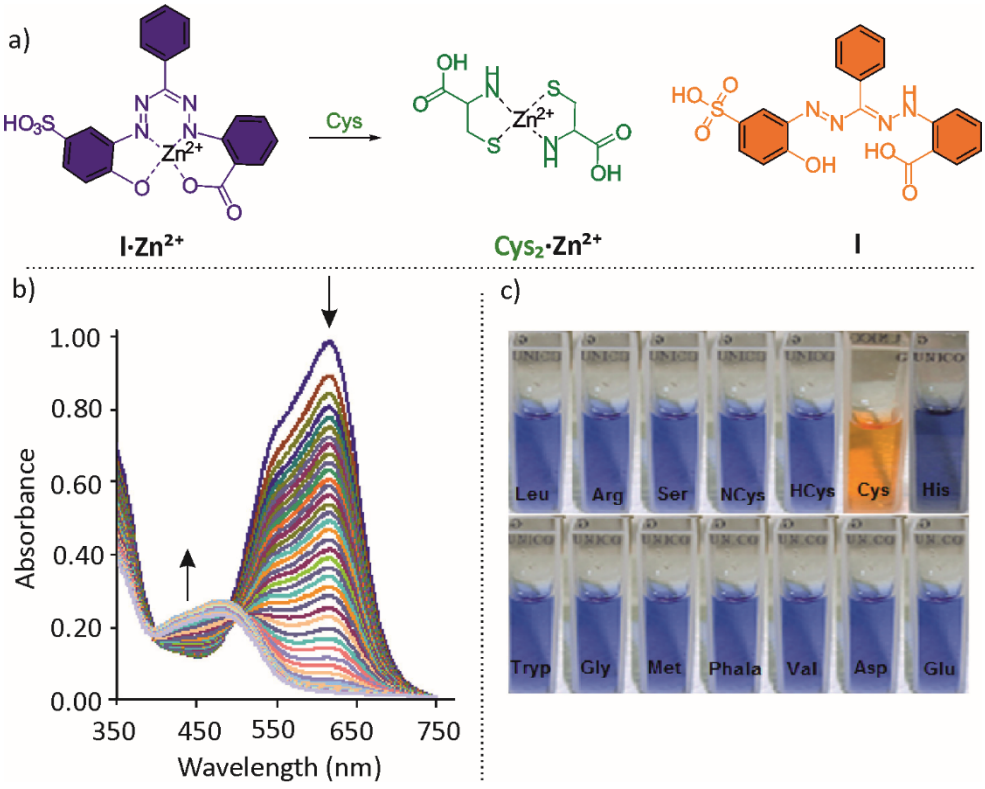

Figure 1.19 a) Line-drawing structures of the zinc (II) complexes of Zincon **I** and cysteine (**Cys**), b) changes in the UV/vis spectra upon the addition of **Cys** (0.0-140.0 µM) to an indicator-receptor complex, c) naked-eye detection of **Cys** (100 µM) over other natural amino acids (80-100 µM) in borate buffer (52.6 Mm, pH 9.0).

The selectivity of the developed IDA for **Cys** detection was evaluated by visual inspection of the color changes experienced by a solution of **I●Zn^{2+}** complex upon addition of other natural amino-acids (AA) like arginine (Arg), asparagine (Asn), glutamine (Gln), glycine (Gly) and others. Only in the presence of **Cys** a noticeable color change from blue to orange-yellow was observed (*Figure 1.19*c). The selectivity, high affinity and linearity, in the range of concentrations of 4.0-94.0 µM, of the developed IDA prompted its application for the selective detection and determination of **Cys** in human urine samples. The recovery values of know added amounts of **Cys** provided a satisfactory precision. The developed IDA represents an example of a simple colorimetric supramolecular chemosensor with feasible medical applications.

Xue et al. reported a related di-nuclear metal-based IDA for the naked-eye detection of **Cys**. The authors took advantages of the intrinsic affinity between Cu^{2+} ions and pyrocathecol violet (**h**) to develop the IDA.[118] To the naked-eye, indicator **h** reversibly binds **Cu^{2+}** ions producing a blue color solution. The subsequent addition of **Cys** strongly competes with **h** for Cu^{2+} binding. As a result, free **h** is released to the bulk solution recovering the original pink color. (*Figure 1.20*).

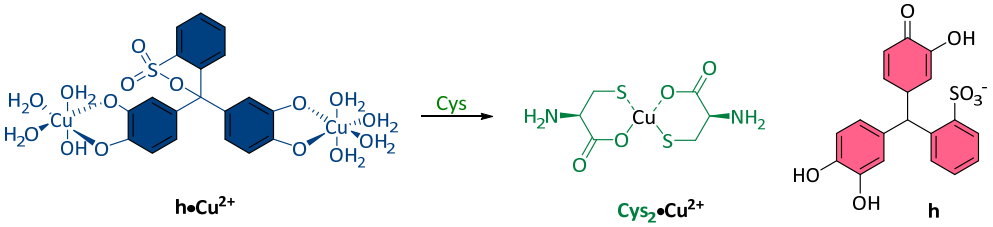

Figure 1.20 Line-drawing structures of **h●Cu^{2+}**, **Cys$_2$●Cu^{2+}** complexes and free indicator **h** used in the IDA-based sensor for **Cys** detection.

The authors also monitored the color changes using UV/vis spectroscopy, both during the titration of **h** with incremental amounts of **Cu^{2+}**, as well as in the displacement reaction of the indicator by competitive coordination the **Cu^{2+}** ions to **Cys**. The addition of **Cu^{2+}** (0-100µM) to a 0.1 M sodium borate buffer solution (pH= 9.0) of 50µM solution of PV, **h**, produced a red shift (Δλ = + 126 nm) to the maximum of the absorption peak of **h** centered at 491 nm, as well as a change in color from pink to blue. The addition of **Cys** to the solution containing **h●Cu^{2+}** ensemble provoked a blue shift (Δλ = -126 nm) of the maximum absorption peak returning to its original position (491 nm). When others natural AA like glycine (Gly), histidine (His), leucine (Leu) were added to the ensemble, no color changes where observed

by the naked-eye, as weel asin the UV/vis absorption spectra of the corresponding titration experiments.

- *Trimethylamine N-oxide (**TMAO**)*

During many years, experts have claimed that the excessive consumption of red meat might raise the risk of heart disease as it is high in saturated fat. Recent studies highlight also that high levels of trimethylamine *N*-oxide (**TMAO**) in blood are directly related with higher risk for CVD. People with high levels of **TMAO** in blood have more than twice the risk of heart attack, stroke, or another serious CVD.[119,120,121] For this reason, the development of sensing approaches for the early detection of TMAO becomes evident.

In 2019, Yu et al. screened different water-soluble macrocycles, including cyclodextrins (α-, β-, and γ-CD), *p*-sulfonatocalix[n]arenes (SCnAs, n = 4, 5, 6) and cucurbit[n]urils (CBn, n = 6, 7, 8, as potential receptors of **TMAO**.[122] They discovered that the guanidinium-modified water soluble calix[5]arene (**12**) as the optimal receptor **TMAO**. The tetra-cationic receptor **12** binds **TMAO** in submicromolar-level.

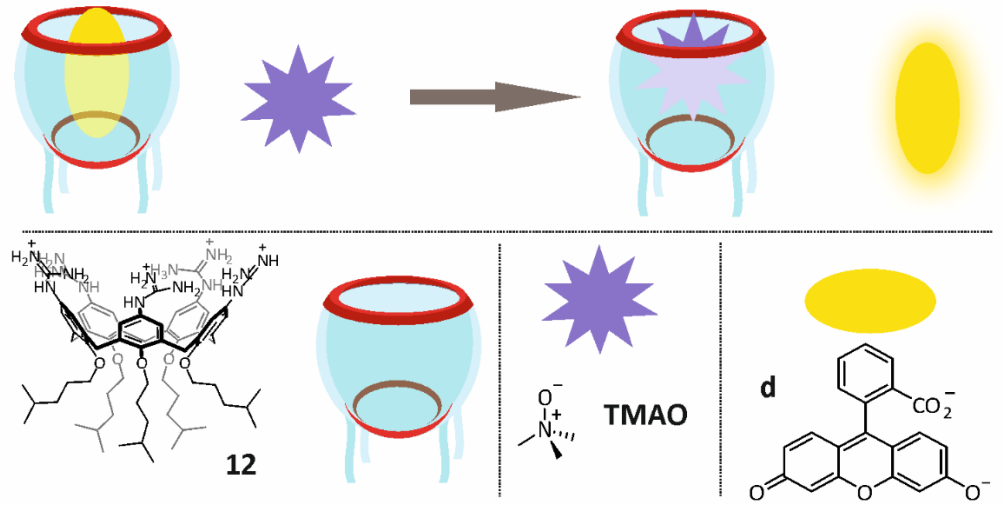

Figure 1.21 Schematic "turn on" fluorescent IDA for selective **TMAO** detection. Adapted from reference 122.

The authors took advantage of the strong interaction established receptor **12** and **TMAO** to design an IDA using fluorescein (**d**) as indicator. The interaction between receptor **12** and indicator **d** was previously characterize using absorption and emission titration experiments (LPA section). The binding constant value for the 1:1

d●12 complex is (5.0 ± 1.0) × 10^6 M^{-1}.[108] As mentioned above, (**LPA** section) the formation of the **d●12** complex caused a decrease on the emission intensity of **d**. The incremental addition of **TMAO** (0-2.52 mM) to a solution of the reporter pair **d●12** (0.8/1μM) displaces the indicator from the calixarene cavity to the bulk solution. Concomitantly, the **TMAO●12** complex is formed. The release of the indicator produced a fluorescence "turn on" (*Figure 1.21*). The fit of the florescence changes of the IDA to a competitive binding model assigned as a binding constant value of 1.61 ± 0.04 × 10^4 M^{-1} to the **TMAO●12** The developed sensing assay was successfully used in the detection of **TMAO** in aqueous media (LOD = 8.98 ± 0.06 μM), artificial urine samples (LOD = 28.88 ± 1.59 μM) and authentic human urine. Interfering analytes commonly found in urine, like creatinine, urea, or glutamic acid (Glu) did not produce detectable changes on the fluorescent properties of the **d●12** complex. It is worthy to mention here, the important interference caused by **LPA** to this reporter pair. Most likely, the hydrophobic effect plays an important role in the stabilization of the **TMAO●12** complex owing to the neutral nature of the analyte. The formation of ionized hydrogen-bonding interactions between the oxygen atom of the *N*-oxide and the NHs of the protonated guanidinium units of the receptor may also be involved in the stabilization of the complex.

1.3.4 Sensing of biomarkers related to Alzheimer´s disease.

The WHO statistics released in 2019, ranked Alzheimer's disease (AD) and other forms of dementia as the 7th leading cause of death worldwide.[50] Women are disproportionately affected. Globally, 65% of deaths from Alzheimer's and other forms of dementia are women.[50] Surprisingly, in Spain this disease rises to the second place (*Figure 1.6*b) with a rate of 90.6 deaths per 100000 population.

This neurodegenerative disease owes its name to the German psychiatrist and neurologist Dr. Alois Alzheimer, who made the first diagnosis of this disease to a German woman named Auguste Deter. After her death in 1906, the number of people diagnosed with AD continues to grow. The diagnosis of AD affects not only the patient but the entire family and their supporting caregivers.[123]

- *Peroxynitrite*

Peroxynitrite ($ONOO^-$)-produced by diffusion-controlled reaction of nitric oxide with superoxide radical- is a short-lived oxidant species considered as a potent inducer of cell death. It can easily diffuse throughout neuronal membranes damaging lipid, proteins and nucleic acids. Particularly in proteins, peroxynitrite mainly reacts with

the phenolic ring of the tyrosines forming nitro-tyrosines affecting dramatically to the physiological functions of the proteins. Protein nitro-tyrosination is an irreversible process that also yields to the accumulation of the modified proteins contributing to the onset and progression of neurodegenerative processes such as Alzheimer's disease and Parkinson's disease.[124]

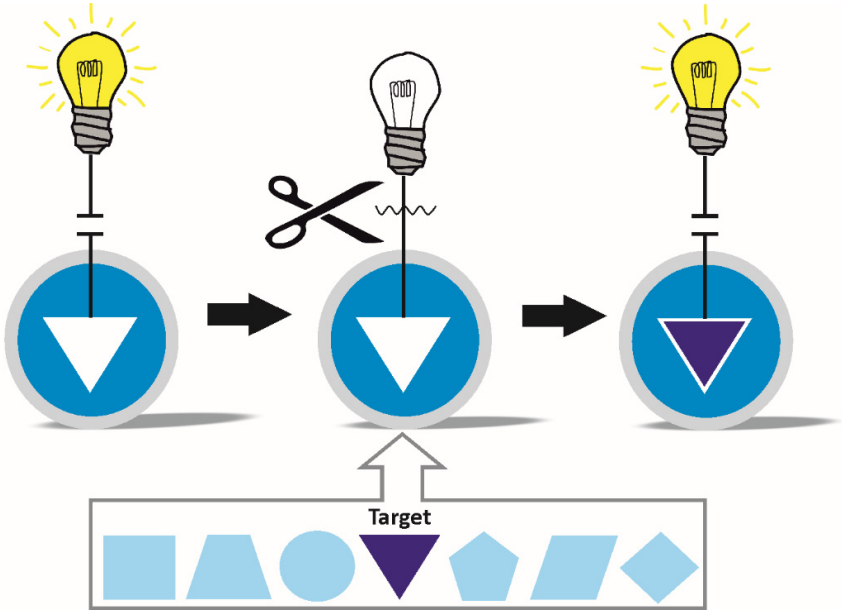

Figure 1.22 Schematic representation of a Reaction-based Indicator Displacement Assay (RIA). Adapted from reference 125

Taking advantage of the properties of peroxynitrite and others reactive oxygen species (ROS), Sun et al. developed a chemosensor in which the functionalized indicator is returned to its original form after reaction with the analyte (peroxinitrite). Indicator-displacement assays that are mediate by a chemical reaction are called Reaction-based Indicator Displacement Assay (RIA) (*Figure 1.22*).[125] In analogy to the IDAs, the design of a RIA involves the initial formation of a host-indicator complex. However, in an RIA the initial complex is not supramolecular. The host and the indicator are covalently connected. The addition of the analyte will produce a chemical transformation breaking the covalent bonds joining the host (receptor) with the indicator. The chemical reaction provides a measurable change of the properties of the solution (e.g. optical signal).

In the RIA developed by Sun et al., the highly fluorescent and dynamically covalent **m-NBA** complex is formed through a boronate ester junction between 2-(*N*,*N*-

dimethylaminomethyl)phenylboronic acid (**NBA**) and Alizarin Red S (**m**). This dynamically covalent complex was used for the selective detection of peroxynitrite. The developed RIA showed a LOD of 5.4 µM (*Figure 1.23*).

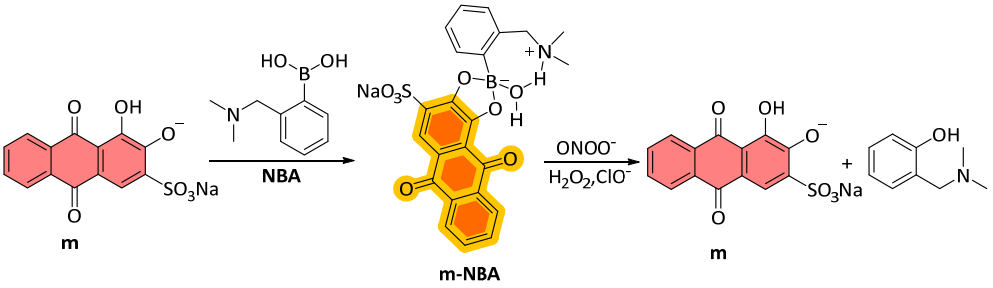

Figure 1.23 Line-drawing structures of the indicator **m**, boronic acid **NBA** (receptor) and the fluorescent and dynamically covalent complex **m**-**NBA** used in the RIA for peroxynitrite detection and quantification.

The authors evaluated the changes experienced by the optical properties of indicator **m** at different pHs and after the addition of three different boronic acids (receptors); phenyl boronic acid (PBA), benzoboroxole (BBA) and 2-(*N,N*-dimethylaminomethyl)phenylboronic acid (**NBA**). At neutral pH, all boronic acid derivatives produced small changes to the optical properties of indicator **m**. On the other hand, at pH 8.10, **NBA** induced more significant changes to the optical properties of **m** than the other boronic acid structures. The optical changes were detected by the naked-eye as a change in the solution color from pink to orange. Moreover, the reaction of **m** with **NBA** produced a *ca*. 15-fold increase of the fluorescence intensity of the former. Absorption spectroscopy evidenced that the reaction between **NBA** and **m** produced a 55 nm blue shift of the maximum of absorbance of the dye, from λ_{max} = 520 nm to λ_{max} = 465 nm. The authors determined that the binding constant for the formation of the cyclic aryl boronate ester complex **m-NBA** was of the order of 10^3 M^{-1}.

The addition of peroxynitrite caused the oxidation of the aryl boronate-**m-NBA** adduct producing the corresponding phenol, from the boronic acid, and releasing indicator **m**. Consequently, the solution experienced a decrease in fluorescence and a bathochromic shift of the absorbance band. The selectivity of the **m**-**NBA** RIA for peroxynitrite over hydrogen peroxide (H_2O_2), hypochlorite (ClO^-) and others ROS species was also demonstrated. The same research group, previously demonstrated that the insertion of an hydroxyl ion in the boronic ester formation caused an enhancement in the interaction between the nitrogen atom of the amino group and

the boron atom.[126] This improved N-B interaction provides a protection for the boronic acid towards oxidation with H_2O_2, ClO^- or other ROS species. Only powerful oxidants as peroxynitrite can overcome the protection given by the N-B interaction.

1.3.5 Sensing of biomarkers related to diabetes disease.

Based on the WHO statistics around 422 million people suffer diabetes worldwide. From 2000 to 2019 diabetes has increased a 70%, entering in the list of top 10 causes of death. It moved from the 15th to 9th leading cause of death worldwide (*Figure 1.6*a).[50]

Diabetes is a chronic disease in which the pancreas does not produce enough insulin or when the body in not able to use properly the insulin it produces. Insulin is a hormone that regulates blood sugar. Over time, diabetes causes serious complications like heart disease, stroke damage to the nerves and kidneys, limb amputation, and blindness.[127] As a result, assays for the selective detection of glucose or other biologically important carbohydrate in blood at physiologically relevant levels are highly desired. The contribution of the supramolecular chemistry in developing molecular sensors for glucose has been nicely collected by Sun and D. James.[127]

- *Saccharides*

Saccharides, also called carbohydrates or natural sugars, are polyhydroxylated aldehydes or ketones with the empirical formula $C_m(H_2O)_n$ (where m could be different from n). These molecules form a wide range of structures going from the most basic form (monosaccharide) to more complex structures composed of hundreds or thousands of monosaccharides (polysaccharides). Saccharides play an important role in many biological processes ranging from molecular composition to functional, physiological, and biochemical behavior. [128]

As already mentioned in the section dealing with the sensing of glycolipids, the reversible interaction of a boronic acid with a 1,2- or 1,3-diol (dynamically covalent formation of a boronate ester) makes boronic acids excellent components of saccharide receptors. In a recent review, Williams et al.,[129] highlighted not only the significance of detecting saccharides for biomedical applications, but also the huge efforts made by several research groups aiming to better understand its binding properties. This knowledge is very important to improve the design of more selective saccharides' chemosensors.

In this vein, Minami´s group has made important contributions. In 2019 they reported a simple colorimetric IDA chemosensor array for detection and discrimination of saccharides.[130] Unlike other saccharide sensors that require demanding synthetic efforts, the approach reported by Minami et al. used an IDA array design based on commercially available and inexpensive compounds: 3-nitrophenylboronic acid (**3-NPBA**) was selected as receptor and combined with four catechol-based indicators (**m**, **n**, **o**, **h**) (*Figure 1.24*). The saccharides' detection was successfully achieved thanks to the dynamic covalent-binding of the boronate esters in which the IDA array is based. The esterification reaction of the boronate group of receptor **3-NPBA** with the catechol indicators (**m**, **n**, **o**, **h** produces a color change of its aqueous solutions). Monosaccharides compete with the indicators for the formation of cyclic boronate ester with the receptor. Thus, saccharides displace the indicators from the dynamically covalent complexes formed with **3-NPBA.** The release of the indicators to the solution induce the recovery of its original optical properties.

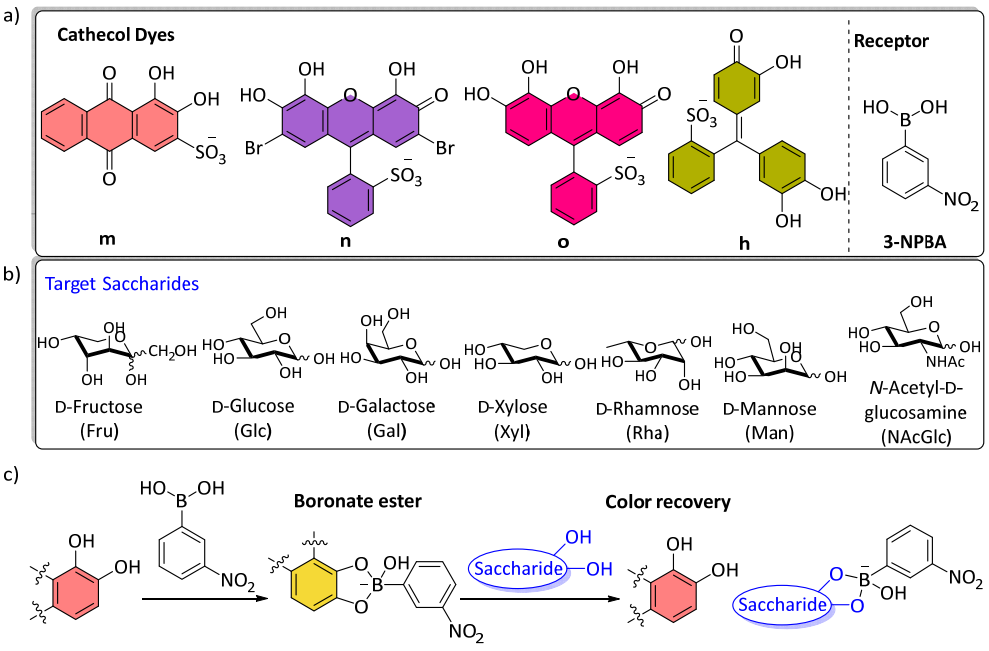

Figure 1.24 Line-drawing structures of: a) cathecol dyes (**m**, **n**, **o**, **h**) and 3-nitrophenylboronic acid (**3-NPBA**) used as a diol receptor, b) target monosaccharides and c) schematic IDA-based boronic acid for saccharide colorimetric detection. Adapted from reference 130.

The saccharide discrimination of the assay was realized because each saccharide produced a different spectrophotometric response (finger print-like response) on

the IDA array. Each one of the four**dye-3-NPBA** complexes of the array experienced a different change of absorption upon the addition of the saccharides. A linear discrimination analysis (LDA) of the array was used for the qualitative sensing of the saccharides achieving a classification success of 100%. Moreover, a support vector machine algorithm (SVM) was also successfully applied for the quantitative application of the assay.

The same research group reported a fluorescent IDA for phosphorylated saccharides. They employed a similar strategy to the one described above. In this case, they selected the same receptor (**3-NPBA**) but combined it with two coumarin derivatives (**p** and **q**) as fluorescent probes (*Figure 1.25*). The spectroscopic changes of the IDA array were monitored using fluorescence spectroscopy. The development of sensing systems for phosphorylated saccharides are of high relevance, since abnormal levels of these biomolecules in glycolysis are related with glycogen storage diseases like von Gierke disease or Pompe disease among others. [131] Qualitative and quantitative analysis were also performed by using LDA and SVM, respectively. For practical purposes, the developed fluorescent IDA array was applied to monitor the glycolytic activity of human induced pluripotent stem (hiPS) cells.

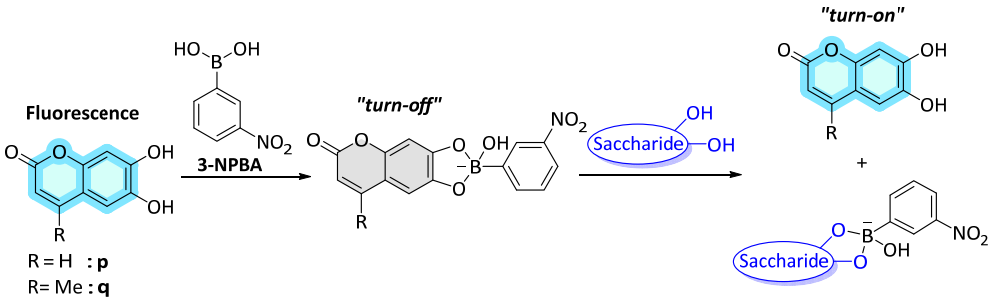

Figure 1.25 Line-drawing structures of receptor (**3-NPBA**) and fluorescent indicators (**p**, **q**) used in the IDA sensor for phosphorylated saccharides detection.

As shown above, boronic acids are extensively used for the sensing of carbohydrates and saccharides in water solution. However, the low binding affinity and solubility of single boronic acids limits their application in physiological conditions. To overcome these limitations, Bonizzoni et al. attached phenylboronic acid moieties to a hydrophilic poly(methacrylic acid) (**PMAA**) generating a water soluble poly(methacrylic acid)-*co*-3-(acrylamido)phenylboronic acid (**PMAA-*co*-AAPBA**). They used this material as a water-soluble polymeric receptor to detect and

differentiate sugars using an IDA array (*Figure 1.26*).[132] In this work, the authors also demonstrated, in agreement with previous NMR and computational studies, that boronic acids bind more efficiently 1,2-diols, forming five-membered cyclic moieties, than 1,3-diols, producing six-membered counterparts.

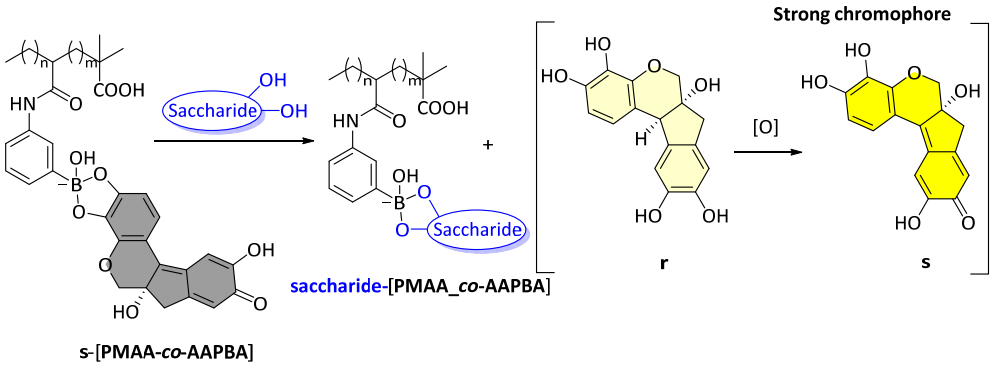

Figure 1.26 Structures of the compounds and polymers involved in the IDA-based on boronic acid polymers for the colorimetric detection mono and di-saccharides. Adapted from reference 132

After screening a series of anionic, cationic and neutral dyes, the authors found that hematoxylin (**r**) binds efficiently to the **PMAA-*co*-AAPBA** resin. However, they observed that a buffered water solution (pH 7.4) of **r** experienced changes in absorption over time. The observed changes were attributed to the oxidation of the dye from **r** to **s** under atmospheric conditions. Since **s** is a stronger chromophore and retains one 1,2-*cis*-diol moiety, it was finally selected as the optimal dye. The authors controlled the oxidation process by adding ascorbate as suitable antioxidant.

The addition of incremental amounts of **PMAA-*co*-AAPBA** to an oxidation stabilized solution of **s** provoked a decrease in the intensity of the absorption band centered at 556 nm. This change was attributed to the formation of the **s**-[**PMAA-*co*-AAPBA**] complex. The release of the indicator dye **s** to the solution caused by the competitive binding of the saccharide to the copolymer [**PMAA-*co*-AAPBA**], gradually restores the absorption intensity. Differentiation of sugars was achieved through multivariable detection and LDA analysis. Two important contributions can be inferred from this work: i) the synthesis of copolymer **s**-[**PMAA-*co*-AAPBA**], as a novel analytical tool for saccharides discrimination in neutral aqueous media and ii) the reported findings extend our understanding of the use of boronic acids for the binding of sugars trough the formation of cyclic boronates in polymers..

1.4. Conclusions

An early detection and clinical diagnosis of a disease allows a promptly medical treatment and could prevent complications and rapid worsening, which may either cure the disease or improve the outcome of the patient. Identification of reliable biomarkers -biological indicators of normal or pathogenic processes- is useful not only for the early detection of a disease but also for monitoring its progression.

Supramolecular chemistry, through semiochemistry, offers a unique and powerful toolkit for the recognition and sensing of biomarkers. Development of chemosensors able to fulfill this task constitutes an active area of research in supramolecular chemistry. In recent years, this area has gained attention because the developed sensors show high sensitivity, selectivity, rapid response time and versatility. A common approach used in the design of chemosensor is binding-based sensing (BBS). The BBS methodology involves the covalent attachment of the recognition site with the signaling unit. In some cases, the synthesis of covalent chemosensors can be very challenging and the signal changes caused by the binding of the analyte can be small. In this chapter, we demonstrated that an elegant and versatile sensing alternative is the development of Indicator Displacement Assays (IDAs). That is, to design reversible indicator-receptor pairs producing changes on the optical properties of the bound indicator compared to the free counterpart. The presence of the target analyte (as a competitive guest for the receptor) displaces the indicator from the receptor binding site forming the analyte-receptor complex and resulting in a recovery of the original indicator´s optical properties.

The pioneering detection of the neurotransmitter acetylcholine reported by Inouye, revealed the potential use of indicator displacement assays in molecular sensing. However, this methodology became popular thanks to the studies of Professor Eric V. Anslyn and his research group at the University of Texas, USA. Prof. Anslyn group and many others groups have reported beautiful examples of the use of indicator displacement assays for the sensing of a wide range of ionic and neutral guests.

In this chapter, we focused on supramolecular sensors for the detection of biomarkers operating by optical IDAs. The development of IDAs represents a positive contribution for the early detection and proper monitoring of diseases. We classified the examples based on different diseases and targeted analytes. Some IDAs can contribute to the diagnosis of several diseases.

Kidney diseases: Citrate (Cit), oxalate (**Ox**) and creatinine (**Cr**).

Cancer: Pyrophosphate (**PPi**), glutathione (**GSH**), carbonic anhydrases (**CAs**), sialic acid (**SA**), lysophosphatidic acid (**LDA**) and glycolipids.

Cardiovascular diseases: Cysteine (**Cys**), homocysteine (**Hcys**) and trimethylamine *N*-oxide (**TMAO**).

Alzheimer´s disease: Peroxynitrite.

Diabetes: Saccharides.

Most of the examples presented here, displayed good selectivity towards the target analyte with outstanding LOD ranging from μM to nM. However, this review reveals the absence of chemosensors operating under IDA mechanism for the detection of biomarkers that can contribute to the diagnosis or monitor neonatal, intestinal or respiratory diseases, which provide a significant number of deaths worldwide. As well as, the lack of IDA-based sensors for other biomarkers apart from peroxynitrite for an early detection of Alzheimer´s disease. We anticipate that the developing of IDA-based chemosensors for AD biomarkers in cerebrospinal fluid (CFS)[133] like tau protein (an indicator of neuronal damage), hyperphosphorylated tau protein (indicative of tau fibrillization and tangle formation) or amyloid $\beta_{1\text{-}42}$ (components of senile plaques) would have a tremendous impact in the current clinical standards for the diagnosis of the disease and would provide a powerful tool for early detection.

On the other hand, from this review becomes evident the lack of diversity of IDA approaches for saccharides detection. Even though the boronic acids have been successfully employed for this purpose, its inherent low water solubility and selectivity (almost any *cis*-1,2 or 1,3 diol moiety binds BA) makes it necessary to develop new IDA-based chemosensors that can overcome these drawbacks.

We are convinced that the supramolecular chemistry will continue providing more and better IDA assays to cover others biomarkers or/and improve existing ones.

1.5. Aims of the thesis

The aim of the research work presented in this thesis is the design and preparation of molecular containers for their use in molecular sensing and catalysis of chemical reactions. For this purpose, we selected calix[4]pyrrole cavitands as binding sites

due to their well-known molecular recognition and inclusion properties towards polar neutral molecules.

More precisely, we based our designs for molecular sensing applications on cavitands featuring phosphonate groups as bridging units connecting the aromatic panels of aryl-extended calix[4]pyrroles. We expected that the unique structure offered by these phosphonate calix[4]pyrrole cavitands could be exploited in the selective recognition of biologically relevant small polar molecules such as creatinine or amino acids.

On the other hand, for catalysis applications we focused our efforts on phosphoramidite calix[4]pyrrole ligands - non-oxidized phosphonate precursors. We expected that these cavitands will not only retain the binding properties of these receptors, but also would allow its use as ligands to prepare coordination complexes with transition metals (e.g. gold) to be used in as supramolecular catalysts.

In order to achieve this main objective, we pursued the following goals.

O.1) Design and synthesis of phosphonate calix[4]pyrrole receptors featuring different number and orientation of the P=O group.

Calix[4]pyrrole cavitands bearing an inwardly oriented P=O group are known to effectively bind creatinine and its derivatives forming 1:1 complexes, which are thermodynamically and kinetically stables. The superior binding displayed by this cavitands towards creatinine is understood in terms of the good size, shape and function complementarity. Moreover, the neutral creatinine is able to stablish four hydrogen bond interaction with the pyrrole NH of the receptor, and the phosphonate group inwardly oriented provide an extra hydrogen bond by interacting with the NH protons of the creatinine. Our purpose is to synthesize a series of calix[4]pyrrole featuring different number and orientation of the P=O group and characterize thermodynamically and kinetically their complexes with creatinine by means of NMR (^{1}H and ^{31}P) and ITC experiments. We envisaged that this characterization will allow to elucidate the contribution of the phosphonate group in the selective recognition of this analyte. The understanding of intermolecular forces involved in the formation of a host-guest complex, should allow the implementation of this knowledge in the design of new phosphonate molecular receptors with improved binding properties.

O.2) Incorporation of fluorophore units in calix[4]pyrrole cavitands and explore their use in the molecular sensing of biologically relevant polar molecules.

The development of chemosensors for the selective recognition of biomarkers would contribute to the early diagnosis of diseases and in this way improve its therapeutic treatments. Our plan is to synthesize and characterize (e.g. 1D and 2D NMR, HR MS, X-ray diffraction) various chemosensors based on phosphonates calix[4]pyrrole cavitands with a fluorescent tag (e.g dansyl group) covalently attached. We plan to evaluate their binding properties in organic solution mainly for creatinine (biomarker of renal function) or its lipophilic analogue. Binding of amino acids (proline, pipecolic acid) will be also pursued. We will characterize the fluorescent cavitands by UV-Vis absorption and emission spectroscopy. We plan to study two different sensing approaches with the developed chemosensors: i) binding-based-sensing (BBS) and ii) indicator-displacement-assay (IDA).

O.3) Design and synthesis of phosphoramidite calix[4]pyrrole gold(I) coordination complexes and study of their catalytic properties for alkyne hydration reaction.

Enzymes- the most efficient nature catalysts- have been a persistent source of inspiration for synthetic reaction development. From a structural point of view, enzymes offer a confined space (binding site) where the substrate is accommodated, and a catalytic site where the chemical transformations take place. We aim to produce synthetic receptors that can mimic enzymes.

In this regard, gold-phosphoramidite calix[4]pyrrole cavitands could be ideal candidates for this purpose. On one hand, the calix[4]pyrrole scaffold will provide a polar cavity for the molecular recognition of a substrate (binding site). On the other hand, the phosphoramidite moiety will provide a coordination site for the incorporation of the transition metal (i.e. Au(I)) necessary for the catalytic site. We plan to study the catalytic performance of the gold(I) complexes in the hydration reaction of a series of terminal alkynes derivatives.

1.6. Outline of the thesis.

The present doctoral thesis is divided in six chapters, as follows: A general introduction (**Chapter 1**), five chapters containing a more specific introduction, results and discussion, and the corresponding experimental section (**Chapter 2-6**). We also included a final section summarizing the conclusions of this research.

In **Chapter 2**, we describe the synthesis of a series of calix[4]pyrrole which differ in the number (0, 1 and 2) and orientation of the bridging phosphonate group with respect to the cavity (inward and outward). We first probed the interaction between the synthesized calix[4]pyrroles and the hexylcreatinine (**HexCr**, the lipophilic version of creatinine) by means of ^{1}H and ^{31}P NMR experiments. We used isothermal titration calorimetry (ITC) experiments to assess accurately the stability constant values for the calix[4]pyrrole complexes in dichloromethane. Thermodynamic parameters (ΔH, ΔS and ΔG) were also extrapolated from the fit of the calorimetric titration data. The direct comparison of these thermodynamic parameters allows to elucidate the contribution of the phosphonate group in the creatinine recognition. We demonstrated that possess a bridging phosphonate group inwardly oriented with respect to the cavity provides a contribution from around 2.0 kcal·mol^{-1} in the **HexCr** complex formation.

Chapter 3 deals with the preparation of two chemosensor based on phosphonate calix[4]pyrrole scaffold and operating through Indicator displacement assay (IDA) for the selective recognition of creatinine. In one of the developed chemosensor, the signaling unit (dansyl group) was covalently attached to the calix[4]pyrrole structure by means of a sulfonamide bond. A first interaction between the fluorescent calix[4]pyrrole and a black hole quencher (**BHQ**) provoked a quenching effect on the characteristic dansyl emission. A subsequent addition of creatinine or hexylcreatinine induced a “turn on” response of the emission of the dansyl unit. For the second IDA, we designed a fluorescent indicator based on pyridyl N-oxide and connected to a pyrene unit by an ethenyl spacer. A quenching effect on the dye emission was detected by complexation with a non-fluorescent monophosphonate calix[4]pyrrole cavitand. The displacement of the dye from the calix[4]pyrrole cavity by incremental addition of creatinine or hexylcreatinine caused the recovery of the fluorescent of the dye. The reported findings demonstrated that calix[4]pyrrole receptors are an excellent alternative as chemosensors for the creatinine detection.

In **Chapter 4**, we report the synthesis of an unprecedent fluorescent calix[4]pyrrole receptor equipped with a signaling unit directly attached on the phosphonate bridging group. We evaluated the ability of the developed calix[4]pyrrole as chemosensor for the detection of L-proline and L-pipecolic acid by using two different sensing approaches; i) binding-based-sensing (BBS) and ii) indicator displacement assay (IDA). We demonstrated that the fluorescent calix[4]pyrrole cavitand can operate through both sensing approaches. However, due to the small changes detected by BBS, is the IDA the most appropriate strategy to achieve the fluorescent sensing of the amino acids.

In **Chapter 5**, we describe the synthesis of a "four wall" calix[4]pyrrole receptor in which two aromatic walls are connected by a phosphonate bridging group, we connected an undecenyl chain on one of the remain aromatic wall and finally, we attached on the last remain aromatic wall a dansyl group via sulfonic ester bond. We demonstrated that this unique design offers three important features: On one hand, the phosphonate group offer an extra hydrogen bonding in the creatinine recognition (**Chapter 1**). Adittionallly, the undecenyl chain will allow the covalent anchoring of this receptor on silicon surfaces for further studies in water media and/or real body samples (e.g blood serum or urine). Finally, we prove that the developed fluorescent calix[4]pyrrole is able to recognize directly the presence of creatinine. In other word, it can operate through a BBS.

Chapter 6 deals with the preparation of two gold phosphoramidite receptor based on calix[4]pyrrole scaffold. We used n-hexyne to prove the catalytic activity of the synthesized receptors and also to find the proper conditions to perform alkyne hydrations. Next, we examine the catalytic performance of the gold calix[4]pyrrole receptor towards alkyne hydration reaction using three different substrates, which differ in the polarity of the knob interacting with the calix[4]pyrrole cavity. We employ GC-FID analysis in order to determine its rate constants values. We conclude that polar substrates can behave as gold ligands or guest for the receptor´s cavity. The results indicate that higher polar substrates have a lower catalytic performance.

1.7. References and notes.

[1] A. Gale, P.; L. Sessler, J.; Král, V. *Chem. Commun.* **1998**, 1-8.
[2] Baeyer, A. *Berichte der deutschen chemischen Gesellschaft* **1886**, *19*, 2184-2185.
[3] Gale, P. A.; Sessler, J. L.; Král, V.; Lynch, V. *J. Am. Chem. Soc.* **1996**, *118*, 5140-5141.

[4] Ballester, P. *Isr. J. Chem.* **2011**, *51*, 710-724.
[5] Blas, J. R.; Márquez, M.; Sessler, J. L.; Luque, F. J.; Orozco, M. *J. Am. Chem. Soc.* **2002**, *124*, 12796-12805.
[6] Sessler, J. L.; Gross, D. E.; Cho, W.-S.; Lynch, V. M.; Schmidtchen, F. P.; Bates, G. W.; Light, M. E.; Gale, P. A. *J. Am. Chem. Soc.* **2006**, *128*, 12281-12288.
[7] Tong, C. C.; Quesada, R.; Sessler, J. L.; Gale, P. A. *Chem. Commun.* **2008**, 6321.
[8] Saha, I.; Lee, J. T.; Lee, C.-H. *Eur. J. Org. Chem.* **2015**, *2015*, 3859-3885.
[9] Villarón, D.; Siegler, M. A.; Wezenberg, S. J. *Chem. Sci.* **2021**, *12*, 3188-3193.
[10] Molina-Muriel, R.; Aragay, G.; Escudero-Adán, E. C.; Ballester, P. *J. Org. Chem.* **2018**, *83*, 13507-13514.
[11] Gale, P. A.; Sessler, J. L.; Král, V. *Chem. Commun.* **1998**, 1-8.
[12] Allen, W. E.; Gale, P. A.; Brown, C. T.; Lynch, V. M.; Sessler, J. L. *J. Am. Chem. Soc.* **1996**, *118*, 12471-12472.
[13] Sun, Q.; Escobar, L.; De Jong, J.; Ballester, P. *Chem. Sci.* **2021**.
[14] Kim, S. K.; Lee, J.; Williams, N. J.; Lynch, V. M.; Hay, B. P.; Moyer, B. A.; Sessler, J. L. *J. Am. Chem. Soc.* **2014**, *136*, 15079-15085.
[15] Gil-Ramírez, G.; Benet-Buchholz, J.; Escudero-Adán, E. C.; Ballester, P. *J. Am. Chem. Soc.* **2007**, *129*, 3820-3821.
[16] Sun, Q.; Escobar, L.; Ballester, P. *Angew. Chem., Int. Ed.* **2021**, *60*, 10359-10365.
[17] Escobar, L.; Villarón, D.; Escudero-Adán, E. C.; Ballester, P. *Chem. Commun.* **2019**, *55*, 604-607.
[18] Moncelsi, G.; Escobar, L.; Dube, H.; Ballester, P. *Chem. Asian J.* **2018**, *13*, 1632-1639.
[19] Sekiya, R.; Díaz-Moscoso, A.; Ballester, P. *Chem. Eur. J.* **2018**, *24*, 2182-2191.
[20] Martínez-Crespo, L.; Sun-Wang, J. L.; Sierra, A. F.; Aragay, G.; Errasti-Murugarren, E.; Bartoccioni, P.; Palacín, M.; Ballester, P. *Chem* **2020**, *6*, 3054-3070.
[21] Martínez-Crespo, L.; Sun-Wang, J. L.; Ferreira, P.; Mirabella, C. F. M.; Aragay, G.; Ballester, P. *Chem. Eur. J.* **2019**, *25*, 4775-4781.
[22] Kim, D. S.; Sessler, J. L. *Chem. Soc. Rev.* **2015**, *44*, 532-546.
[23] Guinovart, T.; Hernández-Alonso, D.; Adriaenssens, L.; Blondeau, P.; Martínez-Belmonte, M.; Rius, F. X.; Andrade, F. J.; Ballester, P. *Angew. Chem., Int. Ed.* **2016**, *55*, 2435-2440.
[24] Guinovart, T.; Hernández-Alonso, D.; Adriaenssens, L.; Blondeau, P.; Rius, F. X.; Ballester, P.; Andrade, F. J. *Biosens. Bioelectron.* **2017**, *87*, 587-592.
[25] Erenas, M. M.; Ortiz-Gómez, I.; De Orbe-Payá, I.; Hernández-Alonso, D.; Ballester, P.; Blondeau, P.; Andrade, F. J.; Salinas-Castillo, A.; Capitán-Vallvey, L. F. *ACS Sensors* **2019**, *4*, 421-426.
[26] Sierra, A. F.; Hernández-Alonso, D.; Romero, M. A.; González-Delgado, J. A.; Pischel, U.; Ballester, P. *J. Am. Chem. Soc.* **2020**, *142*, 4276-4284.
[27] Sierra, A. F.; Aragay, G.; Peñuelas-Haro, G.; Ballester, P. *Org. Chem. Front.* **2021**, *8*, 2402-2412.
[28] Buranaprasertsuk, P.; Tangsakol, Y.; Chavasiri, W. *Catal. Commun.* **2007**, *8*, 310-314.
[29] Cafeo, G.; De Rosa, M.; Kohnke, F. H.; Neri, P.; Soriente, A.; Valenti, L. *Tetrahedron Lett.* **2008**, *49*, 153-155.
[30] Hulanicki, A.; Glab, S.; Ingman, F. *Pure Appl. Chem.* **1991**, *63*, 1247-1250.
[31] Kim, D.; Kang, D. *Sensors* **2008**, *8*, 6605-6641.

[32] Steed, J. W. a. A., J.L. In *Supramol. Chem.*; Wiley, Ed. 2009, p 707-775.
[33] Brzechwa-Chodzyńska, A.; Drożdż, W.; Harrowfield, J.; Stefankiewicz, A. R. *Coord. Chem. Rev.* **2021**, *434*, 213820.
[34] Ward, M. D. *Chem. Soc. Rev.* **1997**, *26*, 365.
[35] Jones, G. A.; Bradshaw, D. S. *Front. Phys.* **2019**, *7*.
[36] Wilkinson, F. *Q Rev Chem Soc* **1966**, *20*, 403.
[37] Li, L.; He, L.; Liu, X.; Liu, H.; Hu, L.; Guo, P.; Bu, W. *RSC Advances* **2017**, *7*, 38581-38585.
[38] Iovan, D. A.; Jia, S.; Chang, C. J. *Inorg. Chem.* **2019**, *58*, 13546-13560.
[39] Tsien, R. Y. *Biochemistry* **1980**, *19*, 2396-2404.
[40] Grynkiewicz, G.; Poenie, M.; Tsien, R. Y. *J. Biol. Chem.* **1985**, *260*, 3440-3450.
[41] Minta, A.; Kao, J. P. Y.; Tsien, R. Y. *J. Biol. Chem.* **1989**, *264*, 8171-8178.
[42] Guo, C.; Sedgwick, A. C.; Hirao, T.; Sessler, J. L. *Coord. Chem. Rev.* **2021**, *427*, 213560.
[43] Maffei, F.; Betti, P.; Genovese, D.; Montalti, M.; Prodi, L.; De Zorzi, R.; Geremia, S.; Dalcanale, E. *Angew. Chem., Int. Ed.* **2011**, *50*, 4654-4657.
[44] Rather, I. A.; Ali, R. *Org. Biomol. Chem.* **2021**, *19*, 5926-5981.
[45] Dsouza, R. N.; Pischel, U.; Nau, W. M. *Chem. Rev.* **2011**, *111*, 7941-7980.
[46] Letters will be assigned to the indicators for reference throughout the chapter.
[47] Numbers will be assigned to the receptors for reference throughout the chapter.
[48] Inouye, M.; Hashimoto, K.-I.; Isagawa, K. *J. Am. Chem. Soc.* **1994**, *116*, 5517-5518.
[49] Metzger, A.; Lynch, V. M.; Anslyn, E. V. *Angew. Chem., Int. Ed. Engl.* **1997**, *36*, 862-865.
[50]The top 10 causes of death. https://www.who.int/news-room/fact-sheets/detail/the-top-10-causes-of-death (accessed 27/10/2021).
[51] Gori, T.; Lelieveld, J.; Münzel, T. *Basic Res. Cardiol.* **2020**, *115*.
[52] Hussain, A.; Bhowmik, B.; Do Vale Moreira, N. C. *Diabetes Res. Clin. Pract.* **2020**, *162*, 108142.
[53] Aveyard, P.; Gao, M.; Lindson, N.; Hartmann-Boyce, J.; Watkinson, P.; Young, D.; Coupland, C. A. C.; Tan, P. S.; Clift, A. K.; Harrison, D.; Gould, D. W.; Pavord, I. D.; Hippisley-Cox, J. *Lancet Respir. Med.* **2021**, *9*, 909-923.
[54] Ito, Y.; Sato, Y.; Teramae, N.; Nishizawa, S. *Bunseki Kagaku* **2021**, *70*, 149-157.
[55] Umemoto, S.; Im, S.; Zhang, J.; Hagihara, M.; Murata, A.; Harada, Y.; Fukuzumi, T.; Wazaki, T.; Sasaoka, S.-I.; Nakatani, K. *Chem. Eur. J.* **2012**, *18*, 9999-10008.
[56] Wang, K.; Cui, J.-H.; Xing, S.-Y.; Dou, H.-X. *Org. Biomol. Chem.* **2016**, *14*, 2684-2690.
[57] Monash, A.; Marciano, D.; Colvin, A.; Fass, R.; Dvash, Y.; Rosen, O. *Talanta* **2021**, *224*, 121927.
[58] Goldberg, H.; Grass, L.; Vogl, R.; Rapoport, A.; Oreopoulos, D. G. *Cmaj* **1989**, *141*, 217-221.
[59] Caudarella, R.; Vescini, F.; Buffa, A.; Stefoni, S. *Frontiers in Bioscience-Landmark* **2003**, *8*, 1084-1106.
[60] Lin, Z.; Wu, M.; Schäferling, M.; Wolfbeis, O. S. *Angew. Chem., Int. Ed.* **2004**, *43*, 1735-1738.
[61] Courbebaisse, M.; Prot-Bertoye, C.; Bertocchio, J. P.; Baron, S.; Maruani, G.; Briand, S.; Daudon, M.; Houillier, P. *Rev Med Interne.* **2017**, *38*, 44-52.
[62] Abarghoei, S.; Fakhri, N.; Borghei, Y. S.; Hosseini, M.; Ganjali, M. R. *Spectrochim. Acta, Part A* **2019**, *210*, 251-259.
[63] Granchi, D.; Baldini, N.; Ulivieri, F. M.; Caudarella, R. *Nutrients* **2019**, *11*, 2576.

[64] Schmuck, C.; Schwegmann, M. *Org. Biomol. Chem.* **2006**, *4*, 836.
[65] Zhu, Z.; Zhou, J.; Li, Z.; Yang, C. *Sens. Actuators B Chem.* **2015**, *208*, 151-158.
[66] Greene, E. L.; Farell, G.; Yu, S.; Matthews, T.; Kumar, V.; Lieske, J. C. *Urological Research* **2005**, *33*, 340-348.
[67] Holmes, R. P.; Knight, J.; Assimos, D. G. *AIP Conf. Proc.* **2007**, *900*, 176-182.
[68] Marengo, S. R.; Romani, A. M. P. *Nat. Clin. Pract. Nephrol.* **2008**, *4*, 368-377.
[69] Crivelli, J. J.; Mitchell, T.; Knight, J.; Wood, K. D.; Assimos, D. G.; Holmes, R. P.; Fargue, S. *Nutrients* **2020**, *13*, 62.
[70] Hirvonen, T.; Pietinen, P.; Virtanen, M.; Albanes, D.; Virtamo, J. *Am. J. Epidemiol.* **1999**, *150*, 187-194.
[71] Ferraro, P. M.; Taylor, E. N.; Gambaro, G.; Curhan, G. C. *Clin J Am Soc Nephrol.* **2013**, *8*, 1389-1395.
[72] Hu, M.; Feng, G. *Chem. Commun.* **2012**, *48*, 6951.
[73] Tang, L.; Park, J.; Kim, H.-J.; Kim, Y.; Kim, S. J.; Chin, J.; Kim, K. M. *J. Am. Chem. Soc.* **2008**, *130*, 12606-12607.
[74] Mittapalli, R. R.; Namashivaya, S. S. R.; Oshchepkov, A. S.; Shumilova, T. A.; Rüffer, T.; Lang, H.; Kataev, E. A. *Chem. Commun.* **2017**, *53*, 11345-11348.
[75] Tavallali, H.; Deilamy-Rad, G.; Mosallanejad, N. *Food Technol. Biotechnol.* **2018**, *56*.
[76] Rothschild, B. M.; Witzke, B. J.; Hershkovitz, I. *The Lancet* **1999**, *354*, 398.
[77] Faguet, G. B. *Int. J. Cancer* **2015**, *136*, 2022-2036.
[78] Schiffman, J. D.; Fisher, P. G.; Gibbs, P. *Am Soc Clin Oncol Educ Book.* **2015**, *35*, 57-65.
[79] Fahrmann, J. F.; Kim, K.; Defelice, B. C.; Taylor, S. L.; Gandara, D. R.; Yoneda, K. Y.; Cooke, D. T.; Fiehn, O.; Kelly, K.; Miyamoto, S. *Cancer Epidemiol. Biomark. Prev.* **2015**, *24*, 1716-1723.
[80] Avioli, L. V.; McDonald, J. E.; Singer, R. A. *J. Clin. Endocrinol. Metab.* **1965**, *25*, 912-915.
[81] Persy, V. P.; McKee, M. D. *Kidney Int.* **2011**, *79*, 490-493.
[82] Anbu, S.; Paul, A.; Stasiuk, G. J.; Pombeiro, A. J. L. *Coord. Chem. Rev.* **2021**, *431*, 213744.
[83] Purohit, A. K.; Kisan, H. K.; Sahu, S.; Kar, P. K. *J. Mol. Struct.* **2021**, *1243*, 130868.
[84] Das, D.; Sutradhar, S.; Singh, A.; Ghosh, B. N. *Z. Anorg. Allg. Chem.* **2021**, *647*, 1234-1238.
[85] Ghosh, K.; Sarkar, A. R.; Samadder, A.; Khuda-Bukhsh, A. R. *Org. Lett.* **2012**, *14*, 4314-4317.
[86] Zwicker, V. E.; Long, B. M.; Jolliffe, K. A. *Org. Biomol. Chem.* **2015**, *13*, 7822-7829.
[87] Yuen, K. K. Y.; Jolliffe, K. A. *Chem. Commun.* **2013**, *49*, 4824.
[88] Liu, X.; Ngo, H. T.; Ge, Z.; Butler, S. J.; Jolliffe, K. A. *Chem. Sci.* **2013**, *4*, 1680.
[89] Long, B. M.; Pfeffer, F. M.; Barrow, C. J. *Sens. Actuators B Chem.* **2017**, *243*, 761-764.
[90] Hamilton, D.; Batist, G. *Curr. Oncol. Rep.* **2004**, *6*, 116-122.
[91] Elie Hatem, N. E. B., and Meng-Er Huang *Antioxid. Redox Signaling* **2017**, *27*, 1217-1234.
[92] Matai, I.; Sachdev, A.; Gopinath, P. *ACS Appl. Mater. Interfaces* **2015**, *7*, 11423-11435.
[93] Feng, T.; Ai, X.; An, G.; Yang, P.; Zhao, Y. *ACS Nano* **2016**, *10*, 4410-4420.
[94] Das, K.; Sarkar, S.; Das, P. K. *ACS Appl. Mater. Interfaces* **2016**, *8*, 25691-25701.
[95] Bourlinos, A. B.; Stassinopoulos, A.; Anglos, D.; Zboril, R.; Georgakilas, V.; Giannelis, E. P. *Chem. Mater.* **2008**, *20*, 4539-4541.
[96] Dulkeith, E.; Morteani, A. C.; Niedereichholz, T.; Klar, T. A.; Feldmann, J.; Levi, S. A.; van Veggel, F. C. J. M.; Reinhoudt, D. N.; Möller, M.; Gittins, D. I. *Phys. Rev. Lett.* **2002**, *89*, 203002.

[97] Zhang, F. X.; Han, L.; Israel, L. B.; Daras, J. G.; Maye, M. M.; K. Ly, N.; Zhong, C.-J. *The Analyst* **2002**, *127*, 462-465.
[98] Thiry, A.; Dogné, J.-M.; Masereel, B.; Supuran, C. T. *Trends Pharmacol. Sci.* **2006**, *27*, 566-573.
[99] Koutnik, P.; Shcherbakova, E. G.; Gozem, S.; Caglayan, M. G.; Minami, T.; Anzenbacher, P. *Chem* **2017**, *2*, 271-282.
[100] Dědová, T.; Braicu, E. I.; Sehouli, J.; Blanchard, V. *Front. Oncol.* **2019**, *9*.
[101] Wang, J.; Zhang, S.; Dai, H.; Zheng, H.; Hong, Z.; Lin, Y. *Biosens. Bioelectron.* **2019**, *142*, 111567.
[102] Wang, J.; Zhao, L.; Yan, B. *ACS Appl. Mater. Interfaces* **2020**, *12*, 12990-12997.
[103] Kandambeth, S.; Mallick, A.; Lukose, B.; Mane, M. V.; Heine, T.; Banerjee, R. *J. Am. Chem. Soc.* **2012**, *134*, 19524-19527.
[104] Houben, A. J. S.; Moolenaar, W. H. *Cancer Metastasis Rev.* **2011**, *30*, 557-565.
[105] Wang, J.; Sun, Y.; Qu, J.; Yan, Y.; Yang, Y.; Cai, H. *Expert Rev. Mol. Diagn.* **2016**, *16*, 1103-1111.
[106] Pua, T. L.; Wang, F.-q.; Fishman, D. A. *Future Oncol.* **2009**, *5*, 1659-1673.
[107] Guo, R.; Kasbohm, E. A.; Arora, P.; Sample, C. J.; Baban, B.; Sud, N.; Sivashanmugam, P.; Moniri, N. H.; Daaka, Y. *Endocrinology* **2006**, *147*, 4883-4892.
[108] Zheng, Z.; Geng, W.-C.; Gao, J.; Wang, Y.-Y.; Sun, H.; Guo, D.-S. *Chem. Sci.* **2018**, *9*, 2087-2091.
[109] Daniotti, J.; Vilcaes, A.; Torres Demichelis, V.; Ruggiero, F.; Rodriguez-Walker, M. *Front. Oncol.* **2013**, *3*.
[110] Hattori, H.; Uemura, K.-I.; Taketomi, T. *Biochim. Biophys. Acta, Lipids Lipid Metab.* **1981**, *666*, 361-369.
[111] Hattori, H.; Uemura, K.-i.; Ishihara, H.; Ogata, H. *Biochim. Biophys. Acta, Lipids Lipid Metab.* **1992**, *1125*, 21-27.
[112] Hakomori, S. *Curr. Opin. Hematol.* **2003**, *10*, 16-24.
[113] Xu, M.; Kelley, S. P.; Glass, T. E. *Angew. Chem., Int. Ed.* **2018**, *57*, 12741-12744.
[114] Rehman, T.; Shabbir, M. A.; Inam-Ur-Raheem, M.; Manzoor, M. F.; Ahmad, N.; Liu, Z. W.; Ahmad, M. H.; Siddeeg, A.; Abid, M.; Aadil, R. M. *Food Sci. Nutr.* **2020**, *8*, 4696-4707.
[115] Ostrakhovitch, E. A.; Tabibzadeh, S. *Ageing Res. Rev.* **2019**, *49*, 144-164.
[116] McNulty, H.; Pentieva, K.; Hoey, L.; Ward, M. *Proc Nutr Soc.* **2008**, *67*, 232-237.
[117] Khajehsharifi, H.; Sheini, A. *Sens. Actuators B Chem.* **2014**, *199*, 457-462.
[118] Xue, Z.; Fu, X.; Rao, H.; Hassan Ibrahim, M.; Xiong, L.; Liu, X.; Lu, X. *Talanta* **2017**, *174*, 667-672.
[119] Nam, H. S. *J. Stroke.* **2019**, *21*, 151-159.
[120] Peng, J.; Xiao, X.; Hu, M.; Zhang, X. *Life Sci.* **2018**, *214*, 153-157.
[121] Kałużna-Czaplińska, J., & Gątarek, P *EXCLI Journal* **2021**, *20*, 301-319.
[122] Yu, H.; Geng, W.-C.; Zheng, Z.; Gao, J.; Guo, D.-S.; Wang, Y. *Theranostics* **2019**, *9*, 4624-4632.
[123] Yang, H. D.; Kim, D. H.; Lee, S. B.; Young, L. D. *Dement Neurocogn Disord.* **2016**, *15*, 115.
[124] Picón-Pagès, P.; Garcia-Buendia, J.; Muñoz, F. J. *Biochim Biophys Acta Mol Basis Dis.* **2019**, *1865*, 1949-1967.

[125] Sun, X.; Lacina, K.; Ramsamy, E. C.; Flower, S. E.; Fossey, J. S.; Qian, X.; Anslyn, E. V.; Bull, S. D.; James, T. D. *Chem. Sci.* **2015**, *6*, 2963-2967.
[126] Sun, X.; Xu, Q.; Kim, G.; Flower, S. E.; Lowe, J. P.; Yoon, J.; Fossey, J. S.; Qian, X.; Bull, S. D.; James, T. D. *Chem. Sci.* **2014**, *5*, 3368.
[127] Sun, X.; James, T. D. *Chem. Rev.* **2015**, *115*, 8001-8037.
[128] Brouns, F. *Front. Nutr.* **2020**, *7*.
[129] Williams, G. T.; Kedge, J. L.; Fossey, J. S. *ACS Sensors* **2021**, *6*, 1508-1528.
[130] Sasaki, Y.; Zhang, Z.; Minami, T. *Front. Chem.* **2019**, *7*.
[131] Sasaki, Y.; Leclerc, É.; Hamedpour, V.; Kubota, R.; Takizawa, S.-y.; Sakai, Y.; Minami, T. *Anal. Chem.* **2019**, *91*, 15570-15576.
[132] Liang, X.; Trentle, M.; Kozlovskaya, V.; Kharlampieva, E.; Bonizzoni, M. *ACS Appl. Polym. Mater.* **2019**, *1*, 1341-1349.
[133] Ausó, E.; Gómez-Vicente, V.; Esquiva, G. *J. Pers. Med.* **2020**, *10*, 114.

UNIVERSITAT ROVIRA I VIRGILI
CALIX[4]PYRROLE CAVITANDS FOR SUPRAMOLECULAR SENSING AND CATALYSIS
Andrés Felipe Sierra Ramos

Chapter 2

Recognition of creatinine with phosphonate calix[4]pyrrole cavitands.

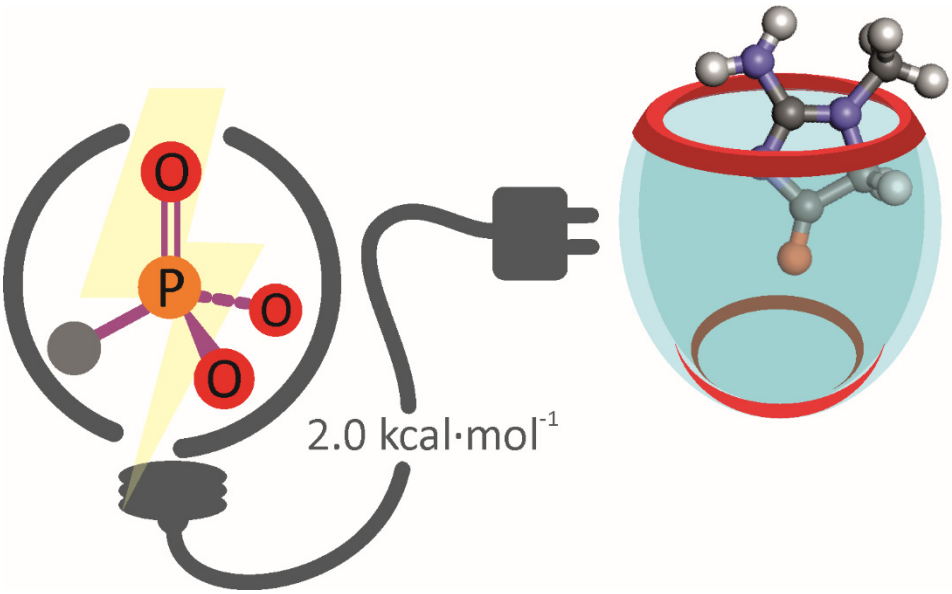

UNIVERSITAT ROVIRA I VIRGILI
CALIX[4]PYRROLE CAVITANDS FOR SUPRAMOLECULAR SENSING AND CATALYSIS
Andrés Felipe Sierra Ramos

2.1 Introduction.

Cavitands are synthetic organic molecules that feature enforced cavities large enough to include a guest.[1] The design of the structure of the cavitand is crucial for its molecular recognition properties that are based on size, shape and functional groups complementarity between the guest and the cavity.[2]

Cavitands derived from resorcinarene are popular for their well-known recognition properties towards cationic inorganic and organic species as well as neutral guests.[3] The selection of the bridging groups connecting the aromatic panels in the upper rim of the resorcinarene scaffold is essential, since it will have an impact on their complexation properties. Among them, the use of bridging P=O groups in resorcinarene cavitands (*a.k.a*. phosphonate cavitands) has been described to provide excellent recognition properties for different guests (e.g. ammonium salts, alcohols, sarcosine, L-lactic acid, methylated amino acids among others) in the solid state,[4,5,6] in solution[7,]and in the gas phase.[8,9] The recognition properties of resorcinarene phosphonate cavitands towards charged and neutral guests are attributed to the presence of CH-π and cation-dipole interactions as well as to hydrogen bonding interactions involving the P=O group.[10] Therefore, the number and orientation of P=O moieties with respect to the cavity (inward or outward) has an impact on their binding affinity.[11]

Inspired by phosphonate resorcinarene cavitands, during the last decade our group has reported several examples of mono-, bis- and tetra-phosphonate receptors built on calix[4]pyrrole scaffolds. [12,13,14] Recently, our group exploited the recognition properties of a mono-phosphonate calix[4]pyrrole cavitand (**3i** in Scheme 2.*1*) for the construction of an ion selective potentiometric sensor for the sensitive and selective determination of creatinine (**Cr**) in biological fluids.[14] Given the significant role of the creatinine -as essential biomarker for kidney diseases- in clinic applications, developing a reliable and sensitive sensing platform for its detection is of great interest and importance. The affinity displayed by the phosphonate calix[4]pyrrole receptors towards **Cr** is attributed to the good size, shape and function complementarity with the binding site defined by the pyrrole rings.

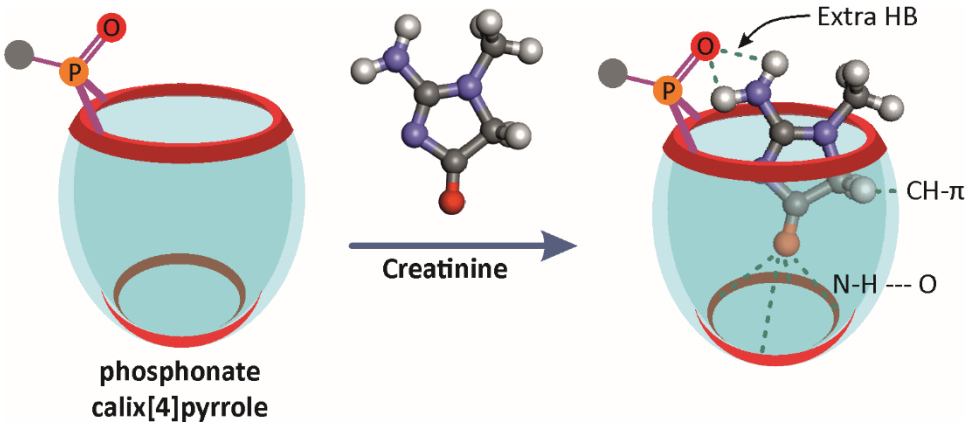

Figure 2.1 Schematic representation of the creatinine complexation with a phosphonate calix[4]pyrrole cavitand.

The X-ray crystal structure of the **Cr⊂3i** complex showed that the oxygen atom of included neutral creatinine established four hydrogen bond interactions with the pyrrole NH protons of the receptor. Moreover, the phosphonate group inwardly oriented offered an extra hydrogen bond by interacting with the NH protons of the creatinine (Figure 2.*1*). The importance of the P=O group inwardly directed to the cavity was supported by comparison of the **Cr** extraction experiments performed in acetone with cavitand **3i** and the doubly methylene bridged analogue **4** (absence of phosphonate group).[14] The results showed that cavitand **3i** extracted 0.4 equiv. of **Cr**, whereas analogous extraction experiments with **4** did not show evidence of **Cr** extraction. These findings demonstrated a larger binding affinity of **3i** towards **Cr** than bis-methylene bridged analogue **4** lacking P=O group. Additionally, adequate selectivity values required for a useful potentiometric electrode were not achieved with this latter receptor. These results threw some light on the fact that the presence and orientation of a phosphonate group plays an important role in the creatinine recognition. In consequence, we become interested in the accurate quantification of the contribution of the hydrogen bonding interaction of the phosphonate group to the thermodynamic stability of the final creatinine complex.

X-ray diffraction of single crystals has been for many years a widespread method for the study of intermolecular hydrogen bonds in supramolecular complexes in the solid state.[15] Currently other methods are being employed not only for the identification of hydrogen bonds but also for their quantification. Among them, several mass spectrometry (MS) techniques have emerged as versatile tools for the study of this and other non-covalent interactions in the gas phase.[16,17] The

development of soft ionization methods allowed the characterization of polar self-assembled macrocycles in the gas phase.[18].

For instance, the combination of MS methods with hydrogen deuterium exchange (HDX) and guest-exchange ion-molecule reactions were efficiently used for the elucidation of the operation of multiple hydrogen bonds in phosphonate cavitands complexes with ethyl-substituted ammonium ions in the gas phase.[8] Nevertheless, application of ion molecular reactions is restricted by the volatility of the neutral reagent and proton affinity difference between the interacting species. Moreover, the repeatability of gas-phase ion molecules reactions with regards to reaction rates is rarely good.

Isothermal Titration Calorimetry (ITC) is a powerful, fast and accurate method that by using appropriate models can be employed to determine the contribution of a hydrogen bond interaction in a host-guest complex in solution.[19] In an ITC experiment, the heat released or absorbed during a binding process is directly measured.[20] The fit of the calorimetric titration data to a specific binding model provides an accurate value of the binding constant (K_a), the stoichiometry of the complex formation, and the binding enthalpy (ΔH). Since K_a can be directly related to the free energy of binding (ΔG), the binding entropy (ΔS) can be easily derived.

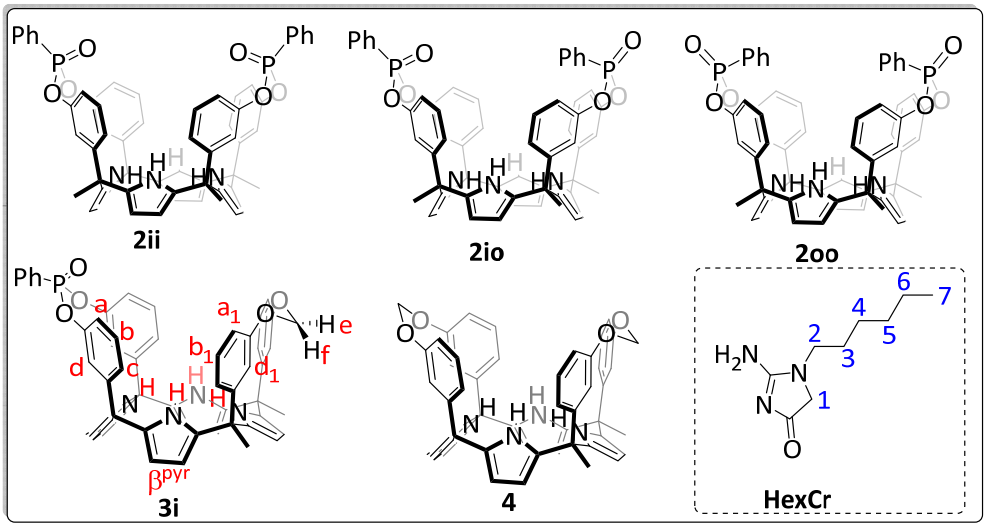

Scheme 2.1 Line-drawing structure of the studied cavitands (**2ii**, **2io**, **2oo**, **3i** and **4**) and hexylcreatinine (**HexCr**) used as guest.

In this chapter, we performed the thermodynamic characterization of a series of calix[4]pyrrole cavitands featuring different number (0, 1, 2) and orientation of the bridging P=O groups (inwardly pointing the cavity or outwardly directed, Scheme 2.*1*). The derived results allowed us to quantify the contribution of the inwardly oriented P=O group to the binding of creatinine and assess the relevance of the P=O in the thermodynamic stabilization of the final complexes. First, the binding interaction between the selected cavitands and hexyl creatinine (**HexCr**, lipophilic version of **Cr**) were probed by ^{1}H and ^{31}P NMR experiments. The accurate determination of the free energy of binding was performed by ITC experiments in dichloromethane. The experimental results were supported by density functional theory (DFT) calculations.

2.2 Results and discussion

2.2.1 NMR Binding studies

Cavitands **2-4** were prepared following the reported procedures (*Scheme 2.2*).[12,14] In brief, the reaction of tetra-phenoxy calix[4]pyrrole **1** with 2 equiv. of phenylphosphonic dichloride using Et_3N as base yields a mixture of three possible diastereoisomers which differ in the orientation of the P=O group with respect to the cavity (**2ii**, **2io** and **2oo**).

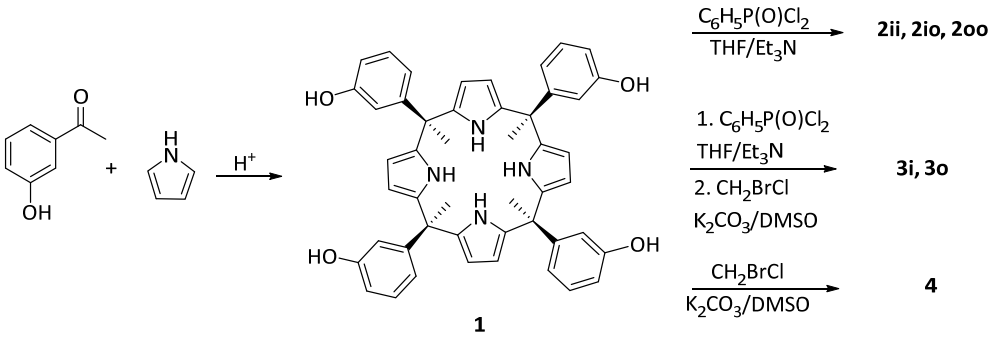

Scheme 2.2 Synthetic scheme for the preparation of receptors **2**, **3i** and **4**.

The three isomers can be separated by column chromatography on silica using CH_2Cl_2:AcOEt as eluent.[21] On the other hand, two diastereoisomers (*in* and *out*) were isolated from the reaction of **1** with 1 equiv. of phenylphosphonic dichloride. After separation and subsequent reaction of each diastereoisomer with $CH_2Br_2Cl_2$ and K_2CO_3 as base we isolated **3i** and **3o**. For these studies, only **3i** was used. We

hypothesized that compound **3o**, featuring one P=O group outwardly oriented with respect to the aromatic cavity might have a similar behavior than bis-methylene bridged cavitand **4** (with no P=O groups).

We performed all the binding studies with the lipophilic derivative of creatinine, hexylcreatinine **HexCr** due to the low solubility of neutral creatinine in organic solvents.[22]

We initially probed the interaction of the selected guest **HexCr** with receptors **2ii**, **2io**, **2oo**, **3i**, **4** using ^{1}H and ^{31}P NMR titration experiments. The ^{1}H NMR spectra of all receptors at millimolar concentration in CD_2Cl_2 solution showed sharp and well resolved proton signals that are in agreement with their respective symmetries, C_{2v} for **2ii**, **2oo**, **4** and C_v for **2io** and **3i**.

For the sake of brevity, we only describe in detail the NMR binding experiments performed with receptors **2ii** and **2oo** with two P=O groups inwardly and outwardly directed with respect to the cavity, respectively. The NMR titration experiments related to the other receptors **2io**, **4** and **3i** can be found in the experimental section at the end of this chapter.

NMR titration of cavitand 2ii with HexCr in CD_2Cl_2. The addition of 0.5 equiv. of **HexCr** to a 2.0 mM CD_2Cl_2 solution of cavitand **2ii** produced the appearance of new set of signals (Figure 2.*2*b, left panel) that was attributed to the protons of bound **2ii**. When 1.0 equiv. of **HexCr** was added to the solution of the cavitand, only the signals assigned to protons of bound **2ii** were observed (Figure 2.*2*c, left panel).

Remarkably, the pyrrole NHs of bound **2ii** resonated as two sharp singlets at δ = 9.8 ppm and 10.0 ppm with a 1:1 integral ratio. These signals moved downfield (Δδ ~ 1.6 ppm) compared to the free receptor, suggesting their involvement in hydrogen-bonding interactions with the bound **HexCr**.

The ^{31}P NMR spectrum of the 1:0.5 molar ratio mixture of **2ii** and **HexCr** displays two separate singlets resonating at δ = 14.9 and 13.6 ppm. The more downfield shifted signal corresponds to the phosphorus atoms of free **2ii**. The other signal was assigned to the phosphorous atom of the P=O group of the bound receptor. Furthermore, the methylene protons (H^1, Figure 2.*1*) of the bound **HexCr** appeared at δ = 1.15 ppm. These protons resonate significantly upfield shifted in comparison to the chemical shift values of the same protons on the free **HexCr** (Δδ = -2.68 ppm).

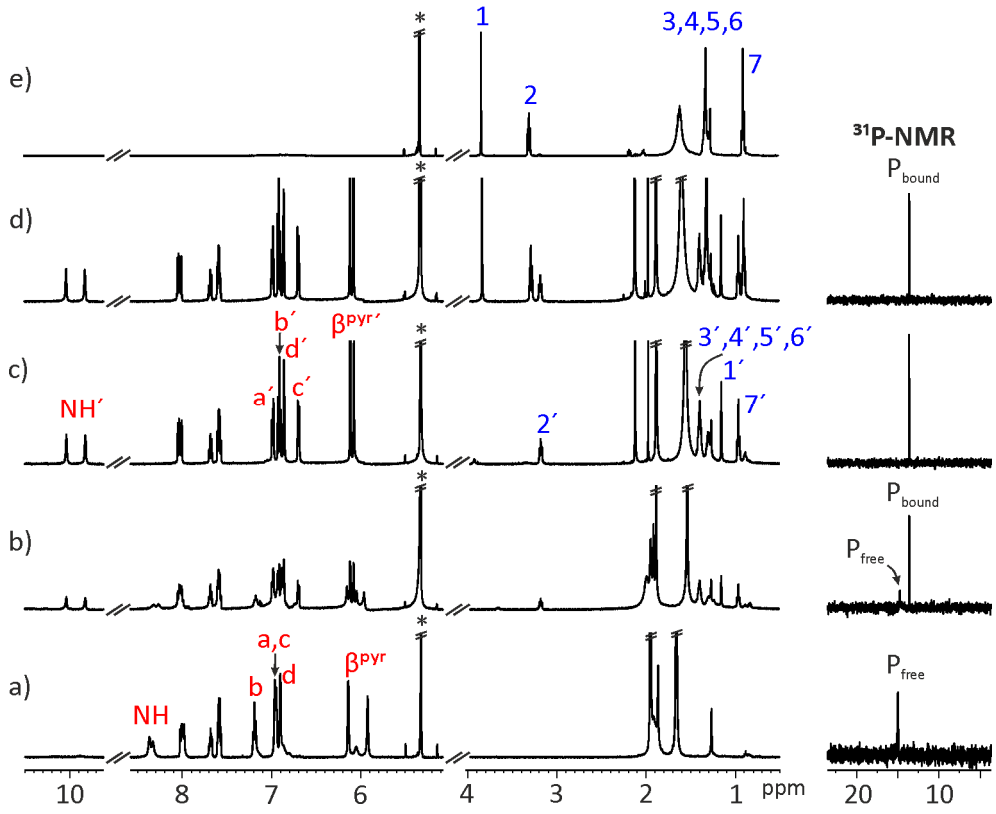

Figure 2.2 Left panel, selected regions of the ^{1}H NMR spectra (500 MHz, 298 K) of CD_2Cl_2 solutions containing receptor **2ii** and **HexCr** in different molar ratios: a) Free **2ii**; b) **2ii** + 0.5 equiv.; c) **2ii** + 1.0 equiv.; d) **2ii** + 2.5 equiv of **HexCr**. Trace e) shows the same regions of the ^{1}H NMR spectrum of **HexCr**. Right panel, corresponding ^{31}P NMR spectra (202 MHz, CD_2Cl_2, 298 K). * Residual solvent peak.

The large upfield shift experienced by the methylene protons of the bound **HexCr**, clearly suggests its deep inclusion in the aromatic cavity of **2ii**. The ^{31}P NMR spectrum of the equimolar mixture showed exclusively an upfield shifted signal for the bound phosphorus atom ($\Delta\delta$ = - 1.34 ppm).

Finally, an excess of **HexCr** did not produce noticeable changes in the signals assigned to protons of bound **2ii** and included **HexCr**. However, new signals corresponding to the free **HexCr** emerged (Figure 2.2d, left panel).

Taken all together, these results indicate that cavitand **2ii** and **HexCr** form a 1:1 complex **HexCr⊂2ii**, which experiences a slow chemical exchange on the chemical shift in the ^{1}H and ^{31}P NMR time scale between the free and bound species.

Moreover, the exclusive observation of **HexCr⊂2ii** complex in the NMR spectrum after the addition of 1 equiv. of guest indicates that the binding constant is larger than 10^4 M^{-1}. In this complex, the **HexCr** is deeply included in the aromatic cavity of **2ii** in its cone conformation.

Similar results were observed during the ^{1}H and ^{31}P NMR titration of receptors **2io** and **3i** with **HexCr** (Figure 2.*6* and Figure 2.*7*).

NMR titration of cavitand 2oo with HexCr. The addition of 0.5 equiv. of **HexCr** causes broadening in most of the proton signals of receptor **2oo**, mainly the ones corresponding to the pyrrole NHs, aromatic and β-pyrrole protons. Protons H^1 and H^2 of the guest also appeared broad at 1.52 and 2.98 ppm, respectively. The addition of an excess of **HexCr** did not produce the appearance of the proton signals corresponding to the free guest but the gradual downfield shift of all the proton signals corresponding to the guest. The ^{31}P NMR spectrum of the free **2oo** receptor show a singlet resonating at δ = 13.2 ppm. The incremental addition of **HexCr**, induce a gradual upfield shift of the phosphorous signals (Δδ = - 0.4 ppm). These results indicated that the binding process displayed a chemical exchange dynamic that is intermediate-fast in the ^{1}H and ^{31}P NMR chemical shift time scale between free and bound counterparts. These results suggest a reduced kinetic stability of the **HexCr⊂2oo** complex compared to the previously described analogue complexes featuring at least one P=O inwardly directed to the cavity**HexCr⊂2ii** and **HexCr⊂3i**.

The sharpening of the proton signals of cavitand **2oo** in the **HexCr⊂2oo** complex (after the addition of 1 equiv. of guest) is given by the lock of the conformation of the receptor in the cone conformation when it is bound to the **HexCr**.

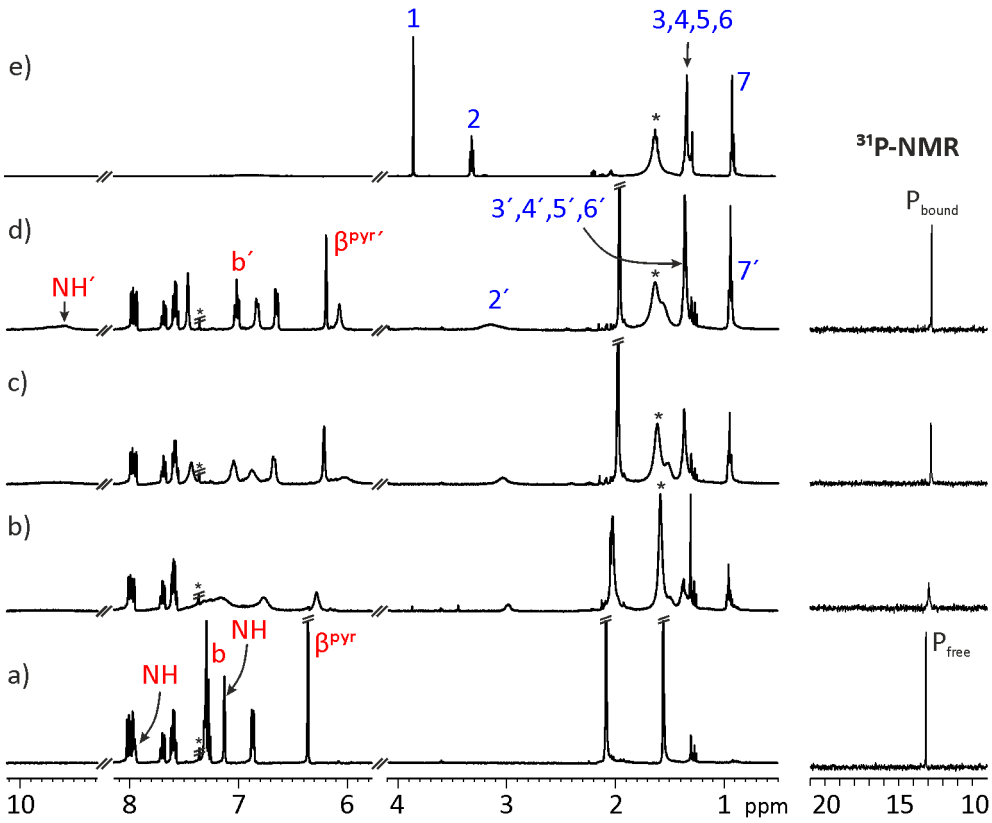

Figure 2. 3 Left panel, selected regions of the ^{1}H NMR spectra (500 MHz, 298 K) of CD_2Cl_2 solutions containing receptor **2oo** and **HexCr** in different molar ratios: a) Free **2oo**; b) **2oo** + 0.5 equiv.; c) **2oo** + 1.0 equiv.; d) **2oo** + 2.5 equiv of **HexCr**. Trace e) shows the same regions of the ^{1}H NMR spectrum of **HexCr**. Right panel, corresponding ^{31}P NMR spectra (202 MHz, CD_2Cl_2, 298 K). * Residual solvent peak.

Analogous results were observed during the ^{1}H and ^{31}P NMR titration of bis-methylene bridged receptor **4** with **HexCr** (Figure 2.*8*).

In both cases (**2oo** and **4**), in the presence of 1 equiv. of **HexCr** the 1:1 complexes are quantitatively formed. Therefore, we estimate a binding constant value K_a larger than 10^4 M^{-1} for both receptors in CD_2Cl_2.

2.2.2 ITC experiments.

We used isothermal titration calorimetry experiments to accurately assess the binding constant values of the five selected receptors towards **HexCr**. The thermodynamic parameters were determined in methylene chloride at 288 K. The sequential injection of a CH_2Cl_2 solution of the receptor into a solution of **HexCr** produced a gradual release of heat corresponding to the binding event. The

normalized integrated heats were corrected with the heat of dilution. All the ITC experiments provided a sigmoidal binding isotherm with an inflection point close to a host:guest ratio of 1 (Figure 2.11 to Figure 2.15), as expected for a 1:1 stoichiometry of the complexes. The fit of the experimental data to a 1:1 binding model was good and provided the thermodynamic parameters (K_a, ΔH and -TΔS) summarized inTable 2.*1*. We draw several conclusions from the tabulated data related to the contribution of the phosphonate group on the hexylcreatinine binding.

Table 2.1 Thermodynamic parameters at 288 K for the 1:1 complexes of the receptors **2ii**, **2io**, **2oo**, **3i** and **4** with **HexCr** in CH_2Cl_2. Binding constant K_a (M^{-1}), free Gibbs energy ΔG (kcal·mol^{-1}), ΔH enthalpy (kcal·mol^{-1}) and entropy TΔS(kcal·mol^{-1}).

Receptor	$K_a \times 10^{-6}$	ΔG	ΔH	-TΔS
2ii	2.1 ± 0.3	-8.3 ± 0.1	-3.5 ± 0.7	4.8 ± 0.7
2io	1.1 ± 0.2	-8.0 ± 0.1	-5.0 ± 0.7	2.9 ± 0.7
2oo	0.021 ± 0.004	-5.7 ± 0.1	-3.9 ± 0.6	1.7 ± 0.6
3i	0.57 ± 0.03	-7.60 ± 0.03	-4.98 ± 0.04	2.61 ± 0.05
4	0.045 ± 0.003	-6.13 ± 0.03	-3.9 ± 0.3	2.3 ± 0.3

On one hand, we determined a reduced thermodynamic stability (lower free energy of binding) of the complexes with cavitands lacking of any phosphonate groups inwardly directed to the cavity (i.e. **4** and **2oo**) compared to their counterparts featuring at least one P=O group pointing towards the cavity. The larger binding constant (i.e. largest ΔG) was determined for the complex with the cavitand featuring the two phosphonate groups inwardly directed to the cavity **2ii** (2.1×10^6 M^{-1}). This value is two orders of magnitude larger than the one determined for **2oo** cavitand with two P=O group outwardly directed to the cavity. We calculated a free energy gain between 2.6-1.5 kcal·mol^{-1} in favor of the complexes with cavitands featuring one or two P=O group inwardly directed to the aromatic cavity compared to the **2oo** or bismethylene bridged **4**. These differences are in agreement with the energetic contribution of an additional hydrogen bond interaction established between the -NH_2 protons of the included hexylcreatinine and the P=O group inwardly oriented to the cavity in **2ii**, **2io** and **3i**.

On the other hand, the complexation of **HexCr** by all the receptor series is both enthalpically and entropically driven and exhibit enthalphy-entropy compensation

effect. These results are in line with previous thermodynamic data obtained for 1:1 complexes of related phosphonate calix[4]pyrrole cavitands with tetra-methyl phosphonium chloride ion-pair in dichloromethane[13] and suggest that solvation/desolvation effects must play a crucial role in the binding process.

From the tabulated data we determined that $K_{HexCr\subset 2ii}$ is two times larger than $K_{HexCr\subset 2io}$ (i.e. $K_{HexCr\subset 2ii} = 2\times K_{HexCr\subset 2io}$). This relationship of binding constants was also confirmed by means of pairwise competitive binding experiments with the two cavitands and HexCr (Figure 2.*10*). Remarkably, the binding process with cavitand receptor **2ii** is mainly entropically driven. This large and negative entropic component underlines the importance of desolvation of the host during the **HexCr** recognition. The larger binding constant determined for cavitand **2ii** might also be attributed to the presence of two energetically and geometrically equivalent interaction modes to **HexCr** guest which increases the entropy of the complex with **2ii** cavitand.More precisely, the **HexCr** stablishes 4 hydrogen bond interactions with the calix[4]pyrrole core and is able to rotate inside the **2ii** cavity and interact with any of the two mirror-related P=O groups (i.e. two equivalent binding geometries). Moreover, **HexCr** stablishes CH-π interactions between its methylene protons (protons H^1 in Scheme 2.*1*) and the aromatic walls of receptor **2ii**. Similar behavior has been reported by Dalcanale and co-workers for resorcin[4]arene derived cavitands with multiple phosphonates groups binding alcohols.[23,24] These latter result were supported by DFT calculations.[25]

The thermodynamic profile of receptors **3i** and **2io** showed that the enthalpic and entropic contribution to the binding of **HexCr** are comparable, suggesting that the presence of a phosphonate group outwardly directed has a limited impact on the binding affinity. Finally, we determined a two-folds increase on the binding constant of cavitand **2oo** compared to the bis-methylene analogue **4**. Most likely, this is due to the differences in solvation/desolvation of the two receptors.

2.2.3 Theoretical studies on the binding geometry of the inclusion complexes.

With the aim to gain some insight on the structures of the inclusion complexes and support the relative energies determined above we performed DFT calculations at the BP86-D3 def2-SVP level of theory using a continuum DCM solvation model (COSMO) as implemented in TURBOMOLE version 7. The energy minimized structures are shown in Figure 2.*4*.

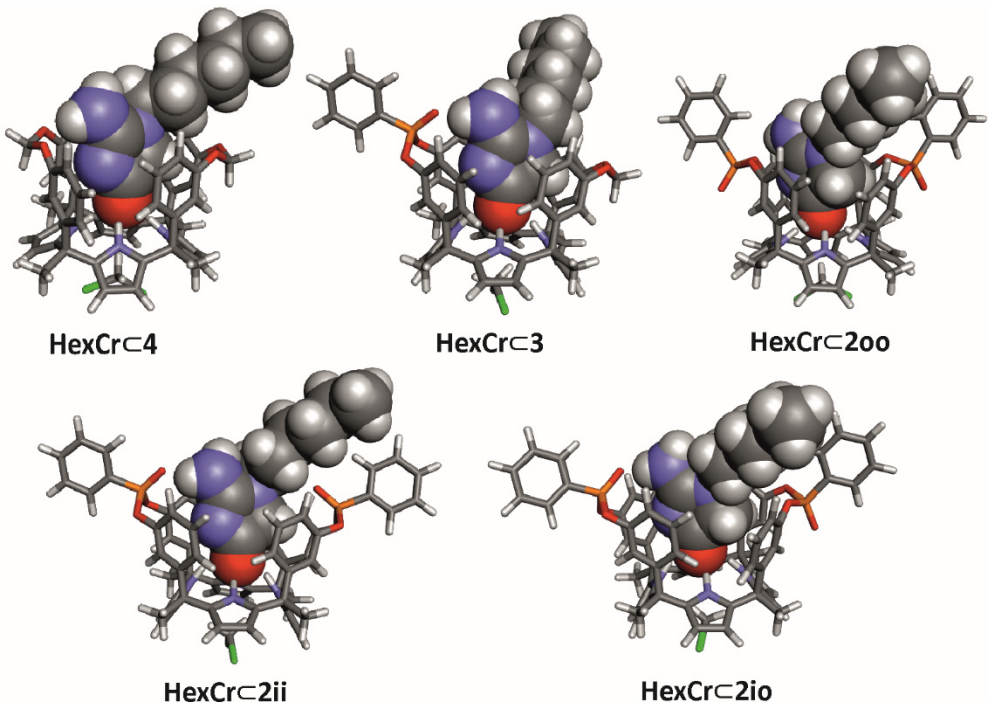

Figure 2.4 Energy minimized structures at PB86-D3-def2-SVP level of theory (solvent COSMO model implemented in Turbomole version 7.) of the inclusion complexes.

In all the complexes, the HexCr is included in the cavity of the calix[4]pyrrole in cone conformation and establishes four hydrogen bond interactions with the pyrrole NHs. As expected, in complexes **2ii**, **2io** and **3** the P=O group inwardly oriented to the cavity establishes an additional hydrogen bond interaction with the -NH_2 moiety of the included HexCr. No significant differences were observed between the hydrogen bond distance of these energy minimized structures (i.e. d(-H_2N···O=P) = 2.7 Å).

Additionally, we were able to obtain single crystals of **HexCre⊂2oo** complex (Figure 2.*5*) by slow evaporation of chloroform at -4 °C. Additionally, the X-ray structure of the inclusion complex between receptor **3i** and neutral creatinine (**Cr**) was previously reported by us (Figure 2.*16*).[14] These X-ray crystal structures were used to evaluate the quality of the theoretical measurements.

In the solid state, thw **HexCr⊂2oo** complex showed the calix[4]pyrrole core in cone conformation with one molecule of **HexCr** deeply included in the polar and aromatic receptor´s cavity. The complex geometry of the x-ray structure is similar to that obtained by molecular modeling.

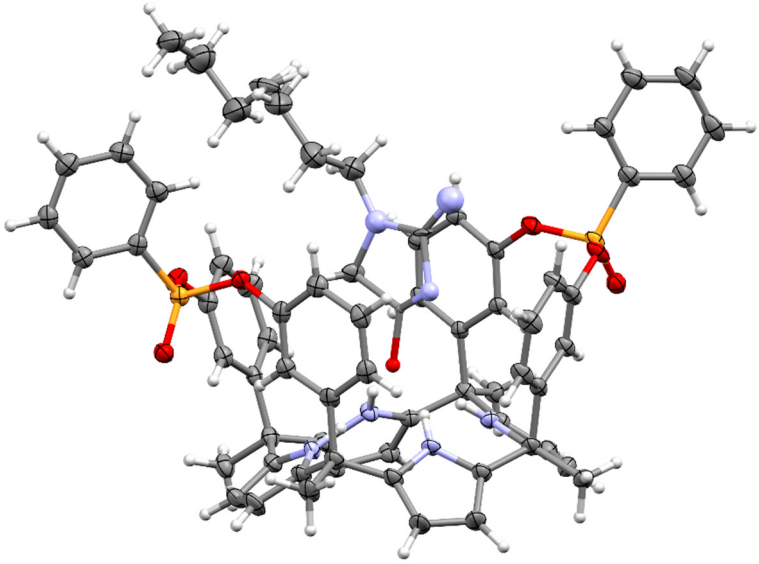

Figure 2.5 X-ray structures of **HexCr⊂2oo**. Thermal ellipsoids for C, N, O and P atoms set at 50% probability, H atoms are shown as spheres of 0,15 Å diameter.

We compared the P=O ··NH_2 distance in the **HexCr⊂3i** complex obtained by the molecular model (Table 2.*2*) with that obtained by the **Cr⊂3i** in solid state (Figure 2.*16*). A difference of 0.201 Å was found between the two complexes. We used this level of coincidence (93 %) to validate the theoretical data.

We subtracted the computed electronic energies of the free species (**HexCr** and free cavitands) from those of the complexes to assign relative stabilities of the complexes with all the cavitand's series. For a fairer comparison of energies (Table 2.1), we introduced an implicit molecule of dichloromethane in the structures of the free cavitand and the complex. The computed data of the complexes involving bisphosphonate cavitands (i.e. **HexCr⊂2ii**, **HexCr⊂2io** and **HexCr⊂2oo**) reproduces the stability trend observed in solution being the complex with cavitand **2ii** the most stable and the one with **2oo** the one producing the least stable complex.

Moreover, the complexes with any P=O pointing towards the aromatic cavity (i.e. **HexCr⊂2oo** and **HexCr⊂4**) are the least stable ones in agreement with the results derived from ITC solution experiments. Computational results ascribe the larger thermodynamic stability to the complex of **HexCr** with cavitand **3i**. The notable changes in structure and the small differences in energy observed experimentally did not allow to reproduce the experimental results (assigning the complex with **2ii** the most thermodynamically stable) with the obtained computed data.

We also computed the chemical shift for the methylene hydrogen atoms of the hexylcreatinine in all the complexes (Table 2.*2*). The trend of the calculated chemical shifts agrees with the experimental results. This agreement supports the geometries assigned to each complex.

Table 2.2 Total energies, energy difference, and the lengths of hydrogens bond for the complexes of the receptors **2ii**, **2io**, **2oo**, **4** with **HexCr** and receptor **3i** with **Cr**. BP86-D3/def2-SVP level of theory.

Complex	ΔE[a] (kcal/mol)	δexp (ppm)	δcalc[b] (ppm)*	Δδexp (ppm)	NICS	P=O ·· N-H (Å)
HexCr⊂2ii	-45.0	1.15	1.48	-2.68	-1.91	2.74
HexCr⊂2io	-43.1	1.39	1.08	-2.50	-2.31	2.73
HexCr⊂2oo	-40.2	1.52	2.29	1.87	-1.10	
HexCr⊂3i	-46.7		n.d.			2.73[c]
HexCr⊂4	-42.5		n.d.			

[a] $\Delta E = E_{complex} - \left(E_{host} + E_{guest}\right)$. [b] Average of the computed values for each of the two methylene protons, H^1. [c] experimental distance 2.943 Å obtained by the x-ray structure of the **Cr⊂3i** complex taken from reference 14.

2.3 Conclusions

In conclusion, phosphonate cavitands are able to form kinetically and thermodynamically stable 1:1 complexes with **Cr** and **HexCr**, operating on principles of size, shape, and functional group complementarity. Structurally, the bound guest stablishes four hydrogen bonds between oxygen group of the creatinine and the pyrrole NHs of the host. One additional hydrogen bond interaction is established between the NH2 group of the included guest and the phosphonate group when it is inwardly directed to the aromatic cavity. The binding of hexylcreatinine was initially proved by ^{1}H and ^{31}P NMR titration experiments in methylene chloride solutions which disclosed binding constants larger than 10^4 M^{-1} for all receptors. ITC experiments quantified a difference of around 2 kcal·mol^{-1} in free energy values of complexes featuring at least one P=O group inwardly oriented to the cavity compared to their analogues lacking this group directed to the cavity. This value is in agreement with the additional energetic contribution of one hydrogen bond interaction displayed by the inwardly directed P=O and the -NH_2 protons of the bound hexylcreatinine The energy minimized structures computed at BP86-

D3/def2-SVP level of theory, evidenced that in all complexes the calix[4]pyrrole adopts a cone conformation and stablishes four hydrogen bond interactions with the oxygen atom of the guest. Moreover, the computed structures of complexes with 2ii, 2io and 3i show an additional hydrogen bond interaction between the -NH2 hydrogens of the included guest and the oxygen atom of the phosphonate group inwardly directed to the cavity. Computational results were also able to reproduce the stability trend observed in solution for the complexes of **HexCr** with bisphosphonate cavitands: **2ii**>**2io**>**2oo**.

2.4 Experimental section

2.4.1 General methods and instrumentation.

Reagents and solvents used in the synthesis were obtained from commercial suppliers and were used without further purification unless otherwise stated. Pyrrole was distilled under vacuum and stored in the freezer for further used. THF was dried under distillation from sodium/benzophenone under argon atmosphere. Triethylamine (Et_3N) was distilled with CaH_2 under argon atmosphere and used it immediately. Flash column chromatography was performed with silica gel, technical grade, pore size 60 Å, and 230–400 mesh particle size.

Automatic column chromatography purifications were done with a Combi-flash® RF^+. Routine ^1H, ^{31}P and ^{13}C NMR spectra were recorded on a Bruker Avance 400 (400 MHz for 1H-NMR), Bruker Avance 500 (500 MHz for 1H-NMR) ultrashield spectrometer. Deuterated solvents were purchase from Aldrich.

2.4.2 Synthesis and characterization data

Synthesis of **1**: To a 2 L round-bottomed flask equipped with a magnetic stir bar, 3´-hydroxyacetophenone (15 g, 108 mmol), AcOEt (1 L) and HCl 36% (73.5 mL, 864 mmol) were added. Under vigorous stirring pyrrole (7.87 mL, 113 mmol) was added slowly via a syringe. The flask was closed with a seal cap and the reaction mixture was stirred at RT for 4h. To quench the reaction a saturated sodium bicarbonate ($NaHCO_3$) solution was added until reaching pH 7. The organic phase was separated and then washed with water (2 × 100 mL), dried over Na_2SO_4, filtered and concentrated under reduced pressure. The resulting solid was washed with Et_2O (500 mL), filtered and the liquid was concentrated. A brown foam was obtained and washed with CH_2Cl_2 (300 mL), filtered and concentrated again. A brown solid was

obtained and recrystallized from acetonitrile. A light brown solid (5.4 g, 27%) was collected.

Melting Point: 220-222 °C, **^{1}H-NMR** (400 MHz, $(CD_3)_2CO$, 298 K): δ (ppm) = 8.78 (bs, 4H), 8.06 (s, 4H), 7.04 (t, 4H, *J* = 7.7 Hz), 6.54 (dd, 4H, *J* = 7.7 Hz), 6.49 (d, 4H, *J* = 7.7 Hz), 6.44 (t, 4H, *J* = 2.5 Hz), 6.01 (d, 8H, *J* = 2.5 Hz), 1.84 (s, 12 H). The ^{13}C-NMR spectrum of this compound agreed with that reported in the literature.[12]

Receptors **2ii***,* **2io***, and* **2oo** were prepared according to a slightly modified published procedure.[12] To a solution of calix[4]pyrrole **1** (1.0 g, 1.35 mmol) in dry THF (70 mL) and freshly distilled triethylamine (0.94 mL, 6.75 mmol), phenylphosphonic dichloride (1.0 mL, 6.92 mmol) was added dropwise (1h) with a syringe pump[26] under argon atmosphere. The reaction mixture was stirred for 2h at room temperature. Next, the solvent was removed *in vacuo* and water (50 mL) was added to solubilize the triethylammonium chloride salts. The suspension was extracted with CH_2Cl_2 (2 × 50 mL). The organic extracts were combined, dried, filtered and the solvent removed. The reaction crude (1.2 g) was purified by column chromatography (60 g SiO_2, from CH_2Cl_2 to CH_2Cl_2:AcOEt 95:5)[21] and further crystallization from acetonitrile to yield **2io** (338 mg, 25.4%), **2oo** (134 mg, 10.1 %) and **2ii** (206 mg, 15.5 %). The ^{1}H and ^{13}C NMR of the three isomers are in complete agreement with those reported previously in literature.[12]

Receptors **3** and **4** were obtained by following the published protocols.[14]

2.4.3 NMR titrations.

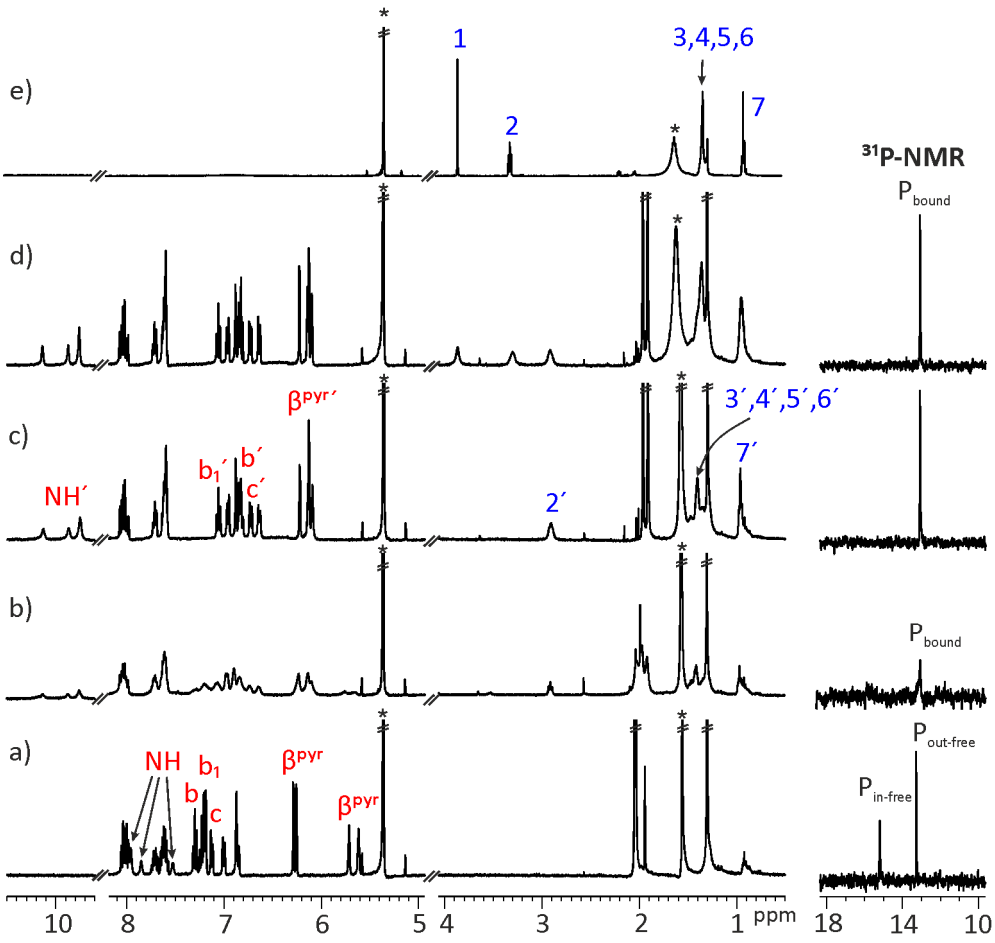

Figure 2.6 Left panel, selected regions of the ^{1}H NMR spectra (500 MHz, 298 K) of CD_2Cl_2 solutions containing receptor **2io** and **HexCr** in different molar ratios: a) Free **2io**; b) **2io** + 0.5 equiv.; c) **2io** + 1.0 equiv.; d) **2io** + 2.5 equiv of **HexCr**. Trace e) shows the same regions of the ^{1}H NMR spectrum of **HexCr**. Right panel, corresponding ^{31}P NMR spectra (202 MHz, CD_2Cl_2, 298 K). * Residual solvent peak.

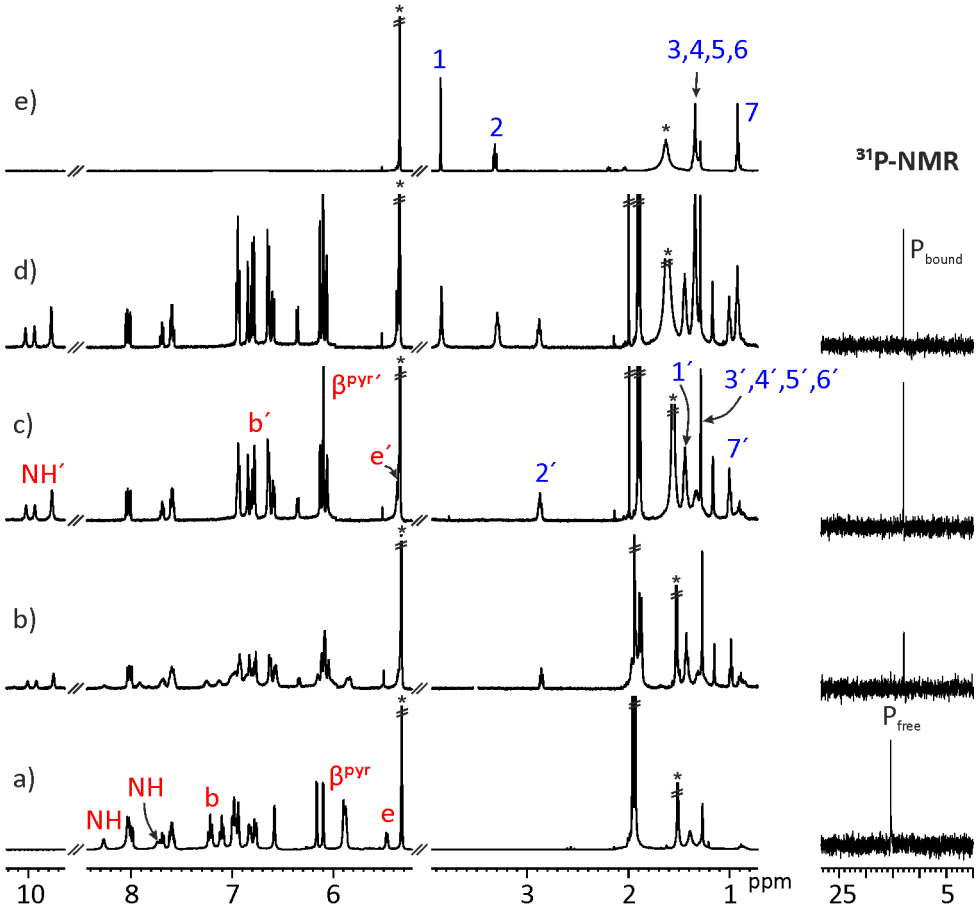

Figure 2.7 Left panel, selected regions of the ^{1}H NMR spectra (500 MHz, 298 K) of CD_2Cl_2 solutions containing receptor **3i** and **HexCr** in different molar ratios: a) Free **3i**; b) **3i** + 0.5 equiv.; c) **3i** + 1.0 equiv.; d) **3i** + 2.5 equiv of **HexCr**. Trace e) shows the same regions of the ^{1}H NMR spectrum of **HexCr**. Right panel, corresponding ^{31}P NMR spectra (202 MHz, CD2Cl2, 298 K). * Residual solvent peak.

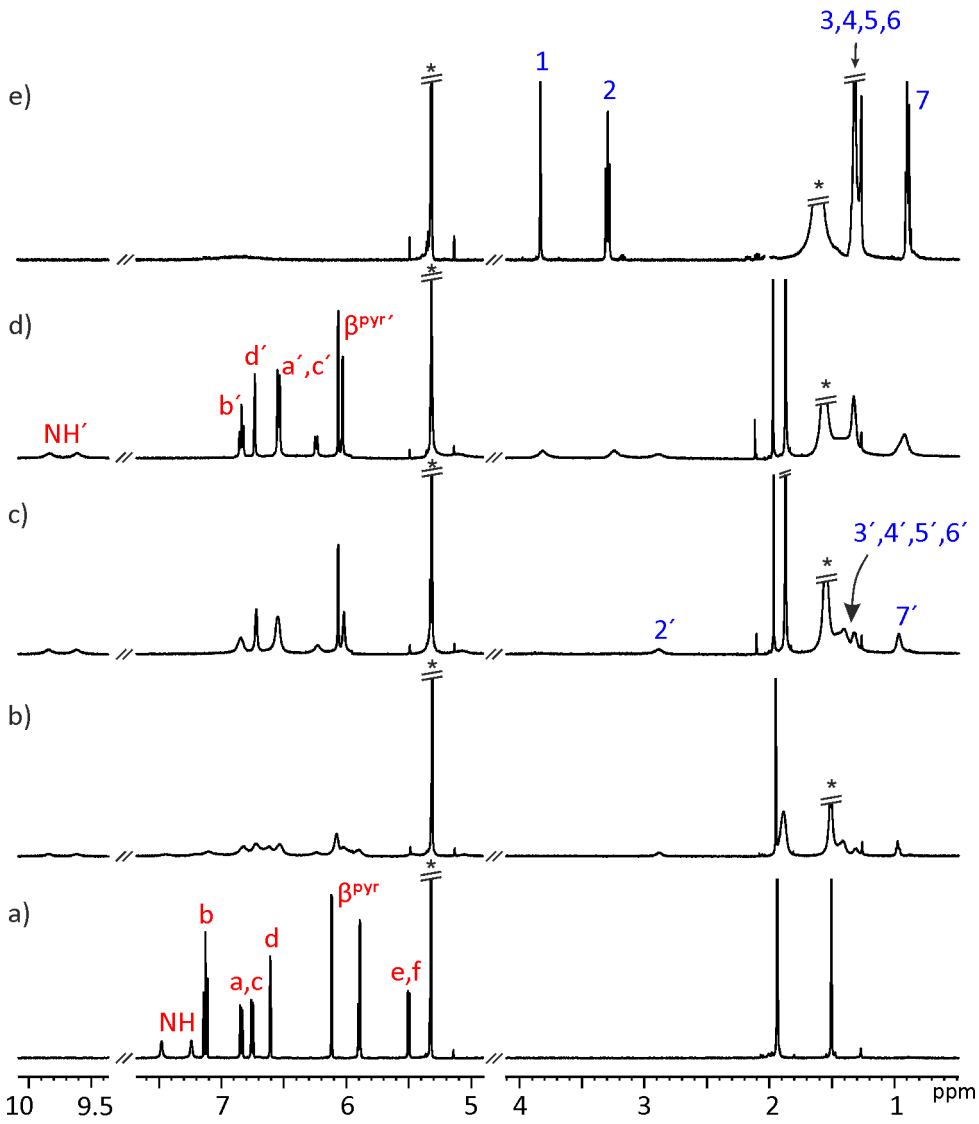

Figure 2.8 Left panel, selected regions of the ^{1}H NMR spectra (500 MHz, 298 K) of CD_2Cl_2 solutions containing receptor **4** and **HexCr** in different molar ratios: a) Free **4**; b) **4** + 0.5 equiv.; c) **4** + 1.0 equiv.; d) **4** + 2.5 equiv of **HexCr**. Trace e) shows the same regions of the ^{1}H NMR spectrum of **HexCr**.

Pairwise NMR competitive experiments.

Speciation profile calculation.

The speciation profile of the displacement of **HexCr⊂2io** with **2ii** was calculated considering that the value of the binding constant of receptor **2ii** is two times higher than that displayed by receptor **2io**. According with the profile, the addition of 1.0

equiv. of **2ii** to a equimolar mixture of **HexCr⊂2io** produces the formation of **HexCr⊂2ii** complex around 60%.

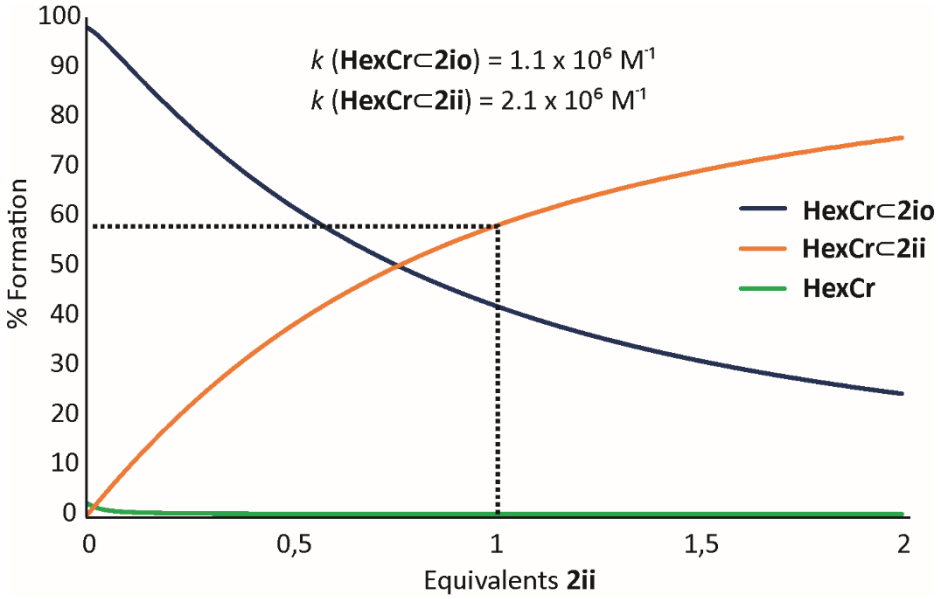

Figure 2.9 Calculated speciation profile for the competitive titration of **HexCr⊂2io** (2.0 mM) with **2ii** considering a binding constant of 1.1 × 10^6 M^{-1} for **HexCr⊂2io** and 2.1 × 10^6 M^{-1} for **HexCr⊂2ii**.

Competitive NMR titration of **HexCr⊂2io** with **2ii**.

The equimolar mixture of **HexCr** and **2io** in CD_2Cl_2, at millimolar concentration, produced the quantitative assembly of **HexCr⊂2io** (2.0 mM, Figure 2.*10*). Subsequently, 0.5 mL of the above solution were transferred to an NMR tube. On the other hand, a solution of **2ii** ten-fold more concentrated was prepared in the same solvent (20-22 mM). The 0.5 mL of the **HexCr⊂2io** complex solution was titrated by manually injecting incremental amounts of the **2ii** solution. The ^{1}H-NMR spectrum of the mixture was acquired after each injection and vigorous hand shaking of the NMR tube.

The addition of 1.0 equiv. of **2ii** to the **HexCr⊂2io** solution produce the appearance of a new set of signals assigned to the **HexCr⊂2ii** complex. For instance, two signals for bound **HexCr** are detected at 3.21 and 2.90 ppm. The more downfield shifted signal was assigned to the H^1 protons of the bound **HexCr** in the complex with **2ii**, while the more upfield shifted to the same protons in complex with **2io**. According with the integration of these proton signals, the **HexCr⊂2ii** complex is formed

around 60% molar ratio. This is in agreement with the speciation profile calculated at 2.0 mM considering the binding constants determined by ITC (Figure 2.*9*).

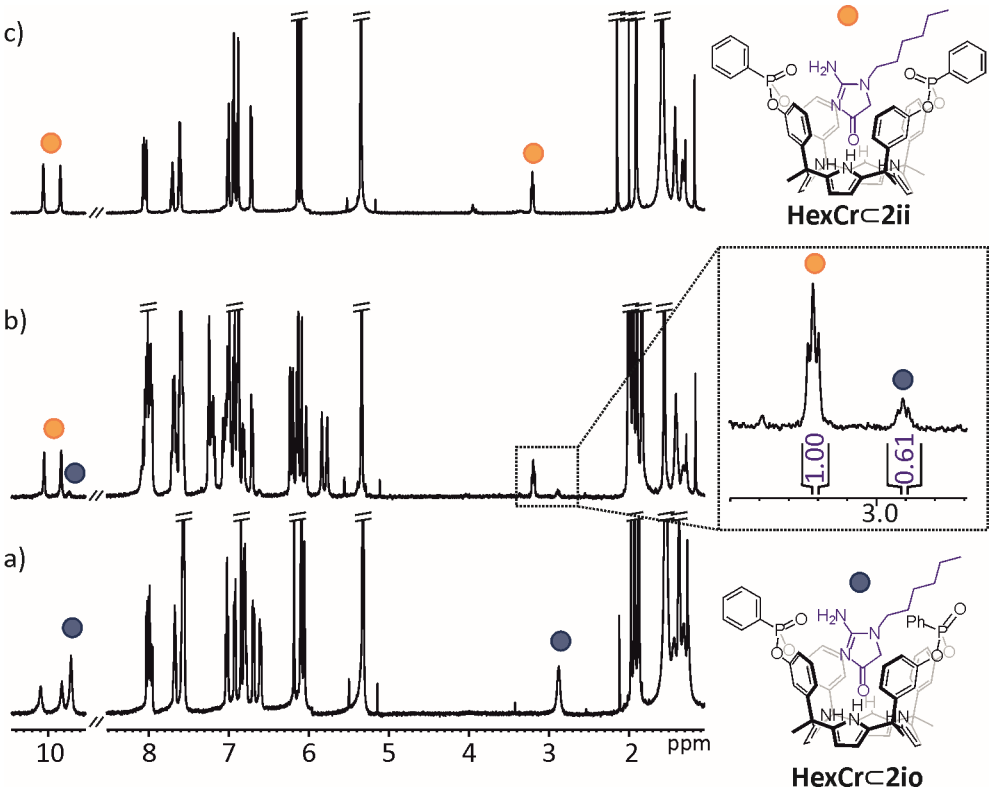

Figure 2.10 selected regions of the ^{1}H-NMR spectra (400 MHz, CD_2Cl_2, 298 K) registered during the competitive titration of a) **HexCr⊂2io** (2.0 mM) with incremental amounts of **2ii**: b) 1.0 equiv. of **2ii**; c) **HexCr⊂2ii.**

2.4.4 ITC experiments.

ITC experiments were performed in a MicroCal VP-ITC Micro Calorimeter with the VP Viewer 2000 software. Due to the low solubility of the hexyl creatinine **HexCr** in methylene chloride, a reverse ITC experiments were performed. The concentration of the solution in the syringe was approximately seven to ten times more concentrated than the cell solution. The association constants and the thermodynamic parameters were obtained from the fit of the titration data to the "one set of sites" binding model implemented in the Microcal ITC Data Analysis module. The enthalpy of binding for each injection is plotted against the molar ratio of guest/host in the cell. The continuous line represents the least-squares-fit of the data to a single-site binding model.

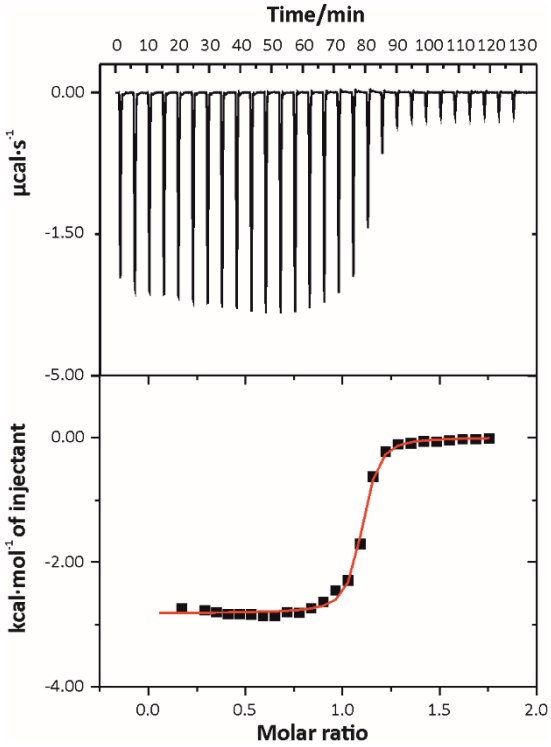

Figure 2.11 On top the raw data for the titration of **HexCr⊂2ii** in methylene chloride are shown. The titration was performed at 288 K. The binding isotherm of the calorimetric titration is shown at the bottom. [**2ii**] = 3.43 mM over [**HexCr**] = 0.42 mM.

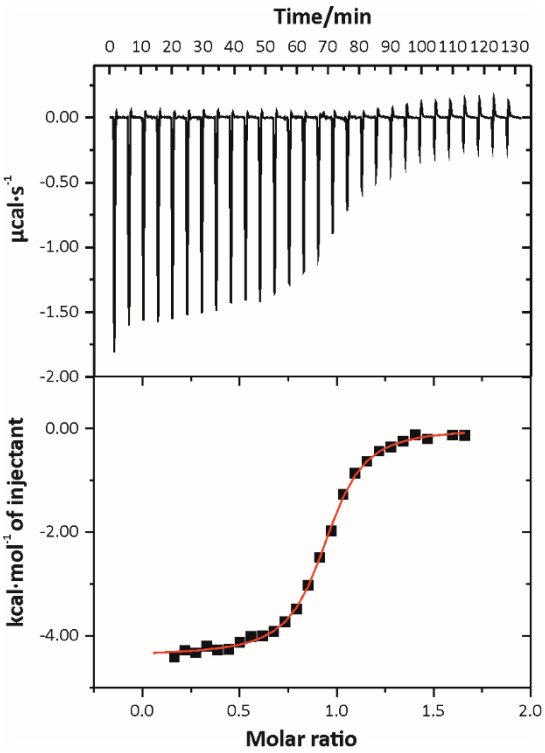

Figure 2.12 On top the raw data for the titration of **HexCr⊂2io** in methylene chloride are shown. The titration was performed at 288 K. The binding isotherm of the calorimetric titration is shown at the bottom. [**2io**] = 0.85 mM over [**HexCr**] = 0.11 mM.

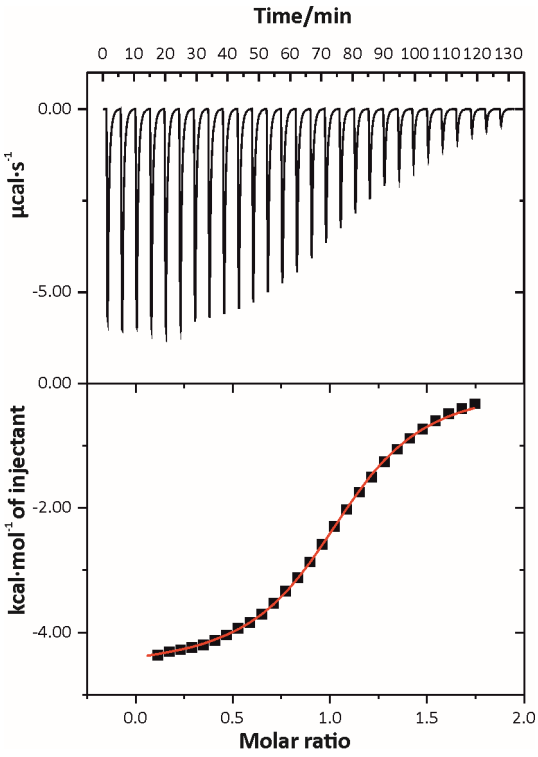

Figure 2.13 On top the raw data for the titration of **HexCr⊂2oo** in methylene chloride are shown. The titration was performed at 288 K. The binding isotherm of the calorimetric titration is shown at the bottom. [**2oo**] = 6.5 mM over [**HexCr**] = 0.8 mM.

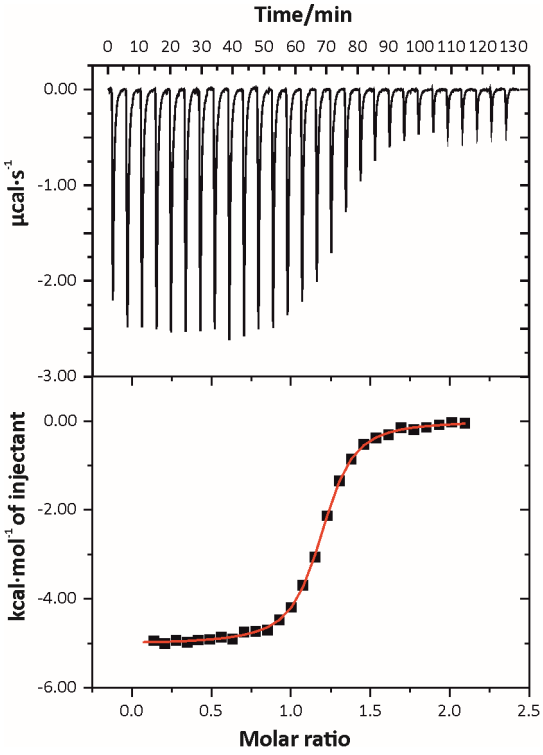

Figure 2.14 On top the raw data for the titration of **HexCr⊂3i** in methylene chloride are shown. The titration was performed at 288 K. The binding isotherm of the calorimetric titration is shown at the bottom. [**3i**] = 1.95 mM over [**HexCr**] = 0.2 mM.

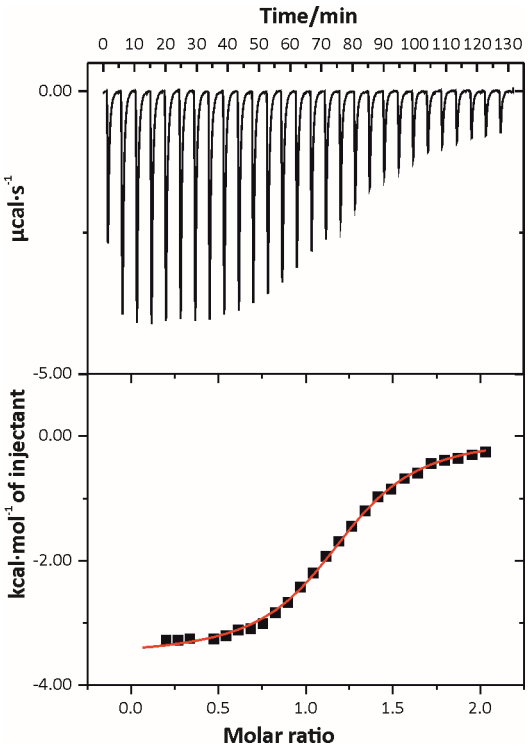

Figure 2.15 On top the raw data for the titration of **HexCr⊂4** in methylene chloride are shown. The titration was performed at 288 K. The binding isotherm of the calorimetric titration is shown at the bottom. [**4**] = 5.01 mM over [**HexCr**] = 0.53 mM.

2.4.5 X-ray structures.

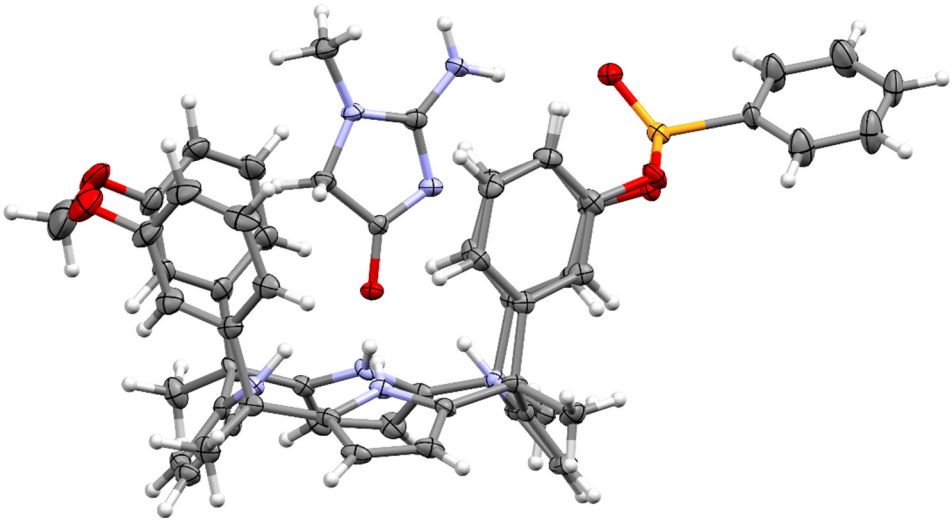

Figure 2.16 X-ray structures of **Cr⊂3i**. Thermal ellipsoids for C, N, O and P atoms set at 50% probability, H atoms are shown as spheres of 0,15 Å diameter. Taken from reference 14.

2.5 References and notes.

[1] Cram, D. J. *Science* **1983**, *219*, 1177-1183.
[2] Biavardi, E.; Tudisco, C.; Maffei, F.; Motta, A.; Massera, C.; Condorelli, G. G.; Dalcanale, E. *Proceedings of the National Academy of Sciences* **2012**, *109*, 2263-2268.
[3] Rudkevich, D. M.; Rebek, J., Julius *Eur. J. Org. Chem.* **1999**, *1999*, 1991-2005.
[4] Biavardi, E.; Favazza, M.; Motta, A.; Fragalà, I. L.; Massera, C.; Prodi, L.; Montalti, M.; Melegari, M.; Condorelli, G. G.; Dalcanale, E. *J. Am. Chem. Soc.* **2009**, *131*, 7447-7455.
[5] Pinalli, R.; Dalcanale, E.; Misztal, K.; Lucentini, R.; Ugozzoli, F.; Massera, C. *Inorg. Chim. Acta* **2018**, *470*, 250-253.
[6] Barboza, T.; Pinalli, R.; Massera, C.; Dalcanale, E. *CrystEngComm* **2016**, *18*, 4958-4963.
[7] Maffei, F.; Brancatelli, G.; Barboza, T.; Dalcanale, E.; Geremia, S.; Pinalli, R. *Supramol. Chem.* **2018**, *30*, 600-609.
[8] Kalenius, E.; Moiani, D.; Dalcanale, E.; Vainiotalo, P. *Chem. Commun. (Cambridge, U. K.)* **2007**, 3865-3867.
[9] Maffei, F.; Betti, P.; Genovese, D.; Montalti, M.; Prodi, L.; De Zorzi, R.; Geremia, S.; Dalcanale, E. *Angew. Chem., Int. Ed.* **2011**, *50*, 4654-4657.
[10] Pinalli, R.; Dalcanale, E. *Acc. Chem. Res.* **2013**, *46*, 399-411.
[11] Menozzi, D.; Pinalli, R.; Massera, C.; Maffei, F.; Dalcanale, E. *Molecules* **2015**, *20*, 4460-4472.

[12] Ciardi, M.; Tancini, F.; Gil-Ramírez, G.; Escudero Adán, E. C.; Massera, C.; Dalcanale, E.; Ballester, P. *J. Am. Chem. Soc.* **2012**, *134*, 13121-13132.
[13] Ciardi, M.; Galán, A.; Ballester, P. *J. Am. Chem. Soc.* **2015**, *137*, 2047-2055.
[14] Guinovart, T.; Hernández-Alonso, D.; Adriaenssens, L.; Blondeau, P.; Martínez-Belmonte, M.; Rius, F. X.; Andrade, F. J.; Ballester, P. *Angew. Chem., Int. Ed.* **2016**, *55*, 2435-2440.
[15] Rissanen, K. In *Analytical Methods in Supramolecular Chemistry* 2007, p 305-336.
[16] Schalley, C. A. *Int. J. Mass Spectrom.* **2000**, *194*, 11-39.
[17] Tullio, A. D.; Reale, S.; Angelis, F. D. *J. Mass Spectrom.* **2005**, *40*, 845-865.
[18] Casas-Hinestroza, J. L.; Bueno, M.; Ibáñez, E.; Cifuentes, A. *Anal. Chim. Acta* **2019**, *1081*, 32-50.
[19] Dethlefs, C.; Eckelmann, J.; Kobarg, H.; Weyrich, T.; Brammer, S.; Näther, C.; Lüning, U. *Eur. J. Org. Chem.* **2011**, *2011*, 2066-2074.
[20] Srivastava, V. K.; Yadav, R. In *Data Processing Handbook for Complex Biological Data Sources*; Misra, G., Ed.; Academic Press: 2019, p 125-137.
[21] In our hands, a semipreparative HPLC separation is not necessary as is reported in literature. Using a gradient elution from CH2Cl2 to CH2CL2:AcOEt 95:5 is possible to separate the three isomers in similar percentages to those reported by semipreparative HPLC.
[22] Beckles, D. L.; Maioriello, J.; Santora, V. J.; Bell, T. W.; Chapoteau, E.; Czech, B. P.; Kumar, A. *Tetrahedron* **1995**, *51*, 363-376.
[23] Melegari, M.; Suman, M.; Pirondini, L.; Moiani, D.; Massera, C.; Ugozzoli, F.; Kalenius, E.; Vainiotalo, P.; Mulatier, J.-C.; Dutasta, J.-P.; Dalcanale, E. *Chemistry – A European Journal* **2008**, *14*, 5772-5779.
[24] Suman, M.; Freddi, M.; Massera, C.; Ugozzoli, F.; Dalcanale, E. *J. Am. Chem. Soc.* **2003**, *125*, 12068-12069.
[25] Jose, D.; Datta, A. *The Journal of Physical Chemistry Letters* **2010**, *1*, 1363-1366.
[26] We realized that a slow addition by using a syringe pump helps to decrease polymers as byproducts (stain clearly observed on the origin of the TLC).

UNIVERSITAT ROVIRA I VIRGILI
CALIX[4]PYRROLE CAVITANDS FOR SUPRAMOLECULAR SENSING AND CATALYSIS
Andrés Felipe Sierra Ramos

Chapter 3

Optical supramolecular sensing of creatinine

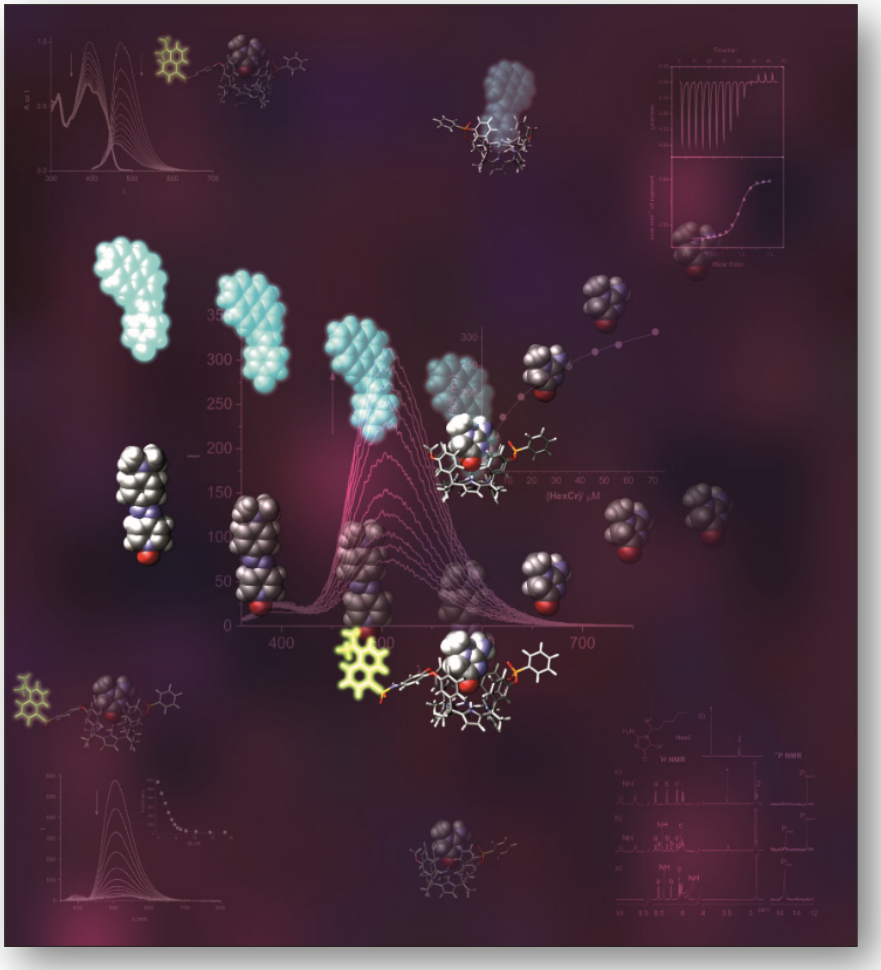

Part of this chapter has been published in:

Sierra, A. F.; Hernández-Alonso, D.; Romero, M. A.; González-Delgado, J. A.; Pischel, U.; Ballester, P. *J. Am. Chem. Soc.* **2020**, *142*, 4276-4284.

UNIVERSITAT ROVIRA I VIRGILI
CALIX[4]PYRROLE CAVITANDS FOR SUPRAMOLECULAR SENSING AND CATALYSIS
Andrés Felipe Sierra Ramos

3.1 Introduction.

The levels of creatinine (**Cr**, see Figure 3.*1*) in human bodily fluids is a widely applied clinical indicator for monitoring kidney and renal function.[1,2] Creatinine is a metabolic waste product, being related to muscle activity, and any anomalous secretion due to organ malfunction leads inevitably to higher concentrations of **Cr** in blood serum and/or urine. Methods for molecular biosensing of creatinine using simple fluorescent probes or in combination with bioconjugates have been reported.[2,3,4,5,6] While these latter approaches rely on unspecific interactions between creatinine and the probe molecule, supramolecular sensing offers distinct benefits for the design of selective and specific sensors by building on size, shape, and function complementarity between the receptor and analyte. Unfortunately, most synthetic receptors designed for creatinine binding are flat and edge-functionalized with divergent hydrogen bonding motifs.[7,8,9,10,11] These characteristics make them a nonideal choice for supramolecular sensing design. Hence, it is not surprising that supramolecular approaches to creatinine sensing, using synthetic receptors, are very scarce in the literature.[12,13]

The selection of synthetic receptor units is a key element in the design of supramolecular sensors. In this respect, aryl-extended calix[4]pyrroles[14] and their cavitand derivatives are well-known receptors for the effective binding of neutral polar species, as well as mono- and polyatomic anions.[15] The superior binding properties of these receptors are inherent to the structural elements that relate to their cone conformation. Moreover, aryl-extended calix[4]pyrroles can be synthetically elaborated at both their upper and lower rims. These structural modifications of the receptor scaffold are translated into modulations of solubility and binding properties. Fluorescent calix[4]pyrrole chemosensors for the recognition of anions[16,17,18,19,20,21,22,23,24,25] and cations[26,27] are known in the literature. In contrast, the development of fluorescent calix[4]pyrrole chemosensors for the detection and quantification of relevant polar biomolecules remains practically unexplored.[28]

In 2016, we introduced an ion-selective electrode (ISE) suitable for the detection of **Cr** in bodily fluids.[29] This ISE hinged on the use of a novel monophosphonate calix[4]pyrrole **1** as an ionophore (Figure 3.*1*). Receptor **1** displayed a high affinity for **Cr** and its protonated form **Cr**·H^+. In contrast to the previously published plane creatinine receptors,[7,10,11,12] macrocycle **1** features a deep aromatic cavity that is

functionalized with a single phosphonate group at the open end (upper rim) and four pyrrole NHs at the closed end.

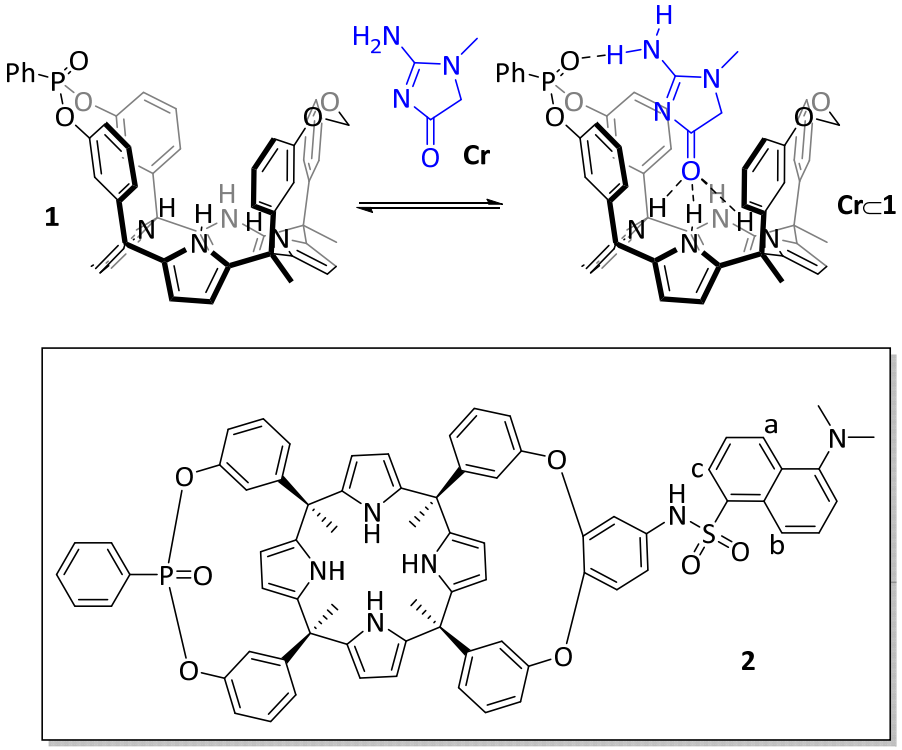

Figure 3.1 Top: molecular structures of receptor **1**, creatinine **Cr**, the 1:1 inclusion complex **Cr⊂1**, and its binding equilibrium. Bottom: structure of the dansyl-modified calix[4]pyrrole receptor **2**.

The cavity dimensions of **1** are ideal for the inclusion of **Cr** by surrounding most of its surface. The polar groups of **1** offer complementary hydrogen-bonding, π–π, and CH–π interactions with the included **Cr**. These attributes translate into an efficient binding for **Cr** in organic solvents. Moreover, the 1:1 **Cr⊂1** inclusion complex is kinetically stable on the ^{1}H NMR chemical shift time scale.

Drawing on calix[4]pyrrole **1**, we present herein optical supramolecular sensors for creatinine and derivatives. In an expansion, the scaffold of **1** was modified with a dansyl fluorophore, yielding receptor **2** (Figure 3.*1*). Using fluorescence emission as an output signal of a molecular sensor provides a convenient way of analyte detection, even with the naked eye. In addition, fluorescence can be monitored for relatively low concentrations (submicromolar) of the sensor, improving the sensitivity further.

A *priori*, two photophysical design strategies (Scheme 3.*1*), based on the popular and functionally flexible competitive indicator displacement assays (IDAs),[30,31] could be followed with receptors **1** and **2**.

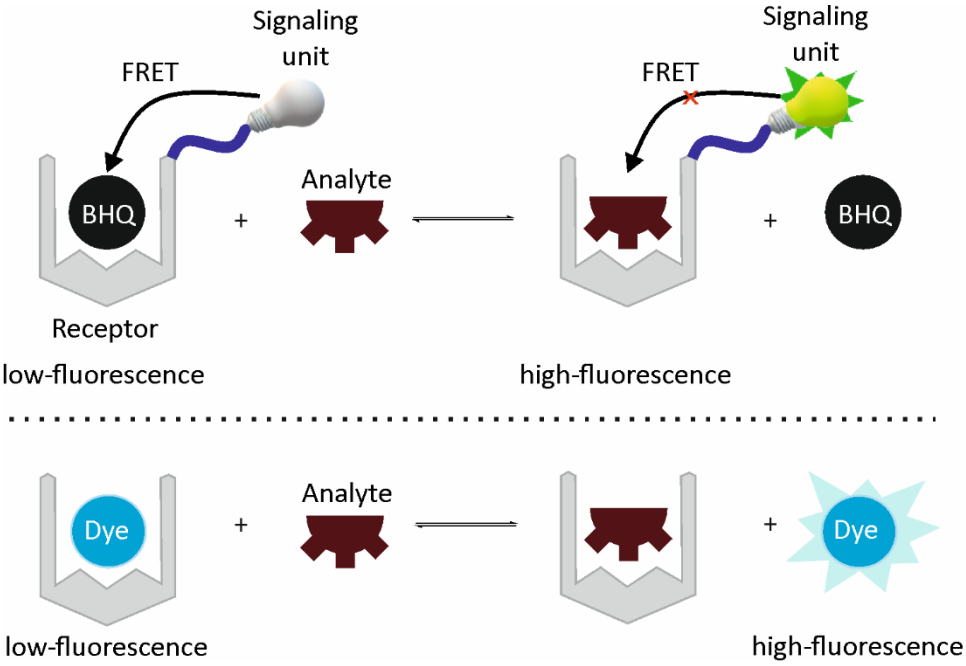

Scheme 3.1 Schematic representation of different approaches to optical supramolecular sensing of creatinine (analyte) using a calix[4]pyrrole scaffold (receptor). Top: Displacement of a black-hole quencher (**BHQ**) and deactivation of FRET quenching of a receptor-appended fluorophore (signaling unit). Bottom: Displacement of a fluorescent dye.

In both cases, we choose pyridyl-*N*-oxides as binding motifs of the indicator guest. Pyridyl-*N*-oxides are known to form host–guest complexes with calix[4]pyrroles having binding constants (10^6–$10^7 M^{-1}$)[32] that are comparable with or slightly higher than those of **Cr** and its derivatives.

On one hand, receptor **2** could be combined with a black-hole quencher guest (**3**, Figure 3.*2*) which on binding deactivates the dansyl fluorescence by Förster resonance energy transfer (FRET). The competitive displacement of the indicator by **HexCr** (as a lipophilic **Cr** analogue) is expected to be signaled by the observation of fluorescence turn-on. On the other hand, receptor **1** could be combined with a fluorescent guest (**4** or **5**, Figure 3.*2*).

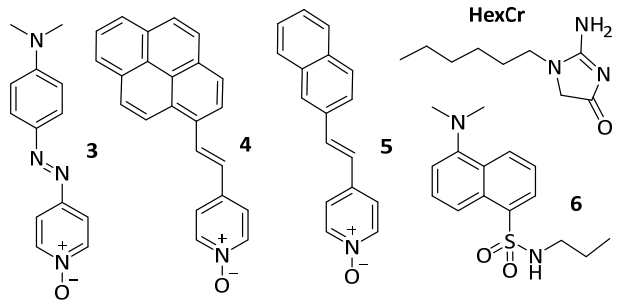

Figure 3.2 Molecular structures of **HexCr**, the *para*-substituted pyridyl-*N*-oxides **3**, **4** and **5**, and the dansyl reference model **6**.

On binding by the receptor, the guest would then undergo fluorescence quenching which is inverted on competitive displacement with **HexCr**. This again yields a fluorescent turn-on sensor. Based on these approaches, highly sensitive optical supramolecular sensors for creatinine derivatives are presented.

Calix[4]pyrroles **1** and **2**, and guests **3**-**5** and **HexCr** were transfer to the group of Prof. Uwe Pischel in order to perform the optical studies. It is worth mentioning that in a preliminary step of the project we realized some optical studies finding similar results. However, prof. Uwe research group performed and extend the experiments at more proper conditions (e.g. concentrations and saturation points).

3.2 Results and Discussion.

3.2.1 Synthesis.

The synthesis of receptor **2** involved four reaction steps starting from the known α,α,α,α-tetrahydroxy-calix[4]-pyrrole **7** (Scheme 3.*2*).[33] The nitro-monoaryl-bridged intermediate **8** was prepared using reaction conditions previously reported for a structurally related compound.[34] The nitro-diol-cavitand **8** was isolated, as a racemic mixture, after column chromatography purification in 32% yield. The incorporation of the bridging phosphonate group was achieved by reacting the nitro-diol **8** with phenylphosphonic dichloride using triethyl-amine as base. The reaction produced a mixture of two diastereoisomers, **9in** and **9out**, which differ in the relative spatial orientation of the P=O group with respect to the aromatic cavity. Diastereoisomers **9in** and **9out** were isolated as pure compounds after column chromatography purification of the reaction crude in 46% and 22% yield, respectively. Gratifyingly, single crystals of **9in** and **9out** (Figure 3.*3*), that were suitable for X-ray diffraction

analysis, were obtained from acetone and dichloromethane solutions, respectively.

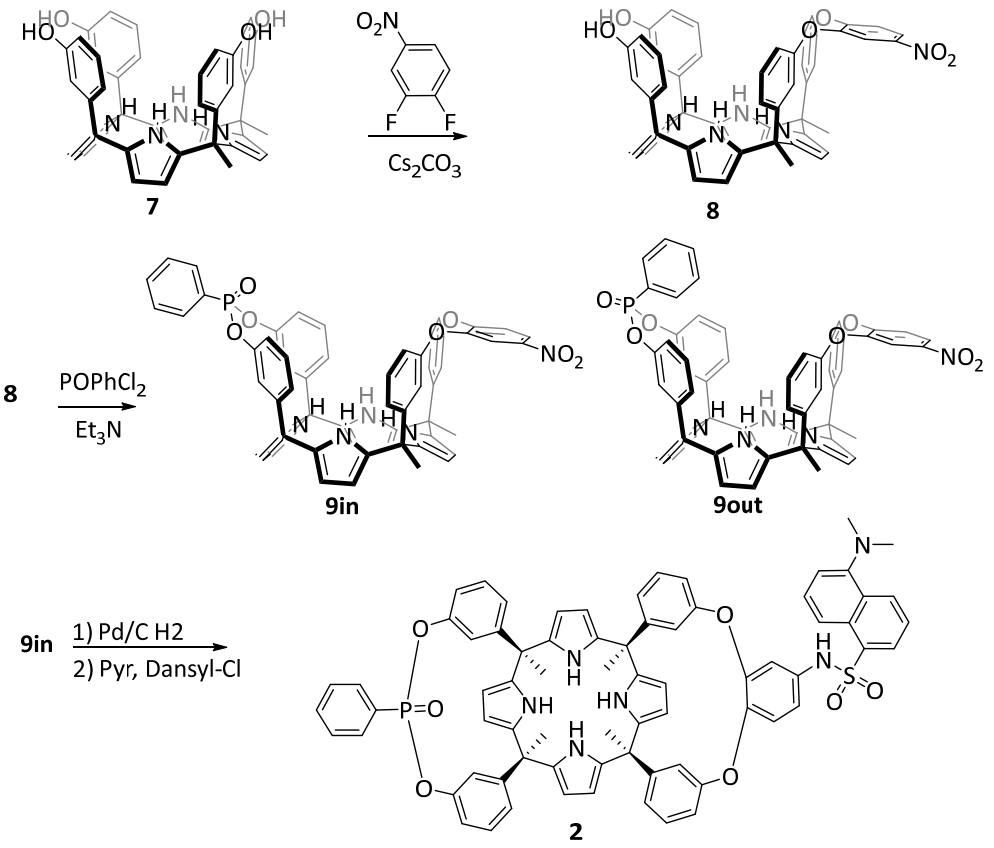

Scheme 3.2 Synthetic scheme for the synthesis of receptor **2**.

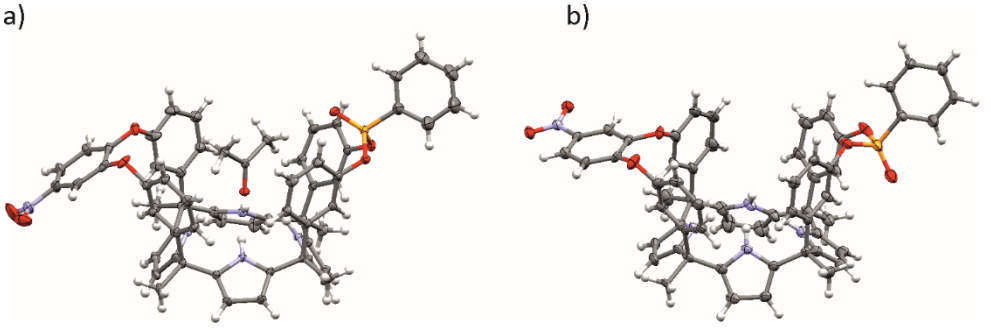

Figure 3.3 X-ray structure of the a) CH_3COCH_3⊂**9in** inclusion complex and b) **9out**. Thermal ellipsoids for C, N, O, and P atoms set at 50% probability; H atoms are shown as spheres of 0.20 Å diameter.

In the solid state, **9in** showed the aryl-extended calix[4]pyrrole core in cone conformation with one molecule of acetone included in the aromatic cavity. The

four pyrrole NHs interact with the acetone guest via hydrogen bonding. The nitro-aryl-bridging group adopted a pseudo equatorial conformation.[35]

The catalytic hydrogenation of the nitro compound **9in**, using 10% Pd/C, yielded quantitatively the corresponding amino derivative, which was used without further purification in the coupling reaction with dansyl chloride. The fluorescent dansylamide monophosphonate cavitand receptor **2** was obtained in 98% yield as a racemic mixture. All attempts to separate the enantiomers of **2**, using chiral HPLC, were unsuccessful. However, because creatinine is nonchiral, no difference for the sensing is expected for the two stereoisomers. Receptor **2** was characterized by a full set of high-resolution spectra (Figure 3.*22* to Figure 3.*27*).

In turn, the precursors of the pyridyl-*N*-oxide dyes **4** and **5** was prepared following reported procedures.[36,37] The *N*-oxidation reaction of the synthesized pyridines was performed using *m*-chloroperoxybenzoic acid (*m*-CPBA).[38]

The fluorescent *N*-oxides **4** and **5** were isolated after column chromatography purification, using neutral alumina, in 58% and 45% yield, respectively. This strategy was not implemented in the synthesis of **3** owing to the presence of additional nitrogen atoms susceptible to *N*-oxidation with the peroxyacid treatment.[39] Instead, we synthesized **3** following a reported procedure that involves the preparation of 4-amino-pyridine-*N*-oxide, its diazotization, and subsequent coupling with dimethyl *N*,*N*-aniline.[40] Starting from 4-Boc-amino-pyridine, we isolated **3** in high purity and 11 % overall yield.

Finally, due to the reduced solubility of **Cr** in organic solvents, we prepared the lipophilic derivative **HexCr**. The compound was obtained, following a known protocol,[41] by treating methyl *N*-cyano-*N*-hexyl-aminoacetate with aqueous ammonia at room temperature. **HexCr** proved to be soluble up to 1.5 mM in dichloromethane and chloroform, thereby enabling binding studies by NMR spectroscopy (see below).

3.2.2 Binding Studies of **2** with **HexCr**.

We initially probed the interaction of **2** with **HexCr** using ^{1}H and ^{31}P NMR spectroscopy. The ^{1}H NMR spectrum of **2** at mM concentration in $CDCl_3$ solution showed sharp and well-resolved proton signals (Figure 3.*4*a, left panel).

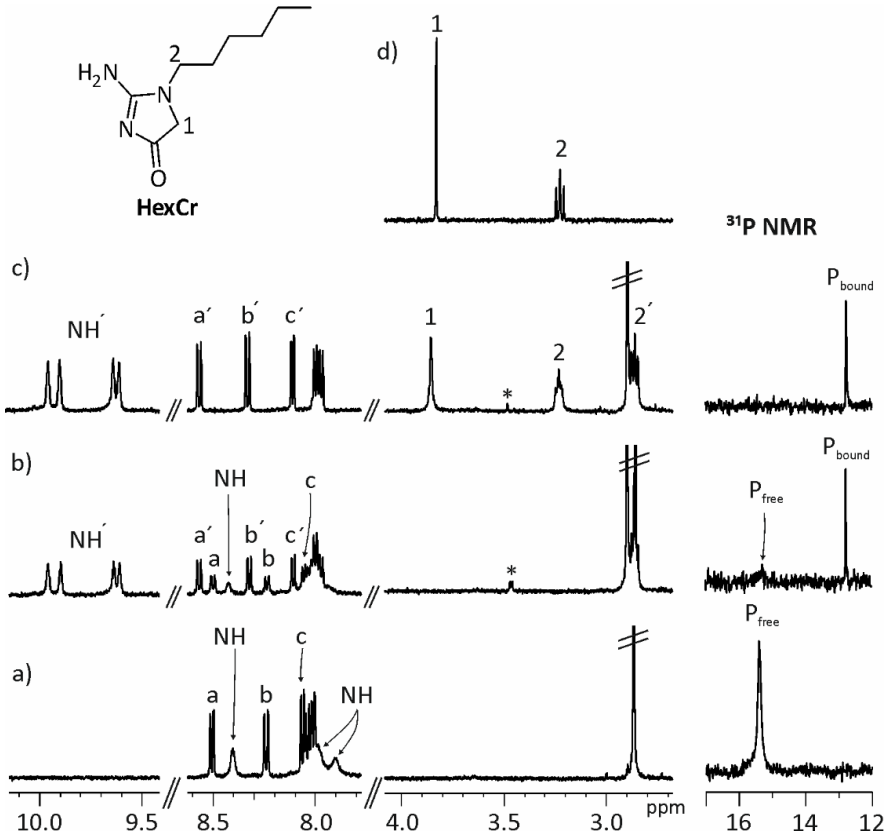

Figure 3.4 Left panel: selected regions of the ^{1}H NMR spectra (500MHz, 298 K) of $CDCl_3$ solutions containing fluorescent receptor **2** and **HexCr** in different molar ratios: a) free **2**; b) **2** + 0.5 equiv.; and c) **2** + 1.5 equiv. d) Trace shows one region of the ^{1}H NMR spectrum of **HexCr**. Right panel: corresponding ^{31}P NMR spectra (202 MHz, $CDCl_3$, 298 K). Primed letters and numbers correspond to the proton signals in the **HexCr⊂2** complex. Proton assignment of **HexCr** is shown in the inset structure. For the proton assignment of **2** see Figure 3.1. * Residual methanol peak. See Experimental Section for a more detailed preparation of the analyzed solution mixtures.

The addition of 0.5 equiv. of **HexCr** to a mM solution of **2** in $CDCl_3$ produced the appearance of a new set of signals that were assigned to the protons of the bound host (Figure 3.*4*b, left panel). Remarkably, the bound pyrrole NHs resonated as four sharp singlets around 9.8 ppm. The significant downfield shift (Δδ = +1.5−1.7 ppm) experienced by the NH protons testifies their involvement in hydrogen bonding interactions with the oxygen atom of the bound **HexCr**. Moreover, we detected two new signals in the aliphatic region of the spectrum. These signals were assigned to the protons H^1 and H^7 of the bound **HexCr**. The H^1 proton experienced a large upfield shift (Δδ = −2.71 ppm) with respect to its chemical shift value in the free **HexCr** (Figure 3.*28*). This observation supports the deep inclusion of **HexCr** in the aromatic

cavity of **2**, where the H^1 proton experiences the shielding effect exerted by the four meso-phenyl groups of the receptor.

The addition of incremental amounts of **HexCr** produced a gradual increase in intensity of the proton signals assigned to bound **2** at the expenses of those of the free counterpart. In the presence of 1 equiv. of **HexCr**, only the proton signals corresponding to the bound host **2** were observable (Figure 3.*29*). Finally, an excess of **HexCr** produced the appearance of the proton signals corresponding to free guest (Figure 3.*4*c, left panel).

An analogous behavior was observed in the acquired ^{31}P NMR spectra of the solutions. The ^{31}P NMR spectrum of **2** showed a somewhat broadened singlet resonating at 15.5 ppm corresponding to the phosphorus atom of the inwardly directed P=O group (Figure 3.*4*a, right panel). In the presence of incremental amounts of **HexCr**, the intensity of this phosphorus signal decreased, and a new sharp singlet, resonating at 13.7 ppm, was observed. In the presence of 1.5 equiv. of **HexCr**, only the phosphorus signal assigned to the P=O group in bound **2** was detected (Figure 3.*4*c, right panel).

In summary, these results indicate that receptor **2** and **HexCr** exclusively formed a 1:1 inclusion complex, **HexCr⊂2**. In this complex, the **HexCr** is deeply immersed in the aromatic cavity of the calix[4]pyrrole **2** in its cone conformation. The binding process displayed slows chemical exchange dynamics in the ^1H and ^{31}P NMR chemical shift time scales between free and bound counterparts.

The kinetic stability of the complex was accompanied by a high thermodynamic stability. Thus, the exclusive observation of the signals of the bound host **2** in the ^1H and ^{31}P NMR spectra acquired in the presence of 1 equiv. of **HexCr** allowed us to estimate that the stability constant of the **HexCr⊂2** complex should be larger than 10^4 M^{-1}.

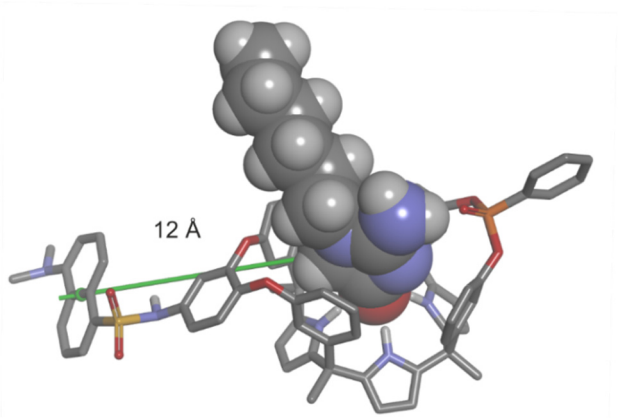

Figure 3.5 Energy-minimized structure of the **HexCr⊂2** complex (PB86-D3/def2-SVP, CPM/chloroform). The nonpolar hydrogen atoms of receptor **2** were removed for the sake of clarity. The encapsulated **HexCr** molecule is shown as the CPK model.

The **HexCr⊂2** complex was fully characterized using 2D NMR experiments (COSY, ROESY Figure 3.*30* to Figure 3.*33*). To gain additional insight into the three-dimensional structure of the **HexCr⊂2** complex, the putative 1:1 inclusion was energy minimized (according to frequency calculation) at theBP86[42,43]-D3[44,45]/def2-SVP[46] level of theory using a polarizable continuum solvent model (PCM) for chloroform as implemented in Gaussian 09.[47] In analogy to the previously described monophosphonate methylene-bridged receptor **1**, the energy-minimized structure of the **HexCr⊂2** complex showed that the aromatic cavity of **2** nicely complements, in terms of size, shape, and functionalization, the included **HexCr** (Figure 3.*5*). The average distance between the centroids of **HexCr** and the dansyl group is in the range of 12 Å.

In order to assess the accurate value of the stability constant of the **HexCr⊂2** complex, we performed isothermal titration calorimetry (ITC) experiments. The successive addition of aliquots of a chloroform solution of receptor **2** (2.2 mM) to a solution of **HexCr** (0.3 mM) in the same solvent produced a gradual release of heat corresponding to the binding event (**Error! Reference source not found.**, top). The normalized integrated heats were corrected for dilution effects. This provided a sigmoidal binding isotherm with an inflection point close to a host:guest ratio of 1 (**Error! Reference source not found.**, bottom), as expected for 1:1 binding.

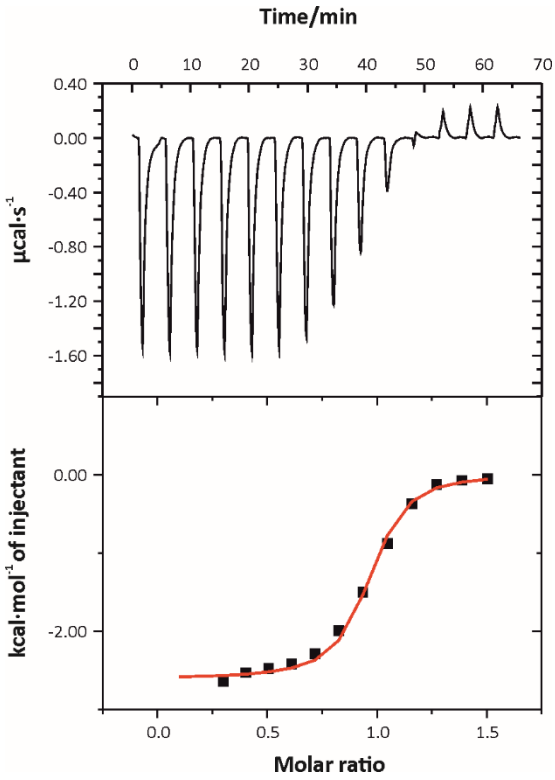

Figure 3.6 Top: raw data (heat vs time) for the calorimetry titration of **HexCr** (0.3 mM) with **2** (2.2 mM) performed at 288 K. Bottom: fit of the integrated and corrected calorimetric data to the one-site binding model. Note that the first two points were excluded from the fitting.

The fit of the calorimetric titration data to a 1:1 binding model returned an accurate value of the binding constant as K_a (**HexCr⊂2**) = (4.5 ± 0.4) × 10^5 M^{-1}. In addition, the fit also provided the binding enthalpy ΔH = −10.9 ± 0.4 kJ·mol^{-1}, which allowed us to calculate TΔS as 20.2 ± 0.6 kJ·mol^{-1} (298 K). These results indicate that the binding of **HexCr** by receptor **2** is mainly entropically driven. In accordance with previous interpretations, the desolvation of the binding partners and the solvation of the formed inclusion complex are thought to play an important role in the complexation process of aryl-extended calix[4]pyrrole cavitand receptors.[48]

3.2.3 Interaction of receptor **2** with dye **3** probed by fluorescence spectroscopy and ITC experiments.

The absorption spectrum of **2** in chloroform (blue line in Figure 3.*7*) shows an intense band with a maximum at 347 nm (ε = 4300 M^{-1}·cm^{-1}), typical for the dansyl chromophore (compared with model **6**; $\lambda_{abs,max}$ = 341 nm, ε = 4400 M^{-1}·cm^{-1}). Further, an intense absorption band with a maximum at 249 nm, which is

characteristic for the π,π*-transitions of the aryl-extended calix[4]pyrrole, is present (see Figure 3.*11*). Excitation at 347nm produces the characteristic and intense fluorescence emission of an intramolecular charge-transfer (ICT) excited state with a maximum at $\lambda_{fluo,max}$ = 509 nm (green line Figure 3.*7*).

For the realization of the IDA with the reporter pair **3**⊂**2**, we characterized the complexation of the pyridyl-*N*-oxide **3**, an analogue of the well-known 4-((4-(dimethylamino)phenyl)-azo)benzoic acid (DABCYL). DABCYL is a very popular black-hole quencher in FRET-based quenching pairs for nucleic acids and proteins.[49,50] Dye **3** is an efficient light absorber between 400 and 550 nm ($\lambda_{abs,max}$= 480 nm, ε= 39 500 $M^{-1}\cdot cm^{-1}$) (see Figure 3.*7*).

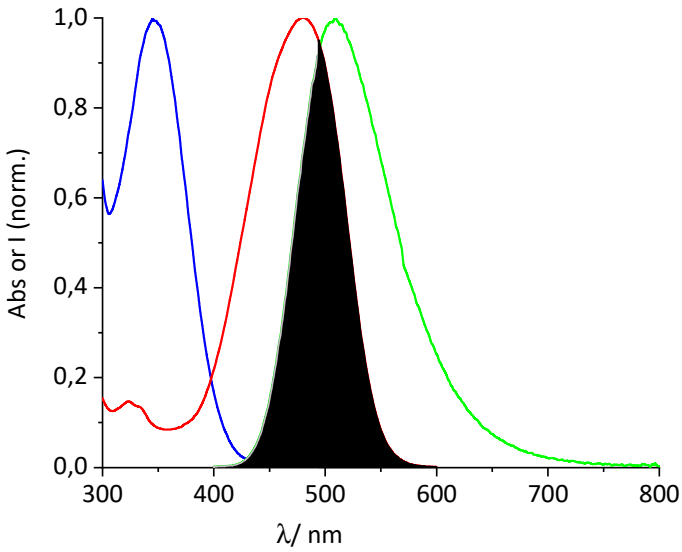

Figure 3.7 UV/vis absorption spectra of **2** (blue) and **3** (red) and the fluorescence spectrum of **2** (green). In grey the spectral overlap is illustrated.

This results in a significant spectral overlap with the dansyl emission (J = 1.2 × 10^{-10} $cm^6\cdot mol^{-1}$), which translates into a critical FRET radius of R_0= 43.7 Å. Taking into account the modeled distance (~13 Å, Figure 3.*46*) between the dansyl energy donor and **3** as the acceptor dye in the **3**⊂**2** complex, a quantitative FRET process should result (Φ_{FRET} ca. 1). Hence, we expected that on complexation of **3** by **2** ([**2**] = 5 μM) the fluorescence of the dansyl chromophore would be efficiently quenched. Indeed, the fluorescence quenching was practically quantitative (ca. 95%) when **2**

equiv of **3** were added. The fluorescence titration curve was fitted according to a 1:1 binding model yielding a binding constant of K_a (**3**⊂**2**) = (1.2 ± 0.5) × 10^7 M^{-1} (corrected for minor inner-filter effects due to the addition of a chromophoric titrator) (see Figure 3.*8*).

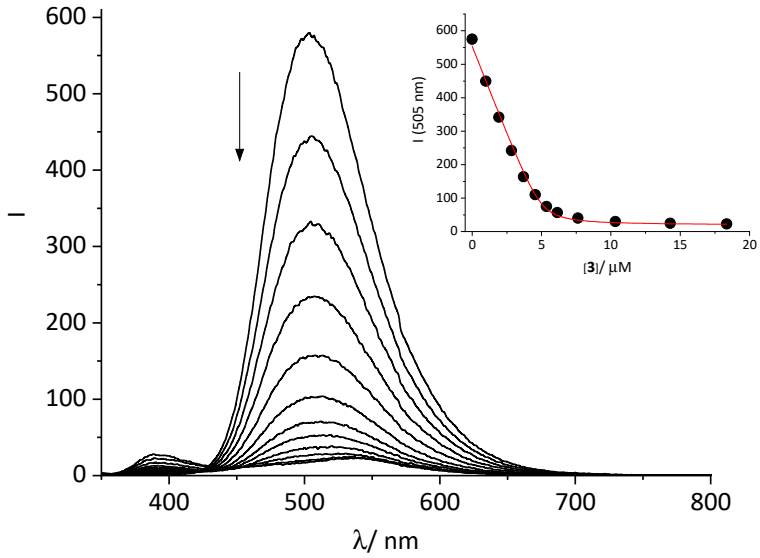

Figure 3.8 Emission spectra of **2** (5μM) registered on addition of increasing amounts of **3** in chloroform; λ_{exc} = 317 nm. Inset: Plot of the emission change at 505 nm (black circles) vs concentration of **3**. The red line corresponds to the fit of the titration data to a binding model that considers the formation of the 1:1 complex, **3**⊂**2**.

Next, we probed the interaction of **3** with receptor **2** by means of ITC experiments (see Figure 3.*9*). The titrations produced rectangular binding isotherms with the height corresponding exactly to ΔH and the sharp increase occurring at the stoichiometric equivalence point: host:guest ratio of **1**. This is the expected result for very tight binding and was only useful to estimate that K_a (**3**⊂**2**) was larger than 10^7 M^{-1}.

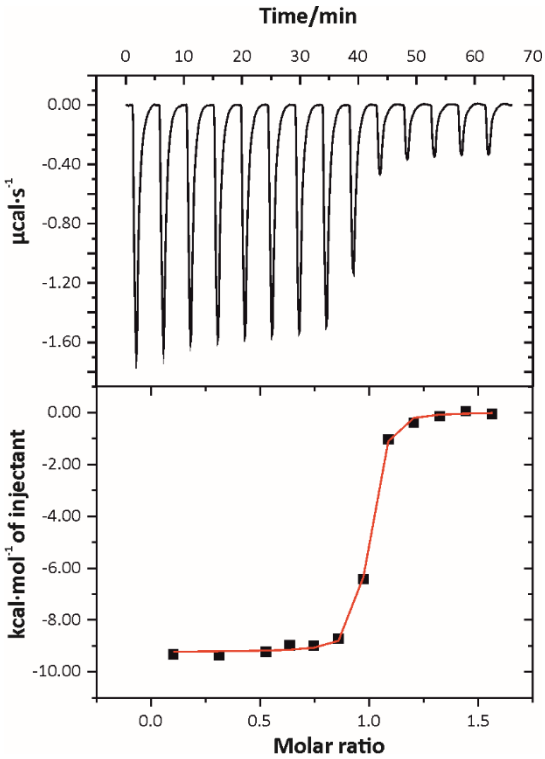

Figure 3.9 Top) Raw data (heat *vs.* time) for the titration of guest **3** over cavitand **2** in chloroform. The titration was performed at 288 K. Bottom) Integrated experimental data (black dots) fitted to a theoretical binding isotherm (red line) for a 1:1 binding model. [**3**] = 0.40 mM over [**2**] = 0.06 mM. Derived thermodynamic parameters: $K_a > 1 \times 10^7$ M^{-1}; ΔH = -35 ± 4.0 kJ mol^{-1}.

The estimated magnitude of the binding constant value is in complete agreement with the value calculated from the fluorescence titrations. While the enthalpic contribution to binding, ΔH, could be accurately determined as −34.7 kJ·mol^{-1} from the height of the isotherm, the corresponding entropic term, which should be positive, could not be derived owing to the estimative nature of K_a (**3**⊂**2**). An accurate determination of K_a (**3**⊂**2**) using ITC experiments required working in more dilute conditions, that is, reducing the "c" value. This approach was not experimentally feasible owing to the reduced heat release of the binding process, which dropped below the instrument's sensitivity (3 − 5 µcal per injection) at lower concentrations. The interaction of **2** with **3** was also probed using ^{1}H NMR spectroscopy (Figure 3.*37*).

3.2.4 Competitive IDA of the **3**⊂**2** Ensemble with **HexCr**.

We prepared an equimolar mixture of **3** and **2** (1 μM) in chloroform solution. At this concentration, complex formation is reached to an extent of 83%. The solution was titrated with incremental amounts of **HexCr**. [51]

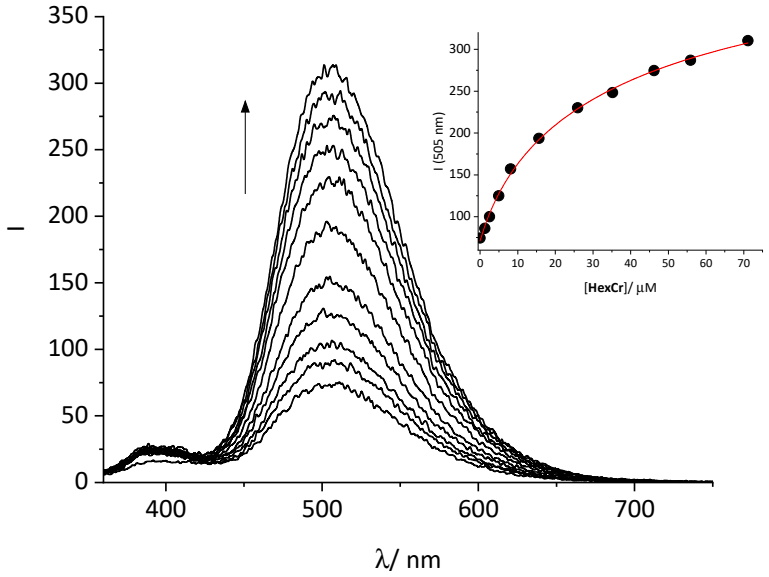

Figure 3.10 Emission spectra registered during the competitive IDA of the **3**⊂**2** ensemble with **HexCr**; λ_{exc} = 317 nm. The initial fluorescence is due to the minor fraction (17 %) of free **2** at the used equimolar concentration (1 μM). Inset: Plot of the changes in emission at 505 nm vs concentration of **HexCr**. The red line corresponds to the fit of the titration data to a competitive binding model that considers the formation of the **3**⊂**2** and **HexCr**⊂**2** complexes.

According to the expectations, on displacement of **3**, as quencher of the dansyl fluorescence, a turn-on effect was observed. For the addition of ca. 70 equiv. of **HexCr**, a 4-fold fluorescence enhancement at 505 nm was registered (see Figure 3.*10*). Noteworthily, **HexCr** does not exercise any significant quenching effect on the dansyl fluorophore when included in the cavity of receptor **2** (Figure 3.*11*). Hence, the observed fluorescence enhancement corresponds to the undisturbed response of the IDA. The fit of the competitive titration data to a competitive binding model of two 1:1 complexes returned a stability constant for the **HexCr**⊂**2** complex of K_a (**HexCr**⊂**2**) = (3.2 ± 0.4) × 10^5 M^{-1}. This value is in excellent agreement with the one obtained in the ITC experiment, (4.5 ± 0.4) × 10^5 M^{-1} (see above).

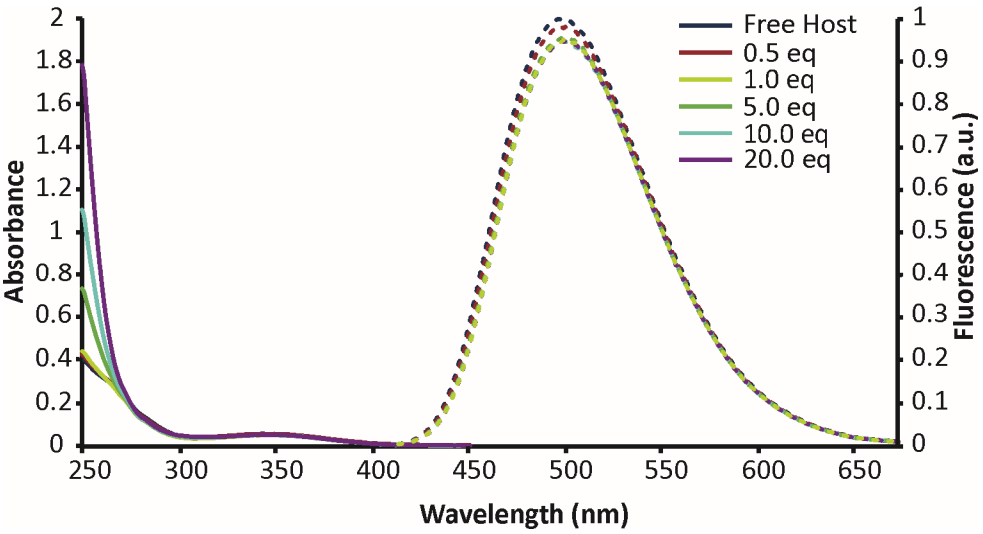

Figure 3.11 Absorption (left panel) and emission (right panel) spectra (λ_{exc} = 340 nm) acquired during the UV/vis and fluorescence titrations of receptor **2** (10 µM) with **HexCr** (0 - 20 equiv).

The need for a large excess of **HexCr** is explained by the difference in the binding constant values of the competitors (see above). Gratifyingly, the concentration range that is required to obtain a visible fluorescence response of the **3⊂2** IDA coincides with or is well below the expected clinical levels of creatinine in blood serum (60–420 µM) or urine (3–25 mM) for healthy individuals.[2] In the case of kidney or renal dysfunction, these values are dramatically increased. We determined the limit of detection (LOD) of the **3⊂2** IDA to be *ca.* 110 nM.

Noteworthily, very similar results were obtained when creatinine (**Cr**) was used instead of the lipophilic version **HexCr** (Figure 3.*12*). On addition of **Cr** to the ensemble **3⊂2** (both components at 1 µM), the fluorescence of the system increased significantly (factor of 2.7 for 50 µM **Cr**). The limited solubility of **Cr** in chloroform (≤ 50µM) precluded the registration of a complete titration curve. However, based on the obtained data, it can be safely stated that a lower limit for the binding constant of the **Cr⊂2** complex is ca. 5×10^4 M^{-1}. Hence, in terms of its sensitivity range, the herein developed fluorescent IDA is fully compatible with **Cr**. The **Cr⊂2** complex was fully characterized by means of 1D and 2D high-resolution NMR experiments (*Figure 3.34* and Figure 3.*35*).

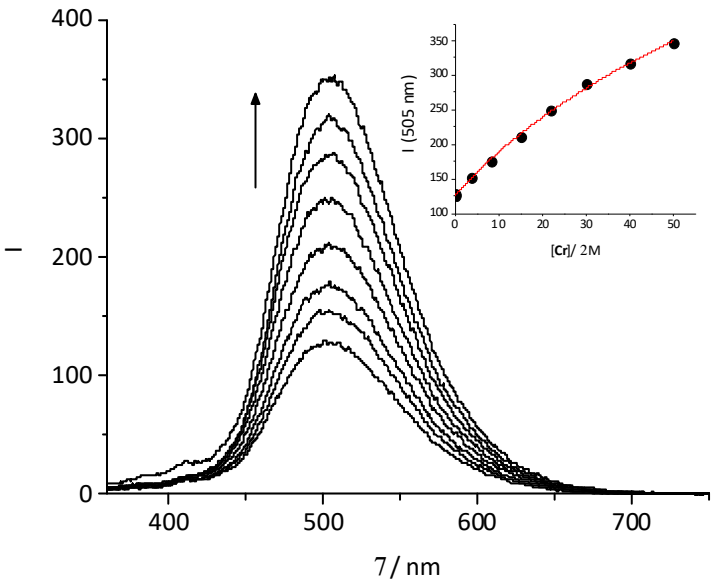

Figure 3.12 Emission spectra registered during the addition of increasing amounts of Cr (up to 50 μM) to the ensemble **3⊂2** (both at 1 μM) in chloroform; λ_{exc} = 317 nm. Inset: Plot of the changes in emission at 505 nm vs concentration of **Cr**. The red line corresponds to the fit of the titration data to a competitive binding model that considers the formation of the **3⊂2** and **Cr⊂2** complexes.

Finally, we tested the possible interference of other biologically relevant analytes. For this purpose, urea and L-proline, as an abundant amino acid, were chosen. The separate addition of these compounds to the ensemble **3⊂2** (both components at 1 μM) yielded fluorescence increase factors of 1.4 (L-proline) and 2.6 (urea) (see Figure 3.*13* and Figure 3. *14*). These responses are significant, however, smaller than those observed for **HexCr** (factor of 2.7, see above).

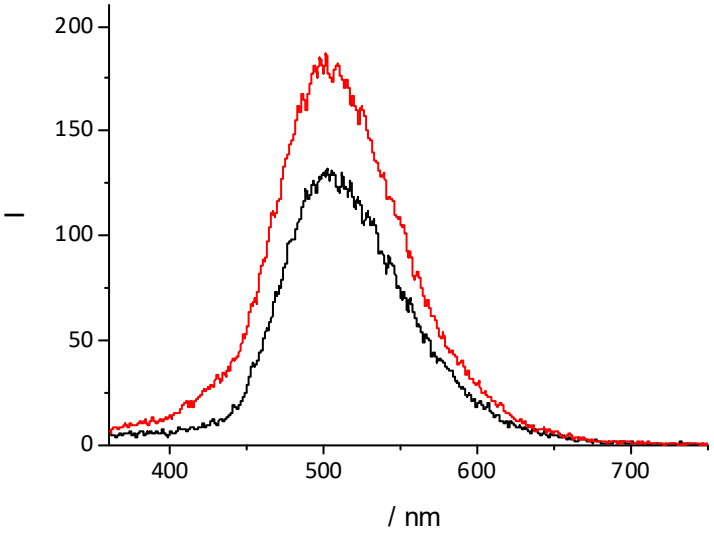

Figure 3.13 Fluorescence spectra registered before (black line) and after (red line) the addition of L-proline (71 μM) to the ensemble **3**⊂**2** (both at 1 μM) in chloroform; λ_{exc} = 317 nm.

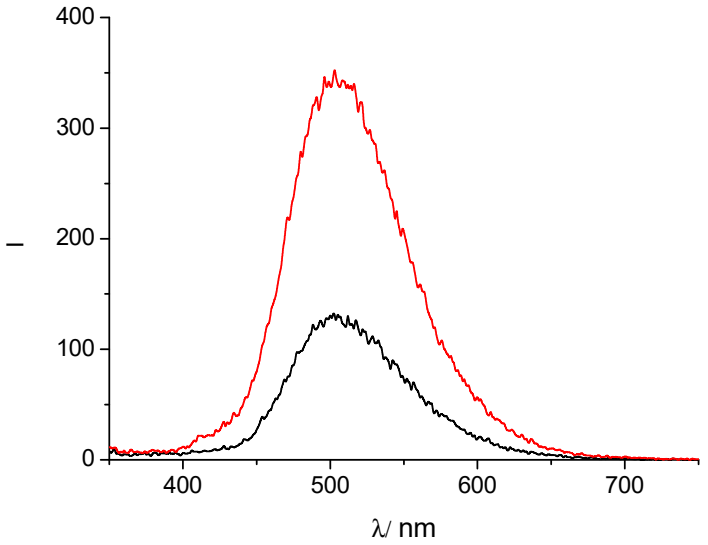

Figure 3. 14 Emission spectra of the ensemble **3**⊂**2** (both at 1 μM) before (black line) and after (red line) the addition of urea (71 μM) in chloroform; λ_{exc} = 317 nm.

3.2.5 Development of an IDA Based on the Non-fluorescent Receptor **1**.

The previously described receptor **1**, which is known to be an excellent host for **Cr**, is non-fluorescent.[29] However, by introducing a fluorescent guest, receptor **1** can be integrated in an optical IDA suitable for **HexCr** sensing. For this purpose, we designed the guest dyes **4** and **5**, containing the pyridyl-*N*-oxide binding motif connected to a pyrene and naphthalene chromophore, respectively, by an ethenyl spacer. Dye **4** features an absorption maximum at 394nm (ε = 32 600 $M^{-1}{\cdot}cm^{-1}$) and fluoresces with a maximum at 474 nm, while dye **5** displayed an absorption maximum at 360 nm (ε = 41 400 $M^{-1}{\cdot}cm^{-1}$) and a maximum of emission at 425 nm.

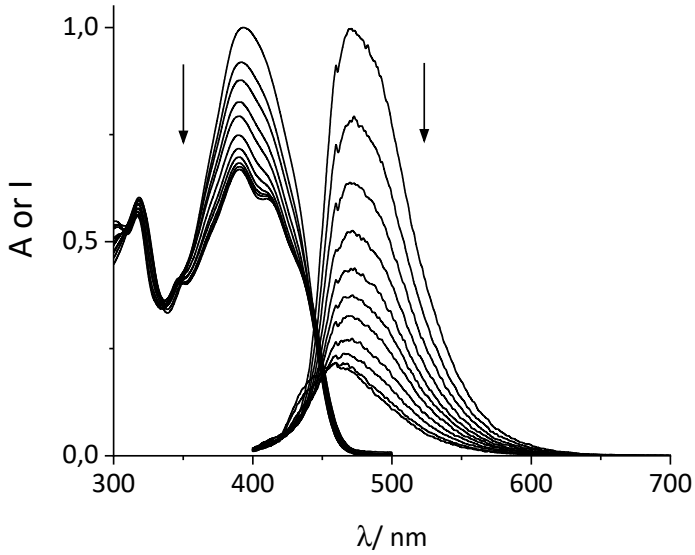

Figure 3.15 UV/vis absorption (left) and fluorescence emission (right) spectra of **4** on addition of increasing amounts of receptor **1** (λ_{exc} = 350 nm).

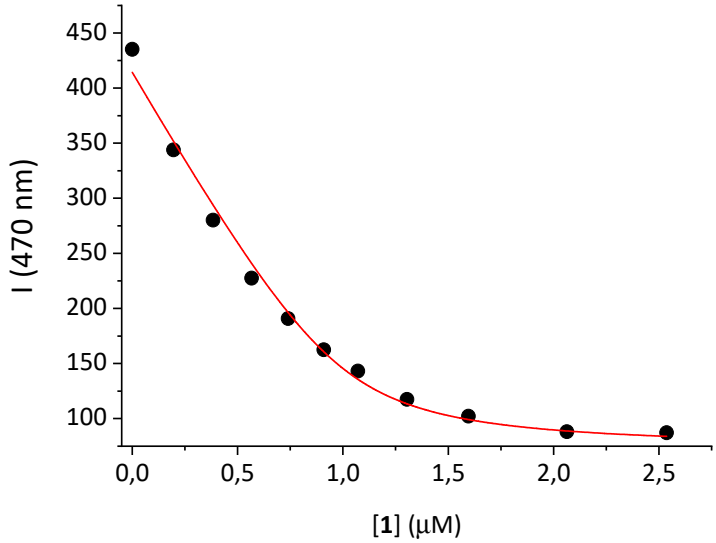

Figure 3.16 Plot of the emission changes at 470 nm of the fluorescence titration of **4** (1 μM) with increasing amounts of **1** in chloroform; λ_{exc} = 350 nm, λ_{obs} = 470 nm. The red line corresponds to the fit of the titration data to a 1:1 binding model that considers the formation of a 1:1: complex **4**⊂**1**.

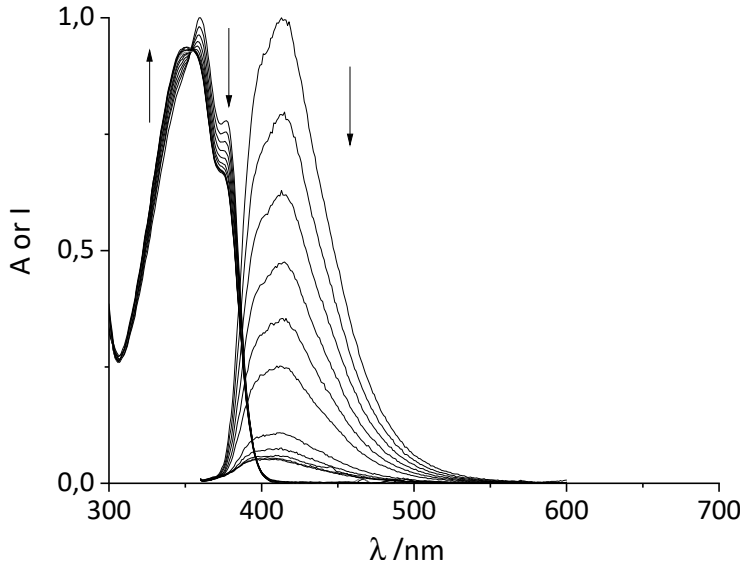

Figure 3.17 UV/vis absorption (left) and fluorescence emission (right) spectra of **5** on addition of receptor **1**. The fluorescence spectra were obtained for excitation at 350 nm.

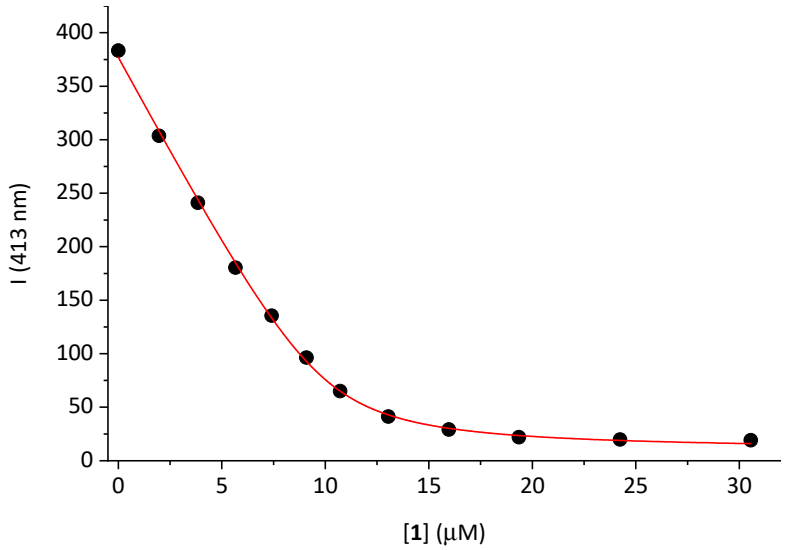

Figure 3.18 Fluorescence titration curve of **5** (10 μM) on addition of increasing amount of **1** in chloroform; λ_{exc} = 350 nm, λ_{obs} = 470 nm. The red line corresponds to a 1:1 binding model.

The UV/vis titrations of the two dyes with incremental amounts of the non-chromophoric receptor **1** provided a set of spectra displaying one isosbestic point (at 350 nm for **4** and at 353 nm for **5**, Figure 3.*15* and Figure 3.*17*). As already mentioned, this is the expected result for the exclusive formation of a 1:1 complex in binding systems involving only two absorbing species: the dye, **4** or **5**, and its inclusion complex with **1**.

We used the observed isosbestic points as excitation wavelength in the fluorescence titrations of the emissive pyridyl-*N*-oxide derivatives, **4** and **5**, with increasing concentrations of **1**. In the course of the titration, the fluorescence was significantly quenched (*ca.* 80% for **4** and 90% for **5** on addition of 2.5 equiv. and 3.0 equiv. of **1**, respectively), and at the end point a slightly blue-shifted emission spectrum (Δλ = −11 nm) were observed in both cases. This is likely the result of the disturbance of the ICT state on an interaction pyridine-*N*-oxide moiety with the host, leading to the observed quenching. The analysis of the emission changes of the dyes vs the concentration of **1**, using a 1:1 binding model, provided the binding constant values for the corresponding inclusion complexes, K_a (**4**⊂**1**) = (1.2 ± 0.2) × 10^7 M^{-1} and K_a (**5**⊂**1**) = 2.5 ± 0.3·× 10^7 M^{-1} (Figure 3.*16* and Figure 3.*18*). ITC experiments of the **4**⊂**1** complex formation (Figure 3.*41*) confirmed the tight and strong 1:1 binding with an exothermic enthalpic contribution of ΔH = −38.0 ± 0.4 kJ·mol^{-1}. However, similar to what was discussed above for the binding of **3** by host **2**, the binding constants could

only be estimated as larger than 10^7 M^{-1}. Noteworthily, this agrees nicely with the more accurate data obtained by fluorescence titration (K_a = (1.2 ± 0.2) × 10^7 M^{-1}). The interaction of **1** with **4** was also probed using ^{1}H NMR spectroscopy (Figure 3.*38*).

Finally, we tested the both ensemble **4⊂1** and **5⊂1** in a competitive IDAs with **HexCr**.[52]

Similarly, to the previous developed IDAs, the sensing ensembles were prepared from equimolar chloroform solutions of their components. We studied the ensembles at two different concentrations: [**4**] = [**1**] = 1 μM, **4⊂1** assembled to ~ 80% extent and [**5**] = [**1**] = 10 μM, **5⊂1** assembled to ~ 90% extent. In both cases, the incremental addition of **HexCr** restored the emission of the dye (fluorescence enhancement factor of 2.3 at 50 μM **HexCr**, Figure 3.*19*).

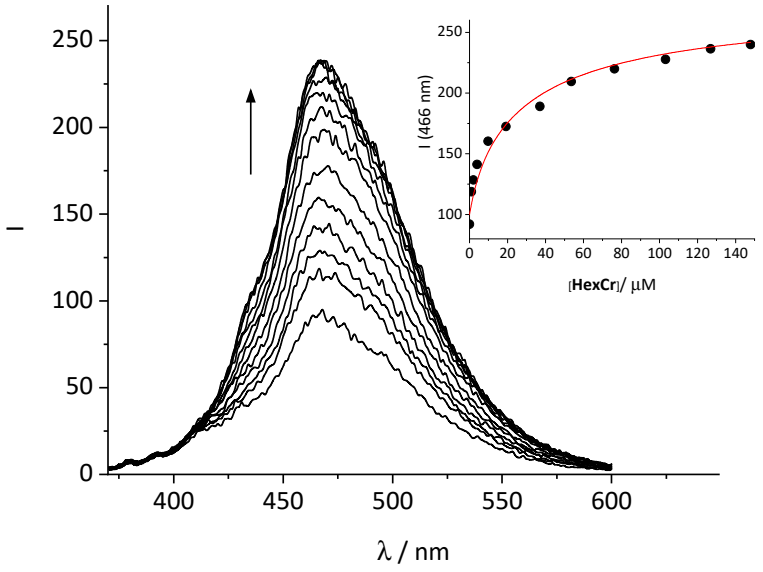

Figure 3.19 Fluorescence response of **4⊂1** ensemble (1 μM each component) on addition of **HexCr** (up to 148 μM); λ_{exc} = 350 nm. Inset: Plot of the changes in emission at 466 nm vs concentration of **HexCr**. The red line corresponds to the fit of the titration data to a competitive binding model that considers the formation of the **4⊂1** and **HexCr⊂1** complexes.

The changes experienced by the fluorescence band of the dye were mathematically analyzed using a theoretical binding model that considers two competitive complexes. The fit of the experimental data provided stability constant values for

the **HexCr⊂1** complex showing the same order of magnitude, K_a (**HexCr⊂1**) = (4.3 ± 0.5) × 10^5 M^{-1} and K_a (**HexCr⊂1**) = (1.5 ± 0.2) × 10^5 M^{-1} using **4** and **5** as external indicators, respectively. These values are again in good agreement with the one determined in ITC experiments, K_a (**HexCr⊂1**) = (1.5 ± 0.3) × 10^5 M^{-1}(Figure 3.*40*). The ITC experiment provided further information on the enthalpic and entropic contributions to binding: ΔH=−7.8 ± 0.1 kJ·mol^{-1} and TΔS as −19.8 ± 0.1 kJ·mol^{-1} (298 K). This data evidenced that the binding of **HexCr** by **1** is mainly entropically driven.

Not surprisingly, the IDA with **Cr** yielded practically the same switch-on response as for **HexCr** (Figure 3.*20*). On addition of 50 µM **Cr**, a fluorescence enhancement factor of 1.8 was obtained. The fitting of the competitive binding titration returned a binding constant of K_a (**Cr⊂1**) = (3.0 ± 1.0) × 10^5 M^{-1}.

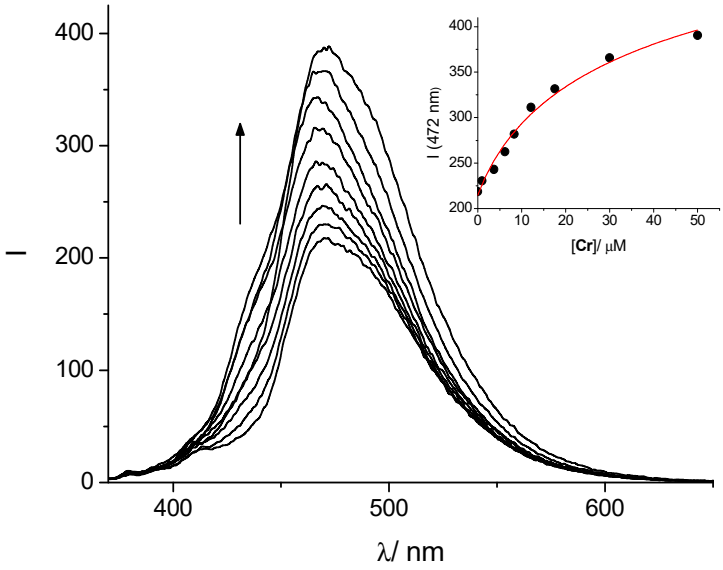

Figure 3.20 Fluorescence response of the ensemble **4⊂1** (both at 1 µM) on addition of increasing amounts of **Cr** (up to 50 µM) in chloroform; λ_{exc} = 350 nm. Inset: Plot of the changes in emisión at 472 nm vs concentration of **Cr**. The red line corresponds to the fit of the titration data to a competitive binding model that considers the formation of the **4⊂1** and **Cr⊂1** complexes.

3.3 Future Challenges and Developments.

The future challenges of the described supramolecular design include the improvement of their sensing selectivity and the compatibility with aqueous media. On one hand, as herein demonstrated, the current design shows interferences with

other biologically relevant analytes, such as proline and urea. In practical terms, this limitation could be avoided by previous extractive separation of creatinine. On the other hand, the issue of water solubility of the calix[4]pyrrole receptor and/or the dyes can be addressed by synthetic modifications involving the incorporation of ionizable and charged groups in their scaffold periphery. However, it is expected that the binding constant of creatinine with the water-soluble versions of the receptor would drop considerably owing to the polar nature of the analyte and the competition of water for hydrogen bonding. This drawback might be partially overcome by performing the sensing experiments in microheterogeneous media, such as micelles and liposomes. We are currently expanding our efforts in these directions, and we expect to report our findings in due course.

3.4 Conclusions.

Calix[4]pyrrole-derived IDAs were designed to enable the efficient sensing of **Cr** and its derivative **HexCr**. The calix[4]pyrrole receptors, **1** and **2**, operate according to the principles of size, shape, and functional complementarity. **Cr** and derivatives are included in the receptor's cavities (K_a ca. 10^5 M^{-1}), establishing five complementary hydrogen bonds: four with pyrrole NHs and one with the upper rim phosphonate group. In one version of the developed sensors, compound **2**, the receptor unit features a covalently attached dansyl fluorophore. This provides a means for FRET-based IDA through the displacement of a black-hole quencher **3** by **Cr** or its lipophilic analogue **HexCr**. In another version, the inherently fluorescent pyrene-based dyes **4** and **5** formed a reporter pairs with receptor **1**. In both developed IDAs, the indicator dyes interact with the calix[4]pyrrole cavitand scaffolds through complexation of the pyridyl-*N*-oxide motif (K_a ca. 10^7 M^{-1}). The two developed IDAs work in organic chlorinated solvents at a range of concentrations that coincide with those in which **Cr** is present in bodily fluids (blood serum and urine). Remarkably, the **3**⊂**2** IDA features a limit of detection as low as 110 nM, drawing on the high sensitivity of the fluorescence measurements and the significant affinity of receptor **2** for **HexCr** and **Cr**. The developed IDAs rely on a combination of hydrogen bonding, π–π, and CH–π interactions, as driving forces of the molecular recognition events. To the best of our knowledge, the reported work describes unprecedented examples of fluorescent supramolecular sensors for creatinine.

3.5 Experimental section

3.5.1 General methods and instrumentation.

Reagents and solvents used in the synthesis were obtained from commercial suppliers and were used without further purification unless otherwise stated. Pyrrole was distilled under vacuum and stored in the freezer for further use. THF was dried by distillation from sodium/benzophenone under argon atmosphere. Triethylamine (Et_3N) was distilled with CaH_2 under argon atmosphere and used immediately. Dried *N*,*N*-dimethylformamide was obtained from a solvent purification system M Braun SPS-800. Flash column chromatography was performed with silica gel (technical grade, pore size 60 Å, 230-400 mesh particle size).

Automatic column chromatography purifications were done with a Combi-flash® RF^+.

Routine ^{1}H-NMR and ^{13}C-NMR spectra were recorded on a Bruker Advance 400 (400 MHz for 1H-NMR) or Bruker Avance 500 (500 MHz for 1H-NMR) ultrashield spectrometer. Deuterated solvents were purchased from Aldrich.

FT-IR measurements were carried out on a Bruker Optics FT-IR Alpha spectrometer equipped with a DTGS detector, KBr beamsplitter at 4 cm^{-1} resolution using a one bounce ATR accessory with diamond windows.

UV/vis absorption measurements were carried out with an Agilent Cary 5000 spectrophotometer or a Shimadzu UV-1603 spectrophotometer. The corrected fluorescence spectra were obtained with a Varian Eclipse fluorimeter. All measurements were done at room temperature (RT) in quartz cuvettes of 1 cm optical pathlength.

3.5.2 Synthesis and characterization data.

Synthesis of **1**: The synthesis of the receptor **1** was performed following previously described procedures.[29]

Synthesis of tetra OH calix[4]pyrrole **7**: To a 2 L round-bottomed flask equipped with a magnetic stir bar, 3´-hydroxyacetophenone (15 g, 108 mmol), AcOEt (1 L) and HCl 36% (73.5 mL, 864 mmol) were added. Under vigorous stirring pyrrole (7.87 mL, 113 mmol) was added slowly via a syringe. The flask was closed with a seal cap and the reaction mixture was stirred at RT for 4 h. To quench the reaction a saturated sodium bicarbonate ($NaHCO_3$) solution was added until reaching pH 7. The organic phase was separated and then washed with water (2 × 100 mL), dried over Na_2SO_4,

filtered and concentrated under reduced pressure. The resulting solid was washed with Et_2O (500 mL), filtered and the liquid was concentrated. A brown foam was obtained and washed with DCM (300 mL), filtered and concentrated again. A brown solid was obtained and recrystallized from acetonitrile. A light brown solid (5.4 g, 27%) was collected.

Melting Point: 220-222 °C, ^{1}H-NMR (400 MHz, $(CD_3)_2CO$, 298 K): δ (ppm) = 8.78 (bs, 4H), 8.06 (s, 4H), 7.04 (t, 4H, *J* = 7.7 Hz), 6.54 (dd, 4H, *J* = 7.7 Hz), 6.49 (d, 4H, *J* = 7.7 Hz), 6.44 (t, 4H, *J* = 2.5 Hz), 6.01 (d, 8H, *J* = 2.5 Hz), 1.84 (s, 12 H). The ^{13}C-NMR spectrum of this compound agreed with that reported in the literature.[33]

Synthesis of mononitro calix[4]pyrrole **8**:[34] **7** (1.5 g, 2.03 mmol) and Cs_2CO_3 (5.28 g, 16.2 mmol) were placed in a previously dried Ace pressure tube (100 mL) equipped with a plunger valve and three cycles of vacuum/Ar were applied. Then, 67.5 mL of anhydrous DMF were added and the mixture was vigorously stirred. 3,4-difluoronitrobenzene (0.25 mL, 2.26 mmol) was added and the mixture was heated at 60 °C for 1 h and at 90 °C overnight in an oil bath. Next day, the reaction was cooled down to RT, diluted with AcOEt (90 mL) and 10% HCl_{aq} was added until reaching pH 1. A white solid precipitated, which was filtered and then washed with AcOEt. The two phases of the filtrate were separated, and the organic layer was washed with water (2 × 40 mL) to remove the DMF. The AcOEt layer was collected, dried over Na_2SO_4, filtered and concentrated to dryness. **8** was isolated by flash column chromatography, absorbing the crude on a minimal amount of SiO_2 and eluting with a continuously changed gradient of DCM:AcOEt from 100% DCM to 70:30. The fraction containing **8** was concentrated until obtaining an oil which was rapidly re-dissolved in DCM. Slow evaporation of the solvent yielded yellow crystals of pure **8** (0.56 g, 32%).

Rf: 0.2 (DCM:AcOEt 98:2, SiO_2), **^{1}H-NMR** (400 MHz, $(CD_3)_2CO$, 298 K): δ (ppm) = 8.66 (bs, 3H, NH), 8.58 (bs, 1H, NH), 8.21 (s, 2H, OH), 8.16 (dd, $^3J_1$ = 9.0Hz, $^4J_2$ = 2.8 Hz, 1H), 8.04 (d, *J* = 2.8 Hz, 1H), 7.41 (d, *J* = 9.0 Hz, 1H), 7.27 (t, *J* = 8.0 Hz, 2H, CH_{Ar}), 7.05 (t, *J* = 8.0 Hz, 2H, CH_{Ar}), 6.98 (d, *J* = 8.0 Hz, 2H, CH_{Ar}), 6.76 (d, *J* = 7.9 Hz, 1H, CH_{Ar}), 6.73 (d, *J* = 7.9 Hz, 1H, CH_{Ar}), 6.57 (d, *J* = 8.0 Hz, 2H, CH_{Ar}), 6.47-6.40 (mult., 4H, CH_{Ar}), 6.01-5.99 (mult., 8H, β^{pyr}), 5.84 (s, 2H, CH_{Ar}), 1.83 (s, 6H, CH_3), 1.77 (s, 3H, CH_3), 1.75 (s, 3H, CH_3). **^{13}C-NMR** (125 MHz, $(CD_3)_2SO$, 298 K): δ (ppm) = 159.1, 158.5, 158.1 (×2), 153.9,153.3, 153.2, 152.3, 152.2, 147.4, 145.2, 138.0 (×2), 137.6, 137.5, 137.4, 137.3, 136.8 (×2), 130.7 (×2), 129.6 (×2), 125.2, 122.7, 122.4, 122.1, 120.5, 118.1

(×2), 116.6, 116.4, 114.5 (×2), 113.8 (×3), 112.5, 105.1-104.9 (× 8 β^{pyr}), 44.7, 44.6, 44.5 (×2), 31.89 (×2), 31.35 (×2).

Synthesis of mononitro phosphonate calix[4]pyrrole **9**: To each of four previously dried Schlenk tubes **8** was added (100 mg, 0.116 mmol), and three cycles of vacuum/Ar were applied. Then, anhydrous THF (6.8 mL) and dried triethylamine (158 µL, 1.13 mmol) were added. Under vigorous stirring, phenylphosphonic dichloride (20 µL, 0.14 mmol) was slowly added over a period of 10 to 15 minutes and the reaction was left to stir at RT for 4 hours. After that time the reaction was quenched by adding water (5 mL) and 10% HCl_{aq} until reaching pH 1. The contents of the four flasks were combined and extracted with AcOEt (3 × 20 mL). The AcOEt extracts were combined, dried over Na_2SO_4, filtered and concentrated under reduced pressure, yielding a light-yellow solid (0.41 g). **9** was isolated by column chromatography on SiO_2 using DCM as eluent until the first product eluted (**9in** isomer), then the polarity was increased until 95:5 DCM:AcOEt, recovering the **9out** isomer. The two isomers were crystallized by using DCM:Hex with a few drops of acetone. **9in** (212 mg, 46%), **9out** (98 mg, 22%). NOTE: In our hands and under the same conditions the scale up of the reaction produced **9** in lower yields.

9in Rf: 0.4 (DCM:AcOEt 96:4, SiO_2) **^{1}H-NMR** (400 MHz, (CD3)2CO, 298 K): δ (ppm) = 8.78 (bs, 2H, NH), 8.54 (bs, 1H, NH), 8.48 (bs, 1H, NH), 8.18 (dd, J_1 = 9.1, J_2 = 2.8 Hz, 1H, CH_{Ar}), 8.11-8.03 (mult., 3H, CH_{Ar}, Ar_{PO}), 7.75 (t, J = 7.5 Hz, 1H, Ar_{PO}), 7.70-7.60 (mult., 2H, Ar_{PO}), 7.45 (d, J = 9.0 Hz, 1H, CH_{Ar}), 7.33 (t, J = 8.0 Hz, 2H, CH_{Ar}), 7.29-7.22 (td, J_1 = 8.0, J2 = 3.8 Hz, 2H, CH_{Ar}), 7.08-7.00 (mult., 4H, CH_{Ar}), 6.86 (t, J = 7.1 Hz, 2H, CH_{Ar}), 6.80 (s, 2H, CH_{Ar}), 6.68 (d, J = 7.8 Hz, 1H, CH_{Ar}), 6.64 (d, J = 7.8 Hz, 1H, CH_{Ar}), 6.16-6.04 (mult., 8H, β^{pyr}), 5.88 (s, 2H, CH_{Ar}), 1.89 (s, 6H, CH_3), 1.78 (s, 3H, CH_3), 1.76 (s, 3H, CH_3). **^{13}C{^{1}H}-NMR** (125 MHz, $CDCl_3$, 298 K): δ (ppm) = 158.5, 157.8, 154.7, 151.5, 151.4, 151.3,150.0, 149.9, 147.7, 144.1, 137-136 (×8, α^{pyr}), 133.2 (Ar_{PO}), 131.2 (d, $^2J_{PC}$ = 10.6 Hz, Ar_{PO}),129.2-128.6 (×4 CH_{Ar}, Ar_{PO}), 127.6 (d, $^1J_{PC}$ = 205.7, Ar_{PO}), 124.0 (×2, CH_{Ar}), 123.6 ($CHNO_2$), 122.2 (CH_{Ar}), 122.0 (×2, CH_{Ar},$CHNO_2$), 120.9 (×2, CH_{Ar}), 120.3 ($ArNO_2$), 120.0 (×2, CH_{Ar}), 116.5 (CH_{Ar}), 116.4 (CH_{Ar}), 115.4 (CH_{Ar}), 113.8 (CH_{Ar}), 106.3-105.9 (×8, β^{pyr}), 44.8 (**C**CH_3), 44.7 (**C**CH_3), 44.6 (×2, **C**CH_3), 29.4 (CH_3), 29.1 (CH_3), 28.8 (CH_3), 28.7 (CH_3). **^{31}P{^{1}H}-NMR** (202 MHz, $CDCl_3$, 298 K): δ (ppm) = 15.4. **9out Rf**: 0.3 (DCM:AcOEt 96:4, SiO_2). **^{1}H-NMR** (500 MHz, THF-d_8, 298 K): δ (ppm) = 9.28 (bs, 1H, NH), 9.22 (bs, 1H, NH), 8.02 (dd, J_1 = 9.6, J_2 = 2.6 Hz, 1H, Ar_{NO2}) 7.99-7.89 (m, 3H, Ar_{NO2}, Ar_{PO}), 7.66-7.59 (m, 2H, NH Ar_{PO}), 7.59-7.50 (m, 3H, NH, Ar_{PO}), 7.30-7.21 (m, 4H, CH_{Ar}), 7.20- 7.00 (m, 9H, Ar_{NO2}, 8 × CH_{Ar}), 6.80-6.73 (m, 2H, CH_{Ar}), 6.12-6.06 (m, 3H, CH_{Ar}, 2 × β^{pyr}), 5.99 (bs, 1H, CH_{Ar}), 5.84-5.79 (m, 2H, β^{pyr}), 5.44 (bs,

1H, β^{pyr}), 5.39 (bs, 1H, β^{pyr}), 5.36-5.29 (m, 2H, β^{pyr}), 1.98 (app s, 6H, 2 × CH_3), 1.86 (s, 3H, CH_3), 1.84 (s, 3H, CH_3). **$^{13}C\{^1H\}$-NMR** (125 MHz, THF-d_8, 298 K): δ (ppm) = 159.7, 159.1, 156.3, 152.6 (d, J_2^{PC} = 12.6 Hz), 152.2 (d, $^2J_{PC}$ = 6.6 Hz), 152.1, 151.9, 149.3, 145.4, 138.6, 138.4, 138.0, 137.9, 136.8 (α^{pyr}), 133.32 (Ar_{PO}), 131.9 (d, $^2J_{PC}$ = 10.2 Hz, Ar_{PO}), 129.5, 129.4, 129.2 (d, $^3J_{PC}$ = 20.0 Hz), 129.1 (×2), 124.5 (CH_{Ar}), 124.4 (CH_{Ar}), 124.3 (CH_{Ar}), 123.7 (CH_{Ar}), 123.3 (CH_{Ar}), 121.8 (CH_{NO2}), 121.1 (CH_{Ar}), 120.9 (CH_{Ar}), 120.3 (CH_{NO2}), 118.0 (CH_{Ar}), 117.9 (CH_{Ar}), 117.6 (CH_{Ar}), 117.2 (CH_{Ar}), 116.7 (CH_{Ar}), 115.6 (CH_{Ar}), 107.3-106.9 (×4 β^{pyr}), 106.1 (β^{pyr}), 106.0 (β^{pyr}), 105.6 (β^{pyr}), 105.5 (β^{pyr}), 46.0 (**C**CH_3), 45.9 (**C**CH_3), 45.8 (×2, CCH_3), 28.1(CH_3), 27.6 (CH_3), 27.1 (CH_3), 27.0 (CH_3). **$^{31}P\{^1H\}$-NMR** (202 MHz, THF-d_8, 298 K): δ (ppm) = 10.3.

Synthesis of dansyl phosphonate calix[4]pyrrole **2**:

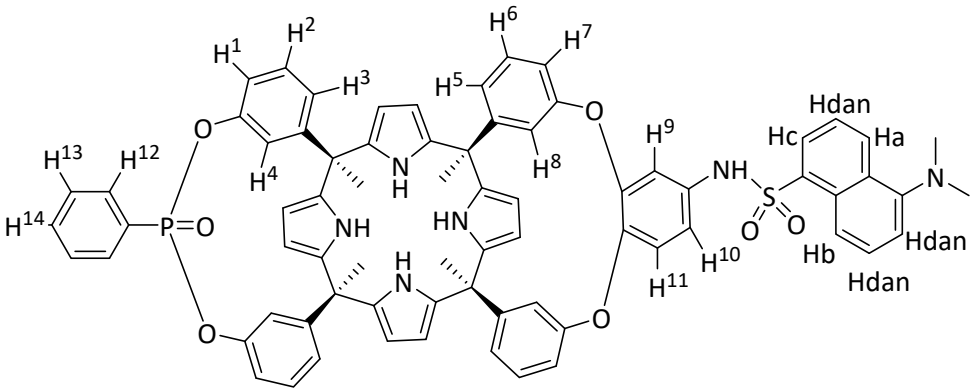

2

Step 1: **9in** (50mg, 0.051 mmol) was dissolved in AcOEt (25 mL, HPLC grade) and the solution was placed in an Ace pressure flask (75 mL). 10% Pd/C (27 mg) was suspended in 3 mL of AcOEt in a vial, and the suspension was sonicated for 5 minutes. Then the catalyst was added to the reaction flask and the remaining catalyst was recovered by washing the vial with more AcOEt (total volume of AcOEt in reaction flask 33 mL). The flask was placed in a parr hydrogenator apparatus and was purged three times with H_2. The flask was pressurized with 4 bar of H_2 and shacked overnight. Next day, the flask was depressurized and the catalyst removed by filtration over zeolite. The zeolite was gently washed with AcOEt and the filtrate was concentrated under reduced pressure yielding a light-pink solid. The solid was immediately used in the next step.

Step 2: The reduction product of **9in** (20 mg, 0.021 mmol) and dansyl chloride (5.38 mg, 0.020 mmol) were dissolved in 1.1 mL of anhydrous pyridine under Ar atmosphere and the reaction was stirred at RT for 3h. Then, the reaction was diluted with 2 mL of DCM and 2 mL of water. The DCM extract was separated and the aqueous phase was extracted two additional times with the same amount of DCM. The DCM extracts were combined, dried over Na_2SO_4, filtered and concentrated under reduced pressure, yielding a yellow solid. **2** was purified by column chromatography on SiO_2 using $CHCl_3$: AcOEt 97:3 yielding pure **2** (24.3 mg, 98%) as a yellow solid.

Rf: 0.1 ($CHCl_3$: AcOEt 97:3, SiO_2) **IR** (film): ν (cm^{-1}) = 3413, 2981, 2938, 2784, 1674, 1579, 1481, 1429, 1370, 1327, 1259, 1227, 1139, 1042, 954, 840, 778, 696, 623, 570, 523. **^{1}H-NMR** (400 MHz, $CDCl_3$, 298 K): δ (ppm) = 8.51 (d, *J* = 8.5 Hz, 1H), 8.47 (bs, 1H), 8.25 (d, *J* = 8.6 Hz, 1H), 8.15 (bs, 2H), 8.06 (dd, J_1 = 7.5, J_2 = 1.3 Hz, 1H), 8.05-7.95 (mult., 3H), 7.66 (td, J_1 = 7.5, J_2 = 1.3 Hz, 1H), 7.56 (td, J_1 = 7.5, J_2 = 4.8 Hz, 2H), 7.51-7.40 (mult., 2H), 7.18-7.09 (mult., 3H), 7.04 (td, J_1 = 7.7, J_2 = 3.2 Hz, 2H), 7.00-6.90 (mult., 7H), 6.84 (d, *J* =2.5 Hz, 1H), 6.82-6.76 (mult., 2H), 6.74 (d, *J* = 8.5 Hz, 1H), 6.67 (t, *J* = 7.7 Hz, 2H), 6.51 (dd, J_1 = 8.5, J_2 = 2.5 Hz, 1H), 6.12- 6.04 (mult., 4H), 5.91-5.80 (mult., 6H), 2.87 (s, 6H), 1.95 (s, 3H), 1.94 (s, 3H), 1.82 (s, 3H), 1.80 (s, 3H). **^{31}P{^{1}H}-NMR** (162 MHz, $(CD_3)_2CO$, 298 K): δ (ppm) = 13.94. **HRMS (ESI-TOF)** m/z: $[M - H]^-$ Calcd for $C_{72}H_{60}N_6O_7PS$ = 1183.3987; found = 1183.3986.

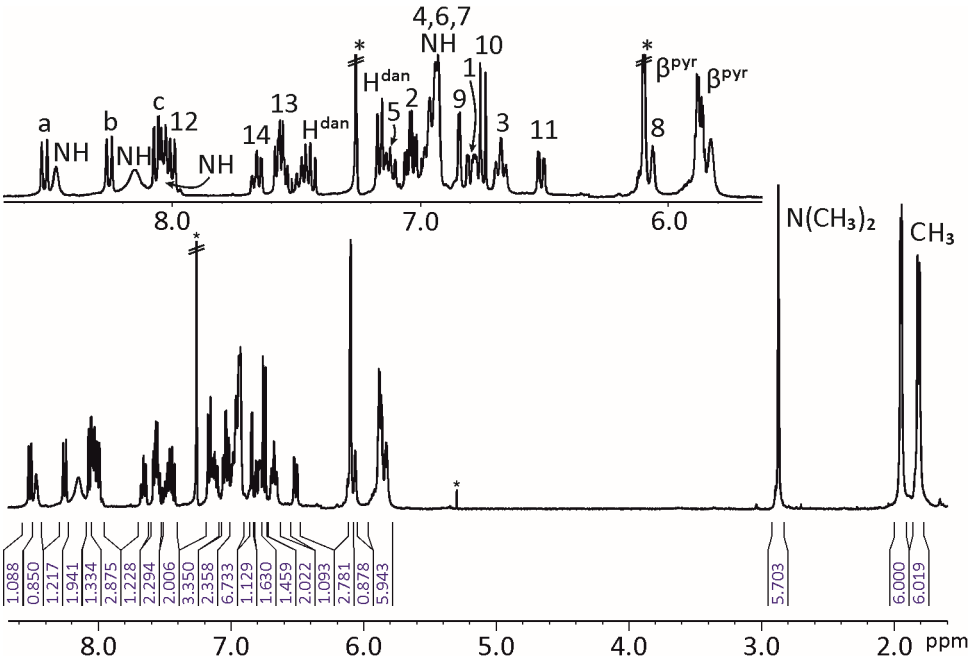

Figure 3.21 ^{1}H-NMR (400 MHz, $CDCl_3$) of compound **2**. * Residual solvent peak.

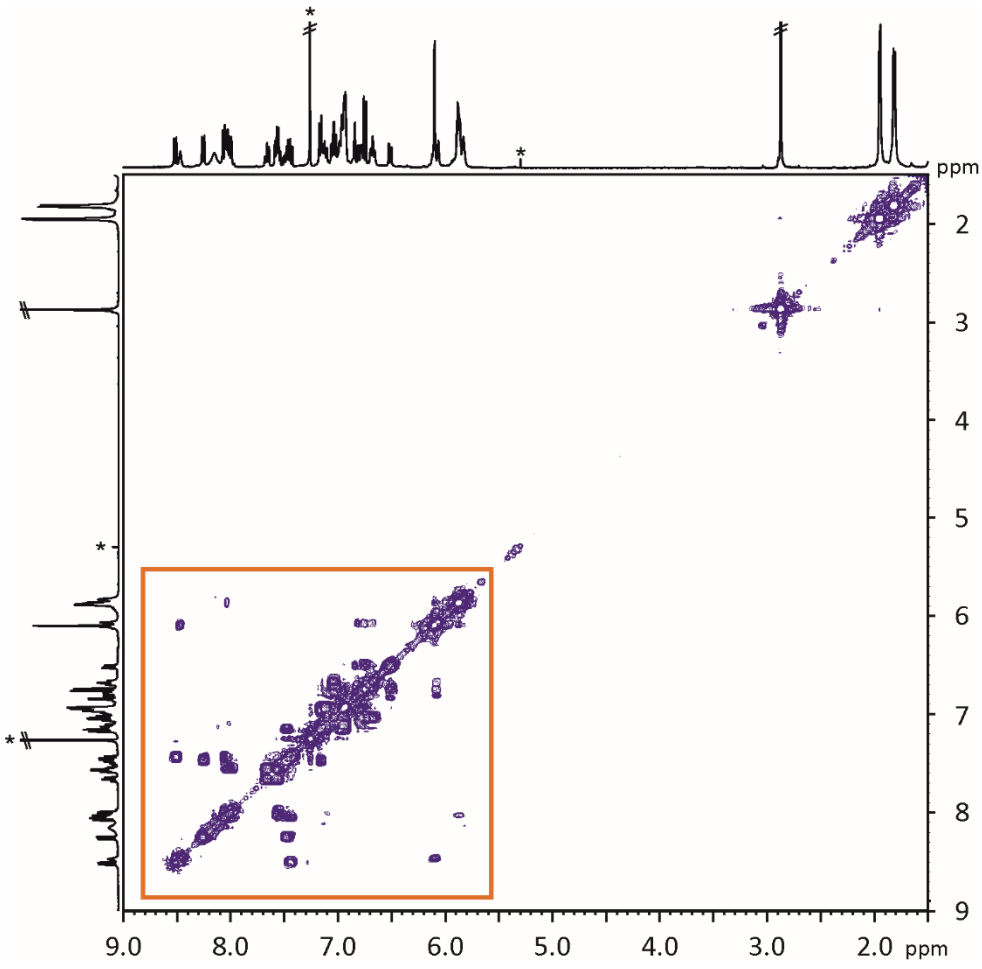

Figure 3.22 2D ^{1}H-^{1}H COSY NMR (400 MHz, $CDCl_3$) spectrum of compound **2**. * Residual solvent peak.

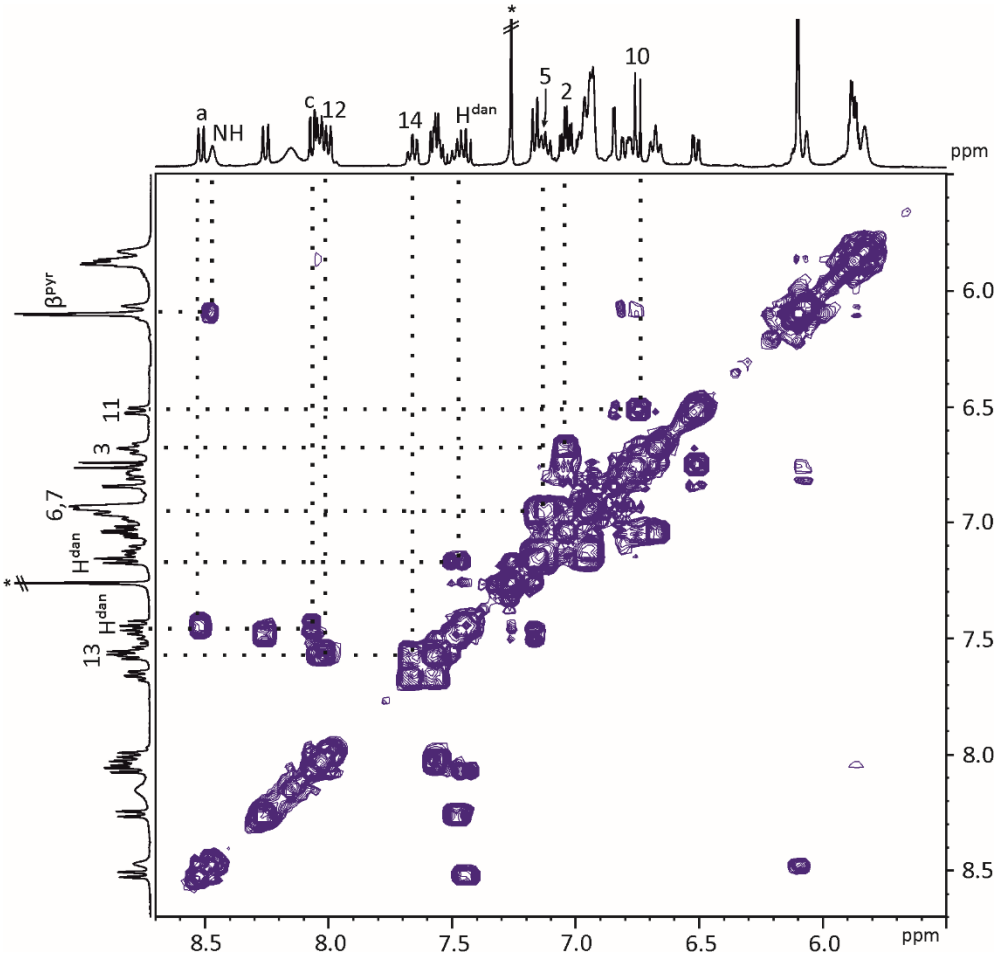

Figure 3.23 Selected region of the 2D ^{1}H-^{1}H COSY NMR (400 MHz, $CDCl_3$) spectrum of compound **2**. * Residual solvent peak.

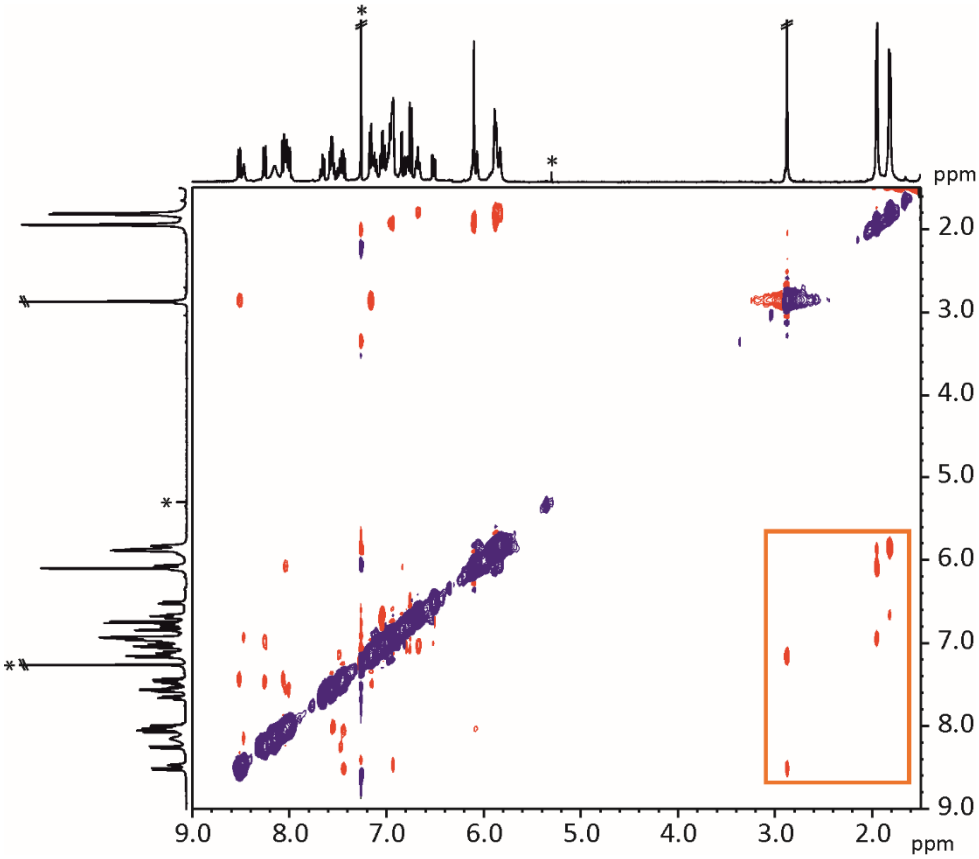

Figure 3.24 2D ^{1}H-^{1}H NOESY NMR (400 MHz, $CDCl_3$, t_{mix} = 0.6 s) spectrum of compound **2**. * Residual solvent peak.

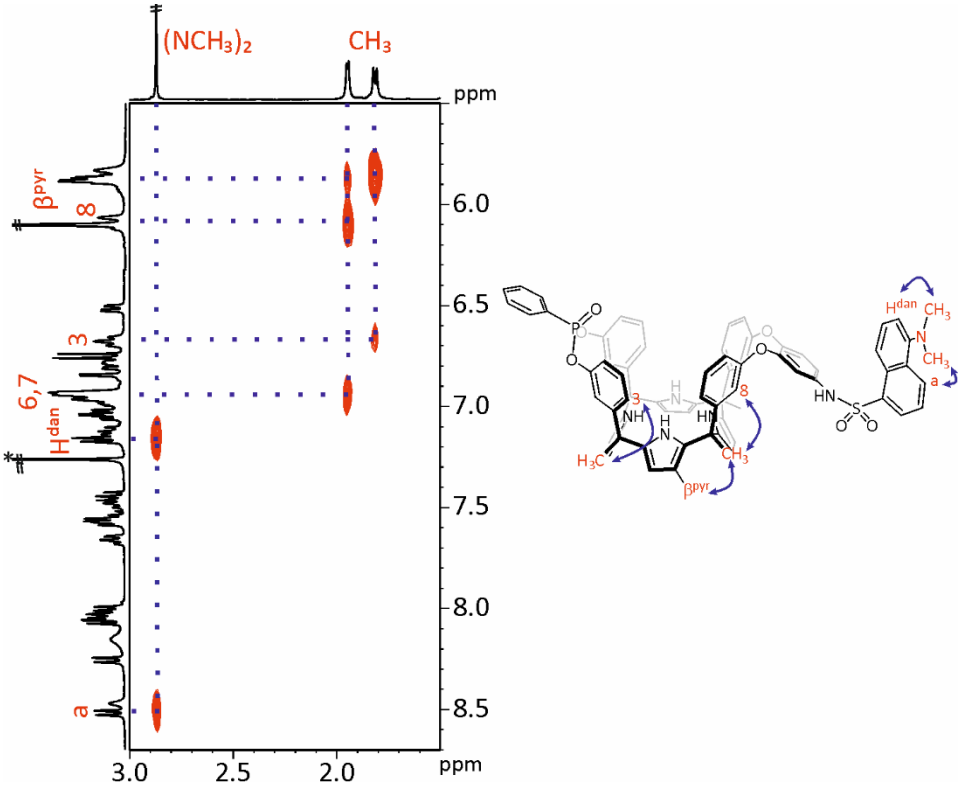

Figure 3.25 Selected region of the 2D ^{1}H-^{1}H NOESY NMR (400 MHz, $CDCl_3$, t_{mix} = 0.6 s) spectrum of compound **2**. * Residual solvent peak.

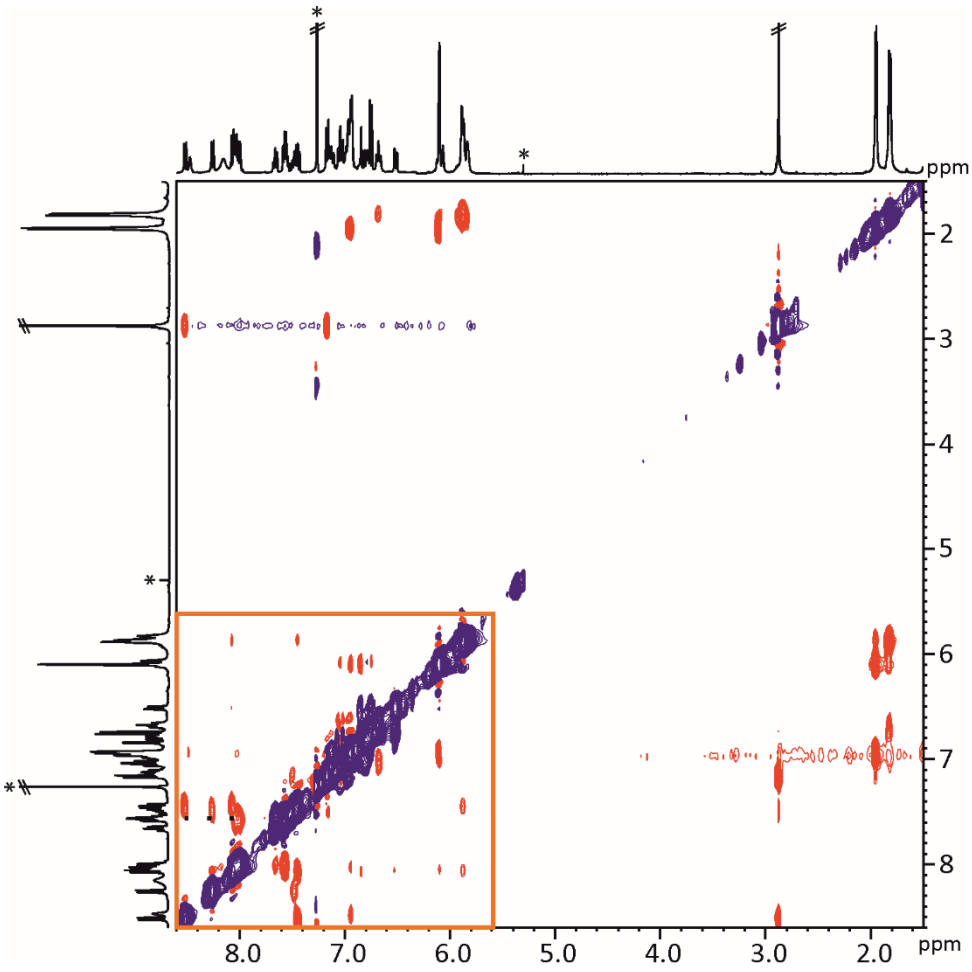

Figure 3.26 2D ^{1}H-^{1}H ROESY NMR (400 MHz, $CDCl_3$, spin-lock = 0.4 s) spectrum of the compound **2**. * Residual solvent peak.

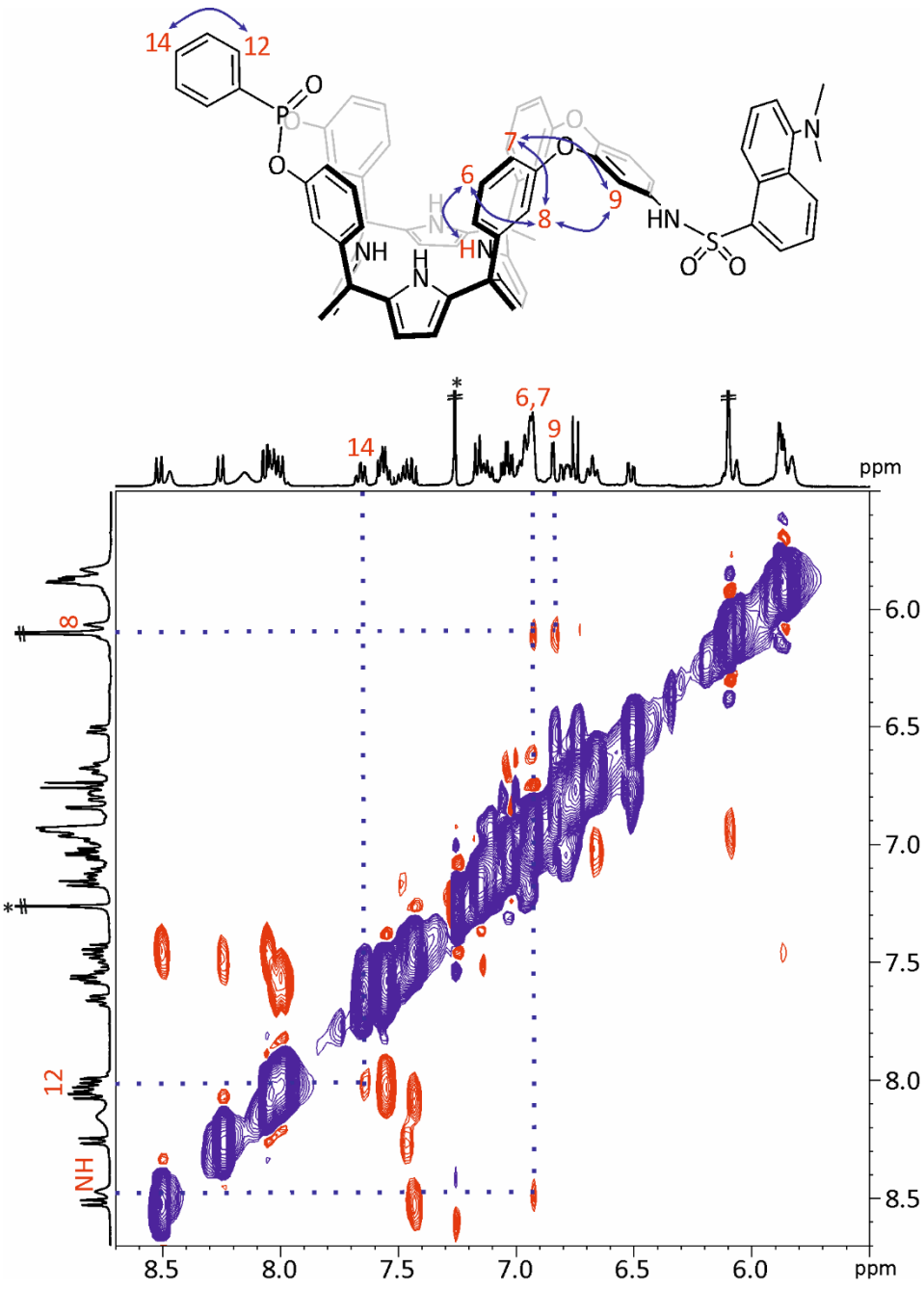

Figure 3.27 Selected region of the 2D ^{1}H-^{1}H ROESY NMR (400 MHz, $CDCl_3$, spin-lock = 0.4 s) spectrum of the compound **2**. * Residual solvent peak.

Synthesis of DABCYL *N*-oxide **3**:[40]

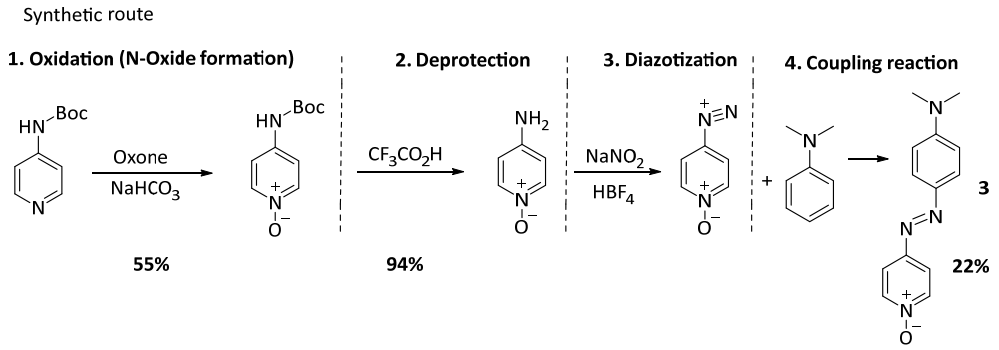

Scheme 3.3 Synthetic scheme for the preparation of **3**.

Oxidation (*N*-oxide) formation

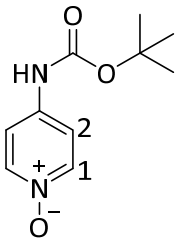

4-(Boc-amino)pyridine (200 mg, 1.03 mmol) and $NaHCO_3$ (605 mg, 7.21 mmol) were dissolved in 1:1 water:2-butanone (30 mL). Oxone® (950 mg, 3.09 mmol) was dissolved in water (1-3 mL) and added gently to the previous solution. The mixture was stirred vigorously at RT overnight. Then the phases were separated. The organic phase was diluted with DCM (20 mL), washed with brine, dried and concentrated. The aqueous phase was extracted with DCM (2 × 20 mL) and all organic phases were combined, washed with brine, dried, concentrated and finally washed with hexane to obtain a white solid (120 mg, 55%).

^{1}H-NMR (500 MHz, $CDCl_3$, 298 K): δ (ppm) = 9.94 (bs, 1H, NH), 8.09 (d, *J* = 7.4 Hz, 2H, H^1), 7.60 (d, *J* = 7.4 Hz, 2H, H^2), 1.46 (s, 9H, CH_3).

Deprotection step.

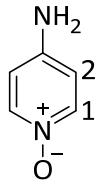

4-(Boc-amino)pyridine *N*-oxide (100 mg, 0.476 mmol) was dissolved in DCM (2.7 mL) and TFA (0.9 mL) was added dropwise. No starting material was detected after 3h of reaction. The solvent was removed (at RT and protected from light) to obtain 100 mg (94%) of the TFA salt of the deprotected compound.

^{1}H-NMR (400 MHz, $(CD_3)_2SO$, 298 K): δ (ppm) = 8.28 (d, *J* = 7.6 Hz, 2H, H^1), 7.90 (bs, 2H, NHs), 6.77 (d, *J* = 7.6 Hz, 2H, H^2).

Diazotization and coupling reaction.

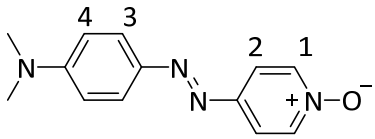

3

Sodium nitrite (36 mg, 0.524 mmol) was slowly added to a stirred solution of 4-aminopyridine (100 mg, 0.476 mmol) in HBF_4 (1 mL), cooled to -15 °C. The reaction mixture was stirred for additional 30 min (yellowish solution with a solid in suspension), keeping it always below -10 °C, whereupon *N*,*N*-dimethylaniline (0.120 mL, 0.952 mmol) was added in one portion (the color turns into intense orange). The reaction mixture was stirred for 2 h and alkalized with a concentrated solution of sodium hydroxide until reaching basic pH. The reaction was diluted with 20 mL DCM and 10 mL H_2O. Three additional extractions were done with DCM. The organic phase was concentrated and 171 mg of the crude were obtained. **3** was purified by column chromatography (20 g basic alumina, DCM:IPA 98:2), yielding 22 mg (22%) of the product as a red solid.

IR (film): ν (cm^{-1}) = 3100, 2912, 1594, 1522, 1449, 1360, 1254, 1147, 1018, 845, 824, 548. **^{1}H-NMR** (400 MHz, $CDCl_3$, 298 K): δ (ppm) = 8.23 (d, *J* = 7.6 Hz, 2H, H^1), 7.86 (d, *J* = 9.3 Hz, 2H, H^3), 7.72 (d, *J* = 7.6, 2H, H^2), 6.75 (d, *J* = 9.3 Hz, 2H, H^4), 3.13 (s, 6H, CH_3).

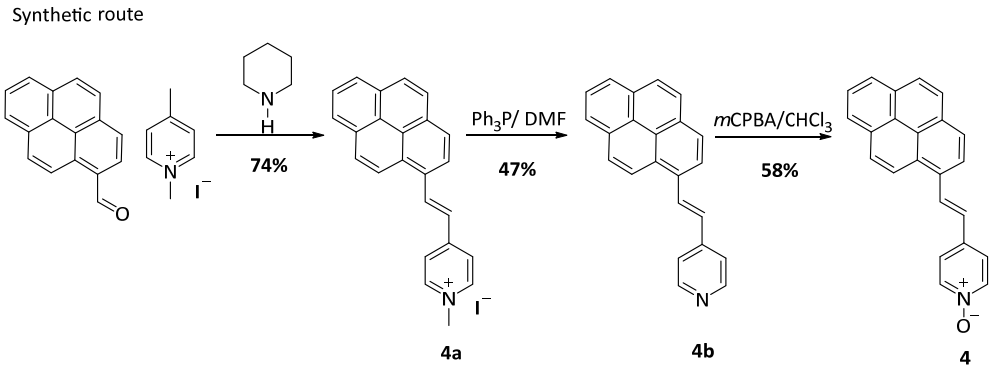

Scheme 3.4 Synthetic scheme for the preparation of **4**.

Synthesis of the vinyl pyridine salt **4a.**

1-Pyrenecarboxaldehyde (0.46 g, 2.0 mmol), dissolved in THF (20 mL), was added to a MeOH solution containing 1,4-dimethylpyridinium iodide (0.47 g, 2.0 mmol) and piperidine (0.17 g, 2.0 mmol). After this mixture was stirred at RT for 6h, the precipitated product was filtrated, yielding 658 mg of **4a** (74%). The characterization data were in accordance with those reported in the literature.[36]

Synthesis of pyrene vinyl pyridine **4b.**

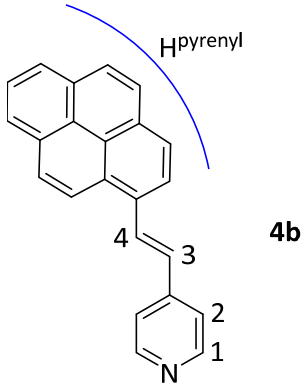

4b

Triphenylphosphine (233 mg, 0.9 mmol) and **4a** (100 mg, 0.2 mmol) were placed in a previously dried Ace pressure tube (100 mL) equipped with a plunger valve and three cycles of vacuum/Ar were applied. Then, DFM (15 mL) was added under argon atmosphere and the mixture was heated at 85 °C overnight. **4b** was isolated by flash column chromatography (6 g SiO_2, AcOEt) yielding 32 mg (47 %) of a yellow solid.

Rf: 0.5 (AcOEt). **^{1}H-NMR** (500 MHz, $CDCl_3$, 298 K): δ (ppm) = 8.65 (d, *J* = 5.9 Hz, 2H, H^1), 8.45 (d, *J* = 9.2 Hz, 1H, $H^{pyrenyl}$), 8.40 (d, *J* = 16.0 Hz, 1H, H^4), 8.31 (d, *J* = 8.1 Hz, 1H, $H^{pyrenyl}$), 8.23- 7.98 (mult., 9H, $H^{pyrenyl}$), 7.52 (d, *J* = 5.9 Hz, 2H, H^2), 7.25 (d, *J* = 16.0 Hz, 1H, H^3).

Synthesis of pyrene vinyl pyridine *N*-oxide **4.**

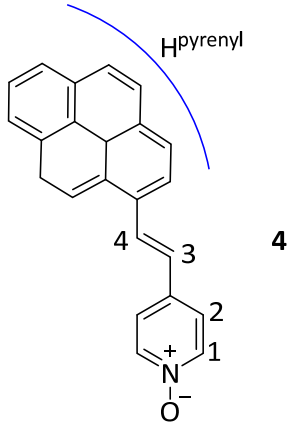

4

4b (52 mg, 0.169 mmol) was dissolved in $CHCl_3$ (2 mL) and the solution was stirred at RT for 15 min Then it was cooled at 0 °C and *m*-CPBA (39 mg, 0.226 mmol) was added portionwise and the reaction was stirred for 1 h at 0 °C and then 3 h at RT.[38] The crude was purified by column chromatography (6 g neutral alumina, DCM:IPA 2%) and 32 mg (58%) of an orange solid was obtained. We also used Oxone® as oxidizing agent, obtaining a lower yield.

Rf: 0.2 (DCM:IPA 98:2, alumina). **IR** (film): ν (cm^{-1}) = 3035, 1588, 1476, 1443, 1251, 1161, 1092, 1026, 941, 848, 810, 720, 610, 566, 517, 458. **^{1}H-NMR** (500 MHz, $CDCl_3$, 298 K): δ (ppm) = 8.42 (d, *J* = 9.2 Hz, 1H, $H^{pyrenyl}$), 8.28 (d, *J* = 8.3 Hz, 1H, $H^{pyrenyl}$), 8.27 (d, *J* = 16.0 Hz, 1H, H^3), 8.22-8.15 (mult., 6H, $H^{pyrenyl}$), 8.21 (d, *J* = 7.0 Hz, 2H, H^1), 8.11-8.05 (mult., 2H, $H^{pyrenyl}$), 8.02 (t, *J* = 7.5 Hz, 1H, $H^{pyrenyl}$), 7.47 (d, *J* = 7.0 Hz, 2H, H^2), 7.20 (d, *J* = 16.0 Hz, 1H, H^4). **^{13}C-NMR** (125 MHz, $CDCl_3$, 298 K): δ (ppm) = 139.4 (×2), 136.1, 131.9, 131.6, 130.9, 130.2, 129.8, 129.0, 128.4, 128.2, 127.5, 126.7, 126.4, 126.0, 125.7, 125.3, 125.2, 124.9, 123.8, 123.2 (×2), 122.5. **HRMS (ESI+)** m/z: $[M + Na]^+$ calcd for $C_{23}H_{15}NONa$: 344.1046, found: 344.1039.

Synthetic route

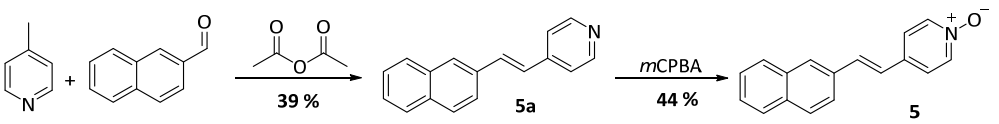

Scheme 3.5 Synthetic scheme for the preparation of **5.**

Synthesis of (E)-4-(2-(naphthalen-2-yl)vinyl)pyridine **5a**.

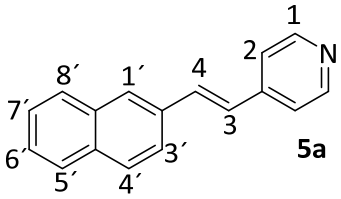

Preparation of **5a** has been described in a previous work and was carry out using the same process.[37]

The 2-naphthaldehyde (15.6 g, 0.1 mol) and 4-picoline (9.5 g, 0.1 mol) were refluxed in Ac_2O (72 g, 0.7 mol) for 48h. The black solid was quenched with H_2O (90 mL) and neutralized with NaOH solution. The mixture was extracted with $CHCl_3$ (3 × 50 mL). Organic phase was dried with Na_2SO_4, filtered and concentrated. Distillation (bp 200 – 210 °C/0.01 mm Hg) gave a yellow solid consisting of **5a** (8.90 g, 39%) with a trace of its Z-isomer. Recrystallization (toluene) gave pure **5a**; light yellow solid.

Melting point: 227-230 °C. **Rf**: 0.3 (AcOEt:n-hexane 70:30). **^{1}H NMR** (400 MHz, $CDCl_3$): δ (ppm) = 8.60 (dd, J_1=4.3 Hz; J_2 = 1.5 Hz, 2H, H^1), 7.91 (s, 1H, $H^{1'}$), 7.88-7.81 (mult., 3H, $H^{4'}$,$H^{5'}$,$H^{8'}$), 7.74 (dd, J_1 = 8.6; J_2=1,70 Hz, 1H, $H^{3'}$), 7.53-7.44 (mult., 3H, H^3,$H^{6'}$,$H^{7'}$), 7.41 (dd, J_1 = 4.3 Hz; J_2 = 1.55 Hz, 2H, H^2), 7.14 (d, J = 16.3 Hz, 1H, H^4).

Synthesis of the naphthalene *N*-oxide **5.**

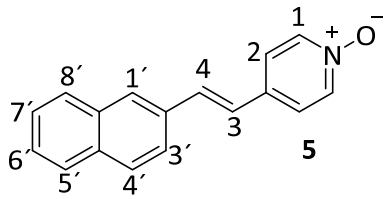

5a (0.5014 g, 2.168 mmol) was dissolved in dichloromethane (50 mL). The solution was stirred at room temperature. Then it was cooled at 0 °C and *m*CPBA (1.2316 g, 7.14 mmol) was added portionwise and the reaction was stirred for 1h at 0 °C and 3h at room temperature. The crude was purified by neutral alumina column chromatography (60g, DCM to DCM:IPA 95:5) and 240 mg (45%) of an yellow solid was obtained.

Melting point: 169-172 °C. **Rf**: 0,2 (CH_2Cl_2:IPA 98:2, Alumina). **IR** (film): ν (cm^{-1}) = 3053, 2922, 1721, 1593, 1479, 1248, 1166, 1023, 959, 816, 753, 579, 539, 471. **^{1}H NMR** (500 MHz, CDCl3): δ (ppm) = 8.17 (d, *J* = 7.3 Hz, 2H, H^1), 7.88 (s, 1H, $H^{1'}$), 7.87-7.81 (mult., 3H, $H^{4'}$, $H^{5'}$, $H^{8'}$), 7.70 (d, *J* = 8.7 Hz, 1H, $H^{3'}$), 7.53-7.48 (mult., 2H, $H^{6'}$, $H^{7'}$), 7.40 (d, *J* = 7.3 Hz, 2H, H^2), 7.32 (d, *J* = 16.3 Hz, 1H, H^3), 7,08 (d, *J* = 16.3 Hz, 1H, H^4). **HRMS (ESI+)** m/z: $[M + Na]^+$ calcd for $C_{17}H_{13}NO$: 270.0889, found: 270.0888.

Synthesis of hexylcreatinine **HexCr**.

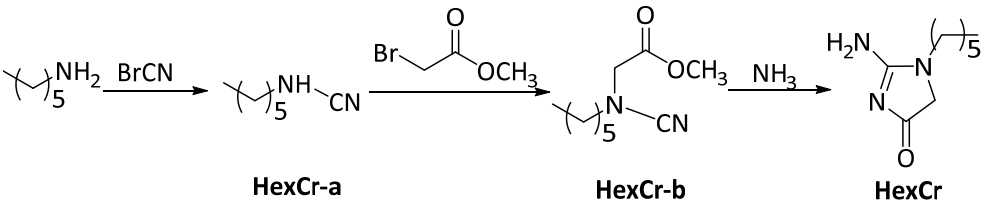

Scheme 3.6 Synthetic scheme for the preparation of **HexCr**.

Step 1: Cyanogen bromide (3.14 g, 29.6 mmol) dissolved in a 1:1 mixture of anhydrous THF:Et_2O and under Ar atmosphere, was added dropwise via a cannula at 0 °C to a previously dried 250 mL round bottom flask, containing a solution of 1-hexylamine (5.0 g, 49.4 mmol) in anhydrous 1:1 THF:Et_2O (50 mL) under Ar. (CAUTION: cyanogen bromide is highly toxic. The chemical should be weight in the fumehood and the reaction should be carried out in the fumehood). During the addition a white solid precipitated. After the addition was completed, the mixture was stirred for further 3.5h. The solid was filtrated and the solution was washed with water (2 × 100 mL). The organic phase was separated and dried (Na_2SO_4), filtered and concentrated under reduced pressure, yielding pure cyanamide (**HexCr-a**) as a yellow oil (3 g, 80%).

^{1}H-NMR (400 MHz, $CDCl_3$, 298 K): δ (ppm) = 3.82 (bs, 1H), 3.05 (dt, *J* = 7.0 Hz, 5.5 Hz, 2H), 1.59 (quin, *J* = 7.4 Hz, 2H), 1.39-1.24 (m, 6H), 0.88 (t, *J* = 6.9 Hz, 3H). **^{13}C{^{1}H}-**

NMR (100 MHz, $CDCl_3$, 298 K): δ (ppm) = 116.5, 46.4, 31.4, 29.8, 26.0, 22.6, 14.0. **HRMS (ESI-TOF)** m/z: $[M + Na]^+$ calcd for $C_7H_{14}N_2Na$ = 149.1049, found = 149.1050.

Step 2: To a solution of the hexylcyanamide (**HexCr-a**) (2.0 g, 15.85 mmol) in anhydrous THF (50 mL), NaH (60 % oil suspension, 0.7g, 17.5 mmol) was added in three portions at 0 °C under Ar atmosphere and the reaction mixture was stirred for 80 min. During that time a precipitate was formed. Then, a solution of methyl 2-bromoacetate (1.5 mL, 15.85 mmol) in anhydrous THF (10 mL) was added at 0 °C and the mixture was stirred overnight. Next day, the reaction mixture was filtered. The filtrate was evaporated to one-half of its total volume and DCM (50 mL) was added. The combined organic layer was washed with water (2 × 50 mL), dried (Na_2SO_4) and filtered. The solvent was evaporated under reduced pressure to give the desired product as a yellow oil 3.08 g (98%). Grease coming from the NaH was observed in the NMR.

^{1}H-NMR (400 MHz, $CDCl_3$, 298 K): δ(ppm) = 3.80 (s, 3H), 3.78 (s, 2H), 3.08 (t, *J* = 7.3 Hz, 2H), 1.67 (quin, *J* = 7.2 Hz, 2H), 1.39-1.24 (m, 6H), 0.88 (m, 3H). **^{13}C{^{1}-NMR** (100 MHz, $CDCl_3$, 298 K): δ(ppm) = 168.4, 116.9, 52.6, 52.4, 52.2, 31.3, 27.5, 26.1, 22.5, 14.0. **HRMS(ESI-TOF)** m/z: $[M + Na]^+$ calcd for $C_{10}H_{18}N_2NaO_2$ = 221.1260, found = 221.1256.

Step 3: The product obtained in step 2 (1 g, 5.04 mmol) was treated with aqueous ammonia (30%, 50 mL, 693 mmol) and the mixture was vigorously stirred at RT for 30 minutes. The resulting solid was filtered and washed with water and methanol, yielding the pure product as a white solid (0.4 g, 43%).

^{1}H-NMR (400 MHz, D_2O, 298 K): δ (ppm) = 4.08 (s, 2H), 3.41 (t, *J* = 7.1 Hz, 2H), 1.64 (quin, *J* = 7.4, 2H), 1.36-1.28 (m, 6H), 0.88 (t, *J* = 7.4 Hz, 3H).

3.5.3 NMR titrations

NMR experiments with different HexCr/2 molar ratios in $CDCl_3$

Stock solutions of the fluorescent receptor **2** (1.0 mM in $CDCl_3$) and **HexCr** (5.0 mM in CH_3OH HPLC grade) were prepared to perform the NMR experiment. In order to reach the desired molar ratio, different volumes of the **HexCr** solution were placed in small vials using high quality micro syringes. The methanol was removed under reduced pressure and the residual solid was redissolved in 0.5 mL of the stock solution of **2**. Each vial was sonicated for five minutes and finally transferred to a NMR tube to acquire the spectrum.

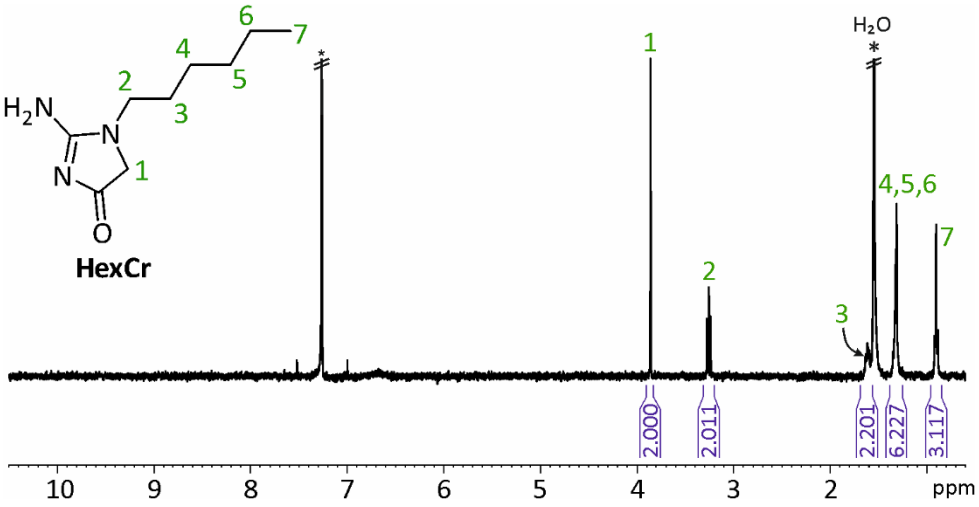

Figure 3.28 ^{1}H-NMR (500 MHz, $CDCl_3$) of **HexCr**. * Residual solvent peak.

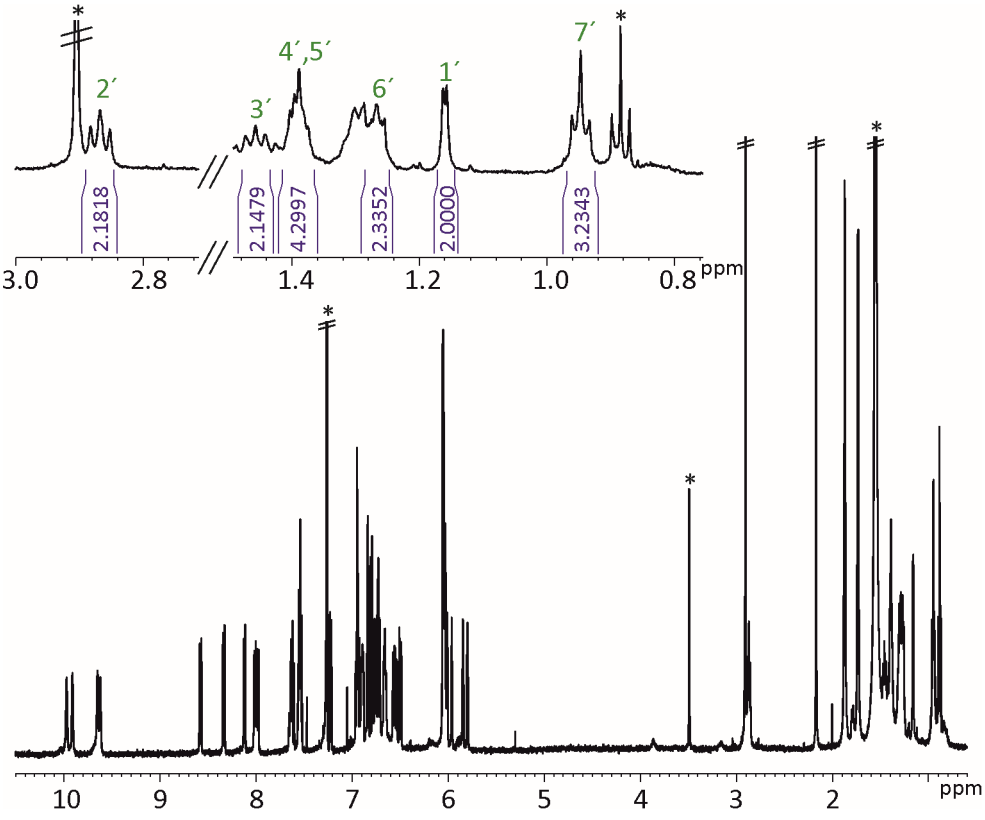

Figure 3.29 ^{1}H-NMR (500 MHz, $CDCl_3$) of **2** + 1.0 equiv. **HexCr**. * Residual solvent peak.

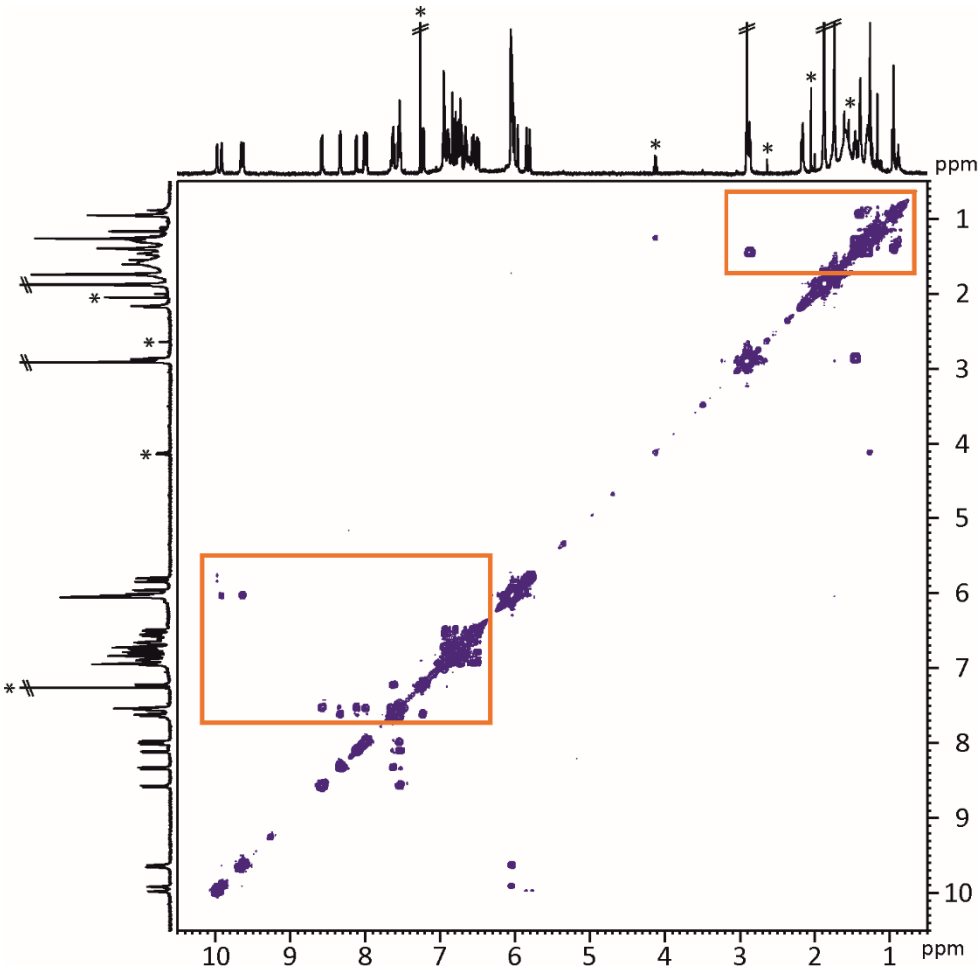

Figure 3.30 2D ^{1}H-^{1}H COSY NMR (400 MHz, $CDCl_3$) spectrum of compound **2** + 1.0 equiv **HexCr**. * Residual solvent peak.

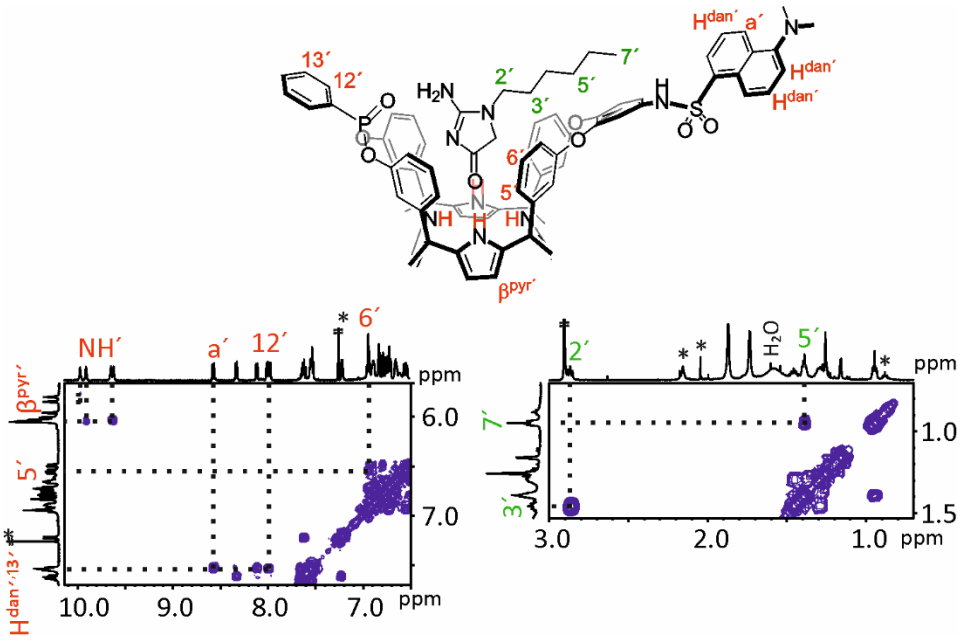

Figure 3.31 Expanded regions of the 2D ^{1}H-^{1}H COSY NMR (400 MHz, $CDCl_3$) spectrum of compound **2** + 1.0 equiv **HexCr**. * Residual solvent peak.

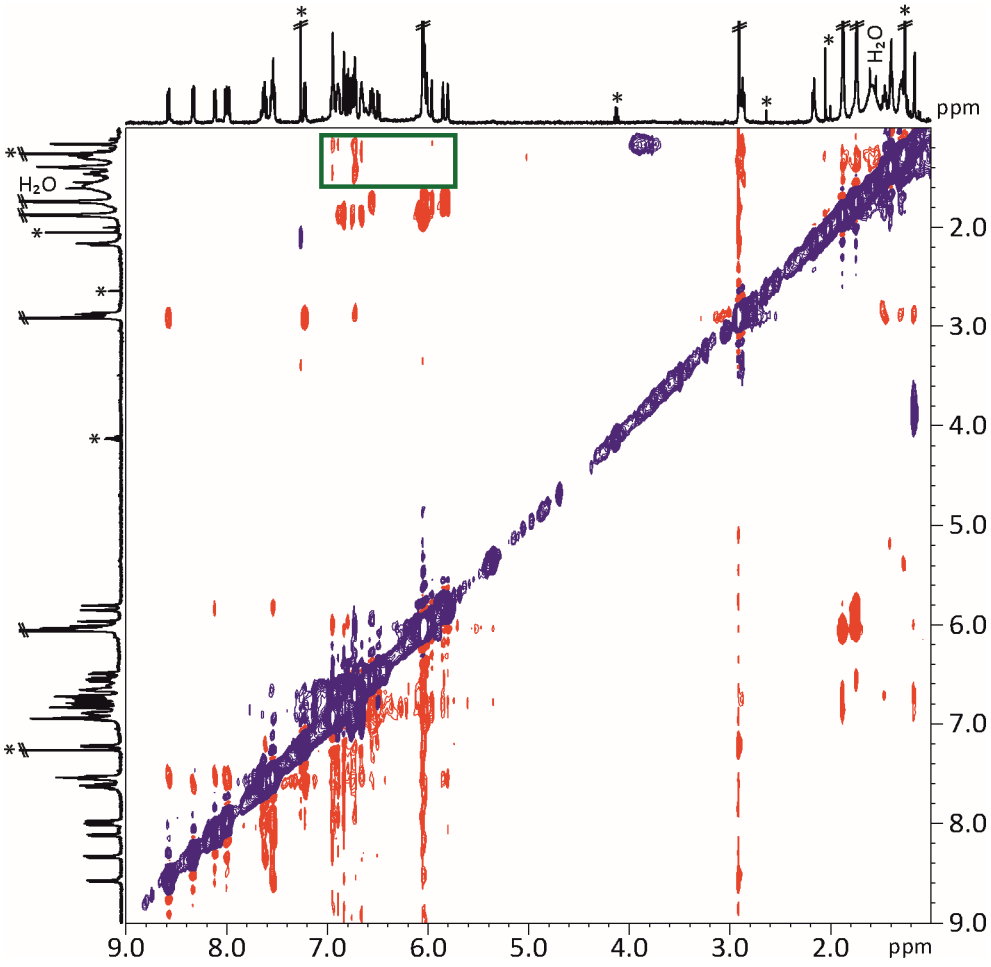

Figure 3.32 2D ^{1}H-^{1}H ROESY NMR (500 MHz, $CDCl_3$, spin-lock = 0.2 s) spectrum of the compound **2** + 1.0 equiv **HexCr**. * Residual solvent peak.

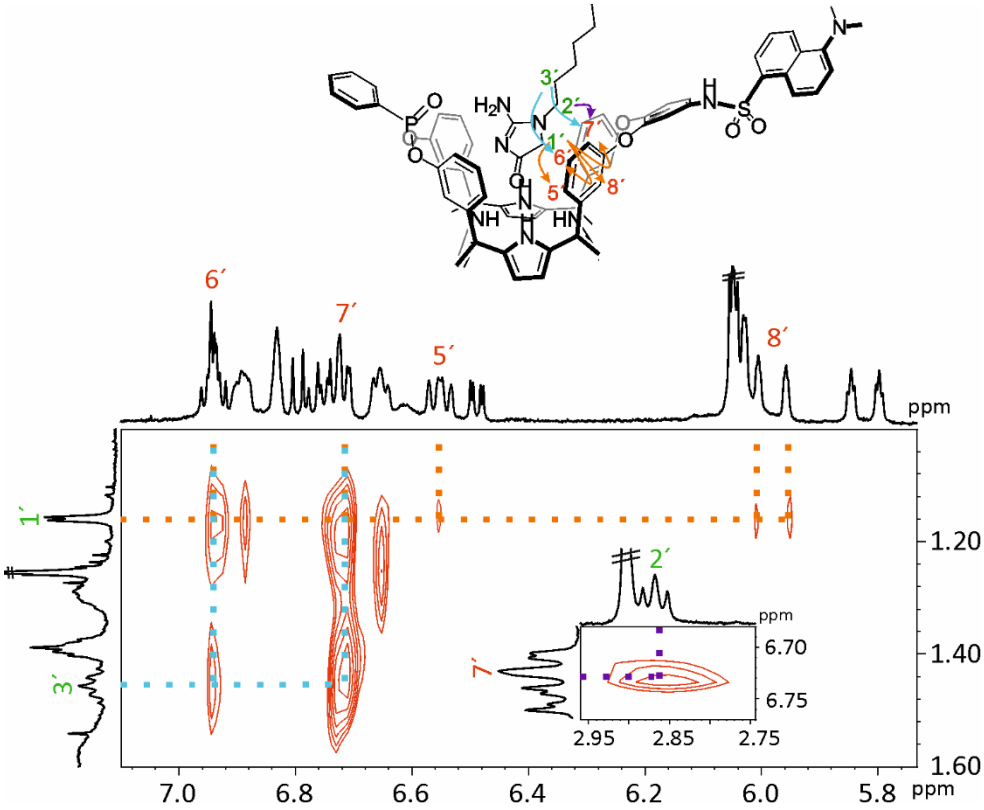

Figure 3.33 Selected region of the 2D ^{1}H-^{1}H ROESY NMR (500 MHz, $CDCl_3$, spin-lock = 0.2 s) spectrum of the compound **2** + 1.0 equiv **HexCr**. * Residual solvent peak.

NMR experiments of Cr⊂2 complex.

Due to the low solubility of the creatinine, we performed a solid-liquid extraction. Solid creatinine and deuterated chloroform solution of **2** (0.5 mL, 2.0 mM) were sonicated during 10 min. After that time, the sample was filtrated directly on an NMR tube.

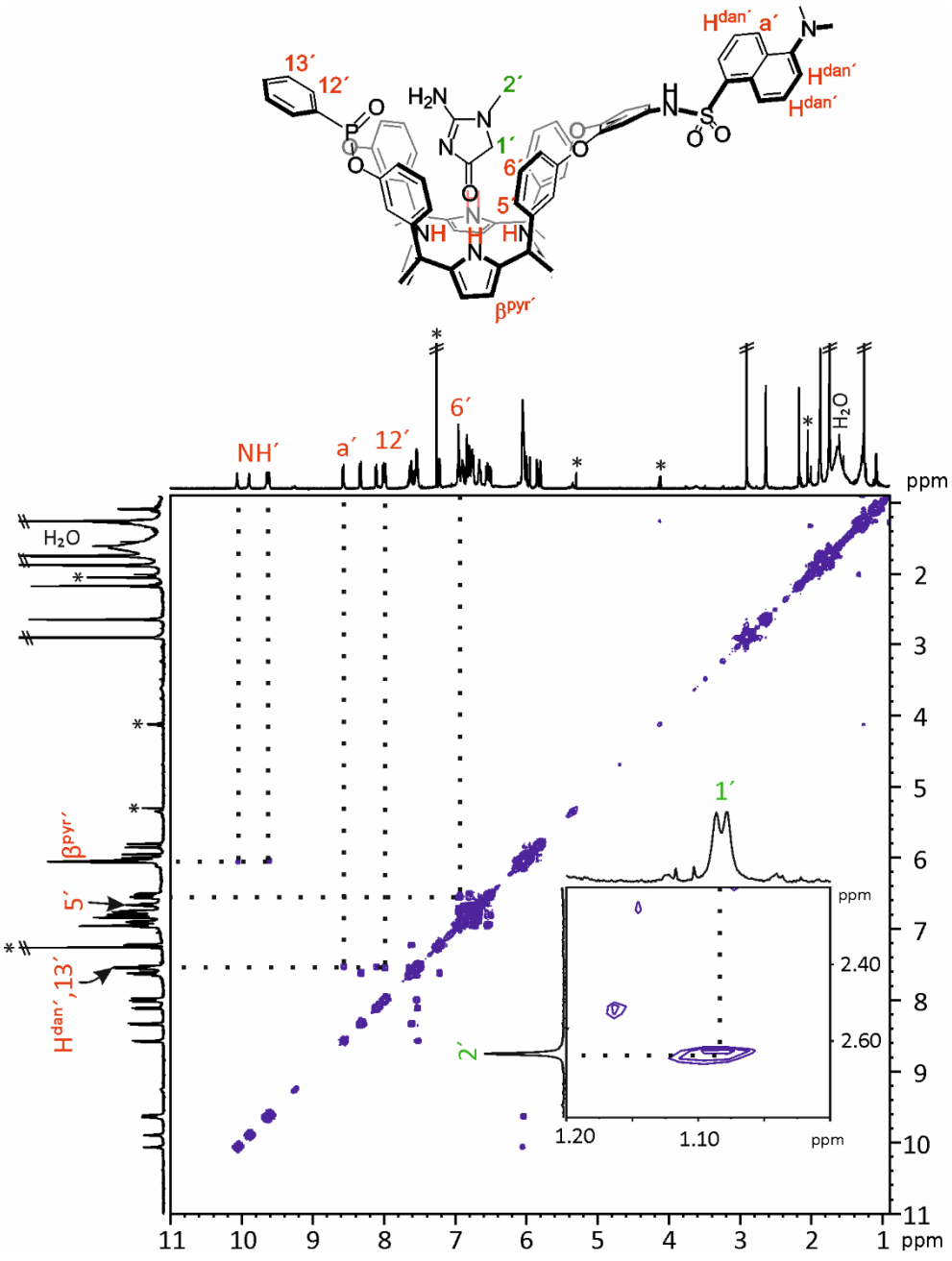

Figure 3.34 2D ^{1}H-^{1}H COSY NMR (500 MHz, $CDCl_3$) spectrum of the **Cr⊂2** complex after the solid-liquid extraction. * Residual solvent peak.

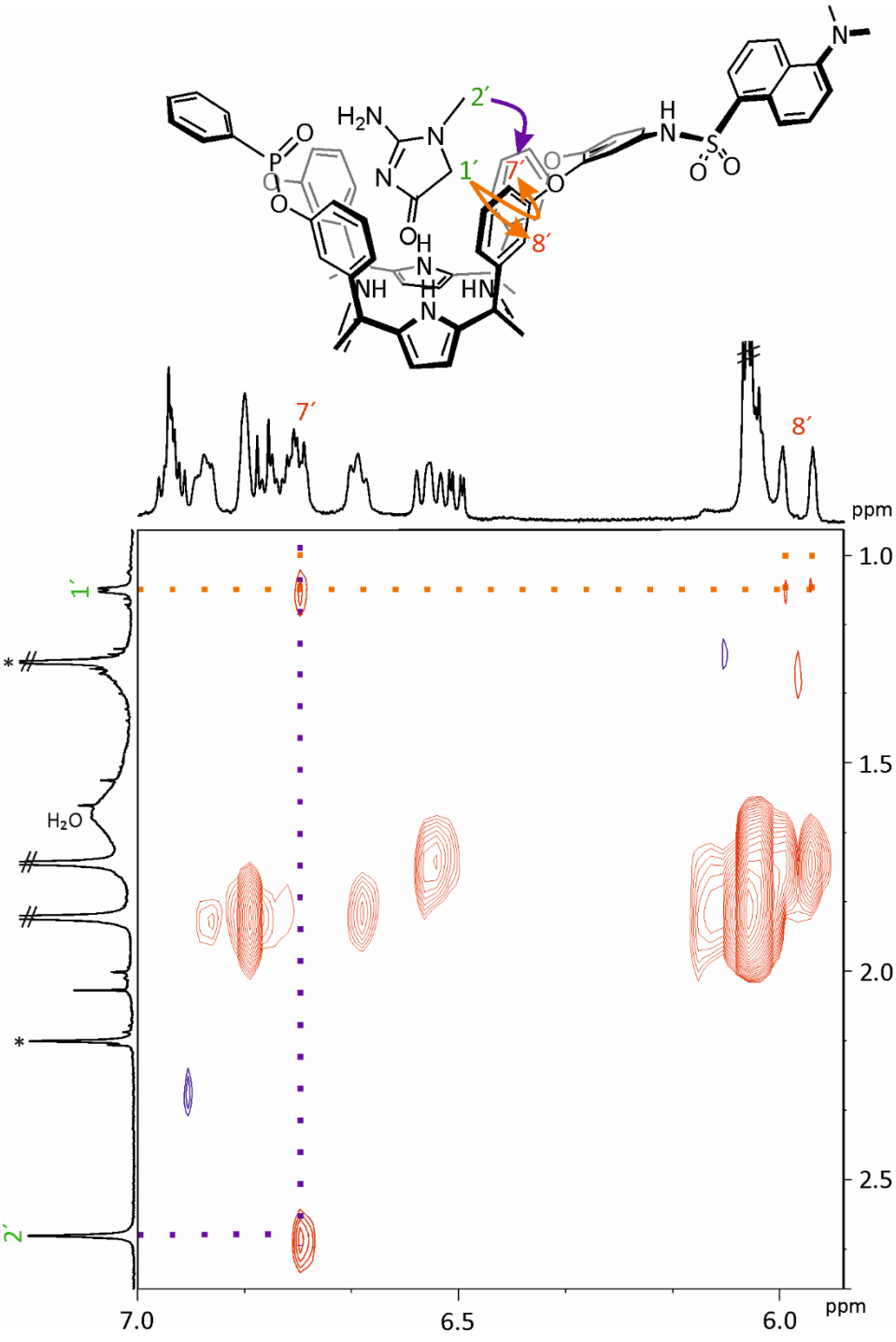

Figure 3.35 Selected region of the 2D ^{1}H-^{1}H ROESY NMR (500 MHz, $CDCl_3$, spin-lock = 0.2 s) spectrum of the **Cr⊂2** complex after the solid-liquid extraction. * Residual solvent peak.

3.5.4 Indicator Displacement Assay (IDA) monitored by ^{1}H and ^{31}P NMR

Speciation profile calculation

The speciation profile of the displacement of **HexCr⊂2** with **3** was calculated considering a difference in the binding constant greater than two orders of magnitude. According with the profile, the addition of 0.5 equiv. of **3** to a solution of **HexCr⊂2** produces the formation of **3⊂2** complex around 50% and more than 80% when 1.0 equiv. is added.

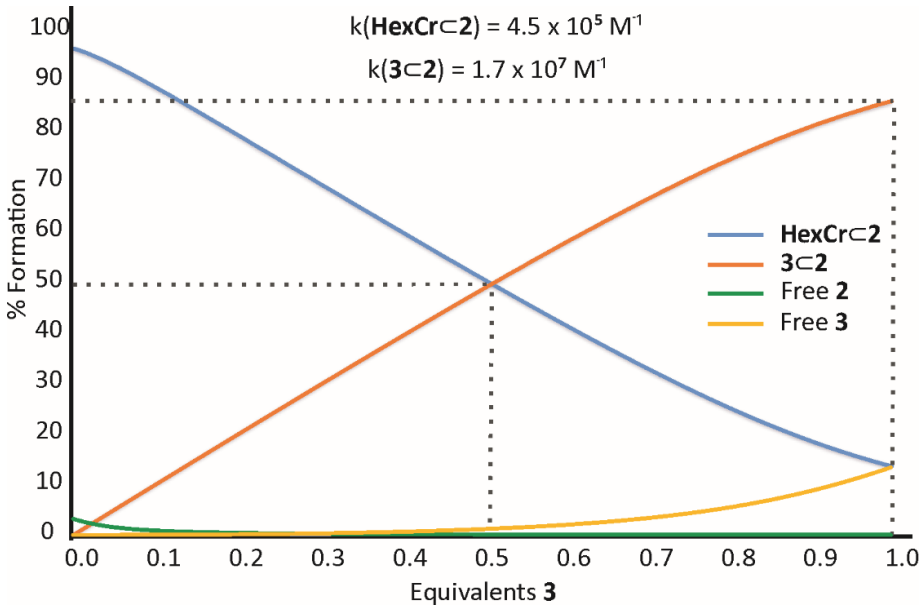

Figure 3.36 Calculated speciation profile for the competitive titration of **HexCr⊂2** with **3** considering a binding constant of 4.5×10^5 M^{-1} for **HexCr⊂2** and 1.7×10^7 M^{-1} for **3⊂2**.

3.5.5 Competitive NMR titration of **HexCr⊂2** with **3**

The equimolar mixture of **HexCr** and **2** in $CDCl_3$, at 2 mM concentration, produced the quantitative assembly of **HexCr⊂2** (2.0 mM) (Figure 3.*37*b). Subsequently, 0.5 mL of the above solution were transferred to an NMR tube. On the other hand, a solution of **3** ten-fold more concentrated was prepared in the same solvent (20-22 mM). The 0.5 mL of the **HexCr⊂2** complex solution was titrated by manually injecting incremental amounts of the **3** solution. The ^{1}H-NMR spectrum of the mixture was acquired after each injection and vigorous hand shaking of the NMR tube.

The addition of 0.5 equiv. of **3** to the **HexCr⊂2** solution produce the appearance of a new set of signals assigned to the **3⊂2** complex. For instance, eight signals appeared in the NHs NMR region (9.4 – 10.2 ppm). Four of these signals were assigned to the **HexCr⊂2** complex and four for the **3⊂2** complex. According with the integration of the signals, the complexes are present around 50% molar ratio, as expected with the speciation profile calculated previously (Figure 3.*37*). With the addition of 1.0 equiv. of **3**, the signals for the free **HexCr** can be clearly observed, supporting its quantitative displacement for the complex with **2**.

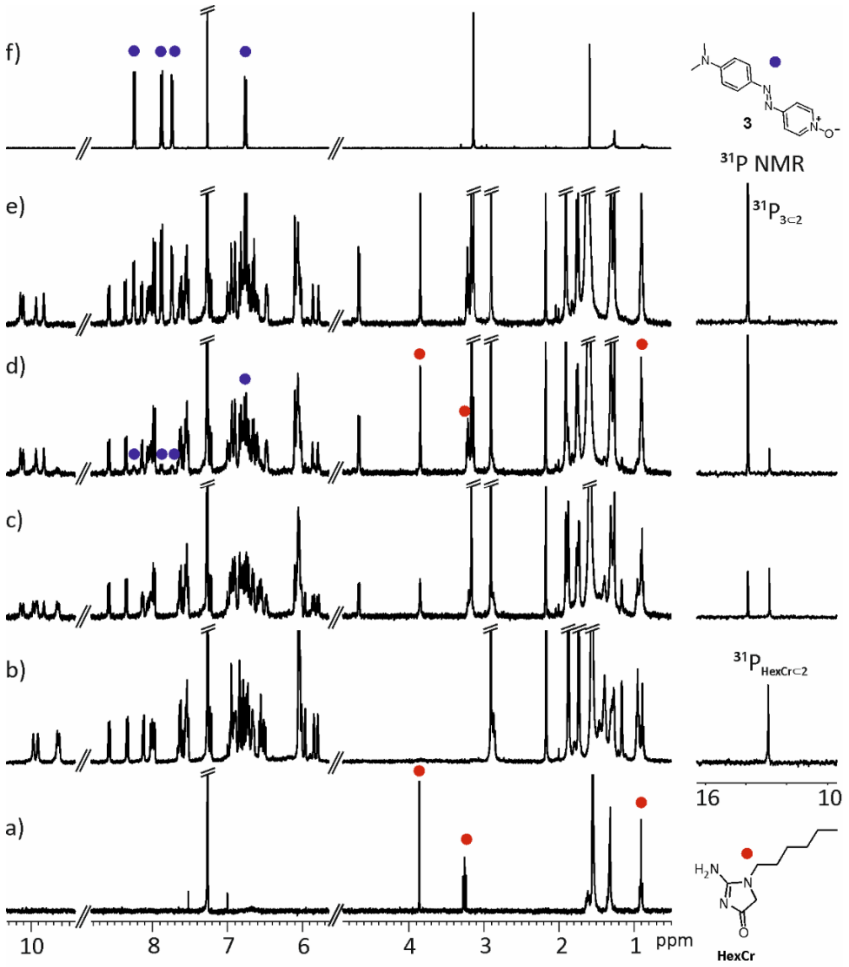

Figure 3.37 Left panel, selected regions of the ^{1}H-NMR spectra (400 MHz, $CDCl_3$, 298 K) registered during the competitive titration of **HexCr⊂2** (2.0 mM) with incremental amounts of **3**: a) free **HexCr**; b) 0.0 equiv. of **3**; c) 0.5 equiv. of **3**; d) 1.0 equiv. of **3**; e)1.5 equiv. of **3**; f) Free **3**. Right panel, corresponding ^{31}P-NMR spectra (162 MHz, $CDCl_3$, 298 K) acquired during the titration experiment.

The obtained results demonstrated the displacement of **HexCr** included in receptor **2** by the addition of dye **3** in a pairwise competitive experiment supporting the existence of the reverse process in the IDA experiments. Moreover, the NMR results of the pairwise competitive experiment are in complete agreement with the ratio of the binding constant values of **3**⊂**2** and **HexCr**⊂**2** derived from the emission and ITC experiments, respectively.

3.5.6 Competitive titration of **HexCr**⊂**1** with **4** monitored by NMR spectroscopy

To probe the interaction between receptor **1** and dye **4**, we performed ^{1}H and ^{31}P NMR titration experiments at millimolar concentration in $CDCl_3$ solutions. The ^{1}H NMR spectrum of **1** at mM concentration in $CDCl_3$ solution showed sharp and well-resolved proton signals (Figure 3.*38*a).

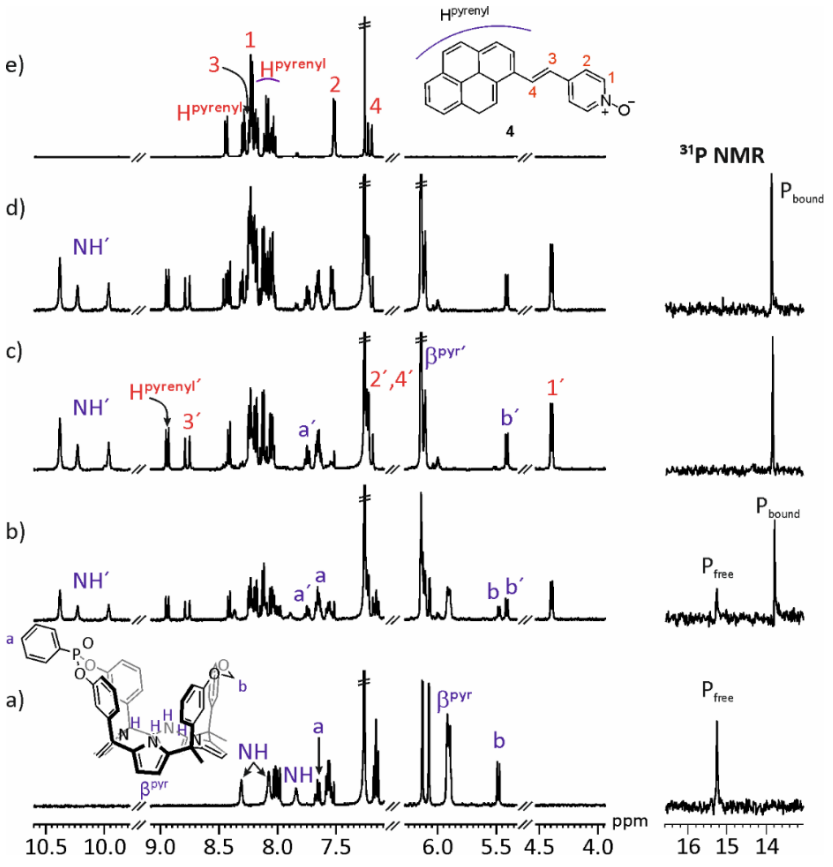

Figure 3.38 ^{1}H NMR (400 MHz, $CDCl_3$, 298 K) spectra registered during the titration of receptor **1** with incremental amounts of **4**. a) Free **1** (2.0 mM); b) **1** + 0.5 equiv.; c) **1** + 1.0 equiv.; d) **1**+ 1.5 equiv.; e) Free **4**. Right panel, corresponding ^{31}P NMR spectra (162 MHz, $CDCl_3$, 298 K). Primed letters and numbers correspond to the proton signals in the **4**⊂**1** complex.

The addition of 0.5 equiv. of **4** to a mM solution of **1** produced the appearance of a new set of signals. The new set of signals was assigned to protons in the **4⊂1** complex (Figure 3.*38*b). Noteworthy, the pyrrole NHs experienced a significant downfield shift (Δδ ~ + 2.3 ppm) providing evidence for the hydrogen bonding interaction with the oxygen atom of bound **4**. The new doublet at 5.41 ppm and the triplet at 7.75 ppm assigned to the bound receptor **1** are also indicative of complex formation. The chemical shift changes experienced by the proton atoms of the bound guest, especially the doublet resonating at 4.39 ppm that is assigned to proton $H^{1'}$, also supported complex formation. $H^{1'}$ moves upfield (Δδ = 3.8 ppm) owing to the deep inclusion of the guest in the receptor's cavity.

The addition of 1.0 equiv. of **4**, produced the exclusive observation of the proton signals assigned to the **4⊂1** complex (Figure 3.*38*c). Finally, the addition of **4** in excess did not produce noticeable changes in the signals assigned to protons of bound **1** and those of included **4**. However, new signals corresponding to the protons of free **4** emerged (Figure 3.*38*d).

A similar behavior was observed in the ^{31}P NMR spectra. The ^{31}P NMR spectrum of free **1** revealed the presence of one singlet at 15.26 ppm (Figure 3.*38*a, right panel). The ^{31}P NMR spectrum of the equimolar mixture (Figure 3.*38*c, right panel) showed exclusively an upfield shifted signal for the phosphorus atom (Δδ = -1.4 ppm). An excess of **4** did not produced observable changes in the ^{31}P NMR spectrum (Figure 3.*38*d, right panel).

Similarly to the NMR experiment described in Figure 3.*37* and with the goal of demonstrating the reversibility of the binding process of **1** with **HexCr** and **4**, we performed NMR competitive titration experiment by adding incremental amounts of **4** to the **HexCr⊂1** complex (Figure 3.*39*). The equimolar mixture of **HexCr** and **1** in $CDCl_3$, at 2 mM concentration, produced the quantitative assembly of **HexCr⊂1** (2.0 mM) (Figure 3.*39*b). The addition of 0.5 equiv. of **4** to the **HexCr⊂1** solution produce the appearance of a new set of signals assigned to the **4⊂1** complex (Figure 3.*39*c). In the NHs NMR region (9.7-10.5 ppm) three new signals emerged, in the same way, a new doublet appeared at 5.41 ppm (protons b in Figure 3.*38*a). These new signals were assigned to bound **1** and included **4**, respectively. In agreement with the integrals of the signals, the two complexes are present in 50% molar ratio (this behavior is also observed in the ^{31}P NMR spectra; Figure 3.*39*c, right panel). This result is in agreement with the speciation profile calculated previously for two complexes differing in two orders of magnitude in binding constant values (Figure

3.*36*). With the addition of 1.0 equiv. of **4** (Figure 3.*39*d) the signals for the free **HexCr** can be clearly observed, supporting its quantitative displacement from complex formed with **1**.

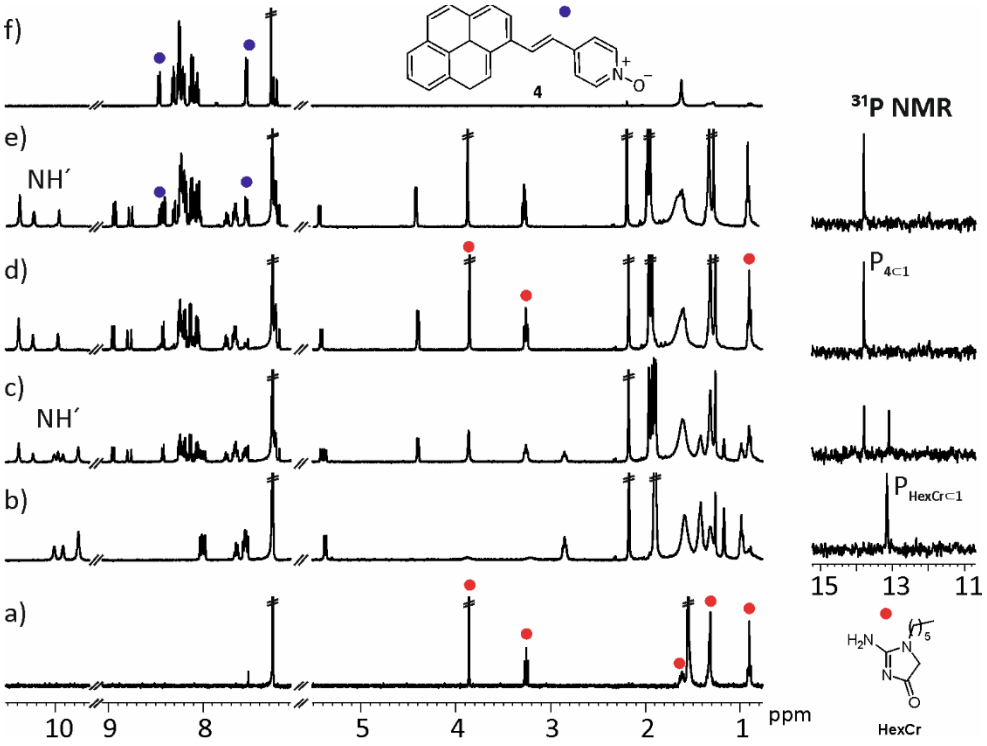

Figure 3.39 Left panel, selected regions of the ^{1}H-NMR spectra (400 MHz, $CDCl_3$, 298 K) registered during the competitive titration of **HexCr⊂1** (2.0 mM) with incremental amounts of **4**: a) free **HexCr**; b) 0.0 equiv. of **4**; c) 0.5 equiv. of **4**; d) 1.0 equiv. of **4**; e)1.5 equiv. of **4**; f) Free **4**. Right panel, corresponding ^{31}P-NMR spectra (162 MHz, $CDCl_3$, 298 K) acquired during the titration experiment.

3.5.7 ITC experiments

ITC Titration experiments of receptors 1 and 2 with pyridyl *N*-oxides (3-5) and hexyl creatinine (HexCr).

ITC experiments were performed in a MicroCal VP-ITC Micro Calorimeter with the VP Viewer 2000 software. In the case of guests **3**-**4**, titrations were carried out by adding small aliquots (10- 20 µL) of a chloroform solution of the guest into a solution of the host in the same solvent. Due to the low solubility of the hexyl creatinine **HexCr** in chloroform, a reverse ITC experiments were performed. The concentration of the solution in the syringe was approximately seven to ten times more concentrated than the cell solution. The association constants and the

thermodynamic parameters were obtained from the fit of the titration data to the "one set of sites" binding model implemented in the Microcal ITC Data Analysis module. The enthalpy of binding for each injection is plotted against the molar ratio of guest/host in the cell. The continuous line represents the least-squares-fit of the data to a single-site binding model. The reduced heat release of the binding process displayed for some calix[4]pyrrole cavitands limits the titrations at lower concentrations.

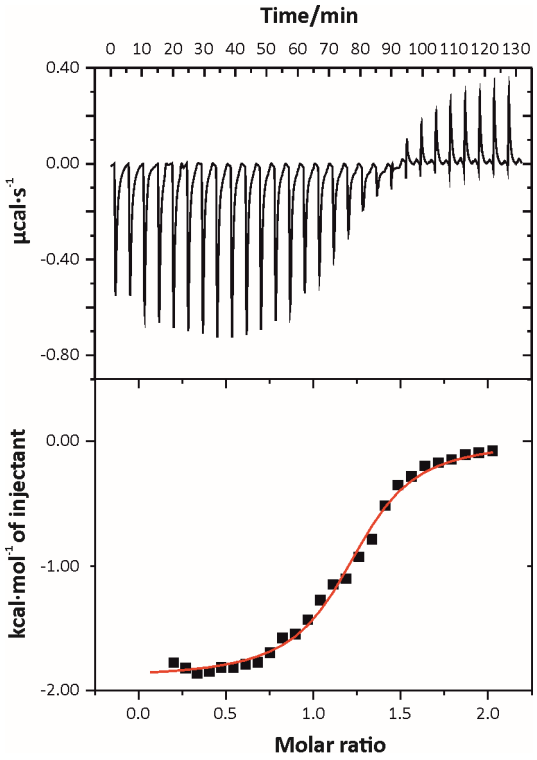

Figure 3.40 On top the raw data for the titration of **HexCr⊂1** in chloroform are shown. The titration was performed at 288 K. The binding isotherm of the calorimetric titration is shown at the bottom. [**1**] = 4.0 mM over [**HexCr**] = 0.42 mM. Derived thermodynamic parameters: K_a = (1.5 ± 0.3) × 10^5 M^{-1}; ΔH = -7.8 ± 0.1 kJ mol^{-1}; TΔS = -19.8 ± 0.1 kJ mol^{-1}.

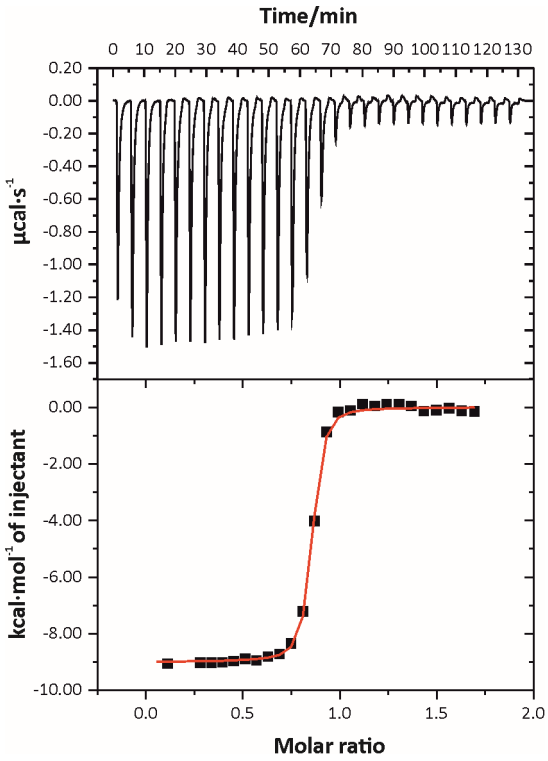

Figure 3.41 On top the raw data for the titration of **4**⊂**1** in chloroform are shown. The titration was performed at 288 K. The binding isotherm of the calorimetric titration is shown at the bottom. [**4**] = 0.69 mM over [**1**] = 0.085 mM. Derived thermodynamic parameters: $K_a > 1 \times 10^7$ M^{-1}; $\Delta H = -38.0 \pm 0.4$ kJ mol^{-1}. Due to the abrupt change in the binding isotherm (saturation curve is defined only by three points) we could not measure accurately neither the binding constant nor the entropic contribution. We can only estimate that the binding constant should be larger than 10^7 M^{-1}.

3.5.8 X-ray structures and molecular modeling

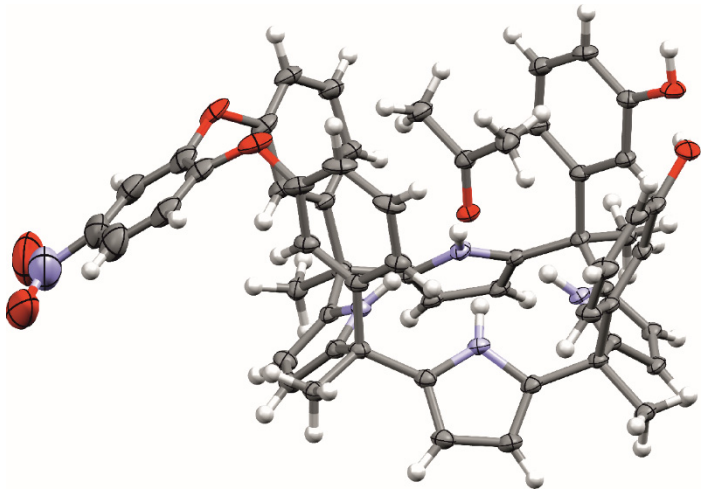

Figure 3.42 a) X-ray structure of **7**, thermal ellipsoids C, N and O atoms set at 50% probability, H atoms are shown as spheres of 0.2 Å.

The X-ray structure of $(CH_3)_2CO\subset_7$ shows the receptor in the cone conformation featuring four hydrogen bonds between the NHs of the receptor and the oxygen atom of the acetone. Additionally, an intramolecular hydrogen bond is observed between the OHs located on the aromatic panel.

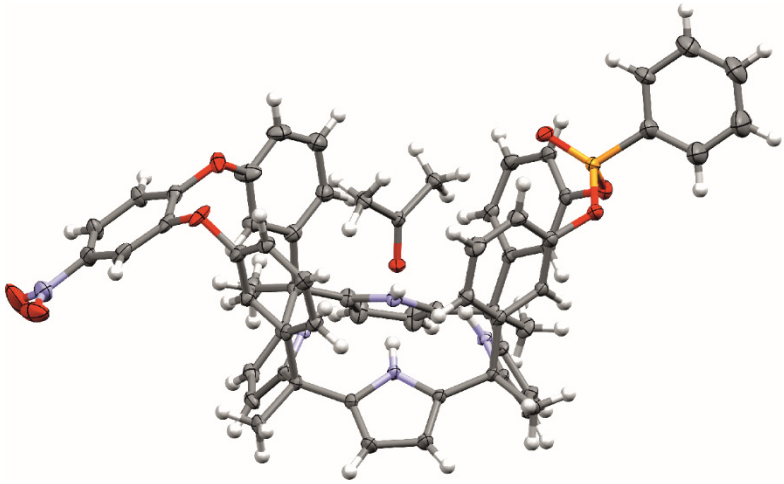

Figure 3.43 a) X-ray structure of **9in**, thermal ellipsoids C, N, O and P atoms set at 50% probability, H atoms are shown as spheres of 0.2 Å.

The X-ray structure of **9in** shows the aryl-extended calix[4]pyrrole core in cone conformation with one molecule of acetone included in the aromatic cavity. The

four pyrrole NHs interact with the acetone guest via hydrogen bonding. The nitro-aryl bridging group adopted a pseudo-equatorial conformation.

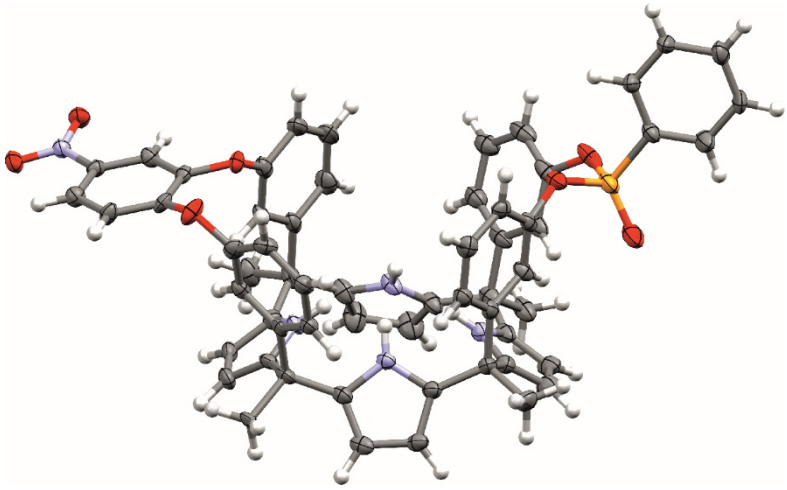

Figure 3.44 a) X-ray structure of **9out**, thermal ellipsoids C, N, O and P atoms set at 50% probability, H atoms are shown as spheres of 0.2 Å.

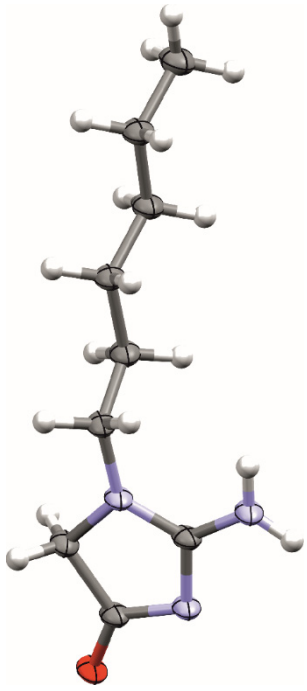

Figure 3.45 a) X-ray structure of **HexCr**, thermal ellipsoids C, N, O and P atoms set at 50% probability, H atoms are shown as spheres of 0.2 Å.

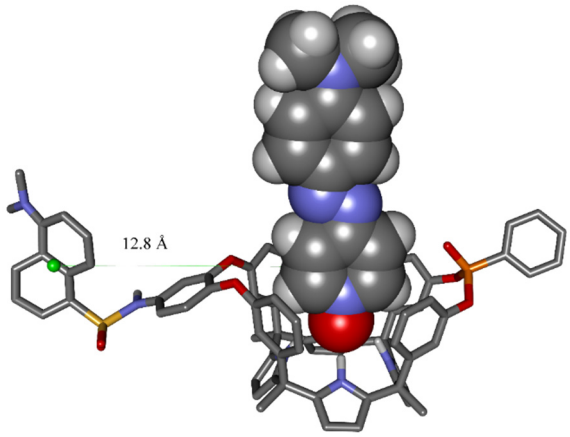

Figure 3.46 Energy-minimized (MM3) structure of the **3**⊂**2** complex. The hydrogen atoms of receptor **2** were removed for the sake of clarity. The encapsulated **3** molecule is shown as CPK model.

3.6 References and notes

[1] Wyss, M.; Kaddurah-Daouk, R. *Physiol. Rev.* **2000**, *80*, 1107-1213.
[2] Cánovas, R.; Cuartero, M.; Crespo, G. A. *Biosens. Bioelectron.* **2019**, *130*, 110-124.
[3] Pal, S.; Lohar, S.; Mukherjee, M.; Chattopadhyay, P.; Dhara, K. *Chem. Commun. (Cambridge, U. K.)* **2016**, *52*, 13706-13709.
[4] Rajamanikandan, R.; Ilanchelian, M. *Anal. Methods.* **2018**, *10*, 3666-3674.
[5] Ellairaja, S.; Shenbagavalli, K.; Vasantha, V. S. *ChemistrySelect* **2017**, *2*, 1025-1031.
[6] Chen, T.; Xie, N.; Viglianti, L.; Zhou, Y.; Tan, H.; Tang, B. Z.; Tang, Y. *Faraday Discuss.* **2017**, *196*, 351-362.
[7] Beckles, D. L.; Maioriello, J.; Santora, V. J.; Bell, T. W.; Chapoteau, E.; Czech, B. P.; Kumar, A. *Tetrahedron* **1995**, *51*, 363-376.
[8] Bell, T. W.; Hext, N. M.; Khasanov, A. B. *Pure Appl. Chem.* **1998**, *70*, 2371-2377.
[9] Bell, T. W.; Firestone, A.; Liu, J.; Ludwig, R.; Rothenberger, S. D. In *Inclusion Phenomena and Molecular Recognition*; Atwood, J. L., Ed.; Springer US: Boston, MA, 1990, p 49-56.
[10] Bühlmann, P.; Badertscher, M.; Simon, W. *Tetrahedron* **1993**, *49*, 595-598.
[11] Bühlmann, P.; Simon, W. *Tetrahedron* **1993**, *49*, 7627-7636.
[12] Bell, T.; Hou, Z.; Luo, Y.; Drew, M.; Chapoteau, E.; Czech, B.; Kumar, A. *Science* **1995**, *269*, 671-674.
[13] Mei, M. H.; Wu, S. K. *Acta Chim. Sin.* **2002**, *60*, 866-869.
[14] Gale, P. A.; Sessler, J. L.; Král, V.; Lynch, V. *J. Am. Chem. Soc.* **1996**, *118*, 5140-5141.
[15] Kim, D. S.; Sessler, J. L. *Chem. Soc. Rev.* **2015**, *44*, 532-546.
[16] Samanta, R.; Kumar, B. S.; Panda, P. K. *Org. Lett.* **2015**, *17*, 4140-4143.
[17] Saha, I.; Lee, J. H.; Hwang, H.; Kim, T. S.; Lee, C.-H. *Chem. Commun. (Cambridge, U. K.)* **2015**, *51*, 5679-5682.
[18] Taner, B.; Kursunlu, A. N.; Güler, E. *Spectrochim. Acta, Part A* **2014**, *118*, 903-907.

[19] Kim, S. K.; Lee, H. G.; Vargas-Zúñiga, G. I.; Oh, J. H.; Lynch, V. M.; Lee, M. H.; Sessler, J. L. *Supramol. Chem.* **2017**, *29*, 651-657.
[20] Ghorpade, T. K.; Patri, M.; Mishra, S. P. *Sens. Actuators, B* **2016**, *225*, 428-435.
[21] Anzenbacher, P.; Jursíková, K.; Sessler, J. L. *J. Am. Chem. Soc.* **2000**, *122*, 9350-9351.
[22] Kataev, E. A.; Backmann, N.; Shumilova, T. A.; Rüffer, T.; Lang, H. *Supramol. Chem.* **2016**, *28*, 53-61.
[23] Sokkalingam, P.; Yoo, J.; Hwang, H.; Lee, P. H.; Jung, Y. M.; Lee, C.-H. *Eur. J. Org. Chem.* **2011**, *2011*, 2911-2915.
[24] Sokkalingam, P.; Kim, D. S.; Hwang, H.; Sessler, J. L.; Lee, C.-H. *Chem. Sci.* **2012**, *3*, 1819-1824.
[25] Mulugeta, E.; He, Q.; Sareen, D.; Hong, S.-J.; Oh, J. H.; Lynch, V. M.; Sessler, J. L.; Kim, S. K.; Lee, C.-H. *Chem* **2017**, *3*, 1008-1020.
[26] Bhatt, K. D.; Shah, H. D.; Panchal, M. *Luminescence* **2017**, *32*, 1398-1404.
[27] Yoo, J.; Jeoung, E.; Lee, C.-H. *Supramol. Chem.* **2009**, *21*, 164-172.
[28] Bell, T. W.; Hext, N. M. *Chem. Soc. Rev.* **2004**, *33*, 589-598.
[29] Guinovart, T.; Hernández-Alonso, D.; Adriaenssens, L.; Blondeau, P.; Martínez-Belmonte, M.; Rius, F. X.; Andrade, F. J.; Ballester, P. *Angew. Chem., Int. Ed.* **2016**, *55*, 2435-2440.
[30] Nguyen, B. T.; Anslyn, E. V. *Coord. Chem. Rev.* **2006**, *250*, 3118-3127.
[31] Nguyen, B. T.; Wiskur, S. L.; Anslyn, E. V. *Org. Lett.* **2004**, *6*, 2499-2501.
[32] Escobar, L.; Aragay, G.; Ballester, P. *Chem.--Eur. J.* **2016**, *22*, 13682-13689.
[33] Ciardi, M.; Tancini, F.; Gil-Ramírez, G.; Escudero Adán, E. C.; Massera, C.; Dalcanale, E.; Ballester, P. *J. Am. Chem. Soc.* **2012**, *134*, 13121-13132.
[34] Lledó, A.; Rebek Jr, J. *Chem. Commun. (Cambridge, U. K.)* **2010**, *46*, 1637.
[35] Galán, A.; Escudero-Adán, E. C.; Frontera, A.; Ballester, P. *J. Org. Chem.* **2014**, *79*, 5545-5557.
[36] Koh, K. N.; Araki, K.; Ikeda, A.; Otsuka, H.; Shinkai, S. *J. Am. Chem. Soc.* **1996**, *118*, 755-758.
[37] Hewlins, M. J. E.; Salter, R. *Synthesis* **2007**, *2007*, 2164-2174.
[38] Han, F. S.; Higuchi, M.; Kurth, D. G. *Org. Lett.* **2007**, *9*, 559-562.
[39] Pentimalli, L. *Tetrahedron* **1960**, *9*, 194-201.
[40] Faessinger, R. W.; Brown, E. V. *Trans. Ky. Acad. Sci.* **1963**, *24*, 106-110.
[41] Kumar, V.; Rana, H.; Kaushik, M. P. *Tetrahedron Lett.* **2012**, *53*, 6423-6425.
[42] Becke, A. D. *Phys. Rev. A* **1988**, *38*, 3098-3100.
[43] Perdew, J. P. *Physical Review B* **1986**, *33*, 8822-8824.
[44] Grimme, S.; Antony, J.; Ehrlich, S.; Krieg, H. *J. Chem. Phys.* **2010**, *132*, 154104.
[45] Sure, R.; Brandenburg, J. G.; Grimme, S. *ChemistryOpen* **2016**, *5*, 94-109.
[46] Weigend, F.; Ahlrichs, R. *Phys. Chem. Chem. Phys.* **2005**, *7*, 3297.
[47] Frisch, M. J.; Trucks, G. W.; Schlegel, H. B.; Scuseria, G. E.; Robb, M. A.; Cheeseman, J. R.; Scalmani, G.; Barone, V.; Petersson, G. A.; Nakatsuji, H.; Li, X.; Caricato, M.; Marenich, A. V.; Bloino, J.; Janesko, B. G.; Gomperts, R.; Mennucci, B.; Hratchian, H. P.; Ortiz, J. V.; Izmaylov, A. F.; Sonnenberg, J. L.; Williams; Ding, F.; Lipparini, F.; Egidi, F.; Goings, J.; Peng, B.; Petrone, A.; Henderson, T.; Ranasinghe, D.; Zakrzewski, V. G.; Gao, J.; Rega, N.; Zheng, G.; Liang, W.; Hada, M.; Ehara, M.; Toyota, K.; Fukuda, R.; Hasegawa, J.; Ishida, M.; Nakajima, T.; Honda, Y.; Kitao, O.; Nakai, H.; Vreven, T.; Throssell, K.; Montgomery Jr., J. A.; Peralta, J.

E.; Ogliaro, F.; Bearpark, M. J.; Heyd, J. J.; Brothers, E. N.; Kudin, K. N.; Staroverov, V. N.; Keith, T. A.; Kobayashi, R.; Normand, J.; Raghavachari, K.; Rendell, A. P.; Burant, J. C.; Iyengar, S. S.; Tomasi, J.; Cossi, M.; Millam, J. M.; Klene, M.; Adamo, C.; Cammi, R.; Ochterski, J. W.; Martin, R. L.; Morokuma, K.; Farkas, O.; Foresman, J. B.; Fox, D. J. Wallingford, CT, 2016.

[48] Aksel, T.; Majumdar, A.; Barrick, D. *Structure* **2011**, *19*, 349-360.

[49] Marras, S. A. E.; Kramer, F. R.; Tyagi, S. *Nucleic Acids Res.* **2002**, *30*, e122-e122.

[50] Aggarwal, M.; Sharma, R.; Kumar, P.; Parida, M.; Tomar, S. *Sci. Rep.* **2015**, *5*, 14753.

[51] The release of 0.5 equiv of **HexCr** from the **HexCr⊂2** complex to the bulk solution induced by adding 0.5 equiv of **3** was evidenced by ^{1}H NMR spectroscopy (Figure 3.*37*). The reverse experiment is not feasible to be performed at mM concentration owing to the reduced solubility of **HexCr** in chloroform solution (∼1.5 mM).

[52] The release of 0.5 equiv of **HexCr** from the **HexCr⊂1** complex to the bulk solution induced by adding 0.5 equiv of **4** was evidenced by ^{1}H NMR spectroscopy (Figure 3.*39*). The reverse experiment is not feasible to be performed at mM concentration owing to the reduced solubility of **HexCr** in chloroform solution (∼ 1.5 mM).

UNIVERSITAT ROVIRA I VIRGILI
CALIX[4]PYRROLE CAVITANDS FOR SUPRAMOLECULAR SENSING AND CATALYSIS
Andrés Felipe Sierra Ramos

Chapter 4

Supramolecular fluorescence sensing of L-proline and L-pipecolic acid.

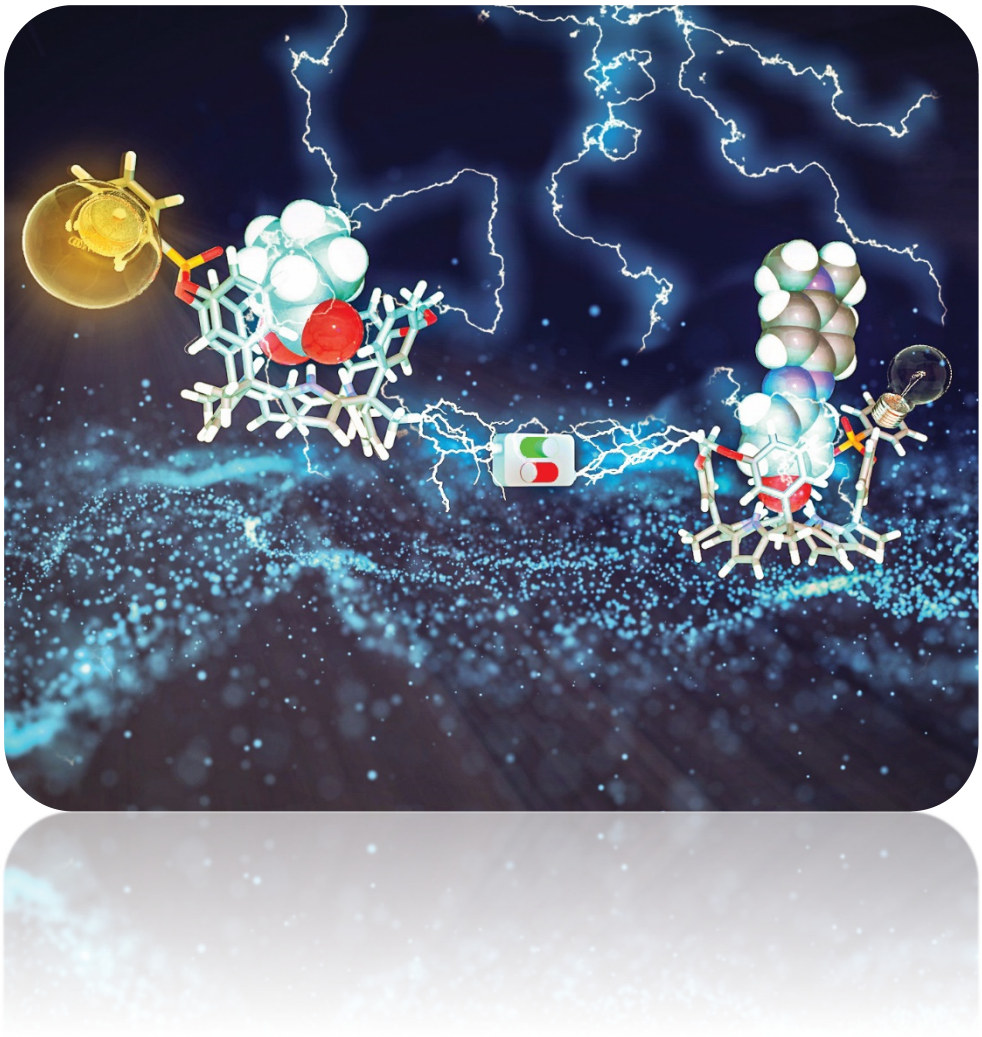

Part of this chapter has been published in:

Sierra, A. F.; Aragay, G.; Peñuelas-Haro, G.; Ballester, P. *Organic Chemistry Frontiers* **2021**, *8*, 2402-2412.

UNIVERSITAT ROVIRA I VIRGILI
CALIX[4]PYRROLE CAVITANDS FOR SUPRAMOLECULAR SENSING AND CATALYSIS
Andrés Felipe Sierra Ramos

4.1 Introduction.

There is an increasing demand in monitoring small polar molecules, which are relevant for disease diagnosis and training status, using portable and even wearable sensing devices.[1] Ideally, the developed sensing devices should be designed for direct manipulation by end-users. This characteristic avoids the intervention of trained medical personnel and the commute to point-of-care facilities or hospitals. Moreover, the devices might transmit the results wirelessly to apps installed in mobile phones and share them with the electronic patient's record or the clinician.[2] Biological and synthetic receptors are fundamental components of many small molecule sensing devices related to human health.[3,4] The principle at work is supramolecular sensing, which relies on transduction mechanisms exclusively activated by molecular recognition events.[5,6] This approach offers significant benefits for the design of synthetic selective molecular sensors, as well as for limiting the interferences caused by non-specific binding. Specific binding, *a.k.a* molecular recognition, builds on shape, size and function complementarity between receptor and analyte. In many cases, the transduction mechanism of the binding event demands the covalent incorporation of reporter units to the receptor's scaffolds i.e. the fluorescence, absorbance or redox properties of the receptor itself are not suitable for transduction in practical applications. As we mentioned in the chapter 1, the constructs resulting from the covalent connection of a synthetic receptor to a reporter unit are referred as molecular sensors. Molecular sensors are also key in the design of selective sensor nanomaterials able to discriminate analytes by molecular structure (specific binding) rather than by physical/chemical properties i.e. polarity (nonspecific binding).

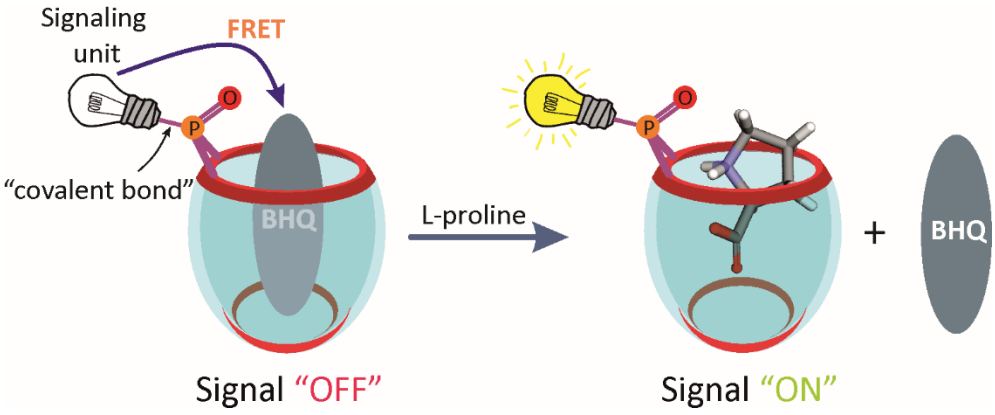

Scheme 4.1 Cartoon representation of the IDA-based sensor for L-proline sensing.

In Chapter 2, we showed that the monophosphonate calix[4]pyrrole cavitand **5in** (Figure 4.*1*) provided a three-dimensional polar aromatic cavity suitable for including creatinine and surrounding most of its surface.[7] The receptor's aromatic cavity is functionalized with an inwardly directed phosphonate group at its open upper rim and by four pyrrole NHs at the opposed and closed end. These polar groups offer complementary hydrogen bonding donor and acceptor interactions to those of the included guest. The contribution of the phosphonate group in the creatinine recognition was quantified by ITC experiments to be around 2.0 kcal·mol^{-1} (see Chapter 2). We used the mono-phosphonate calix[4]pyrrole cavitand scaffold for the construction of ion selective electrodes, molecular sensors and indicator displacement assays for creatinine sensing and quantification (see Chapter 3).[8,9] More recently, we demonstrated that the mono-phosphonate calix[4]pyrrole cavitand was also an effective synthetic carrier facilitating the selective diffusion of L-proline across membranes of liposomes and living cells.[10] L-Proline is also included in the aromatic cavity of the mono-phosphonate receptors establishing multiple charged hydrogen-bonds (carboxylate-pyrrole NHs, ammonium-phosphonate) and CH–π interactions.

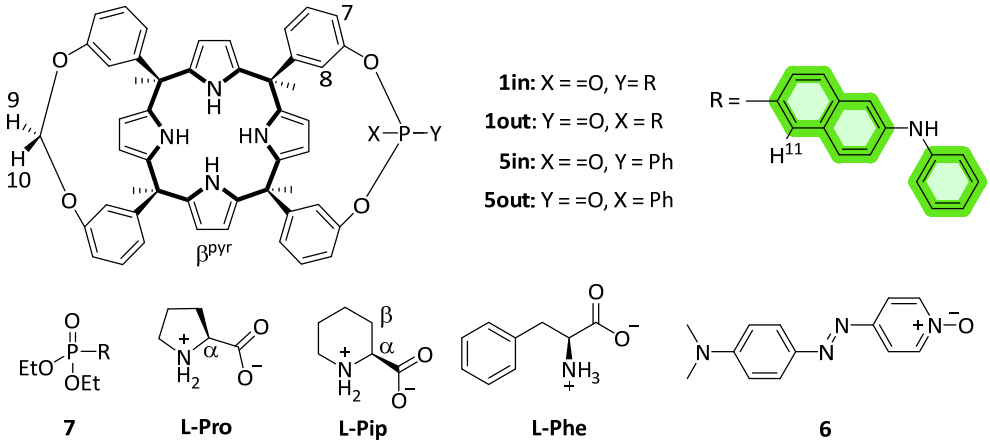

Figure 4.1 Line drawing molecular structures of the monophosphonate calix[4]pyrrole cavitands **1in**/**1out** and **5in**/**5out**, the pyridine *N*-oxide quencher **6**, diethyl 6-(phenylamino)naphthalene-2-phosphonate **7** and the substrates used in the work (L-**Pro**, L -**Pip** and L-**Phe**). Proton assignment of calix[4]pyrrole cavitands and amino acids is shown in the structure.

Herein, we describe the synthesis of two novel fluorescent molecular sensors based on a mono-phosphonate calix[4]pyrrole cavitand scaffold. The introduced approach hinges on the covalent attachment of the fluorescent signaling unit directly to the phosphonate bridging group (**Scheme 4.*1***).

The design is inspired by the work of Dalcanale and co-workers with monophosphonate fluorescent cavitands based on resorcin[4]arene scaffolds.[11] We also report the binding properties of monophosphonate calix[4]pyrrole cavitands and their fluorescent derivatives with a reduced series of amino acids: L-proline (L-**Pro**), L-pipecolic acid (L-**Pip**) and L-phenylalanine (L-**Phe**). Using a direct binding-based sensing (BBS) approach, we determined that the binding constant of the fluorescent **1in** isomer for L-Pro was one order of magnitude larger than that of L-Pip. Surprisingly to us, the direct BBS experiments of L-Pro and L-Pip with the **1out** isomer produced larger changes in emission intensity in comparison to those of the **1in** counterpart. Nevertheless, the binding constant values determined for the 1:1 inclusion complexes of **1out** and the amino acids were one order of magnitude smaller than those of the **1in** isomer. Due to the small changes observed with the direct BBS approach, we considered that an improved fluorescent sensing of the amino acids required the development of indicator displacement assays (IDA).[12] To this end, we used the pyridine-*N*-oxide **6** as analogue of the well-known DABCYL ((4-dimethylaminoazo) benzene-4-carboxylic acid) black-hole quencher (Figure 4.*1*). Pyridine *N*-oxide **6** formed thermodynamically and kinetically highly stable 1:1 non-emissive complexes with **1in** and **1out**. The displacement of **6** from the 1:1 complexes produced fluorescence "turn-on". The BBS and IDA experiments produced analogous binding constant values for all complexes. They assigned a superior stability to the L-**Pro⊂1in** complex compared to L-**Pip⊂1in** and L-**Phe⊂1in** analogues, and the **1out** counterparts.

4.2 Results and discussion.

4.2.1 Synthesis

The fluorescent phosphonate calix[4]pyrrole cavitands **1in** and **1out** were prepared in two synthetic steps starting from the known α,α,α,α-isomer of tetra-meta hydroxyphenyl-tetra-methyl-calix[4]pyrrole **2** (Scheme 4.*2*).[13] Firstly, the mono-methylene bridged calix[4]pyrrole **3** was obtained by reacting α,α,α,α-**2** tetrol with 1.2 equiv. of bromochloromethane in DMSO solution in the presence of potassium carbonate as base. The mono-methylene bridged compound **3** was isolated in 48% yield after column chromatography purification of the reaction crude and crystallization of the isolated fraction in acetonitrile.

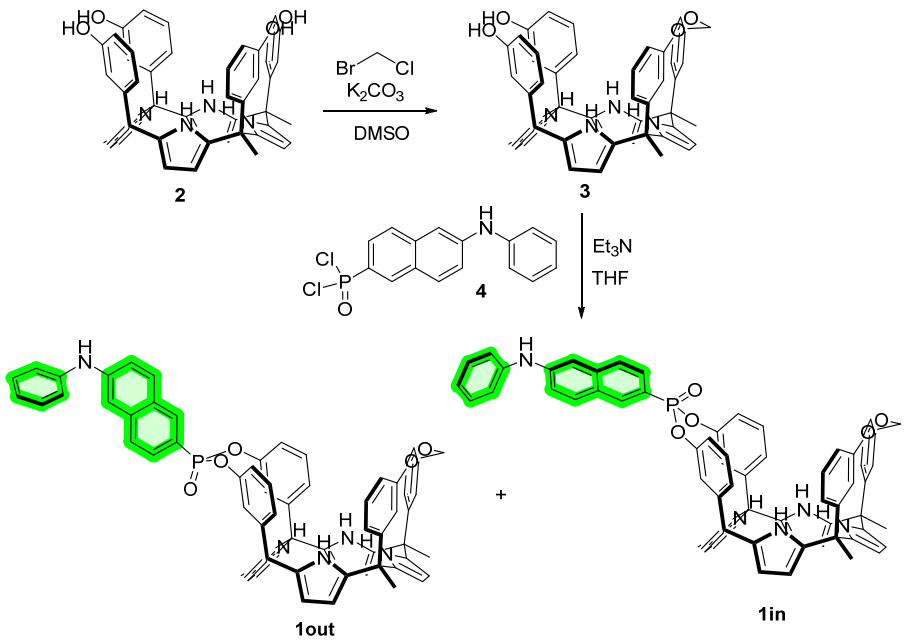

Scheme 4.2 Synthetic scheme for the preparation of the isomeric mono-phosphonate mono-methylene fluorescent calix[4]pyrrole cavitands **1in** and **1out.**

Secondly, the incorporation of the fluorescent unit at the upper rim of **3** involved the room temperature reaction with freshly prepared 6-(phenylamino)-naphthalen-2-yl phosphonic acid dichloride **4**,[11] in THF solution during 2h and using tri-ethylamine as base. The reaction produced a mixture of the two mono-phosphonate diastereoisomers **1in** and **1out**. The two pure stereoisomers were isolated by separation of an enriched fraction of the reaction crude (see experimental section for details) by means of analytical HPLC (Waters Spherisorb®, 5.0µm Silica,4.6 mm × 250 mm) using isocratic elution (DCM:AcOEt 90:10).

The **1out** isomer eluted first. The **1in** isomer, presenting the P=O group inwardly oriented with respect to its aromatic cavity, was more polar and eluted second. This latter arrangement of functional groups should allow that suitable bound guests can establish simultaneous hydrogen-bonding intermolecular interactions with both the P=O group and the NHs of the calix[4]pyrrole core of the fluorescent receptor. The isolated **1out** isomer will be used as a control to validate this hypothesis.

The configurational assignment of the two diastereoisomeric cavitands, **1in** and **1out**, was achieved by a combination of ^{1}H, ^{31}P NMR spectroscopy and X-ray crystallographic analysis. Single crystals of **1in** grew from a deuterated acetone

solution used to acquire its NMR spectra. On the other hand, we used acetonitrile to obtain single crystals of **1out**. The solid-state structures of the two fluorescent calix[4]pyrrole isomers are depicted in Figure 4.*2*.

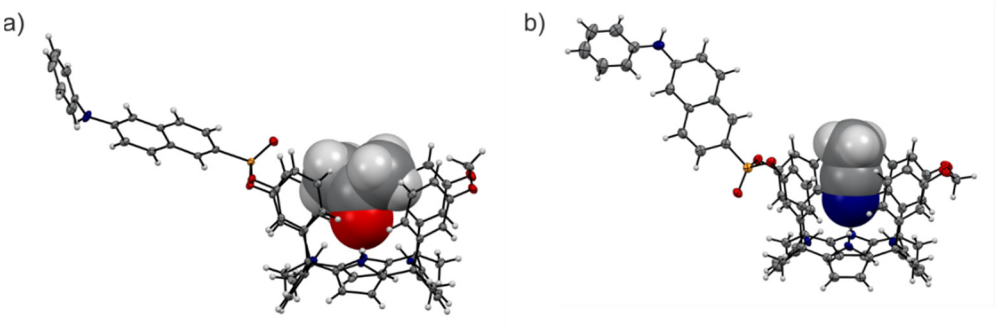

Figure 4.2 X-ray structure of the a) (**$CH_3)_2CO$⊂1in** inclusion complex and b) **CH_3CN⊂1out**. Thermal ellipsoids for C, N, O, and P atoms set at 50% probability; H atoms are shown as spheres of 0.15 Å diameter.

In both of them, the calix[4] pyrrole core adopts the cone conformation and one molecule of the solvent, used to grow the crystals, is included in its polar aromatic cavity. The included solvent forms four simultaneous hydrogen-bonding interactions between its heteroatom (oxygen or nitrogen) and the pyrrole NHs. In the solid state and for the two isomers, the 14-membered rings delineated by the bridged phosphonate-group, two *meso*phenyl groups, their corresponding *meso*-carbons and one pyrrole ring, present a conformation locating the phenyl-amino-naphthyl substituent of the phosphorous atom in equatorial orientation and pointing away from the aromatic cavity.

The outwardly oriented fluorescent unit, which is observed in both solid-state structures of the calix[4]pyrrole diastereo-isomers, is in striking contrast to the observation made in structurally related isomers of mono-phosphonate resorcin[4]arene cavitands.[11] In the latter case, the ^{1}H NMR spectrum of the *out* isomer showed the protons assigned to the phenyl-amino-naphthyl substituent upfield shifted compared to those of the *in* counterpart. This difference was attributed to dissimilar orientations of the substituent with respect to the receptor's aromatic cavity. In short, the resorcin[4]arene out isomer directs the fluorescent substituent towards the receptor's cavity experiencing the shielding effect exerted by the aromatic rings.

We did not observe significant chemical shift changes for the signals of the hydrogen atoms of the fluorescent substituent when comparing the ^{1}H NMR spectra of the **1in** and **1out** isomers in acetone-d_6 or dichloromethane-d_2 solutions (Figure 4.*3*).

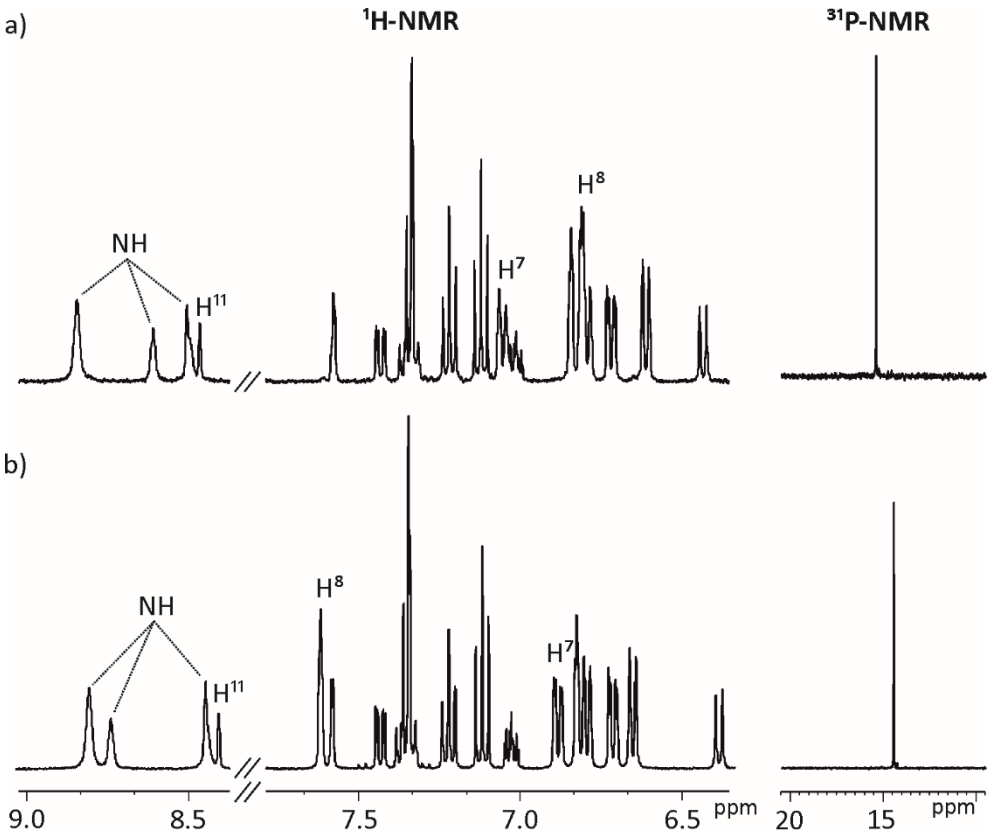

Figure 4.3 Selected regions of the ^{1}H (400 MHz, 298 K) and ^{31}P (161 MHz, 298 K) NMR spectra of a) **1in** and b) **1out** isomers in acetone-d_6 solution. The pyrrole NH, β^{pyr}, $H^{11}$and the two proton signals of the meso-aryl groups, H^8 and H^7, that are ortho with respect to the phosphonate bridging groups are indicated. See Figure 4.1 for proton assignment.

This finding indicated that in agreement with the solid-state structures, in solution, the two isomers of **1** also featured the fluorescent substituent outwardly directed with respect to their aromatic cavities. However, the signals for H^8 and H^7 (Figure 4.*1*), corresponding to the *meso*-aryl hydrogen atoms that are ortho with respect to the bridging phosphonate group, showed very different chemical shift values in the two isomers. For example, in the **1out** isomer H^8 resonates significantly down-field shifted compared to the chemical shift value for the analogous proton signal in the **1in** counterpart (Figure 4.*3*). This chemical shift difference is due to the positioning of H^8 in the deshielding zone of the magnetic anisotropy cone generated by the *out*

P=O group. For the same token, proton H^7 becomes partially deshielded when the P=O group is inwardly directed.

The chemical shift values of the phosphorous atoms of the **1in** and **1out** isomers are in agreement with those observed for structurally related mono- and bis-phosphonate calix[4]pyrrole cavitands (Figure 4.*23* and Figure 4.*31*).[7,13,] The phosphorous atom of the *out* isomer resonates slightly upfield, possibly due to the shielding effect exerted by the aromatic cavity. In acetone-d_6 solution, both isomers showed three highly downfield shifted signals for the pyrrole NHs. This is due to the involvement of the NHs in hydrogen bonding interactions with the oxygen atom of one included acetone molecule. The bound acetone molecule locks the cavitands in their cone conformation as observed for **1in** in the solid-state (Figure 4.*2*a). The ^{1}H NMR spectra of the two isomers in chlorinated solvents (see below) are significantly different to those registered in acetone. Most likely, in dichloromethane-d_2 solution the receptors adopted alternate conformations of their calix[4]pyrrole core and are involved in conformation exchange processes that are fast on the chemical shift timescale.

4.2.2 NMR binding studies

We became interested in investigating the binding properties of these type of cavitands as receptors for L-**Pro** and the 6-membered ring α-amino acid analogue, L-pipecolic acid (L-**Pip**). L-**Pip** has been described as a diagnostic marker of pyridoxine-dependent epilepsy.[14]

We first performed separate solid–liquid extraction experiments with L-**Pro** or L-**Pip** and the fluorescent cavitand **1in** in CD_2Cl_2. We added an excess of the solid amino acid (~2mg L-**Pro** or L-**Pip**) to a 2 mM CD_2Cl_2 solution of the cavitand **1in**.We hand-shook the suspensions for several minutes and filtered off the remaining solid. The ^{1}H NMR spectra of the filtered solutions showed significant differences compared to that of the free cavitand **1in** in the same solvent (Figure 4.*4*). In both cases, only a single set of sharp signals was observed for the hydrogen atoms of the receptor.

The signals corresponding to the pyrrole NHs were the ones experiencing the most important chemical shift changes. These signals moved downfield compared to those in free **1in** (Δδ = 1.8–1.5 and 2.3–1.1 ppm, for L-**Pro** and L-**Pip**, respectively), suggesting their involvement in hydrogen bonding interactions with the corresponding included guest. On the other hand, we observed the appearance of a new set of signals in the upfield region of the spectra. These signals were indicative

of the inclusion of the guests in the polar aromatic cavity of **1in**. Specifically for L-**Pro** extraction, we observed a broad signal centered at δ= 2.7 ppm. We attributed this signal to the proton α to the carboxylate group of the bound L-**Pro**. This signal appeared upfield shifted compared to that of the free guest in $(CD_3)_2SO$ solution (Δδ = −1.2 ppm). Thus, the proton atoms of the included L-**Pro** experienced the shielding effect exerted by the four *meso*-phenyl substituents of **1in**. Analogously, the signals of bound L-**Pip** also appeared upfield shifted compared to those in the free guest in $(CD_3)_2SO$ solution. The integral values of selected proton signals for the host and the guest indicated the quantitative formation of 1:1 complexes: L-**Pro⊂1in** and L-**Pip⊂1in**. That is, receptor **1in** extracted 1 equiv. of L-**Pro** and L-**Pip** in the independent solid–liquid extractions experiments.

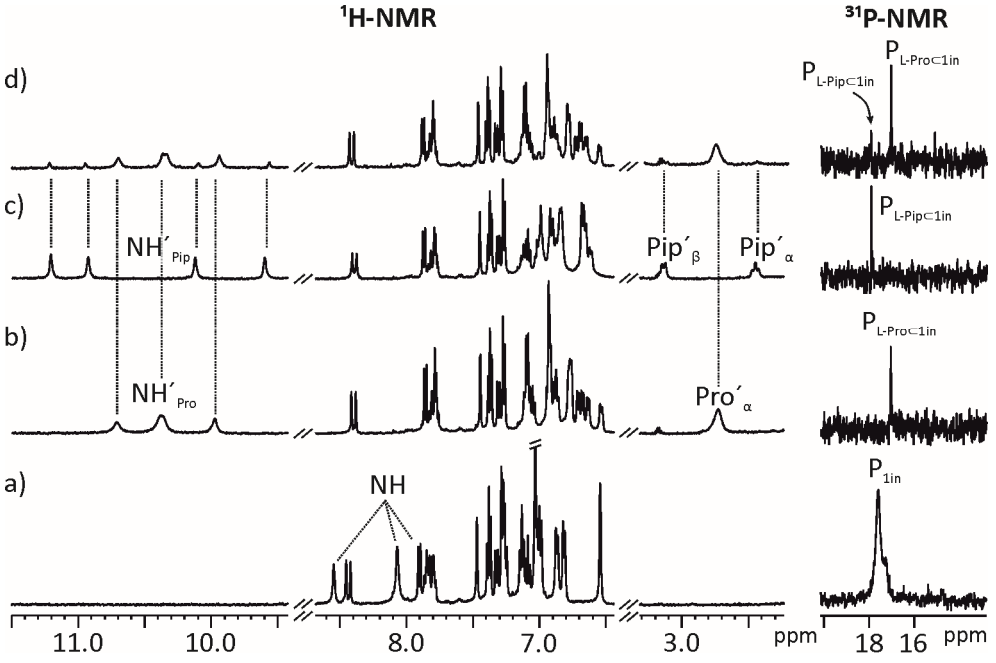

Figure 4.4 ^{1}H NMR (400 MHz, 298 K) and ^{31}P (161 MHz, 298 K) NMR spectra of a 2 mM CD_2Cl_2 solution of **1in** a) before and after (b–d) solid–liquid extraction with solid b) L-**Pro** and solid c) L-**Pip** (c) and d) with equal amounts of solid L-**Pro** and L-**Pip**.

The binding of the guest was also supported by the chemical shift changes observed in the ^{31}P NMR spectra of the filtered solutions. The ^{31}P NMR spectrum of free **1in** shows a singlet resonating at δ= 17.3 ppm. Remarkably, after the extraction experiments of L-**Pro** and L-**Pip**, the phosphorous signal of bound **1in** resonated at δ= 17.0 ppm and 17.9 ppm, respectively (*Figure 4.4* right).

Next, we performed a competitive solid–liquid extraction experiment by adding equimolar amounts of solid L-**Pro** and L-**Pip** (~2 mg of each guest) to a millimolar CD_2Cl_2 solution of the fluorescent receptor **1in**. The ^1H NMR spectra of the filtered solution clearly showed two sets of proton signals for the NHs of bound **1in**. Moreover, the integral values of the two sets of NH signals were significantly different (Figure 4.*4*d). By comparison to the ^1H NMR spectra of the solid–liquid extraction experiments performed separately, we easily assigned the two sets of signals to the protons of the bound receptor in the L-**Pro⊂1in** and L-**Pip⊂1in** complexes (*Figure 4.4*b and c). Integration of the pyrrole NH signals for the two complexes assigned a 5:1 molar ratio to the mixture of L-**Pro⊂1in** and L-**Pip⊂1in** complexes.[15] Considering that the solubility of L-**Pro** is slightly higher than that of L-**Pip**, the result of the competitive extraction experiment is not conclusive in assigning a larger binding affinity of **1in** for L-**Pro** compared to L-**Pip**.[16] Nevertheless, it provides an initial hint in this direction.

We were also interested in evaluating the importance of the hydrogen bonding interaction established between the inwardly directed P=O group of cavitand **1in** and the protonated amino group of the bound amino acid guests. With this aim, we performed analogous solid–liquid extraction experiments of L-**Pro** with non-fluorescent cavitands **5in** and **5out**. We used the non-fluorescent receptors as model compounds of the fluorescent counterparts due to their ease of synthesis (Figure 4.*1*). We hypothesized that **5out** could bind and extract L-**Pro** through the formation of four hydrogen bonds with the pyrrole NHs and additional CH–π interactions. In contrast, the outwardly directed P=O group of **5out** should not participate in hydrogen bonding interactions with the protonated amino group of bound L-**Pro**. Thus, we expected a decrease in the binding constant of the L-**Pro⊂5out** complex compared to that of the **5in** isomer.

The solid–liquid extraction experiments of L-**Pro** using the non-fluorescent model receptor **5in** produced similar changes in the ^1H and ^{31}P NMR spectra to those described above for the fluorescent cavitand **1in** (Figure 4.*4*). To our surprise, the ^1H NMR spectrum of the filtered solution obtained after extraction of L-**Pro** with **5out** showed broad proton signals. The corresponding ^{31}P NMR spectrum did not produce any observable signal. We detected a significant increase in the signal-to-noise ratio of the spectra. We considered this observation as indicative of a diminution of the concentration of **5out** in solution after the extraction experiment. To clarify this issue, we evaporated the CD_2Cl_2 and re-dissolved the solid residue in $(CD_3)_2SO$. The obtained $(CD_3)_2SO$ solution was analysed using ^1H NMR spectroscopy. We observed

the diagnostic signals of the protons of free **5out** and free L-**Pro**. The L-**Pro** signals displayed a significantly reduced intensity. This result suggested that **5out** was not able to extract 1 equiv. of L-**Pro**. To investigate the insolubility of the putatively formed L-**Pro⊂5out** complex in CD_2Cl_2, we acquired a ^1H NMR spectrum of the filtered solid by dissolving it in $(CD_3)_2SO$. The ^1H NMR spectrum of the solution displayed the diagnostic signals of free **5out** and free L-**Pro**. The observation of the signals of free **5out** indicates that the L-**Pro⊂5out** complex features a reduced solubility in CD_2Cl_2, falling out of solution during the solid–liquid experiment and hampering its use for quantitative purposes.

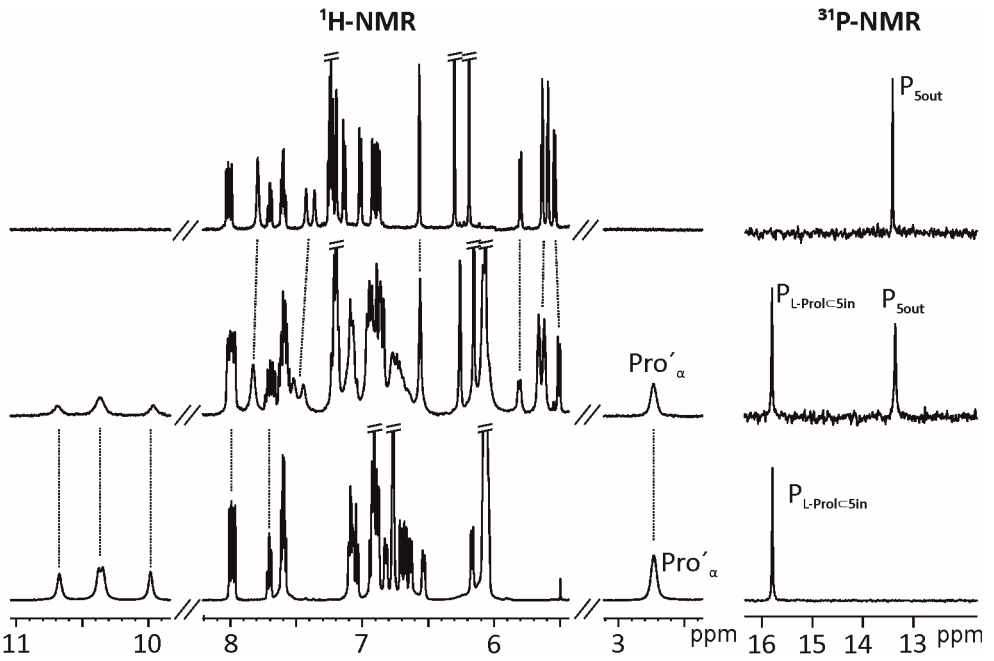

Figure 4.5 ^1H NMR (400 MHz, 298 K) and ^{31}P (161 MHz, 298 K) NMR spectra of a CD_2Cl_2 solution of L-**Pro⊂5in** complex a) before and b) after the addition of 1 equiv. of **5out**; c) ^1H and ^{31}P NMR of a CD_2Cl_2 solution of **5out**.

For this reason, we decided to perform a competitive binding experiment starting from a millimolar CD_2Cl_2 solution of the L-**Pro⊂5in** complex. The addition of 1 equiv. of the **5out** isomer to the above solution did not induce significant changes to the proton signals of the L-**Pro⊂5in** complex (*Figure 4.5*b). We detected the appearance of a new set of proton signals that almost coincided with those of the free **5out** receptor. The broadening and small chemical shift changes observed for the new set of signals (*Figure 4.5*b) suggested the existence of a binding equilibrium in solution. In short, we propose that the L-**Pro⊂5out** complex is formed in solution to a reduced

extent and the binding equilibrium between free and bound **5out** shows fast/intermediate exchange dynamics on the chemical shift timescale. The ^{31}P NMR spectrum of the mixture also supports this hypothesis. It displayed two singlets centered at δ= 15.8 and 13.4 ppm. The one appearing downfield is quite sharp and corresponds to the L-**Pro⊂5in** complex.

In contrast, the upfield-shifted singlet is slightly broadened due to the chemical exchange between free and bound **5out**. The lack of separate signals for the phosphorous atoms of free **5in** results from its low concentration in solution (*Figure 4.5*b, right). Taken together, these results indicate that the binding affinity of **5in** for L-**Pro** is significantly larger (approximately 7–10-fold, see below) than that of the **5out** isomer. In close analogy to the results obtained in chapter 2 for creatinine, we attributed the increased binding affinity to the additional hydrogen bond interaction provided by the inwardly directed P=O group in the L-**Pro⊂5in** complex.

4.2.3 UV/vis and emission spectroscopy binding studies.

Direct binding-based sensing (BBS).

After having demonstrated the important contribution of the inwardly directed P=O group for the binding of L-**Pro** with the **5in** model cavitand, we carried out direct binding-based sensing (BBS) studies with the analogous fluorescent **1in** cavitand. Some years ago, Dalcanale and co-workers reported the use of somewhat structurally related fluorescent resorcin[4]arene receptors for the optical sensing of alkyl-chain C_1–C_4 alcohols.[11] The authors claimed that the hydrogen bonding interaction established between the alcohol OH function and the P=O group of the receptor could decrease the electronic density on the phosphorus atom and modify the energy of the excited state of the naphthalene unit directly attached to it. The electronic modification was expected to alter the maximum of the emission band.

The UV/vis absorption spectra of **1in** and **1out** showed very similar features (Figure 4.*6*). Concretely, two intense absorption bands with maxima at 275 (ε = 34 000 M^{-1} cm^{-1}) and 328 nm (ε = 24 000 M^{-1} cm^{-1}) and a shoulder at 370 nm. These bands are characteristic of π–π* and n–π*-transitions of the phenylamino-naphthyl moiety, as demonstrated by simple comparison with the UV/vis spectrum of diethyl 6-(phenylamino) naphthalene-2-phosphonate **7** (Figure 4.*1*) used as model compound (Figure 4.32).

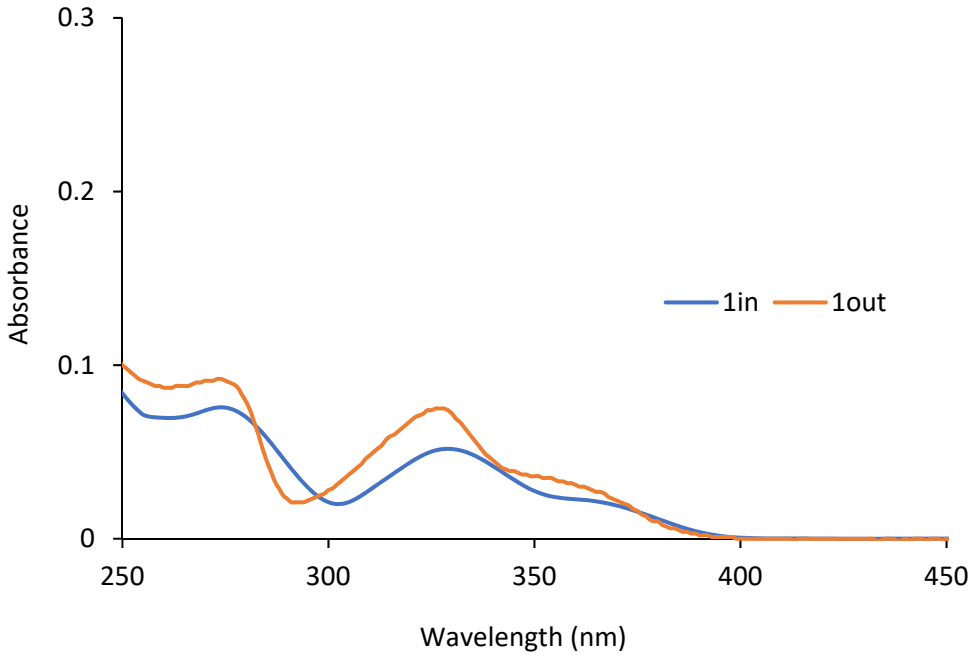

Figure 4.6 UV/vis spectra of a 2.5 μM solution of **1in** (blue line) and **1out** (orange line) in DCM.

The incremental addition of L-**Pro** to separate micromolar dichloromethane solutions of **1in** and **1out** did not produce changes in their corresponding UV/vis spectra (Figure 4.*34*). Spectral changes were more evident using emission spectroscopy to monitor the titration experiment. The excitation at 335 nm of a 5×10^{-7} M dichloromethane solution of **1in** resulted in an intense and broad emission band with a maximum at 422 nm. The incremental addition of L-**Pro** provoked a concomitant red-shift of the maximum ($\Delta\lambda_{max}$ = 3–4 nm) and a decrease in emission intensity (Figure 4.*7*). Similar changes were observed during the incremental addition of L-**Pip** to **1in** using analogous experimental conditions (Figure 4.*36*).

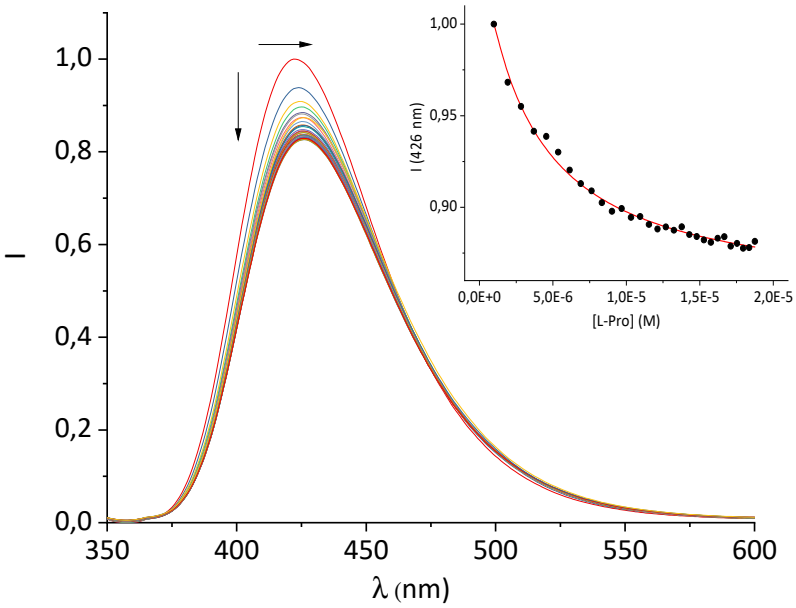

Figure 4.7 Normalized emission spectra of **1in** (0.5 μM) registered during the addition of incremental amounts of L-**Pro** (up to 30) in dichloromethane solution: λ_{exc} = 335 nm. Inset: Plot of the emission change at 426 nm (black circles) vs. concentration of L-**Pro**. The red line corresponds to the fit of the titration data to a 1:1 binding model considering two emissive species: the free cavitand and the 1:1 complex with the corresponding amino acid.

We also performed emission titration experiments with the fluorescent compound **7**. This compound was used as reference of the fluorescent signaling unit incorporated in the **1in** and **1out** receptor cavitands. In this case, the incremental addition of L-**Pro** did not produce noticeable changes in the emission of **7** (Figure 4.*33*). This result evidenced the relevance of the aryl-extended calix[4]pyrrole scaffold for the efficient binding of L-**Pro** by **1in** and the transduction of the binding event in the modification of the emission properties of the signaling unit.

The changes in emission intensity observed during the titrations of **1in** with L-**Pro** and L-**Pip** were rather small. Even so, we fit the obtained experimental titration data to a theoretical 1:1 binding model considering two emissive species: free and bound **1in**. We determined the binding constant values for the complexes of **1in** with L-**Pro** and L-**Pip** as, K(L-**Pro**⊂**1in**)$_{BBS}$ = 3.2 × 10^5 M^{-1} and K(L-**Pip**⊂**1in**)$_{BBS}$ = 6.3 × 10^4 M^{-1}, respectively. Surprisingly to us, the titrations of the **1out** isomer with L-**Pro** and L-**Pip** produced greater emission intensity changes (Figure 4.*8* and Figure 4.*37*).[17] Conversely, the bathochromic shift experienced by the emission band of **1out** was reduced compared to that of **1in** ($\Delta\lambda_{max}$ < 1 nm). The mathematical analysis of the

titration data of **1out**, using a 1:1 binding model considering two emissive species, returned very similar binding constant values for the two complexes of the aminoacids, K(L-**Pro**⊂**1out**)$_{BBS}$ = 3.9 × 10^4 M^{-1} and K(L-**Pip**⊂**1out**)$_{BBS}$ = 2.3 × 10^4 M^{-1}. The magnitudes of the binding constants for the complexes with **1out** are close to one order of magnitude lower than those of the **1in** isomer.

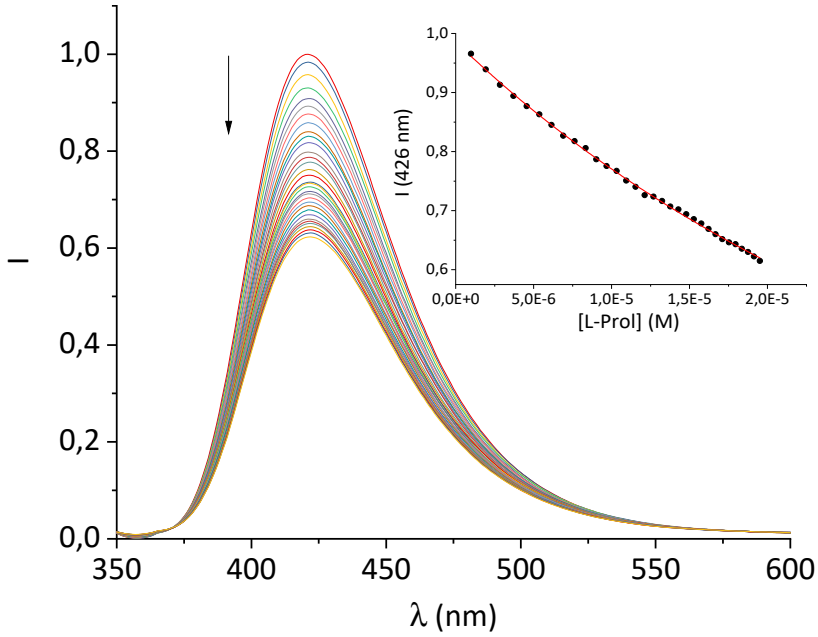

Figure 4.8 Normalized emission spectra of **1out** (1.0 μM) registered during the addition of incremental amounts of L-Pro (up to 20) in dichloromethane solution: λ_{exc} = 335 nm. Inset: Plot of the emission change at 426 nm (black circles) vs. concentration of L-**Pro**. The red line corresponds to the fit of the titration data to a 1:1 binding model considering two emissive species: the free cavitand and the 1:1 complex with the corresponding amino acid.

The observation of larger emission changes in the titrations of the **1out** isomer was completely unexpected. The spatial orientation of the P=O group in the free isomer and its complexes is not geometrically suitable for the involvement in charged hydrogen bonding interactions with the bound guests. Dalcanale et al. hypothesized that hydrogen bonding interactions with the inwardly directed P=O group were responsible for the observed emission changes in the gas phase sensing of short alkyl chain alcohols using structurally related phosphonate resorcin[4]arene cavitands. The authors did not observe emission changes in the sensing experiments using the *out* isomer. Based on our findings, we suggest that the cavitand-amino acid binding, especially for the **1out** isomer, induces changes in the conformation (and possibly steric effects) of the receptor, which directly affects the properties of

the signaling unit. These changes are transduced into non-radiative decay processes of the excited states of the 1:1 complexes. Accordingly, the binding event is responsible for the observed decrease in fluorescence intensity of the signaling unit.[18]

Development of an Indicator Displacement Assay (IDA): a study of the interaction of the fluorescent receptors 1in and 1out with *N*-oxide 6.

The reduced changes observed in the direct BBS fluorescence titrations of **1in** with the two amino acids prompted us to explore an alternative sensing approach using an Indicator Displacement Assay (IDA). In chapter 3, we described the synthesis and characterization of the pyridyl-*N*-oxide derivative **6** (Figure 4.*1*). The molecular structure of **6** is based on the popular and efficient acceptor 4-(dimethylaminoazo) benzene-4-carboxylic acid (DABCYL) ($\lambda_{abs,max}$ = 480 nm, ε = 39 500 M^{-1} cm^{-1}). DABCYL is used in the development of Förster resonance energy transfer (FRET)-based nucleic acid probes. We already applied *N*-oxide **6** for the optical sensing of creatinine using an IDA (Chapter 3). We used a calix[4] pyrrole phosphonate cavitand equipped with a dansyl group as fluorophore. We reported that the binding of **6** in the cavity of the receptor produced the efficient quenching of the fluorescence of the dansyl group through a FRET process.[9]

We calculated the spectral overlap between the absorption spectrum of *N*-oxide **6** and the emission spectrum of **1in** to be $J = 2.5 \times 10^{-9}$ cm^6 mol^{-1} (Figure 4.*38*). This value is even larger than the one calculated for the FRET pair formed by **6** and the phosphonate calix[4]pyrrole containing the dansyl fluorophore, which resulted in ca. 95% quenching of the receptor's fluorescence in the 1:1 complex. The addition of 1 equiv. of **6** to a 5 μM dichloromethane solution of **1in** produced a strong quenching of the emission band of the receptor at 422 nm (>95%, λ_{exc} = 335 nm) (Figure 4.*40*).[19] The fluorescence quenching is the direct consequence of the FRET process operating in the formed 1:1 inclusion complex. The phenyl-amino naphthyl substituent of the **1in** receptor acts as energy donor and the bound *N*-oxide **6** as the acceptor. We obtained analogous results for the equimolar mixture of **1out** and **6** (Figure 4.*41*). The quantitative formation of the complexes **6⊂1in** and **6⊂1out** in the presence of 1 equiv. of the *N*-oxide allowed us to estimate their binding constants as larger than 10^7 M^{-1}. We expected similar binding constant values for the two complexes owing to the lack of additional interaction of guest **6** with the P=O group of the receptors. We performed a titration of **1in** with **6** using more diluted

conditions ([**1in**] = 5 × 10^{-8} M, Figure 4.*9*) and determined the accurate binding constant of the 1:1 complex to be *K*(**6**⊂**1in**) = 3.2 × 10^{7} M^{-1}.[20]

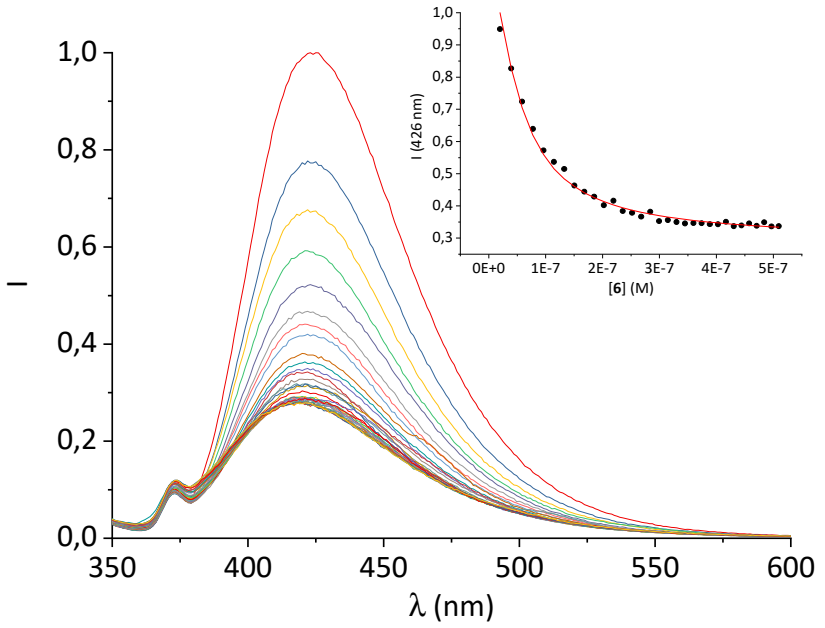

Figure 4.9 Normalized emission spectra registered for the titration of **1in** (0.05 μM) with incremental amounts of **6** in dichloromethane solution: λ_{exc} = 335 nm. Inset: plot of the emission change at 426 nm (black circles) vs concentration of **6**. The red line corresponds to the fit of the titration data to a 1:1 binding model considering two emissive species: free receptor and 1:1 complex with **6**.

The incremental addition of **6** to a 1μM solution of **7**, used as reference of the fluorescent substituent of the receptors, did not produce noticeable emission changes. This result demonstrated that the formation of the 1:1 complexes induces the observation of the FRET-quenching process.

Competitive IDA experiments.

Initially, we probed the competitive binding of **6** and L-**Pro** with the **1in** receptor using ^{1}H NMR spectroscopy. We prepared an equimolar CD_2Cl_2 solution of **1in** and L-**Pro** ([**1in**] = [L-**Pro**] = 2.0 mM) by performing a solid–liquid extraction experiment (Figure 4.*10*a). The ^{1}H NMR spectrum of the obtained solution revealed the exclusive presence of the diagnostic signals for the quantitative formation of the L-**Pro**⊂**1in** complex. The subsequent addition of 0.5 equiv. of **6** produced the appearance of a separate set of signals (Figure 4.*10*b). We attributed the new set of signals to the protons of the receptor in the **6**⊂**1in** complex. The observation of two separate sets

of signals for the receptor's protons in the L-**Pro⊂1in** and **6⊂1in** complexes indicated that its chemical exchange is slow on the chemical shift timescale. The protons of the pyridyl-*N*-oxide residue of **6** were shifted upfield, in comparison to the free counterpart, placing them within the aromatic walls of the cavitand. Compound **6** is included in the cavity of **1in** by establishing four hydrogen bonds between the oxygen atom of the pyridyl-*N*-oxide knob and the four pyrrole NHs of the receptor in addition to π–π and CH–π interactions. We also observed a new set of signals in the downfield region of the spectrum and we assigned them to the protons of free L-**Pro**. The addition of 1 equiv. of **6** induced the exclusive observation of the proton signals of the receptor in the **6⊂1in** complex. Concomitantly, the signals of free L-**Pro** grew in intensity (Figure 4.*10*c). This result is in complete agreement with the binding constant of L-**Pro⊂1in** being two orders of magnitude smaller (see above). It also demonstrates that the guest exchange process is fast on the human timescale (i.e. min.).[21]

Next, we studied the competitive displacement of the indicator *N*-oxide **6**, involved in the **6⊂1in** complex, by L-**Pro** and L-**Pip** at micromolar concentrations using emission spectroscopy. We prepared an equimolar dichloromethane solution of **6** and **1in** (1 μM). At this concentration and taking in consideration the binding constant determined in the previous section, the **6⊂1in** complex is present in 84% extent. Thus, the fluorescence observed for the ensemble is assigned to the 16% of dye **6** remaining free in solution (Figure 4.*11*).

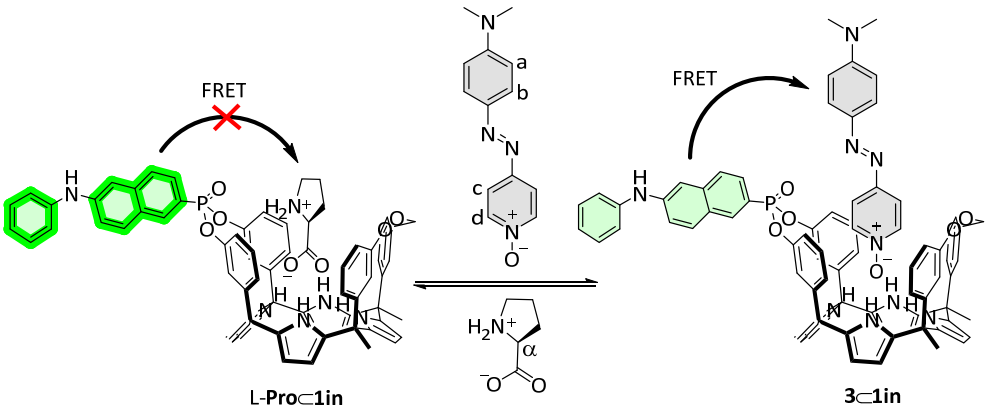

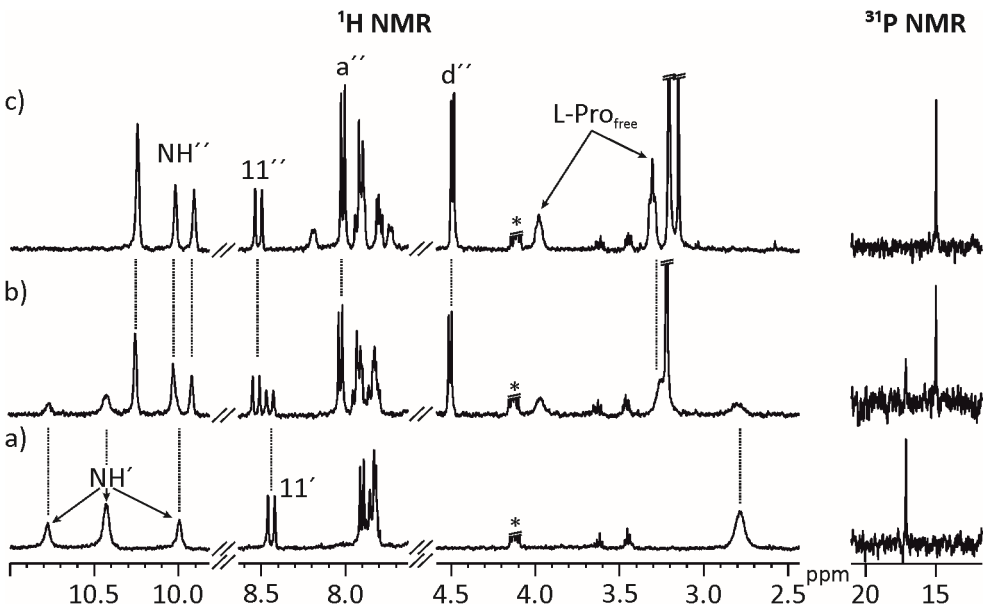

Figure 4.10 (Top) Competitive IDA binding equilibrium. (Bottom) ^{1}H and ^{31}P NMR spectra of 2 mM solution of L-**Pro**⊂**1in** in CD_2Cl_2 after the addition of a) 0, b) 0.5 and c) 1.0 equiv. of **6**.* Residual solvent peak.

The titration of the solution with incremental amounts of L-**Pro** evidenced a gradual increase of the fluorescence emission. In the presence of 30 equiv. of L-**Pro**, the observed intensity for the maximum of the emission band was 2.5 times higher than the initial one (I_0). We rationalized the noticed fluorescence "turn-on" by considering the displacement of **6**, as quencher of the fluorescence of the phenyl-amino-naphthyl group in the **6**⊂**1in** complex, by L-**Pro**. This displacement leads to the formation of the fluorescent L-**Pro**⊂**1in** complex. It is worthy to note that the identical titration monitored using absorption spectroscopy produced negligible changes in the registered spectra.

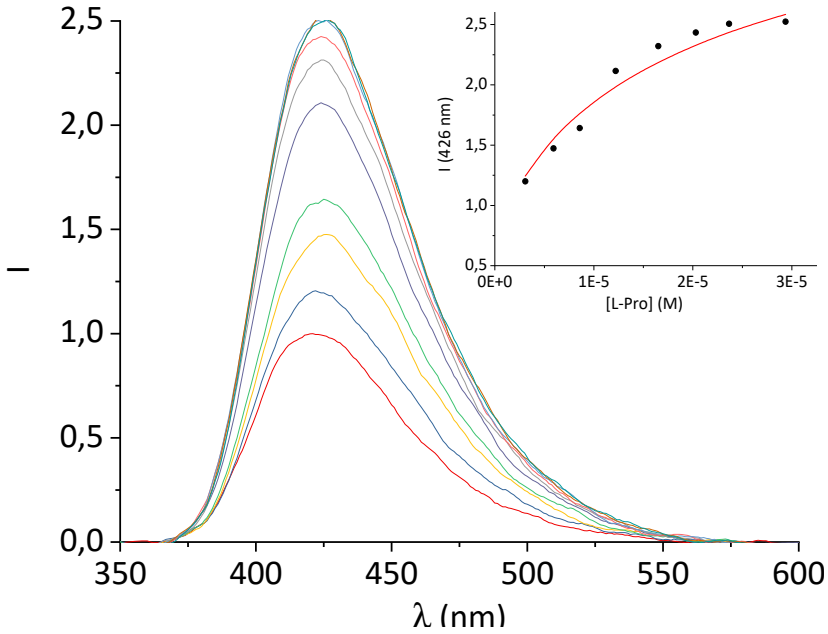

Figure 4.11 Emission spectra registered during the competitive IDA experiments of **6⊂1in** complex (1 μM) with incremental addition of L-**Pro** (up to 30 equiv.) in dichloromethane solution; λ_{exc}= 335 nm. Inset: plots of the emission change at 426 nm (black circles) vs. concentration of the amino acid. The red line corresponds to the fit of the titration data to a 1:1 theoretical binding model considering only two emissive species: the free cavitand and the 1:1 complex with the corresponding amino acid.

We analysed mathematically the titration data obtained in the emission IDA experiment using a theoretical binding model considering the competitive formation of two 1:1 complexes (**6⊂1in** and L-**Pro⊂1in**). We assigned emissive properties to only two (free **1in** and L-**Pro⊂1in**) of the five species involved the binding model.[22] We fixed the binding constant of the **6⊂1in** complex to the previously determined value of K = 3.2 × 10^7 M^{-1} (see above). The fit of the experimental data to the model was good and returned the stability constant value for the L-**Pro⊂1in** as K(L-**Pro⊂1in**)$_{IDA}$ = 4.5 × 10^5 M^{-1}. This value is in good agreement with the one determined previously using direct BBS titration experiments (K(L-**Pro⊂1in**)$_{BBS}$ = 3.2 × 10^5 M^{-1}, see above). The fit of the experimental data also provided the calculated emission spectra for **1in** and L-**Pro⊂1in**. The calculation of the spectra of the emissive (*a.k.a*. coloured) species is one of the advantages of performing global fitting multivariate data analysis compared to the simpler single or even multiple wavelength fitting alternatives. Obtaining sensible calculated spectra for the coloured species is a necessary condition to support the quality and fit of the data analysis. To our delight, the calculated spectra showed a nice agreement with the experimental ones registered in separate experiments. We also

tested the performance of the ensemble of **6** and **1out** in emission IDA experiments with L-**Pro** (Figure 4.*42*). Using this methodology, the calculated binding constant for the L-**Pro**⊂**1out** complex was K(L-**Pro**⊂**1out**)$_{IDA}$ = 7.9 × 10^4 M^{-1}. In short, the emission IDA experiments reflected that the difference in the binding constant values of the L-**Pro**⊂**1in** and L-**Pro**⊂**1out** inclusion complexes is close to one order of magnitude, in favour of the former. In addition, the binding constant values measured for the complexes using IDA and BBS experiments are fully consistent.

We carried out analogous IDA experiments with L-**Pip**. We observed a 1.7 times fluorescence enhancement for the ensemble of **6** and **1in** in the presence of 30 equiv. of L-**Pip** (i.e. I_{30} = 1.2 × I_0) (Figure 4.*43*). The measured fluorescence enhancement factor is reduced when compared to the 2.5-fold observed for L-**Pro** under identical conditions. The fit of the data of the IDA experiments to the same theoretical binding model used before for L-**Pro** returned a binding constant for L-**Pip**⊂**1in** complex of K(L-**Pip**⊂**1in**)$_{IDA}$ = 6.3 × 10^4 M^{-1}. Again, this value is in line with the one obtained in direct BBS experiments. It is worthy to mention that under the used experimental conditions for the IDA, and considering the calculated binding constant for the L-**Pip**⊂**1in** complex, this species is only formed in a 20% extent. The reduced extension in which the L-**Pip**⊂**1in** complex is formed diminishes the accuracy of the calculated binding constant value. Unfortunately, the low solubility of L-**Pip** in dichloromethane hampered the formation of the L-**Pip**⊂**1in** complex to a larger extent.

We also determined the binding constant of L-phenylalanine (L-**Phe**) with **1in** using analogous competitive IDA experiments. We observed a 1.5 times fluorescence enhancement in the presence of 30 equiv. of L-**Phe** (Figure 4.*12*). This result hinted to similar binding constant values for the L-**Phe**⊂**1in** and L-**Pip**⊂**1in** complexes. The fit of the experimental data returned a binding constant of K(L-**Phe**⊂**1in**)$_{IDA}$ = 3.5 × 10^4 M^{-1}.

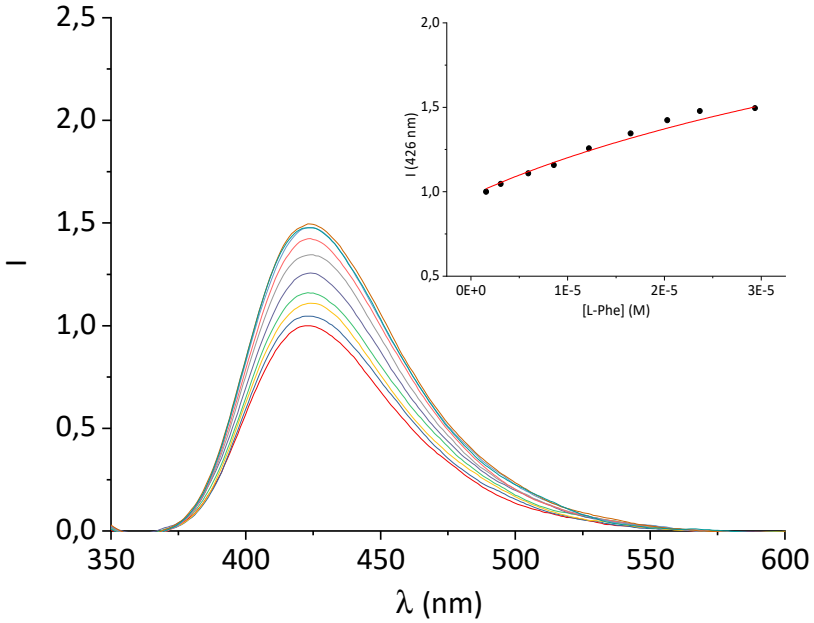

Figure 4.12 Emission spectra registered during the competitive IDA experiments of **6⊂1in** complex (1 μM) with incremental addition of L-**Phe** (up to 30 equiv.) in dichloromethane solution; λ_{exc} = 335 nm. Insets: plots of the emission change at 426 nm (black circles) vs. concentration of the amino acid. The red line corresponds to thefit of the titration data to a 1:1 theoretical binding model considering only two emissive species: the free cavitand and the 1:1complex with the corresponding amino acid.

Influence of the polar hydrogen bonding in the inclusion complexes of 1in.

In previous studies, we learned that in water solution six-membered ring lactams produced more stable inclusion complexes with bis-phosphonate cavitand than the five-membered analogues.[23] These results were rationalized based on the superior size and shape fit of the 6-membered ring, with respect to the receptor's cavity, and its increased hydrophobicity. Considering our previous findings, we were surprised to calculate a larger binding constant for the L-**Pro⊂1in** complex, involving a 5-membered cyclic guest, than for the analogous complex with L-**Pip** (6-membered ring).

To gain some insight on the structures of the amino acid's inclusion complexes with receptor **1in**, we computed their energy-minimized structures at the BP86[24,25]/def2SVP level of theory using GAUSSIAN 09.[26] In all the computed inclusion complexes, the calix[4]pyrrole core adopts the cone conformation by establishing four hydrogen bonding interactions with one of the oxygen atoms of the carboxylate group of the included guest (Figure 4.*13* and Figure 4.*44*). It is also possible to infer

the presence of multiple CH–π and O–π interactions in the complexes (Figure 4.*45*). Moreover, all complexes display a charged hydrogen bonding interaction between the inwardly directed P=O group of the receptor and the protonated amino group of the zwitterionic form of the bound amino acids (Figure 4.*45*).

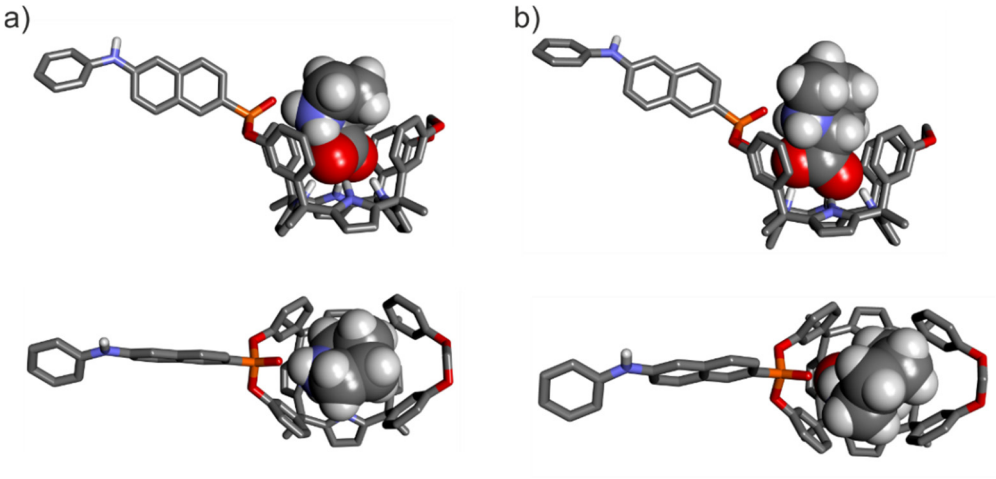

Figure 4.13 Side and top views of the energy-minimized inclusion complexes a) L-**Pro⊂1in** and b) L-**Pip**$_{eq}$**⊂1in**. The structures are energy minima at the BP86/def2-SVP level of theory. The receptors are shown in stick representation. Non-polar hydrogen atoms were removed for clarity. The included amino acids are depicted as CPK models.

In the particular case of the L-**Pip⊂1in** complex, we computed two different binding geometries. One of them involved the energetically more favorable conformation of L-**Pip**, L-**Pip**$_{eq}$ (i.e. COO^- substituent equatorial in the protonated piperidine chair conformation). The other one considers the higher energy conformer, L-**Pip**$_{ax}$ (i.e. COO− substituent is axial in the protonated piperidine chair conformation). The results of the calculations indicated that both inclusion complexes were isoenergetic.

A simple visual inspection of the energy-minimized structures of the amino acid's inclusion complexes revealed that those of L-**Pro** featured a superior match in size and shape between the cavity of **1in** and the included amino acid (Figure 4.*13*). Most likely, the L-**Pro⊂1in** inclusion complex establishes energetically more favorable dispersive, van der Waals and hydrogen bonding intermolecular interactions than the other counterparts (L-**Pip⊂1in** and L-**Phe⊂1in**) (Figure 4.*44*).

Table 4.1 Binding constants K_a (M^{-1}) at 298 K for the 1:1 inclusion complexes of the **1in** and **1out** receptors in dichloromethane and free Gibbs energy ΔG (kcal mol^{-1}).

		1in	**1out**	$\Delta\Delta G_{(\mathbf{1in}\text{-}\mathbf{1out})}$
L-**Pro**	K_a	$3.2 \pm 0.6 \times 10^{5a}$ $4.5 \pm 0.9 \times 10^{5b}$	$3.9 \pm 0.8 \times 10^{4a}$ $7.9 \pm 1.5 \times 10^{4b}$	~-1.1
	Δ*G*	-7.5 ± 0.1^{a} -7.7 ± 0.1^{b}	-6.3 ± 0.1^{a} -6.7 ± 0.1^{b}	
L-**Pip**	K_a	$6.3 \pm 1.3 \times 10^{4a}$ $6.3 \pm 1.3 \times 10^{4b}$	$2.3 \pm 0.5 \times 10^{4a}$	-0.5^{a}
	Δ*G*	-6.5 ± 0.1^{a} -6.5 ± 0.1^{b}	-6.0 ± 0.1^{a}	
L-**Phe**	K_a	$3.5 \pm 0.7 \times 10^{4b}$	*n.d.*	*n.d.*
	Δ*G*	6.2 ± 0.1^{b}	*n.d.*	

K_a and ΔG are the average values from two independent titrations. Errors are reported as standard deviation for K_a and propagated for ΔG. [a] Determined by direct BBS experiments. [b] Determined by IDA experiments. n.d. Not determined.

The experimentally determined values for the association constants of the complexes of the amino acids with receptors **1in** and **1out** are summarized in Table 4.*1*. We draw the following conclusions from the tabulated data.

On the one hand, the determined ΔG values for L-**Pro**⊂**1in** and L-**Pro**⊂**1out** complexes assigned a free energy gain of ∼−1.1 kcal mol^{-1} ($\Delta\Delta G_{(\text{L-}\mathbf{Pro}\subset\mathbf{1in}-\text{L-}\mathbf{Pro}\subset\mathbf{1out})}$) in favour to L-**Pro**⊂**1in** complex. We attributed this difference to the additional polar hydrogen bonding interaction established in the inclusion complex with **1in**. This interaction involves the oxygen atom of the P=O group inwardly directed towards the receptor's cavity and the protonated amino group of the included L-**Pro**. This results are in line with those presented in the Chapter 2 for inwardly directed phosphonate calix[4]pyrroles. Due to geometrical reasons, this interaction is not present in the L-**Pro**⊂**1out** complex. Thus, receptor **1out** binds L-**Pro** through the formation of only four hydrogen bonds involving the carboxylate group of the L-**Pro** and pyrrole NHs of **1out**. Additional CH–π interactions also assist in the stabilization of both complexes.

On the other hand, the calculated free energy difference between the analogous complexes of L-**Pip** ($\Delta\Delta G_{(\text{L-}\mathbf{Pip}\subset\mathbf{1in}-\text{L-}\mathbf{Pip}\subset\mathbf{1out})}$ is reduced to just −0.5 kcal mol^{-1}. Most likely, this is due to the formation of a weaker polar hydrogen bond in the L-**Pip**⊂**1in** complex in comparison to the L-**Pro** counterpart.

We measured a small free energy difference for the complexes of L-**Pro** and L-**Pip** with the **1out** receptor (∼−6.3 and −6.0 kcal mol^{-1}, respectively) that we assigned to

the better fit of the former in the cavity of the latter. Taken together, these results indicate that the polar intermolecular hydrogen bond interaction N–H···O=P plays a pivotal role in the binding selectivity featured by **1in** for L-**Pro** over L-**Pip**, $\Delta\Delta G_{(\text{L-Pro}\subset\textbf{1in}-\text{L-Pip}\subset\textbf{1in})}$ ~-1.0 kcal mol^{-1}.

4.3 Conclusions.

We report the synthesis of two unprecedented diastereoisomeric mono-phosphonate calix[4]pyrrole cavitands featuring a *N*-phenyl-naphthalamine fluorophore directly attached to its phosphorous atom. The two isomers differ in the relative orientation (in/out) of the P=O bridging group with respect to its polar aromatic cavity (**1in** and **1out**). We characterized the two isomers in solution using NMR and optical (UV/vis absorption and emission) spectroscopies and in the solid state by X-ray diffraction studies. We used the non-fluorescent model receptors **5in** and **5out** to perform a competitive binding experiment with L-**Pro**. The analyses of the mixtures using ^{1}H and ^{31}P NMR spectroscopy showed that the L-**Pro** was preferentially bound to the **5in** isomer. We attributed the higher thermodynamic stability exhibited by the L-**Pro**⊂**5in** complex to the existence of an additional charged hydrogen bonding interaction between the protonated amino group of bound L-**Pro** and the inwardly directed bridging P=O function of the receptor. We developed two different supramolecular approaches for the sensing of L-**Pro** and L-**Pip** using the fluorescent receptor **1in**: direct binding-based sensing (BBS) and a FRET-based indicator displacement assay (IDA). The BBS strategy produced a small reduction of the emission intensity of **1in** upon binding L-**Pro** or L-**Pip**. The fit of the reduced emission changes to a simple 1:1 binding model allowed us to determine the binding constants of the inclusion complexes of **1in** with L-**Pro** and L-**Pip** as, K(L-**Pro**⊂**1in**)$_{BBS}$ = 3.2 × 10^{5} M^{-1} and K(L-**Pip**⊂**1in**)$_{BBS}$ = 6.3 × 10^{4} M^{-1}, respectively. Analogous titration experiments of the **1out** isomer with the two amino acids resulted in greater decreases of the emission intensity of the free receptor. In contrast, the binding constant values determined for the complexes of **1out** with L-**Pro** and L-**Pip** are close to one order of magnitude lower than those of **1in**. The increased binding affinity of the amino acids for the **1in** receptors is assigned to the charged hydrogen-bonding interaction established between the protonated amino group of the bound guest and the bridging P=O function inwardly directed with respect to the polar aromatic cavity of the receptor.

The sensing of amino acids (e.g. L-**Pro**, L-**Pip** and L-**Phe**) using IDA experiments with the ensemble composed by **1in** and *N*-oxide **6** produced more significant emission changes than those of the direct BBS strategy. Remarkably, the IDA experiments induced fluorescence "turn on" instead of quenching. The binding constant values determined for the amino acid's inclusion complexes with **1in** using IDA experiments were in complete agreement with those derived from the direct BBS counterparts. Receptor **1in** showed binding selectivity for L-**Pro** over the other amino acids tested. Conversely, receptor **1out** did not feature a noticeable selectivity in the amino acids' binding. We assign the dissimilar receptors' binding selectivity to the existence of an intermolecular hydrogen bond interaction between the bound amino acid and the P=O group of the receptor. For geometrical reasons, the required arrangement of functional groups is only possible for the **1in** diastereoisomer. The obtained results demonstrate the importance of dedicated polar interactions in determining binding selectivity.

4.4 Experimental section.

4.4.1 General methods and instrumentation.

All chemicals were purchased from commercial sources and used without further purification unless otherwise stated. Compounds **5in** and **5out** were synthesized following described procedures.[7] Pyrrole was distilled under vacuum and freshly used or stored in a freezer for further use. THF was dried from sodium/benzophenone and distilled under argon atmosphere. Triethylamine (Et_3N) was distilled from CaH_2 under argon atmosphere and was immediately used. Dried *N*,*N*-dimethylformamide was obtained from a solvent purification system M Braun SPS-800.

Flash column chromatography was performed with silica gel (technical grade, pore size 60 Å, 230-400 mesh particle size). Automatic column chromatography purifications were done with a Combi-flash® RF^+. Analytical HPLC instrument consisted of an Agilent 1100 with autosampler and UV/vis detector using a Waters Spherisorb® (5.0 µm Silica, 4.6 mm × 250 mm) column and isocratic elution (DCM:AcOEt 90:10).

Routine ^{1}H-NMR, ^{31}P-NMR and ^{13}C-NMR spectra were recorded on a Bruker Advanced 400 (400 MHz for ^{1}H-NMR) or Bruker Advance 500 (500 MHz for ^{1}H-NMR) ultrashield spectrometer. Deuterated solvents were purchased from Aldrich. FT-IR

measurements were carried out on a Bruker Optics FT-IR Alpha spectrometer equipped with a DTGS detector, KBr beam splitter at 4 cm^{-1} resolution using a one bounce ATR accessory with diamond windows.

Solutions for optical spectroscopy studies were prepared in HPLC grade dichloromethane supplied by Scharlab, S.L. UV/vis measurements were carried out on a Shimadzu UV-2401PC spectrophotometer equipped with a photomultiplier detector, double beam optics and D2 and W light sources. Fluorescence measurements were carried out on a Fluorolog Horiba Jobin Yvon spectrofluorimeter equipped with photomultiplier detector, double monochromator and Xenon light source.

4.4.2 Synthesis and characterization data

Synthesis of 6-(phenylamino)naphthalene-2-yl phosphonic dichloride **4**.

The phosphonic acid dichloride **4** was synthesized following the procedure reported by Dalcanale et al.5 The synthetic route is shown in Scheme 4.*3*.

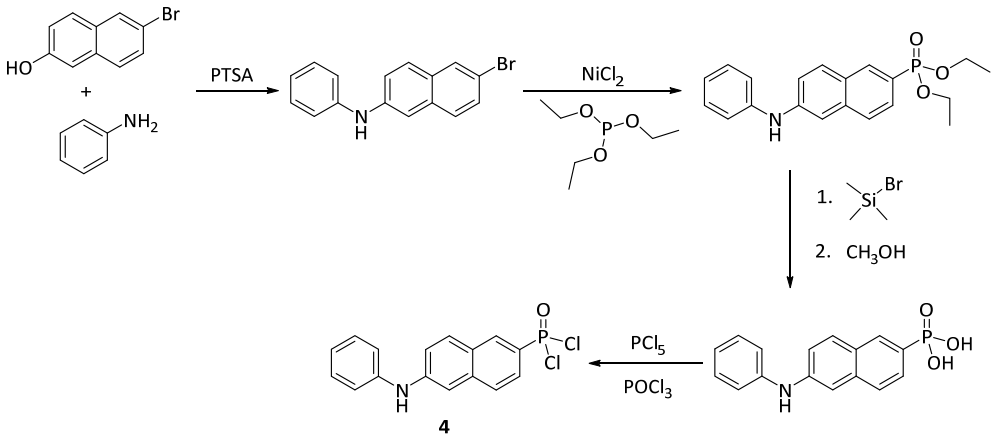

Scheme 4.3 Synthetic scheme for the synthesis of compound **4**.

Synthesis of the mono-methylene bridged calix[4]pyrrole receptor **3**.

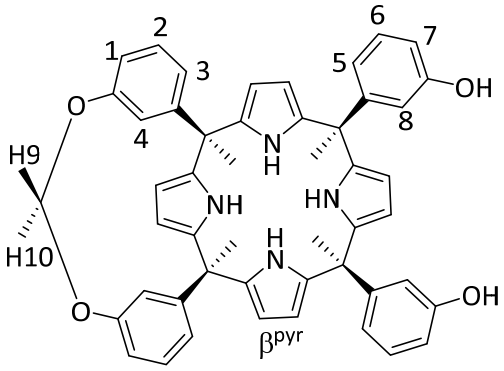

3

To an Ace pressure tube equipped with a magnetic stir bar and plunger valve, tetrol 26 (1.50 g, 2.9025 mmol), and K2CO3 (2.24 g, 16.20 mmol, 8 equiv.) were added. The system was left under vacuum for one hour and then anhydrous DMSO (80 mL) was added under Ar atmosphere. To the resulting mixture, bromochloromethane (0.158 µl, 2.43 mmol, 1.2 equiv.) was added in one portion. The flask was sealed and heated overnight at 60 °C in an oil bath. The reaction mixture was then cooled down to RT and poured into 10% HCl(aq) (80 mL). The resulting suspension was extracted with DCM (3 × 50 mL). The organic portions were collected and washed with water (3 × 50 mL), dried over Na2SO4, filtered and evaporated under reduced pressure to yield a pale yellow powder (1.48 g). The final product was purified by combi-flash chromatography on a silica gel column (40 g silica column, DCM:AcOEt 90:10) to yield a white powder (800 mg). Finally, the white powder was further recrystallized in acetonitrile (5 ml) with some drops of DCM (720 mg, 48 % yield).

Receptor **3**. **Rf**: 0.5 (DCM:AcOEt 90:10, SiO_2) **Melting Point**: 255 °C. **^{1}H NMR** (500 MHz, $(CD_3)_2CO$, 298 K): δ (ppm) = 8.77 (bs, 2H, NH), 8.73 (bs, 1H, NH), 8.53 (bs, 1H, NH), 8.16 (s, 2H, OH), 7.07 (t, *J* = 7.85 Hz, 2H, H^2), 7.04 (t, *J* = 7.85 Hz, 2H, H^6), 6.79 (s, 2H, H^4), 6.70 (d, *J* = 8.02 Hz, 1H, H^1), 6.67 (dd, J_1 =8.02 Hz, J_2 = 1.92 Hz, 2H, H^3), 6.55 (dd, J_1 =8.02 Hz, J_2 = 1.92 Hz, 2H, H^5), 6.42 (d, *J* = 7.85 Hz, 2H, H^7), 6.38 (s, 2H, H^8), 6.36 (d, *J* = 8.25 Hz, 1H, H^9), 6.06 - 6.00 (m, 8H, β^{pyr}), 5.33 (d, *J* = 8.25 Hz, 1H, H^{10}), 1.88 (s, 6H, CH_3), 1.84 (s, 6H, CH_3). **^{13}C NMR** (100 MHz, CD_2Cl_2, 298 K): δ (ppm) = 155.9, 154.9, 137.8, 137.7, 137.2, 136.7, 128.9, 128.8, 121.9, 120.4, 117.1, 116.9, 115.0, 113.3, 105.7, 105.1, 44.7, 44.6, 1.4.

Synthesis of fluorescent receptors **1in** and **1out**.

In a 25 mL Schlenk flask, compound 4 (180 mg, 0.535 mmol, 2.0 equiv.) was dried overnight under reduced pressure. Next day, the solid was dissolved on freshly dried THF (15 mL, 18 mM) and triethylamine (0.5 mL, 3.59 mmol, 13.5 equiv.) was added in one portion under Ar atmosphere. The mixture left under vigorous stirring for 15 min. This solution was added via cannula to a 5mL THF solution of mono-methylene bridged cavitand 3 (200 mg, 0.266 mmol, 1.0 equiv.) under Ar atmosphere.

The reaction was stirred at RT for 2h. Then, the solvent was evaporated, and the resulting solid was solubilized in DCM (20 mL). The organic solution was washed with 10 mL of HCl (aq.) 10% and 10 mL of brine solution. Then, the aqueous phase was washed with DCM (2 × 20 mL). The organic portions were collected, dried over Na_2SO_4, filtered, and concentrated under reduced pressure yielding a pale brown solid (250 mg). The reaction produced a mixture of the two mono-phosphonate diastereoisomers **1in** and **1out**.

Analytical HPLC separation of diastereoisomers 1in and 1out.

The reaction crude (after work-up) was passed through silica gel column chromatography as a pre-treatment using DCM as eluent. The collected combined fractions containing the desired products were analyzed by HPLC. After an optimization process, the elution mixture DCM/AcOEt 90:10 showed the best isomeric separation (Figure 4.*14*).

HPLC parameters:

Column: Waters Spherisorb® (5.0 µm Silica, 4.6 mm × 250 mm) column.

Mobile phase: DCM/AcOEt 90:10

Flux: 1 mL/min

Injection volume: 50 µL

Sample concentration: 1 mg/ml

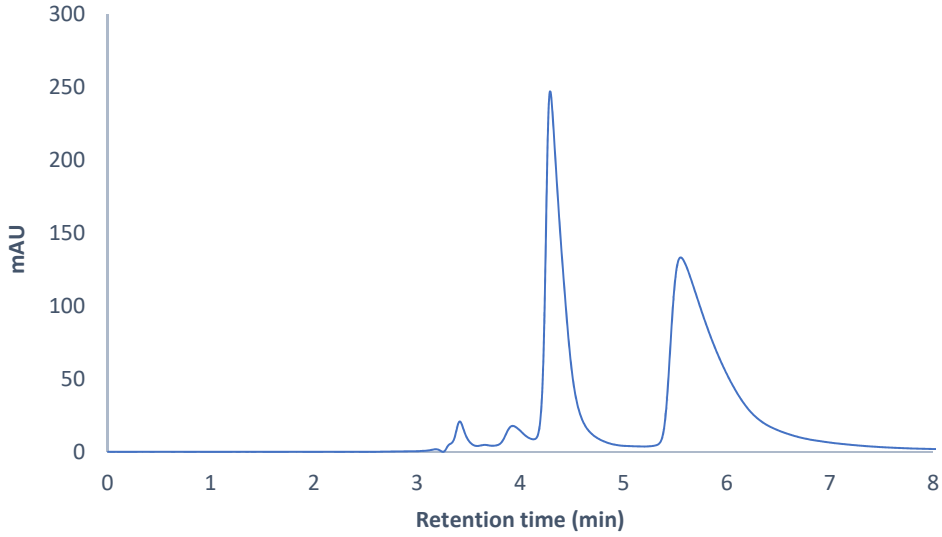

Figure 4.14 HPLC Chromatogram of the combined organic fractions containing receptors **1in** and **1out**.

After optimizing the analytical conditions, we performed a loading study using the same column and eluent mixture. We ran different injections (10 mg mL^{-1} in DCM) increasing the injection volume from 5 µL to 100 µL. The results from the loading study are shown in Figure 4.*15*.

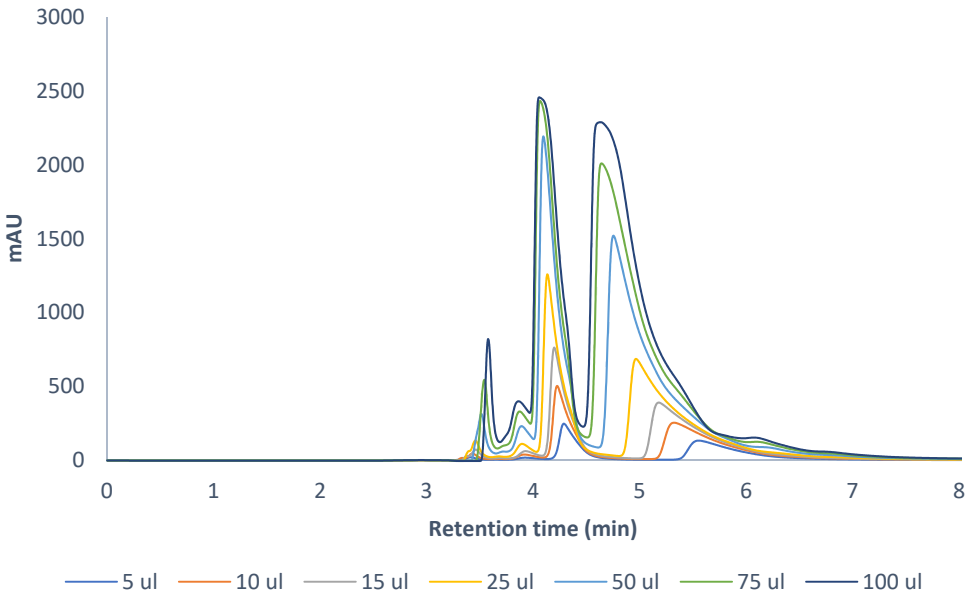

Figure 4.15 Stacked HPLC chromatograms obtained during the loading study of combined organic fractions containing receptors **1in** and **1out**.

Repetitive injections of the isomers' mixture (10 mg mL^{-1} in DCM) under the optimized conditions yielded 20 mg (15%) of each separated isomer. Crystals of **1in** and **1out** spontaneously grew in the NMR tubes from deuterated acetone or acetonitrile solutions. According to the X-ray diffraction results, the fraction with the shorter retention time (4.2 min) corresponded to the *out* isomer, while the fraction eluting later at 5 min corresponded to the *in* isomer.

Mono-phosphonate Calix[4]pyrrole cavitand **1in.**

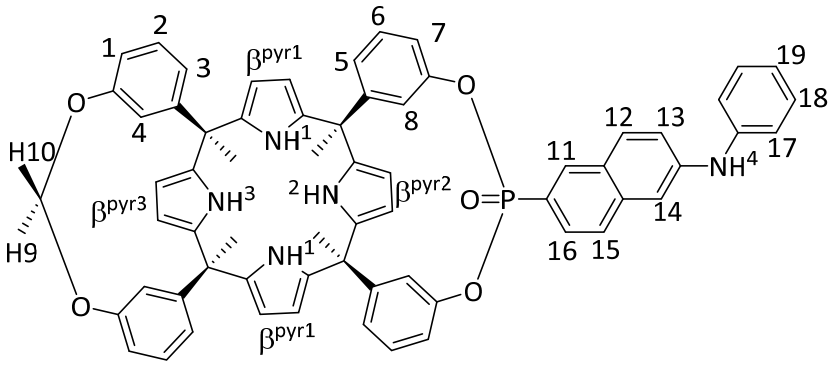

1in

Receptor **1in**. Rf: 0.3 (DCM:AcOEt 98:2, SiO_2). **^{1}H NMR** (400 MHz, $(CD_3)_2CO$, 298 K): δ (ppm) = 8.85 (bs, 2H, NH^1), 8.62 (bs, 1H, NH^2), 8.51 (bs, 1H, NH^3), 8.49 (d, 1H, H^{11}), 8.00 (d, 1H, *J* = 8.74 Hz, H^{12}), 7.98 (bs, 1H, NH^4), 7.93-7.83 (m, 2H, $H^{15,16}$), 7.58 (d, 1H, *J* = 2.20 Hz, H14), 7.44 (dd, 1H, J_1 = 8.82 Hz, J_2 = 2.20 Hz, H^{13}), 7.39-7.31 (m, 4H, $H^{17,18}$), 7.22 (t, 2H, *J* = 7.87 Hz, H^6), 7.13 (t, 2H, *J* = 7.87 Hz, H^2), 7.06 (d, 2H, *J* = 8.05 Hz, H^7), 7.02 (tt, 1H, J_1 = 6.51 Hz, J_2 = 1.84 Hz, H^{19}), 6.85 (s, 2H, H^4), 6.82 (s, 2H, H^8), 6.83-6.78 (m, 4H, $H^{5,8}$), 6.72 (dd, 2H, J_1 = 8.10 Hz, J_2 = 1.30 Hz, H^1), 6.62 (d, 2H, *J* = 7.87 Hz, H^3), 6.44 (d, 1H, *J* = 8.06 Hz, H^9), 6.14 (d, 2H, *J* = 2.60 Hz, β^{pyr2}), 6.11 (d, 4H, *J* = 2.60 Hz, β^{pyr1}), 6.08 (d, 2H, *J* = 2.60 Hz, β^{pyr3}), 5.35 (d, 1H, *J* = 8.06 Hz, H^{10}), 1.91 (s, 6H, CH_3), 1.90 (s, 6H, CH_3). **^{31}P NMR** (161 MHz, $(CD_3)_2CO$, 298 K): δ (ppm) = 15.31.

Note: 2D-NMR experiments (COSY and ROESY) were performed for the fully proton assignment of cavitand **1in** (Figure 4.*17* to Figure 4.*22*).

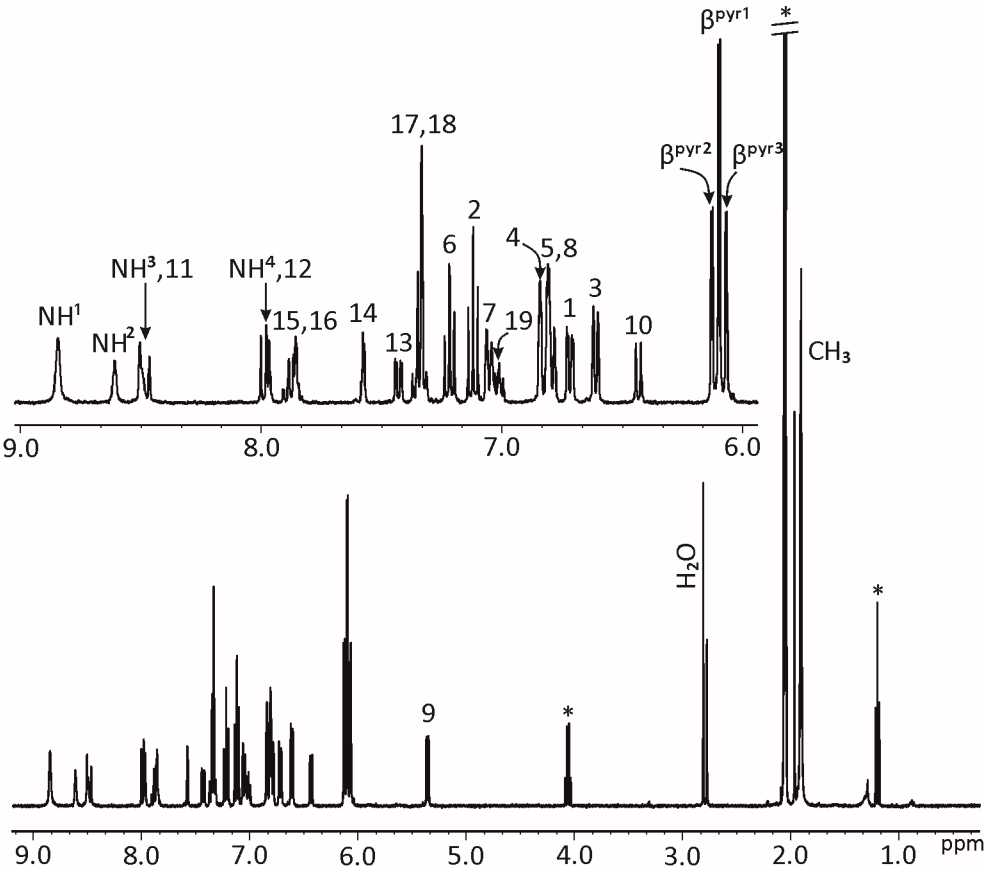

Figure 4.16 ^{1}H NMR (400 MHz, $(CD_3)_2CO$, 298 K) spectrum of **1in**. A zoom of the spectral window from 6.0 to 9.0 ppm is shown. *Residual solvent peak.

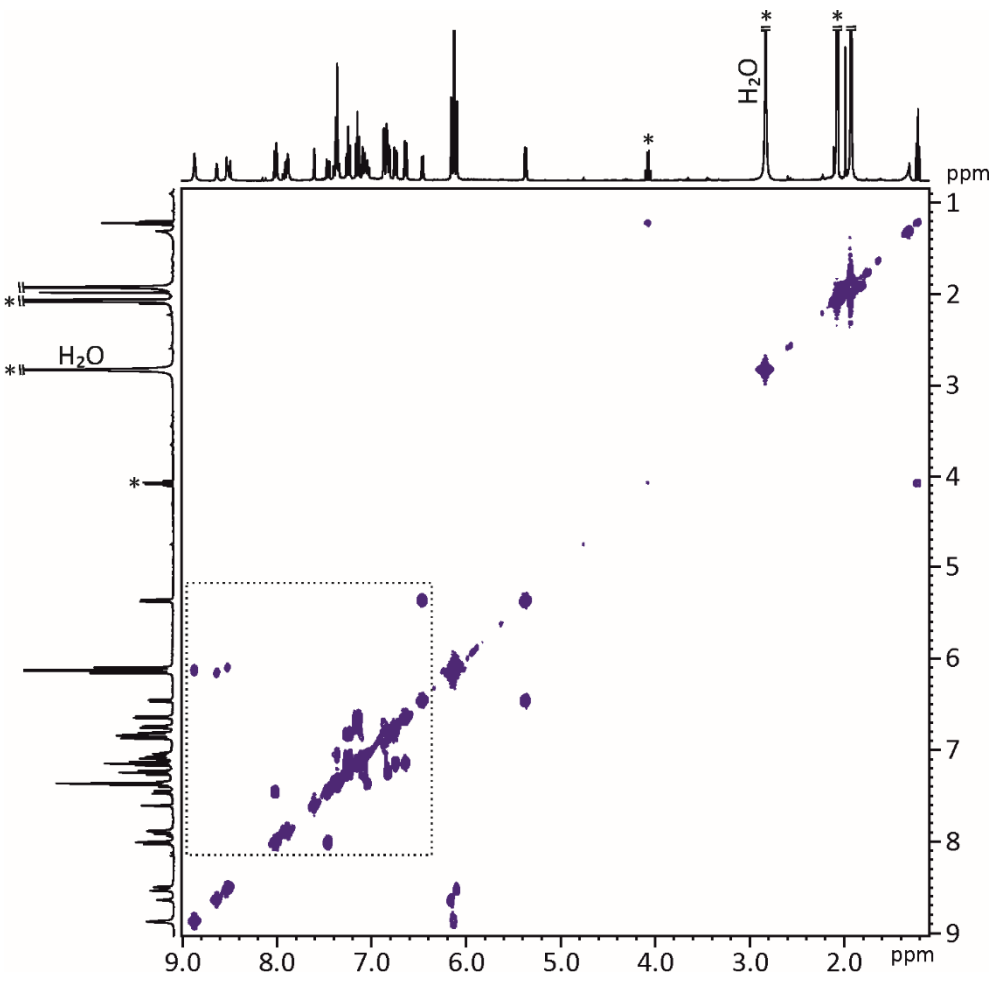

Figure 4.17 COSY NMR (400 MHz, $(CD_3)_2CO$, 298 K) spectrum of compound **1in**. * Residual solvent peak.

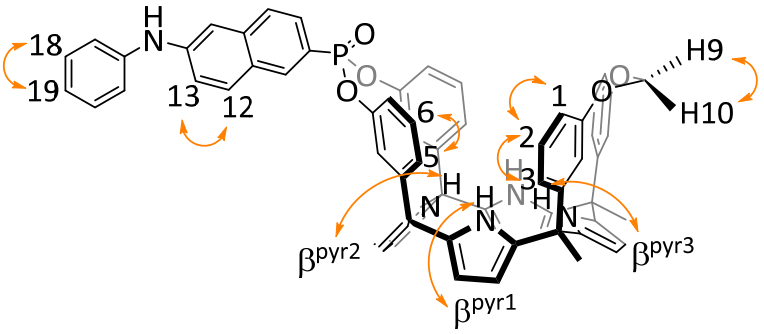

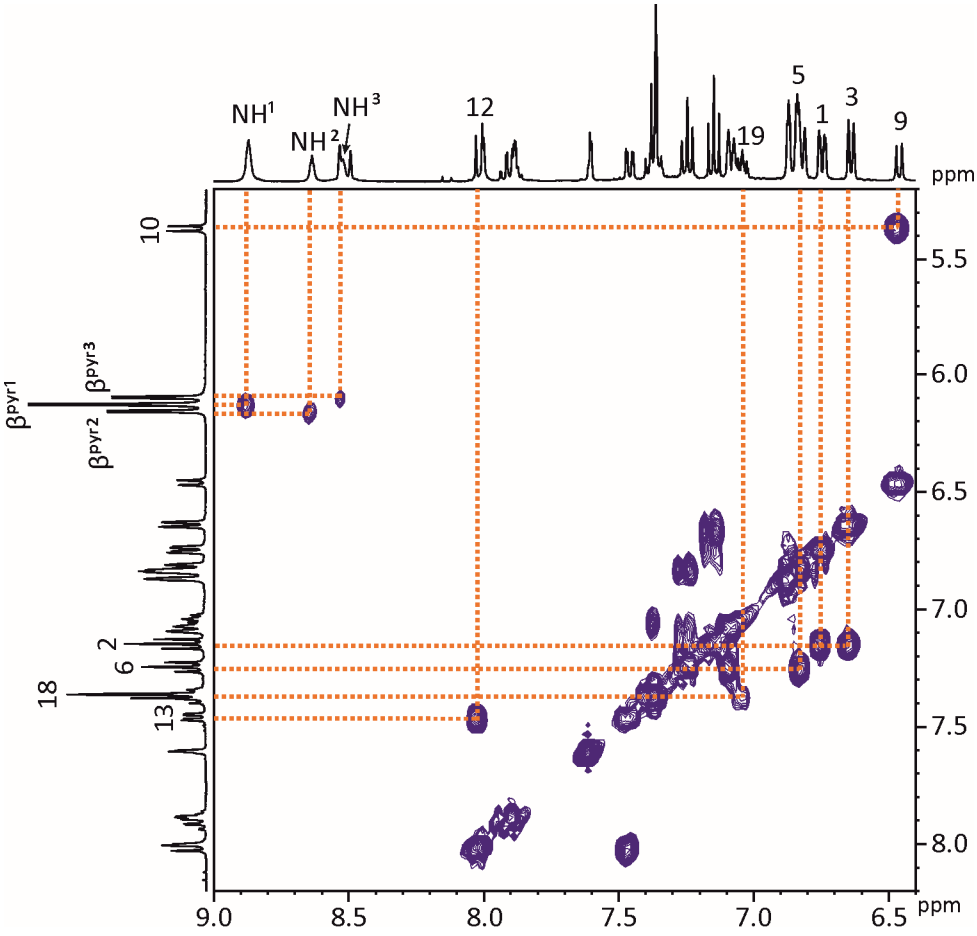

Figure 4.18 Selected region of the COSY NMR spectrum of the cavitand **1in**.

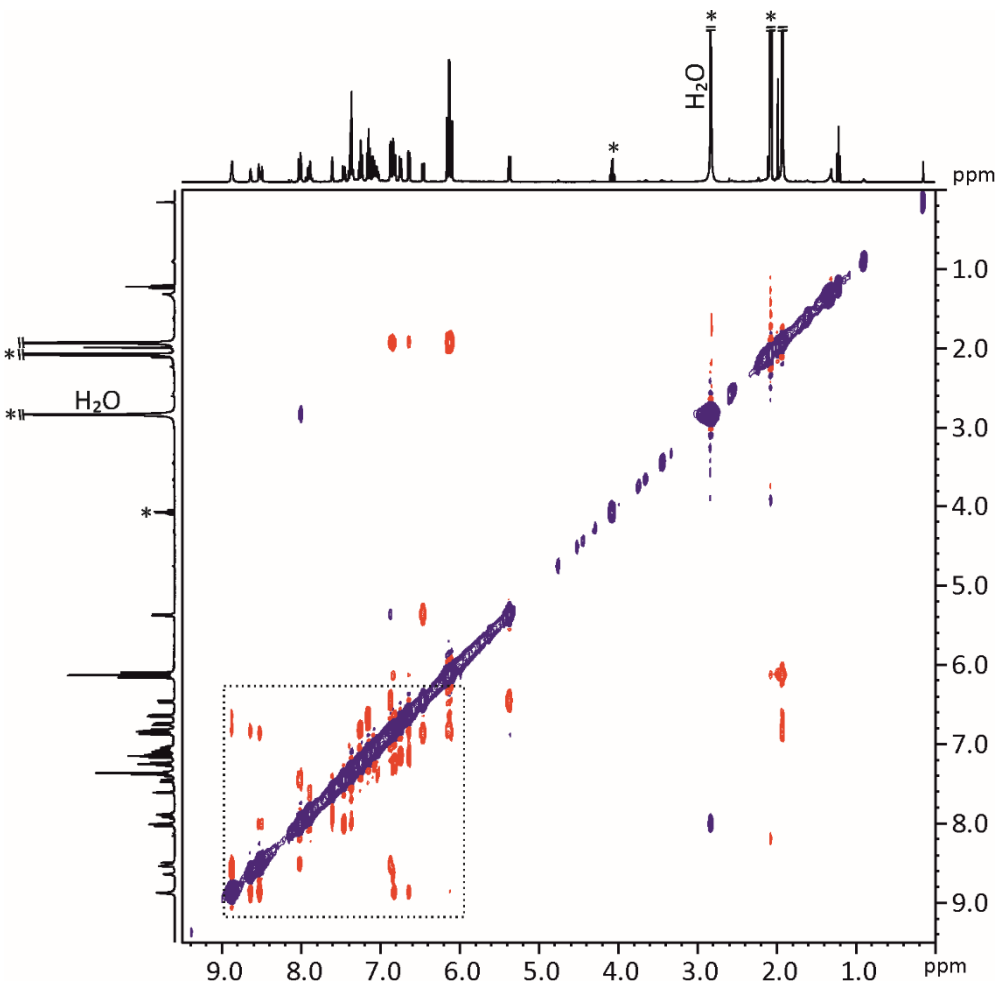

Figure 4.19 NOESY NMR (400 MHz, $(CD_3)_2CO$, 298 K) spectrum of cavitand **1in**. * Residual solvent peak.

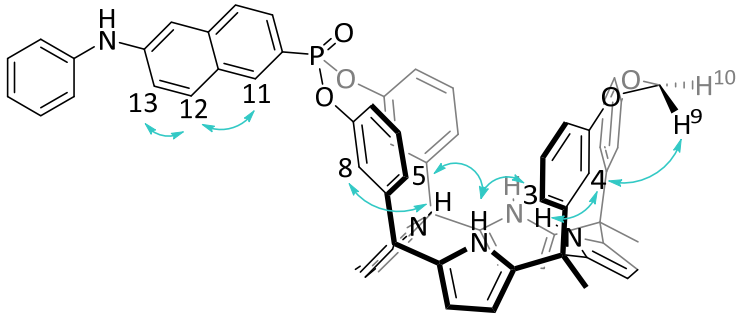

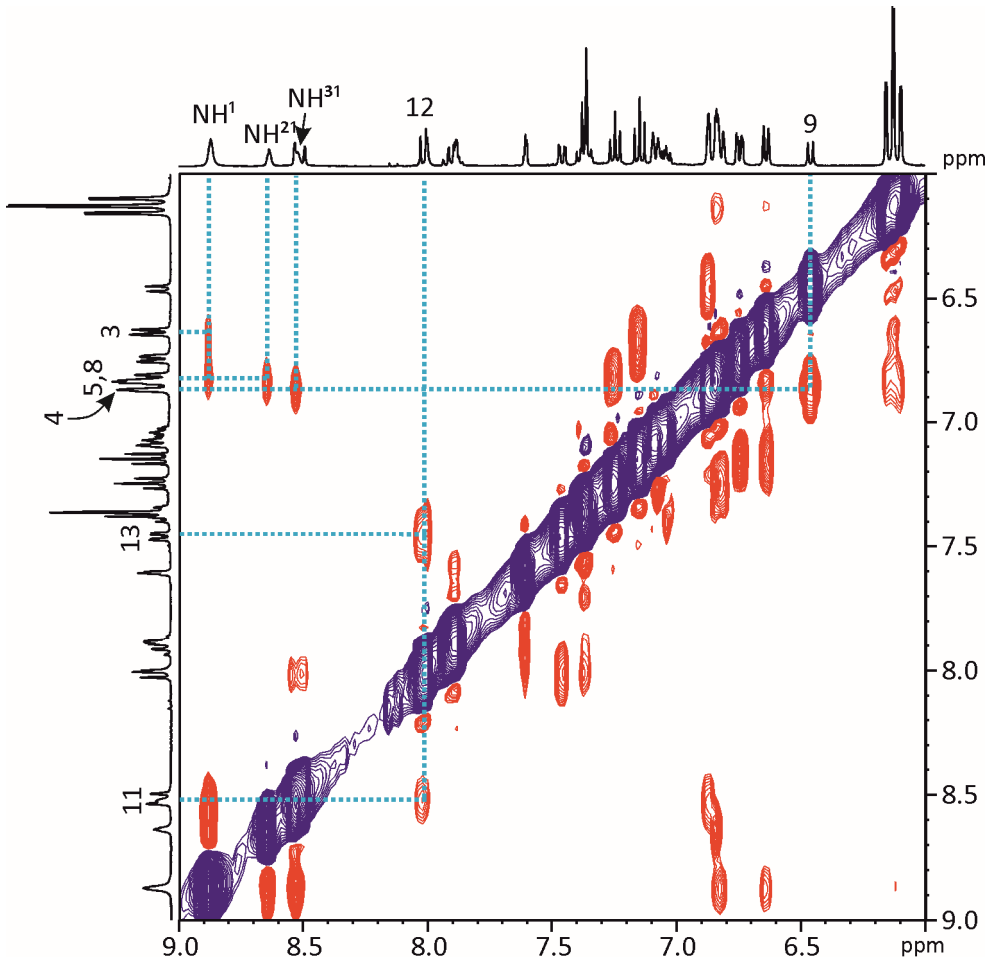

Figure 4.20 Expansion of a selected region of the 2D NOESY NMR (400 MHz, $(CD_3)_2CO$, 298 K) spectrum of the cavitand **1in**.

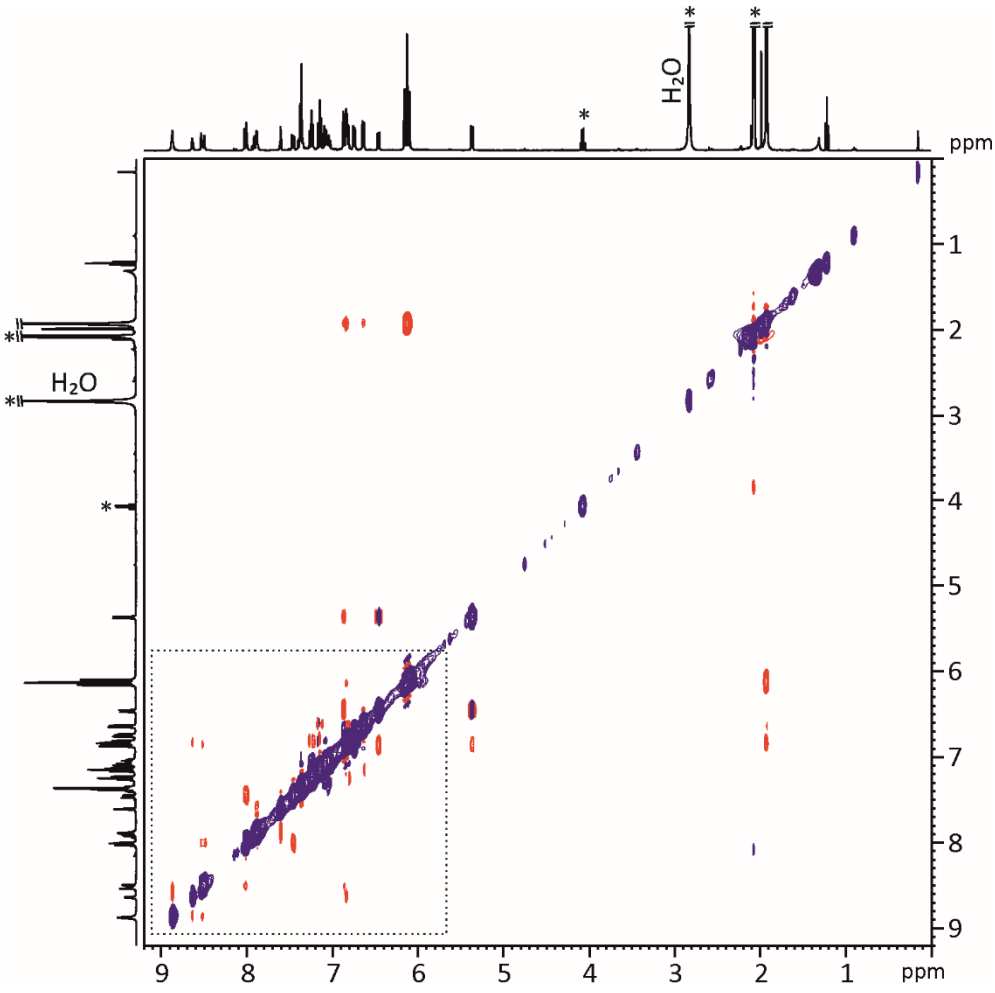

Figure 4.21 ROESY NMR (400 MHz, $(CD_3)_2CO$, 298 K) spectrum of the cavitand **1in**. * Residual solvent peak.

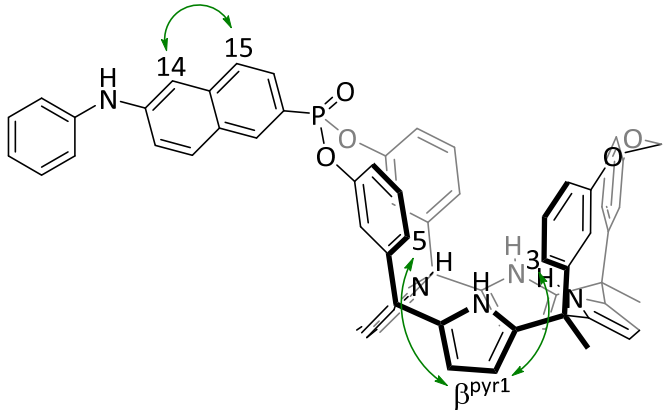

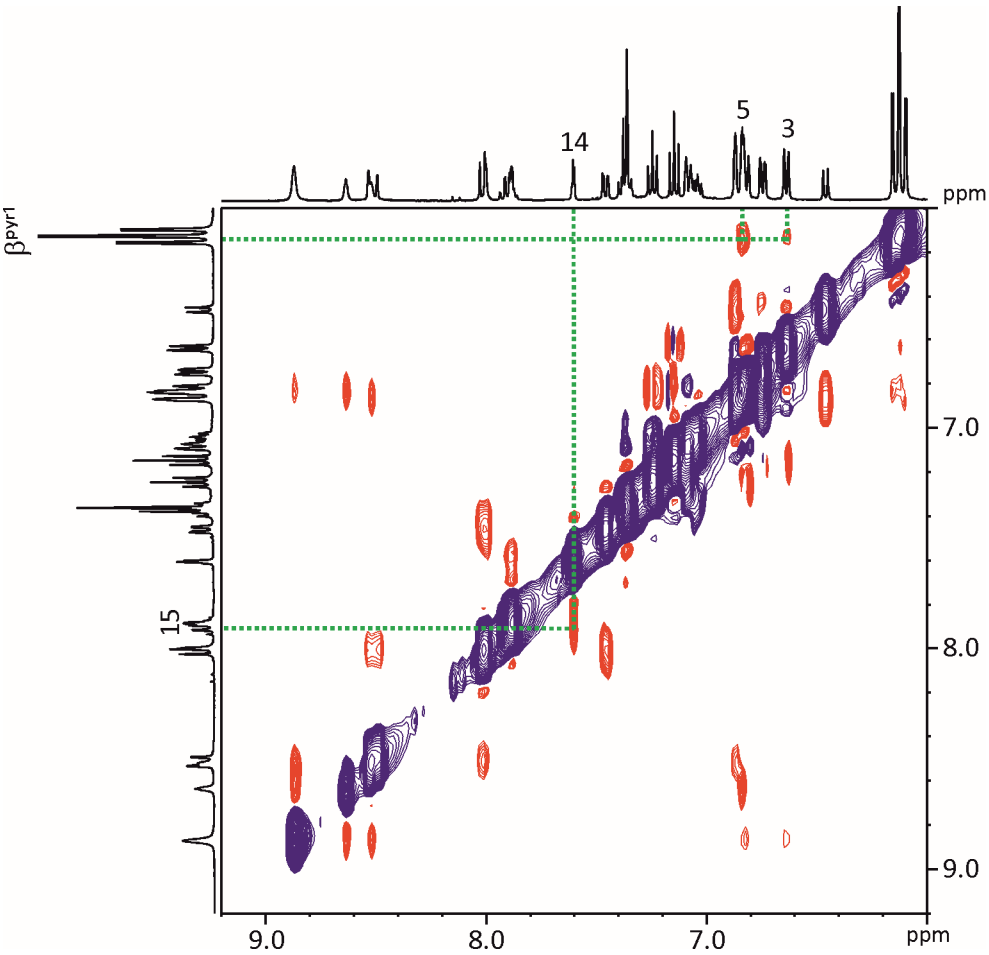

Figure 4.22 Expansion of a selected region of the 2D ROESY NMR (400 MHz, $(CD_3)_2CO$, 298 K) spectrum of the cavitand **1in**.

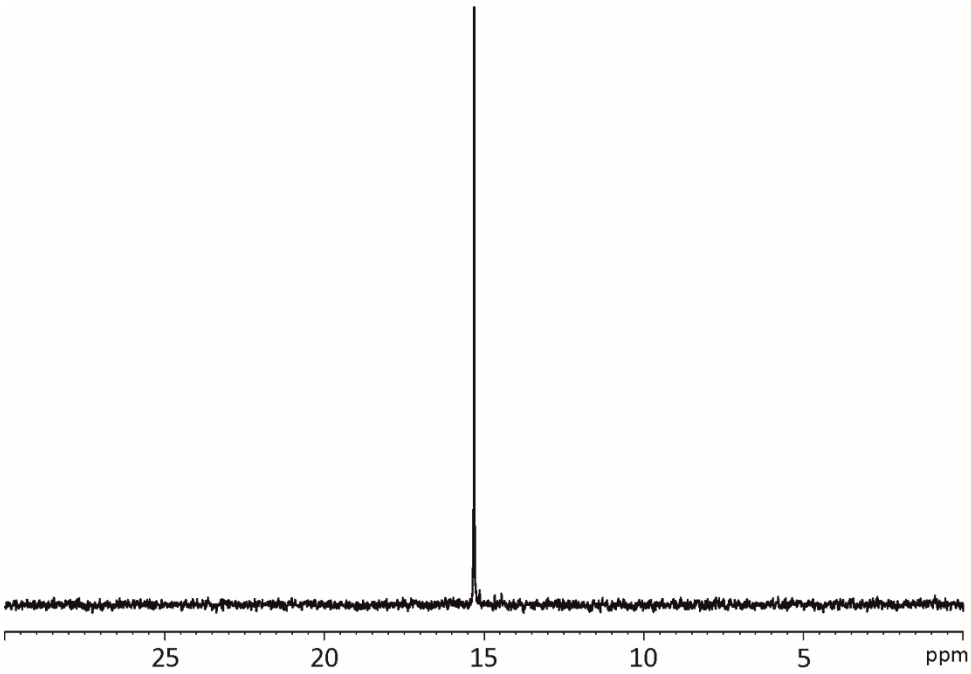

Figure 4.23 ^{31}P NMR (161 MHz, $(CD_3)_2CO$, 298 K) of cavitand **1in**.

Mono-phosphonate Calix[4]pyrrole cavitand **1out.**

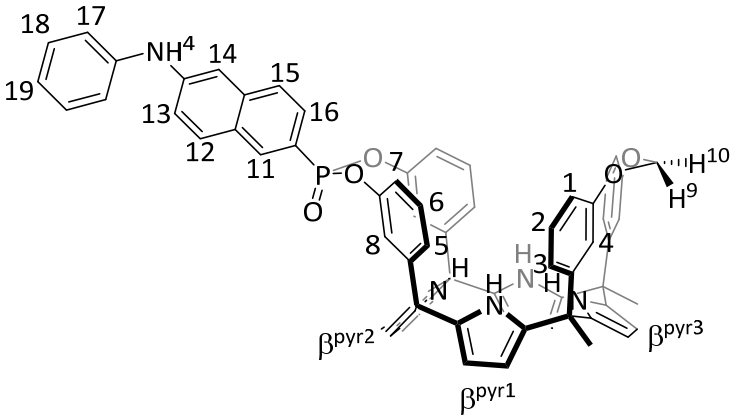

Receptor **1out**. **Rf**: 0.3 (DCM:AcOEt 98:2, SiO_2). **^{1}H NMR** (400 MHz, $(CD_3)_2CO$, 298 K): δ (ppm) = 8.81 (bs, 2H, NH^1), 8.74 (bs, 1H, NH^2), 8.45 (bs, 1H, NH^3), 8.43 (d, 1H, J = 16.38 Hz, H^{11}), 7.98 (bs, 1H, NH^4), 7.97 (d, 1H, J = 8.90 Hz, H^{12}), 7.86-7.81 (m, 2H, $H^{15,16}$), 7.61 (s, 2H, H^8), 7.58 (d, 1H, J = 2.25 Hz, H^{14}), 7.43 (dd, 1H, J_1 = 8.90 Hz, J_2 = 2.25 Hz, H^{13}), 7.39-7.30 (mult., 4H, H^{17}-H^{18}), 7.22 (t, 2H, J = 7.94 Hz, H^6), 7.11 (t, 2H, J = 7.94 Hz, H^2), 7.02 (tt, 1H, J_1 = 6.60 Hz, J_2 = 2.05 Hz, H^{19}), 6.88 (dd, 2H, J_1 = 8.35 Hz,

J_2 = 2.35 Hz, H^5), 6.82 (s, 2H, H^4), 6.79 (d, 2H, *J* = 7.94 Hz, H^7), 6.71 (dd, 2H, J_1= 8.35 Hz, J_2 = 2.60 Hz, H^1), 6.65 (d, 2H, *J* = 7.94 Hz, H^3), 6.38 (d, 1H, *J* = 8.02 Hz, H^9), 6.12 (d, 2H, *J* = 2.60 Hz, β^{pyr2}), 6.07 (d, 2H, *J* = 2.60 Hz, β^{pyr3}), 6.05 (d, 4H, *J* = 2.60 Hz, β^{pyr1}), 5.35 (d, 1H, *J* = 8.02 Hz, H^{10}), 1.93 (s, 6H, CH_3), 1.90 (s, 6H, CH_3). **^{31}P-NMR** (161 MHz, (CD3)2CO, 298 K): δ (ppm) = 14.45.

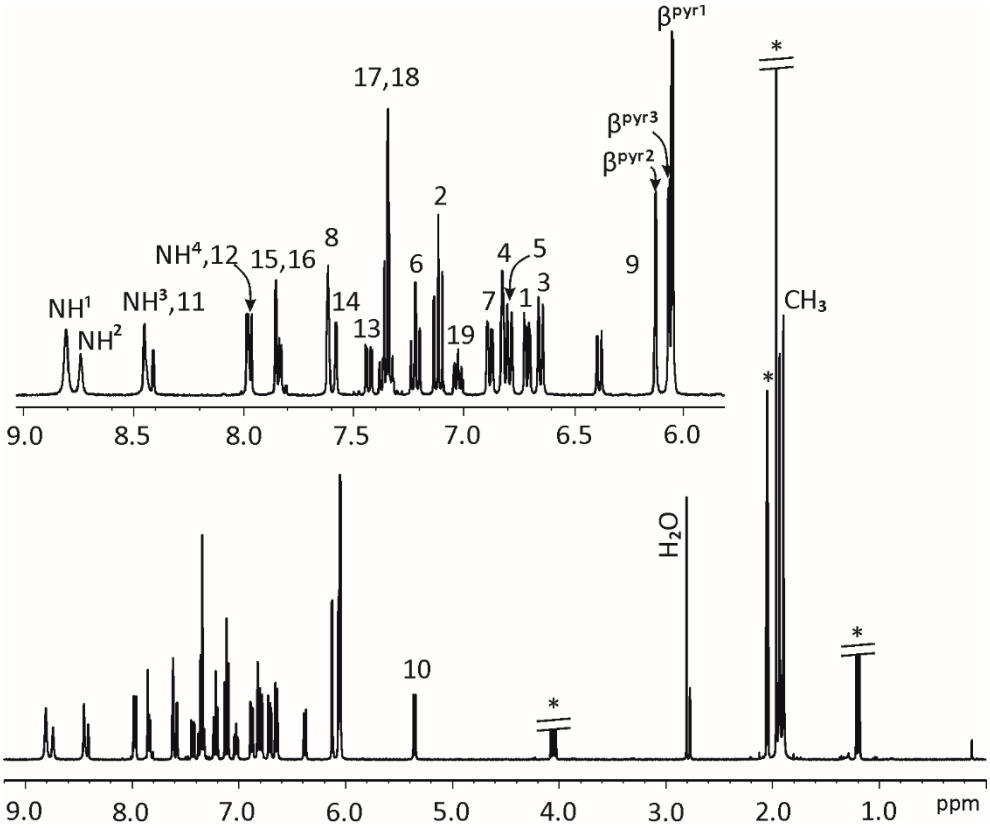

Figure 4.24 ^{1}H NMR (400 MHz, $(CD_3)_2CO$, 298 K) spectrum of cavitand **1out**.

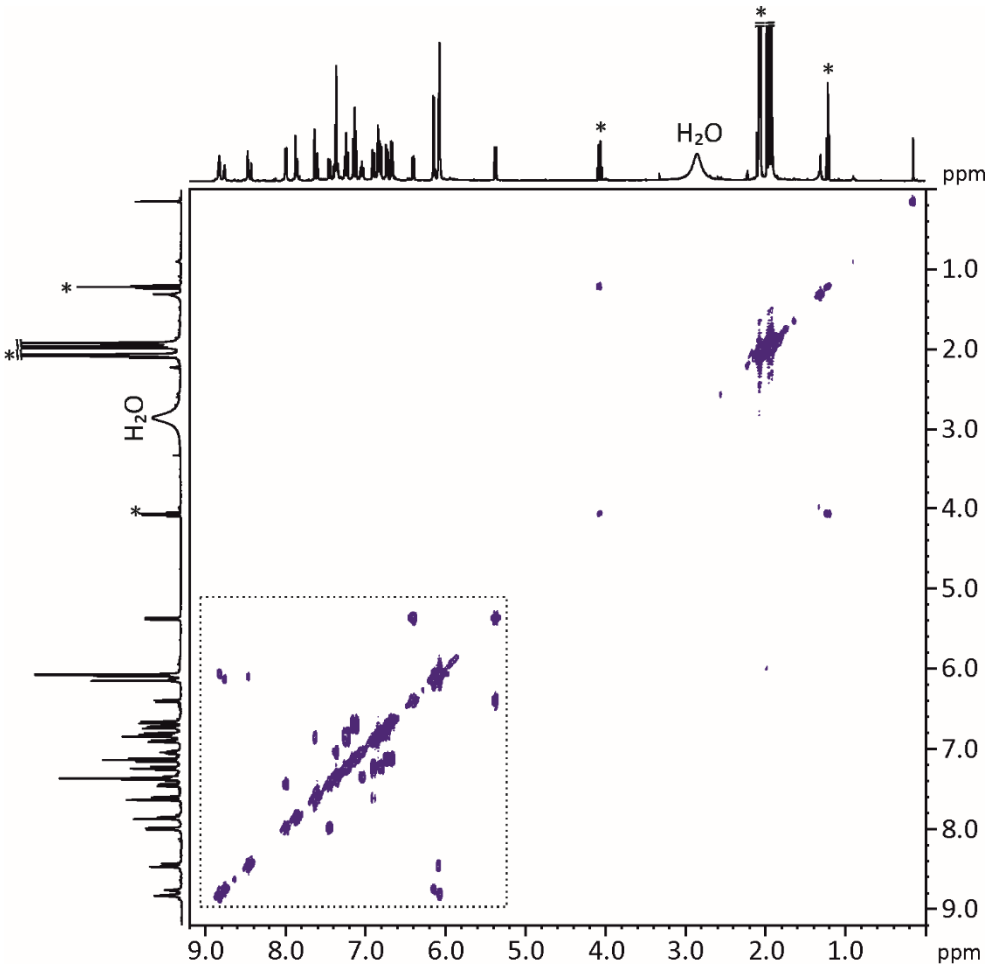

Figure 4.25 2D COSY NMR (400 MHz, $(CD_3)_2CO$, 298 K) spectrum of cavitand **1out**. * Residual solvent peak

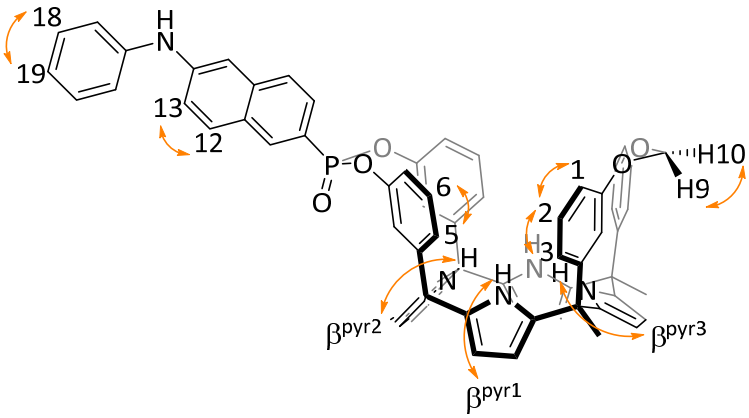

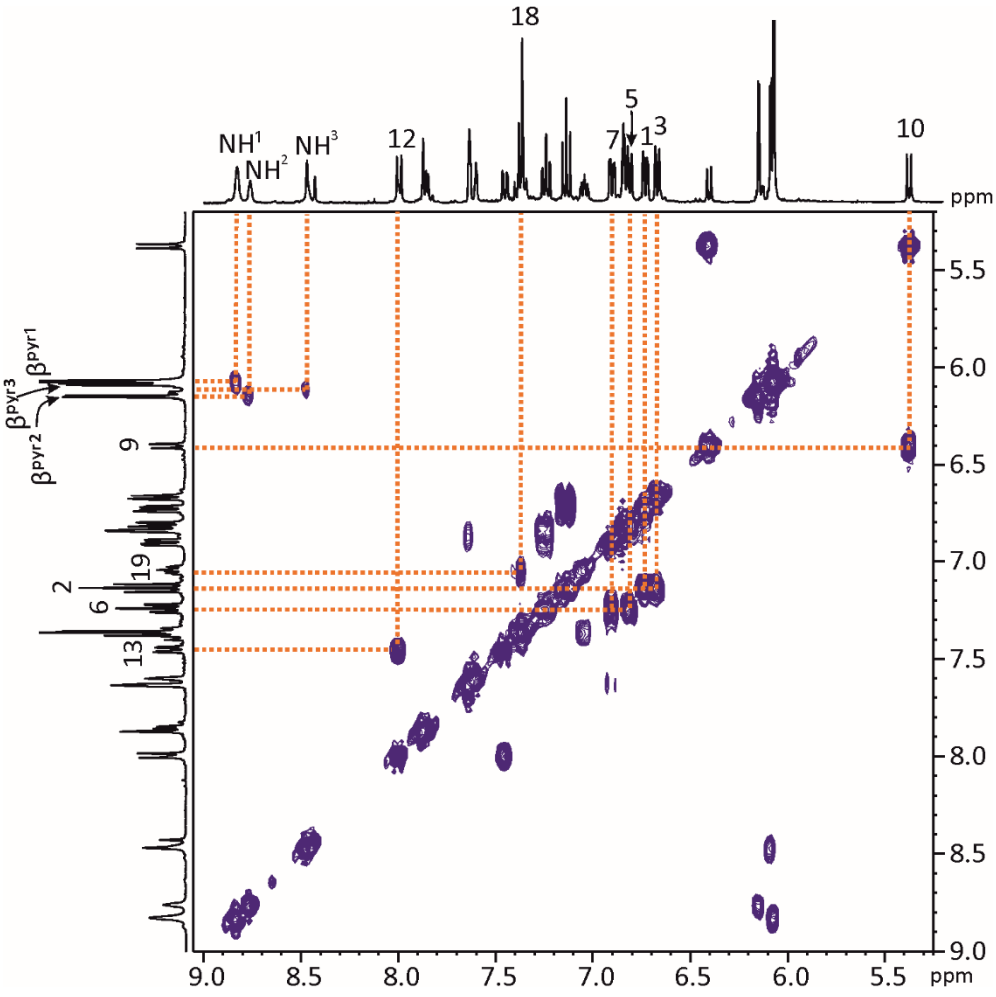

Figure 4.26 Expansion of a selected region of the 2D COSY NMR (400 MHz, $(CD_3)_2CO$, 298 K) spectrum of cavitand **1out**.

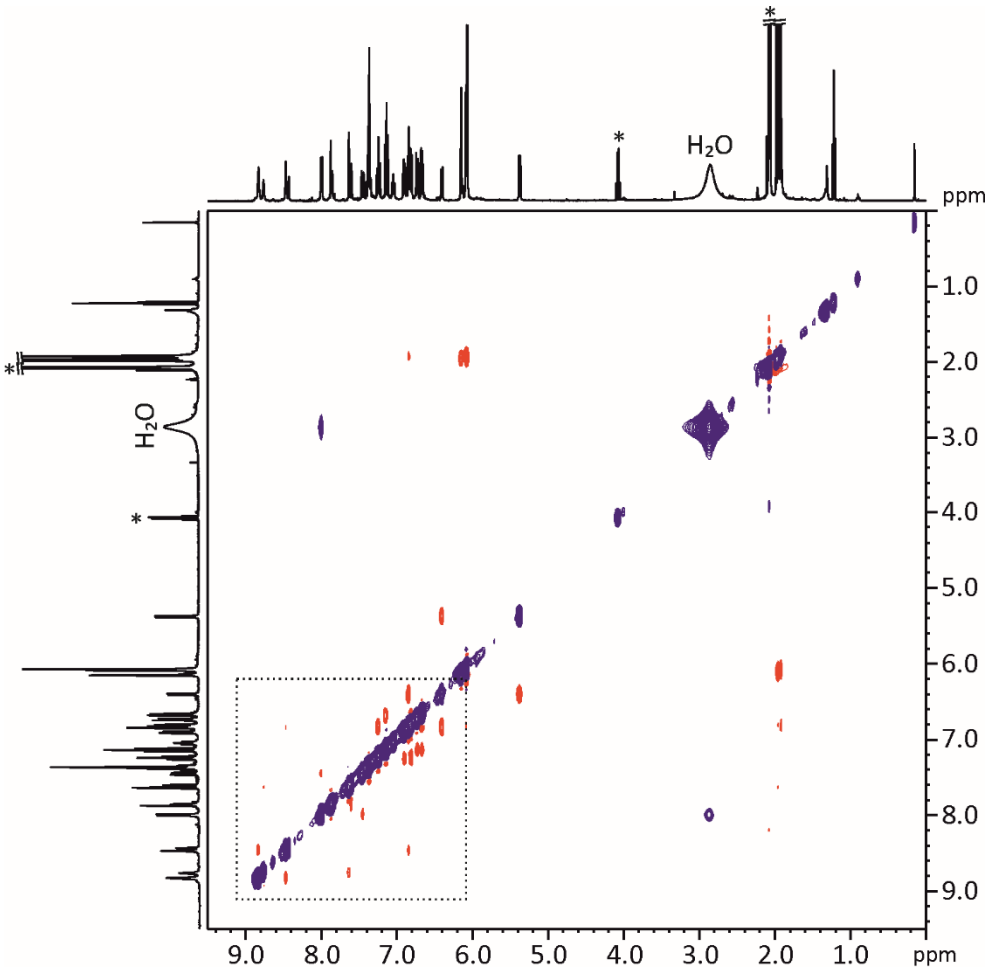

Figure 4.27 NOESY NMR (400 MHz, $(CD_3)_2CO$, 298 K) spectrum of cavitand **1out**. * Residual solvent peak.

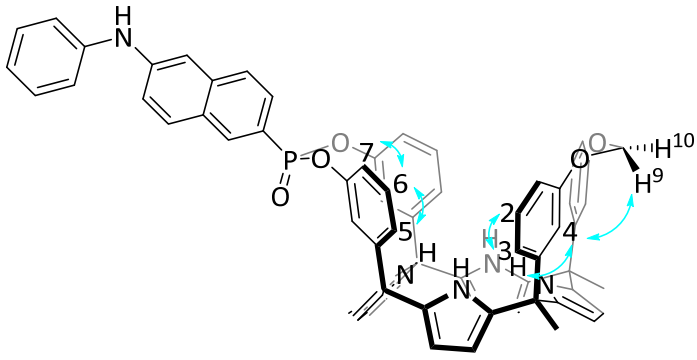

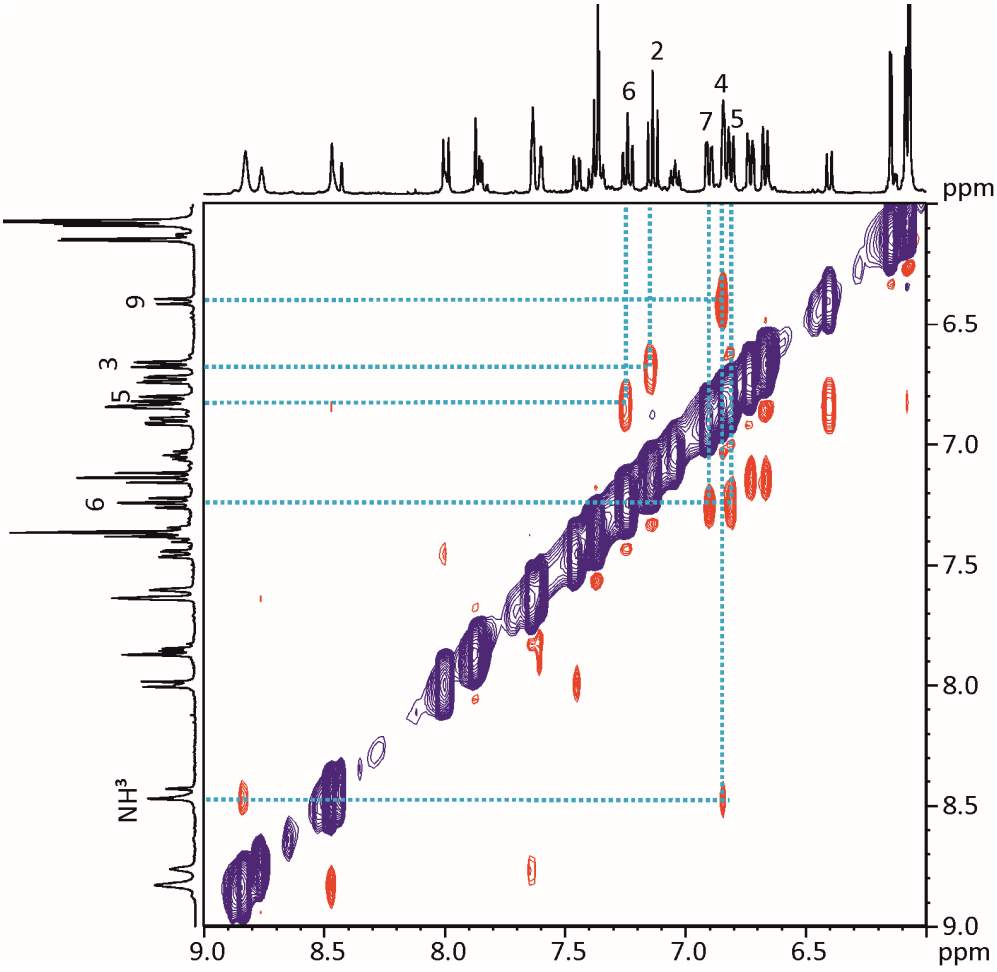

Figure 4.28 Expansion of a selected region of the 2D NOESY NMR (400 MHz, $(CD_3)_2CO$, 298 K) spectrum of cavitand **1out.**

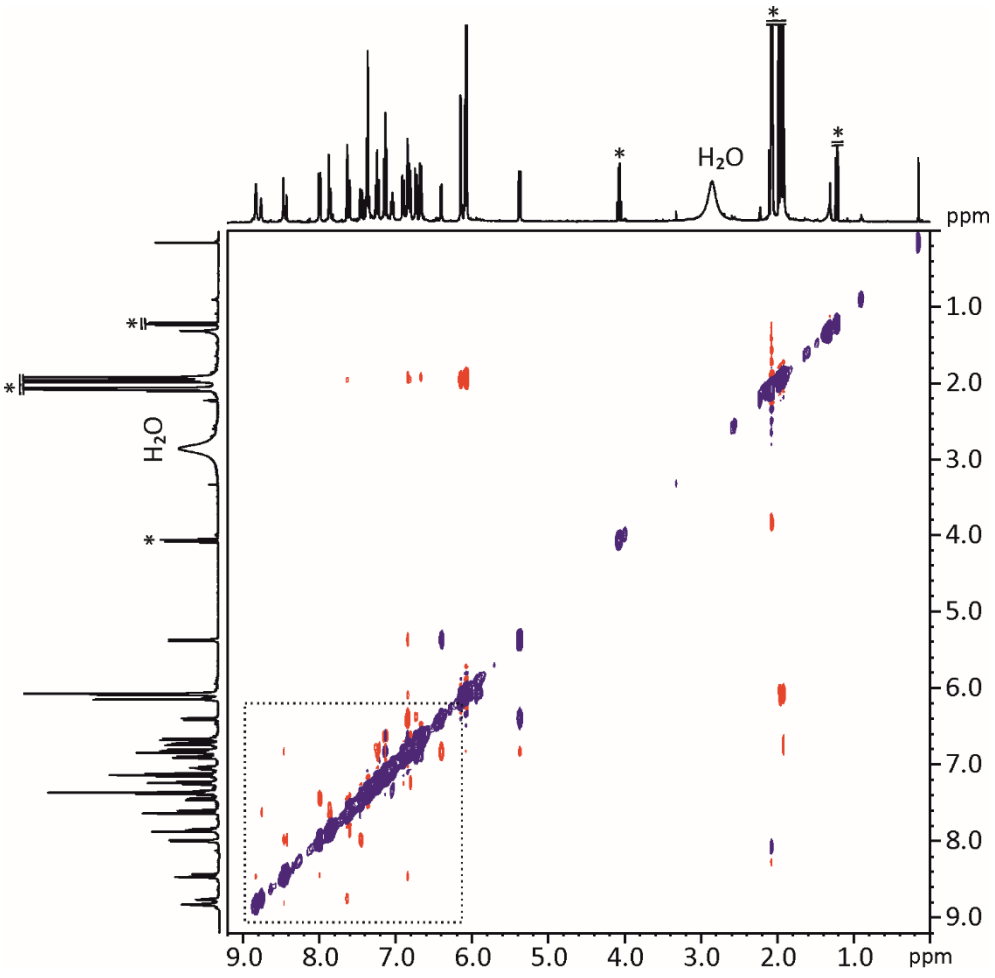

Figure 4.29 ROESY NMR (400 MHz, $(CD_3)_2CO$, 298 K) spectrum of the compound **1out**. * Residual solvent peak.

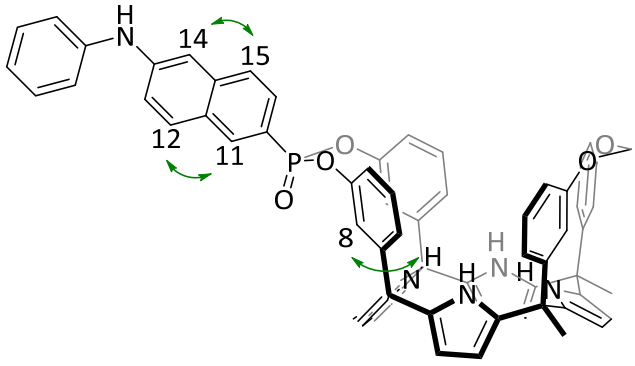

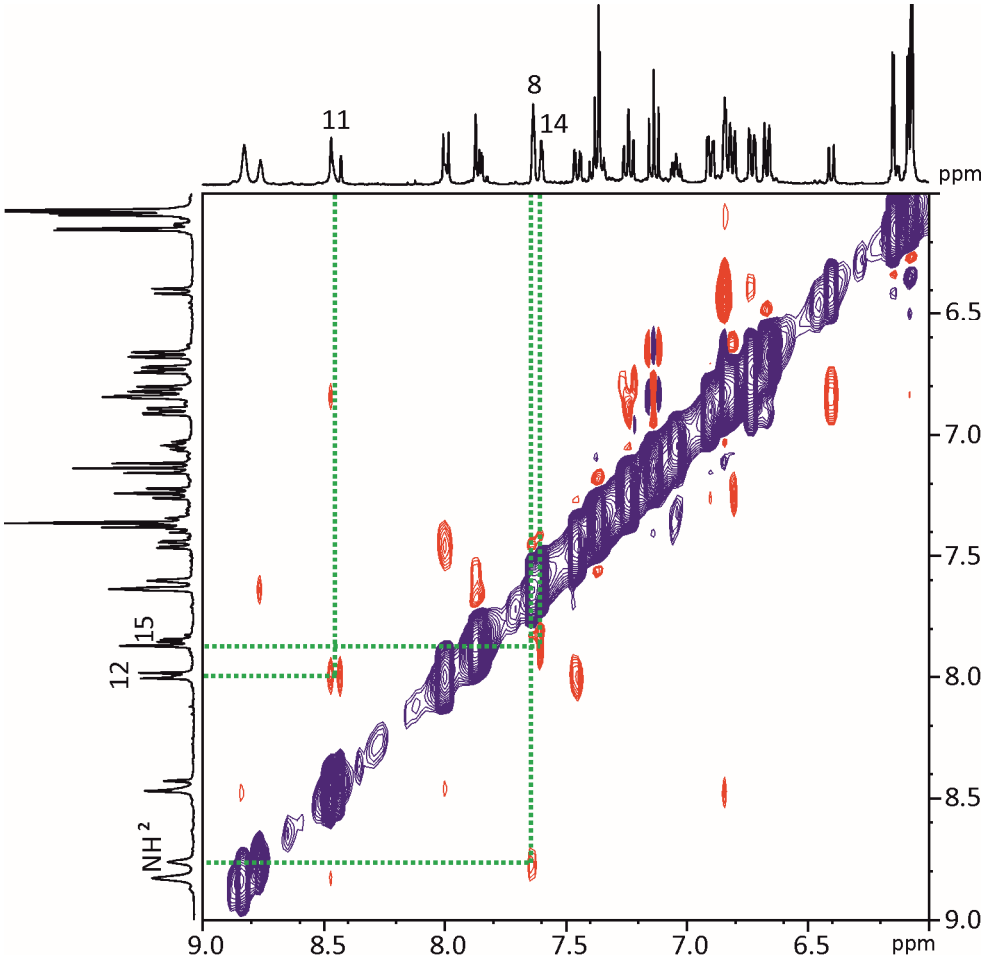

Figure 4.30 Expansion of a selected region of the 2D ROESY NMR (400 MHz, $(CD_3)_2CO$, 298 K) spectrum of cavitand **1out**.

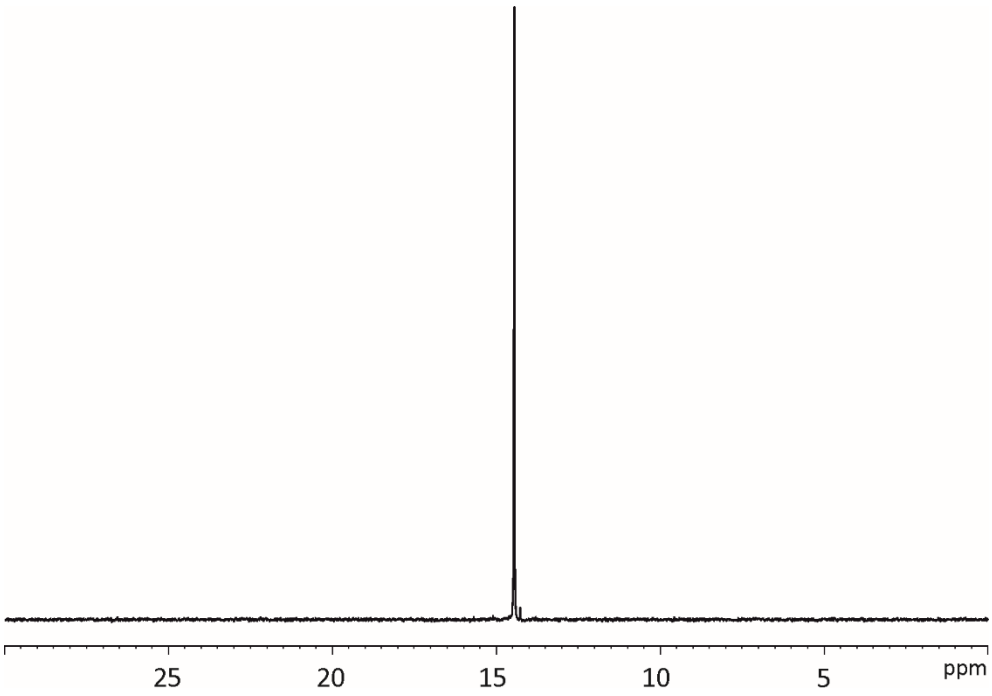

Figure 4.31 ^{31}P NMR (161 MHz, $(CD_3)_2CO$, 298 K) spectrum of compound **1out**.

4.4.3 Direct binding-based sensing (**BBS**): UV/vis absorption and emission titrations.

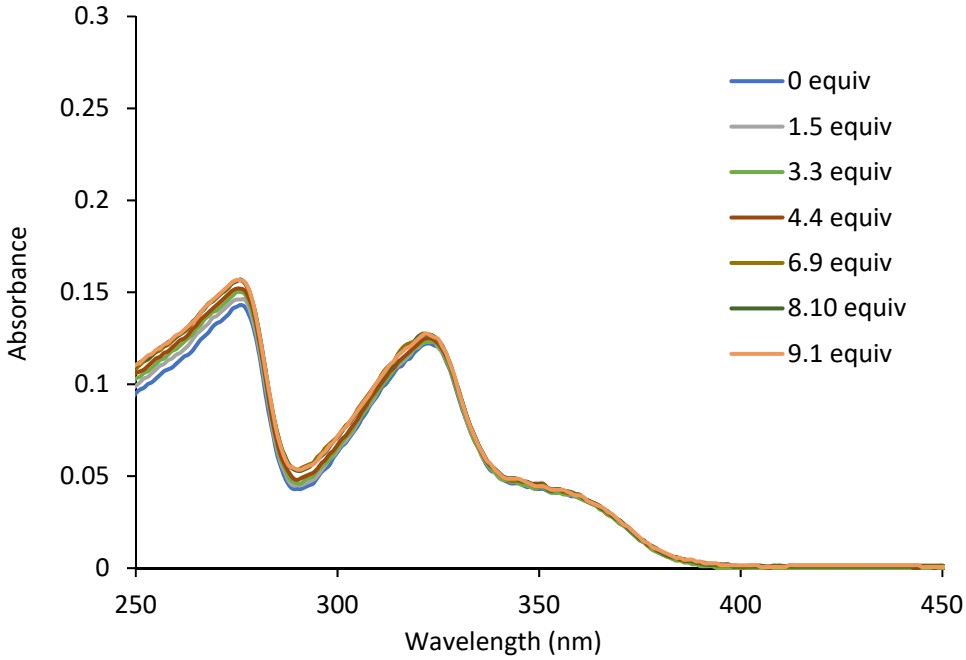

Figure 4.32 UV/vis spectra of a 1 µM solution of **7** in DCM registered during the addition of incremental amounts of L-**Pro**.

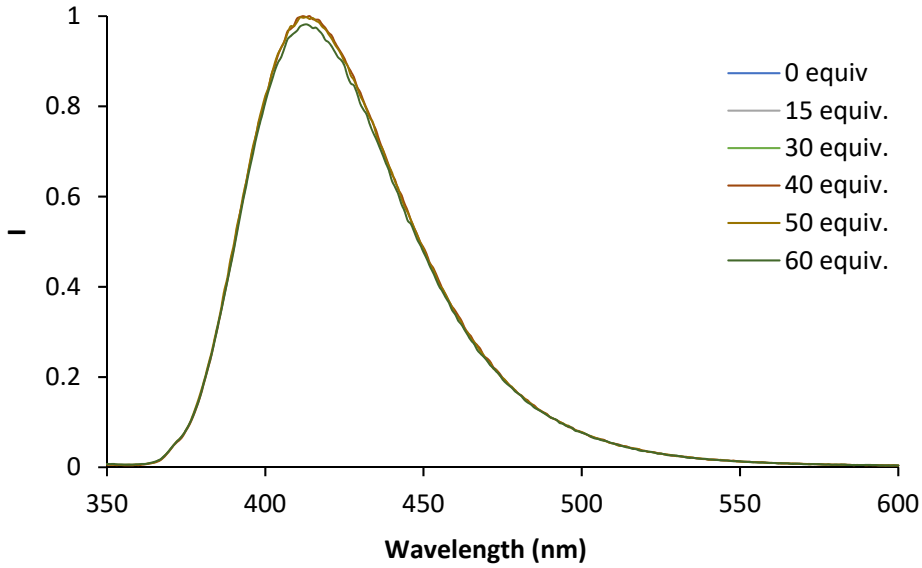

Figure 4.33 Normalized emission spectra (λ_{exc} = 335 nm) of **7** (1 µM) in DCM registered during the addition of incremental amounts of L-**Pro**.

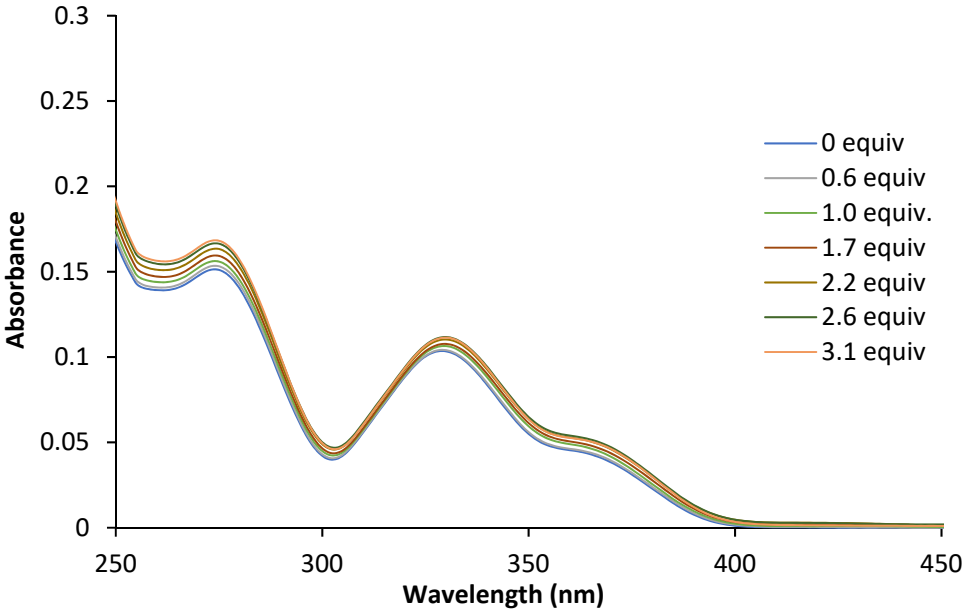

Figure 4.34 UV/vis spectra of a 1 µM solution of **1in** in DCM registered during the addition of incremental amounts of L-**Pro**.

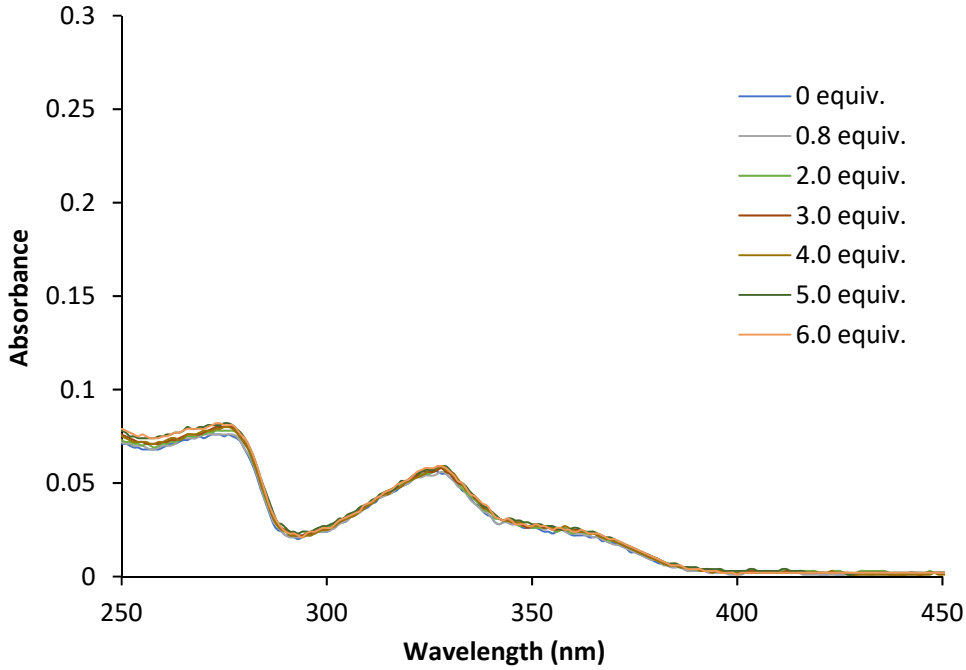

Figure 4.35 UV/vis spectra of a 0.5 μM solution of **1in** in DCM registered during the addition of incremental amounts of L-**Pip**.

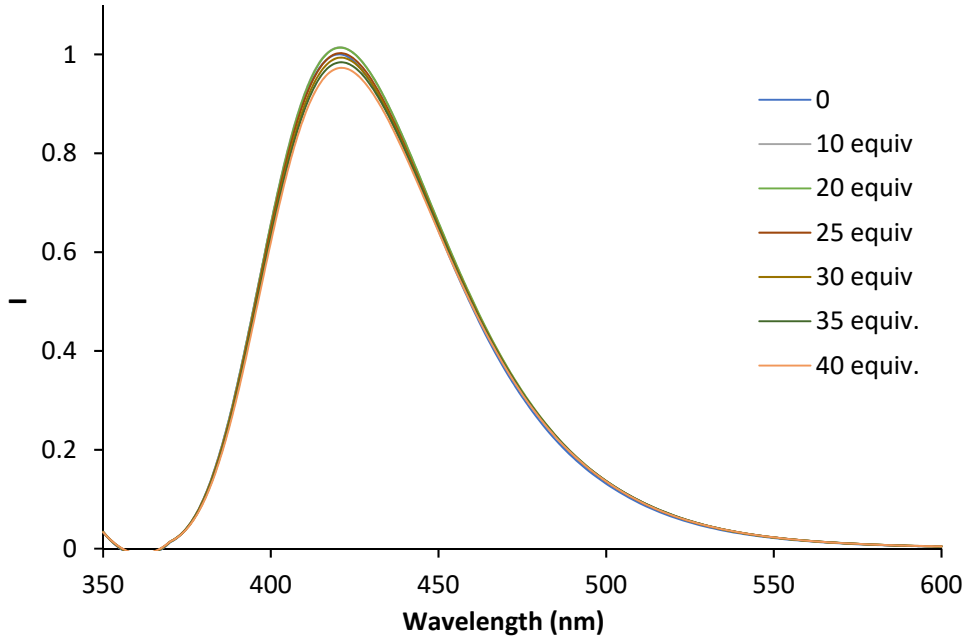

Figure 4.36 Normalized emission spectra (λ_{exc} = 335 nm) of **1in** (1 μM) in DCM registered during the addition of incremental amounts of L-**Pip**.

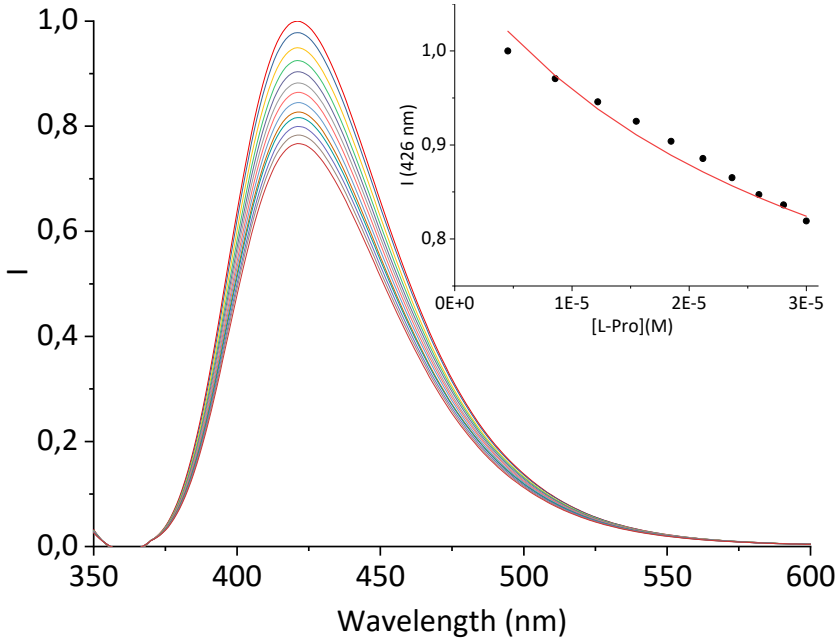

Figure 4.37 Normalized emission spectra (λ_{exc} = 335 nm) of **1out** (1 μM) in DCM registered during the addition of incremental amounts of L-**Pip**. Inset: Plot of the emission change at 426 nm (black circles) vs concentration of L-**Pip**. The red line corresponds to the fit of the titration data.

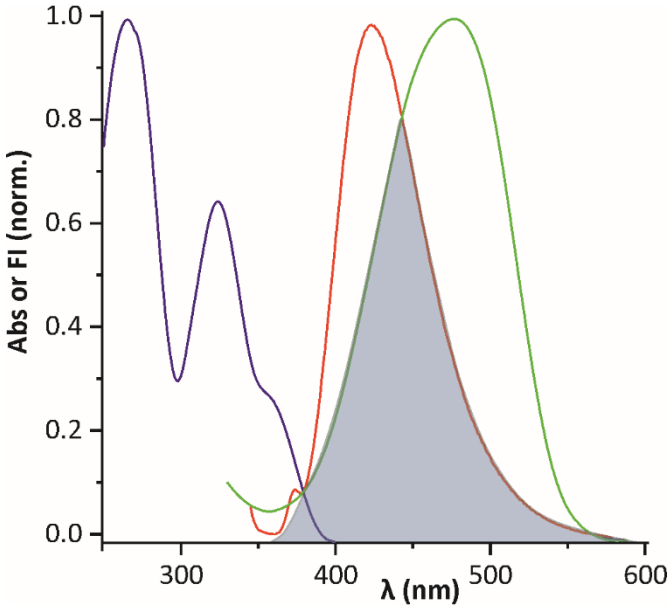

Figure 4.38 UV/vis absorption spectra of **1in** (blue) and **6** (red) and the fluorescence spectrum of **1in** (green). The spectral overlap is highlighted in grey.

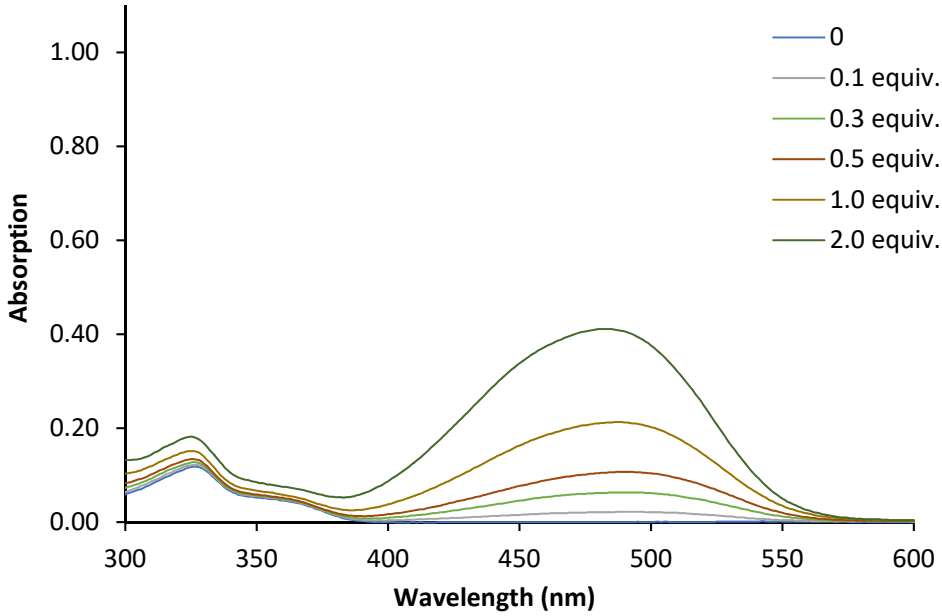

Figure 4.39 UV/vis spectra of a 0.5 µM solution of **1in** in DCM registered during the addition of incremental amounts of **6**.

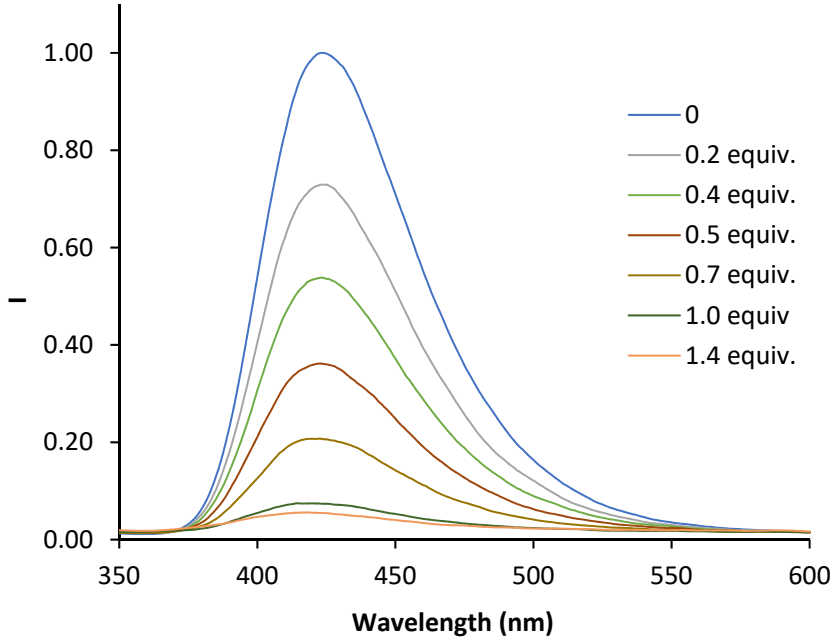

Figure 4.40 Normalized emission spectra (λ_{exc} = 335 nm) of **1in** (5 µM) in DCM registered during the addition of incremental amounts of **6**.

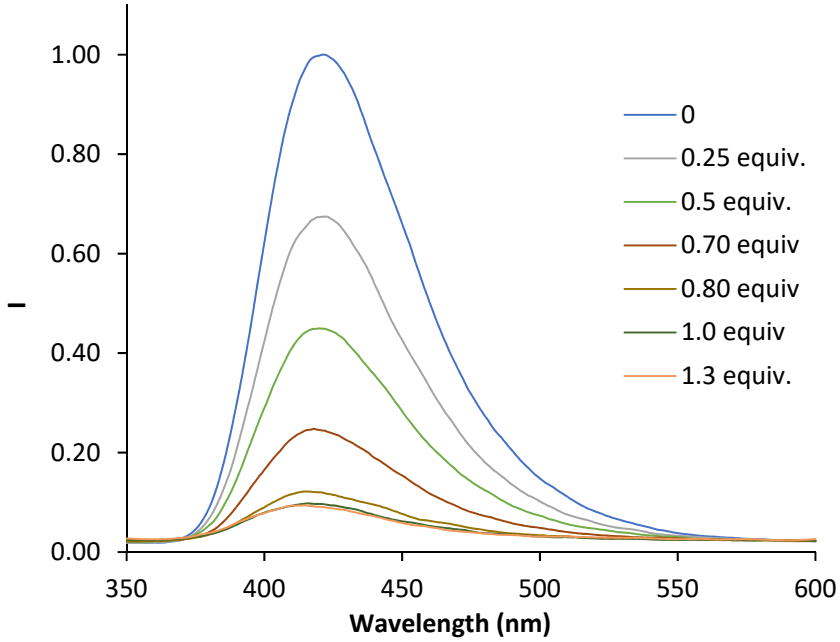

Figure 4.41 Normalized emission spectra (λ_{exc} = 335 nm) of **1out** (5 µM) in DCM registered during the addition of incremental amounts of **6**.

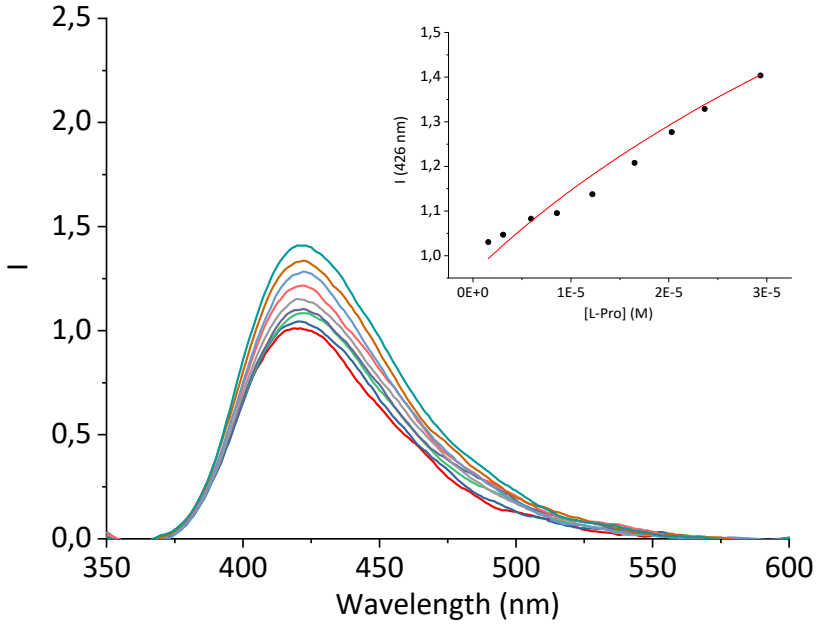

Figure 4.42 Normalized emission spectra registered during the competitive IDA experiments of **6⊂1out** complex with incremental addition of L-**Pro** in dichloromethane solution; λ_{exc} = 335 nm. Inset: Plot of

the emission change at 426 nm (black circles) vs concentration of L-Pro. The red line corresponds to the fit of the titration data.

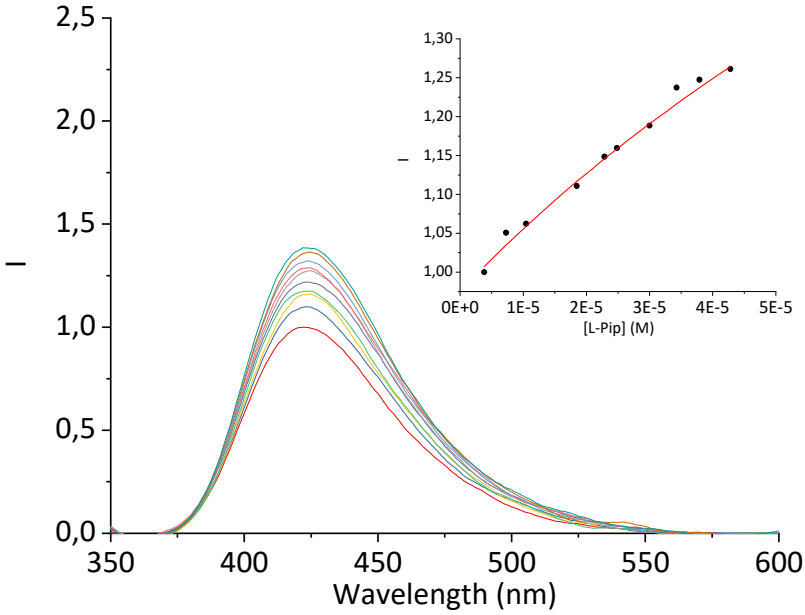

Figure 4.43 Normalized emission spectra registered during the competitive IDA experiments of **6⊂1in** complex with incremental addition of L-**Pip** in dichloromethane solution; λ_{exc} = 335 nm. Inset: Plot of the emission change at 426 nm (black circles) vs concentration of L-**Pip**. The red line corresponds to the fit of the titration data.

4.4.4 Molecular modeling

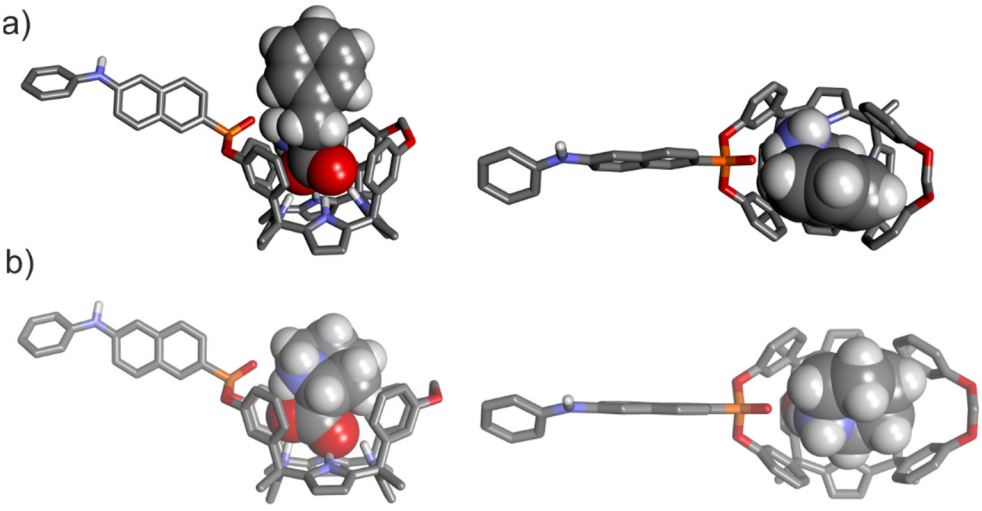

Figure 4.44 Side and top views of the energy-minimized inclusion complexes a) L-**Phe⊂1in** and b) L-**Pip$_{ax}$⊂1in**. The structures are energy minima at the BP86/def2-SVP level of theory. The receptors are shown in stick representation. Non-polar hydrogen atoms of the host were removed for clarity. The included amino acids are depicted as CPK models.

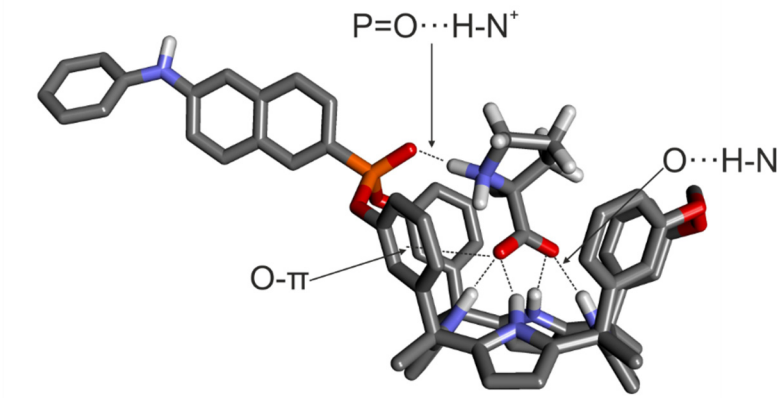

Figure 4.45 Side view of the energy-minimized inclusion complex L-**Pip$_{eq}$⊂1in**. Hydrogen bond and O-π interactions are indicated. The structures are energy minima at the BP86/def2-SVP level of theory. The receptor and the included amino acid are shown in stick representation. Non-polar hydrogen atoms of the receptor were removed for clarity.

4.5 References and notes.

[1] Lou, Z.; Wang, L.; Shen, G. *Advanced Materials Technologies* **2018**, *3*, 1800444.
[2] Purohit, B.; Kumar, A.; Mahato, K.; Chandra, P. *Current Opinion in Biomedical Engineering* **2020**, *13*, 42-50.
[3] Subrahmanyam, S.; Piletsky, S. A.; Turner, A. P. F. *Analytical Chemistry* **2002**, *74*, 3942-3951.
[4] Pinalli, R.; Pedrini, A.; Dalcanale, E. *Chemical Society Reviews* **2018**, *47*, 7006-7026.
[5] Guo, C.; Sedgwick, A. C.; Hirao, T.; Sessler, J. L. *Coordination Chemistry Reviews* **2021**, *427*, 213560.
[6] Pirondini, L.; Dalcanale, E. *Chem. Soc. Rev.* **2007**, *36*, 695-706.
[7] Guinovart, T.; Hernández-Alonso, D.; Adriaenssens, L.; Blondeau, P.; Martínez-Belmonte, M.; Rius, F. X.; Andrade, F. J.; Ballester, P. *Angewandte Chemie International Edition* **2016**, *55*, 2435-2440.
[8] Erenas, M. M.; Ortiz-Gómez, I.; De Orbe-Payá, I.; Hernández-Alonso, D.; Ballester, P.; Blondeau, P.; Andrade, F. J.; Salinas-Castillo, A.; Capitán-Vallvey, L. F. *ACS Sensors* **2019**, *4*, 421-426.
[9] Sierra, A. F.; Hernández-Alonso, D.; Romero, M. A.; González-Delgado, J. A.; Pischel, U.; Ballester, P. *Journal of the American Chemical Society* **2020**, *142*, 4276-4284.
[10] Martínez-Crespo, L.; Sun-Wang, J. L.; Sierra, A. F.; Aragay, G.; Errasti-Murugarren, E.; Bartoccioni, P.; Palacín, M.; Ballester, P. *Chem* **2020**, *6*, 3054-3070.
[11] Maffei, F.; Betti, P.; Genovese, D.; Montalti, M.; Prodi, L.; De Zorzi, R.; Geremia, S.; Dalcanale, E. *Angewandte Chemie International Edition* **2011**, *50*, 4654-4657.
[12] Sedgwick, A. C.; Brewster, J. T.; Wu, T.; Feng, X.; Bull, S. D.; Qian, X.; Sessler, J. L.; James, T. D.; Anslyn, E. V.; Sun, X. *Chemical Society Reviews* **2021**, *50*, 9-38.
[13] Ciardi, M.; Tancini, F.; Gil-Ramírez, G.; Escudero Adán, E. C.; Massera, C.; Dalcanale, E.; Ballester, P. *Journal of the American Chemical Society* **2012**, *134*, 13121-13132.
[14] Plecko, B.; Hikel, C.; Korenke, G. C.; Schmitt, B.; Baumgartner, M.; Baumeister, F.; Jakobs, C.; Struys, E.; Erwa, W.; Stöckler-Ipsiroglu, S. *Neuropediatrics* **2005**, *36*, 200-205.
[15] We performed an additional solid–liquid extraction competitive experiment in which we left the suspension under stirring overnight. The ^{1}H NMR spectra of the filtered solution did not show significant changes to the one obtained after5 minutes hand-shook extraction.
[16] Solubility was calculated by preparing 1 mL saturated solutions of L-**Pro** and L-**Pip** in dichloromethane at 298 K. Evaporation of the solvent and accurate weight of the resulting solids returned the solubility of L-**Pro** and L-**Pip** in dichloromethane as 8×10^{-4} and 5×10^{-4} mol L^{-1}, respectively.
[17] We did not find significant differences in the fluorescence emission of **1in** and **1out** in dichloromethane.
[18] We did not see the formation of any precipitate after the addition of L-**Pip** to a micromolar dichloromethane solution of **1out** as observed in the analogous experiments at millimolar concentration (i.e. NMR experiments). We consider that at micromolar concentration the L-**Pip⊂1out** complex is soluble in dichloromethane. Therefore, we conclude that the decrease in fluorescence intensity is not related to the precipitation of the complex.
[19] Slit width of the monochromator as 1 nm.
[20] These experimental conditions forced us to modify the slit width of the mono-chromator settings (from 1 nm to 5 nm). These new parameters did not allow us to consider the **6⊂1in**

host–guest complex non-emissive as occurred with the previous instrument set-up. Hence, the titration data was fit to a theoretical 1:1binding model that considered two emissive species (free and bound **1in**).

[21] The competitive displacement of guest **6** from the cavity of **1in** by L-**Pro** in CD_2Cl_2 was not possible at millimolar concentration due to the poor solubility of L-Pro in this solvent.

[22] The **6⊂1in** complex was considered non-emissive under the experimental conditions and the instrument set up used for the titration (slit width of the monochromator = 1 nm).

[23] Peñuelas-Haro, G.; Ballester, P. *Chemical Science* **2019**, *10*, 2413-2423.

[24] Perdew, J. P. *Physical Review B* **1986**, *33*, 8822-8824.

[25] Becke, A. D. *Physical Review A* **1988**, *38*, 3098-3100.

[26] Frisch, M. J.; Trucks, G. W.; Schlegel, H. B.; Scuseria, G. E.; Robb, M. A.; Cheeseman, J. R.; Scalmani, G.; Barone, V.; Petersson, G. A.; Nakatsuji, H.; Li, X.; Caricato, M.; Marenich, A. V.; Bloino, J.; Janesko, B. G.; Gomperts, R.; Mennucci, B.; Hratchian, H. P.; Ortiz, J. V.; Izmaylov, A. F.; Sonnenberg, J. L.; Williams; Ding, F.; Lipparini, F.; Egidi, F.; Goings, J.; Peng, B.; Petrone, A.; Henderson, T.; Ranasinghe, D.; Zakrzewski, V. G.; Gao, J.; Rega, N.; Zheng, G.; Liang, W.; Hada, M.; Ehara, M.; Toyota, K.; Fukuda, R.; Hasegawa, J.; Ishida, M.; Nakajima, T.; Honda, Y.; Kitao, O.; Nakai, H.; Vreven, T.; Throssell, K.; Montgomery Jr., J. A.; Peralta, J. E.; Ogliaro, F.; Bearpark, M. J.; Heyd, J. J.; Brothers, E. N.; Kudin, K. N.; Staroverov, V. N.; Keith, T. A.; Kobayashi, R.; Normand, J.; Raghavachari, K.; Rendell, A. P.; Burant, J. C.; Iyengar, S. S.; Tomasi, J.; Cossi, M.; Millam, J. M.; Klene, M.; Adamo, C.; Cammi, R.; Ochterski, J. W.; Martin, R. L.; Morokuma, K.; Farkas, O.; Foresman, J. B.; Fox, D. J. Wallingford, CT, 2016.

UNIVERSITAT ROVIRA I VIRGILI
CALIX[4]PYRROLE CAVITANDS FOR SUPRAMOLECULAR SENSING AND CATALYSIS
Andrés Felipe Sierra Ramos

Chapter 5

Direct supramolecular sensing of creatinine

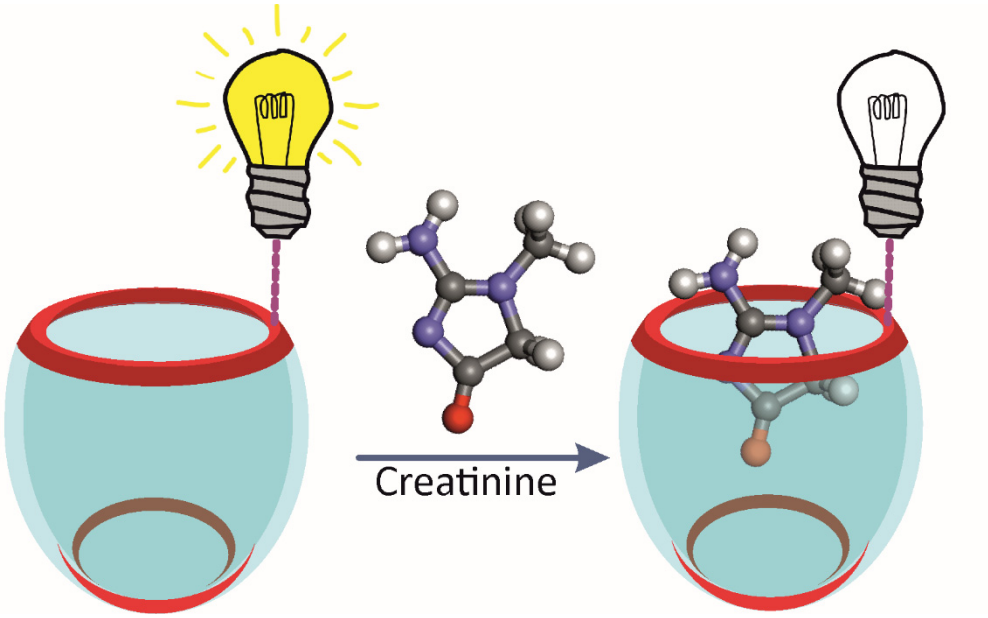

UNIVERSITAT ROVIRA I VIRGILI
CALIX[4]PYRROLE CAVITANDS FOR SUPRAMOLECULAR SENSING AND CATALYSIS
Andrés Felipe Sierra Ramos

5.1 Introduction.

In **Chapter 3** and **4**, we presented calix[4]pyrrole based IDAs for the sensing of creatinine and L-proline, respectively.[1,2] However, the fluorescent calix[4]pyrrole cavitands were not useful for the direct binding based sensing of the analytes. That is, the receptor itself was not able to translate the binding event into a measurable signal (i.e. small or no fluorescent changes were observed between the free and bound cavitands).

In the present chapter, we report the synthesis and binding properties of two unprecedented fluorescent monophosphonate C4P receptors, **4** and **5** (Figure 5.*1*), decorated with a dansyl group as signaling unit.

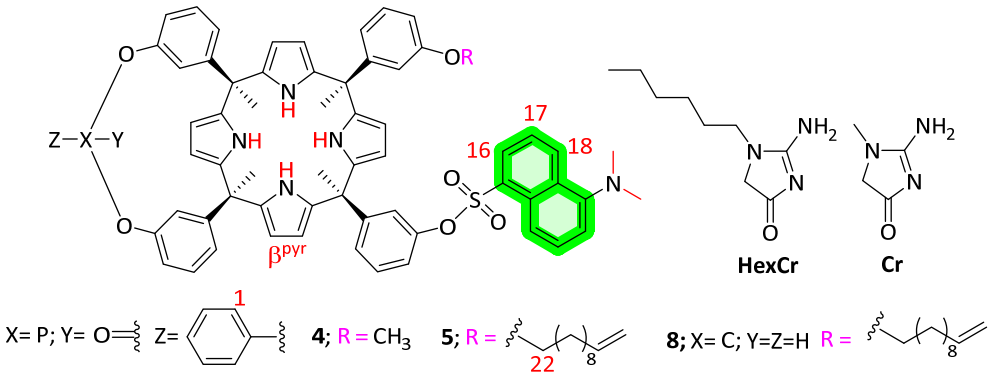

Figure 5.1 Line drawing structures of fluorescent receptors **4** and **5** and guests **Cr** and **HexCr**.

Interestingly, receptors **4** and **5** displayed significant changes in their emission properties upon **Cr** and **HexCr** binding (Figure 5.*2*). In other words, the new developed receptors are able to perform an efficient molecular recognition for the analytes and produce a transducible signal as a response for this binding event. Specifically, the addition of increasing amounts of **HexCr** resulted in the gradual quenching of the fluorescence of the fluorophore covalently attached to the cavitand.

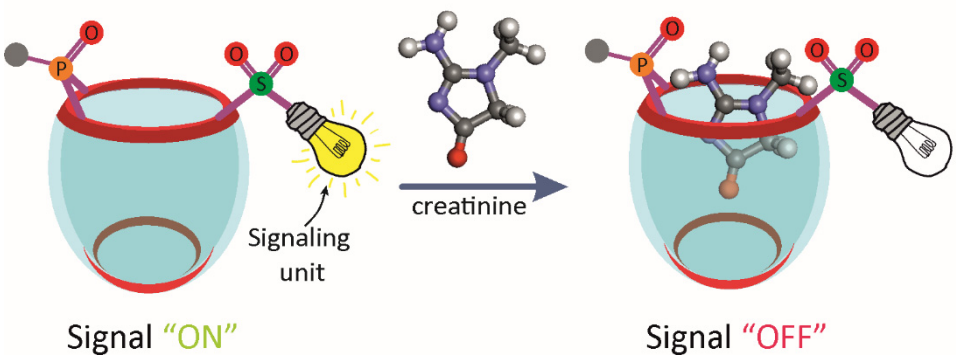

Figure 5.2 Cartoon representation of a binding-based sensing of creatinine.

5.2 Results and discussion.

5.2.1 Synthesis

Receptors **4** and **5** (Scheme 5.*1*), were prepared starting from the known α,α,α,α-tetrahydroxycalix[4]pyrrole **1**. First, receptor **1** was reacted with an equimolar mixture of phenylphosphonic dichloride in THF using triethylamine as a base to yield the mono-phosphonate bridged calix[4]pyrrole **2**. This reaction mainly produced a mixture of two phosphonate diastereoisomers (**2i** and **2o**) which differ in the spatial orientation of the phosphonate group with respect to the cavity (inward or outward, respectively). The two isomers were separated by column chromatography purification on silica gel of the crude reaction mixture and obtained in 20% yield. Considering the demonstrated relevance of the P=O bond orientation in the binding properties of the receptor, we continued the synthetic pathway only with the isomer with the P=O group inwardly oriented (**2i**).

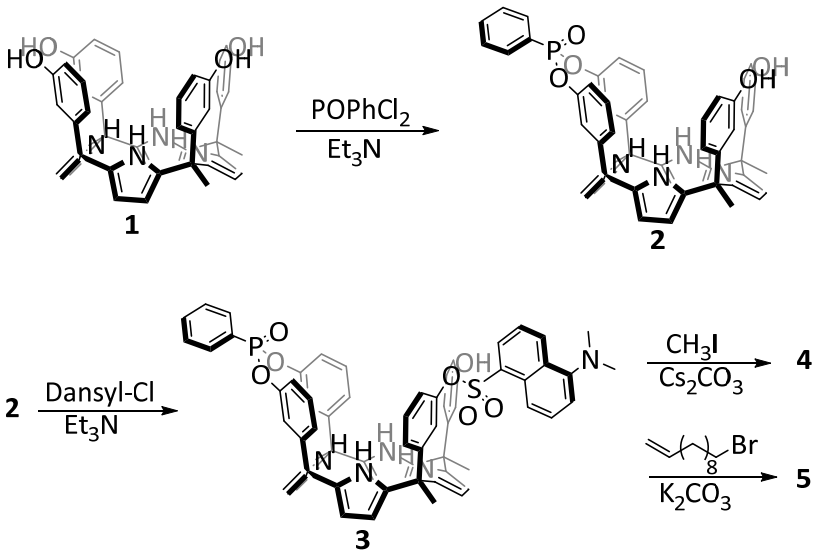

Scheme 5.1 Synthetic Scheme for the preparation of the fluorescent cavitands **4** and **5**.

The nucleophilic substitution reaction of the mono-phosphonate receptor **2i** with 1.0 equiv. of dansyl chloride in dry acetonitrile, produced a green precipitate. A further crystallization of this precipitate in hot acetonitrile afforded the corresponding fluorescent calix[4]pyrrole **3**, featuring the dansyl group covalently attached directly to the aromatic wall through a sulfonic ester bond. Finally, reaction of receptor **3** with methyl iodine and 11-bromo-1-undecene, produced receptors **4** and **5**, respectively. Compound **4** was obtained without further purification. We isolated pure **5** after column chromatography using CH_2Cl_2 as eluent in 40% yield. The installation of the long alkyl chain with a terminal alkene will be used in a near future as grafting moiety for Si (1,0,0) surfaces by hydrosilylation reaction.

Single crystals of **3** and **4** suitable for X-ray diffraction analysis were obtained from the slow evaporation of a 1:1 acetone:dichloromethane mixture and acetone solution, respectively (Figure 5.*3*, Figure 5.*32*). In both crystal structures, the calix[4]pyrrole core adopts a cone conformation with one acetone molecule included in the aromatic cavity, establishing four hydrogen bonding interactions with the pyrrole NHs. Additionally, the solid-state structure of receptor **3** has a dichloromethane molecule accommodated on the electronic rich aromatic cavity define by the pyrrole rings of the receptor in the cone conformation. In both receptors the dansyl group is located in equatorial position far from the receptor´s cavity.

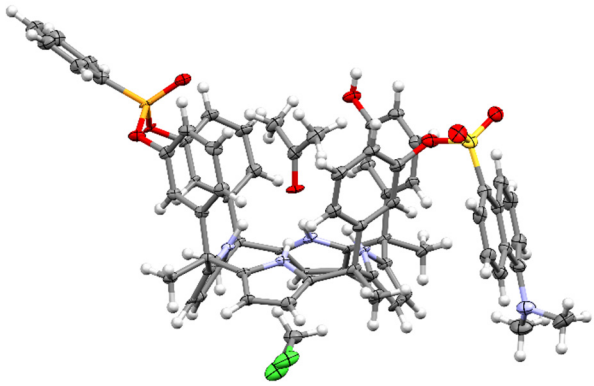

Figure 5.3 X-ray structure of the receptor **3**. Thermal ellipsoids set at 50% probability; H atoms are shown as spheres of 0.20 Å diameter.

We also synthesized receptor **8**, the methylene-bridged analogue of **5** following similar reaction conditions to those used for receptor **5** (Scheme 5.*2*).

Receptors **3**, **4**, **5** and **8** and some of their intermediates were fully characterized by means of 1D and 2D high-resolution NMR experiments. We only include the 2D NMR analysis for the final receptors with the attached undecenyl chain (Figure 5.*10* to Figure 5.*21*).

5.2.2 NMR binding studies of receptor **5** with **HexCr**.

We performed binding studies of receptors **4** and **5** with **HexCr** in dichloromethane solution. For the sake of brevity, and considering the analogous behavior observed for both receptors, we only report here the experiments performed with receptor **5**.

We probed the interaction of the fluorescent receptor **5** with **HexCr**, using ^{1}H and ^{31}P NMR titration experiments in CD_2Cl_2 solutions at millimolar concentration.

The ^{1}H NMR spectrum of **5** showed a set of sharp and well-defined proton signals (Figure 5.4a, left). In particular, the pyrrole NHs emerged at 9.07, 8.17 and 8.11 ppm as three broad singlets. Moreover, we detected the protons belonging to the dansyl unit. For example, the doublet at 8.59 ppm and the triplet at 7.43 ppm displaying the same *J*-coupling (8.01 MHz) were assigned to protons H^{18} and H^{17}, respectively. Besides, the singlet resonating at 2.86 ppm assigned to the *N*-methyl protons of the dansyl group support the covalent attachment to one of the aromatic walls of the calix[4]pyrrole structure.

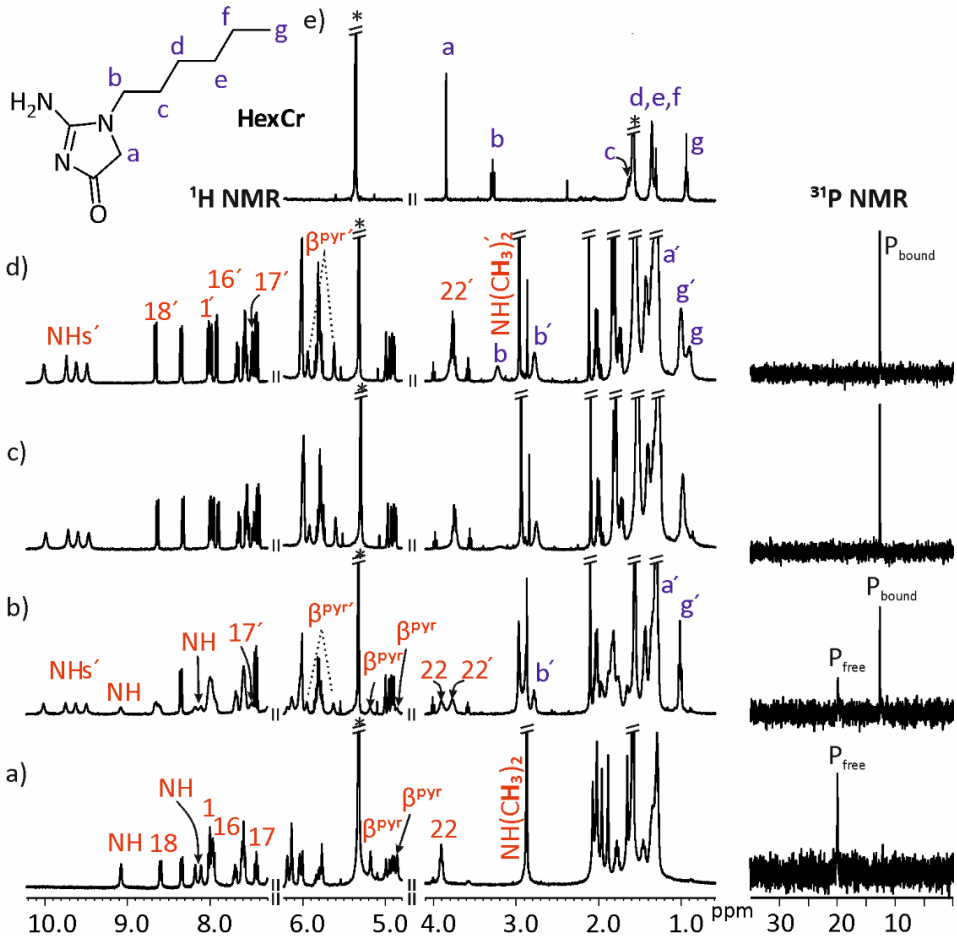

Figure 5.4 Selected regions of the ^{1}H NMR (left) (400 MHz, 298 K, CD_2Cl_2) and ^{31}P NMR (right) (202 MHz, 298 K, CD_2Cl_2) spectra of a) free **5** and after the addition of **HexCr** e): 0.5 equiv. b); 1.0 equiv. c) and 1.5 equiv. d). Primed letters and numbers correspond to the signals assigned to complex **HexCr⊂5**. See Figure 5.1 for the proton assignment of receptor **5**. * Residual solvent peaks.

Additionally, the ^{31}P NMR spectrum revealed the presence of a single phosphorous signal centered at 20.0 ppm (*Figure 5.4*a, right).

The addition of 0.5 equiv. of **HexCr** produced the broadening and decrease in intensity of the proton signals assigned to the free receptor (*Figure 5.4*b, left). Concomitantly, a new set of signals appeared in the aromatic and aliphatic regions of the ^{1}H NMR spectrum. This new set of signals was assigned primarily to a complex of unknown stoichiometry between receptor **5** and **HexCr**. Remarkably, four proton

signals were detected around 9.8 ppm and were assigned to the pyrrole NHs, highly downfield shifted with respect to the same protons in the free counterpart (Δδ = 1.7 ppm). The proton signals observed between 3.0-1.0 ppm were assigned to the protons of bound **HexCr** (H^a, H^b), which appear highly upfield shifted when compared to free **HexCr** (Δδ = -2.5 ppm and Δδ = -0.4 ppm, respectively). (Figure 5.*4*e, left). The ^{31}P NMR spectrum of the mixture revealed the presence of two singlets: one corresponding to the phosphorous atom of free **5** while the other assigned to the bound receptor (Figure 5.*4*b, right). The appearance of this new phosphorus signal supports their involvement of the P=O group in hydrogen bonding interaction with the NH protons of the bound creatinine.

The addition of up to 1.0 equiv. of **HexCr** produced the complete disappearance of the protons related to the free receptor and an increase in the intensity of the signals assigned to the bound **5** and bound **HexCr**. The ^{31}P NMR spectrum of the equimolar mixture showed exclusively an upfield shifted signal for the phosphorous atom at 12.67 pm (Δδ = 7.31 ppm) (Figure 5.*4*c, left).Finally, the addition of more than 1.0 equiv. of **HexCr** produced only the appearance of a new set of proton signals attributed to free **HexCr** (Figure 5.*4*d, left). The ^{31}P NMR spectrum did not experience further changes (Figure 5.*4*d, right).

Taken together, these results advocate for the formation of complex **HexCr⊂5** experiencing a slow equilibrium in the ^{1}H and ^{31}P NMR chemical shift timescale with its free components. The **HexCr** is included in the cavity of **5** establishing 4 hydrogen bond interactions between its oxygen atom and the pyrrole NHs of the host. This binding was supported by the downfield shift observed for the pyrrole NHs in the complex. Most likely, **HexCr** also establishes an additional hydrogen bonding interaction with the P=O group of **5** similarly to the geometries described in previous chapters with analogous phosphonate receptors (Figure 5.*5*).

Moreover, proton H^a of **HexCr** experienced a dramatic upfield shift upon binding **5**. This is attributed to the shielding effect exerted by aromatic cavity of **5**. Interestingly, protons H^{16}, H^{17}, H^{18} and $N(C\mathbf{H}_3)_2$ proton of the dansyl group move also downfield affected upon inclusion of **HexCr.** Most likely, this is due to the conformational changes of the fluorescent unit upon complex formation.

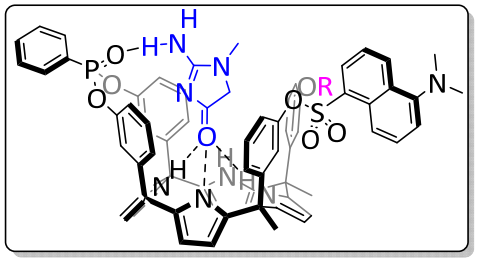

Figure 5.5 Line-drawing structure of the creatine complex with **4** or **5.**

Finally, since the ^{1}H and ^{31}P NMR spectra of the equimolar mixture of **5** and **HexCr** only display the signals assigned to the **HexCr⊂5** complex, we estimate a binding constant larger than 10^4 M^{-1}.

5.2.3 Absorption and emission titration experiments of receptor **5** with **Cr** and **HexCr**.

The absorption spectrum of **5** (10 μM) in DCM displays an intense band at 354 nm (ε = 4470 $M^{-1}{\cdot}cm^{-1}$) attributed to the dansyl group (orange line in Figure 5.*6*). Excitation at 354 nm produced an intense emission band with a maximum at $\lambda_{fluo,\ max}$ = 522 nm (green line in Figure 5.*6*).

We first tested if the binding of **Cr** and **HexCr** affected the emission properties of **5** by performing solid-liquid extraction experiments in micromolar DCM solutions.

We registered the absorption and emission spectra of two separate micromolar solutions of **5** before and after a solid-liquid extraction with **Cr** and **HexCr**. In both cases, we did not observed changes in the absorption spectrum before and after the extraction (Figure 5.*6* and Figure 5.*26*, respectively). Interestingly, we observed a fluorescence quenching of *ca*. 69% and 75% after extraction experiments of **Cr** and **HexCr**, respectively.

Receptor **4** exhibited similar results (Figure 5.*24*).

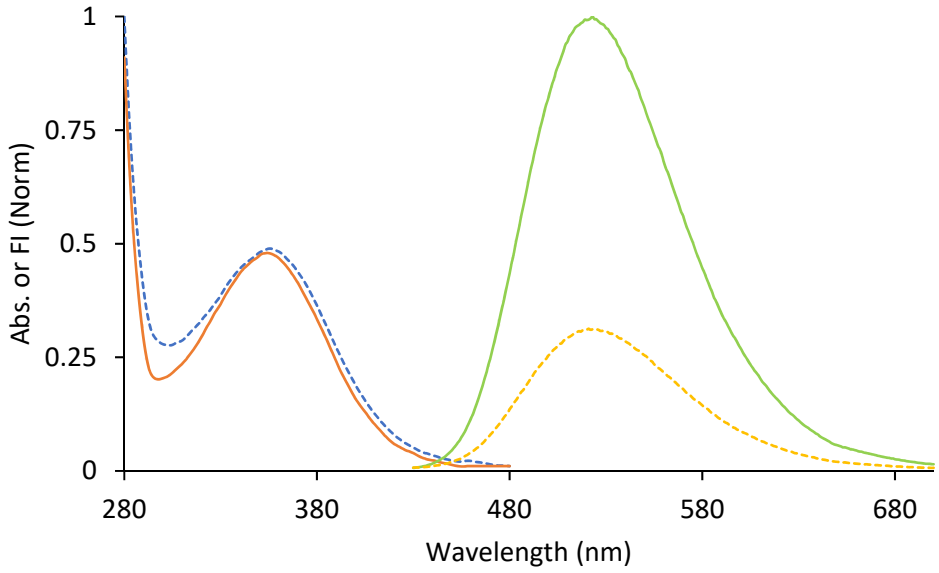

Figure 5.6 Uv/vis absorption and emission spectra of **5** at 10 µM before (orange and green) and after (blue and yellow dash lines) **Cr** solid extraction.

The emission changes upon the binding of **Cr** or **HexCr** by receptor **5** could be ascribed to conformational changes of the fluorescent unit upon complex formation that could favor the occurrence of *non-radiative* relaxation processes. However, additional experiments need to be performed and other processes cannot be discarded.

These results contrast with the results obtained with the previously described receptors in Chapters 3 and 4 of the present thesis, in which the fluorescent receptors did not experience any significant change in their emission properties upon binding **HexCr**. These experimental results open an alternative for the development of a fluorescent sensor able to perform a direct sensing of creatinine.

5.2.4 Determination of the binding constant for receptor **4** and **HexCr**.

We performed emission titration experiments to determine the value of the binding constant of complex **HexCr⊂4** in dichloromethane solution.

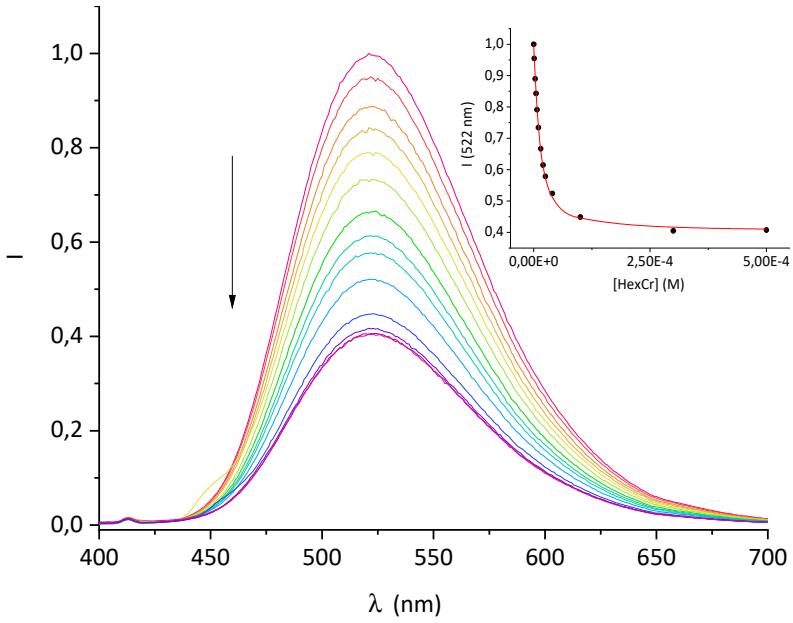

Figure 5.7 Emission spectra of **4** (10 μM) registered upon addition of increasing amounts of **HexCr** in diclorometane; λ_{exc} = 367 nm. Inset: Plot of the emission change at 522 nm (black circles) vs equivalents of **HexCr**. The red line corresponds to the fit of the titration data to a 1:1 binding model considering two emissive species: The free cavitand and the 1:1 complex, **HexCr⊂4**.

The incremental addition of **HexCr** to a micromolar solution of receptor **4** produced a gradual decrease on the emission intensity. The fluorescence titration data was adjusted to a mathematical model that assumed the formation of a 1:1 complex and considered two emissive species: Free and bound **4**. It returned a value for the binding constant of K_a = 1.38 × 10^5 M^{-1}. This value is in agreement with those reported in Chapter 2 of this thesis and in literature using analogous calix[4]pyrrole cavitands and **HexCr**.[1, 3]

We performed analogous emission titration experiments with methylene cavitand receptor **8** lacking the phosphonate group. As expected, receptor **8** also displayed a modulation in its fluorescence intensity in the presence of **HexCr** (Figure 5.*30*), however the binding constant determined by emission titration (Figure 5.*31*) is one order of magnitude lower in comparison to that obtained for receptor **4**. These findings are in complete agreement with the additional contribution expected for an extra hydrogen bonding provided for phosphonate calix[4]pyrrole in the creatinine recognition (Chapter 2).

5.3 Future developments.

The long alkyl chain with a terminal alkene moiety displayed in receptors **5** and **8** will be used for the immobilization of the receptors in Si (1,0,0) solid surfaces using hydrosilylation reaction. We are currently evaluating different thermal hydrosilylation conditions (e.g. reaction times, washing steps, concentrations) as well as photochemical grafting (i.e. using UV light) which resulted to be less efficient. We plan to characterize the surfaces and perform fluorescent binding experiments at the solid-liquid interface with the grafted surfaces and **HexCr**/**Cr**.

5.4 Conclusions.

We have synthesized three fluorescent C4P receptors **4**, **5** and **8** combining the binding properties of the calix[4]pyrrole core with the well-known emission properties of the dansyl group. The receptors formed thermodynamically and kinetically stable complexes with **Cr** and **HexCr** with binding affinity constants larger than 10^4 M^{-1}.

The formation of complexes was confirmed by ^{1}H and ^{31}P NMR studies. In the complex, the NHs of the **HexCr** established hydrogen bonding interactions with the P=O group inwardly directed to the cavity of the receptor.

Solid-liquid extraction experiments showed that the binding of **HexCr** or **Cr** to the fluorescent complexes produced a decrease on their fluorescence intensity. We determined by emission titration a binding constants of K_a (**HexCr**⊂**4**) = 1.38×10^5 M^{-1} and K_a (**HexCr**⊂**8**) = 3.89×10^4 M^{-1}.

These results augur well for the development of fluorescent sensors for the direct detection of creatinine. We are currently working in the laboratory to graft these receptors into Si (1,0,0) surfaces to transfer the binding event from solution to surface and advance in the development of a creatinine sensing platform.

5.5 Experimental section.

5.5.1 General methods and instrumentation.

Reagents and solvents used in the synthesis were obtained from commercial suppliers and were used without further purification unless otherwise stated. Pyrrole was distilled under vacuum and stored in the freezer for further use. THF was dried by distillation from sodium/benzophenone under argon atmosphere. Triethylamine (Et_3N) was distilled with CaH_2 under argon atmosphere and used

immediately. Dried *N*,*N*-dimethylformamide was obtained from a solvent purification system M Braun SPS-800. Flash column chromatography was performed with silica gel (technical grade, pore size 60 Å, 230-400 mesh particle size).

Automatic column chromatography purifications were done with a Combi-flash® RF^{+}.

Routine ^{1}H-NMR and ^{13}C-NMR spectra were recorded on a Bruker Advance 400 (400 MHz for ^{1}H-NMR) or Bruker advance 500 (500 MHz for ^{1}H-NMR) ultrashield spectrometer. Deuterated solvents were purchased from Aldrich.

FT-IR measurements were carried out on a Bruker Optics FT-IR Alpha spectrometer equipped with a DTGS detector, KBr beamsplitter at 4 cm^{-1} resolution using a one bounce ATR accessory with diamond windows.

UV/vis measurements were carried out on a Shimadzu UV-2401PC spectrophotometer equipped with a photomultiplier detector, double beam optics and D2 and W light sources. Fluorescence measurements were carried out on a Fluorolog Horiba Jobin Yvon spectrofluorimeter equipped with photomultiplier [or InGaAs if using the nitrogen cooled detector] detector, double monochromator and Xenon light source.

Synthesis of receptors **1** and **2** were performed following previously described procedures.[3,1]

Synthesis of mono-phosphonate dansyl-OH **3**: In a 50 ml schlenk flask (three purges Ar/Vacuum previously done), **2** (100 mg, 0.116 mmol) was dissolved in 20 mL of dry acetonitrile (**2** is not complete soluble) and tryethylamine (65 µL, 0.464 mmol) was added in one portion with vigorous stirring. The reaction mixture was stirred for 20 min, and then dansyl chloride (31 mg, 0.116 mmol, dissolved in 1.5 mL of acetonitrile) was added drop by dropf. The reaction mixture was stirred at room temperature under argon atmosphere for 14h. A green solid appeared and it was filtered and washed with acetonitrile. **3** was finally purified by crystallization on Acetonitrile with some drops of dichloromethane, yielding 30 mg (24 %) of the pure compound.

Rf: 0.25 (DCM:AcOEt 96:4), ^{1}H NMR (500 MHz , acetone-d_6, 298 K): δ (ppm) = 8.77 (bs, 2H), 8.72 (d, *J* = 8.51 Hz, 1H), 8.70 (bs, 1H), 8.64 (bs, 1H), 8.40 (d, *J* = 8.51 Hz, 1H), 8.17 (s, 1H), 8.10-8.03 (mult., 2H), 7.99 (d, *J* = 7.33 Hz, 1H), 7.74 (t, *J* = 7.47 Hz,

1H), 7.68-7.63 (mult., 2H), 7.63-7.57 (mult., 2H), 7.38 (d, *J* = 7.53 Hz, 1H), 7.30-7.18 (mult., 3H), 7.05 (t, *J* = 7.85 Hz, 1H), 7.02-6.92 (mult., 4H), 6.79 (d, *J* = 8.38 Hz, 1H), 6.77 (s, 1H), 6.75 (s, 1H), 6.69 (d, *J* = 7.67 Hz, 1H), 6.58 (dd, *J* = 7.85, 1.86 Hz, 1H), 6.36 (s, 1H), 6.32 (d, *J* = 7.85 Hz, 1H), 6.14 (s, 1H), 6.11-6.07 (mult., 2H), 5.99 (s, 2H), 5.94 (t, *J* = 2.90 Hz, 1H), 5.72 (s, 1H), 5.68 (t, *J* = 2.90 Hz, 1H), 5.56 (s, 1H), 2.96 (s, 6H), 1.88 (s, 3H), 1.87 (s, 3H), 1.82 (s, 3H), 1.43 (s, 3H). $^{31}P\{^{1}H\}$ NMR (202 MHz, acetone-d_6, 298 K): δ (ppm) = 14.32. Nominal mass (ESI): Calcd for $C_{66}H_{58}N_5O_7PS$= 1096.2518; Found =1096.2.

Synthesis of mono-phosphonate dansyl-methoxy **4**: Methyl Iodide (10 µL, 0.16 mmol) was added to a solution of **3** (24 mg, 0.022 mmol) and Cs_2CO_3 (30 mg, 0.092 mmol) in 50 mL of acetonitrile. The mixture was refluxed for 1h and the solvent was removed under vacuum. The residue was dissolved in diethyl ether (2 × 100 mL), washed with water (3 × 30 mL) and the combined ethereal layers were dried over Na_2SO_4, and evaporated. **4** was obtained as a green solid (22 mg, 98%).

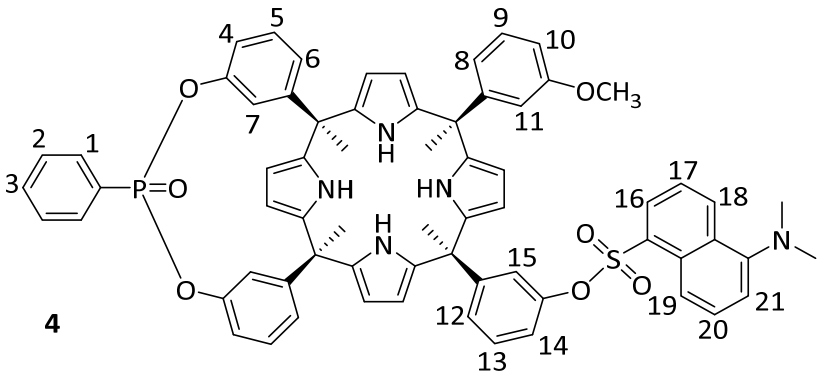

Rf: 0.90 (DCM:AcOEt 90:10), **^{1}H NMR** (500 MHz, acetone-d_6, 298 K): δ (ppm) = 8.79 (bs, 3H), 8.72 (d, *J* = 8.58 Hz, 2H), 8.42 (d, *J* = 8.58 Hz, 1H), 8.06 (dd, *J* = 14.30 Hz, 2H), 8.00 (d, *J* = 7.35 Hz, 1H), 7.75 (t, *J* = 7.50 Hz, 1H), 7.68-7.56 (mult., 4H), 7.38 (d, *J* = 7.50 Hz, 1H), 7.30-7.15 (mult., 3H), 7.02-6.91 (mult., 5H), 6.84-6.67 (mult., 5H), 6.45 (d, *J* = 7.69 Hz, 1H), 6.42 (s, 1H), 6.15 (t, *J* = 2.02 Hz, 1H), 6.10 (mult., 2H), 6.04 (s, 1H), 5.99 (t, *J* = 3.08 Hz, 1H), 5.95 (t, *J* = 3.08 Hz, 1H), 5.69 (t, *J* = 3.08 Hz, 1H), 5.64 (s, 1H), 5.46 (s, 1H), 3.77 (s, 3H), 2.96 (s, 6H), 1.89(s, 3H), 1.88 (s, 3H), 1.85 (s, 3H), 1.45 (s, 3H). **^{31}P{^{1}H} NMR** (202 MHz, acetone-d_6, 298 K): δ (ppm) = 14.43.

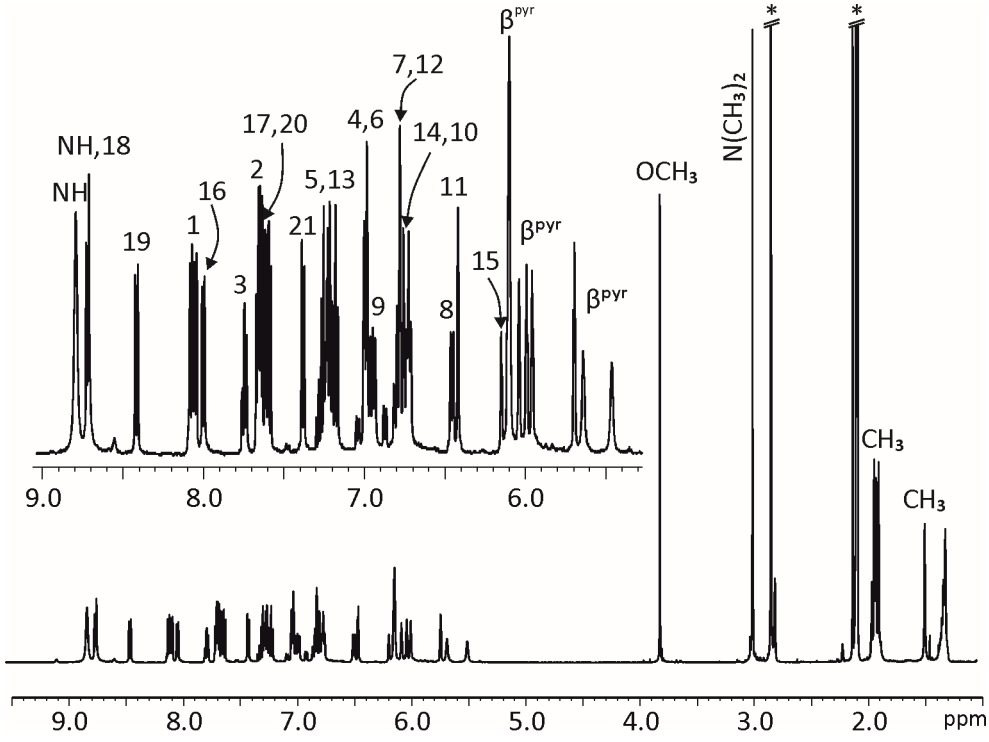

Figure 5.8 ^{1}H-NMR (500 MHz, acetone-d_6) of compound **4**. * Residual solvent peak.

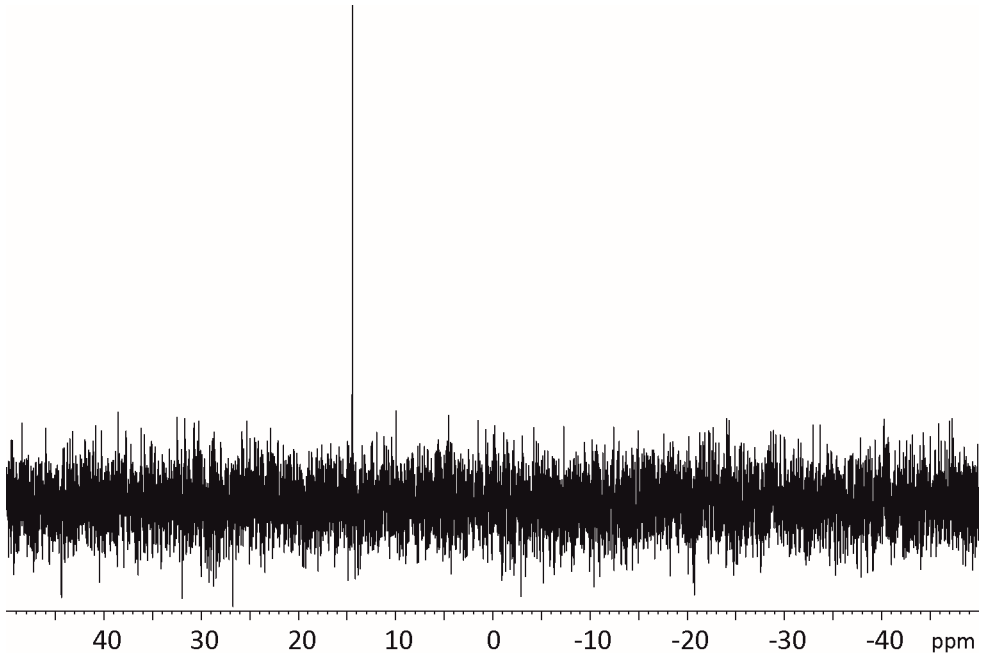

Figure 5.9 ^{31}P-NMR (202 MHz, acetone-d_6) of compound **4**.

Synthesis of mono-phosphonate dansyl-undecene **5**: Receptor **3** (20 mg, 18 µmol), 11-bromo-1-undecene (6.3 µL, 27 µmol) and K_2CO_3 (3.8 mg, 27 µmol) were introduced into an Ace Pressure tube, and 5 mL of dry DMF was added. The reaction mixture was stirred at 80 °C for 2h. DMF was removed under vacuum, the residue was dissolved in dichloromethane and washed with water (3 × 20 mL), the organic phase was collected, dry on Na_2SO_4, filtered and the solvent was removed under vacuum. The solid residue was dissolved in CH_2Cl_2 and submitted to silica-gel column chromatography using CH_2Cl_2 as eluent, which provided 8 mg (40%) as a green powder.

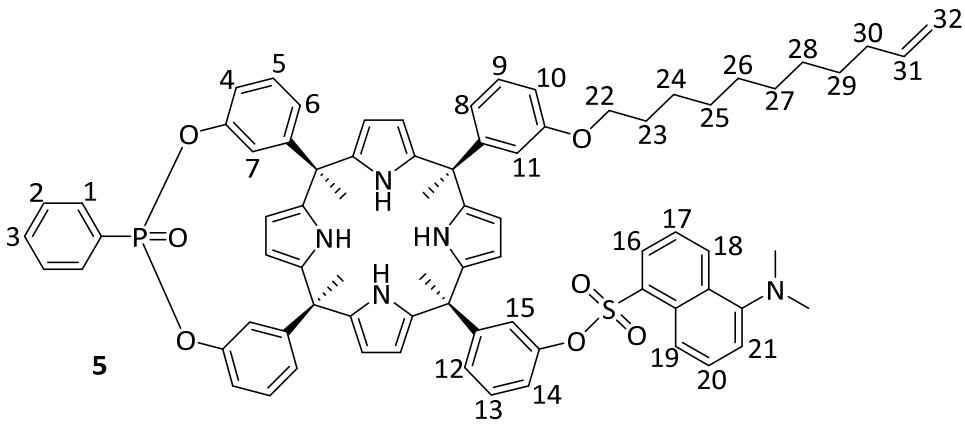

5

^{1}H NMR (400 MHz, acetone-d_6, 298 K): δ (ppm) = 8.78 (bs, 3H), 8.72 (d, *J* = 8.42 Hz, 2H), 8.41 (d, *J* = 8.42 Hz, 1H), 8.06 (d, *J* = 7.47 Hz, 2H), 8.00 (d, *J* = 7.40 Hz, 1H), 7.74 (t, *J* = 7.53 Hz, 1H), 7.68-7.55 (mult., 4H), 7.37 (d, *J* = 7.53 Hz, 1H), 7.30-7.12 (mult., 4H), 7.04-6.90 (mult., 4H), 6.83-6.65 (mult., 5H), 6.45 (d, *J* = 7.84 Hz, 1H), 6.41 (s, 1H), 6.14-6.07 (mult., 3H), 6.03 (s, 1H), 5.99 (t, *J* = 3.04 Hz, 1H), 5.95 (t, *J* = 3.04 Hz, 1H), 5.85-5.72 (mult., 1H), 5.69 (t, *J* = 3.04 Hz, 1H), 5.62 (s, 1H), 5.45 (s, 1H), 4.93 (dd, J_1 = 17.12, J_2 = 10.18 Hz, 2H), 3.93 (t, *J* = 6.42 Hz, 2H), 2.95 (s, 6H), 2.01 (t, *J* = 7.20 Hz, 2H), 1.89 (s, 3H), 1.88 (s, 3H), 1.85 (s, 3H), 1.83-1.75 (mult., 2H), 1.54-1.43 (mult.,5H), 1.43-1.27 (mult., 10H). **^{31}P{^{1}H} NMR** (162 MHz, acetone-d_6, 298 K): δ (ppm) = 14.54.

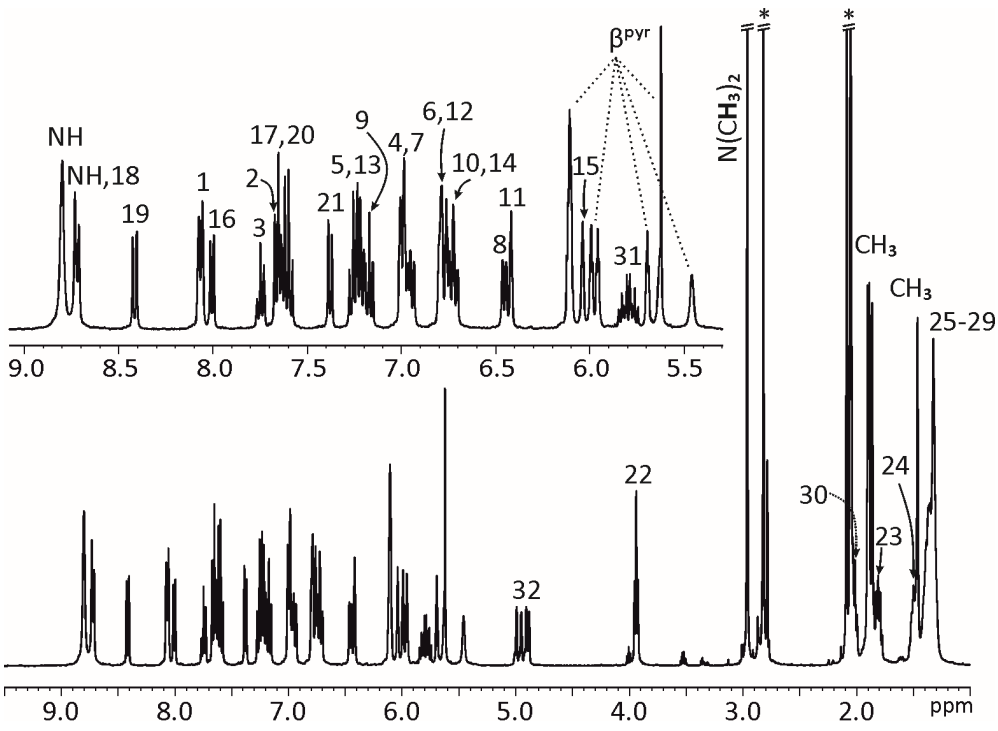

Figure 5.10 ^{1}H-NMR (400 MHz, acetone-d_6) of compound **5**. * Residual solvent peak.

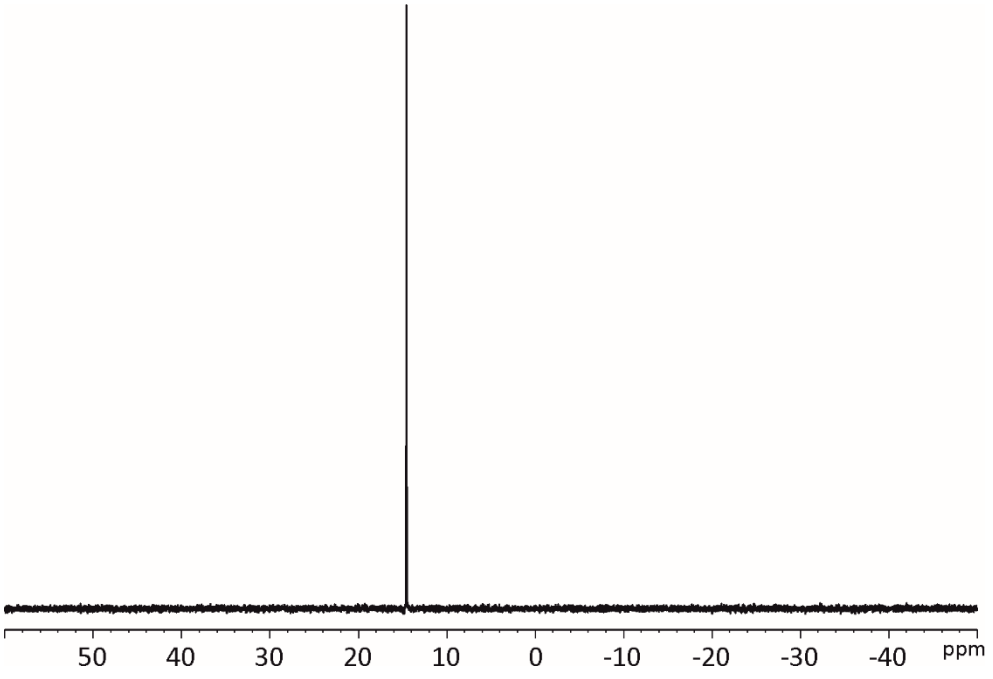

Figure 5.11 ^{31}P-NMR (162 MHz, acetone-d_6) of compound **5**.

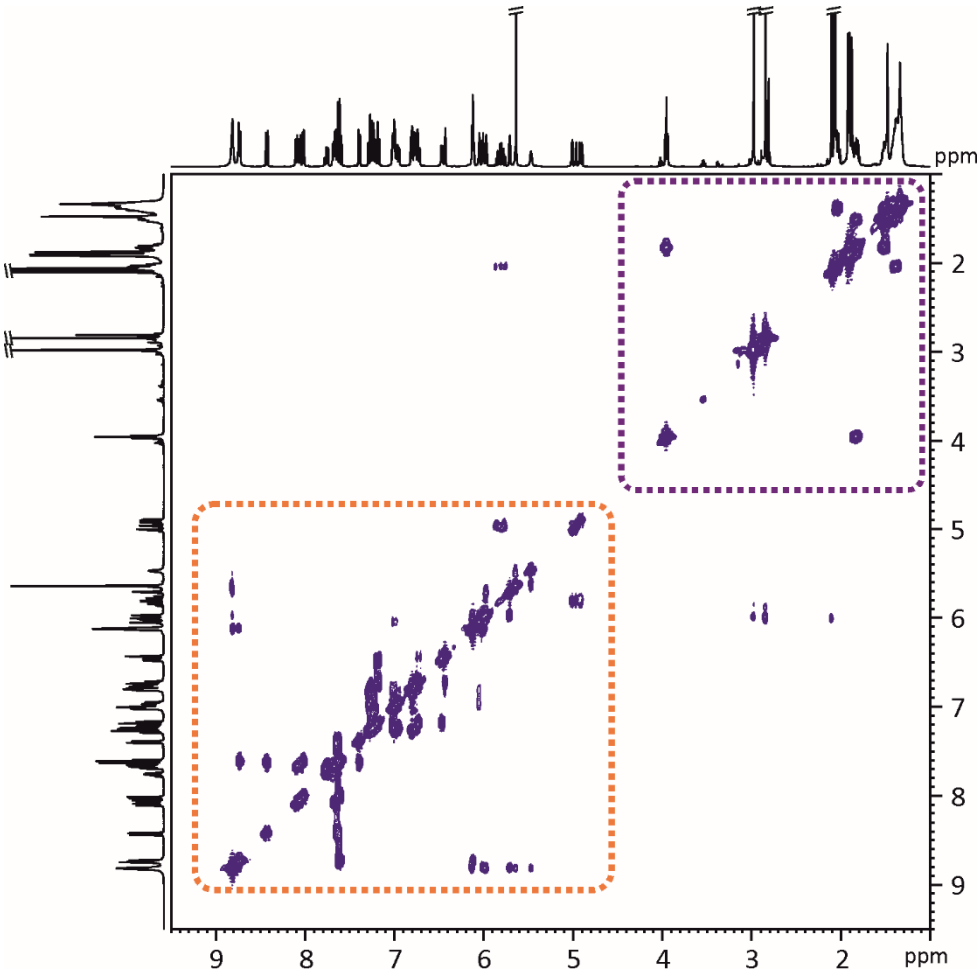

Figure 5.12 2D ^{1}H-^{1}H COSY NMR (400 MHz, acetone-d_6) spectrum of compound **5**.

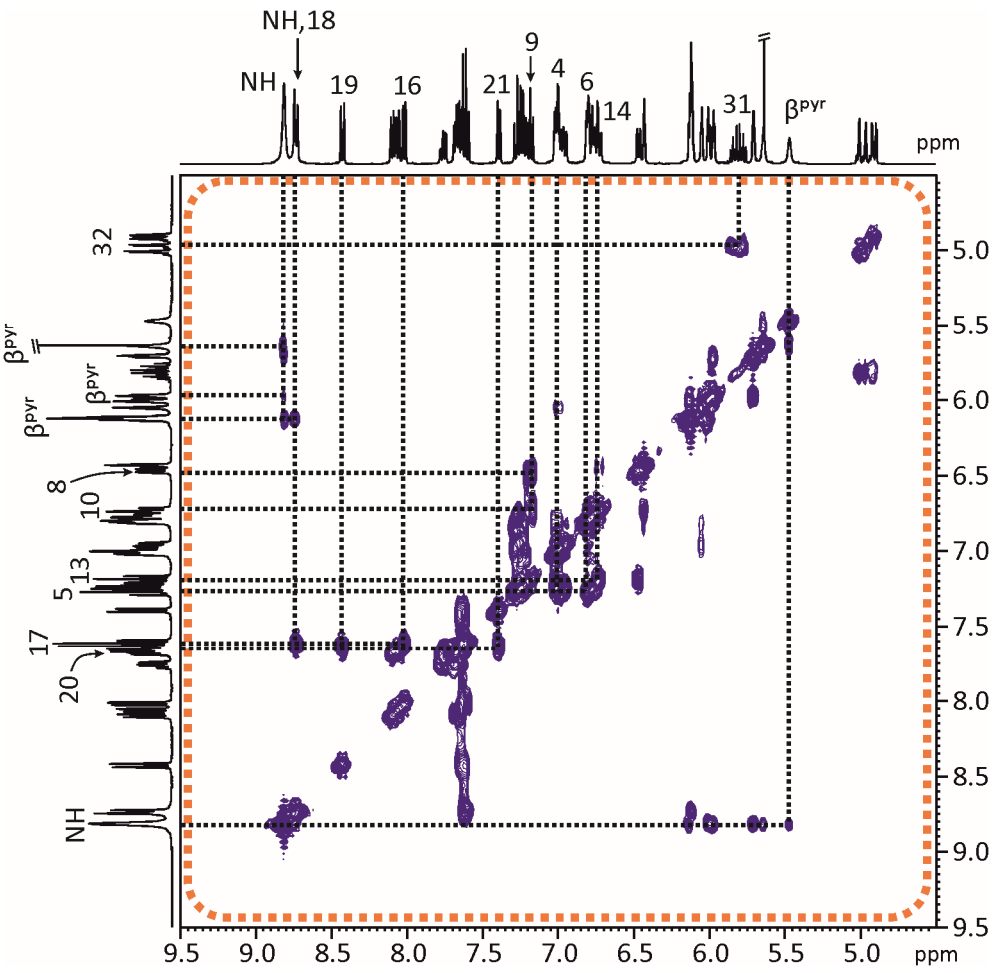

Figure 5.13 Selected region of the 2D ^{1}H-^{1}H COSY NMR (400 MHz, acetone-d_6) spectrum of compound **5**.

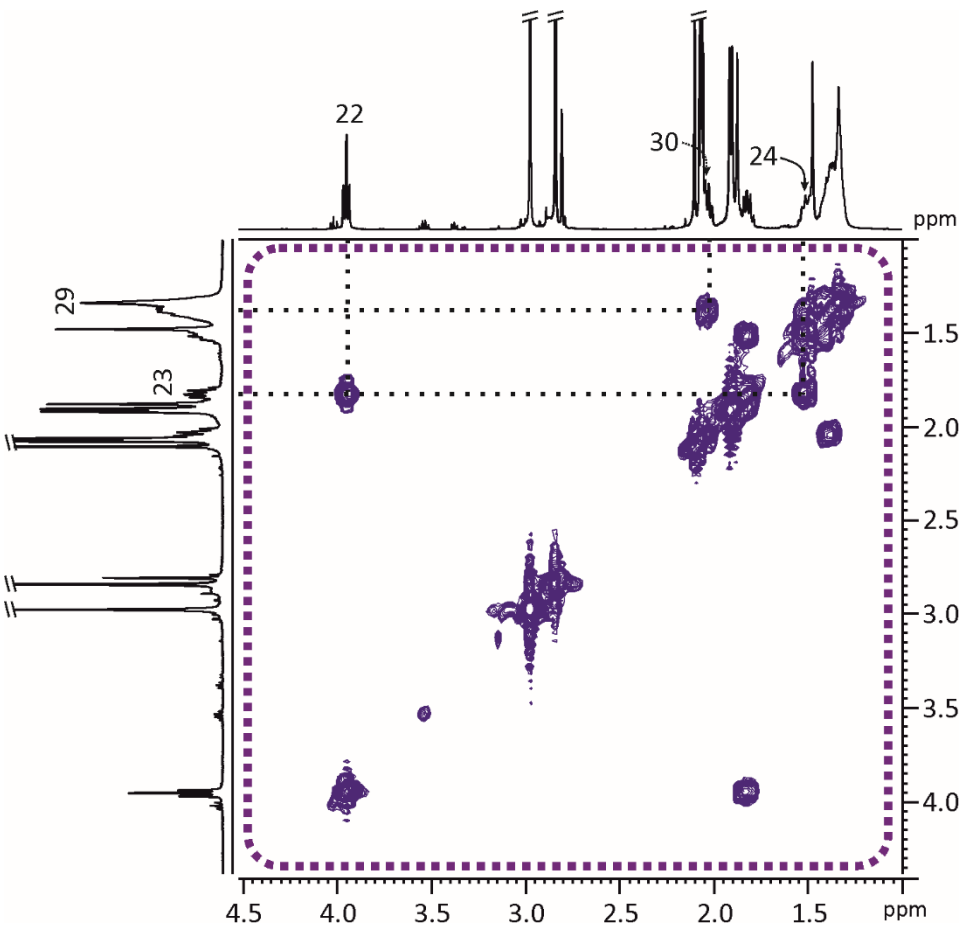

Figure 5.14 Selected region of the 2D ^{1}H-^{1}H COSY NMR (400 MHz, acetone-d_6) spectrum of compound **5**.

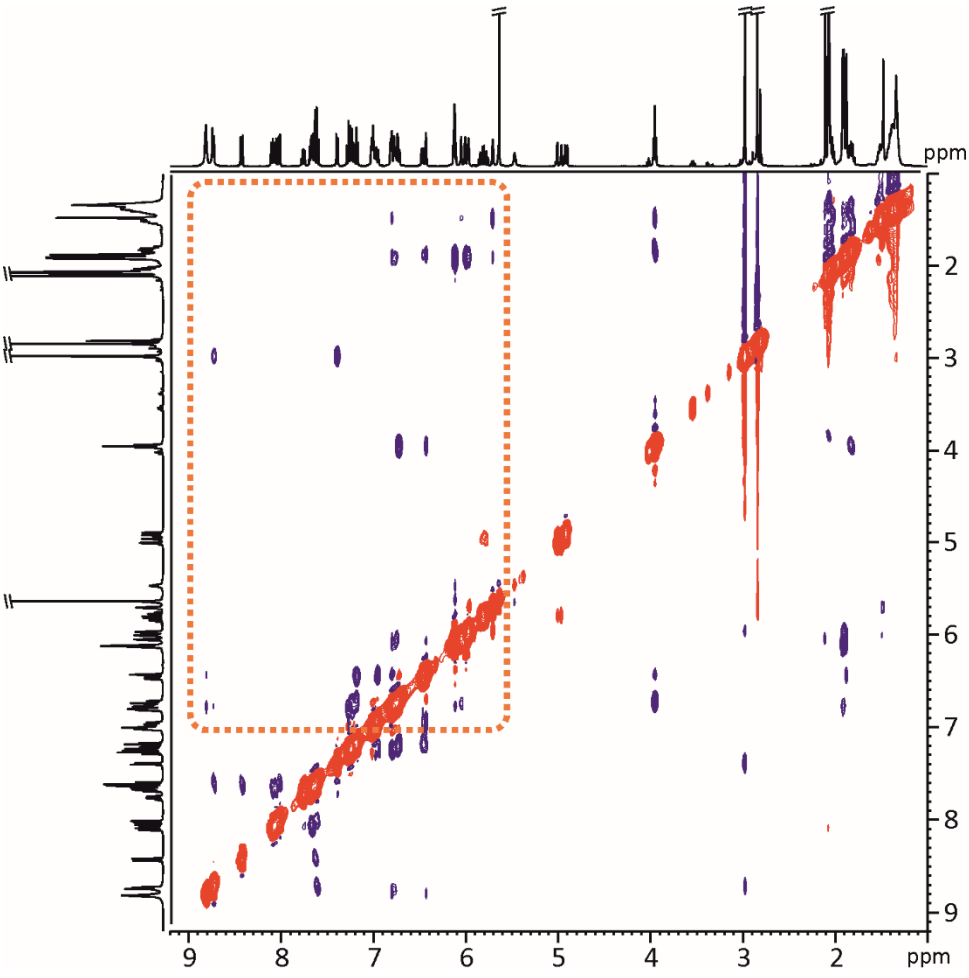

Figure 5.15 2D ^{1}H-^{1}H ROESY NMR (400 MHz, acetone-d_6, spin-lock = 0.4 s) spectrum of the compound **5**.

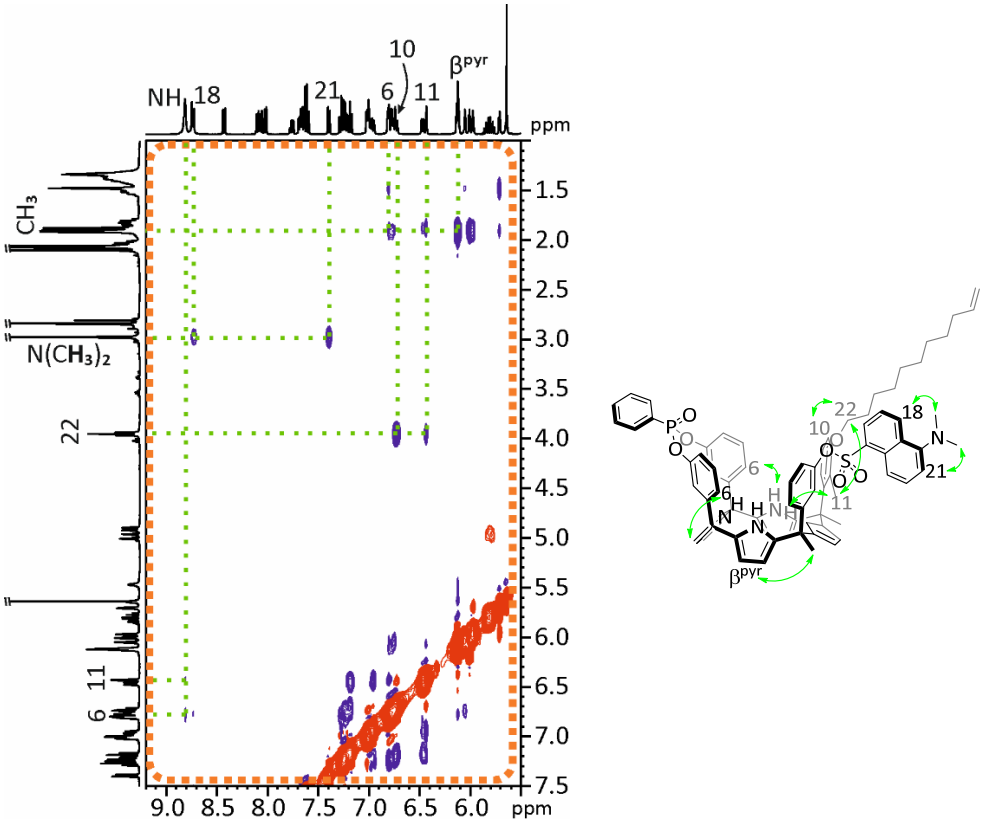

Figure 5.16 Selected region of the 2D ^{1}H-^{1}H ROESY NMR (400 MHz, acetone-d_6, spin-lock = 0.4 s) spectrum of the compound **5**.

Synthesis of methylene-bridge dansyl-undecene (8).

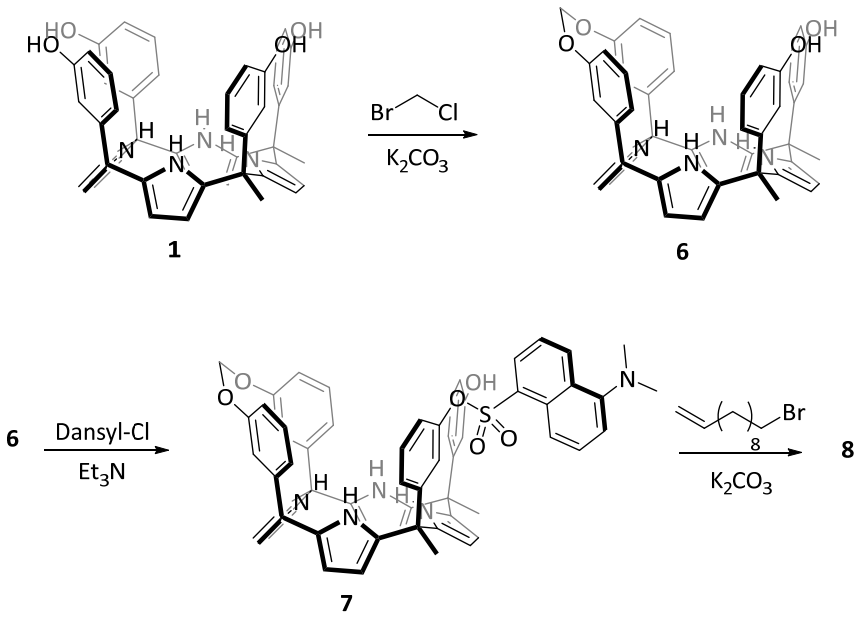

Scheme 5.2 Synthetic Scheme for the preparation of the fluorescent cavitands **8**.

Synthesis of receptors **1** and **6** were synthesized according with the protocols reported in literature.[4,2]

Synthesis of monomethylene bridge dansyl-OH **7**: In a 50 ml schlenk flask (three purges Ar/Vacuum previously done), receptor **6** (100 mg, 0.133 mmol) was dissolved in acetonitrile (dry previously on CaH_2 and distill during 1h) (25 mL, it is complete soluble) and Et_3N (0.5 mL, 3.59 mmol) was added in one portion with vigorous stirring. The reaction mixture was stirred for 20 min, and then dansyl chloride (35.8 mg, 0.133 mmol, dissolved in 1.5 mL) was added drop by drop. The reaction mixture was stirred at room temperature under argon atmosphere for 14h. The solution was diluted with DCM and the organic phase was washed with HCl 10% and brine (4 × 50 mL). The organic phase was collected, dryed and concentrated resulting a green solid. The target product was purified by column chromatography (5.0 g SiO_2, DCM) obtaining 82 mg (63 %) of the pure fraction.

Rf: 0.14 (DCM 100%), **^{1}H NMR** (400 MHz, acetone-d_6, 298 K): δ (ppm) = 8.72 (d, J = 8.67 Hz, 1H), 8.60 (bs, 1H), 8.57 (bs, 2H), 8.40 (d, J = 8.67 Hz, 1H), 8.36 (bs, 1H), 8.16 (s, 1H), 7.97 (dd, J_1 = 7.28 Hz, J_2 = 1.22 Hz, 1H), 7.62-7.55 (mult., 2H), 7.38 (d, J = 7.31 Hz, 1H), 7.24 (t, J =7.93 Hz, 1H), 7.09 (t, J = 7.93 Hz, 1H), 7.05 (t, J = 7.93 Hz, 1H), 7.02 (t, J = 7.93 Hz, 1H), 6.79-6.72 (mult., 3H), 6.71-6.64 (mult., 3H), 6.54 (dd, , J_1 = 7.99

Hz, J_2 = 2.47 Hz, 1H), 6.43 (d, *J* = 7.53 Hz, 1H), 6.33 (d, *J* = 8.10 Hz, 1H), 6.31 (t, *J* = 2.07 Hz, 1H), 6.26 (d, *J* = 7.72 Hz, 1H), 6.04-5.99 (mult., 3H), 5.97 (t, *J* = 2.97 Hz, 1H), 5.92-5.88 (mult., 2H), 5.83 (t, *J* = 3.06 Hz, 1H), 5.77 (t, *J* = 3.07 Hz, 1H), 5.60 (t, *J* = 3.07 Hz, 1H), 5.33 (d, *J* = 8.10 Hz, 1H), 2.97 (s, 6H), 1.96 (s, 3H), 1.85 (s, 6H), 1.79 (s, 3H).

Synthesis of monomethylene bridge dansyl-undecene **8**: Receptor **6** (200 mg, 0.203 mmol), 11-bromo-1-undecene (222 µL, 1.01 mmol) and K_2CO_3 (280 mg, 2.03 mmol) were introduced into 100 mL Schlenk tube, and 50 mL of dry DMF was added. The reaction mixture was stirred for 2h at 80 °C. DMF was removed under vacuum, the residue was dissolved in dichloromethane and washed with water (3 × 20 mL), the organic phase was collected, dry on Na_2SO_4, filtered and the solvent was removed under vacuum. The solid residue was dissolved in CH_2Cl_2 and submitted to silica-gel column chromatography using CH_2Cl_2 as eluent. The resulting solid was washed with hexane to remove the excess of the 11-bromo-1-undecene, yielding 62 mg (27 %) as a green powder.

^{1}H NMR (400 MHz, acetone-d_6, 298 K): δ (ppm) = 8.73 (d, *J* =7.7 Hz, 1H), 8.63 (bs, 2H), 8.58 (bs, 1H), 8.41 (d, *J* = 7.7 Hz, 1H), 8.38 (bs, 1H), 7.97 (d, *J* = 7.0 Hz, 1H), 7.63-7.55 (mult., 2H), 7.39 (d, *J* = 7.4 Hz, 1H), 7.23 (t, *J* =7.9 Hz, 1H), 7.13 (t, *J* = 7.9 Hz, 1H), 7.10-7.01 (mult., 2H), 6.98 (dd, J_1 = 7.2 Hz, J_2 = 2.3 Hz, 1H), 6.81-6.61 (mult., 7H), 6.45 (d, *J* = 7.7 Hz, 1H), 6.39-6.28 (mult., 3H), 6.05-5.99 (mult., 3H), 5.97 (t, *J* = 2.9 Hz, 1H), 5.89 (bs, 2H), 5.83 (t, *J* = 2.9 Hz, 1H), 5.79 (mult., 1H), 5.74 (t, *J* = 2.7 Hz, 1H), 5.60 (t, *J* = 2.7 Hz, 1H), 5.34 (d, *J* = 8.1 Hz, 1H), 4.98 (d, *J* = 17.1 Hz, 1H), 4.90 (d, *J* = 10.2 Hz, 1H), 3.90 (t, *J* =6.5 Hz, 2H), 2.98 (s, 6H), 1.85 (s, 6H), 1.81 (s, 3H), 1.79 (mult., 2H), 1.49 (mult., 2H), 1.43-1.22 (mult., 13H), 0.88 (mult., 2H).

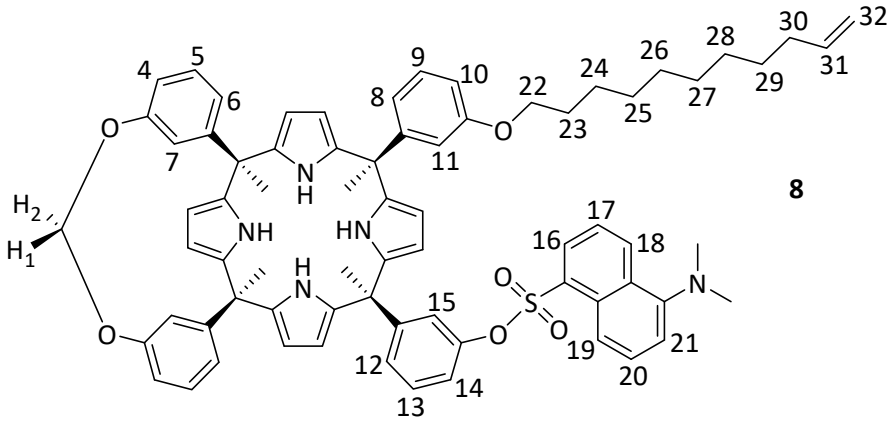

8

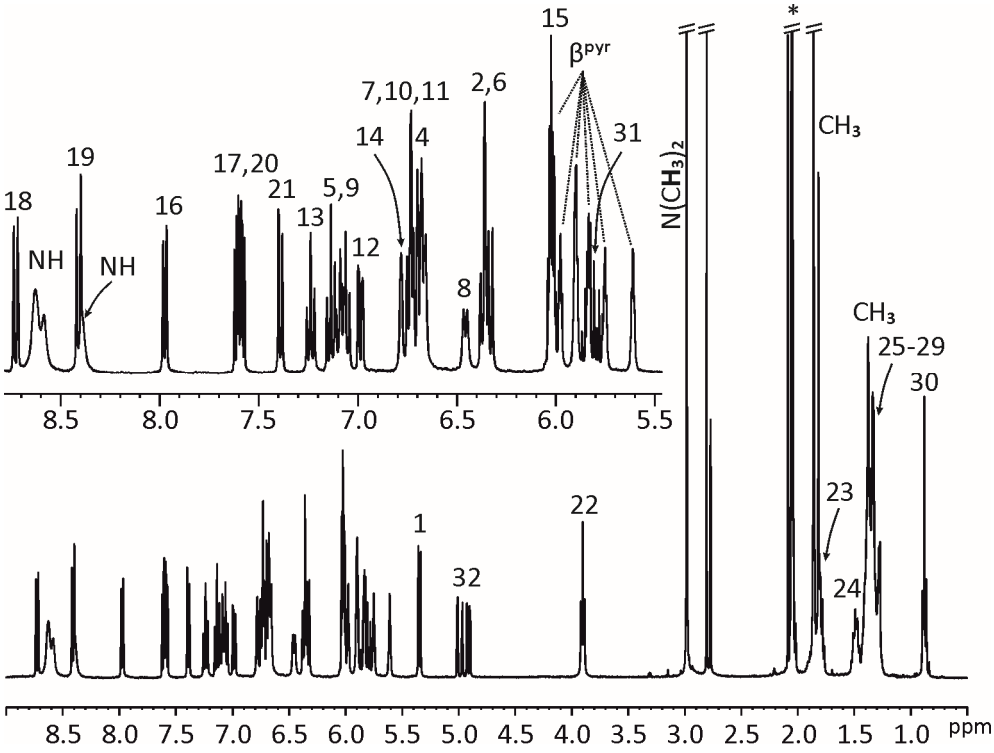

Figure 5.17 ^{1}H-NMR (400 MHz, acetone-d_6) of compound **8**. * Residual solvent peak.

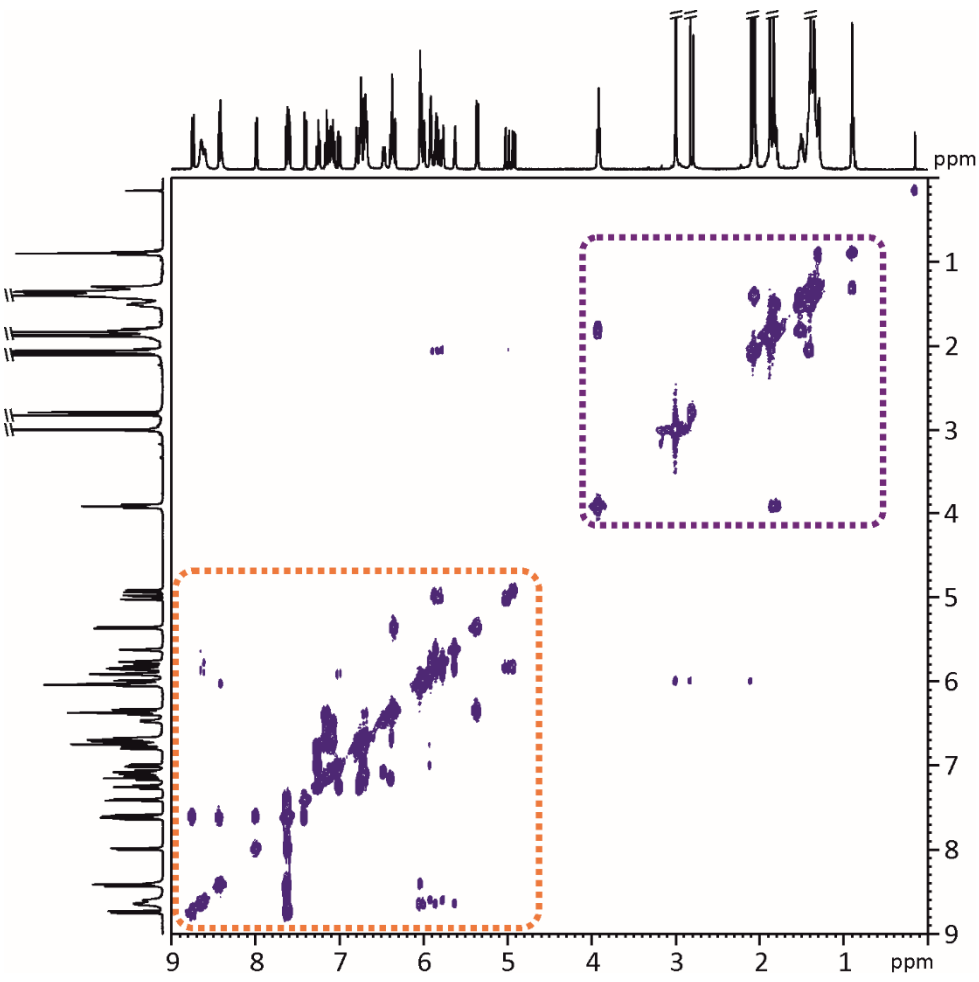

Figure 5.18 2D ^{1}H-^{1}H COSY NMR (400 MHz, acetone-d_6) spectrum of compound **8**.

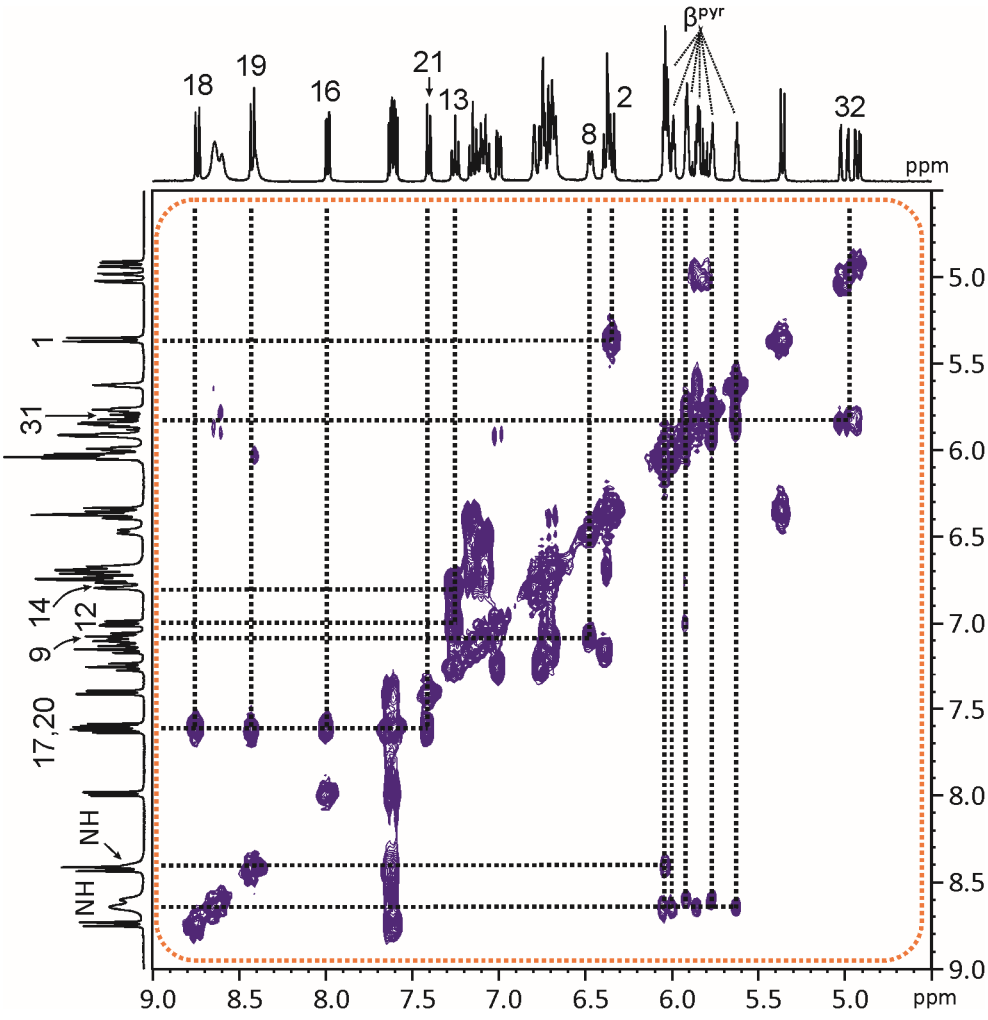

Figure 5.19 Selected region of the 2D ^{1}H-^{1}H COSY NMR (400 MHz, acetone-d_6) spectrum of compound **8**.

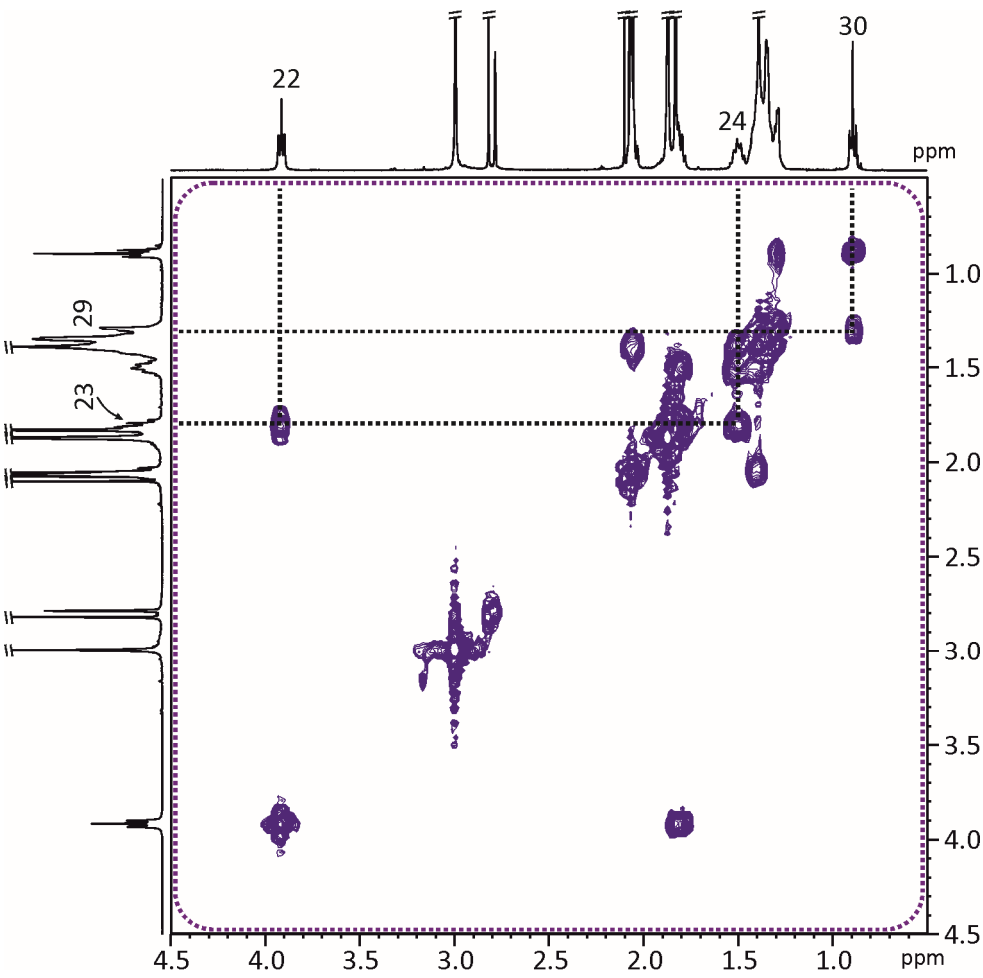

Figure 5.20 Selected region of the 2D ^{1}H-^{1}H COSY NMR (400 MHz, acetone-d_6) spectrum of compound **8**.

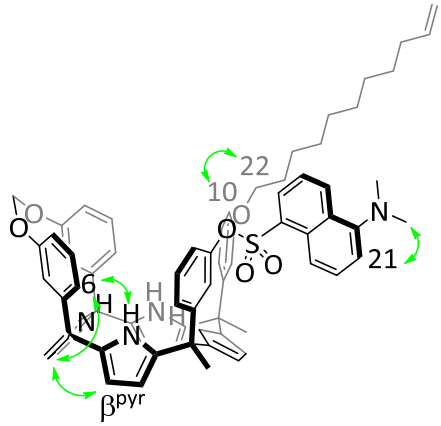

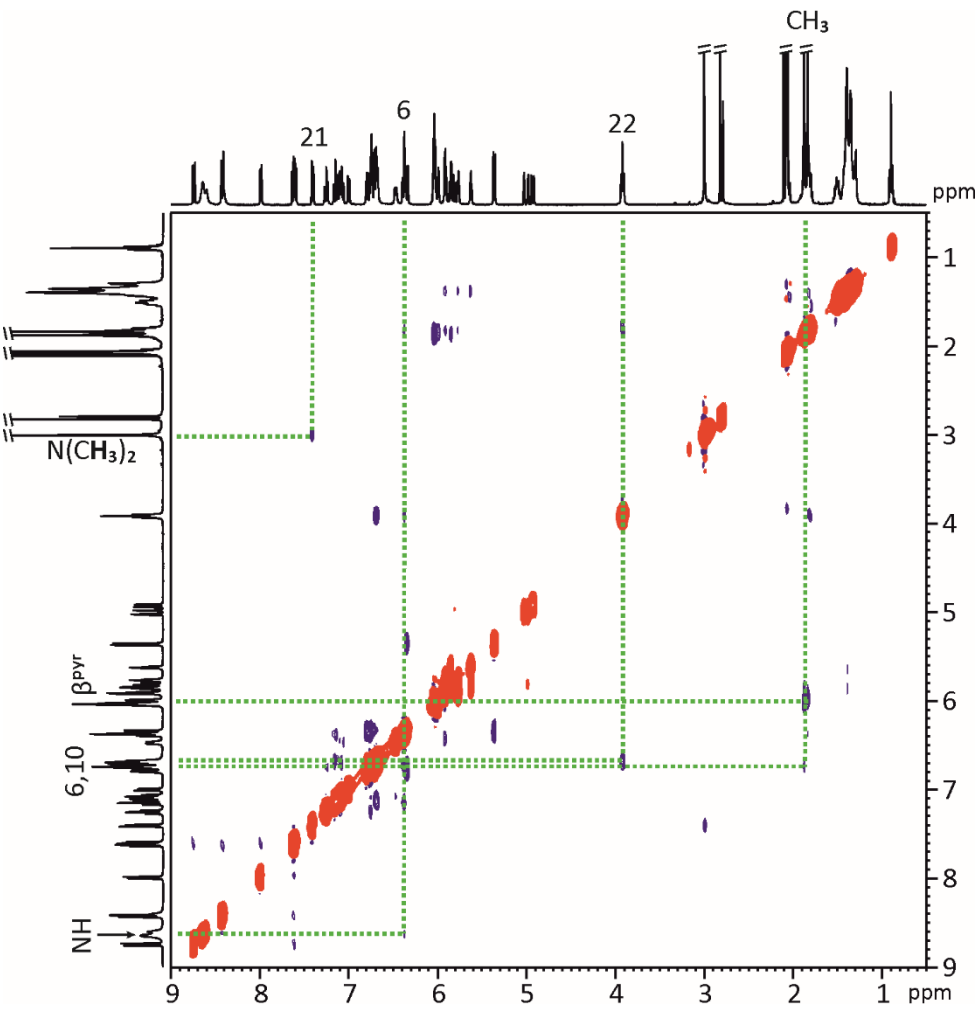

Figure 5.21 2D ^{1}H-^{1}H ROESY NMR (400 MHz, acetone-d_6, spin-lock = 0.4 s) spectrum of the compound **8**.

5.5.2 Optical spectroscopy studies.

Liquid-liquid extractions with Cr and HexCr.

In a normal liquid-liquid extraction experiment, 10 mL of a methylene chloride solution of **4** or **5** (10 -14 µM) is prepared. One portion was used to fill one of the emission cuvettes (2.5 mL). Another part of the solution was used to perform a solid-liquid extraction with creatinine or hexylcreatinine (~ 2 mg).

Receptor 4 and HexCr.

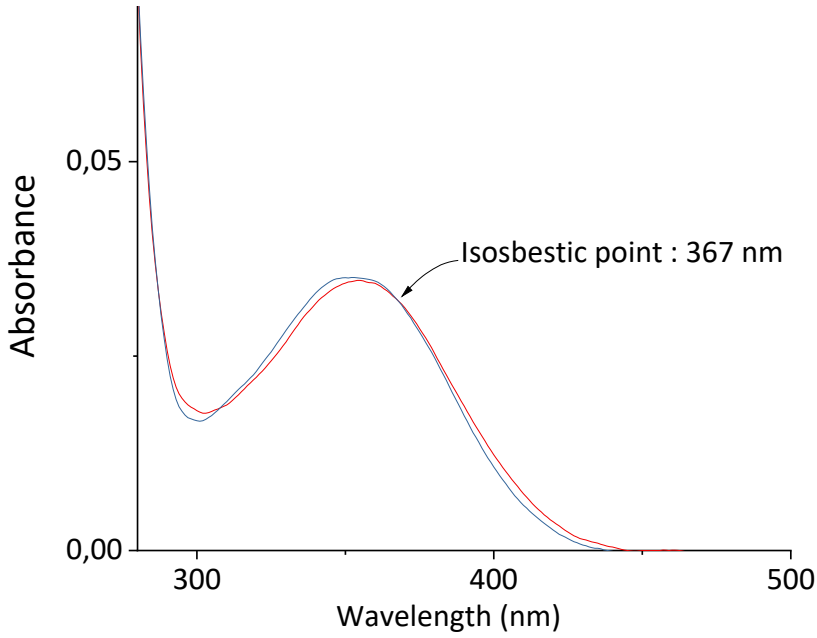

Figure 5.22 UV/vis spectrum of **4** (10 µM, red line) and after solid-liquid extraction with **HexCr** (blue line) in CH_2Cl_2.

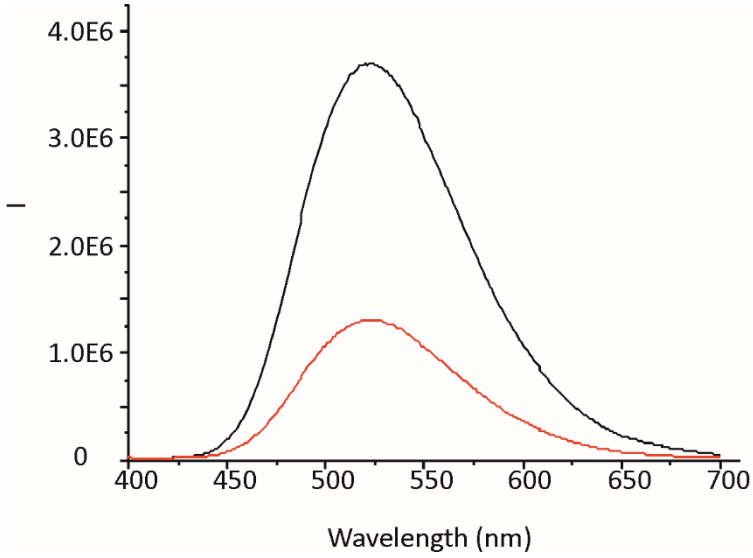

Figure 5.23 Emission spectrum of **4** (10 µM, black line, λ_{exc} = 367 nm) and after solid-liquid extraction with **HexCr** (red line) in CH_2Cl_2.

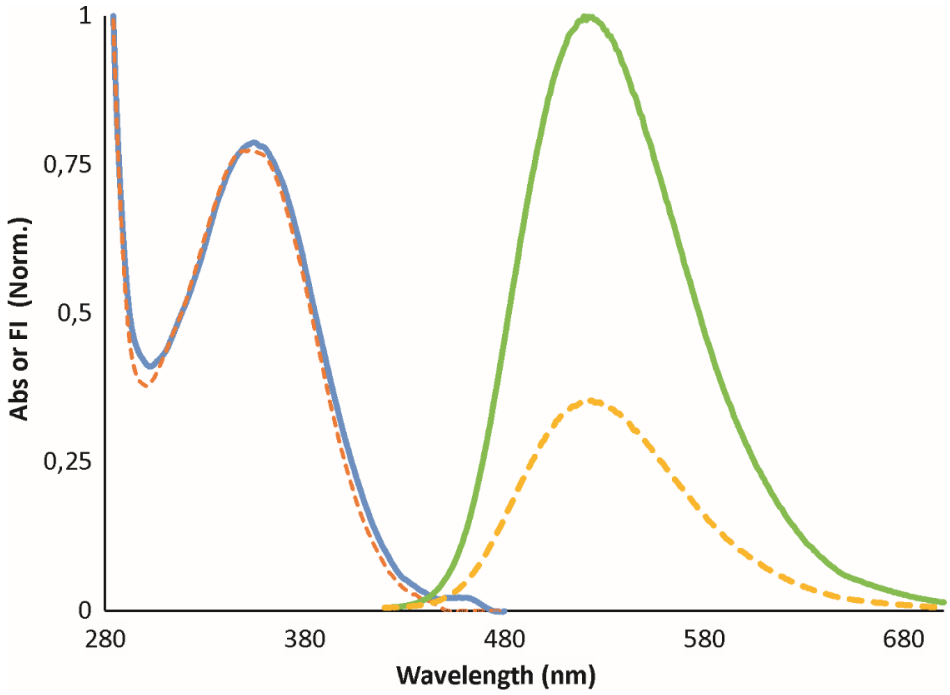

Figure 5.24 UV/vis absorption and emission spectra of **4** before (blue and green) and after (orange and yellow dash lines) **HexCr** solid-liquid extraction, respectively.

Receptor 5 and HexCr.

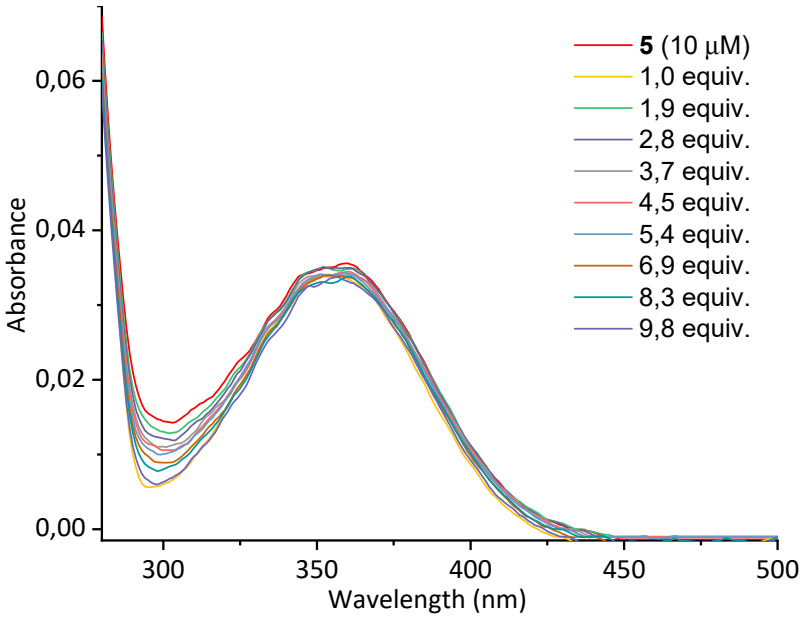

Figure 5.25 Absorption spectra of **5** (10 μM) registered on addition of increasing amounts of **HexCr** in CH_2Cl_2.

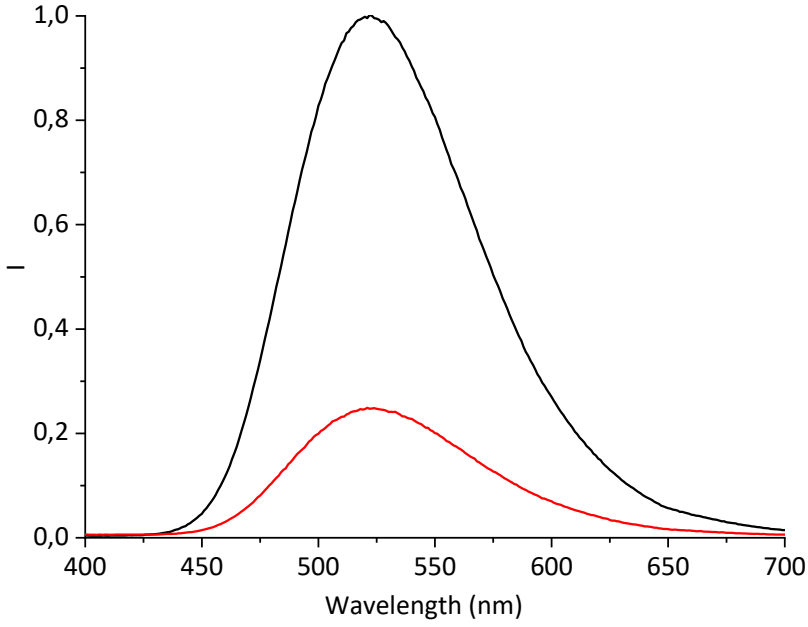

Figure 5.26 Emission spectrum of **5** (10 μM, black line, λ_{exc} = 354 nm) and after solid-liquid extraction with **HexCr** (red line) in CH_2Cl_2.

Receptor 5 and Cr.

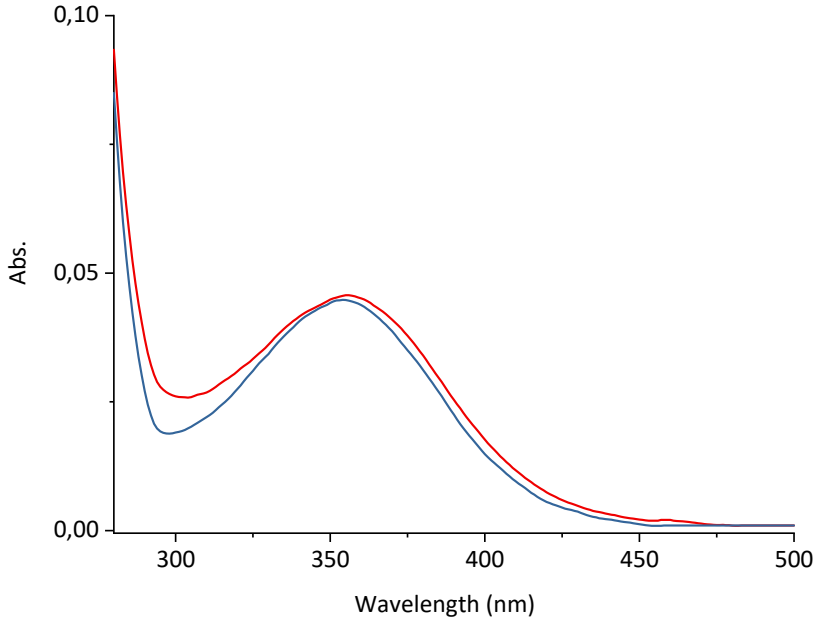

Figure 5.27 UV/vis spectrum of **5** (10 µM, red line) and after solid-liquid extraction with **Cr** (blue line) in CH_2Cl_2.

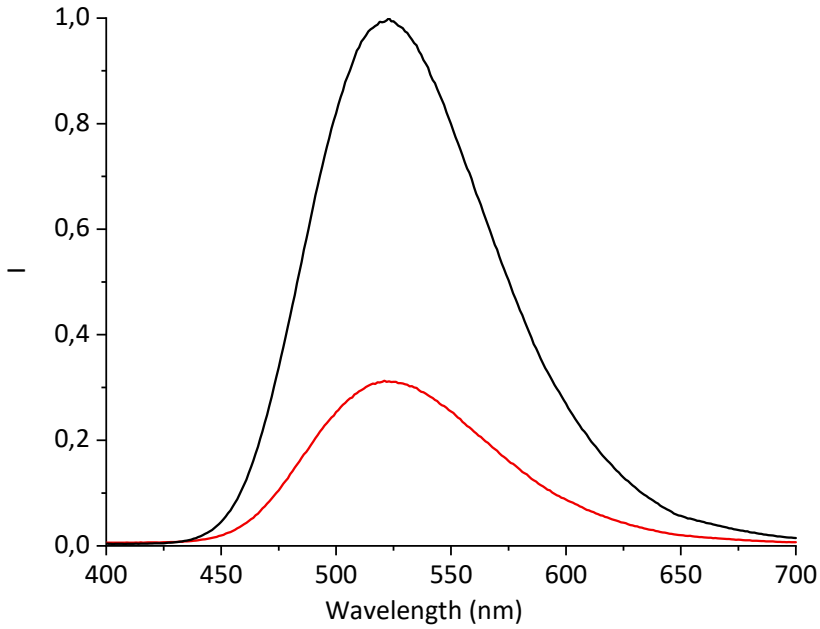

Figure 5.28 Emission spectrum of **5** (10 μM, black line, λ_{exc} = 354 nm) and after solid-liquid extraction with **Cr** (red line) in CH_2Cl_2.

Receptor 8 and HexCr.

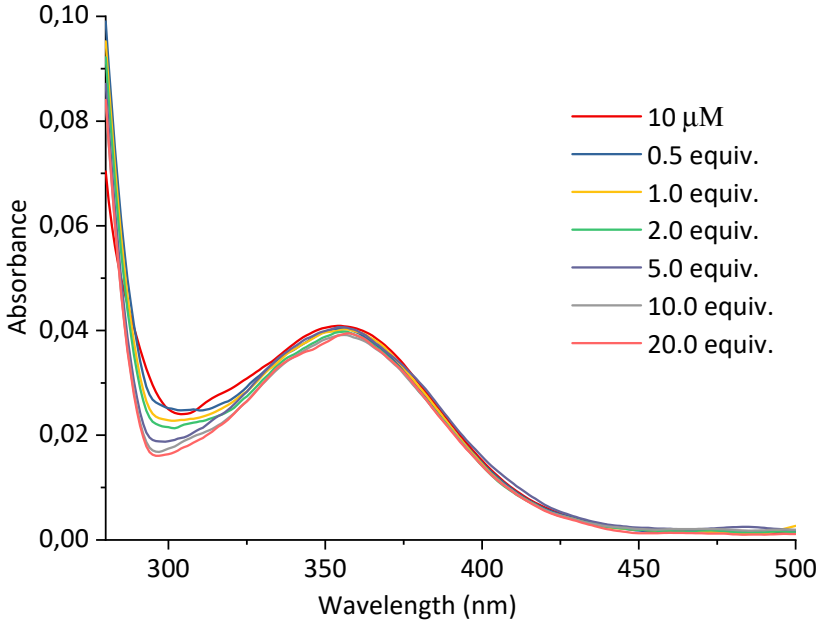

Figure 5.29 Absorption spectra of **8** (10 µM) registered on addition of increasing amounts of **HexCr** in CH_2Cl_2.

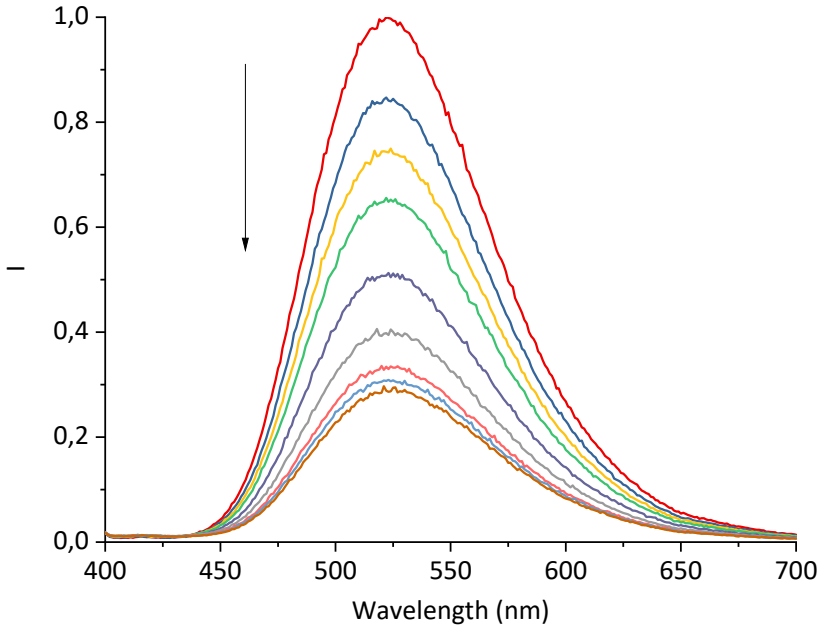

Figure 5.30 Emission spectra of **8** (10 µM) registered on addition of increasing amounts of **HexCr** in dicloromethane; λ_{exc} = 356 nm.

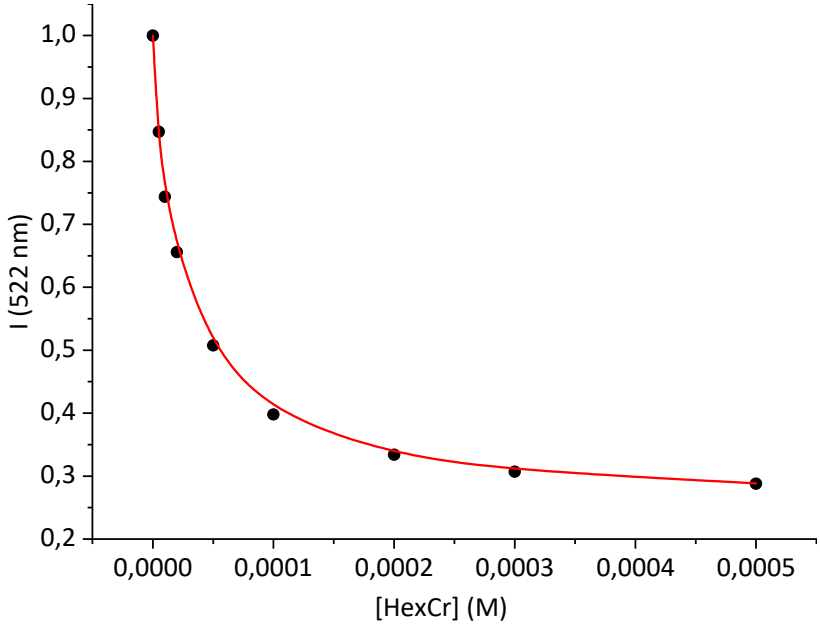

Figure 5.31 Fitting of the emission spectra recorded during the titration of **8** (10 μM) with incremental amounts of **HexCr** (λ_{exc} = 356 nm) at 522 nm using HypSpec version 1.1.16 considering a binding constant of 3.89×10^4 M^{-1}.

5.5.3 X-Ray structures and molecular modeling

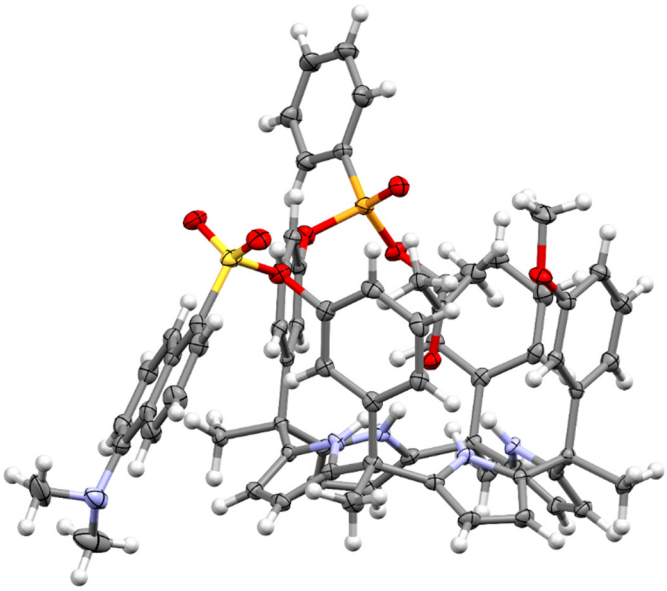

Figure 5.32 X-ray structure of the receptor **4**. Thermal ellipsoids set at 50% probability; H atoms are shown as spheres of 0.20 Å diameter.

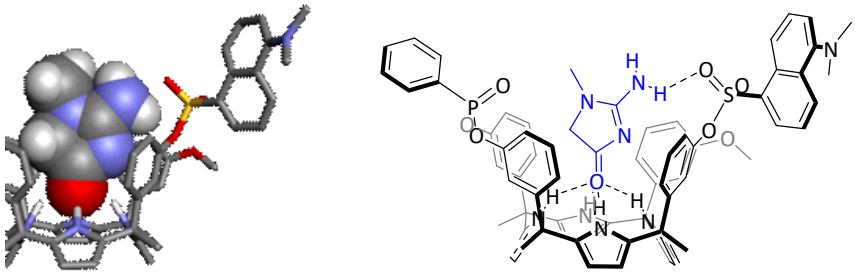

Figure 5.33 a) Energy-minimized (MM3) structure of the complex. The hydrogen atoms of receptor **4** were removed for the sake of clarity. The encapsulated **Cr** molecule is shown as CPK model; b) Line-drawing structure of the **Cr⊂4** complex.

5.6 References and notes.

[1] Sierra, A. F.; Hernández-Alonso, D.; Romero, M. A.; González-Delgado, J. A.; Pischel, U.; Ballester, P. *J. Am. Chem. Soc.* **2020**, *142*, 4276-4284.
[2] Sierra, A. F.; Aragay, G.; Peñuelas-Haro, G.; Ballester, P. *Organic Chemistry Frontiers* **2021**, *8*, 2402-2412.

[3] Guinovart, T.; Hernández-Alonso, D.; Adriaenssens, L.; Blondeau, P.; Martínez-Belmonte, M.; Rius, F. X.; Andrade, F. J.; Ballester, P. *Angew. Chem., Int. Ed.* **2016**, *55*, 2435-2440.
[4] Ciardi, M.; Tancini, F.; Gil-Ramírez, G.; Escudero Adán, E. C.; Massera, C.; Dalcanale, E.; Ballester, P. *J. Am. Chem. Soc.* **2012**, *134*, 13121-13132.

Chapter 6

Gold supramolecular catalysis towards alkyne activation

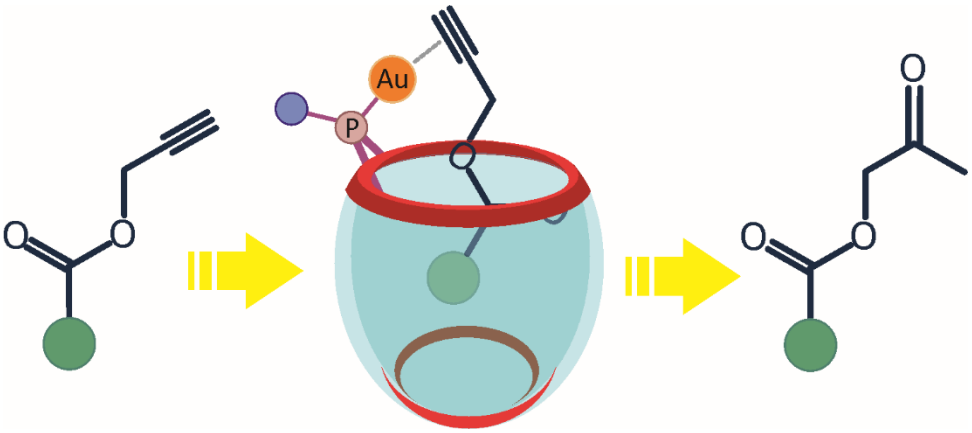

UNIVERSITAT ROVIRA I VIRGILI
CALIX[4]PYRROLE CAVITANDS FOR SUPRAMOLECULAR SENSING AND CATALYSIS
Andrés Felipe Sierra Ramos

6.1 Introduction.

Supramolecular catalysis[1,2] is inspired in living biological systems particularly by nature´s most efficient catalysts, enzymes, because their supramolecular properties such as molecular recognition, self-assembly, self-organization, and kinetic and thermodynamic complementarity.[3] Enzymes offer a confined space (the active site) able to recognize the specific substrate through numerous interactions (hydrophobic, hydrogen bonding, Lewis acid-base), creating a well-organized chemical catalytic site in order to carry out multiple biological operations (Figure 6.*1*).[4] Supramolecular chemistry has developed artificial receptors able to provide confined spaces with different functional groups such as cavitands,[5,6,7,8] cryptands,[9,10] metallocages,[11,12,13] and capsules.[14,15]

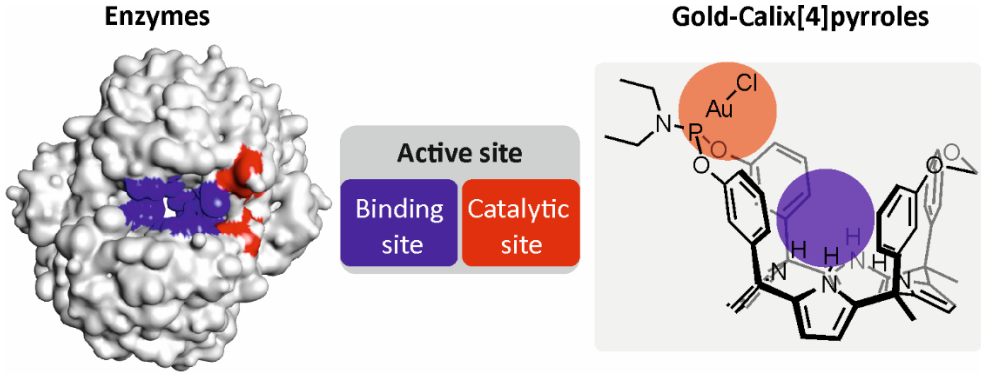

Figure 6.1 Natural(enzymes) and synthetic (gold-calix[4]pyrroles) catalyst.

In the last years, there has been a growing interest in connect transition-metals to the supramolecular receptor as a way to increase the selectivity and activity given by the confined space during the catalytic process.[16] Within the transition metals, gold complexes have evidenced remarkably reactivity and regioselectivity, partially understood by its relativistic effects,[17] becoming in an excellent alternative as catalyst in many organic reactions such as nucleophilic additions, Friedel-Crafts reactions, C-H activation, hydrogenations, oxidations and others.[18]

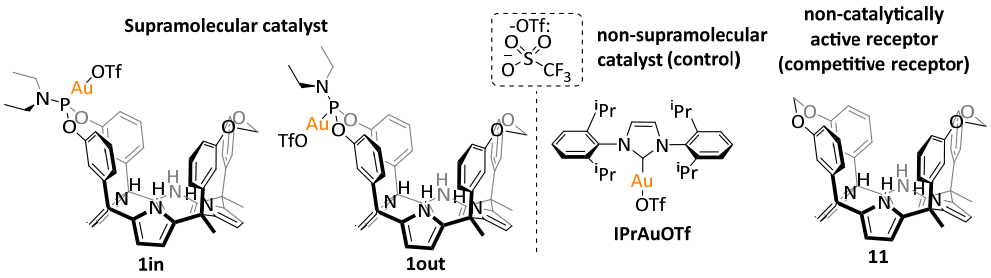

Figure 6.2 Molecular structure of gold-supramolecular catalyst **1in**, **1out**, control catalyst **IPrAuOTf** and non-active receptor **11**.

Considering what said above, gold-supramolecular complexes offer a unique way to impact the catalytic performance in various organic transformations. On one hand, gold atom provides the active site where the catalytic process will occur. On the other hand, the specific conformation of the cavity in the supramolecular receptor induces different selectivity and reactivity towards a pre-organized guest (Figure 6.*1*). We envisioned that a synergy between these two important features will bring new opportunities for calix[4]pyrroles in the supramolecular catalysis field.

Recently, Iwasawa and co-workers developed a resorcin[4]arene based cavitand with a gold center attached to a phosphorous atom inwardly oriented to the cavity. The gold-cavitand complex displayed catalytic activity in the hydration of terminal alkynes and cyclization of diketo-alkynes.[19] It is worth mentioning that addition of water to alkynes is an environmentally friendly method to prepare ketones with 100% atomic economy. In the past, mercury salts[20,21] were frequently used to this purpose.

Calix[4]pyrroles[22] and derivatives have been widely studied as effective receptors in the recognition of polar molecules, as well as mono- and polyatomic anions.[23] However, their use as a possible synthetic platform for supramolecular catalysis remain almost unexplored.[24,25]

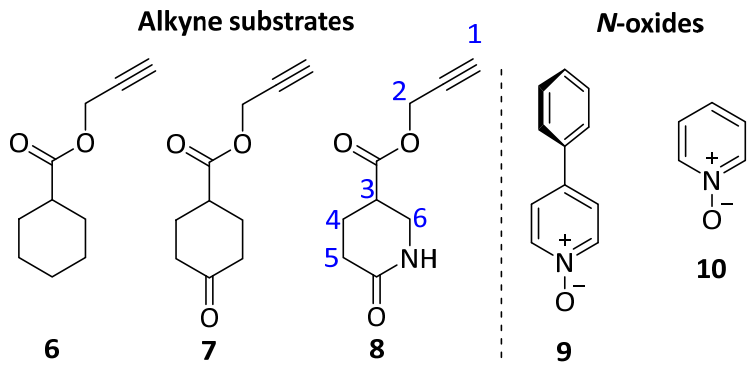

Figure 6.3 Molecular structures of alkyne substrates (**6**, **7** and **8**) and pyridine *N*-oxides (**9** and **10**) used in this study.

Similarly to what previously reported by Rebek and co-workers for a resorcinarene-palladium complex,[26] here, we describe the synthesis of two unprecedented gold-calix[4]pyrrole cavitands **1in** and **1out**, bearing a P-Au bond inwardly and outwardly oriented with respect to the cavity, respectively (Figure 6.*2*). After disclose the catalytic properties towards terminal alkyne activation (**6**, **7** and **8,** Figure 6.*3*), we demonstrated the role of its cavity on the catalytic process, 1) when a *N*-oxide molecules (**9** and **10**) are present, 2) by comparison the results with a non-supramolecular gold-catalyst **IPrAuOTf** (Figure 6.*2*) and finally, 3) the effect of a non-catalytically active receptor **11**, as a competitive receptor.

6.2 Results and discussion.

Synthesis. The synthetic route followed to obtain the gold-calix[4]pyrrole cavitands **1in** and **1out** (Scheme 6.*1*) involves four reaction steps. The synthesis of the α,α,α,α-tetrahydroxycalix[4]pyrrole **2** is the first one.[27]

Mono-methylene bridge cavitand **3** was synthesized by reacting overnight the calix[4]pyrrole **2** with 1 equiv. of bromochloro methane using potassium carbonate as a base in anhydrous DMSO at 60 °C, according to the procedure described in literature.[28] The incorporation of the phosphoramidite group was achieved by reacting cavitand **3** with diethylphosphoramidous dichloride in presence of triethylamine.[19] The reaction produces a mixture of two diasteroisomers **4in** and **4out**, which differ in the spatial orientation of the lone pair of the phosphorous atom with respect to the cavity.

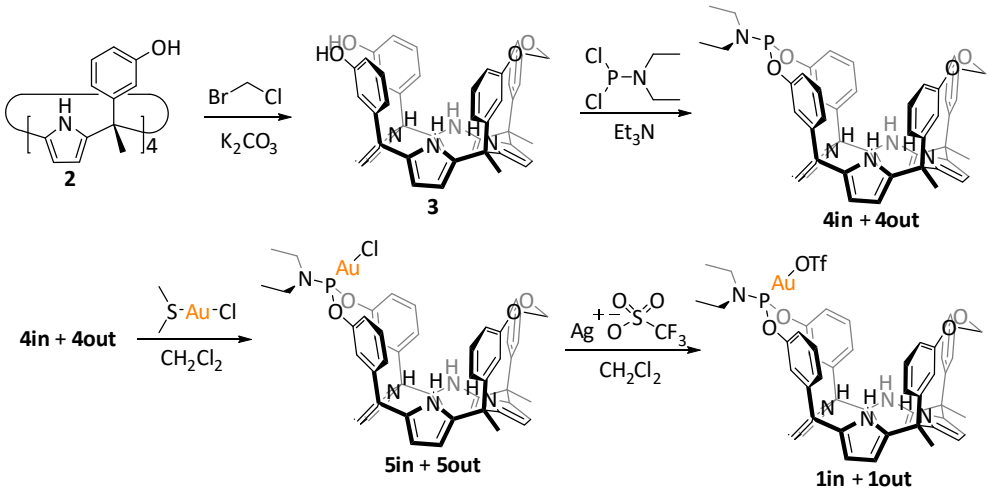

Scheme 6.1 Synthetic scheme for the preparation of the gold calix[4]pyrrole cavitands **1in** and **1out**.

After several attempts the diasterotopic separation using conventional and HPLC chromatography resulted unsuccessful. Indeed, after column chromatography purification we obtained fractions with isomeric mixture enriched with each isomer. Gratifyingly, crystals of **4in** spontaneously grew into the NMR tube containing an enriched fraction in a deuterated acetone solution (Figure 6.*77*). Unfortunately, crystallization as separation method was not reproducible working with bigger scales.

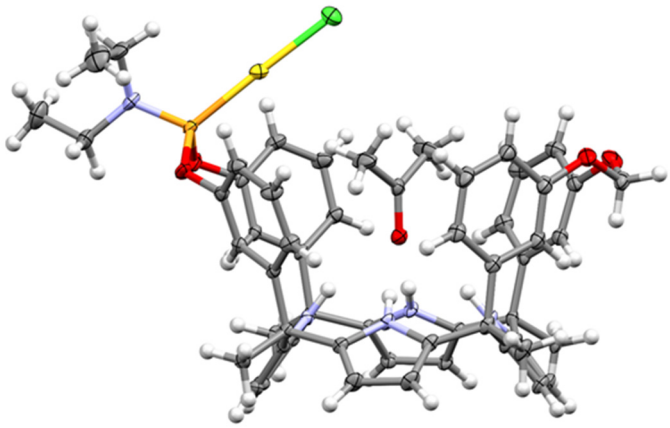

Figure 6.4 X-ray structure of the CH_3COCH_3⊂**5in** inclusion complex. Thermal ellipsoids for C, N, O, P, Cl and Au atoms set at 50% probability; H atoms are shown as spheres of 0.20 Å diameter.

Gold calix[4]pyrrole receptors **5in** and **5out** were obtained by reaction between phosphoramidite cavitand **4** (as an isomer mixture of **4in** and **4out**) and $AuCl{\cdot}S(CH_3)_2$

following a literature procedure.[19] The two isomers were properly separated from the crude of reaction by column chromatography on silica gel, obtaining for each isomer in 20% yield. Slow evaporation of an acetone solution yielded single crystals of both isomers that were suitable for X-ray diffraction. The solid-state structure of the **5in** and **5out** stereoisomers are shown in Figure 6.*4* and Figure 6.*78* respectively. In both cases, the calix[4]pyrrole core adopts a cone conformation having one molecule of acetone included in its aromatic cavity, interacting by hydrogen bond interactions with the pyrrole NHs. Finally, the catalytically active species **1in**, **1out** and **IPrAuOTf** (Figure 6.*2*) were obtained from an anion metathesis reaction with silver triflate and **5in**, **5out** and **IPrAuCl**, respectively. The mixtures were filtered under Argon atmosphere via cannula and preserve as dichloromethane solution to use directly on the catalytic reactions.

The synthesis of the alkyne substrates **6**, **7** and **8** were carried out at room temperature using 1-ethyl-3-(3-dimethylaminopropyl)carbodiimide (EDC) as a carboxyl activating agent for the coupling between propargyl alcohol and cyclohexanecarboxylic acid, 4-oxocyclohexanecarboxylicacid and 6-oxopiperidine-3-carboxylic acid, respectively (Scheme 6.*5***,** Scheme 6.*6***,** Scheme 6.*7*) in the presence of DMAP as a base and dichloromethane as solvent. No further purification was required for the alkyne substrates.

6.2.1 Alkyne hydration

Catalytic activity

We first prove the catalytic activity of the gold-calix[4]pyrrole **1in** towards alkyne hydration using the condition showed in the Scheme 6.*2*, where the catalytic species are obtained *in-situ*. Terminal *n*-hexyne was chosen as a model experiment based on the results previously reported by Iwasawa and co-workers.[19]

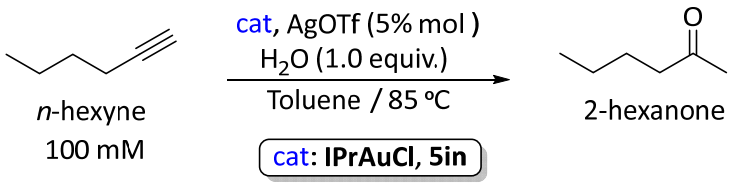

Scheme 6.2 Catalytic hydration reaction of *n*-hexyne.

Control experiment. For the control experiment, we used IPrAuCl a well-known and commercial gold catalyst.[29] After 1 hour we observed the complete hydration of *n*-hexyne, and only proton NMR signals for 2-hexanone were detected (Figure 6.*29*).

Catalytic activity of 1in and 1out. Gold calix[4]pyrrole receptor **1in** also provided catalytic activity towards alkyne hydration. We could observe the appearance in NMR spectra of a signal relative to the CH_3 protons of 2-hexanone (at 1.62 ppm) accompanied by the disappearance of the alkyne proton signal (at 1.73 ppm) after 24 hours of catalysis (Figure 6.*5*). According to the NMR-signal integration a conversion of 60% were reached. Notably, we also detected catalytic activity at lower catalysis loading (2% mol) for **1out** (Scheme 6.*10*, Figure 6.*31*). The reaction was also monitored after 48h of catalysis; however, no noticeable changes were detected. Instead, the formation of black metal precipitate was gradually observed, indicating that the Au atom might separate from the ligand producing a complex decomposition.

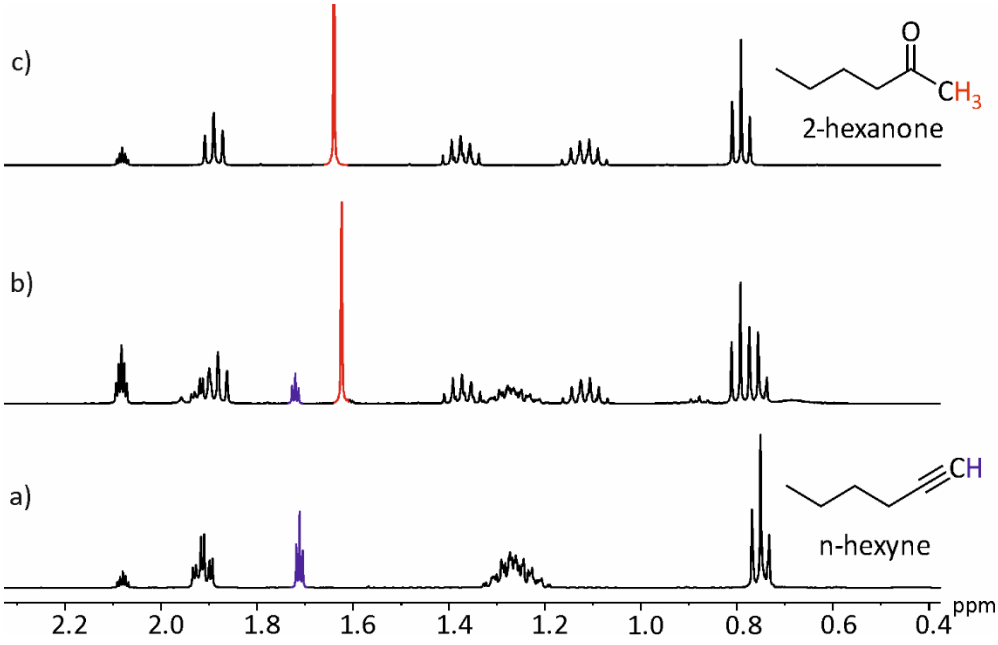

Figure 6.5 Selected region of the ^{1}H NMR spectra (400 MHz, toluene-*d8*, 298 K) for hydration of *n*-hexyne; a) n-hexyne, b) 24h of catalysis with **5in** and c) 2-hexanone.

In an additional experiment, the catalytic activity of **1in** towards *n*-hexyne hydration was studied blocking the access to the cavity using 4-phenylpyridine *N*-oxide (**9**). Interestingly, no noticeable conversion was observed under the same reaction conditions. These results threw some light on the fact that the cavity plays an

important role in the catalytic process (Scheme 6.*11*, Figure 6.*32*). In further experiments we will discuss more in detail the effect of the *N*-oxides on the catalytic process.

Once we evidenced the catalytic activity of receptor **1in**, we studied the role of the calix[4]pyrrole cavity in the catalytic hydration of terminal alkynes (**6**, **7** and **8**).

6.2.2 Binding studies

We probed the interaction of receptor **1in** and guest **8** using ^{1}H and ^{31}P NMR titration experiments in CD_2Cl_2 solutions. We anticipated a higher binding affinity of the receptor towards guest **8** based on the more elevated basicity of its oxygen atom (Figure 6.*10*) The ^{1}H NMR spectrum of receptor **1in** in CD_2Cl_2 solution (Figure 6.*6*a, left panel) showed sharp and well-defined NMR proton signals. The addition of 0.5 equiv. of **5** produced broadening in some of the proton signals of the receptor **1in** (Figure 6.*6*b, left panel), indicating intermediate chemical exchange in the NMR chemical shift time scale between free and bound counterparts. The ^{31}P NMR spectrum of the mixture showed the disappearance of the phosphorous signal (Figure 6.*6*a, right panel). Similar results were observed when 1.0 equiv. was added (Figure 6.*6*c).

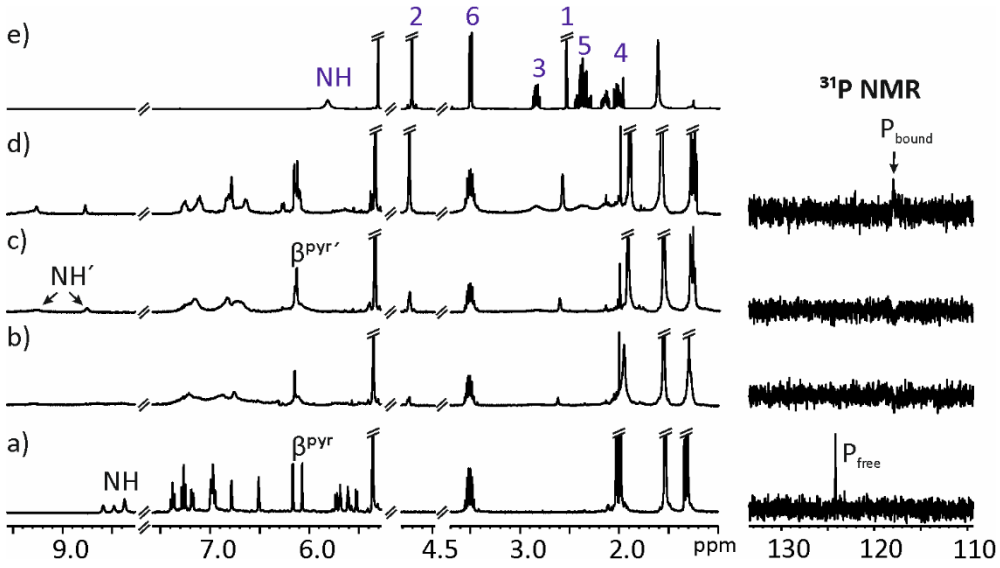

Figure 6.6 Selected regions of the ^{1}H NMR and ^{31}P NMR spectra registered during the titration of a milimolar solution of receptor **1in** with incremental amounts of **8** in CD_2Cl_2 solution. a) Free **1in**; b) **1in** + 0.5 equiv; c) **1in** + 1.0 equiv; d) **1in** + 3.0 equiv; e) Free **8**. See Figure 6.3 for proton assigment of **8**.

The addition of 3.0 equiv. of **8** revealed clearer signals relative to the bound pyrrole NHs, which experience a significant downfield shift (Δδ = + 0.4-0.8 ppm), indicating the hydrogen bonding interactions with the oxygen atom of the bound **8**. The ^{31}P NMR spectrum showed exclusively an upfield shifted for the phosphorus atom (Δδ = - 6.3 ppm), relative to the bound host.

6.2.3 Supramolecular catalysis: Kinetic studies.

After screening two reaction conditions, we found that the hydration of **8** promoted by **5in** proceed more appropriately under methylene chloride at 40 °C (Figure 6.*39*) instead toluene at 85 °C (Figure 6.*38*).We measured the rate constants under conditions showed in Scheme 6.*3* by Gas Chromatography (GC).

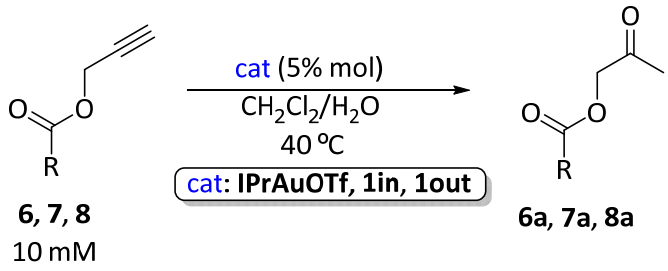

Scheme 6.3 Catalytic hydration reaction of **6**, **7** and **8**.

The presented gold-calix[4]pyrrole receptors (**1in** and **1out**) feature not only a binding cavity where HB-acceptor guests can accommodate, but also contain a gold atom in which chemical transformation and catalysis can be performed. In this study, we focus on the catalytic hydration of guest **6**, **7** and **8** (Figure 6.*3*)**.** All of them are alkyne ester that differ in the substituent group on the carbonyl carbon and its interaction with the cavity and the gold atom. Polar substrates **7** and **8** present a dual nature, they can behave either as a guest interacting with the calix[4]pyrrole cavity, or as a ligand coordinating the gold atom. While non-polar guest **6** has not interaction neither with the cavity or with the gold atom.

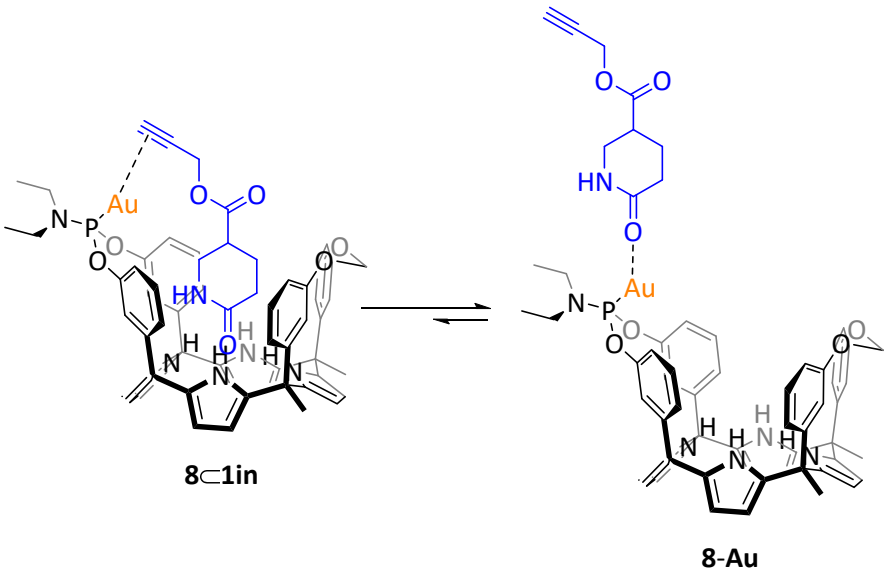

Scheme 6.4 Molecular structures of the 1:1 inclusion complex **8⊂1in**, **8**-Au interaction and its binding equilibrium.

We performed kinetic studies for the hydration of substrates **6**, **7** and **8** promoted by supramolecular receptors **1in** and **1out** and compare the results with a non-supramolecular receptor **IPrAuOTf**. The experiments in dichloromethane solutions and in the presence of the catalyst provided relevant information about the effect of the basicity of the substrate on the supramolecular kinetic results.

Reactions were followed by GC system equipped with a Flame Ionization Detector (FID) and an HP-5 capillary column (30 × 0.32 mm × 0.25 µm). The solutions (1 µl) were injected in a manual mode, with a split ratio of 1:50. The initial oven temperature was 50 °C increased at 20 °C/min up to 325 °C. Using this CG method, each alkyne (**6**, **7** and **8**) and their hydration products (**6a**, **7a** and **8a**) displayed a different retention times (Figure 6.*7*).

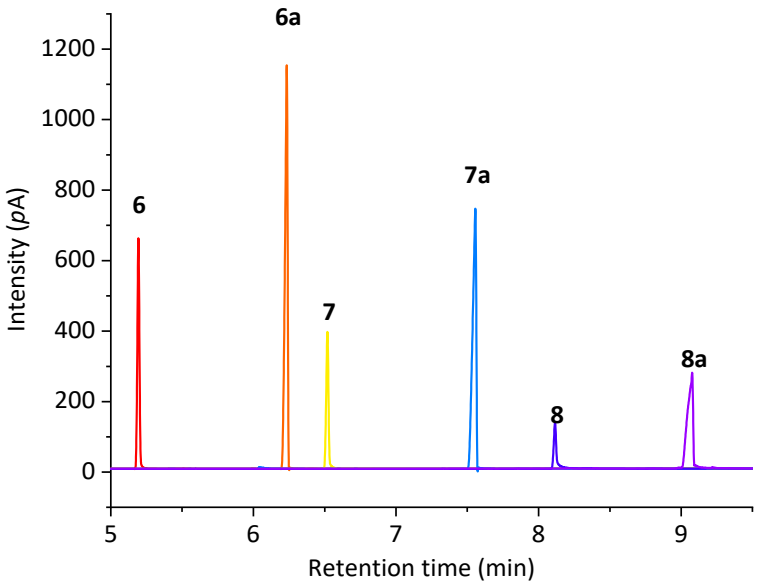

Figure 6.7 GC-FID chromatogram of alkynes **6**, **7**, **8** and their hydration products **6a**, **7a** and **8a**. Note that the differences in the peak intensities is because each compound was injected independently at different concentrations.

In a typical kinetic experiment, a known concentration aliquot of the active specie was added to a water-saturated methylene chloride solution of the substrate (1.0 mL, 10 Mm) and the resulting solution was preserved at 40 °C. Noteworthy, reproducibility problems were observed when the active species were generated *in-situ*.

Integration of the chromatographic peaks provide the percentage of hydration conversion at different reaction times considering the same detector response factor for each alkyne and their respective hydration product (Figure 6.*9*)

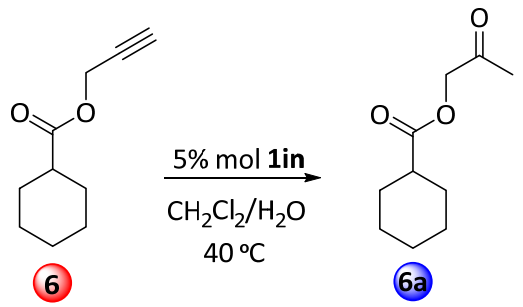

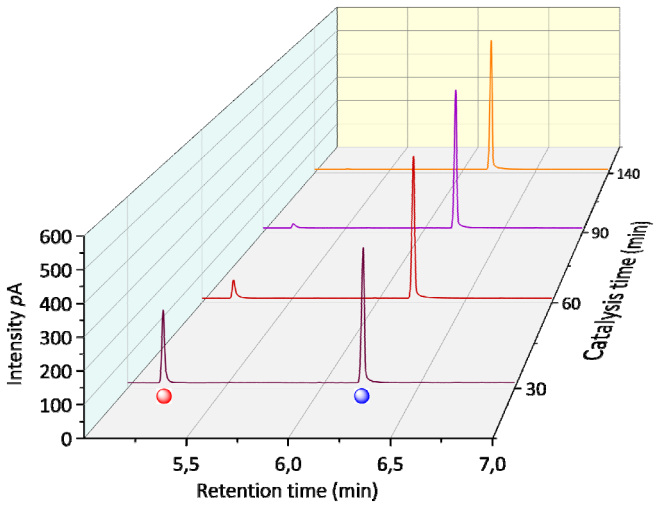

Figure 6.8 Evolution of the GC chromatogram during the hydration of **6** promoted by 5 mol % of **1in**.

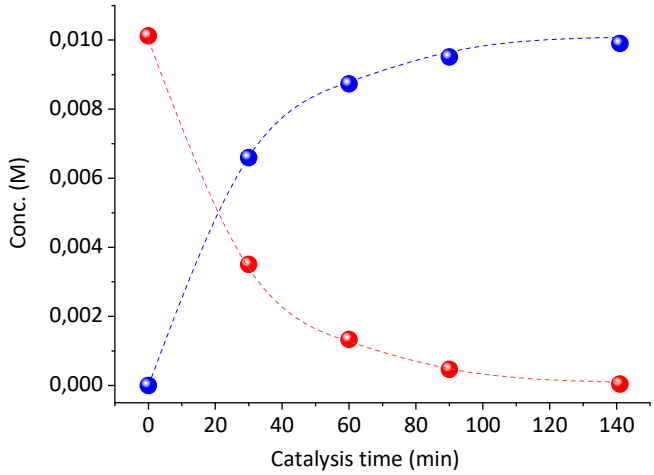

Figure 6.9 Kinetic curves for the alkyne hydration of **6** with 5% mol of **1in**. Red and blue circles represent the experimental data. Red and blue dash lines represent the fit of the kinetic data considering a bimolecular reaction.

The fit of the kinetic results returns a rate constant of k = (0.9±0.1 M^{-1}·min^{-1}) for the hydration of **6** assisted by 5 mol % of receptor **1in**. All the kinetic results are summarized in Table 6.*1*.

Table 6.1 Rate constants values (313 K) for substrates **6**, **7** and **8** promoted by catalyst **1in**, **1out** and **IPrAuOTf**.

	k (M^{-1} min^{-1})		
Sub/Cat	**6**	**7**	**8**
1in	0.9 ± 0.1	0.29 ± 0.04	$< 8.0 \times 10^{-4}$ [a]
1out	> 5.0 [a,b]	0.48 ± 0.06	$(4.4 \pm 0.7) \times 10^{-3}$
IPrAuOTf	0.57 ± 0.01	0.29 ± 0.03	$(8.0 \pm 0.2) \times 10^{-3}$

[a] Estimation using COPASI software version 4.34, [b] 1.53 ± 0.02 M^{-1}·min^{-1} when compound **9** was used as inhibitor.

Several conclusions can be drawn from Table 6.*1*. A dramatic decrease of catalyst activity using polar substrates can be ascribed to the interaction between the gold atom of the catalysts with the oxygen atom of the guest, which makes the interaction with the calix[4]pyrrole cavity less favorable (Scheme 6.*4*).

To substantiate this rationale and, hence, to offer theoretical support to our premise, the electrostatic surface potential (ESP, Scheme 6.*10*) was calculated to illustrate the electrostatic and topographic complementarity of substrates **6**, **7** and **8** in a hypothetical interaction with the catalysts. Particularly, alkyne lactam compound **8** is more electron rich than the guest **7** and even more than guest **6**, this produce an increase in the interaction of the guest with the calix[4]pyrrole cavity but at the same time an increase with the binding with the gold atom, blocking the catalytic site. In this manner, guest **8** presented the lowest rate constant in all cases while compound **6** have the largest values.

Alkyne hydration of **6** promoted by catalyst **1in** and **IPrAuOTf** showed the same order of magnitude in the rate constant while catalyst **1out** is at least five times more active. We found that even in more diluted conditions of guest **6** (5.0 mM) and same catalyst loading (5% mol), the catalyst **1out** displayed very good activity (Figure 6.*59*). Since no interaction are present neither with the cavity nor with the gold atom with compound **6**, we consider the two supramolecular receptors just as two new gold-catalysts. Considering that the environment surrounding the gold atom is different for each catalyst, we expect variations in the catalytic process with non-polar guest.

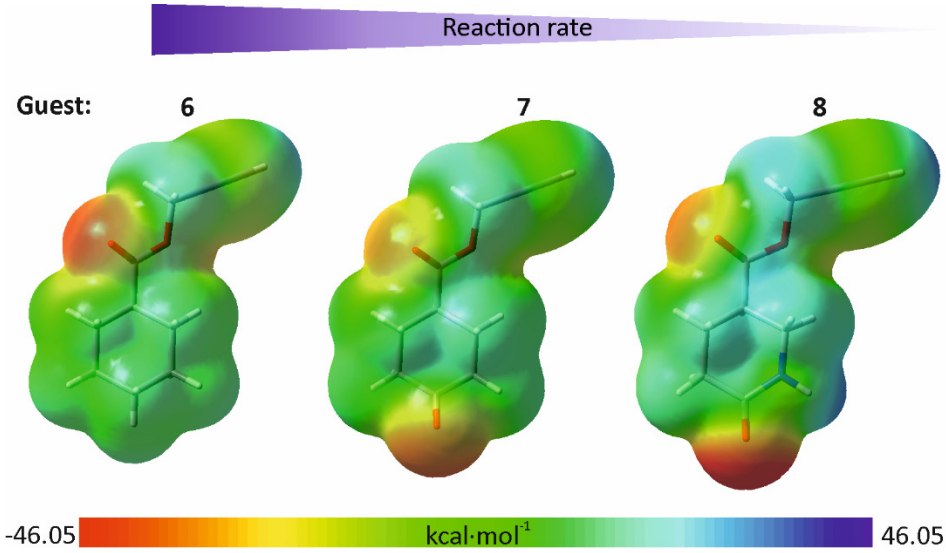

Figure 6.10 Representation of the molecular electrostatic potential surfaces corresponding to substrates **6**, **7** and **8**. Structures were energy-minimized at the B3LYP 3-21G level of theory using GAUSSIAN version 09.

Opposite to substrate **6**, alkyne lactam **8** exhibit the highest basicity located on the oxygen atom of the carbonyl group of the lactam ring (Figure 6.*10*), this cause an increase in the gold-substrate interaction becoming substrate **8** in an inhibitor itself. The two supramolecular catalyst are more affected by this effect since the rate constant decrease three orders of magnitude, but only 72 times less active for the **IPrAuOTf** for the same substrate. Although we expected some reversibility in the **8**-**Au** interaction, because of the very favorable geometry of the **8**⊂**1in** (Figure 6.*4*) and **8**⊂**1out** complexes, the competition of the cavity for the substrate is reduce considerable.

Interestingly, due to the substrate **7** present an intermediate basicity (Figure 6.*10*), the **7**-**Au** interaction is reduced relating with **8** and, in consequence a higher reversibility process can be observed, resulting in substantially increase of around two order of magnitude in the rate constants compare with the magnitude obtained for **8** with the three catalysts. These experimental results not only threw some light on the fact that the cavity and the gold atom compete for polar substrates, but also appropriately correlate the substrate basicity.

Since gold (I) catalyst under anhydrous conditions could favor other reactions, it is the case of gold-catalyzed dearomative spirocyclization of aryl alkynoate esters.[30] A free water reaction was performed at the same conditions in order to evaluate the

presence of other products instead of the hydration one. However, the singlet at 2.12 ppm assigned to the methyl protons of ketone **8a** was also detected, obtaining 25% of conversion according with NMR signal integration (Figure 6.*40*). The water present inherently in the deuterated solvent could promote the hydration reaction.

6.2.4 Kinetic studies at diluted conditions.

We proposed that the alkyne hydration assisted by supramolecular receptors involved a complexation step previous to the catalysis, hence, the catalytic process take place once the complex is formed (intramolecular reaction, Scheme 6.*4*, left side of the equilibrium). In contrast, the gold-oxygen bonding (Scheme 6.*4*, right side of the equilibrium) should be understood as an intermolecular interaction. With the intention of favoring the intramolecular event, experiments at diluted conditions were investigated. When the concentration of **6** was reduced to 0.1 mM, all of these catalytic systems failed to promoted the alkyne hydration and only peak for the starting material was detected by GC-FID (Figure 6.*65* to Figure 6.*68*).

6.2.5 Role of the cavity: *N*-oxides studies

We are interested in elucidate the role of the cavity on the catalytic process, for this reason we used *N*-oxides compounds **9** and **10** (Figure 6.*3*), as strong polar compounds able to interact with the calix[4]pyrrole cavity but also to coordinate the gold atom.

The catalytic process was evaluated after the addition of 1.0 equiv. (regards to the catalysts) of compounds **9** and **10** to a reaction mixture containing the substrate and the catalyst (Figure 6.*11*a).

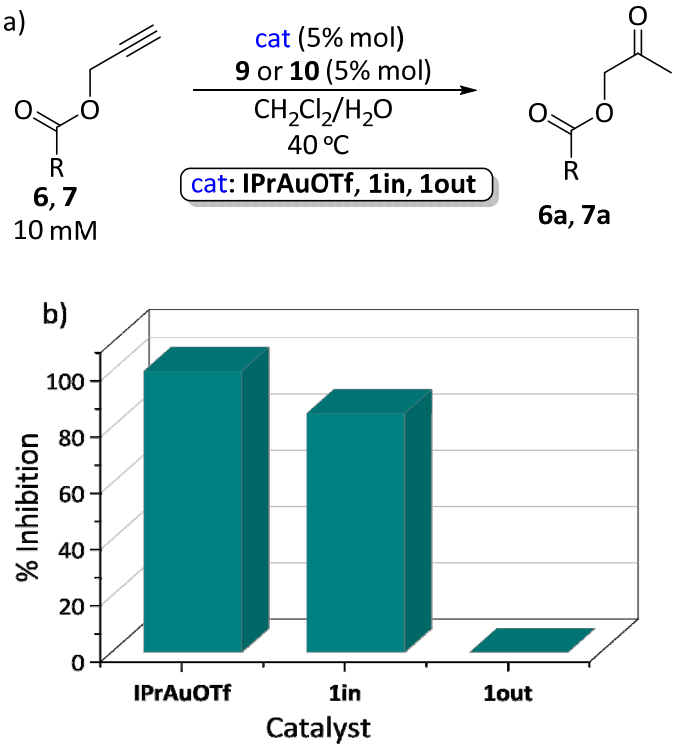

Figure 6.11 a) Inhibition of the catalytic hydration reaction using *N*-oxides, b) Percentage inhibition graph of catalytic hydration of **6** using conditions showed in a), after around 24h of reaction.

Compound **9** presented a total inhibition of the catalytic alkyne hydration of **6** and **7** (Figure 6.*69*, Figure 6.*70*) promoted by **IPrAuOTf**. On the other hand, partial inhibition was observed by compound **9** when **1in** was used to catalyst alkyne hydration of guest **6** and **7.** In fact, inhibitions of 85% and 91% were reached, respectively, after almost 24h of reaction (Figure 6.*71*, Figure 6.*72*). Although this indicate small percentages of conversions, the results suggest that the cavity have a slight effect on the inhibition by compound **9**. However, the most fascinating result took place when we evaluated the catalytic inhibition of compound **9** in the alkyne hydration of **6** promoted by **1out**. In this particular case, the *N*-oxide compound barely affect the catalytic performance of **1out** (Figure 6.*73*). The system experienced just a three-fold decrease in the rate constant (Table 6.*1*, Figure 6.*74*). We attributed this to the fact that the gold atom is blocked in the **9⊂1in** complex (Figure 6.*79*), but not in the case of the **9⊂1out** complex, since the P-Au bond is outwardly oriented with respect to the cavity.

We observed analogous behavior during the catalytic inhibition by compound **10** (Figure 6.*75*). Remarkably, after 24.5h of reaction just 64% of inhibition was reached for the hydrolysis of **6** promoted by catalyst **1in**. We performed simple molecular modeling studies (MM3) to derive the putative structures for the inclusion complexes **9⊂1in** and **10⊂1in** (Figure 6.*79*). The energy-minimized structures of both complexes showed the guest included deep in the aromatic cavity of the receptor. The oxygen atom of the *N*-oxides formed four hydrogen bonds with the pyrrole NHs of the receptor that adopted the cone conformation. Clearly, the guest inclusion of the guest **9** provoked a major blocking of the gold atom making it less available to perform the catalytic activity.

6.2.6 Role of the cavity: addition of a non-catalytically active receptor.

To prove the positive effect of the receptor cavity on the catalytic process, we conducted experimental studies using receptor **11** as a competitive receptor. First, we added 1.0 equivalent of **9** to a solution containing 10 mM of **6** and 5% mol of catalyst. Control experiments showed that, in the present of **9** and in the absence of receptor **11**, the reaction cannot proceed at all in the case of **IPrAuOTf** (Figure 6.*76*) or reduced considerably the catalytic activity in the case of **1in** (18% of conversion after 2.5 h, red dash-line in Figure 6.*12*), because the *N*-oxide bind strongly both binding sites, the gold atom and the cavity. Subsequently to the addition of receptor **11** to the solution with **IPrAuOTf**, we observed 25% and 48% of conversion after 24h and 72h of reaction, respectively. Remarkably, the reaction with **1in** exhibited 70% of conversion after 1h of the addition of receptor **11**. These results suggested that the addition of 10 equiv. of receptor **11** induced the gradual recovery of the catalytic because the **9⊂11** complex formation, delivering free catalyst to the bulk solution.

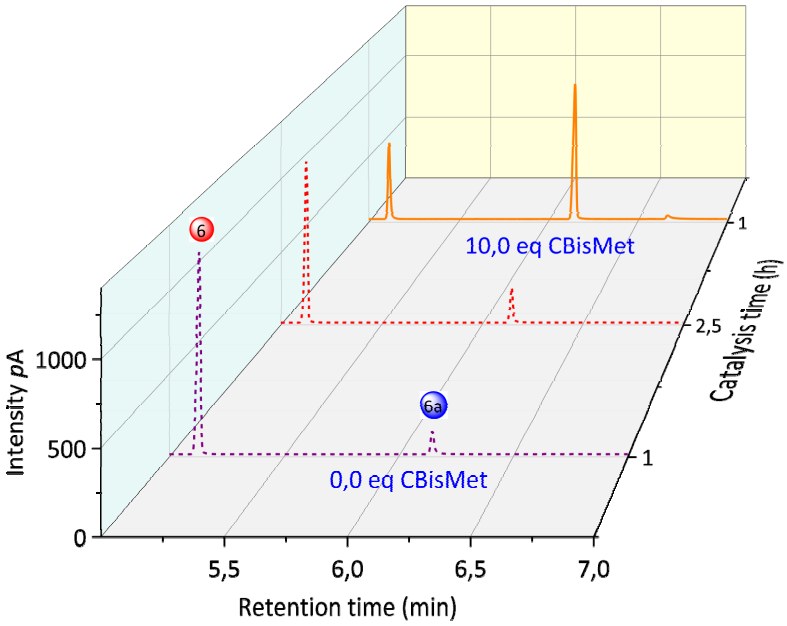

Figure 6.12 Evolution of the GC chromatogram during the recovery of the hydration of **6** promoted by **1in**, before (dash lines, inhibited with **9**) and after (solid line) the addition of receptor **11**.

6.3 Conclusions.

In summary, we described the synthesis of two unprecedented gold-calix[4]pyrrole receptors, **1in** and **1out**, and their non-supramolecular analogous **IPrAuOTf**. We also used 1-ethyl-3-(3-dimethylaminopropyl)carbodiimide (EDC) as a carboxyl activating agent to successfully synthesized guests **6**, **7** and **8**, in order to used it during the kinetic studies.

Experiments with *n*-hexyne demonstrated that supramolecular and non-supramolecular catalysts are actives towards alkyne hydration reaction. Only proton signals relative to the Markonikov product were detected in the ^{1}H NMR spectra, showing the regioselectivity of the catalyst.

Kinetic experiments of **6**, **7** and **8**, followed by GC-FID, showed a good correlation between the polarity of the guest with the magnitude of the rate constant. Higher polarity of the guest, lower rate constant. This finding was supported by theoretical calculation of the electrostatic surface potential (ESP) of the guests. Receptor **1out** showed a higher catalytic performance for alkyne hydration of **6** and **7**, but fairly similar than **IPrAuOTf** for alkyne hydration of **8**.

Finally, we proved the role of the cavity on the catalytic process by the addition of compound **9**, since for alkyne hydration of **6** a total, partial and slightly inhibition was observed with **IPrAuOTf**, **1in** and **1out**, respectively. A subsequent addition of non-catalytically active receptor **11** to the inhibited reaction, generated a gradual recovery on the catalytic effect for catalyst **IPrAuOTf** and **1in**.

We follow in a permanent pursuit for other catalytic reactions or guest structures which allow us more effective results using phosphoramidite calix[4]pyrrole as catalyst. We are convinced that the use of calix[4]pyrrole scaffolds bearing a P-Au bond, will open new possibilities in supramolecular catalysis.

6.4 Experimental section.

6.4.1 General methods and instrumentation.

Reagents and solvents used in the synthesis were obtained from commercial suppliers and were used without further purification unless otherwise stated. Pyrrole was distilled under vacuum and stored in the freezer for further use. THF was dried by distillation from sodium/benzophenone under argon atmosphere. Triethylamine (Et_3N) was distilled with CaH_2 under argon atmosphere and used immediately. Dried *N,N*-dimethylformamide was obtained from a solvent purification system M Braun SPS-800. Flash column chromatography was performed with silica gel (technical grade, pore size 60 Å, 230-400 mesh particle size).

Automatic column chromatography purifications were done with a Combi-flash® RF^+.

Routine ^{1}H-NMR and ^{13}C-NMR spectra were recorded on a Bruker Avance 400 (400 MHz for ^{1}H-NMR) or Bruker Avance 500 (500 MHz for ^{1}H-NMR) ultrashield spectrometer. Deuterated solvents were purchased from Aldrich.

FT-IR measurements were carried out on a Bruker Optics FT-IR Alpha spectrometer equipped with a DTGS detector, KBr beamsplitter at 4 cm^{-1} resolution using a one bounce ATR accessory with diamond windows.

6.4.2 Synthesis and characterization data.

Synthesis of receptors **2** and **3** were synthesized following conditions reported previously in literature.[27,28]

Synthesis of receptor **4**: In a 5 mL Schlenk flask and under Ar atmosphere, receptor 3 (250 mg, 0.33 mmol) was dissolved in 10 mL of THF (previously dried), next TEA (0.25 mL, 1.8 mmol, 5.4 eq) was added in one portion. The diethylphosphoramidous dichloride (0.060 mL, 0.4 mmol, 1.2 eq) was added dropwise. After 5 min of stirring at rt a precipitated started to appear.

After 1 hour of reaction the starting material is complete consumed. The solution was filtered and the solvent was evaporated. The resulting solid was dissolved in DCM and liquid-liquid extractions (3 × 20 mL) with saturated sodium bicarbonate solution were made. The organic phase was washed with water (3 × 10 mL), dried and filtered yielding 150 mg of crude. The product was purified by column chromatography (10 g SiO_2, DCM). Receptor **4** was obtained as an isomeric mixture (125 mg, 44%).

4in, **^{1}H NMR** (500 MHz, acetone-d_6, 298 K) δ (ppm) 8.73 (bs, 2H), 8.5 (bs, 2H), 7.08 (qui, 4H), 6.81 (t, 2H), 6.74 (dd, 2H), 6.74 (dq, 2H), 6.61 (dt, 2H), 6.58 (mult., 2H), 6.56 (t, 2H), 6.43 (d, 1H), 6.05 (mult., 8H), 6.41 (d, H^6, 1H), 3.27 (mult., 4H), 1.86 (s, 3H), 1.85 (s, 3H), 1.15 (t, 6H). **^{31}P NMR** (202 MHz, acetone-d_6, 298 K) δ (ppm) 152.12.

4out, **^{1}H NMR** (500 MHz, acetone-d_6, 298 K) δ (ppm) 8.73 (bs, 2H), 8.80 (bs, 1H), 8.48 (bs, 1H), 7.28 (t, 2H), 7.25 (bs, 2H), 7.13 (t, 2H), 6.92 (d, 2H), 6.88 (d, 2H), 6.77 (bs, 2H), 6.75 (d, 2H), 6.70 (d, 2H), 6.24 (d, 1H), 6.14 (d, 2H), 6.05 (d, 2H), 5.96 (d, 4H), 5.38 (d, 1H), 3.55 (m, 4H), 1.96 (s, 6H), 1.90 (s, 6H), 1.26 (t, 6H). **^{31}P NMR** (202 MHz, acetone-d_6, 298 K) δ (ppm) 117.34.

Synthesis of receptor **5in** and **5out**: On a 5ml Schlenk flask and under an Ar atmosphere, to a solution of 4 (4in and 4out, 138 mg, 0.167 mmol, 1 eq) in anhydrous CH_2Cl_2 (15 mL) at room temperature was added $AuCl{\cdot}S(CH_2CH_3)_2$ (73.8 mg, 0.251 mmol, 1.5 eq). After stirring for 30 min, receptor **4** had been completely consumed (TLC monitoring). The reaction mixture was concentrated in vacuum to give a crude product as a pink solid. Purification by column chromatography (5 g SiO_2, DCM:Hex 80:20) allow us separate the two isomers **5in** and **5out** in 20% each one.

5in. **^{1}H NMR** (500 MHz, acetone-d_6, 298 K) δ (ppm) 8.98 (bs, 2H), 8.6 (bs, 2H), 7.27 (mult., 4H), 7.17 (t, 2H), 6.91 (dd, 2H), 6.82 (t, 2H), 6.78 (dd, 2H), 6.69 (mult., 2H), 6.66 (d, 2H), 6.31 (d, 1H), 6.14 (d, 2H), 6.08 (d, 2H), 6.02 (mult., 4H), 5.39 (d, 1H), 3.56 (mult., 4H), 1.92 (s, 6H), 1.29 (t, 6H). **^{31}P NMR** (202 MHz, acetone-d_6, 298 K) δ (ppm) 122.15.

5out. **^{1}H NMR** (500 MHz, acetone-d_6, 298 K) δ (ppm) 8.98 (bs, 2H), 8.82 (bs, 1H), 8.50 (bs, 1H), 7.30 (t, 2H), 7.26 (q, 2H), 7.14 (t, 2H), 6.93 (dt, 2H), 6.90 (dt, 2H), 6.79 (bs, 2H), 6.73 (mult., 4H), 6.26 (d, 1H), 6.15 (d, 2H), 6.06 (d, 2H), 5.97 (d, 4H), 5.40 (d, 1H), 3.56 (m, 4H), 1.97 (s, 3H), 1.91 (s, 3H), 1.28 (t, 6H). **^{31}P NMR** (202 MHz, acetone-d_6, 298 K) δ (ppm) 117.41.

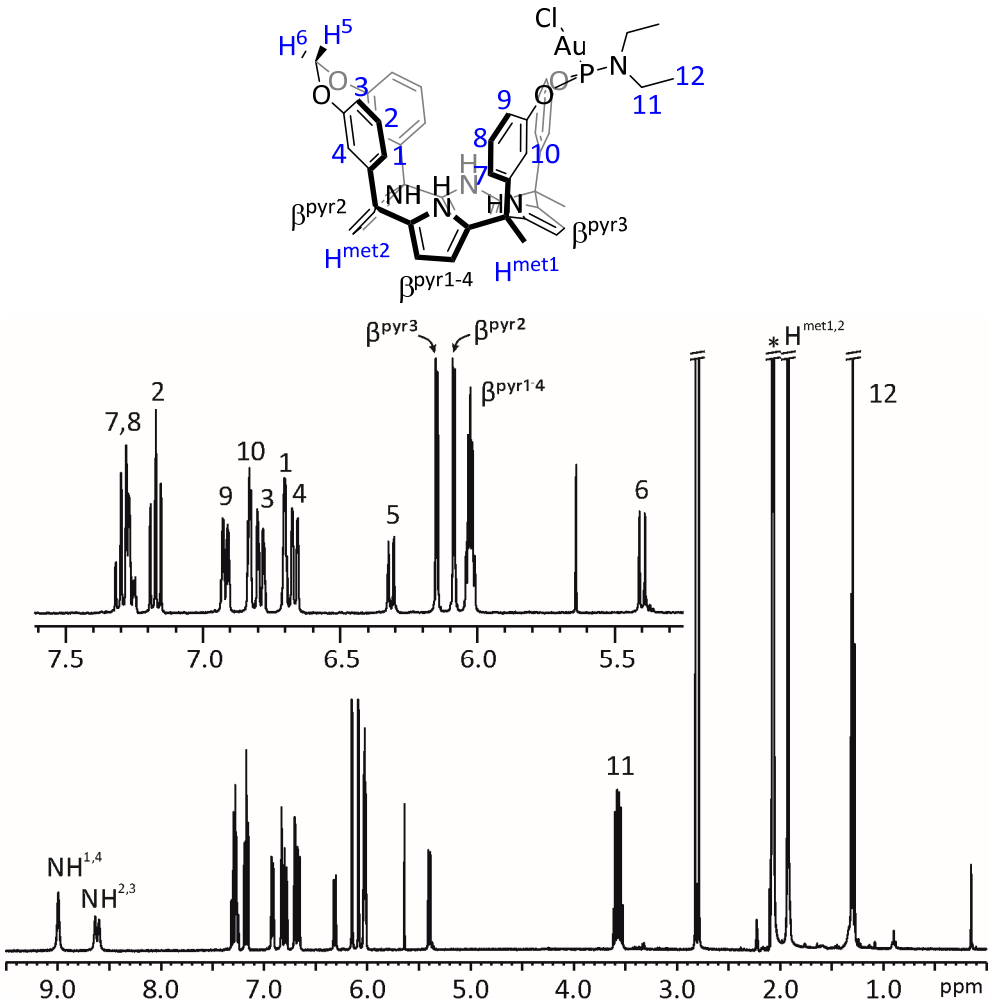

Figure 6.13 ^{1}H NMR (500 MHz, acetone-d_6) of **5in**.

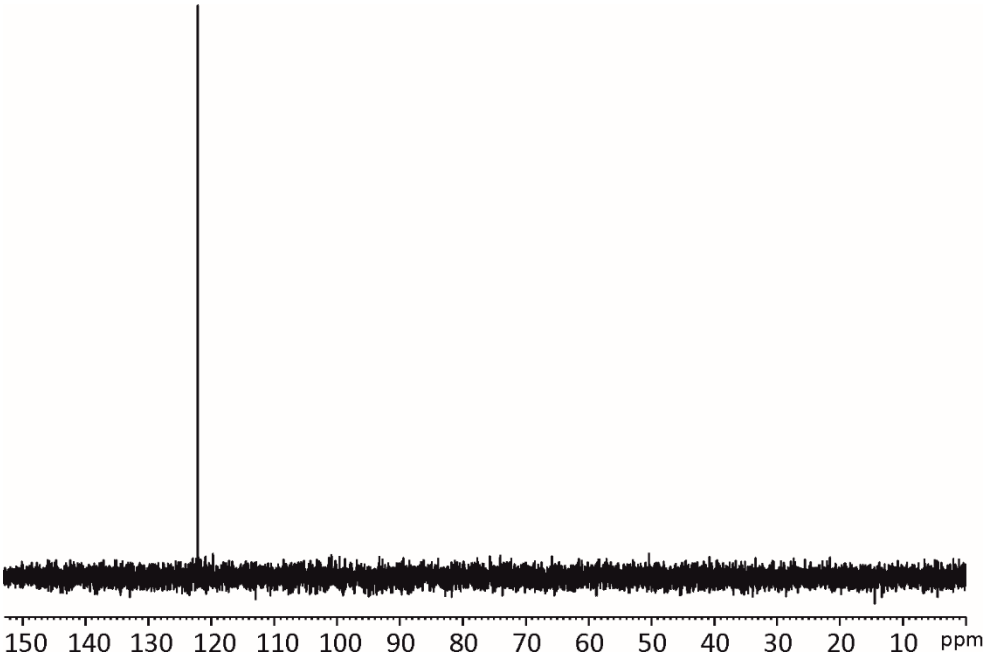

Figure 6.14 ^{31}P NMR (202 MHz, acetone-d_6) of **5in**.

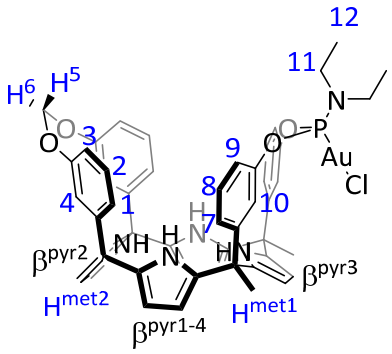

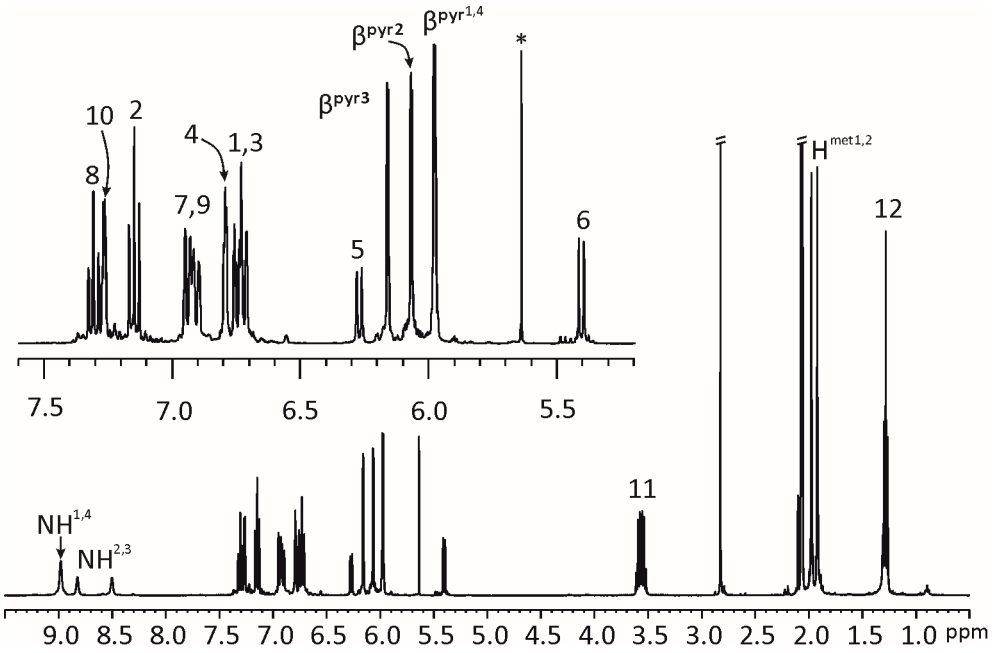

Figure 6.15 ^{1}H NMR (500 MHz, acetone-d_6) of **5out**.

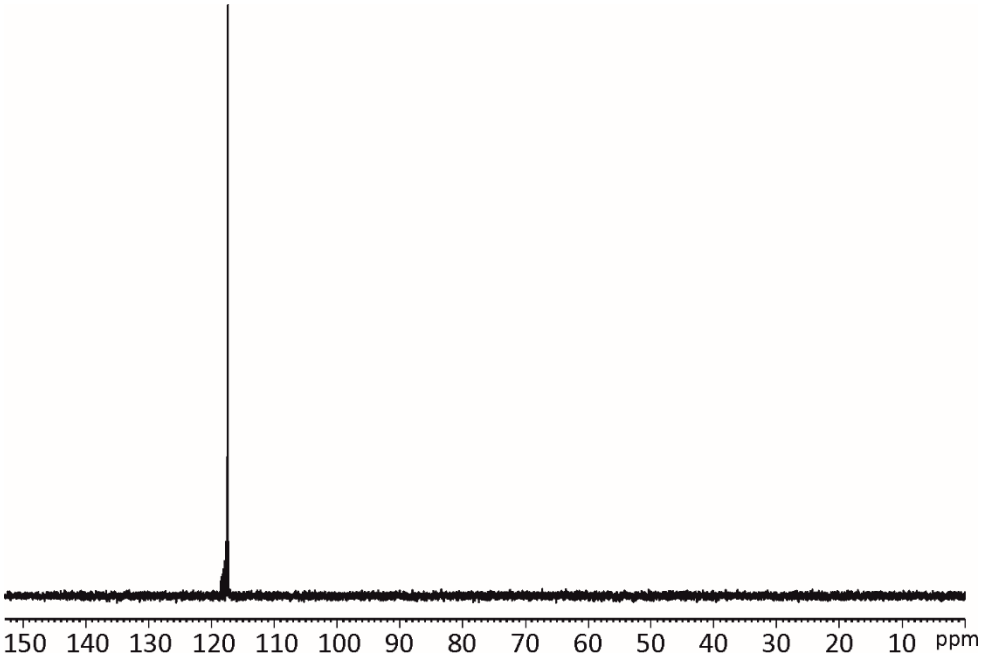

Figure 6.16 ^{31}P NMR (202 MHz, acetone-d_6) of **5out**.

Synthesis of receptors **1in** and **1out**: **5in** (21.861 mg, 0.20 mmol, 1.0 equiv.) and AgOTf (5.071 mg, 0.20 mmol, 1.0 equiv.) were added to a dry-oven 10 mL RBF and 5 mL Schlenk flask respectively, and keep under vacuum for 1h. Three Ar/Vacuum purges were done for both flasks and preserve under Argon atmosphere. Schlenk flask containing the AgOTf was covered with aluminum foil to protect it from light. Dry DCM (2.0 mL) was added to dissolved **5in** and added to the Schlenk flask via cannula. The reaction was stirred at rt for 3h. After that time, a gray precipitate was observed. The suspension was filtered thought Celite® under Argon atmosphere and collected on an external Schlenk. **1in** was preserved as methylene chloride solution. Same protocol was followed in order to obtain **1out**.

^{1}H NMR (400 MHz, acetone-d_6, 298 K) δ (ppm) 9.04 (bs, 2H), 8.62 (bs, 2H), 7.30 (d, J = 4.08 Hz,4H), 7.16 (t, J = 7.47 Hz, 2H), 6.91 (bs, 2H), 6.81 (bs, 2H), 6.77 (bd, 2H), 6.70 (s, 2H), 6.64 (bd, 2H), 6.32(d, J = 7.70 Hz, 1H), 6.08 (bs, 8H), 5.38(d, J = 7.70 Hz, 1H), 3.54 (mult.,4H), 1.92 (s, 12H), 1.26 (t, J = 7.09 Hz, 6H). **^{19}F {1H} NMR** (376 MHz, acetone-d_6, 298 K) δ (ppm) -78.74. **^{31}P {1H} NMR** (162 MHz, acetone-d_6, 298 K) δ (ppm) 117.49.

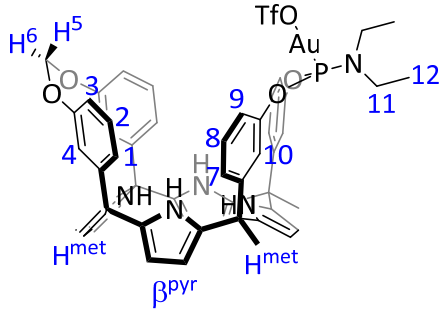

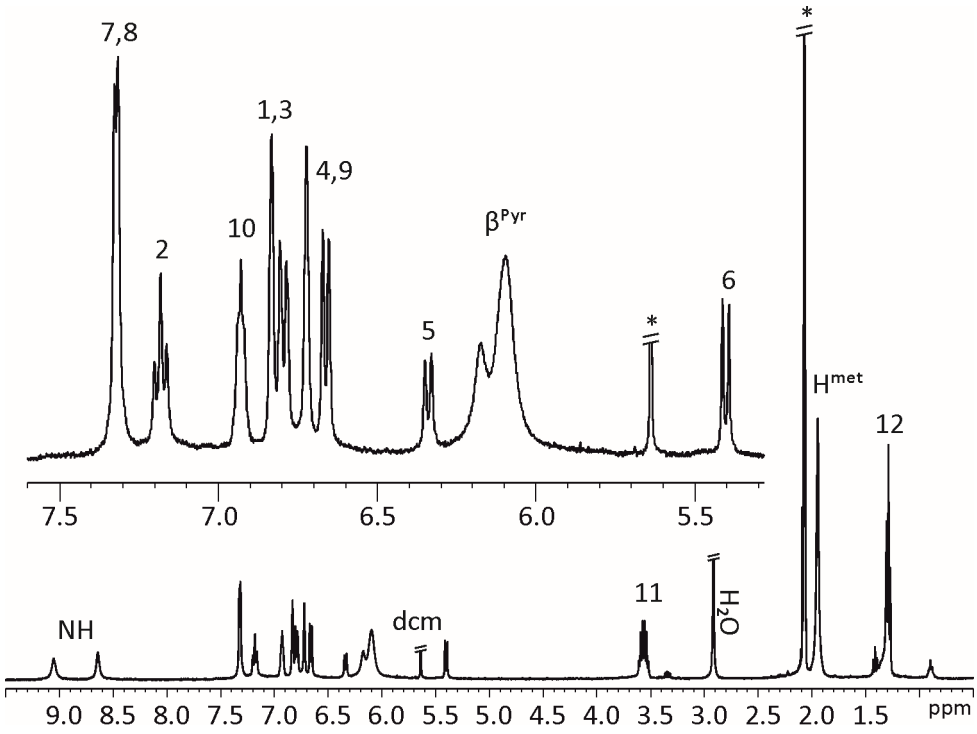

Figure 6.17 ^{1}H NMR (400 MHz, acetone-d_6) of **1in**.

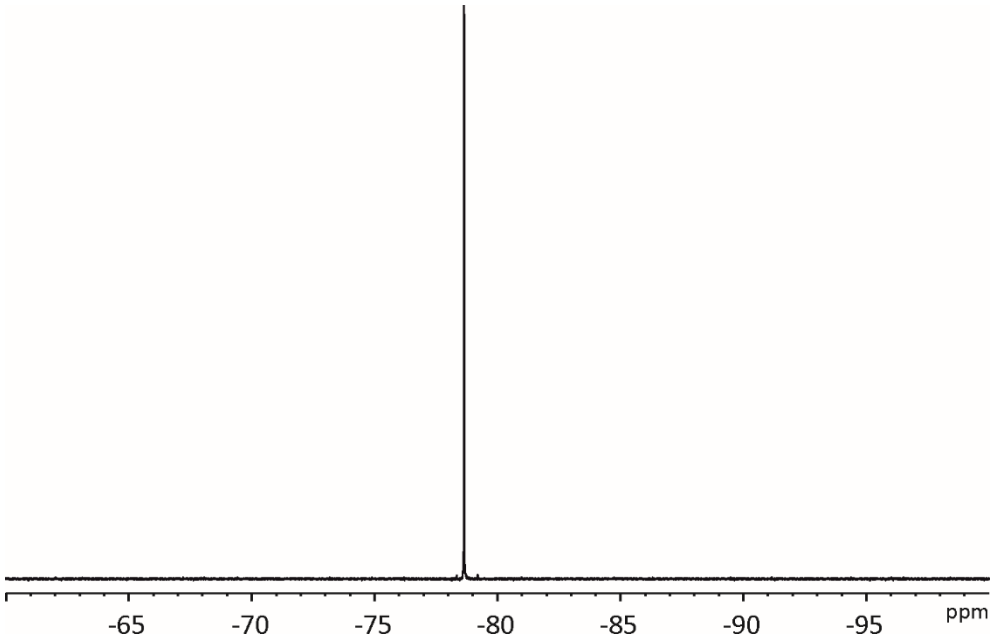

Figure 6.18 ^{19}F{^{1}H} NMR (376 MHz, acetone-d_6) of **1in**.

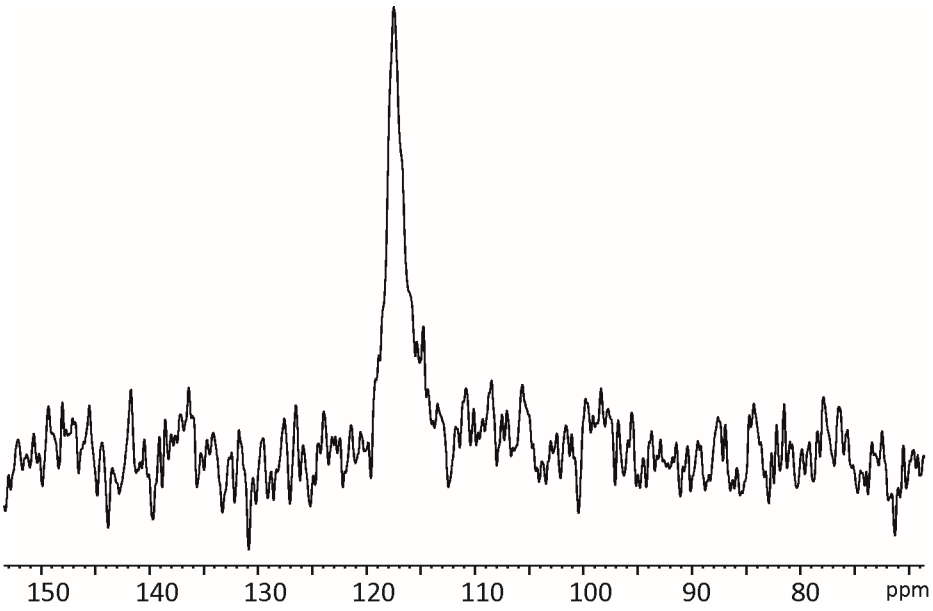

Figure 6.19 $^{31}P\{^{1}H\}$ NMR (162 MHz, acetone-d_6) of **1in**.

Synthesis of **IPrAuOTf**: IPrAuCl (31.025 mg, 0.50 mmol, 1.0 equiv.) and AgOTf (14.675 mg, 0.57 mmol, 1.14 equiv.) were added to a dry-oven 10 mL RBF and 10 mL Schlenk flask respectively, and keep under vacuum for 1h. Three Ar/Vacuum purges were done for both flasks and preserve under Argon atmosphere. Schlenk flask containing the AgOTf was covered with aluminum foil to protect it from light. Dry DCM (5.0 mL) was added to dissolved the IPrAuCl and added to the Schlenk flask via cannula. The reaction was stirred at rt for 2.5h. After that time, a gray precipitate was observed. The suspension was filtered through Celite® under Argon atmosphere and collected on an external Schlenk. IPrAuOTf was preserved as methylene chloride solution. An aliquot of 53 µL of the IPrAuOTf was added to a 1 ml solution (10 mM) of each substrate.

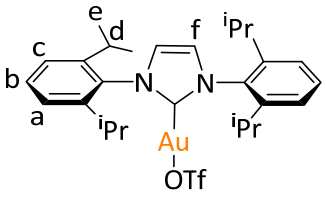

^{1}H NMR (400 MHz, chloroform-*d*, 298 K) δ (ppm) 7.54 (t, *J* = 7.61 Hz, 2H), 7.32 (d, *J* = 7.61 Hz, 4H), 7.25 (bs, 2H), 2.48 (mult., *J* = 7.10 Hz, 4H), 1.32 (d, *J* =7.05 Hz, 12 H),

1.22 (d, *J* =7.05 Hz, 12 H). **^{19}F {1H} NMR** (376 MHz, chloroform-d, 298 K) δ (ppm) -77.30.

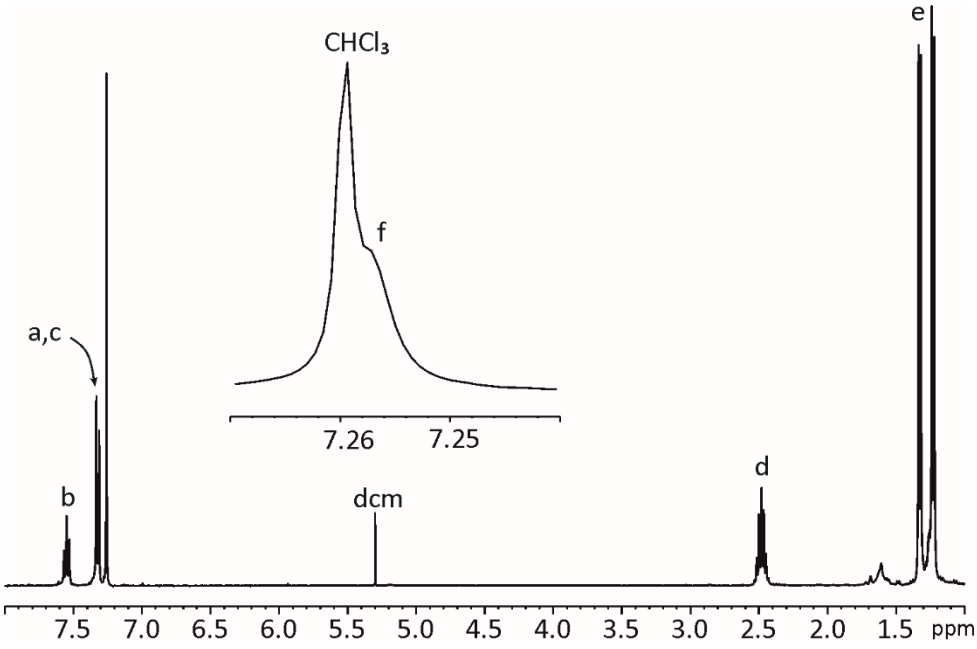

Figure 6. 20 ^{1}H NMR (400 MHz, chloroform-*d*, 298 K) of **IPrAuOTf**.

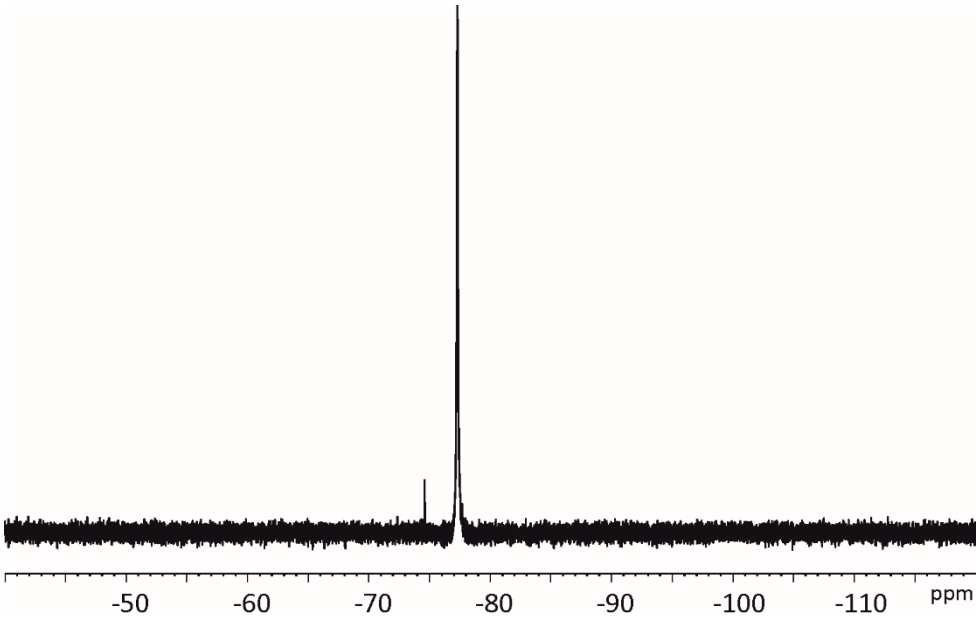

Figure 6.21 ^{19}F NMR (376 MHz, chloroform-*d*, 298 K) of **IPrAuOTf**.

Synthesis of the alkyne substrates (6, 7 and 8).

Synthesis of **6**.

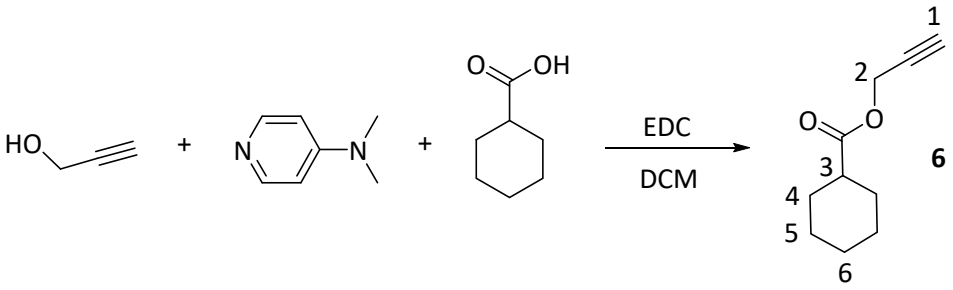

Scheme 6.5 Synthetic scheme for the preparation of substrate **6**.

Propargyl alcohol (337 µL, 5.85 mmol, 1.5 eq), cyclohexanecarboxylic acid (500 mg, 3.90 mmol, 1 eq) and DMAP (238 mg, 1.95 mmol, 0.5 eq) were dissolved in 25 mL of dry DCM. After stirring at room temperature for 30 min, EDC (1070 µL, 5.85 mmol, 1.5 eq) was added to the solution. Reaction mixture was stirred 16 h at room temperature. Then the solid residue was filtered, and the solvent was evaporated in vacuum. Yielding 524 mg (80.8 %) of pure **6**.

IR (film): ν (cm^{-1}) = 3293, 2932, 2856, 1734, 1450, 1380, 1311, 1245, 1161, 1129, 1041, 670. **^{1}H NMR** (400 MHz, CD_2Cl_2, 298 K) δ (ppm) = 4.64 (d, *J* = 2.41 Hz, 2H), 2.49 (t, *J* = 2.50 Hz, 1H), 2.33 (tt, J_1 = 11.33 Hz, J_2 = 3.70 Hz, 1H), 1.94-1.83 (mult., 2H), 1.80-1.68 (mult., 2H), 1.67-1.58 (mult., 1H), 1.50-1.36 (mult., 2H), 1.36-1.15 (mult., 3H).

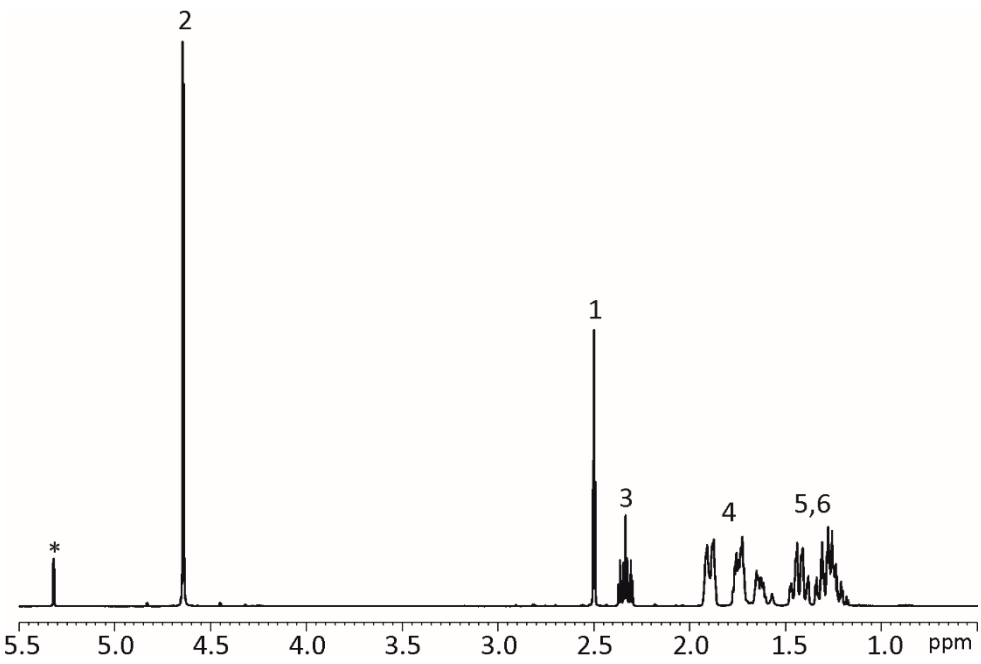

Figure 6.22 ^{1}H NMR (400 MHz, methylene chloride-d_2) of **6**.

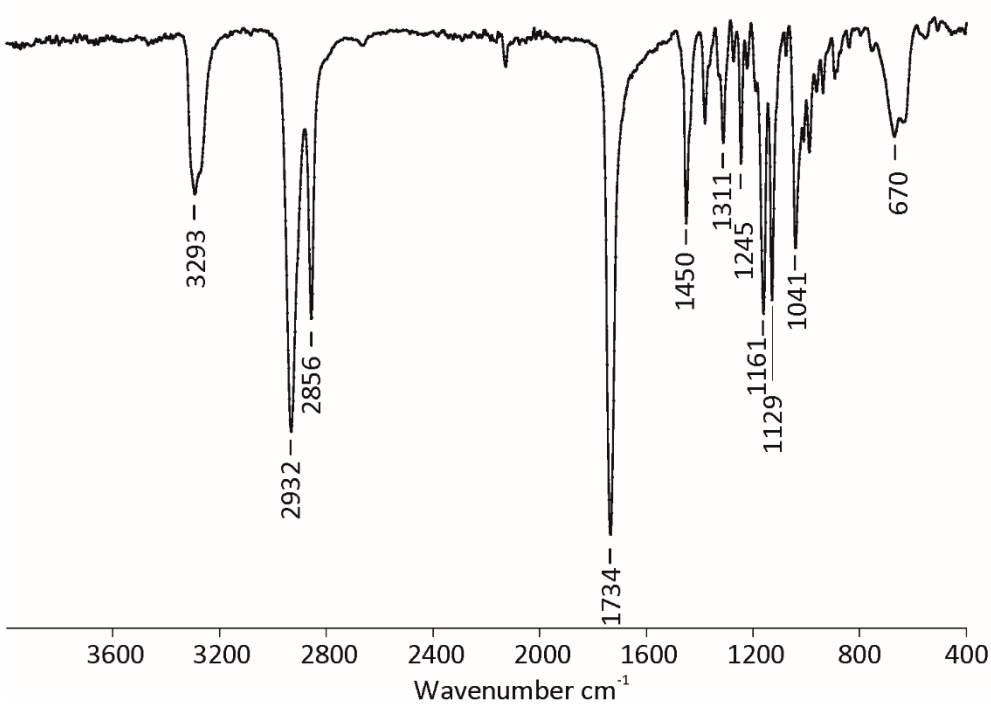

Figure 6.23 FTIR-ATR spectrum of **6**.

Synthesis of **7**.

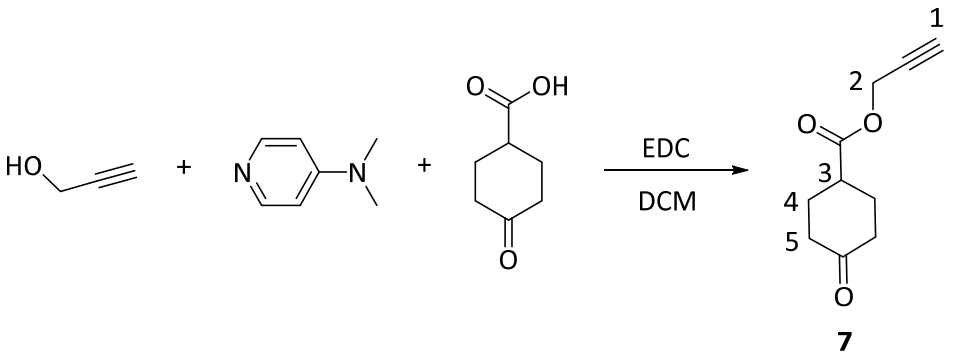

7

Scheme 6.6 Synthetic scheme for the preparation of substrate **7**.

Propargyl alcohol (242 µL, 4.19 mmol, 1.2 eq), 4-oxocyclohexanecarboxylic acid (500 mg, 3.52 mmol, 1 eq) and DMAP (215 mg, 1.76 mmol, 0.5 eq) were dissolved in 25 mL of dry DCM. After stirring at room temperature for 30 min, EDC (770 µL, 4.22 mmol, 1.2 eq) was added to the solution. Reaction mixture was stirred 16 h at room temperature. Then the solid residue was filtered, and the solvent was evaporated in vacuum. Yielding 320 mg (50.5%) of pure **7**.

IR (film): ν (cm^{-1}) = 3270, 2955, 2923, 2875, 2126, 1710, 1438, 1383, 1305, 1158, 1034, 999, 677. **^{1}H NMR** (400 MHz, CD_2Cl_2, 298 K) δ (ppm) 4.70 (d, *J* = 2.50 Hz, 2H), 2.83-2.75 (mult., 1H), 2.53 (t, J_1 = 2.50 Hz, 1H), 2.46-2.28 (mult., 4H), 2.25-2.16 (mult., 2H), 2.05-1.93 (mult., 2H).

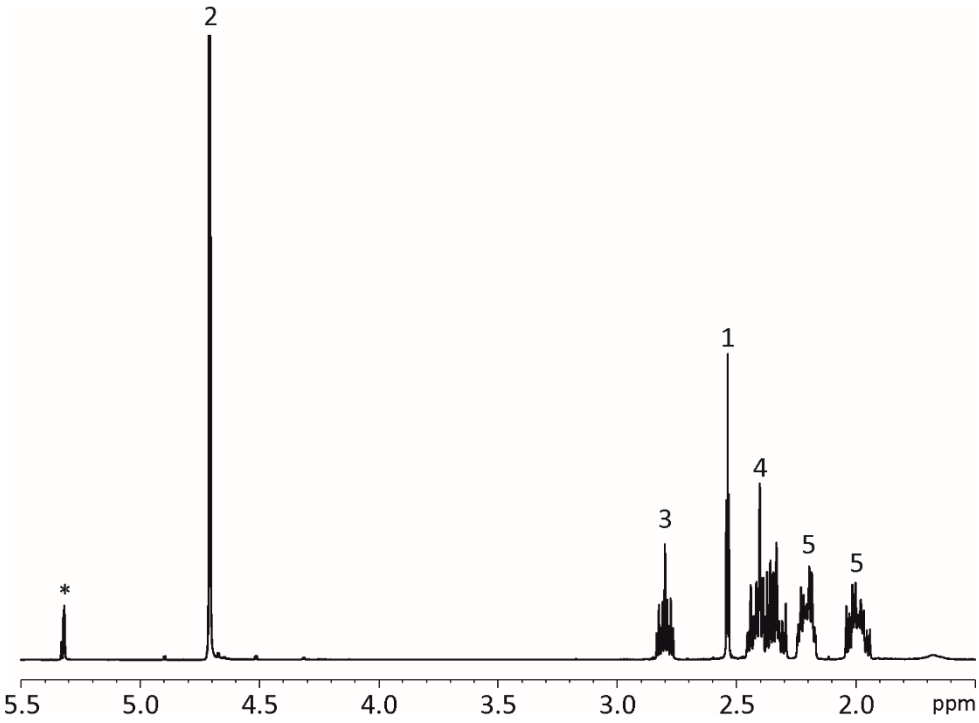

Figure 6.24 ^{1}H NMR (400 MHz, methylene chloride-d_2) of **7**.

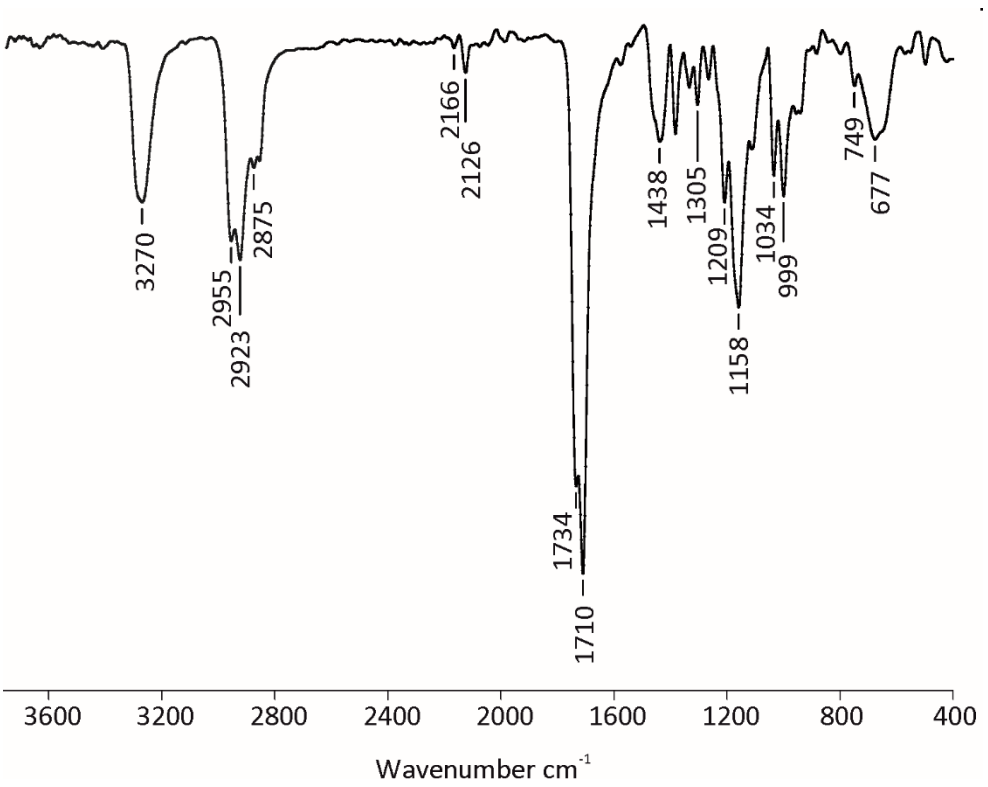

Figure 6.25 FTIR-ATR spectrum of **7**

Synthesis of **8**.

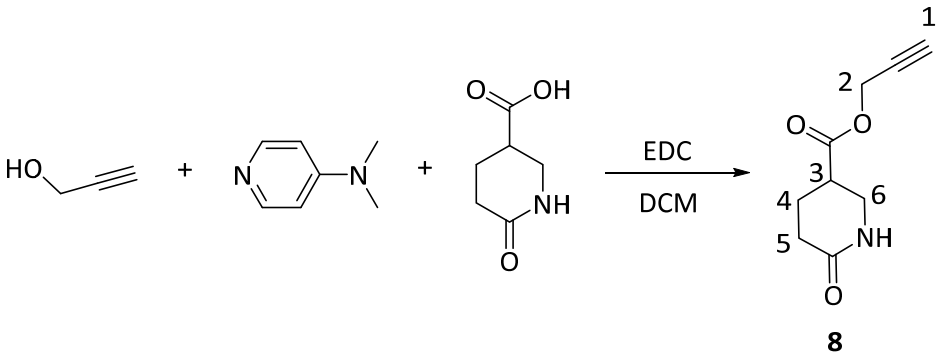

Scheme 6.7 Synthetic scheme for the preparation of substrate **8**.

Propargyl alcohol (242 µL, 4.19 mmol, 1.2 eq), 6-oxopiperidine-3-carboxilic acid (500 mg, 3.49 mmol, 1 eq) and DMAP (213 mg, 1.75 mmol, 0.5 eq) were dissolved in 25 mL of dry DCM. After stirring at room temperature for 30 min, EDC (765 µL, 4.19

mmol, 1.2 eq) was added to the solution. Reaction mixture was stirred 16h at room temperature. Then the solid residue was filtered, and the solvent was evaporated in vacuum. Yielding 220 mg (34.8%) of pure **8**.

IR (film): ν (cm^{-1}) = 3223, 3045, 2962, 2893, 2126, 1732, 1655, 1501, 1413, 1385, 1303, 1222, 1169, 1138, 1004, 954, 834, 690, 631, 514, 450. **^{1}H NMR** (400 MHz, CD_2Cl_2, 298 K) δ (ppm) 5.83 (br, NH, 1H), 4.72 (dd, J_1 = 2.41 Hz, J_2 = 1.02 Hz, H^2, 2H), 3.51 (dd, J_1 = 7.50 Hz, J_2 = 2.30 Hz, H^6, 2H), 2.88-2.79 (m, H^3, 1H), 2.55 (t, J_1 = 2.50 Hz, H^1, 1H), 2.45-2.27 (m, H^5, 2H), 2.19-2.09 (m, H^4, 1H), 2.06-1.94 (m, H^4, 1H). **HRMS (ESI-TOF)** m/z: $[M+Na]^+$ Calcd for $C_9H_{11}NNaO_3$ = 204.0637; found = 204.0640.

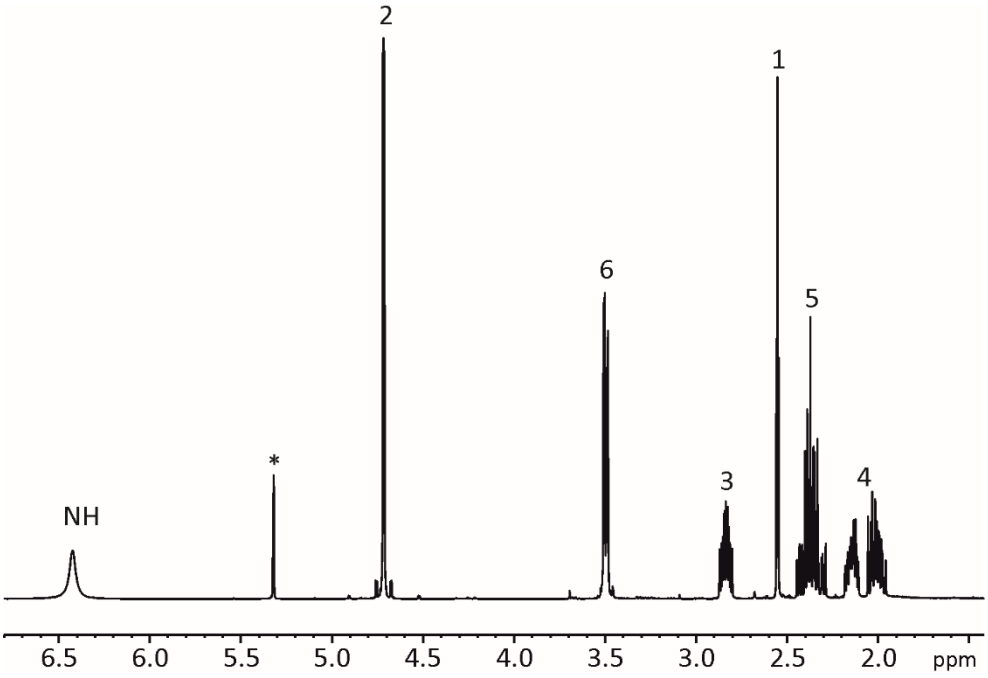

Figure 6.26 ^{1}H NMR (400 MHz, methylene chloride-d_2) of **8**.

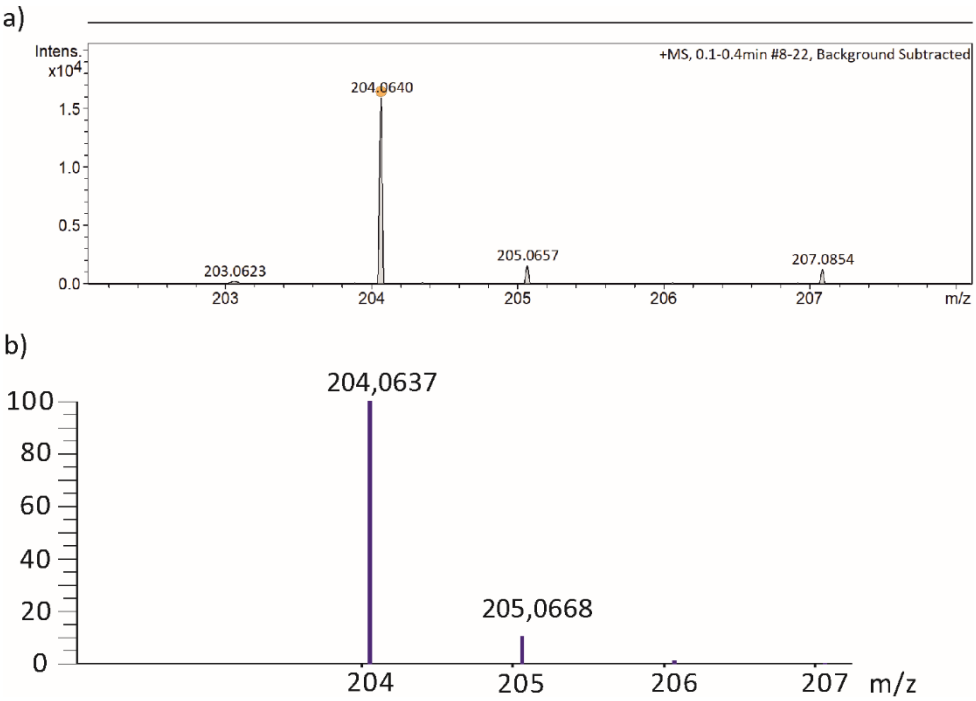

Figure 6.27 a) HR-MS spectrum of compound **8** and b) theoretical isotope patterns.

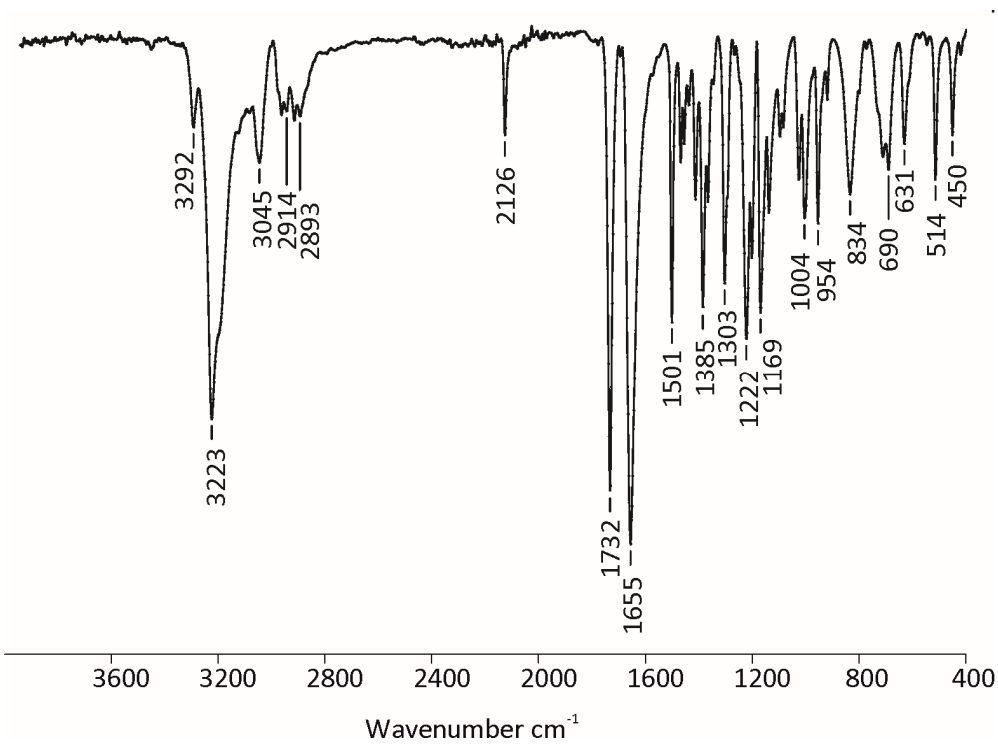

Figure 6.28 FTIR-ATR spectrum of **8**.

6.4.3 Study of the catalytic activity.

Towards *n*-hexyne hydration.

- Catalysis with IPrAuOTf.

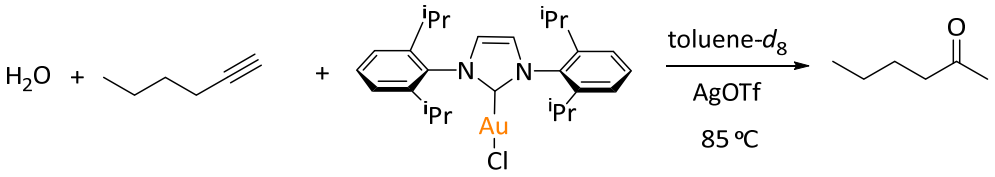

Scheme 6.8 Scheme of the *n*-hexyne hydration promoted by **IPrAuCl**.

In an NMR Young tube were solubilized 1.751 mg of **IPrAuCl** (0.05 eq, 2.82 µmol), and 0.725 mg of AgOTf (0.05 eq, 2.82 µmol), in 0.55 mL of toluene-d_8. After 6.63 µL of *n*-hexyne (1 eq, 0.056 mmol), and 1 µL of water (1 eq, 0.056 mmol) were added. The mixture was heated at 85 °C.

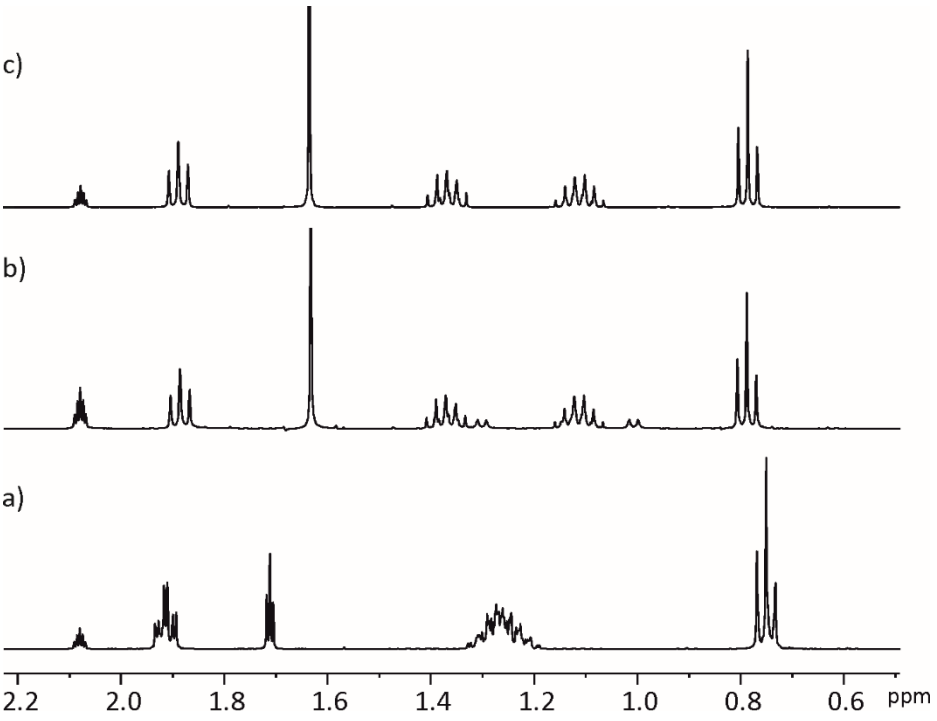

Figure 6.29 ^{1}H NMR (400 MHz, toluene-d_8, 298 K) during hydration of *n*-hexyne promoted by **IPrAuCl**: a) reacting mixture at the beginning of the reaction; b) reacting mixture after 1h; c) 2-hexanone.

- Catalysis with **5in**.

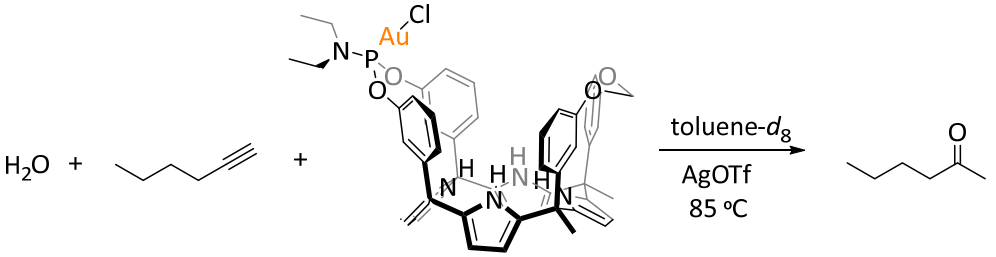

Scheme 6.9 Scheme of the *n*-hexyne hydration promoted by **5in**.

In an NMR Young tube were solubilized 3.04 mg of **5in** (0.05 eq, 2.8 µmol), and 0.293 mg of AgOTf (0.02 eq, 1.140 µmol), in 0.55 mL of toluene-d$_8$. After 6.63 µL of *n*-hexyne (1 eq, 0.056 mmol), and 1 µL of water (1 eq, 0.056 mmol). The mixture was heated at 85 °C.

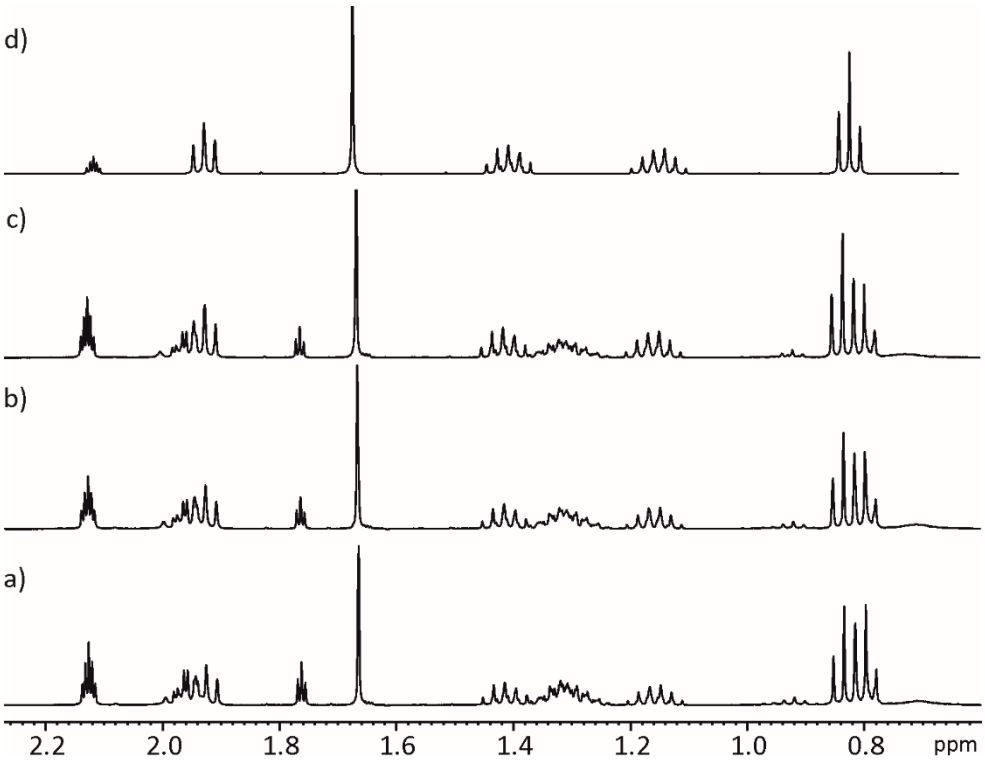

Figure 6. 30 Selected region of ^{1}H NMR (400 MHz, toluene-d_8, 298 K) of: a) reacting mixture after 1h; b) reacting mixture after 2h; c) reacting mixture after 24h; d) 2-hexanone.

- Catalysis with **5out**.

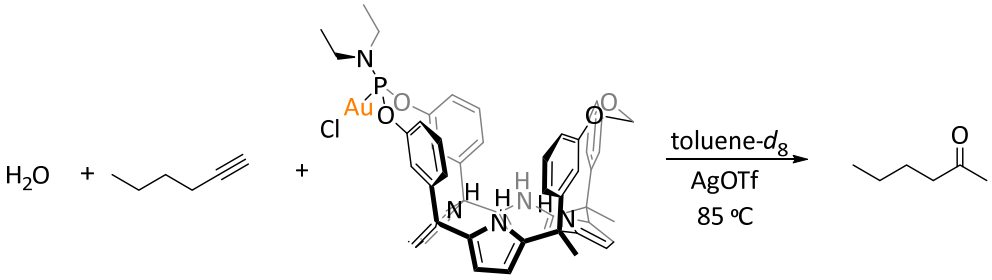

Scheme 6.10 Scheme of the *n*-hexyne hydration promoted by **5out**.

In an NMR Young tube were solubilized 1.148 mg of **5out** (0.019 eq, 1.085 µmol), and 0.293 mg of AgOTf (0.020 eq, 1.140 µmol), in 0.55 mL of toluene-d_8. After 6.63 µL of *n*-hexyne (1 eq, 0.056 mmol), and 1 µL of water (1 eq, 0.056 mmol). The mixture was heated at 85 °C.

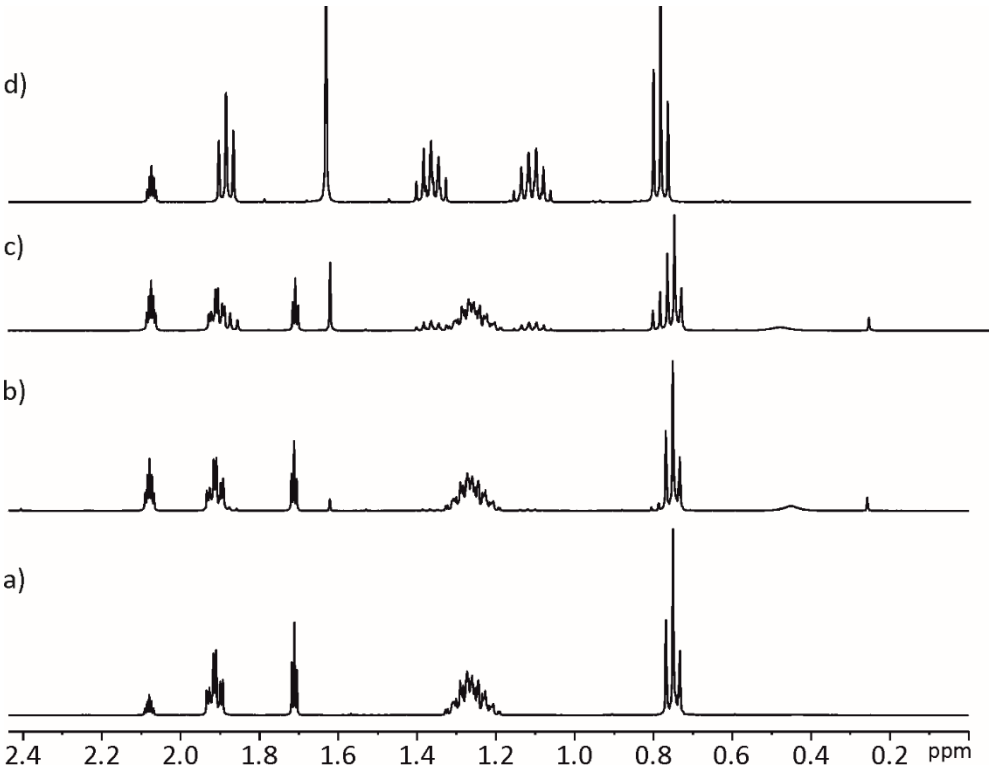

Figure 6.31 ^{1}H NMR (400 MHz, toluene-d_8, 298 K) of: a) reacting mixture at the beginning of the reaction; b) reacting mixture after 1h; c) reacting mixture after 12h; d) 2-hexanone.

- Catalysis with **5in** and 4-phenylpyridine *N*-oxide (**9**).

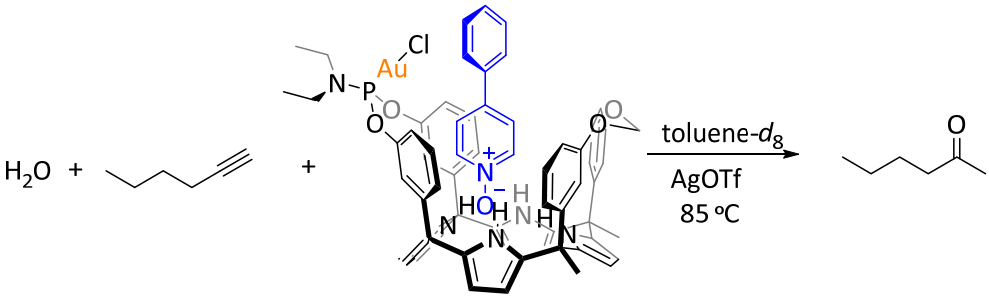

Scheme 6.11 Scheme of the *n*-hexyne hydration promoted by **5in** and compound **9** as inhibitor.

In an NMR Young tube were solubilized 2.98 mg of **5in** (0.05 eq, 2.98 µmol), 0.704 mg of AgOTf (0.05 eq, 2.74 µmol) and 0.469 mg of 4-phenylpyridine *N*-oxide (**9**) (0.05 eq, 2.74 µmol), in 0.55 mL of toluene-d_8. After 6.63 µL of *n*-hexyne (1 eq, 0.056 mmol), and 1 µL of water (1 eq, 0.056 mmol). The mixture was heated at 85 °C.

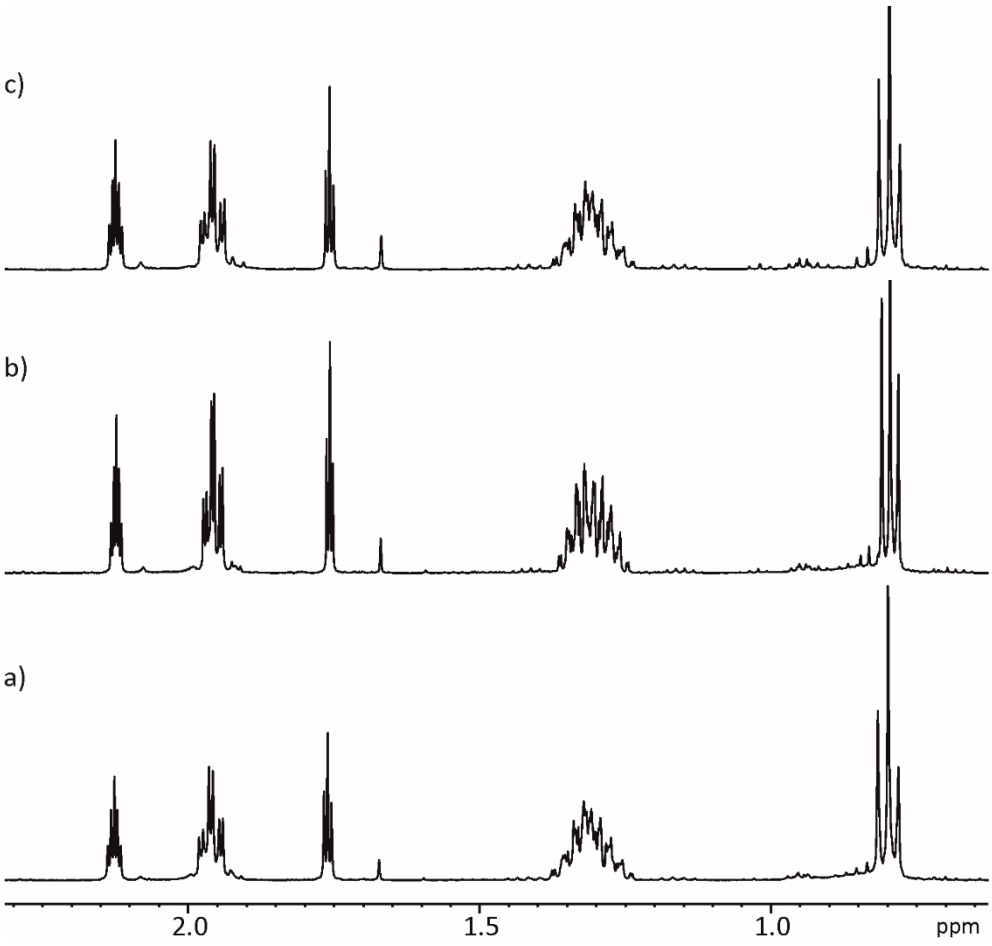

Figure 6.32 ^{1}H NMR (400 MHz, toluene-d_8, 298 K) of: a) reacting mixture after 1h; b) reacting mixture after 2h; c) reacting mixture after 24h.

Towards alkyne hydration of 6.

- Catalysis with **IPrAuCl.**

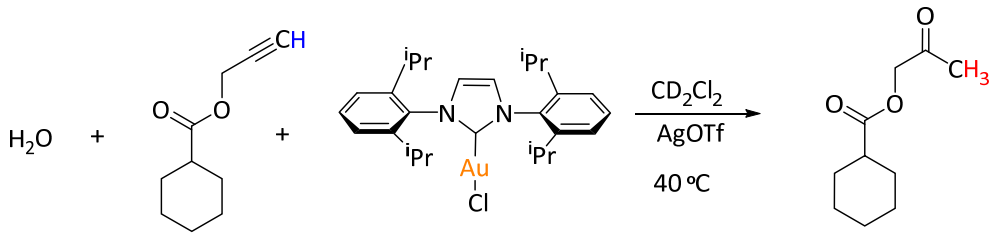

Scheme 6.12 Scheme of the alkyne hydration of **6** promoted by **IPrAuCl** as catalyst.

In an NMR Young tube were solubilized 1.95 mg of **IPrAuCl** (0.05 eq, 3.13 µmol), 0.770 mg of AgOTf (0.05 eq, 3.00 µmol) in 0.55 mL of methylene chloride-d_2. After 10 mg of **6** (1 eq, 0.060 mmol), and 1 µL of water (1 eq, 0.056 mmol). The mixture was heated at 40 °C.

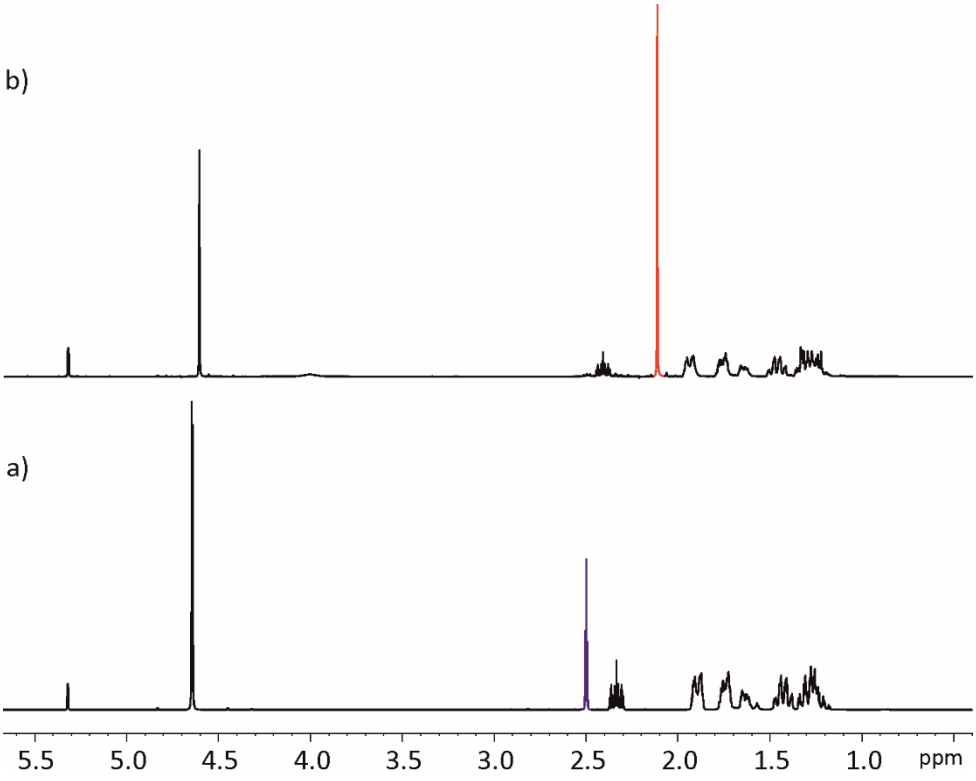

Figure 6.33 ^{1}H NMR (400 MHz, methylene chloride-d_2, 298 K) of: a) free **6**; b) reacting mixture after 1h.

- Catalysis with **5in.**

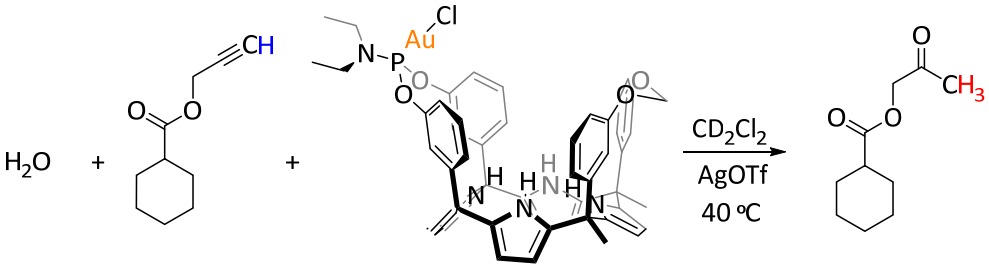

Scheme 6.13 Scheme of the alkyne hydration of **6** promoted by **5in**.

In an NMR Young tube were solubilized 3.55 mg of **5in** (0.05 eq, 3.20 µmol), 0.700 mg of AgOTf (0.05 eq, 3.00 µmol) in 0.55 mL of methylene chloride-d_2. After 10 mg of **6** (1 eq, 0.060 mmol), and 1 µL of water (1 eq, 0.056 mmol). The mixture was heated at 40 °C.

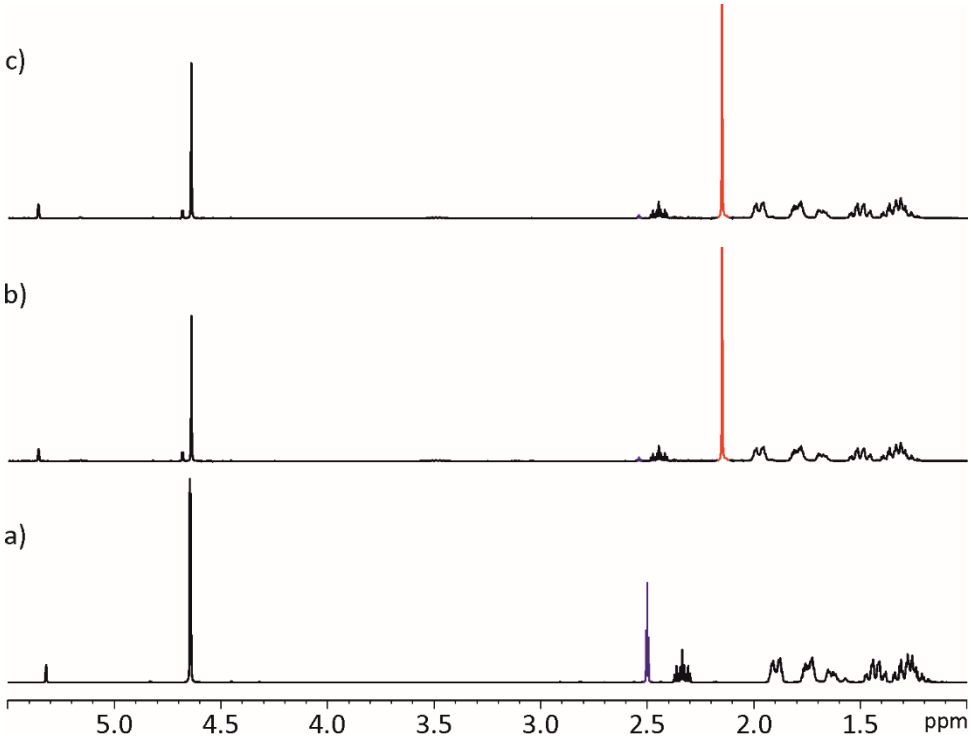

Figure 6.34 Selected region of the ^{1}H NMR spectra (400 MHz, methylene chloride-d_2, 298 K) for a) free 6, b) 1h of catalysis and c) 2h of catalysis with **5in**.

Towards alkyne hydration of 7.

- Catalysis with **IPrAuCl.**

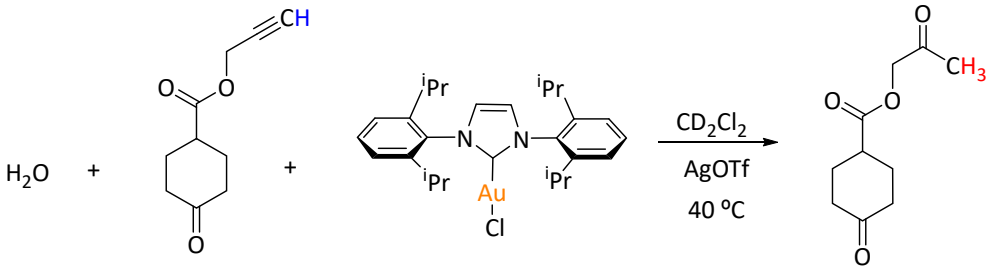

Scheme 6.14 Scheme of the alkyne hydration of **7** promoted by **IPrAuCl**.

In an NMR Young tube were solubilized 1.70 mg of **IPrAuCl** (0.05 eq, 2.80 µmol), 0.710 mg of AgOTf (0.05 eq, 2.80 µmol) in 0.55 mL of methylene chloride-d_2. After 10 mg of **7** (1 eq, 0.055 mmol), and 1 µL of water (1 eq, 0.056 mmol). The mixture was heated at 40 °C.

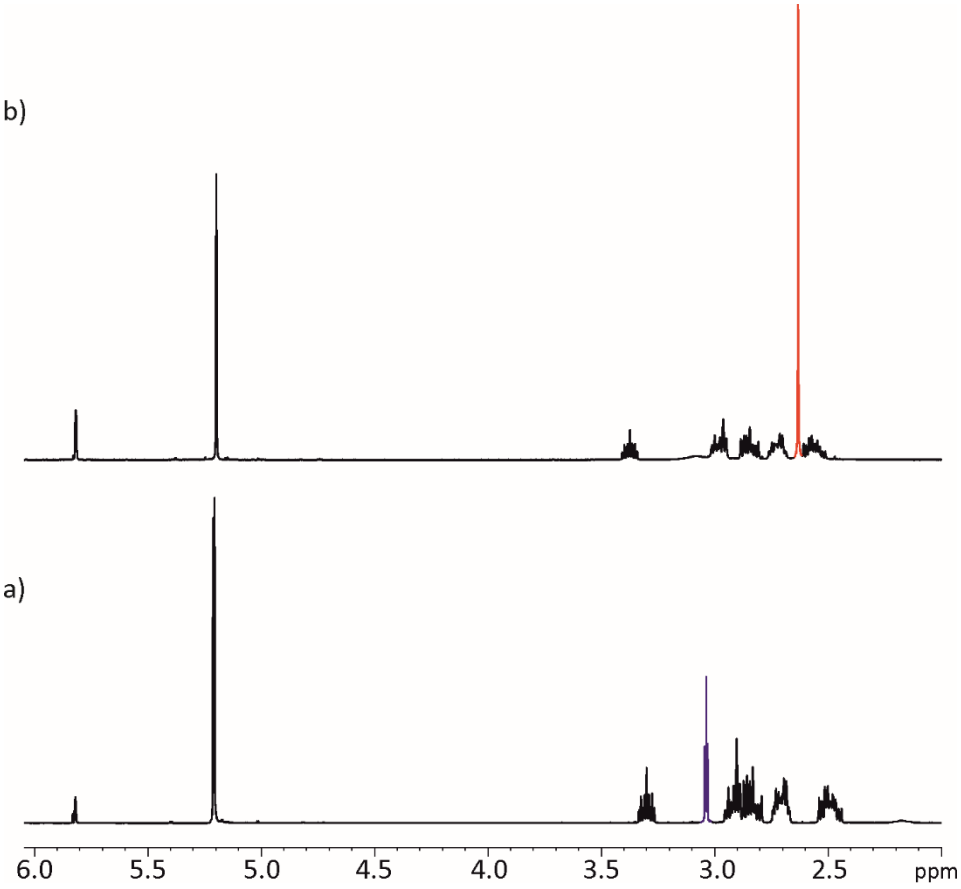

Figure 6.35 Selected region of the ^{1}H NMR spectra (400 MHz, methylene chloride-d_2, 298 K) for a) free **7**, b) 1h of catalysis with **IPrAuCl**.

- Catalysis with **5in.**

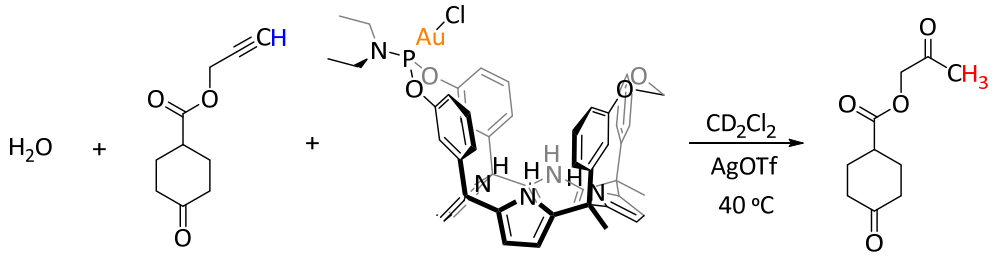

Scheme 6.15 Scheme of the alkyne hydration of **7** promoted by **5in**.

In an NMR Young tube were solubilized 3.585 mg of **5in** (0.05 eq, 3.30 µmol), 1.005 mg of AgOTf (0.06 eq, 3.91 µmol) in 0.55 mL of methylene chloride-d_2. After 11.89 mg of **7** (1 eq, 0.066 mmol), and 1 µL of water (1 eq, 0.056 mmol). The mixture was heated at 40 °C.

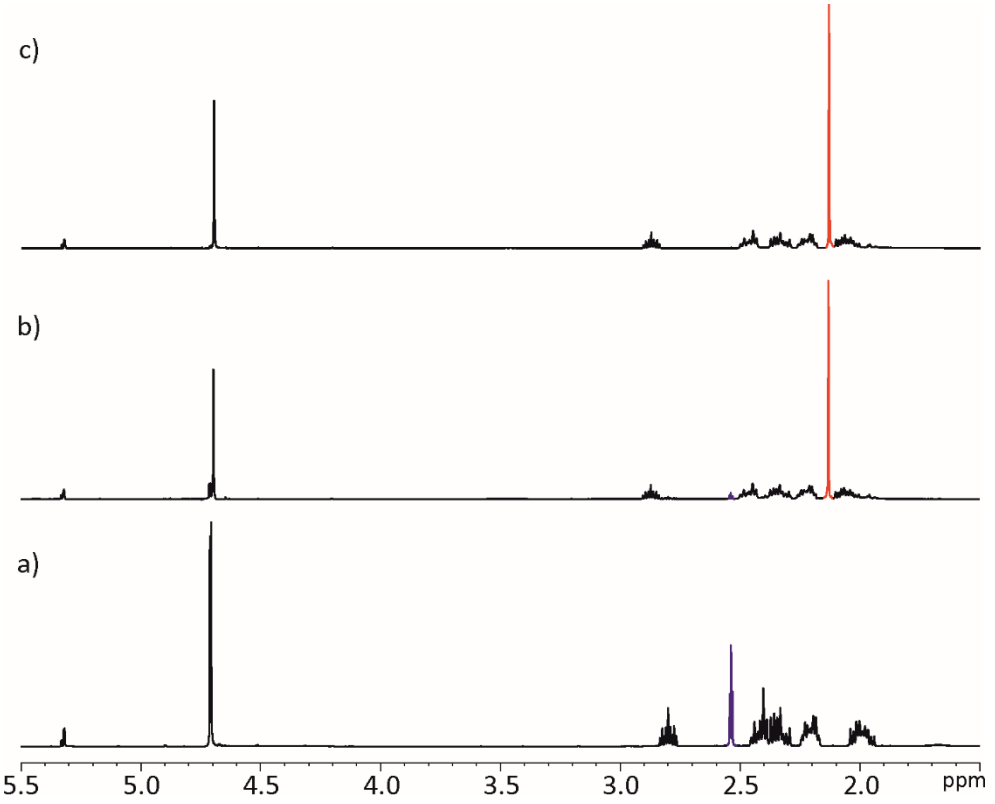

Figure 6.36 Selected region of the ^{1}H NMR spectra (400 MHz, methylene chloride-d_2, 298 K) for a) free 7, b) 1h of catalysis and c) 2h of catalysis with **5in**.

Towards alkyne hydration of 8.

- Catalysis with **IPrAuCl.**

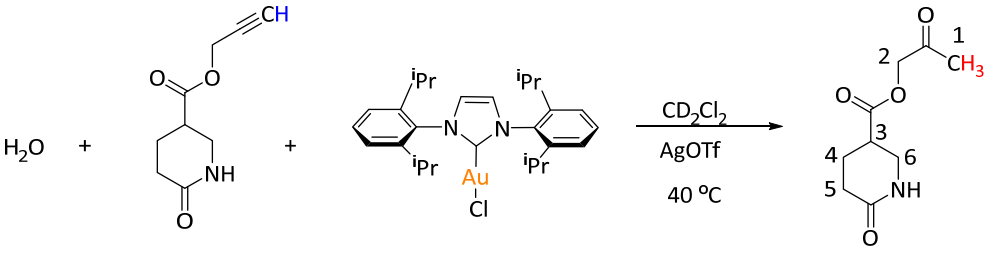

Scheme 6.16 Scheme of the alkyne hydration of **8** promoted by **IPrAuCl**.

In an NMR Young tube were solubilized 1.856 mg of **IPrAuCl** (0.055 eq, 2.98 µmol), and 0.715 mg of AgOTf (0.052 eq, 2.78 µmol), in 0.55 mL of methylene chloride-d_2. After 9.76 mg of **8** (1 eq, 0.054 mmol), and 1 µL of water (1 eq, 0.056 mmol). The mixture was heated at 40 °C.

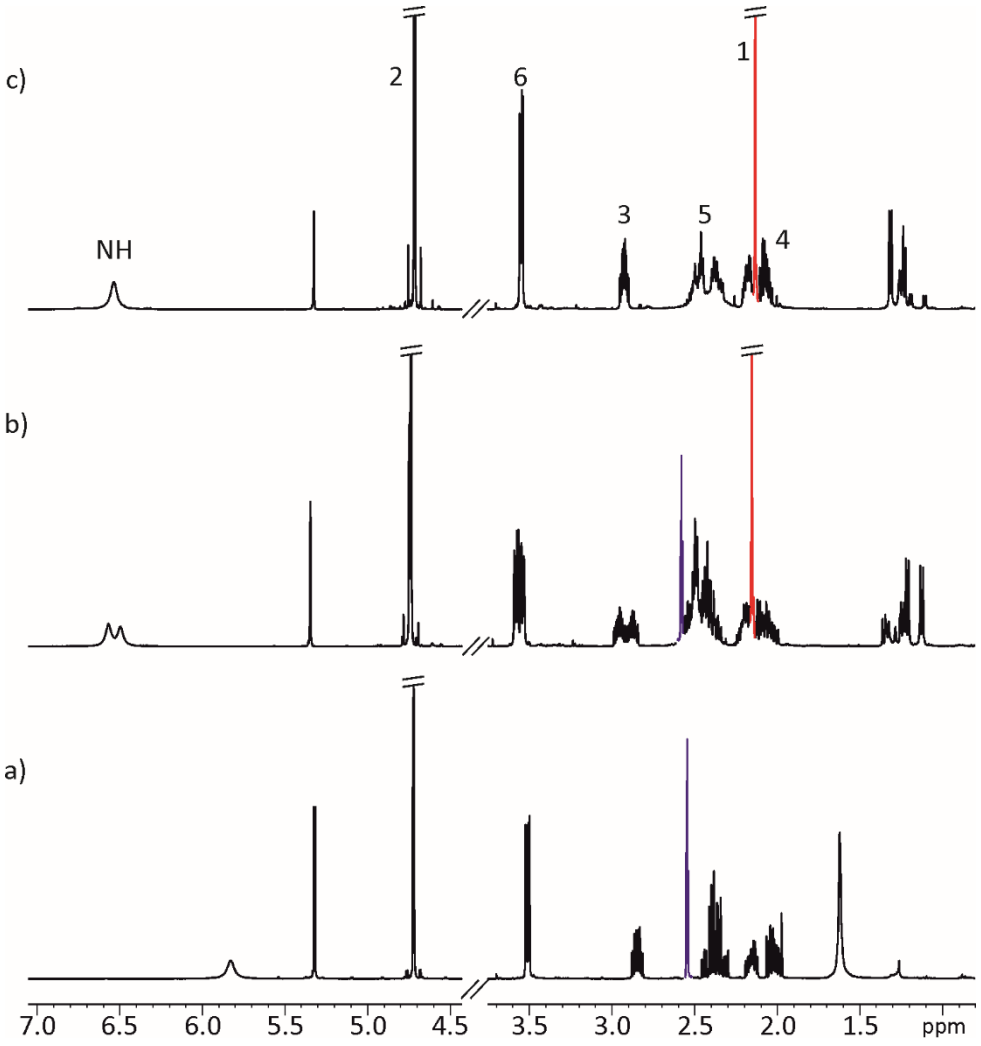

Figure 6.37 ^{1}H NMR (400 MHz, methylene chloride-d_2, 298 K) of: a) free **8**; b) reacting mixture after 1h of catalysis; and c) after 48 h with **IPAuCl**.

- Catalysis with **5in** in toluene**.**

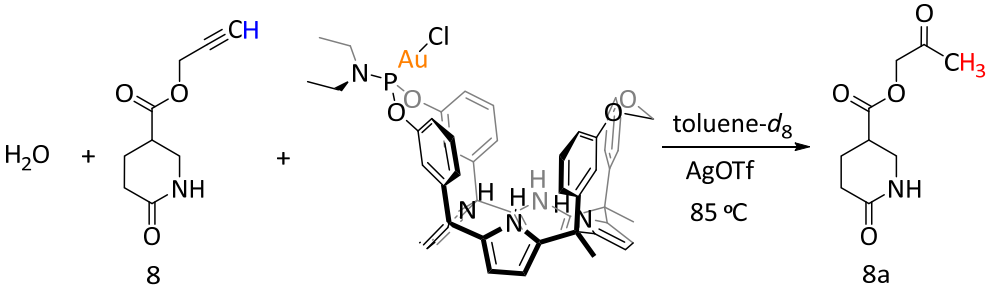

Scheme 6.17 Scheme of the alkyne hydration of **8** promoted by **5in** in toluene.

In an NMR Young tube were solubilized 3.111 mg of **5in** (0.051 eq, 2.86 µmol), and 0.905 mg of AgOTf (0.06 eq, 3.52 µmol), in 0.55 mL of toluene-d_8. After 10.10 mg of **8** (1 eq, 0.056 mmol), and 1 µL of water (1 eq, 0.056 mmol). The mixture was heated at 85 °C.

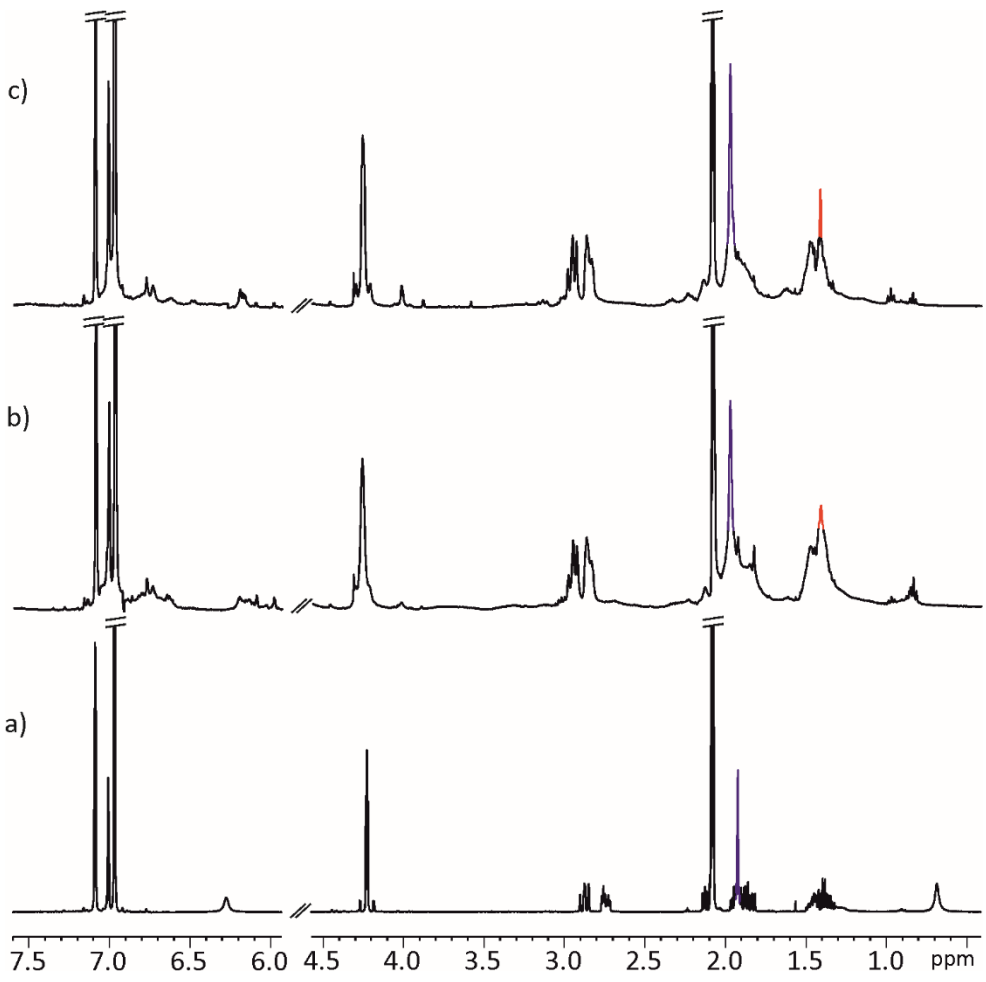

Figure 6.38 ^{1}H NMR (400 MHz, toluene-d_8, 298 K) of: a) free **8**; b) reacting mixture after 1h; c) reacting mixture after 24h with **5in**.

- Catalysis with **5in** in DCM**.**

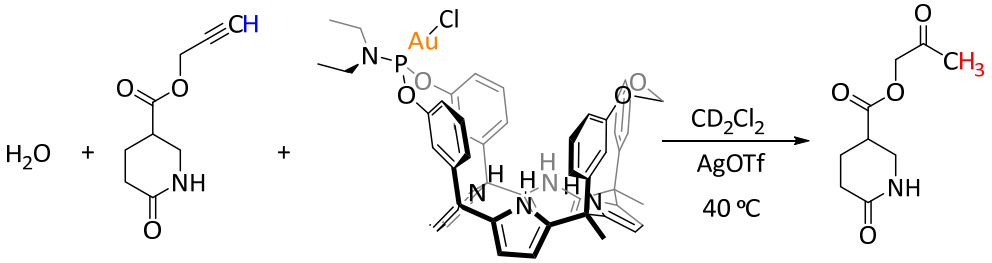

Scheme 6.18 Scheme of the alkyne hydration of **8** promoted by **5in** in methylene chloride.

In an NMR Young tube were solubilized 3.111 mg of **5in** (0.051 eq, 2.86 µmol), and 0.905 mg of AgOTf (0.06 eq, 3.52 µmol), in 0.55 mL of methylene chloride-d_2. After 10.10 mg of **8** (1 eq, 0.056 mmol), and 1 µL of water (1 eq, 0.056 mmol). The mixture was heated at 40 °C.

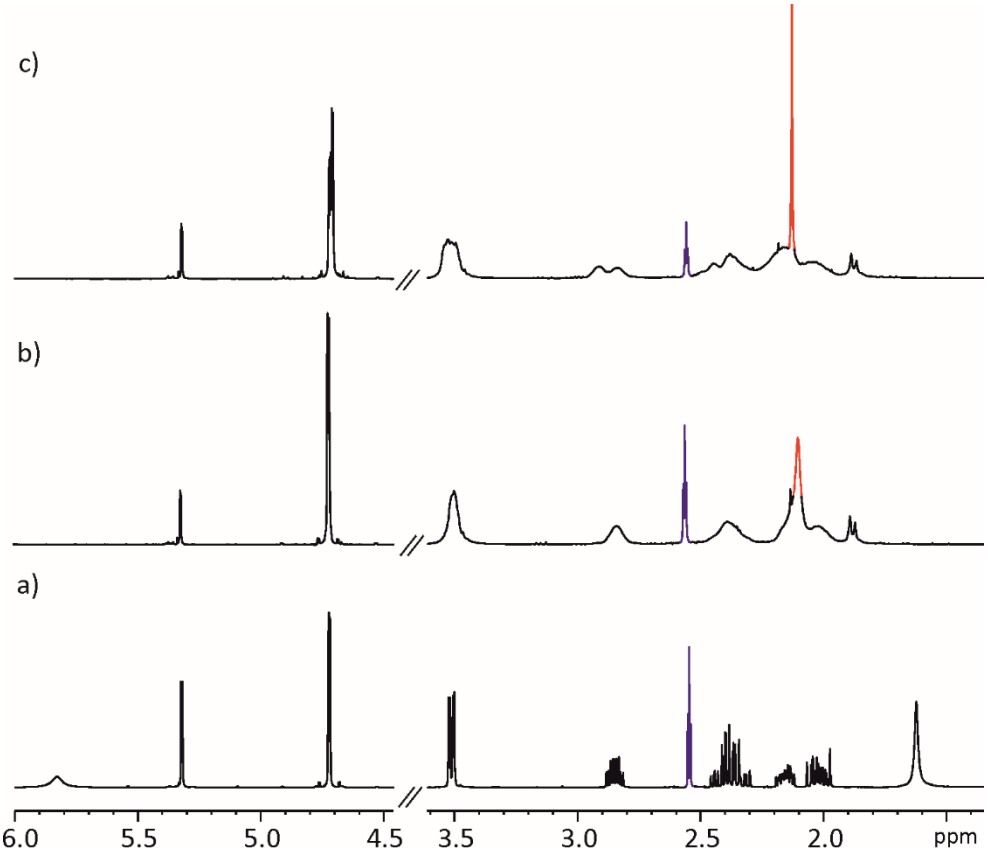

Figure 6.39 ^{1}H NMR (400 MHz, methylene chloride-d_2, 298 K) of: a) free **8**; b) 1h of catalysis; c) 72h of catalysis.

- Catalysis with **5in** in absence of water**.**

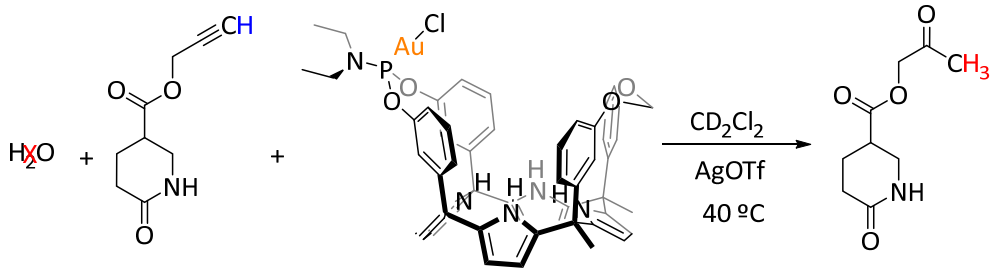

Scheme 6.19 Scheme of the alkyne hydration of **8** promoted by **5in**.

In an NMR Young tube were solubilized 3.125 mg of **5in** (0.052 eq, 2.9 µmol), and 0.770 mg of AgOTf (0.05 eq, 2.80 µmol), in 0.55 mL of methylene chloride-d_2. After 10.12 mg of **8** (1 eq, 0.056 mmol). The mixture was heated at 40 °C.

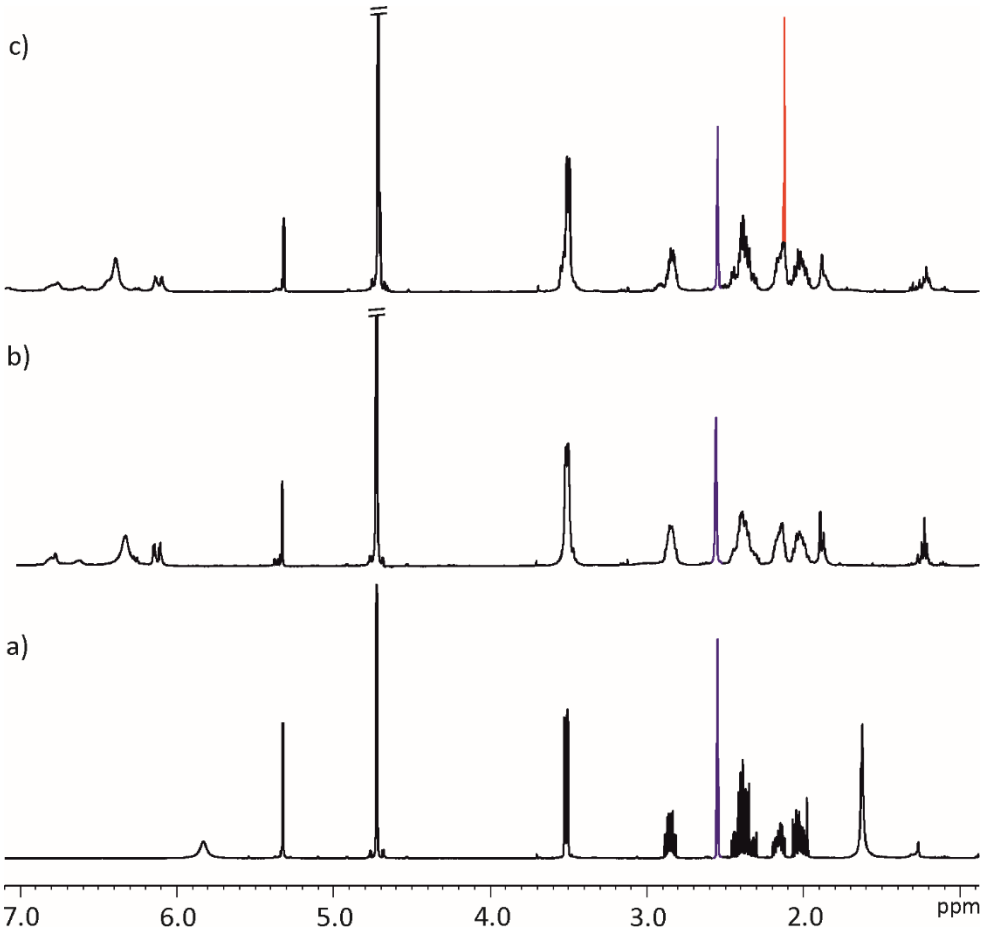

Figure 6.40 ^{1}H NMR (400 MHz, methylene chloride-d_2, 298 K) of: a) free **8**; b) reacting mixture after 1h; c) reacting mixture after 72h with **5in**.

Alkocyclization catalysis.

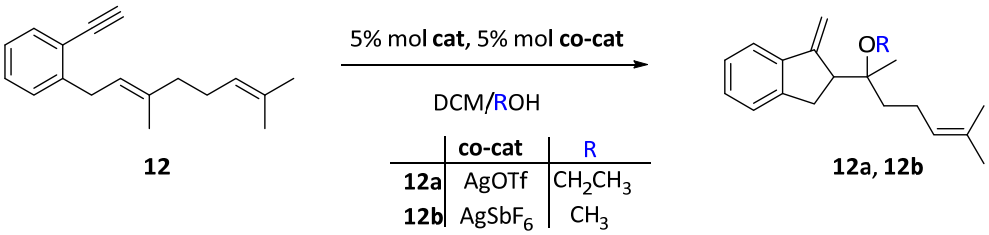

	co-cat	R
12a	AgOTf	CH_2CH_3
12b	$AgSbF_6$	CH_3

Scheme 6.20 Scheme of the alkocyclization catalysis of **12** promoted by **5in**.

On an small vial (HPLC vial) 12 mg of alkyne substrate **12** (0.05 mmol) was solubilized in 0.5 mL of DCM:ROH solvent mixture (1:1). The gold-catalyst (0.05 equiv.) and co-catalyst (0.05 eq) were added under vigorous stirring. The mixture was reacting during 1h at room temperature. The final product was purified by chromatography column (SiO_2, from Hexane to Hex:AcOEt 98:2).

12a: AgOTf in CH_3CH_2-OH.

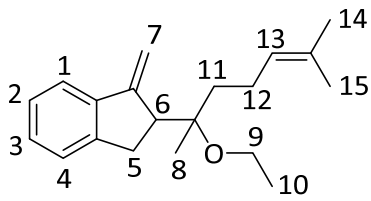

12a

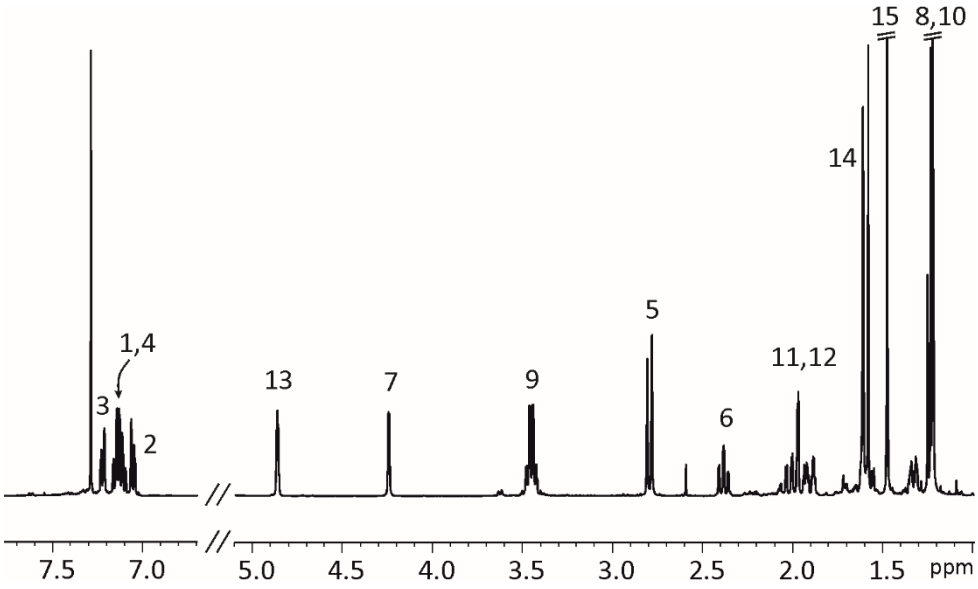

Figure 6.41 ^{1}H NMR (400 MHz, chloroform-*d*, 298 K) of **12a**.

12b: $AgSbF_6$ in CH_3-OH.

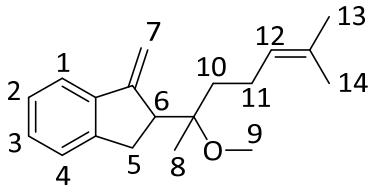

12b

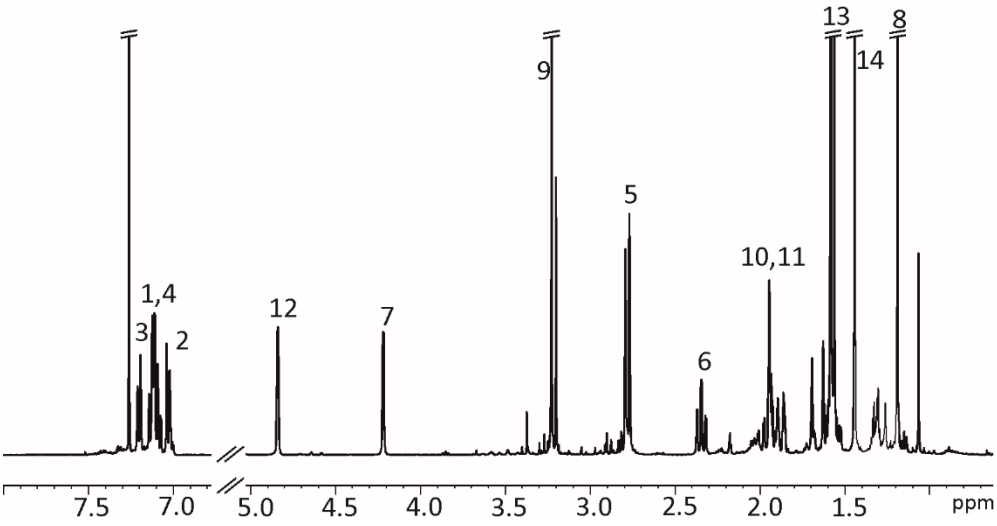

Figure 6.42 ^{1}H NMR (400 MHz, chloroform-*d*, 298 K) of **12b**.

6.4.4 Development of a GC–FID method.

Standard solutions of **6**, 7, **8** and their respective hydration products **6a**, **7a** and **8a** were prepared in CH_2Cl_2. The standard solutions were analyzed using a Gas Chromatography (GC, Figure 8) system equipped with a Flame Ionization Detector (FID) and an HP-5 capillary column (30 × 0.32 mm × 0.25 µm). The solutions (1 µl) were injected in a manual mode, with a split ratio of 1:50. The initial oven temperature was 50 °C increased at 20 °C/min up to 325 °C.

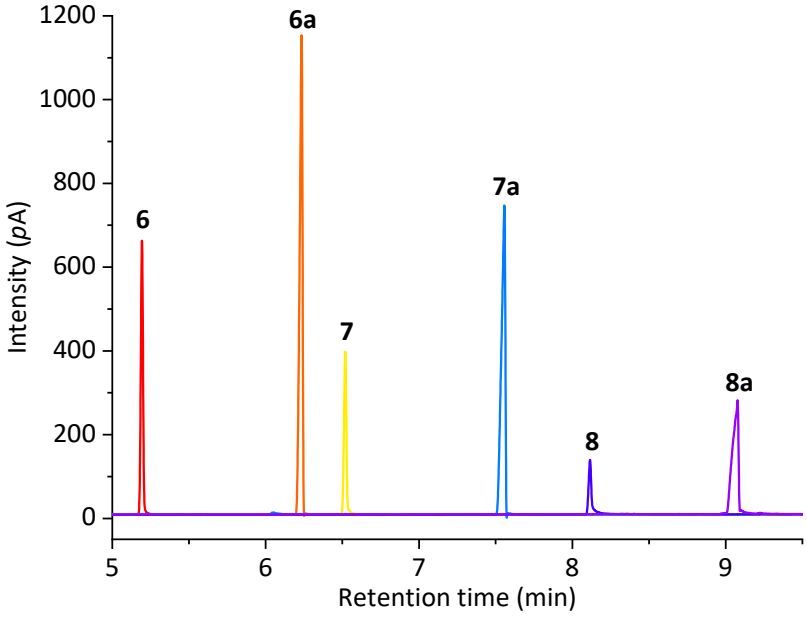

Figure 6.43 GC-FID chromatogram of alkynes **6**, **7**, **8** and their hydration products **6a**, **7a** and **8a**. Note that the differences in the peak intensities is because each compound was injected independently at different concentrations.

6.4.5 Kinetic studies.

In a typical kinetic experiment, a known concentration aliquot of the active specie was added to a water-saturated methylene chloride solution of the substrate (1.0 mL, 10 mM) and the resulting solution was preserved at 40 °C. Noteworthy, reproducibility problems were observed when the active species were generated *in-situ*.

- Kinetic studies with **IPrAuOTf**.

Towards alkyne hydration of 6.

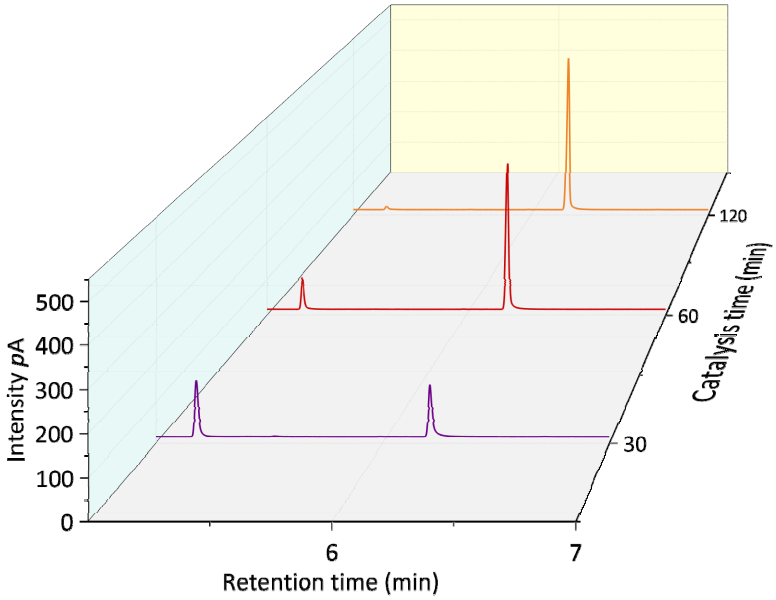

Figure 6.44 Evolution of the GC chromatogram during the hydration of **6** promoted by **IPrAuOTf**.

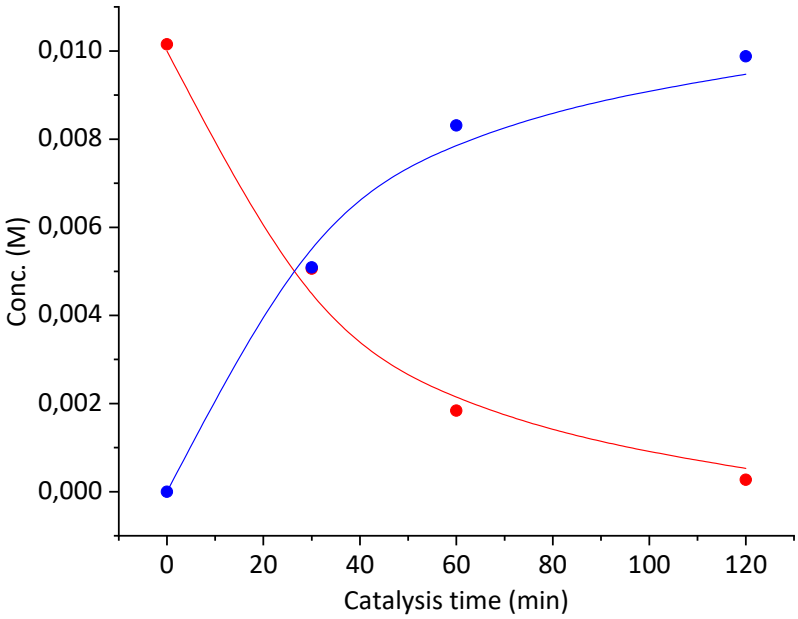

Figure 6.45 Kinetic curves for the alkyne hydration of **6** promoted by **IPrAuOTf**. Red and blue circles represent the experimental data. Red and blue lines represent the fit of the kinetic data considering a bimolecular reaction.

$$k\ (40\ °C) = 0.57\ \pm 0.01\ M^{-1}min^{-1}$$

Towards alkyne hydration of 7.

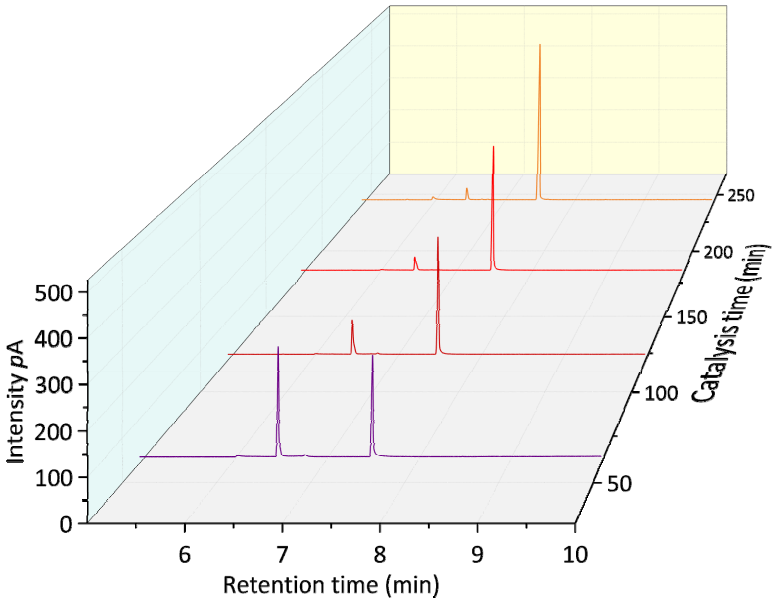

Figure 6.46 Evolution of the GC chromatogram during the hydration of **7** promoted by **IPrAuOTf**.

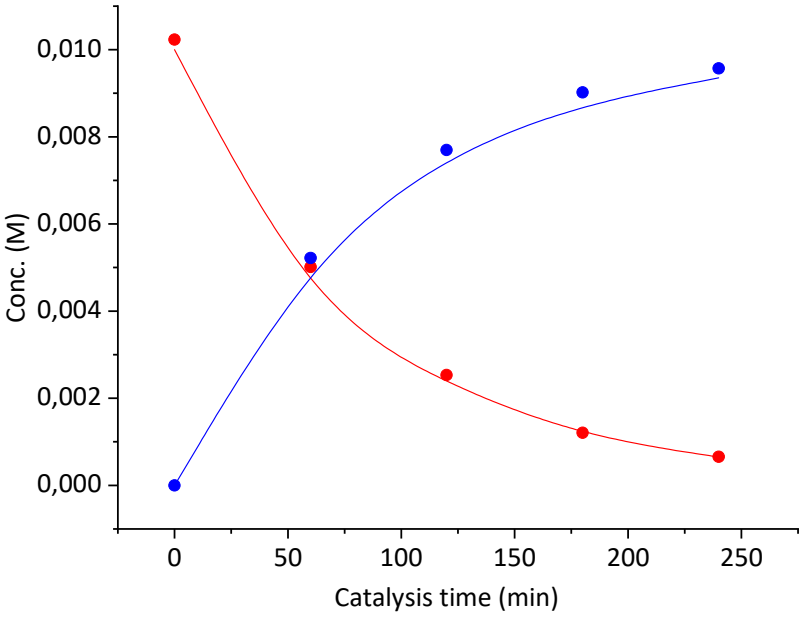

Figure 6.47 Kinetic curves for the alkyne hydration of **7** promoted by **IPrAuOTf**. Red and blue circles represent the experimental data. Red and blue lines represent the fit of the kinetic data considering a bimolecular reaction.

$$k\ (40\ °C) = 0.29\ \pm 0.03\ M^{-1}min^{-1}$$

Towards alkyne hydration of 8.

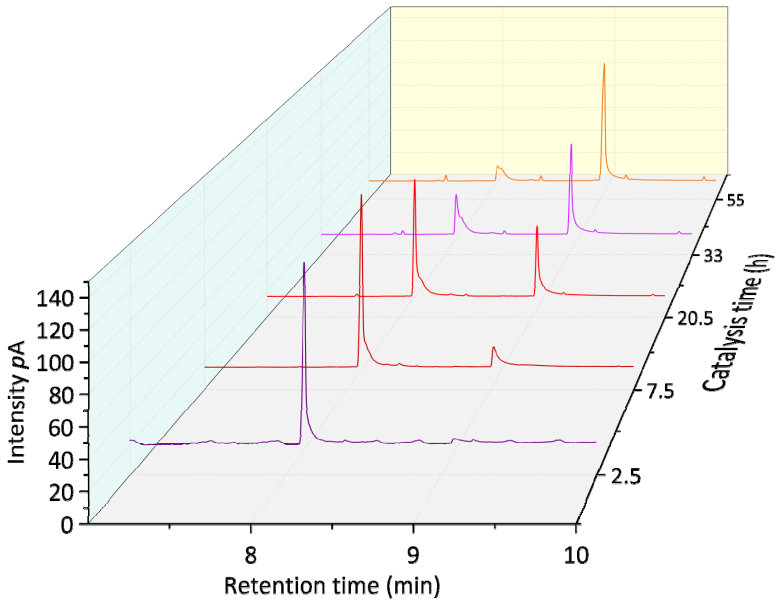

Figure 6.48 Evolution of the GC chromatogram during the hydration of **8** promoted by **IPrAuOTf**.

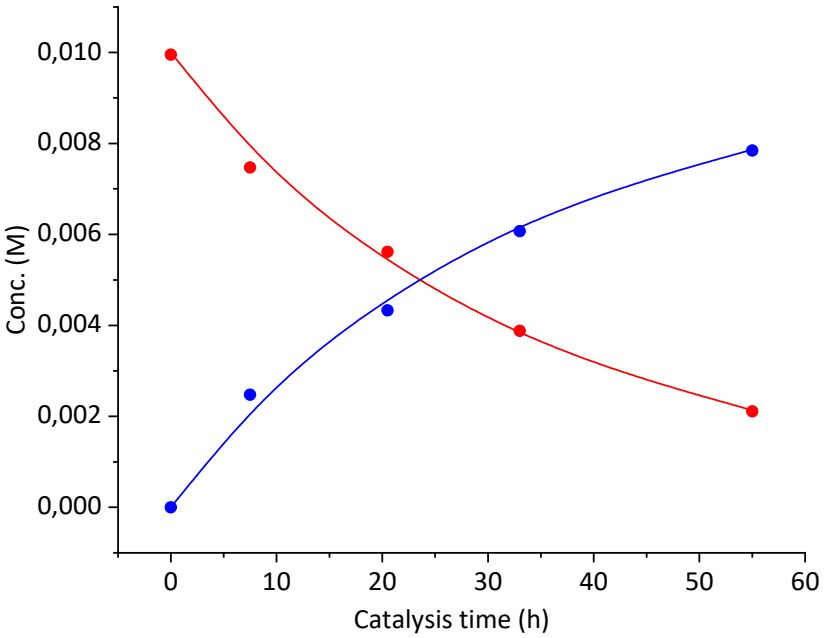

Figure 6.49 Kinetic curves for the alkyne hydration of **8** promoted by **IPrAuOTf**. Red and blue circles represent the experimental data. Red and blue lines represent the fit of the kinetic data considering a bimolecular reaction.

$$k\ (40\ °C) = 0.008\ \pm 0.002\ M^{-1}min^{-1}$$

- Kinetic studies with **1in**.

Towards alkyne hydration of 6.

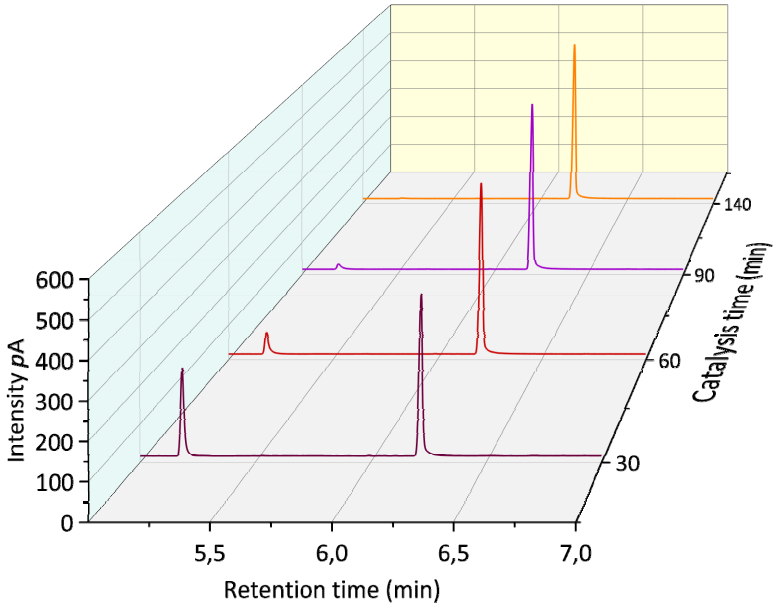

Figure 6.50 Evolution of the GC chromatogram during the hydration of **6** promoted by **1in**.

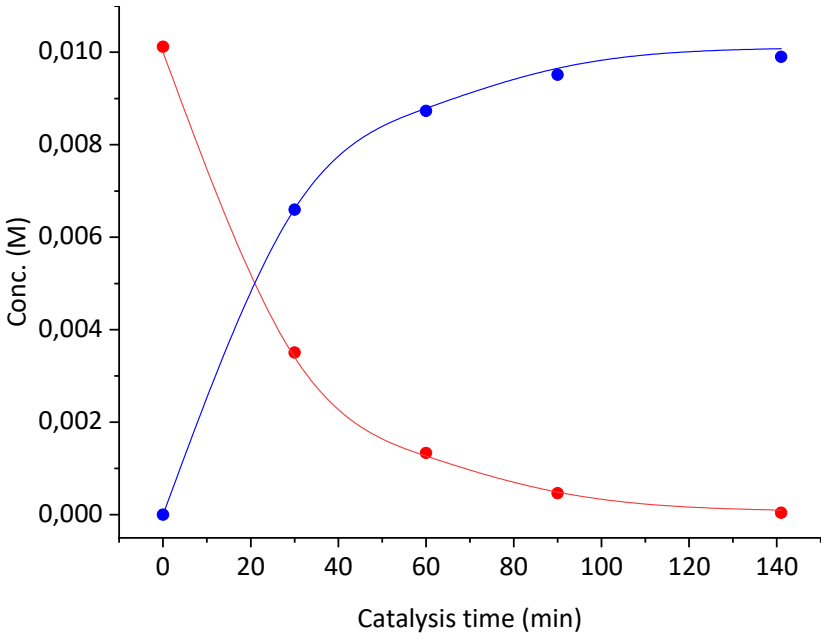

Figure 6. 51 Kinetic curves for the alkyne hydration of **6** promoted by **1in**. Red and blue circles represent the experimental data. Red and blue lines represent the fit of the kinetic data considering a bimolecular reaction.

$$k\ (40\ °C) = 0.9\ \pm 0.1\ M^{-1}min^{-1}$$

Towards alkyne hydration of 7.

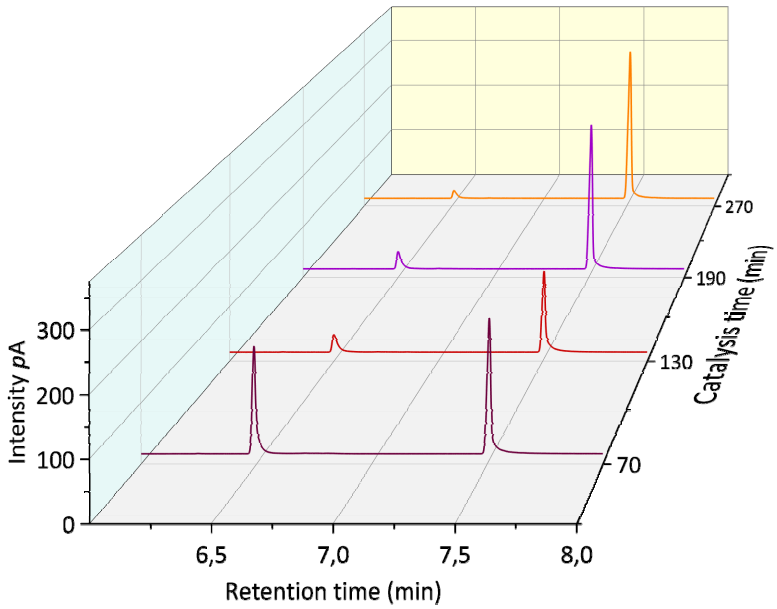

Figure 6.52 Evolution of the GC chromatogram during the hydration of **7** promoted by **1in**.

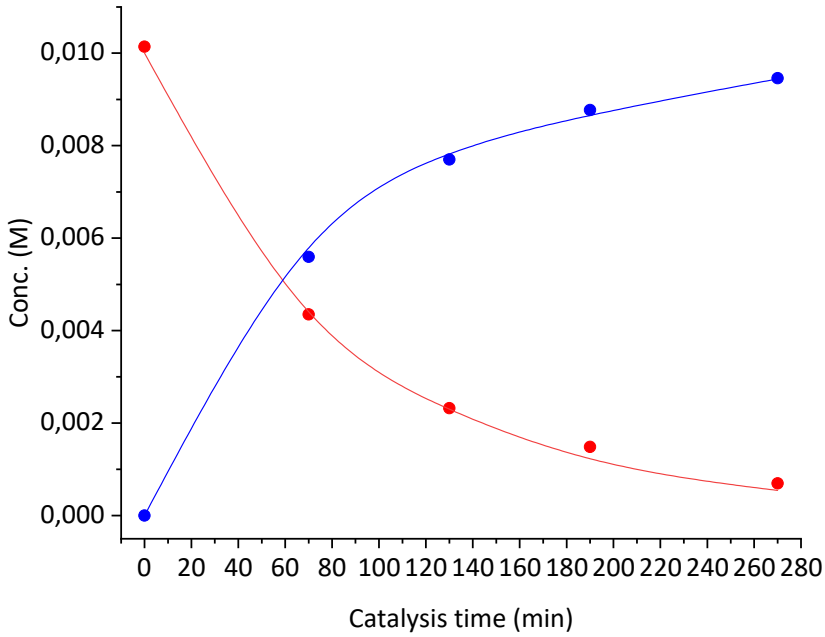

Figure 6.53 Kinetic curves for the alkyne hydration of **7** promoted by **1in**. Red and blue circles represent the experimental data. Red and blue lines represent the fit of the kinetic data considering a bimolecular reaction.

$$k\ (40\ °C) = 0.29\ \pm 0.04\ M^{-1}min^{-1}$$

Towards alkyne hydration of 8.

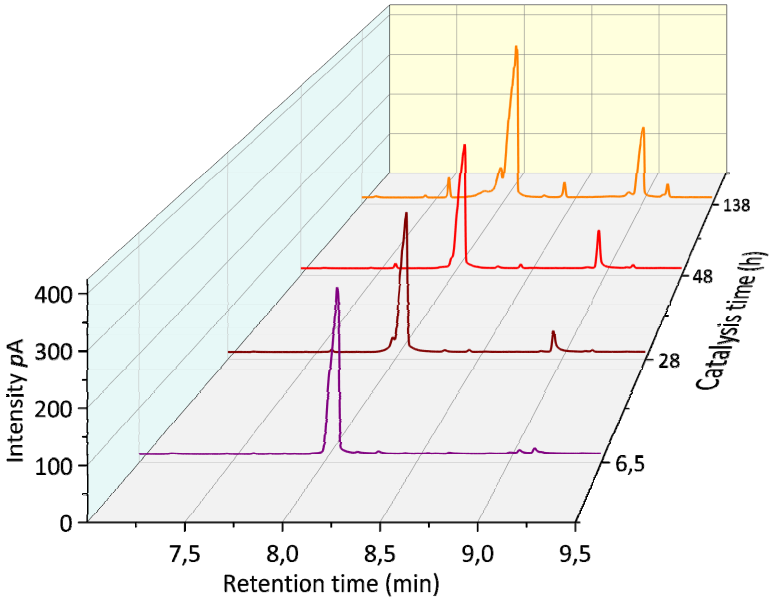

Figure 6.54 Evolution of the GC chromatogram during the hydration of **8** promoted by **1in**.

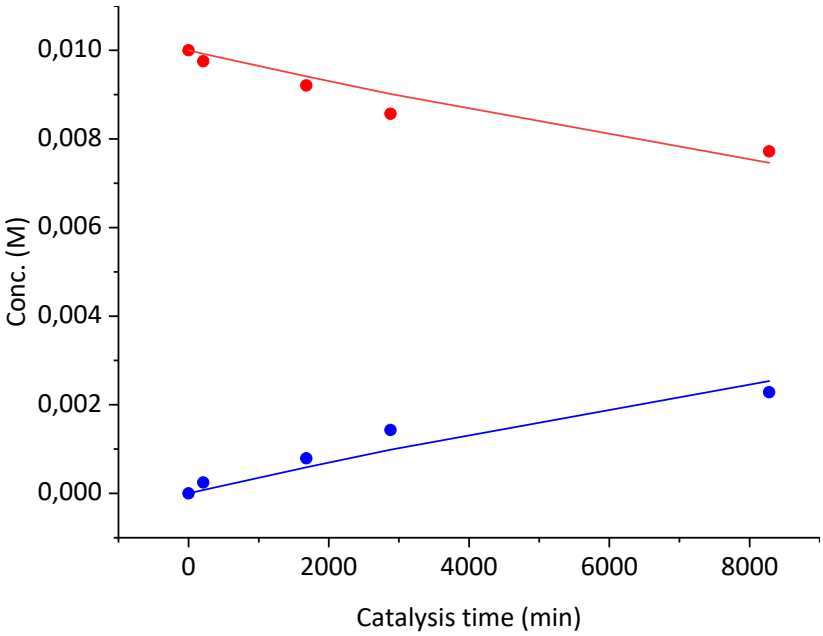

Figure 6.55 Kinetic curves for the alkyne hydration of **8** promoted by **1in**. Red and blue circles represent the experimental data. Red and blue lines represent the fit of the kinetic data considering a bimolecular reaction.

$$k\ (40\ °C) = (7.2\ \pm 0.6) \times 10^{-4}\ M^{-1} min^{-1}$$

The magnitude of the rate constants at this reaction conditions translate into long acquisition times. We used COPASI ® software to estimate a rate constant that describe the behaviour observed for this kinetic. A rate constant of 8.0×10^{-4} $M^{-1}min^{-1}$ return a similar tendency that the observed experimentally.

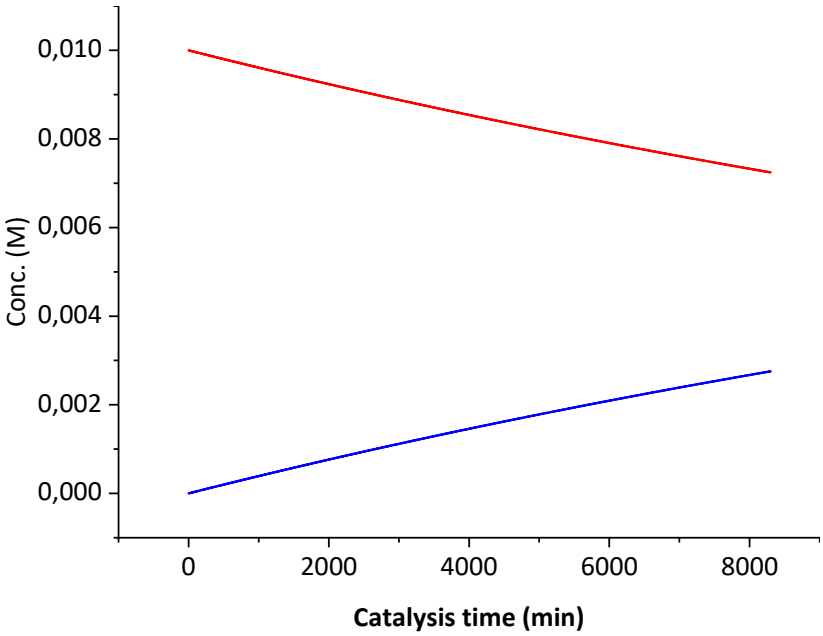

Figure 6.56 Estimation of the kinetic performance for the alkyne hydration of **8** promoted by **1in** considering a rate constant less than 8.0×10^{-4} $M^{-1} \cdot min^{-1}$ using COPASI® software version 4.34.

- Kinetic studies with **5out**.

Towards alkyne hydration of 6 (10 mM).

Interestingly, in just 15 min all **6** was converted into **6a**. We used COPASI® software in order to estimate a rate constant which can describe this kinetic performance. We found total alkyne hydration in 15 minutes when the rate constant is higher than 5.0 $M^{-1} \cdot min^{-1}$.

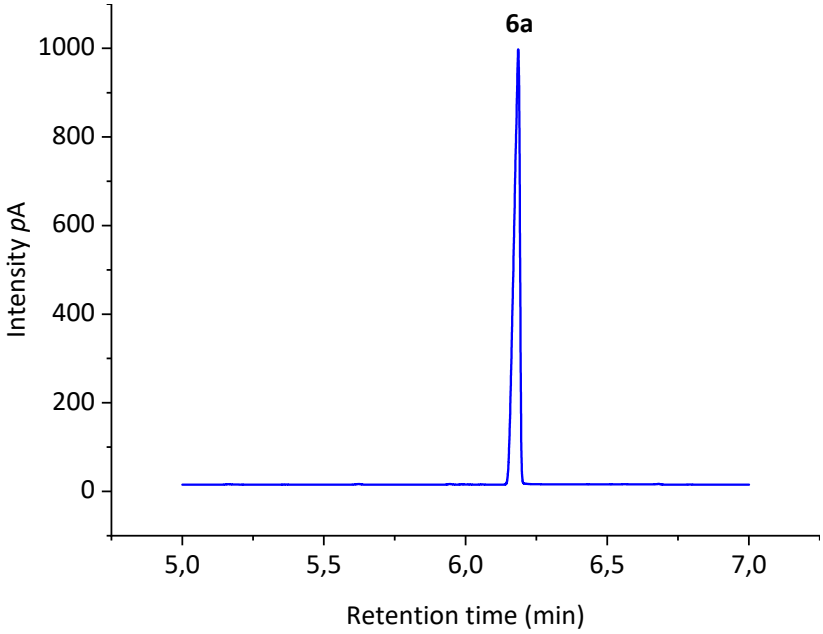

Figure 6.57 GC-FID chromatogram of hydration of **6** (10 mM) promoted by **1out**.

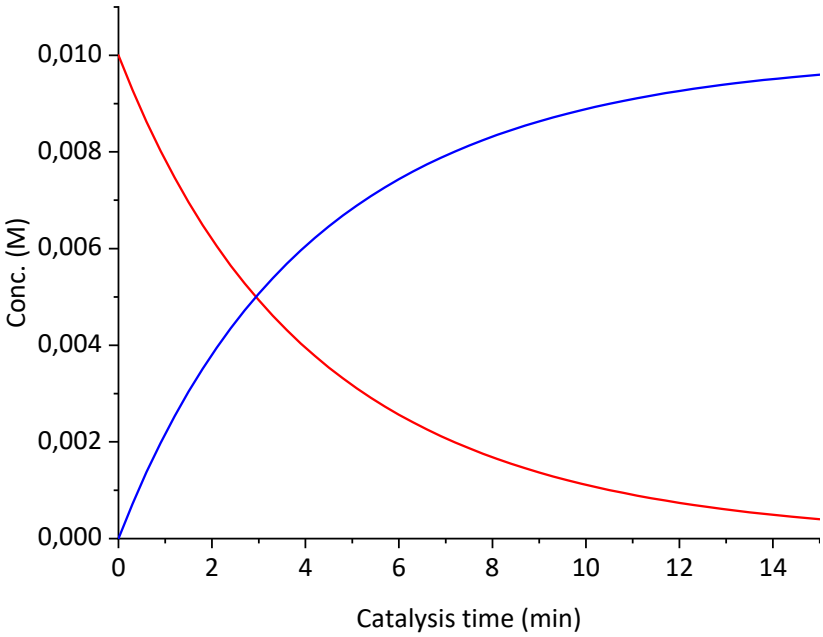

Figure 6.58 Estimation of the kinetic performance for the alkyne hydration of **6** promoted by **1out** considering a rate constant greater than 5.0 $M^{-1}{\cdot}min^{-1}$ using COPASI® software version 4.34.

Towards alkyne hydration of 6 (5.0 mM).

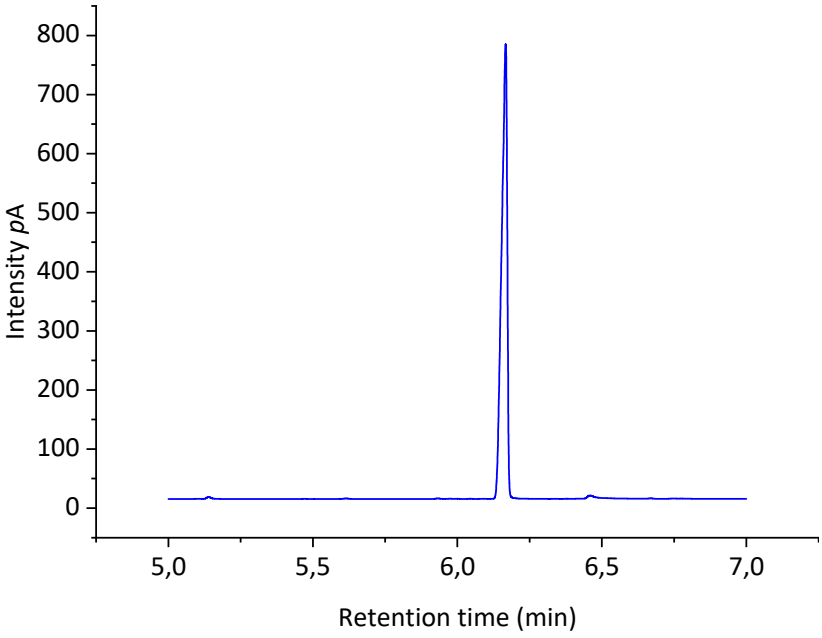

Figure 6.59 GC-FID chromatogram of hydration of **6** (5 mM) promoted by **1out**.

Towards alkyne hydration of 6 (1.0 mM).

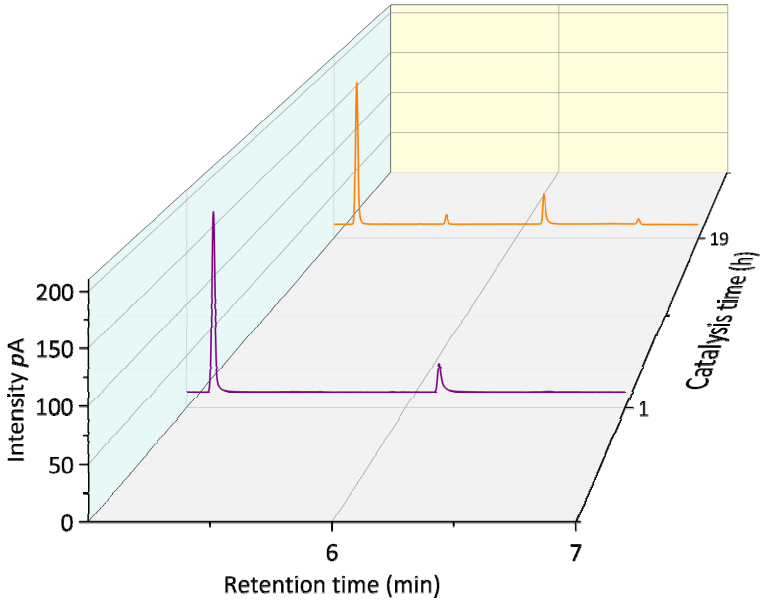

Figure 6.60 Evolution of the GC chromatogram during the hydration of **6** (1.0 mM) promoted by **1out**.

Towards alkyne hydration of 7 (1.0 mM).

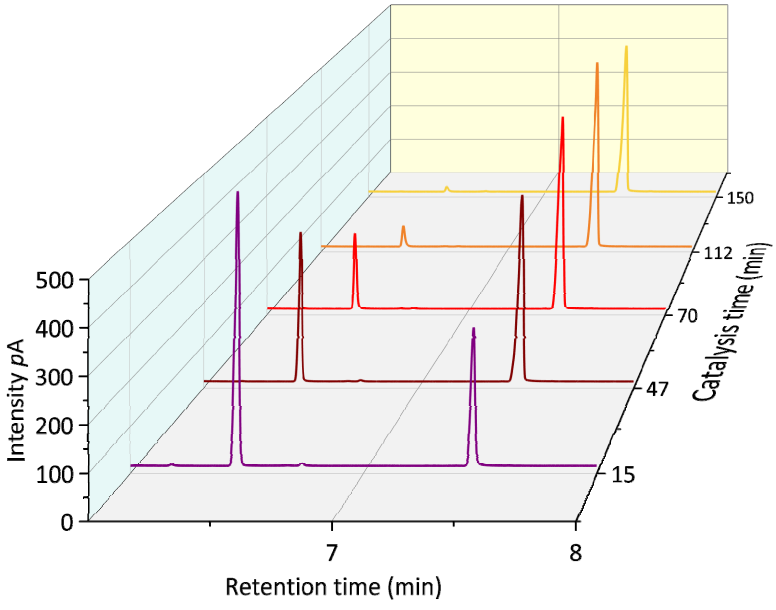

Figure 6.61 Evolution of the GC chromatogram during the hydration of **7** promoted by **1out**.

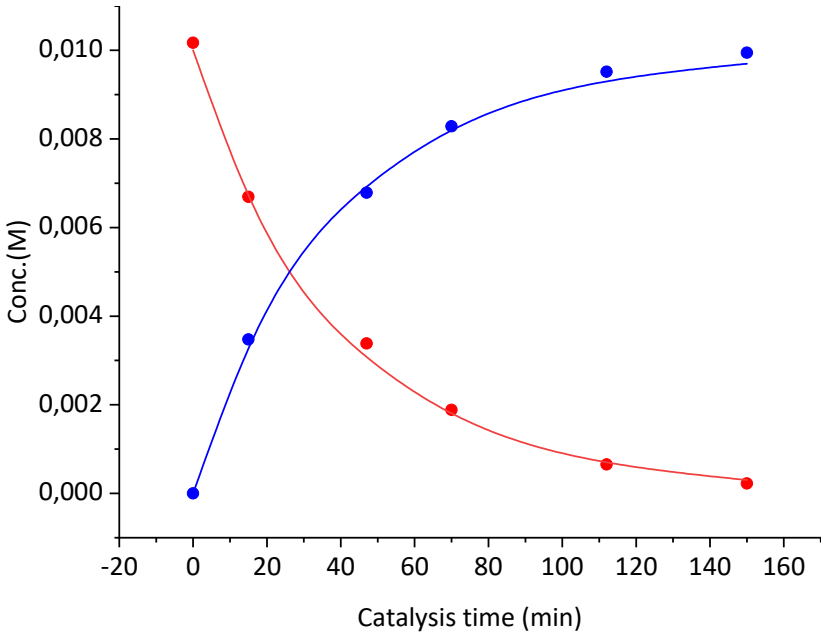

Figure 6.62 Kinetic curves for the alkyne hydration of **7** promoted by **1out**. Red and blue circles represent the experimental data. Red and blue lines represent the fit of the kinetic data considering a bimolecular reaction.

$$k\ (40\ °C) = 0.48\ \pm 0.06\ M^{-1}min^{-1}$$

Towards alkyne hydration of 8.

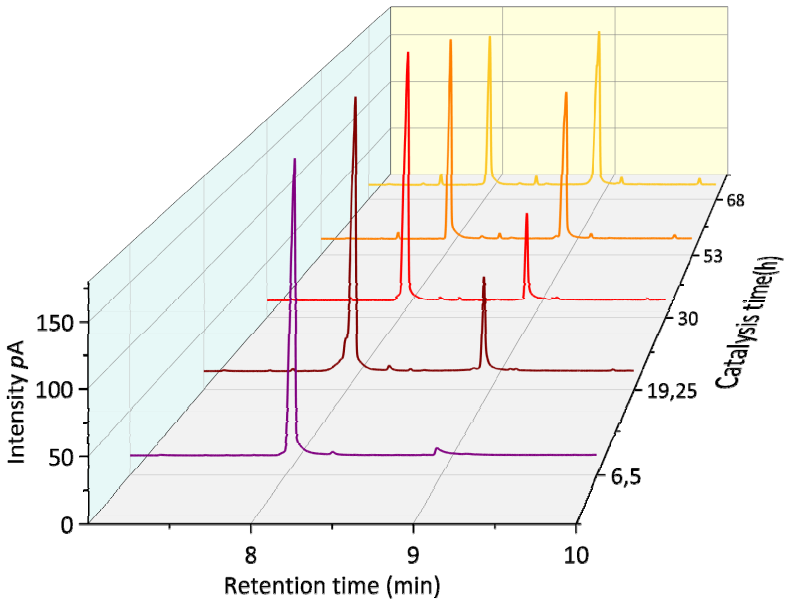

Figure 6.63 Evolution of the GC chromatogram during the hydration of **8** promoted by **1out**.

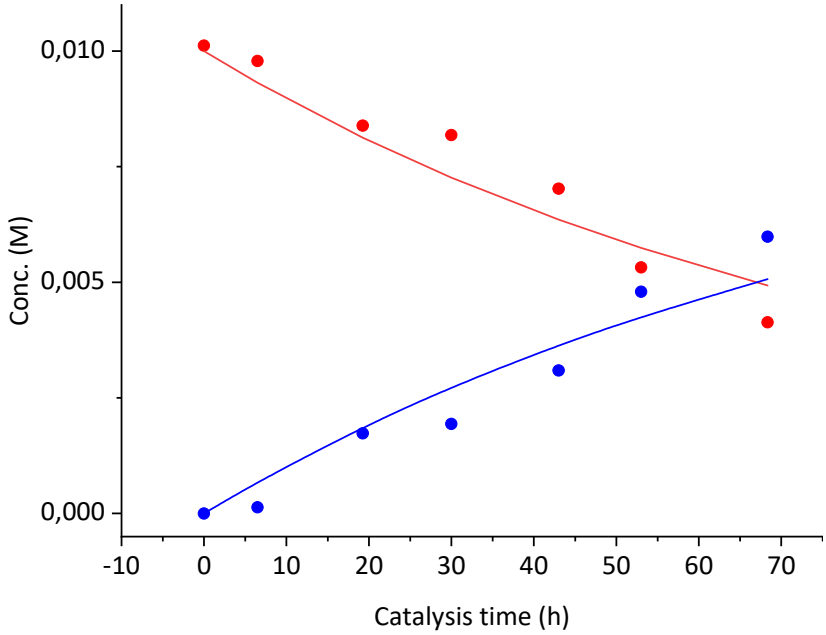

Figure 6.64 Kinetic curves for the alkyne hydration of **8** promoted by 1out. Red and blue circles represent the experimental data. Red and blue lines represent the fit of the kinetic data considering a bimolecular reaction.

$$k\ (40\ °C) = 0.0044\ \pm 0.0007\ M^{-1}min^{-1}$$

6.4.6 Kinetic studies at diluted conditions (0.1 mM).

We hypothesized that at very diluted conditions the role of the cavity becomes more favorable.

- Kinetic studies with **IPrAuOTf**.

Towards alkyne hydration of 6.

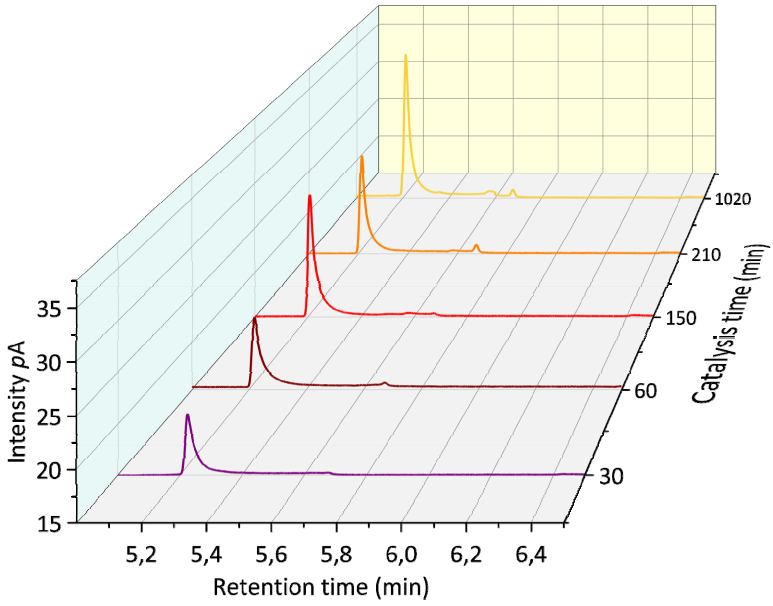

Figure 6.65 Evolution of the GC chromatogram during the hydration of **6** (0.1 mM) promoted by **IPrAuOTf**.

- Kinetic studies with **1in**.

Towards alkyne hydration of 6.

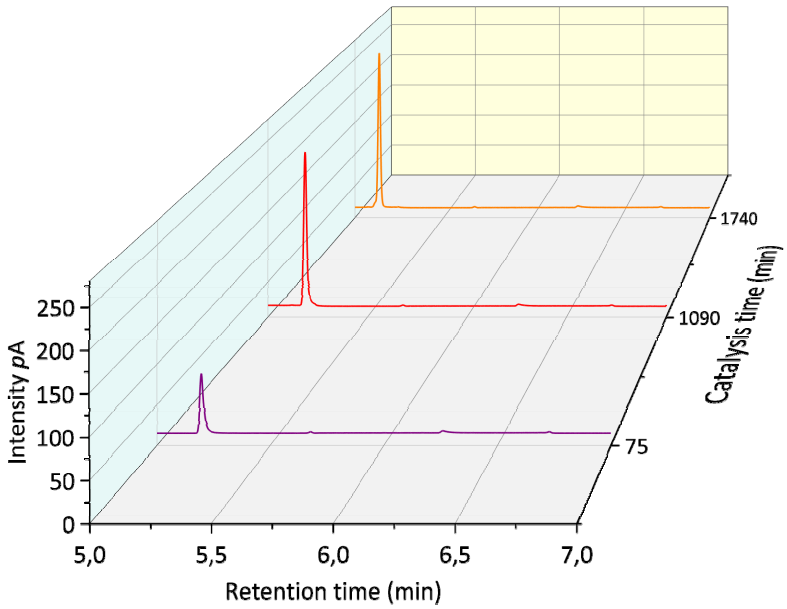

Figure 6.66 Evolution of the GC chromatogram during the hydration of **6** (0.1 mM) promoted by **1in**.

Towards alkyne hydration of 7.

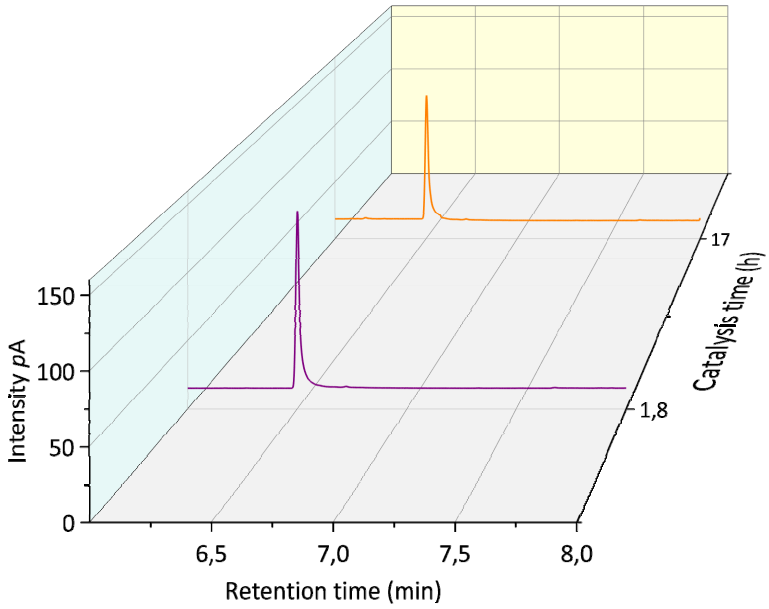

Figure 6.67 Evolution of the GC chromatogram during the hydration of **7** (0.1 mM) promoted by **1in**.

Towards alkyne hydration of 8.

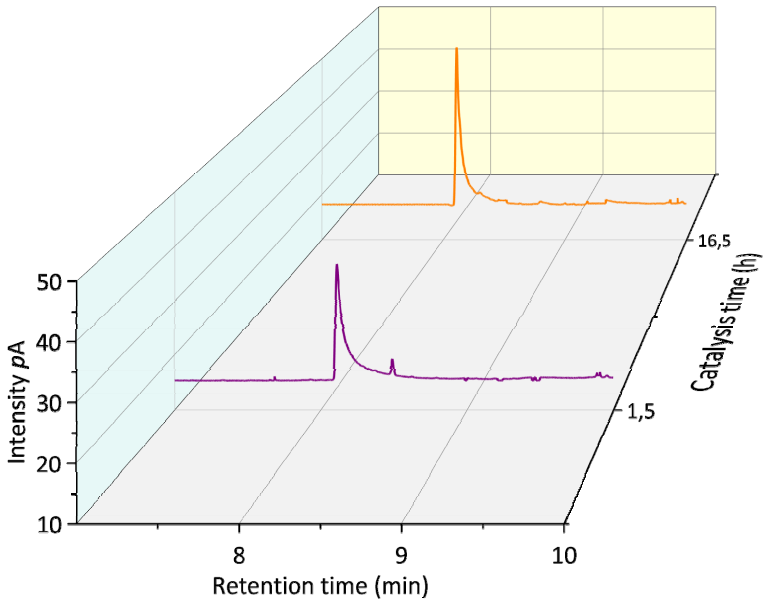

Figure 6.68 Evolution of the GC chromatogram during the hydration of **8** (0.1 mM) promoted by **1in**.

6.4.7 Evaluating the role of the cavity: a) kinetic studies with *N*-oxides

- Effect of compound **9** on the catalysis with **IPrAuOTf**.

Towards alkyne hydration of 6.

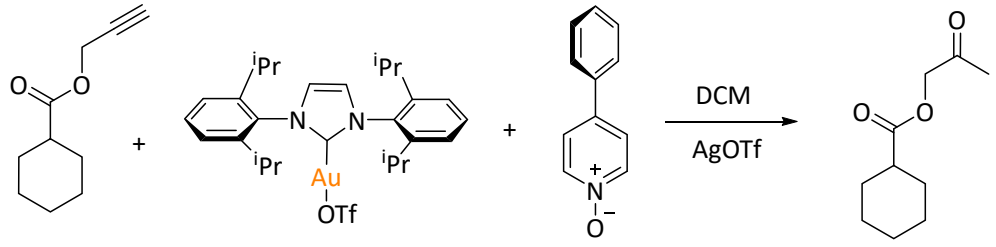

Scheme 6.21 Scheme of the alkyne hydration of **6** promoted by **IPrAuOTf** and compound **9** as inhibitor.

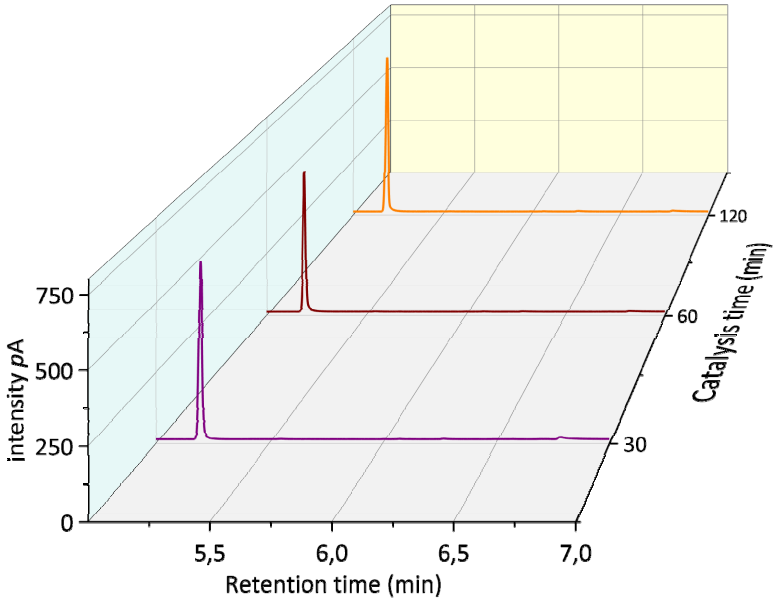

Figure 6.69 Evolution of the GC chromatogram during the hydration of **6** promoted by **IPrAuOTf** and compound **9** as inhibitor.

Towards alkyne hydration of 7.

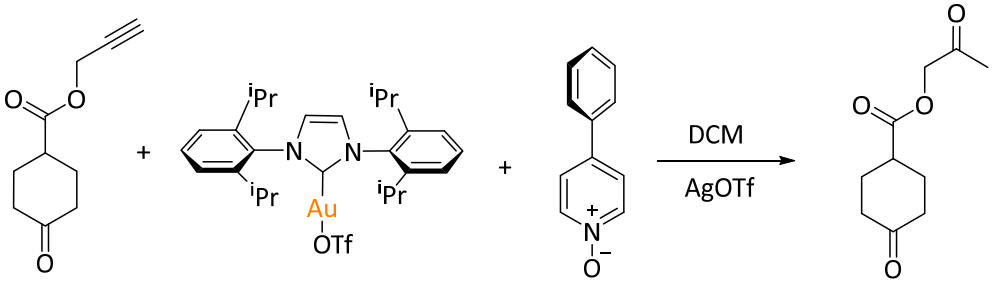

Scheme 6.22 Scheme of the alkyne hydration of **7** promoted by **IPrAuOTf** and compound **9** as inhibitor.

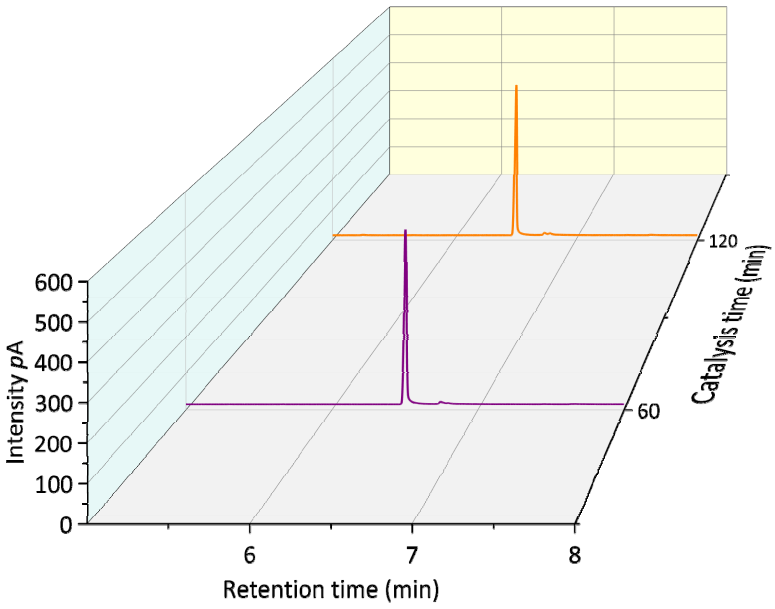

Figure 6.70 Evolution of the GC chromatogram during the hydration of **7** promoted by **IPrAuOTf** and compound **9** as inhibitor.

- Effect of compound **9** on the catalysis with **1in**.

Towards alkyne hydration of 6.

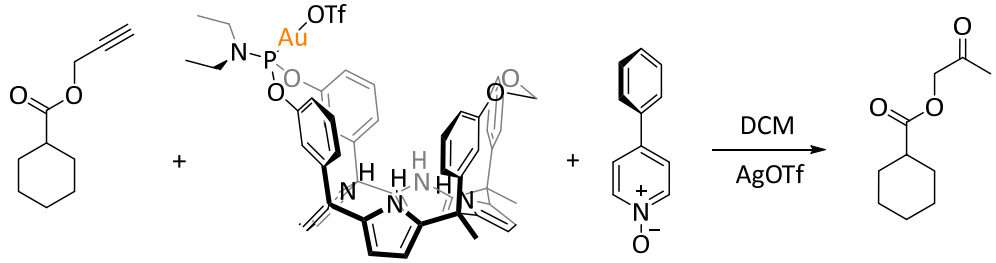

Scheme 6.23 Scheme of the alkyne hydration of **6** promoted by **1in** and compound **9** as inhibitor.

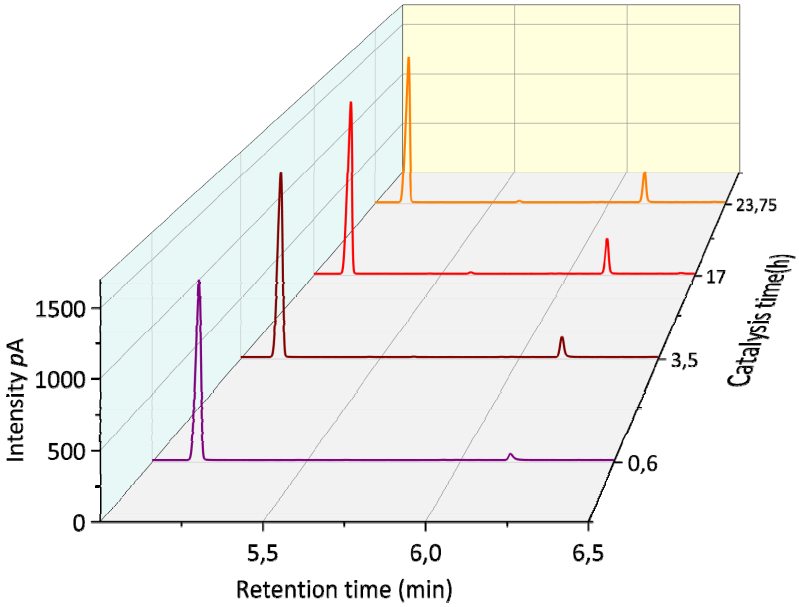

Figure 6.71 Evolution of the GC chromatogram during the hydration of **6** promoted by **1in** and compound **9** as inhibitor.

Towards alkyne hydration of 7.

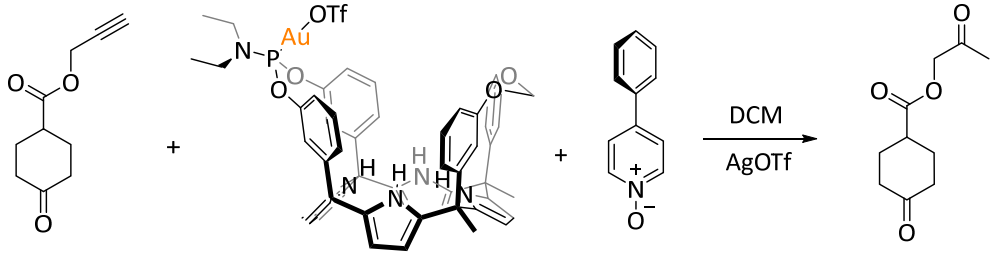

Scheme 6.24 Scheme of the alkyne hydration of **7** promoted by **1in** and compound **9** as inhibitor.

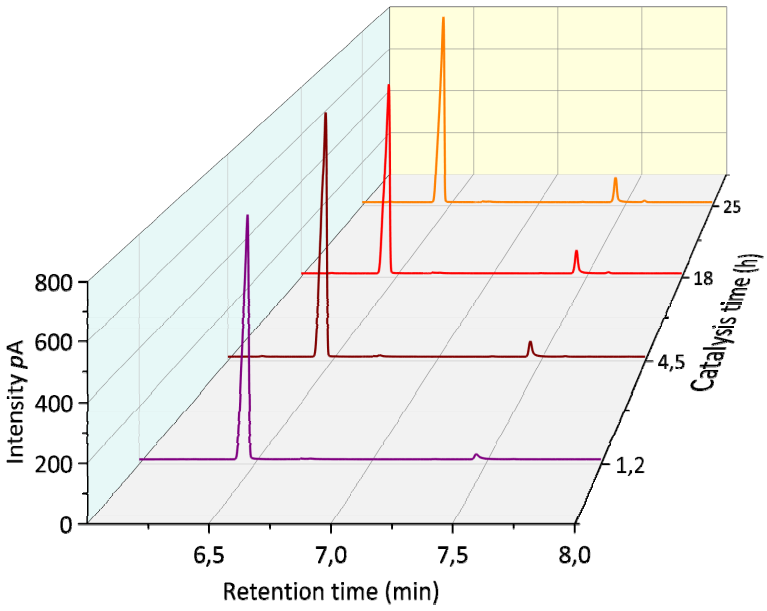

Figure 6.72 Evolution of the GC chromatogram during the hydration of **7** promoted by **1in** and compound **9** as inhibitor.

- Effect of compound **9** on the catalysis with **1out**.

Towards alkyne hydration of 6.

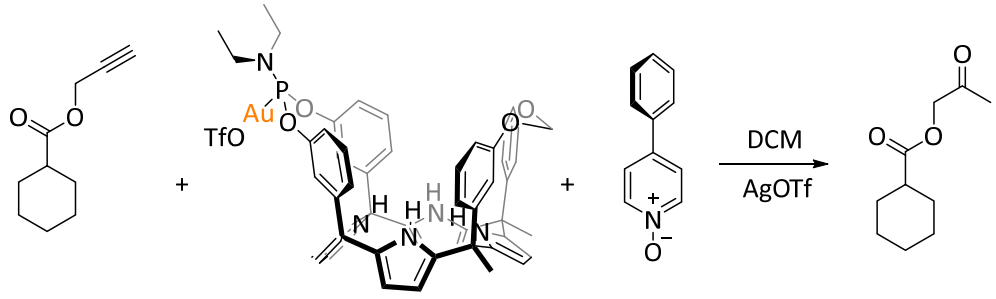

Scheme 6.25 Scheme of the alkyne hydration of **6** promoted by **1out** and compound **9** as inhibitor.

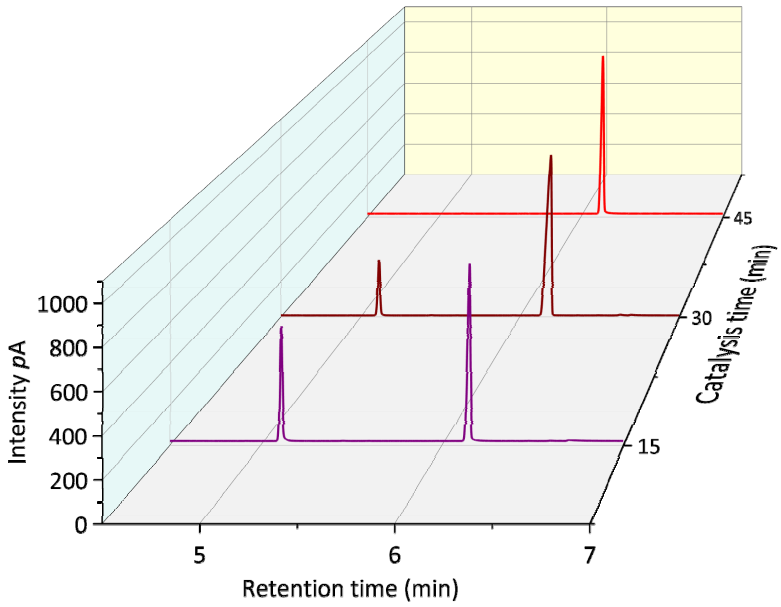

Figure 6.73 Evolution of the GC chromatogram during the hydration of **6** promoted by **1out** and compound **9** as inhibitor.

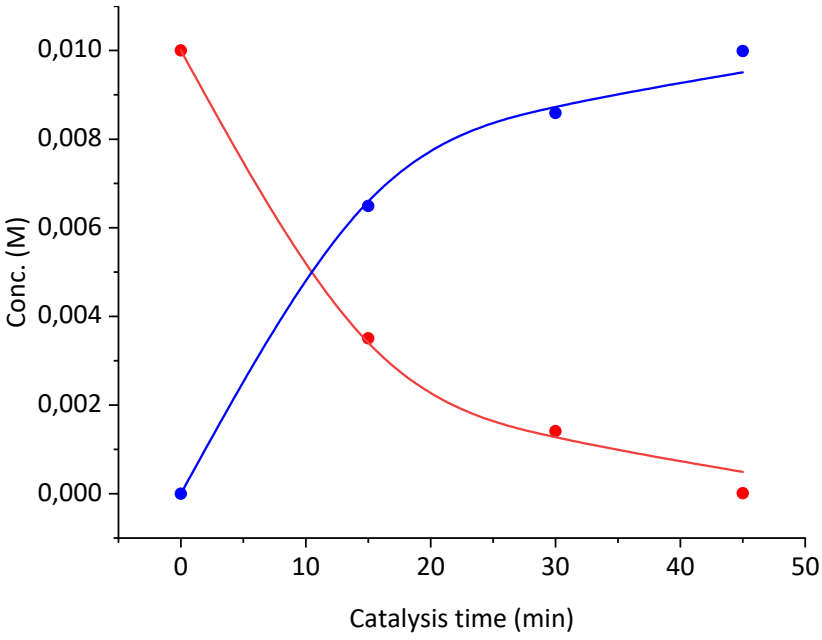

Figure 6.74 Kinetic curves for the alkyne hydration of **6** promoted by **1out** and compound **9** as inhibitor. Red and blue circles represent the experimental data. Red and blue lines represent the fit of the kinetic data considering a bimolecular reaction.

$$k\ (40\ °C) = 1.53\ \pm 0.02\ M^{-1}min^{-1}$$

- Effect of compound **10** on the catalysis with **1in**.

Towards alkyne hydration of 6.

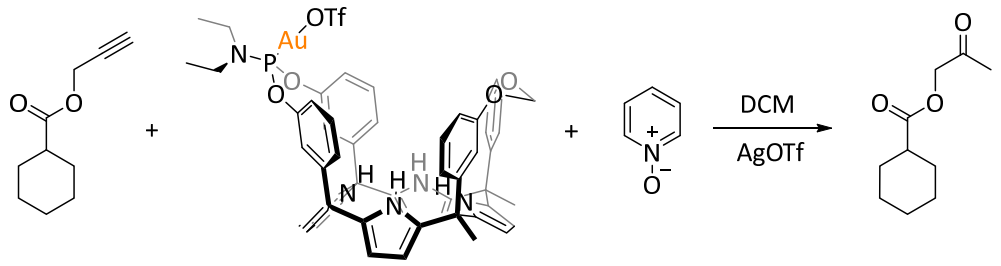

Scheme 6.26 Scheme of the alkyne hydration of **6** promoted by **1in** and compound **10** as inhibitor.

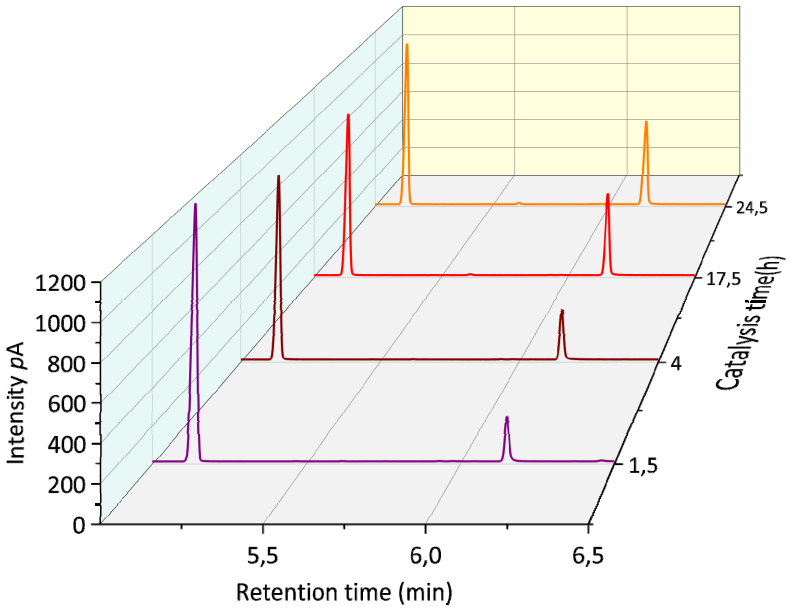

Figure 6.75 Evolution of the GC chromatogram during the hydration of **6** promoted by **1in** and compound **10** as inhibitor.

6.4.8 Evaluating the role of the cavity: b) addition of receptor **11**.

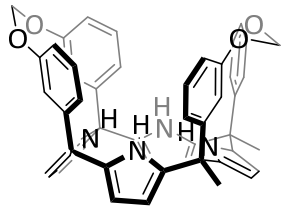

11

- Effect of receptor **11** on the catalysis with **IPrAuOTf**.

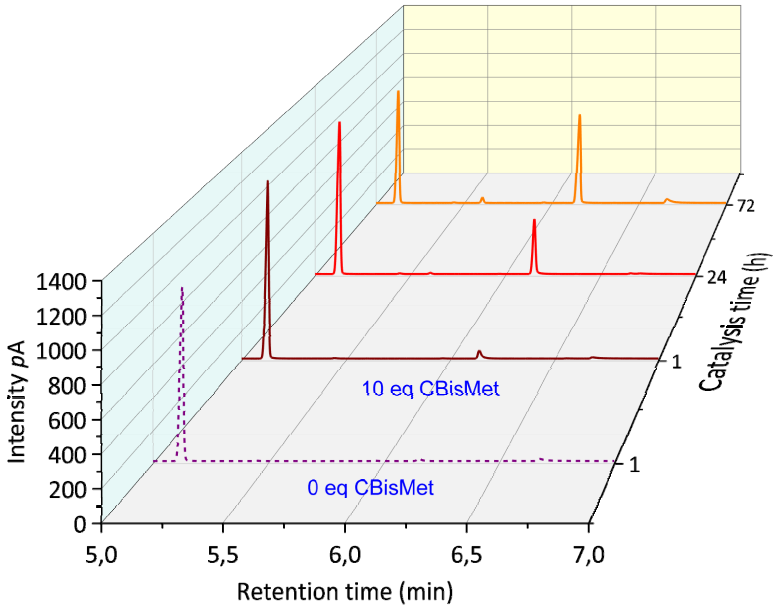

Figure 6.76 Evolution of the GC chromatogram during the recovery of the hydration of **6** promoted by **IPrAuOTf**, before (dash lines, inhibited with **9**) and after (solid line) the addition of receptor **11**.

6.4.9 X-ray structures and molecular modeling.

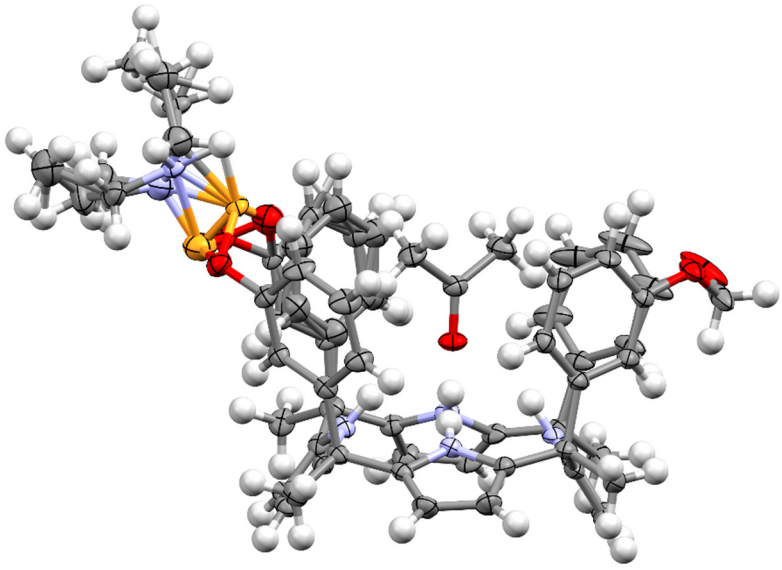

Figure 6.77 X-ray structure of **4in**. Thermal ellipsoids for C, N, O and P atoms set at 50% probability; H atoms are shown as spheres of 0.20 Å diameter.

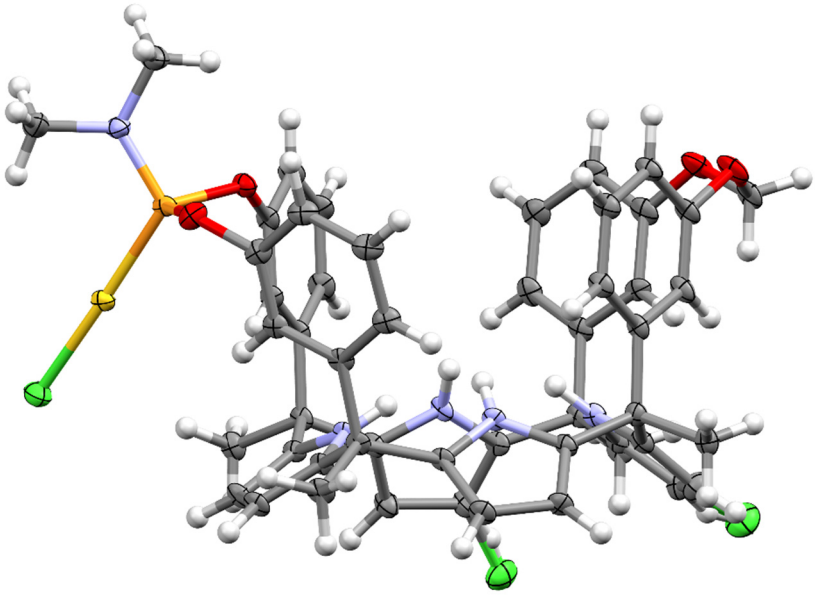

Figure 6.78 X-ray structure of **5out**. Thermal ellipsoids for Au, Cl, C, N, O and P atoms set at 50% probability; H atoms are shown as spheres of 0.20 Å diameter.

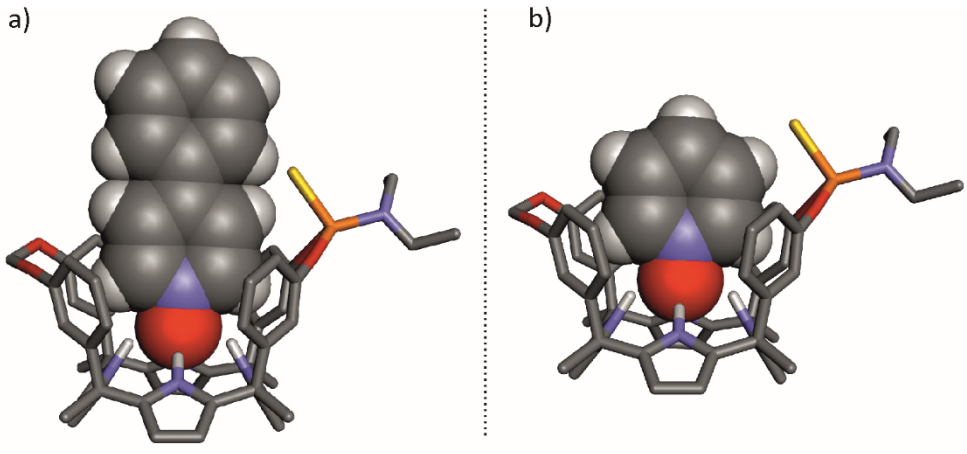

Figure 6.79 Energy-minimized structure of a) **9⊂1in** and b) **10⊂1in** complexes (MM3). The nonpolar hydrogen atoms of receptor **1in** were removed for the sake of clarity. The encapsulated **9** and **10** molecules are shown as the CPK model.

6.5 References and notes.

[1] Ballester, P.; Scarso, A. *Front. Chem.* **2019**, *7*.
[2] Ballester, P.; van Leeuwer, P.; Vidal-Ferran, A. In *Reference Module in Chemistry, Molecular Sciences and Chemical Engineering*; Elsevier: 2015.
[3] Pappalardo, A.; Puglisi, R.; Sfrazzetto, G. T. *Catalysts* **2019**, *9*.
[4] Skerra, A. *J. Mol. Recognit.* **2000**, *13*, 167-187.
[5] Rudkevich, D. M.; Hilmersson, G.; Rebek, J. *J. Am. Chem. Soc.* **1998**, *120*, 12216-12225.
[6] Petroselli, M.; Angamuthu, V.; Rahman, F.-U.; Zhao, X.; Yu, Y.; Rebek, J. *J. Am. Chem. Soc.* **2020**, *142*, 2396-2403.
[7] Inoue, M.; Kamiguchi, S.; Ugawa, K.; Hkiri, S.; Bouffard, J.; Sémeril, D.; Iwasawa, T. *Eur. J. Org. Chem.* **2019**, *2019*, 6261-6268.
[8] Wu, N.-W.; Petsalakis, I. D.; Theodorakopoulos, G.; Yu, Y.; Rebek Jr., J. *Angew. Chem., Int. Ed.* **2018**, *57*, 15091-15095.
[9] Rivera, D. G.; Wessjohann, L. A. *J. Am. Chem. Soc.* **2006**, *128*, 7122-7123.
[10] Wang, X.; Shyshov, O.; Hanževački, M.; Jäger, C. M.; von Delius, M. *J. Am. Chem. Soc.* **2019**, *141*, 8868-8876.
[11] Chen, L.; Chen, Q.; Wu, M.; Jiang, F.; Hong, M. *Acc. Chem. Res.* **2015**, *48*, 201-210.
[12] Amouri, H.; Desmarets, C.; Moussa, J. *Chem. Rev. (Washington, DC, U. S.)* **2012**, *112*, 2015-2041.
[13] Fujita, M.; Tominaga, M.; Hori, A.; Therrien, B. *Acc. Chem. Res.* **2005**, *38*, 369-378.
[14] Conn, M. M.; Rebek, J. *Chem. Rev. (Washington, DC, U. S.)* **1997**, *97*, 1647-1668.
[15] Martí-Centelles, V.; Spicer, R. L.; Lusby, P. J. *Chem. Sci.* **2020**, *11*, 3236-3240.
[16] Jans, A. C. H.; Caumes, X.; Reek, J. N. H. *ChemCatChem* **2019**, *11*, 287-297.
[17] Gorin, D. J.; Toste, F. D. *Nature* **2007**, *446*, 395-403.

[18] Li, Z.; Brouwer, C.; He, C. *Chem. Rev. (Washington, DC, U. S.)* **2008**, *108*, 3239-3265.
[19] Schramm, M. P.; Kanaura, M.; Ito, K.; Ide, M.; Iwasawa, T. *Eur. J. Org. Chem.* **2016**, *2016*, 813-820.
[20] Hintermann, L.; Labonne, A. *Synthesis* **2007**, *2007*, 1121-1150.
[21] Nishizawa, M.; Imagawa, H.; Yamamoto, H. *Org. Biomol. Chem.* **2010**, *8*, 511-521.
[22] Gale, P. A.; Sessler, J. L.; Král, V.; Lynch, V. *J. Am. Chem. Soc.* **1996**, *118*, 5140-5141.
[23] Kim, D. S.; Sessler, J. L. *Chem. Soc. Rev.* **2015**, *44*, 532-546.
[24] Cafeo, G.; De Rosa, M.; Kohnke, F. H.; Soriente, A.; Talotta, C.; Valenti, L. *Molecules* **2009**, *14*, 2594-2601.
[25] Cafeo, G.; De Rosa, M.; Kohnke, F. H.; Neri, P.; Soriente, A.; Valenti, L. *Tetrahedron Lett.* **2008**, *49*, 153-155.
[26] Gibson, C.; Rebek, J. *Org. Lett.* **2002**, *4*, 1887-1890.
[27] Ciardi, M.; Tancini, F.; Gil-Ramírez, G.; Escudero Adán, E. C.; Massera, C.; Dalcanale, E.; Ballester, P. *Journal of the American Chemical Society* **2012**, *134*, 13121-13132.
[28] Sierra, A. F.; Hernández-Alonso, D.; Romero, M. A.; González-Delgado, J. A.; Pischel, U.; Ballester, P. *Journal of the American Chemical Society* **2020**, *142*, 4276-4284.
[29] Li, F.; Wang, N.; Lu, L.; Zhu, G. *J. Org. Chem.* **2015**, *80*, 3538-3546.
[30] Aparece, M. D.; Vadola, P. A. *Org. Lett.* **2014**, *16*, 6008-6011.

General Conclusions.

In this Thesis we describe the design and synthesis of a series of phosphonate-based calix[4]pyrrole cavitands and their application as chemosensors for biologically relevant molecules and as ligands for the catalysis of the hydration of terminal alkynes.

We draw the following conclusions from the results obtained:

1) The synthesized calix[4]pyrrole cavitands form thermodynamically and kinetically stable complexes with **HexCr**, featuring binding constant values larger than 10^4 M^{-1} in dichloromethane solution.

2) Structurally, in all complexes the calix[4]pyrrole receptors adopt a cone and establish four hydrogen bonding interactions between the pyrrole NHs and the oxygen atom of the bound **HexCr**. In addition, cavitands featuring a P=O group inwardly oriented to the aromatic cavity offer an extra hydrogen bond interaction with the -NH_2 protons of the included guest.

3) Isothermal titration calorimetry (ITC) experiments assigned a 2 kcal/mol stabilization to the complexes of **HexCr** with cavitands featuring a phosphonate group inwardly oriented in comparison with their analogous lacking this group or having it outwardly directed.

4) The developed monophosphonate calix[4]pyrrole cavitands used in indicator displacement assays (IDAs) display binding constant values larger than 10^5 M^{-1} for creatinine and derivatives (**HexCr**) and larger than 10^7 M^{-1} for the pyridine *N*-oxides used as indicators/quenchers.

5) The designed chemosensor having covalently attached a dansyl fluorophore on the calix[4]pyrrole structure via sulfonamide bond produced unnoticeable changes on its absorption or emission properties upon binding creatinine or hexylcreatinine. However, complexation with DABCYL *N*-oxide acting as a black hole quencher (**BHQ**) provoked a quenching on the emission intensity through Förster resonance energy transfer (FRET). The displacement of the BHQ from the calix[4]pyrrole cavity by complexation with **HexCr** caused a deactivation of the FRET effect and in consequence the recovery on the emission properties of the dansyl unit. The limit of

detection (LOD) for HexCr of this IDA was determined to be 110 nM. This value is in line with levels of creatinine displayed either in health and sick patients.

6) The second IDA design, based on the interaction of a non-fluorescent calix[4]pyrrole cavitand and a fluorescent pyridyl *N*-oxide connected to a pyrene moiety was also useful for the sensing of **HexCr.**

7) The synthesized diastereoisomeric monophosphonate calix[4]pyrrole cavitands featuring a *N*-phenyl-naphthalamine fluorophore directly attached to its phosphorous atom (in and out) bind L-Proline and L-Pipecolic acid in organic solution with binding constants in the order of 10^5-10^4 M^{-1}. Binding constants determined with the out isomer were close to one order of magnitude lower than those determined with the in counterpart. This was attributed to the charged hydrogen-bonding interaction established between the protonated amino group of the bound guest and the bridging P=O function inwardly directed with respect to the polar aromatic cavity of the receptor.

8) The synthesized monophosphonate calix[4]pyrrole cavitands bearing a dansyl group attached to one of the aromatic walls via sulfonic ester bond showed noticeable changes on the emission properties upon binding Cr and **HexCr** in dichloromethane (i.e. quenching of the emission). These chemosensors display binding constants larger that 10^5M^{-1} in organic solution and allow the direct sensing of creatinine.

9) The synthesized two isomeric gold ligands based on phosphoramidite calix[4]pyrrole cavitands showed catalytic activity in the alkyne hydration reaction of a series of substrates featuring a terminal alkyne and a six-membered ring substituent with and without a carbonyl group of different basicity.

10) The prepared calix[4]pyrrole gold coordination complexes showed different catalytic performance depending on the basicity of the carbonyl group on the cyclic residue of the substrate and the orientation of the P-Au bond of the complex.

List of Abbreviations.

°C	-	Celsius
3-NPBA	-	3-nitrophenylboronic acid
AA	-	Amino Acids
ACD	-	Anionic Carbon Dots
AD	-	Alzheimer's disease
AEE	-	Aggregation-Enhanced Emission
Arg	-	Arginine
Asn	-	Asparagine
BA	-	Boronic acids
BBA	-	Benzoboroxole
BBS	-	Binding-Based Sensing
BBS	-	Binding-Based Sensing
bCAII	-	Bovine carbonic anhydrase isozyme II
BHQ	-	Black-Hole Quencher
C4P	-	Calix[4]pyrrole
CAC	-	Citric Acid Cycle
CAC	-	Critical Aggregation Concentration
CAs	-	Carbonic anhydrases
CB	-	Cucurbit[8]uril
CD	-	Carbon Dots
CD	-	Cyclodextrins
Cit	-	Citrate

COSY	-	Correlation spectroscopy
CPK	-	Corey-Pauling-Koltun model
Cr	-	Creatinine
CSF	-	Cerebrospinal fluid
CVD	-	Cardiovascular diseases
Cys	-	Cysteine
DCM	-	Dichloromethane
DLS	-	Dynamic Light Scattering
DMF	-	Dimethyl formamide
DMSO	-	Dimethyl sulfoxide
DPA	-	Zinc(II)-dipicolylamine
DSA	-	9,10-Distyrylanthracene
EET	-	Electronic Energy Transfer
ET	-	Energy Transfer
FRET	-	Fluorescence Resonance Energy Transfer
GL	-	Glycolipid
Gln	-	Glutamine
Glu	-	Glutamic acid
Gly	-	Glycine
GNP	-	Gold Nanoparticles
GSH	-	Glutathione
GSSG	-	Gluthathione oxidized
Has	-	Human serum albumin

Hcys	-	Homocysteine
HexCr	-	Hexylcreatinine
His	-	Histidine
HPLC	-	High Performance Liquid Chromatography
HPPi	-	Hydrogen pyrophosphate
ICT	-	Intramolecular Charge Transfer
IDA	-	Indicator Displacement Assay
IHD	-	Ischaemic Heart Disease
IHD	-	Ischaemic Heart Disease
ISR	-	Indicator-Spacer-Receptor
ITC	-	Isothermal Titration Calorimetry
IUPAC	-	International Union of Pure and Applied Chemistry
LDA	-	Linear Discrimination Analysis
Leu	-	Leucine
LOD	-	Limit of Detection
LPA	-	Lysophosphatidic acid
MHz	-	Megahertz
MM3	-	Molecular mechanics force field
NBA	-	2-(*N*,*N*-dimethylaminomethyl)phenylboronic acid
NMR	-	Nuclear magnetic resonance
OMC4P	-	Octamethylcalix[4]pyrrole
Ox	-	Oxalate
Pa	-	*p*-phenylenendiamine

PBA	-	Phenyl boronic acid
PET	-	Photoinduced Electron Transfer
PMAA	-	Poly(methacrylic acid)
PMAA-co-AAPBA	-	Poly(methacrylic acid)-co-3-(acrylamido)phenylboronic acid
PPi	-	Pyrophosphate
PV	-	Pyrocatechol violet
RIA	-	Reaction-based Indicator Displacement Assay
ROESY	-	Rotating-frame Overhauser Enhancement SpectroscopY
ROS	-	Reactive Oxygen Species
SA	-	Sialic Acid
SCnAs	-	*p*-sulfonatocalix[n]arenes
SVM	-	Support Vector Machine
TLC	-	Thin Layer Chromatography
TMAO	-	Trimethylamine *N*-oxide
Tp	-	1,3,5-triformylphloroglucinol
UV	-	Ultraviolet
WHO	-	World Health Organization

UNIVERSITAT ROVIRA I VIRGILI
CALIX[4]PYRROLE CAVITANDS FOR SUPRAMOLECULAR SENSING AND CATALYSIS
Andrés Felipe Sierra Ramos

UNIVERSITAT
ROVIRA i VIRGILI